AD-A219 740

AGARD

ADVISORY GROUP FOR AEROSPACE RESEARCH & DEVELOPMENT

7 RUE ANCELLE 92200 NEUILLY SUR SEINE FRANCE

AGARD REPORT No.764

DTIC
ELECTE
MAR 22 1990
S E

Special Course
on
Three-Dimensional
Supersonic/Hypersonic Flows
Including Separation

NORTH ATLANTIC TREATY ORGANIZATION

**DISTRIBUTION AND AVAILABILITY
ON BACK COVER**

90 03 22 037

NORTH ATLANTIC TREATY ORGANIZATION

ADVISORY GROUP FOR AEROSPACE RESEARCH AND DEVELOPMENT

(ORGANISATION DU TRAITE DE L'ATLANTIQUE NORD)

AGARD Report No.764

SPECIAL COURSE

ON

THREE-DIMENSIONAL

SUPERSONIC/HYPERSONIC FLOWS

INCLUDING SEPARATION

Accession For

NTIS GRA&I

DTIC T.:

Unannounced

Justification

By

Distribution/

Avail ility Code

i and/or

Dist   Special

A-1

THE MISSION OF AGARD

According to its Charter, the mission of AGARD is to bring together the leading personalities of the NATO nations in the fields of science and technology relating to aerospace for the following purposes:

- Recommending effective ways for the member nations to use their research and development capabilities for the common benefit of the NATO community;

- Providing scientific and technical advice and assistance to the Military Committee in the field of aerospace research and development (with particular regard to its military application);

- Continuously stimulating advances in the aerospace sciences relevant to strengthening the common defence posture;

- Improving the co-operation among member nations in aerospace research and development;

- Exchange of scientific and technical information;

- Providing assistance to member nations for the purpose of increasing their scientific and technical potential;

- Rendering scientific and technical assistance, as requested, to other NATO bodies and to member nations in connection with research and development problems in the aerospace field.

The highest authority within AGARD is the National Delegates Board consisting of officially appointed senior representatives from each member nation. The mission of AGARD is carried out through the Panels which are composed of experts appointed by the National Delegates, the Consultant and Exchange Programme and the Aerospace Applications Studies Programme. The results of AGARD work are reported to the member nations and the NATO Authorities through the AGARD series of publications of which this is one.

Participation in AGARD activities is by invitation only and is normally limited to citizens of the NATO nations.

PREFACE

The objective of this AGARD-FDP-VKI Special Course was to provide a status report on our understanding and ability to predict three-dimensional compressible flows including the complex effects of flow separation. Stimulation for this course arose from a variety of projects underway or receiving strong consideration in many countries. the next generation supersonic transport, HERMES, the National Aerospace Plane, HOTOL, SANGER, the "Orient Express", etc.

An overview of the applications and problem areas set the stage for the course and was followed by two lectures which discussed topics that are basic to all that followed. First, the capabilities and limitations of computational fluid dynamics to describe these complex flows was addressed, and second a review of turbulence models appropriate to compressible flows was presented.

The remainder of the lectures concentrated on a series of generic problems which may be viewed as either a means to understand flow physics or as building blocks for vehicle design. They were:

- interactions of the shock-shock type which can lead to locally high pressures and heat transfer rates;

- corner flows which are characterized by multiple shock wave-boundary layer interactions;

- glancing shock wave-boundary layer interactions which provoke local separations and high heat transfer rates in re-attachment regions;

- unsteadiness which seems to characterize nearly all shock-induced flow separations.

The course closed with a discussion on how the chemical reactions present in highly hypersonic flows will influence three-dimensional hypersonic flows fields.

Short contributions from members of the audience who described relevant research in progress at their respective organizations were presented on the last day of the course.

The course and the material assembled in this book were prepared under the combined sponsorship of the Fluid Dynamics Panel, the von Kármán Institute, and the Consultant and Exchange Program of AGARD. Presentations were made at the von Kármán Institute, Rhode-Saint-Genèse, Belgium, on 8—12 May 1989 and at NASA's Ames Research Center, Moffett Field, California, USA, on 10—14 July 1989.

<div style="text-align: right;">

John F.Wendt
Special Course Director
von Kármán Institute for Fluid Dynamics

</div>

AVANT-PROPOS

L'objectif de ce cours spécial AGARD/FDP/VKI fut de présenter un rapport de synthèse sur l'état des connaissances et des capacités en matière de prévision des écoulements compressibles tridimensionnels, y compris les effets complexes de séparation de l'écoulement.

La raison d'être de ce cours se trouve dans un certain nombre de projets qui sont soit en cours, soit au stade final d'étude dans plusieurs pays à savoir: l'aéronef de transport supersonique de la prochaine génération, HERMES, l'aéronef national aérospatial, HOTOL, SANGER, "L'Orient Express" etc.

Le cours a commencé par un tour d'horizon des applications et des domaines problématiques, suivi de deux communications sur des aspects fondamentaux de la question. D'abord les possibilités et les limites des méthodes du calcul en dynamique des fluides en ce qui concerne la caractérisation de ces écoulements complexes, et ensuite les modèles de turbulence les plus adaptés aux écoulements compressibles.

Les autres communications concernaient une série de problèmes génériques qui peuvent être vus soit comme un élément clé pour la compréhension de la physique des écoulements, soit comme des modules de la conception des véhicules aériens.

Il s'agit des problèmes suivants:

— les interactions du type choc-choc, qui peuvent conduire localement à des fortes pressions et à des taux de transfert de chaleur élevés

— les écoulements d'angle qui sont caractérisés par des interactions du type onde de choc multiple-couche limite

— les interactions du type onde de choc rasante-couche limite, qui provoquent des séparations locales et engendrent des taux de transfert de chaleur élevés dans les zones de reattachement

— l'instabilité qui semble être caractéristique de la quasi-totalité des cas de décollement de l'écoulement sous l'effet de l'onde de choc.

Le cours s'est terminé par une discussion sur le thème de l'influence des réactions chimiques qui se produisent dans les écoulements fortement hypersoniques sur les champs d'écoulement hypersoniques tridimensionnels

Le dernier jour du cours, certains membres de l'assistance ont présenté des résumés des travaux de recherche en cours à ce sujet au sein de leurs organisations respectives.

Le cours et les textes du présent recueil ont été préparés sous l'égide conjointe du Panel AGARD de la Dynamique des Fluides, l'Institut von Kármán et le programme AGARD des Consultants et des Echanges. Les présentations ont été données au von Kármán Institute, Rhode-Saint-Genèse, en Belgique, le 8—12 mai 1989 et au NASA Ames Research Center, Moffet Field, California, au Etats-Unis, le 10—14 juillet 1989.

John F.Wendt
Directeur du Cours Spécial
Institut von Kármán de la Dynamique des Fluides

SPECIAL COURSE STAFF

Special Course Director: Professor J.F.Wendt
Von Kármán Institute for Fluid Dynamics
72 Chaussee de Waterloo
1640 Rhode-Saint-Genèse
Belgium

Dr Ing. D.Hänel
Aerodynamisches Institut
RWTH Aachen
Templergraben 55
D-5100 Aachen
Federal Republic of Germany

Dr G.V.Candler
Aerothermodynamics Br. M/S 230-2
NASA Ames Research Center
Moffett Field, CA 94035
United States

Prof. Dr Ing. D.Hummel
Inst. für Strömungsmechanik
T.U. Braunschweig
Bienroder Weg 3
D-3300 Braunschweig
Federal Republic of Germany

Professor G.S.Deiwert
Aerothermodynamics Br. M/S 230-2
NASA Ames Research Center
Moffett Field, CA 94035
United States

Mr B.Aupoix
Departement d'Aerothermodynamique
ONERA-CERT
2 Av. Edouard Belin
31055 Toulouse Cedex
France

Professor D.S.Dolling
Dept. of Aerospace & Eng. Mech.
University of Texas
Austin, TX 78712
United States

Mr J.Cousteix
Departement d'Aerothermodynamique
ONERA-CERT
2 Av. Edouard Belin
31055 Toulouse Cedex
France

Dr M.S.Holden
Calspan Corporation
P.O. Box 400
Buffalo, NY 14225
United States

Professor J.L.Stollery
College of Aeronautics
Cranfield Institute of Technology
Cranfield
Bedford MK43 0AL
United Kingdom

Mr R.Jones
Manager, High Speed Aerodynamics
Division
NASA Langley Research Center
Hampton, VA 23665
United States

LOCAL COORDINATORS

Professor J.F.Wendt
Von Kármán Institute for Fluid Dynamics
72 Chaussee de Waterloo
1640 Rhode-Saint-Genèse
Belgium

Mr M.Green
M/S 258-1
NASA Ames Research Center
Moffett Field, CA 94035
United States

AGARD REPRESENTATIVE

Mr M.C.Fischer
Fluid Dynamics Panel Executive
AGARD
7 rue Ancelle
92200 Neuilly-sur-Seine
France

v

CONTENTS

OPPORTUNITIES FOR IMPROVED UNDERSTANDING OF SUPERSONIC
AND HYPERSONIC FLOWS

by

Robert A.Jones
Manager, Hypersonic Technology Office
NASA Langley Research Center
Hampton, VA 23665
United States

*Note: The author has not provided a formal copy of this paper.
What follows comprises copies of the viewgraphs used
during the lecture and their associated texts.*

I. INTRODUCTION

THIS OVERVIEW DESCRIBES SOME OF THE DIVERSE APPLICATIONS WHICH ARE
FORESEEN IN THE SUPERSONIC AND HYPERSONIC REGIME, AND POINTS OUT BOTH
THE NEED AND THE OPPORTUNITY FOR IMPROVED UNDERSTANDING OF THE SUBJECT.

NEW FACILITIES AND EXPERIMENTAL TEST TECHNIQUES COMBINED WITH
COMPUTATIONAL FLUID DYNAMICS METHODS ARE DESCRIBED TO ILLUSTRATE
CHALLENGING FLOWS OVER SUPERSONIC WINGS, SEPARATED FREE-SHEAR MIXING
LAYERS, AND IN SCRAMJET-AIRFRAME INTEGRATION.

II. LOW DISTURBANCE TUNNELS FOR SUPERSONIC AND HYPERSONIC FLOW RESEARCH

IT HAS BEEN WELL KNOWN FOR A NUMBER OF YEARS THAT BOUNDARY-LAYER TRANSITION MEASURED IN WIND TUNNELS OCCURRED AT LOWER REYNOLDS NUMBERS THAN FOR MEASUREMENTS MADE IN FLIGHT FOR SUPERSONIC SPEEDS. THIS EARLY TRANSITION IN WIND TUNNELS IS DUE TO THE ACOUSTIC NOISE RADIATED FROM THE NOZZLE WALL TURBULENT BOUNDARY LAYERS. WHAT IS NEEDED IS A "QUIET" TUNNEL THAT HAS LAMINAR FLOW ON THE NOZZLE WALLS, YET OPERATES AT HIGH ENOUGH REYNOLDS NUMBERS TO MATCH THOSE OF FLIGHT VEHICLES.

NEED FOR QUIET TUNNEL

PROBLEM

- ALL EXISTING WIND TUNNELS FOR M > 2.5 HAVE HIGH INTENSITY ACOUSTIC NOISE RADIATED FROM NOZZLE WALL TURBULENT BOUNDARY LAYERS

  - RMS PRESSURE DISTURBANCES FROM ~1 TO 8 PERCENT OF MEAN

  - FREQUENCIES TO ~150 KHz

- NOISE DOMINATES OR INTERACTS WITH:

  ————▶ ● BOUNDARY LAYER TRANSITION

  - FREE TURBULENT SHEAR FLOWS AND SEPARATION

  - UNSTEADY FLOWS

NASA LANGLEY RESEARCH CENTER HAS DEVELOPED A SUPERSONIC QUIET TUNNEL THAT MAINTAINS LAMINAR WALL BOUNDARY LAYERS AND THUS HAS NO NOISE RADIATION IN ITS TEST SECTION FROM TURBULENT NOZZLE WALL BOUNDARY LAYER.

NASA LANGLEY APPROACH TO PROBLEM OF M > 1 QUIET TUNNEL

PILOT FACILITY

● HIGH QUALITY PARTICLE FILTERS - *1 micron*

● SETTLING CHAMBER TREATMENT

    ● ACOUSTIC BAFFLES (HIGH DENSITY POROUS PLATES)
    ● HONEYCOMB
    ● TURBULENCE SCREENS

● UNIQUE TWO-DIMENSIONAL NOZZLE DESIGN

    ● MAINTAINS LAMINAR WALL BOUNDARY LAYERS ("ZERO" NOISE RADIATION) ON CONTOUR
    WALLS TO HIGH REYNOLDS NUMBERS

        - BOUNDARY LAYER REMOVAL UPSTREAM OF THROAT
        - HIGHLY POLISHED WALLS
        - RAPID EXPANSION CONTOUR

A PILOT "QUIET" TUNNEL CALLED THE SUPERSONIC LOW-DISTURBANCE TUNNEL IS
CURRENTLY IN OPERATION. THIS CHART ILLUSTRATES THE KEY FEATURES OF THE
FACILITY AND SHOWS THE REGION OF TEST SECTION FLOW THAT IS FREE OF
RADIATED NOISE.

SUPERSONIC LOW-DISTURBANCE TUNNEL

Mach 3.5 pilot nozzle
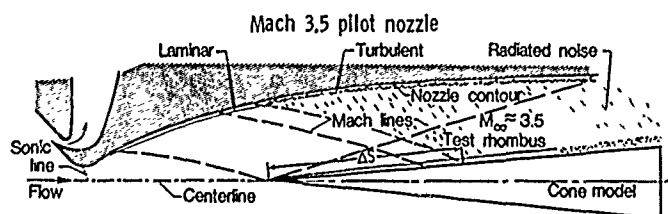
● Blow-down tunnel - high valve and pipe noise

● Settling chamber treatment
● Subsonic boundary-layer removal
● Highly polished walls
● Laminar boundary-layer on nozzle walls

● Laminar to turbulent transition on test models same as flight data
● Incident noise can be varied

MEASUREMENT OF THE ROOT-MEAN-SQUARE PRESSURE COEFFICIENT OBTAINED IN
TEST SECTION OF THE MACH 3.5 QUIET TUNNEL AT AN ORDER OF MAGNITUDE LOWER
THAN THOSE OBTAINED IN CONVENTIONAL SUPERSONIC TUNNELS.

COMPARISONS OF RMS PRESSURE COEFFICIENTS
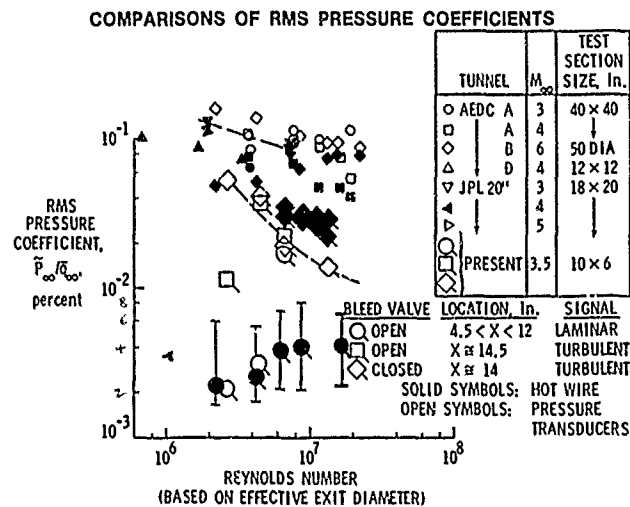
BOUNDARY-LAYER TRANSITION DATA MEASURED ON SHARP SLENDER CONES IN
CONVENTIONAL WIND TUNNELS AND IN FLIGHT TESTS ARE COMPARED WITH DATA
TAKEN IN THE MACH 3.5 QUIET TUNNEL. DATA FOR THE ORIGINAL NOZZLE WALL
WHICH HAD A SURFACE FINISH OF 100μ-INCH ROUGHNESS SHOWED, FOR THE
FIRST TIME AT UNIT REYNOLDS NUMBER OF UP TO 8×10^6, THAT FLIGHT LEVEL OF
TRANSITION REYNOLDS NUMBERS WERE MAINTAINED OUT TO MUCH HIGHER UNIT
REYNOLDS NUMBER. IN FACT, WITH THE NEW NOZZLE (20μ-INCH ROUGHNESS),
VIRTUALLY NO VARIATION OF TRANSITION REYNOLDS NUMBER WITH UNIT REYNOLDS
IS OBSERVED.

TRANSITION REYNOLDS NUMBERS ON SHARP CONES
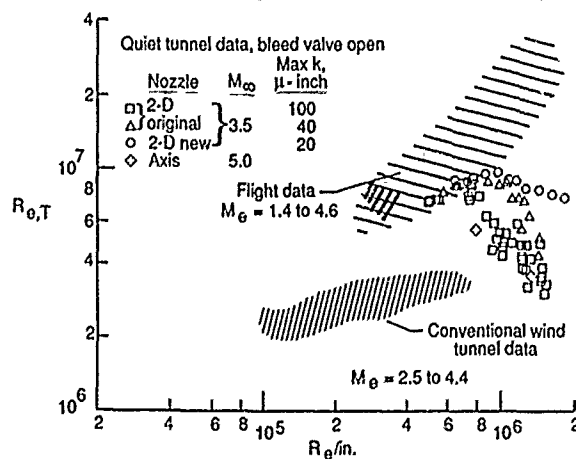
THERE HAS BEEN A LONG STANDING DISCREPANCY BETWEEN BOUNDARY-LAYER
TRANSITION PREDICTIONS FROM LINEAR STABILITY THEORY AS APPLIED TO CONES
AND FLAT PLATES AND DATA OBTAINED IN LARGE CONVENTIONAL WIND TUNNELS.
THEORY PREDICTS THE RATIO OF CONE TO FLAT PLATE VALUES TO BE LESS THAN
ONE WHERE AS THE RESULTS FROM CONVETIONAL TUNNEL SHOWS THIS RATIO TO
VARY FROM ONE TO 2.5 DEPENDING ON MACH NUMBER. IT TURNS OUT THAT FLAT
PLATES ARE MORE SENSITIVE TO THE LOWER FREQUENCY RADIATED NOISE THAN
CONES AND IT IS SHOWN BY THE DATA FROM THE QUIET TUNNEL THAT WHEN
RADIATED NOISE IS ABSENT THE RATIO MEASURED AGREES WITH PREDICTIONS FROM
STABILITY THEORY.

RATIO OF CONE-TO-FLAT-PLATE TRANSITION REYNOLDS NUMBERS

O Data: LaRC Pilot Quiet Tunnel
X Prediction for N = 10
+ Extrapolated to N = 10: Mack
— Pate's data correlation AEDC, '69-'69

$$\frac{(Re_T)_{cone}}{(Re_T)_{planar}}$$

Mach number
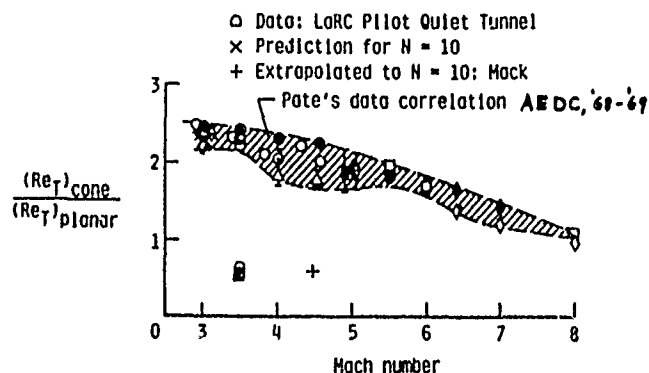
DATA TAKEN FROM THE NEW QUIET TUNNEL FOR BOUNDARY-LAYER TRANSITION ON
BOTH CONES AND FLAT PLATES ARE IN AGREEMENT WITH PREDICTIONS FROM
STABILITY THEORY AND SHOW THAT FLAT PLATES ACTUALLY HAVE TRANSITION
REYNOLDS NUMBERS HIGHER THAN CONES WHEN THERE ARE NO DISTURBANCES
PRESENT. THIS IS A RESULT THAT HAS NEVER BEEN MEASURED IN WIND TUNNELS
BEFORE. THIS RESULT INDICATES THAT LINEAR STABILITY THEORY CAN BE USED
AS FOR VALID PREDICTIONS OF BOUNDARY-LAYER TRANSITION AT SUPERSONIC
SPEEDS.

TRANSITION ON CONES AND FLAT PLATES

	Model	Mach no.	Wind tunnel	Ref
O	Cone	3.5 }	LaRC low disturb.	19
□	Flat plate	3.5 }		19
----	Flat plate	3.0	AEDC	27
—·—	Flat plate	3.7	JPL 20 in.	28,29

Flat plate prediction for N = 10

Cone prediction for N = 10

Re_T

Tunnel A (40" × 40")
JPL 20"
Tunnel D (12" × 12")

Re/in.
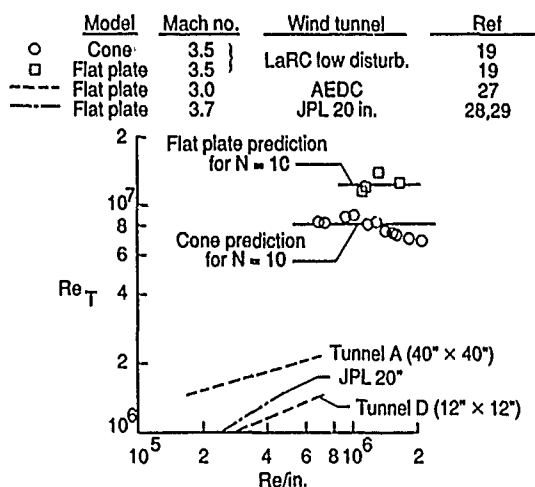
A DISTURBANCE GROWTH RATE OR LINEAR AMPLIFICATION RATE OBTAINED FROM STABILITY THEORY OF e^N WHERE N IS DEFINED AS INDICATED ON THE CHART IS A GOOD PREDICTION OF THE ONSET OF BOUNDARY-LAYER TRANSITION FROM LAMINAR TO TURBULENT FLOW.

e^N METHOD FOR TRANSITION PREDICTION
(Smith, 1952)

- Calculate mean boundary layer profiles

- Calculate linear amplification rate by using "appropriate stability model"

- Transition occurs when disturbances in the boundary layer are first amplified by a factor e^N, where

$$N = \ln(A/A_0) = \int_{x_0}^{x_T} \text{(linear amplification rate) } dx$$

COMPARISON OF DATA FROM A VARIETY OF CONFIGURATIONS SHOW THAT WHEN THE DOMINANT PHYSICAL EFFECTS ARE INCLUDED IN THE STABILITY THEORY AND INPUT DISTURBANCES ARE SMALL AS THEY ARE IN FLIGHT OR IN A QUIET FACILITY, A VALUE OF N OF APPROXIMATELY 10 IS A GOOD PREDICTION OF TRANSITION.

TRANSITION CORRELATIONS WITH e^N THEORY

$N = \ln A/A_o$

Flow	Instability	N	Reference
● Concave walls, low speed	Taylor-Görtler vortices (TG)	6-12	Smith, 1955
● Two-dimensional wings, low speed	Tollmien-Schlichting waves (TS)	9-12	Jaffe, et al, 1970
● Heated bodies, water	TS	9-12	Wazzan, et al, 1979
● Rotating disc	Cross-flow vortices (CF)	11	Malik, et al, 1981
● Cones, $\alpha \approx 0$ $M = 1.2 - 3.5$	TS	9-11	Malik, 1984
● Swept cylinder, low speed	CF	11	Malik, et al, 1984
● Concave walls, supersonic	TG	9-11	Present

Conclude: When dominant physical effects are included in theory and input disturbances are small; $N \approx 9-12$

SINCE NOISE DOMINATES OR AT LEAST INTERACTS WITH SEVERAL VERY IMPORTANT TYPES OF FLOW OTHER THAN BOUNDARY-LAYER TRANSITION, RESEARCH WITH THE NEW QUIET TUNNELS THAT ARE NOW UNDER CONSTRUCTION FROM MACH 3.5 TO 20 WILL OPEN NEW OPPORTUNITIES FOR IMPROVING OUR UNDERSTANDING OF BOUNDARY-LAYER SEPARATION, FREE SHEAR LAYER FLOWS AND MIXING OF DIFFERENT GASES IN FREE-SHEAR LAYER FLOWS AS WELL AS BOUNDARY-LAYER TRANSITION.

"QUIET" TUNNELS MAY PROVIDE IMPROVED

UNDERSTANDING OF SUPERSONIC AND

HYPERSONIC FLOWS

RADIATED NOISE DOMINATES OR INTERACTS WITH:
● BOUNDARY LAYER TRANSITION
● FREE-SHEAR LAYER FLOWS
● MIXING IN FREE-SHEAR LAYER FLOWS
● SEPARATION

SEVERAL NEW QUIET TUNNELS ARE PRESENTLY PLANNED AT NASA LANGLEY
● SMALL MACH 6 QUIET TUNNEL RECENTLY PUT INTO OPERATION
● MACH 8 TUNNEL (18" DIAM TEST SECTION) NOW BEING MODIFIED TO PROVIDE QUIET FLOW
● MACH 20 HELIUM TUNNEL (20" DIAM TEST SECTION) NOW BEING MODIFIED TO PROVIDE QUIET FLOW

III. A GENERALIZED CFD BASED DESIGN PROCEDURE FOR ACTIVELY COOLED HYPERSONIC WIND-TUNNEL NOZZLES SUBJECT TO WALL SHAPE CONSTRAINTS

THE DESIGN OF SUPERSONIC AND HYPERSONIC WIND-TUNNEL NOZZLES HAVE USED TECHNIQUES BASED ON THE METHOD OF CHARACTERISTICS WITH BOUNDARY LAYER CORRECTIONS FOR MANY YEARS. THESE TECHNIQUES ARE RESTRICTED TO EITHER 2-D OR AXISYMMETRIC FLOWS. THREE-DIMENSIONAL DESIGNS OR DESIGNS WHOSE CONSTRAINTS FACE THE RELAXATION OF THE REQUIREMENT OF SHOCKLESS FLOW REQUIRE MORE SOPHISTICATED CFD TOOLS. THE NEXT CHART AND SKETCH DESCRIBE THE CONVENTIONAL DESIGN PROCEDURES.

Conventional Design Procedure

1) $P_{tot}, T_{tot}, M_{ex} \longrightarrow r_{th}$

2) Gradual subsonic contraction:
$r'(z) = r''(z) = 0 \longrightarrow$ straight sonic line

3) An expansion wall profile is specified based on wall heating and flow separation criteria.

4) Downstream of the inflection point, the wall angle is chosen to cancel waves that intersect it.

5) A displacement thickness δ^* is added to the inviscid contour.
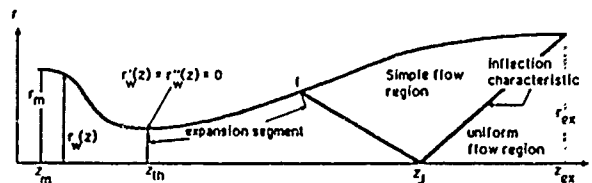
THE EFFORT TO DESIGN NOZZLE CONTOURS FOR THE NASA LANGLEY 8-FOOT HIGH-TEMPERATURE TUNNEL (8'HTT) PROVIDES AN EXAMPLE OF THE USE OF ADVANCED CFD CODES IN NOZZLE DESIGN. UNDER THIS EFFORT, A MACH 4 AND MACH 5 NOZZLE WERE DESIGNED SUCH THAT THEY SMOOTHLY BLENDED WITH THE EXISTING MACH 7 NOZZLE ABOUT 200 INCHES UPSTREAM OF THE TEST SECTION. THE PHYSICAL DESIGN CONSTRAINTS OF THESE NOZZLES ARE SHOWN HERE.

DESIGN CONSTRAINTS FOR MACH 5 HIGH TEMPERATURE
TUNNEL NOZZLE
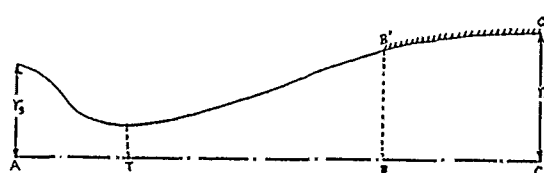
- AXIAL POSITION A AND ENTRANCE RADIUS r_s SPECIFIED FOR SUBSONIC REGION

- THROAT LOCATION T SPECIFIED

- TEST SECTION RADIUS r_t SPECIFIED

- AXIAL LOCATION OF STATION B WHERE CURRENT AND EXISTING NOZZLE WALL BLEND SMOOTHLY IS SPECIFIED TOGETHER WITH THE LENGTH BC OF THE CURRENT NOZZLE WALL BEING RETAINED

THE FLOW QUALITY REQUIREMENTS WERE THAT THE MACH NUMBER VARIATION BE LESS THAN +0.1 FROM ITS MEAN VALUE ACROSS 60% OF THE CORE FLOW. THIS WAS COMPLICATED BY THE FACT THAT THE HIGH TEMPERATURE FLOW IN THE TUNNEL REQUIRED COOLING OF THE NOZZLE THROATS BY TRANSPIRATION OF A FOREIGN GAS. FURTHERMORE, THE LARGE STATIC TEMPERATURE VARIATION IN THE NOZZLES RESULTED IN A SIGNIFICANT VARIATION IN GAS PROPERTIES AND THOSE VARIATIONS HAD TO BE PROPERLY MODELED.

FLOW QUALITY REQUIREMENTS

EXIT PLANE

$$M = M_{ex} \pm \cdot 1$$
$$T = T_{ex} \pm 50^\circ \text{ R/ft}$$

OVER 60% OF CORE FLOW

AXIS

$$\frac{\Delta T}{\Delta Z} \leq 50^\circ \text{ R/ft}$$

WITH THESE CONSTRAINTS, THE CONVENTIONAL SHOCKLESS NOZZLE DESIGN PROCEDURE WAS NOT APPLICABLE. A NEW ITERATIVE DESIGN PROCEDURE WAS DEVELOPED THAT COUPLED AN EULER CODE, A METHOD OF CHARACTERISTICS CODE, AND A BOUNDARY-LAYER CODE. A NAVIER-STOKES CODE WAS USED TO CHECK THE OVERALL FLOW QUALITY OF THE FINAL DESIGN. ALL CODES INCLUDED CONSISTENT REAL GAS CHEMISTRY PACKAGES FOR THE HYDROGEN-CARBON, OXYGEN, NITROGEN COMBUSTION PRODUCTS OF THE HEATER. IN ADDITION, THE NAVIER-STOKES AND BOUNDARY-LAYER CODES HAD THE CAPABILITY TO ACCOUNT FOR THE FOREIGN GAS INJECTION USED FOR TRANSPIRATION COOLING OF THE THROAT.

### NEW CFD BASED DESIGN PROCEDURE

- DUE TO IMPOSED CONSTRAINTS, CONVENTIONAL SHOCKLESS NOZZLE DESIGN PROCEDURE NOT APPLICABLE

- A NEW CFD BASED DESIGN PROCEDURE DEVELOPED THAT ITERA-TIVELY COUPLES AN EULER CODE, A METHOD OF CHARACTERISTICS CODE, AND A BOUNDARY-LAYER CODE

- FINAL DESIGN CHECKED BY FULL NAVIER-STOKES CODE

- CODES IN THE DESIGN PROCEDURE INCLUDE

  - GENERALIZED EQUILIBRIUM GAS CHEMISTRY OF COMBUSTION PRODUCTS

  - TRANSPIRATION COOLING OF THROAT WITH A FOREIGN GAS

- NEW DESIGN PROCEDURE APPLICABLE TO CONVENTIONAL NOZZLE DESIGNS ALSO

THE NEXT TWO FIGURES SHOW SOME RESULTS OBTAINED FROM THE DESIGN OF THE MACH 5 NOZZLE. THE FIRST FIGURE SHOWS THE MACH NUMBER PROFILES IN THE EXIT PLANE OF THE NOZZLE CALCULATED BY THE NAVIER-STOKES AND EULER CODES. THE PROFILE HAS A MEAN VALUE OF 4.96 WITH A VARIATION OF +0.06 OVER MORE THAN 70% OF THE TEST SECTION RADIUS, THUS SATISFYING THE MACH NUMBER VARIATION CONSTRAINT. HOWEVER, A WEAK SHOCK FORMS NEAR THE NOZZLE THROAT AND INTERSECTS THE EXIST PLANE, AS IS CLEARLY SEEN FROM THE MACH NUMBER CONTOURS IN THE SECOND FIGURE. IT APPEARS THAT THE WEAK SHOCK CANNOT BE AVOIDED UNDER THE SPECIFIED GEOMETRIC CONSTRAINTS. THESE FIGURES ALSO ILLUSTRATE THE QUALITATIVE SIMILARITIES IN THE FLOW SOLUTION OBTAINED FROM THE ITERATIVE DESIGN PROCEDURE AND THE NAVIER-STOKES CODE.

**EXIT PLANE MACH NUMBER
PROFILE IN THE DESIGNED MACH 5 NOZZLE**

Navier-Stokes

Euler

Mach number

Radial coordinate, in.

Radial coordinate, in.
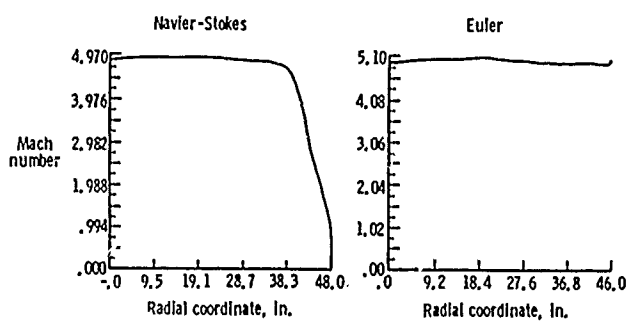
**MACH NUMBER CONTOURS
IN THE DESIGNED MACH 5 NOZZLE**

Navier-Stokes

Euler
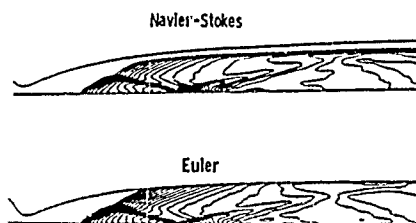
IV. WING LEESIDE FLOWS AT

SUPERSONIC SPEEDS

SUPERSONIC WING DESIGNS OF THE 1960's AND 1970's WERE BASED ON ATTACHED-FLOW CONCEPTS.
THESE DESIGNS WERE SEVERELY LIMITED (LOW TO MODERATE C_L) AND CONSTRAINED (WEAK SHOCKS AND
NO ADVERSE PRESSURE GRADIENTS).

THE 1980's BROUGHT ON REQUIREMENTS OF SUPERSONIC MANEUVERABILITY AND THE DEVELOPMENT OF
ADVANCED COMPUTER CODES WHICH COULD HANDLE, TO SOME DEGREE, SEPARATED VORTEX FLOWS. WITH
THESE NEW REQUIREMENTS AND NEW TOOLS, IT WAS NATURAL TO EXTEND WING DESIGN CONCEPTS TO
INCLUDE SEPARATED FLOWS.

ONE OF THE FIRST STEPS WAS TO DETERMINE UNDER WHAT CONDITIONS FLOW SEPARATION OCCURRED AND
WHAT DIFFERENT FLOW STRUCTURES WOULD BE PRODUCED. A LEESIDE FLOW CHARACTERIZATION STUDY
WAS CONDUCTED IN TWO PHASES: IN 1984 OVER A MACH NUMBER RANGE ROM 1.5-2.8 USING
CONVENTIONAL VAPOR-SCREEN TECHNIQUES AND IN 1988 THE MACH NUMBER RANGE EXTENDED TO 4.6
USING LASER VAPOR SCREEN. IN BOTH PHASES, DELTA WING SERIES WAS TESTED WITH LEADING-
EDGE-SWEEP ANGLES OF 52.5^0, 60.0, 67.5, 75.0^0.

THE RESULTS OF THESE TWO PHASE STUDY ARE SHOWN IN THE FIGURE. ALTHOUGH THE PARAMETERS OF
THE STUDY WERE THREE (MACH NUMBER, WING LEADING-EDGE SWEEP, AND ANGLE OF ATTACK) THE
RESULTS COULD BE PRESENTED IN TERMS OF TWO PARAMETERS (MACH NUMBER NORMAL TO THE WING
LEADING EDGE, M_N, AND ANGLE OF ATTACK NORMAL TO THE WING LEADING EDGE, α_N).

THE 1984 STUDY RESULTS SHOWED THAT SIX BASIC TYPES OF FLOW COULD OCCUR; THE DASHED LINE
INDICATES THE TEST MATRIX OF THE 1988 STUDY. THE 1988 STUDY EXTENDED THE MACH NUMBER
RANGE AND, USING THE LASER VAPOR SCREEN, IDENTIFIED SOME NEW SUBCLASSES OF FLOW TYPES NOT
SEEN IN THE PREVIOUS STUDY.

ONE OF THE NEW TYPES OF FLOW OCCURS IN THE CLASSICAL VORTEX-WITH-SHOCK REGION AND TWO
SUBREGIONS EXIST AS SHOWN IN THIS FIGURE. ONE WITH A VORTEX STRING AND TWO WITH A
CENTERLINE SHOCK.

CLASSIFICATION OF LEESIDE FLOW TYPES

Miller, Wood 1984
Vapor screen, tuft, oil flow
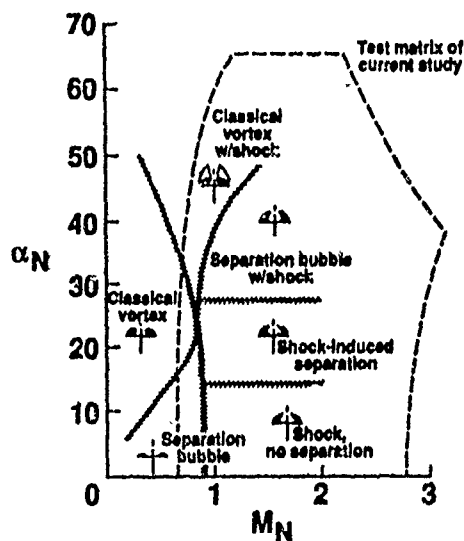
Covell, Wesselmann 1988
Laser vapor screen

ONE OF THE NEW TYPES OF FLOW OCCURS IN THE CLASSICAL VORTEX-WITH SHOCK
REGION AND TWO SUBREGIONS EXIST AS SHOWN IN THIS FIGURE--ONE WITH A
VORTEX STRING AND THE SECOND WITH A CENTERLINE SHOCK.

CLASSIFICATION OF LEESIDE FLOW TYPES
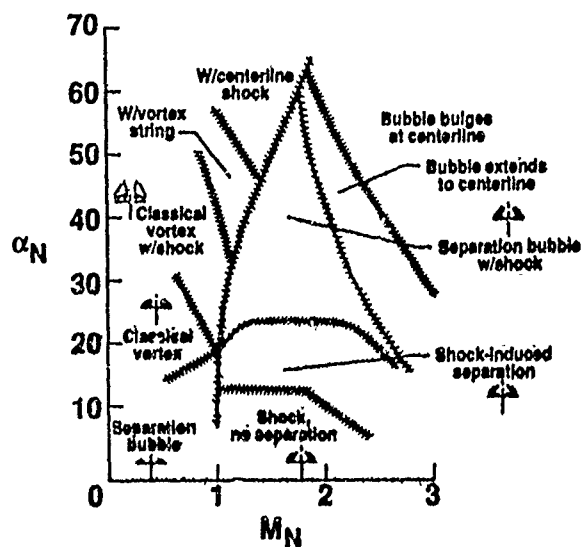
Classical vortex with shock, vortex string,
and centerline shock

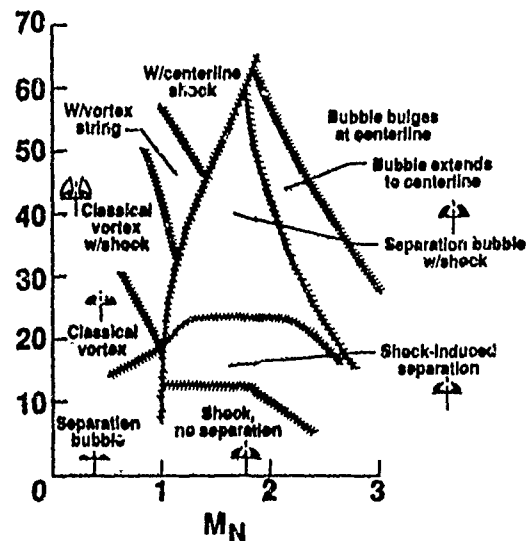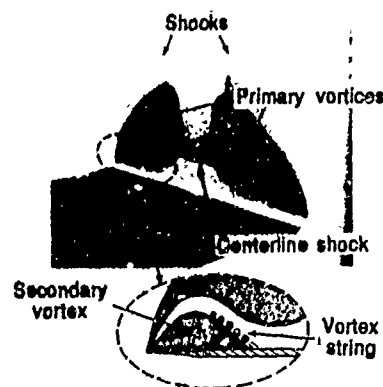ANOTHER NEW TYPE OF FLOW THAT WAS FOUND IS ILLUSTRATED IN THE NEXT TWO
FIGURES. IN THE SEPARATION BUBBLE WITH SHOCK REGION, TWO SUBREGIONS
ALSO EXIST. ONE IN WHICH THE BUBBLE IS EXTENDED TO THE CENTERLINE.

SEPARATION BUBBLES 'BULGE' INBOARD OF SHOCK

$\Lambda = 75°$ $M = 4.6$ $\alpha = 28°$

THE OTHER SUBREGION IS ONE IN WHICH THE BUBBLE BULGES AT THE
CENTERLINE. STUDIES ARE PRESENTLY UNDERWAY TO DETERMINE IF CFD CODES
CAN PREDICT THESE FLOW TYPES AND TO EXTEND THE EXPERIMENTAL FLOW
CLASSIFICATION TO INCLUDE THE EFFECTS OF AIRFOIL PROFILE AND WING
CAMBER.

MODERN FLOW VISUALIZATION TECHNIQUES WHICH SHOW THE COMPLEX STRUCTURE OF
THE SEPARATED FLOW OVER WINGS PROVIDE ANOTHER OPPORTUNITY TO IMPROVE OUR
UNDERSTANDING OF SUPERSONIC AND HYPERSONIC FLOWS.

SEPARATION BUBBLES EXTEND TO CENTERLINE

$\Lambda = 75°$ $M = 4.6$ $\alpha = 20°$
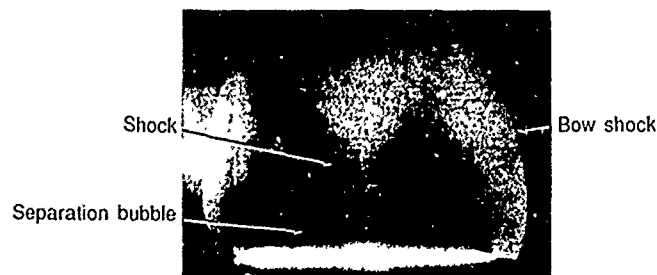
V. TURBULENT FREE-SHEAR LAYER MIXING

EXPERIMENTAL DATA OBTAINED IN SUPERSONIC FLOW WITH TURBULENT FREE-SHEAR LAYERS SHOW TWO IMPORTANT PHENOMENA. IN THE NEAR FIELD (A LOW LENGTH LESS THAN 25 BOUNDARY-LAYER THICKNESSES FROM THE SEPARATION POINT), THE SPREADING ANGLE AND THUS THE MIXING RATE IS UNAFFECTED BY MACH NUMBER AS SHOWN BY THE SOLID SYMBOLS. HOWEVER, IN THE FAR FIELD (MORE THAN 25 BOUNDARY-LAYER THICKNESSES FOR THE SEPARATION POINT), THE SPREADING ANGLE AND THE MIXING RATE DECREASES RAPIDLY WITH INCREASING MACH NUMBER AS SHOWN BY THE OPEN SYMBOLS.

SUPERSONIC FLOW DECREASES TURBULENT FREE SHEAR LAYER MIXING
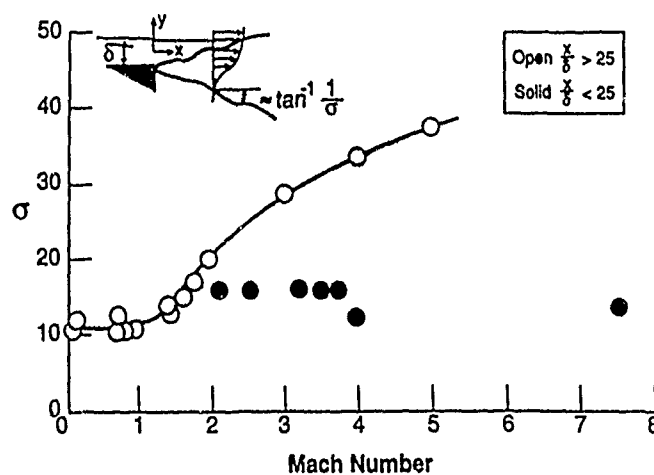
AT SUPERSONIC SPEEDS, EDDY SHOCKLETS FORM ABOUT THE TURBULENT EDDIES IN THE FREE-SHEAR LAYER AS INDICATED BY A CFD SOLUTION USING THE DIRECT SIMULATION TECHNIQUE. THE DENSITY CONTOURS SHOWN IN THE FIGURE CLEARLY SHOW THE FORMATION OF SHOCKS ABOUT THE EDDIES. ONE THEORY IS THAT THESE SHOCKS PREVENT COMUNICATION OF THE PRESSURE FIELD BETWEEN THE EDDIES AND THUS PREVENT THE EDDIES FROM ROLLING UP AND MERGING AS THEY DO IN SUBSONIC FLOWS.

WE WILL REVISIT THE SUBJET OF MIXING IN SEPARATED FREE-SHEAR LAYER FLOWS LATER IN THIS PRESENTATION AS THE REDUCED MIXING WITH INCREASED MACH NUMBERS IS A CRITICAL MATTER IN THE DESIGN OF SUPERSONIC COMBUSTION RAMJET ENGINES (SCRAMJETS). METHODS TO ENHANCE THIS MIXING AT HIGH MACH NUMBERS ARE NEEDED.

Direct-simulation for compressible flows

S.K. Lele Simulation of supersonic mixing layers

Density contours

A : $M_1 = 4.0$, $M_2 = 2.4$, $M_c = 1$
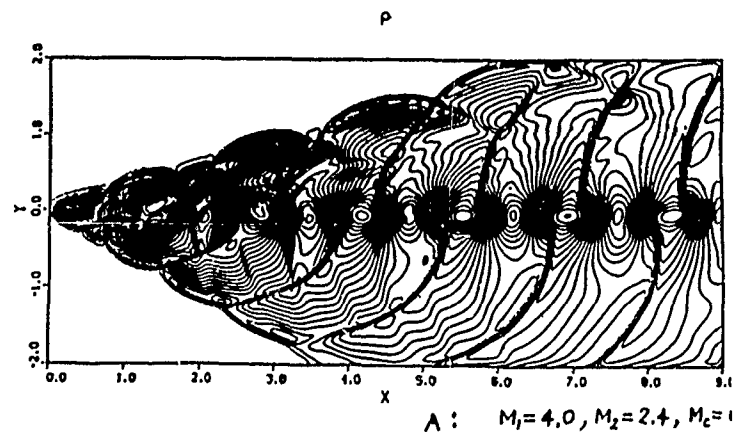
VI. VORTEX FLOWS ENHANCE SUPERSONIC VEHICLE PERFORMANCE

THE VORTEX FLAP (A CONCEPT WHICH HAS BEEN SUCCESSFULLY APPLIED AT
TRANSONIC SPEEDS) IS ONE OF THE SIMPLEST AND MOST STRAIGHT FORWARD
APPLICATIONS OF SEPARATED VORTEX FLOWS TO SUPERSONIC WING DESIGN.
STATED SIMPLY, THE CONCEPT EMPLOYES A SHARP LEADING EDGE TO GENERATE A
VORTEX OF MAXIMUM STRENGTH WHILE CONTAINING ITS INFLUENCE ON THE SURFACE
OF A DEFLECTED LEADING-EDGE FLAP.

THE FIRST SUPERSONIC EXPLORATION OF THE VORTEX FLAP WAS PERFORMED ON A
75^0 DELTA WING. RESULTS FOR $M = 1.7$ AND $= 4.5^0$ ARE SHOWN IN THE
FIGURE FOR FLAP DEFLECTIONS OF 5^0 AND 10^0. THE SURFACE TUFT PHOTOGRAPHS
IN THE CENTER OF THE FIGURE CLEARLY INDICATE THAT THE VORTEX INFLUENCE
IS CONFINED TO THE FLAP FOR A FLAP DEFLECTED 5^C BUT EXTENDS WELL INBOARD
OF THE FLAP DEFLECTD 10^0. THE LATTER SITUATION IS APPARENTLY CAUSED BY
HINGELINE SEPARATION WHICH WAS FOUND TO BE MUCH MORE A PROBLEM AT
SUPERSONIC SPEEDS THAN AT TRANSONIC SPEEDS. THE SPANWISE PRESSURE
DISTRIBUTION SHOWS THE EXTREMELY LARGE INFLUENCE OF THE HINGELINE
SEPARATION AND MEASURED AERODYNAMIC FORCES (NOT SHOWN IN FIGURE) SHOWED
THAT A DEGRADATION IN PERFORMANCE ACCOMPANIED THIS SEPARATION.

SUPERSONIC VORTEX FLAP

75° Delta wing

$M = 1.70 \quad \alpha = 4.5°$

$\delta_f = 5°$ $\delta_f = 10°$

Hingeline(HL)   HL

Hingeline separation
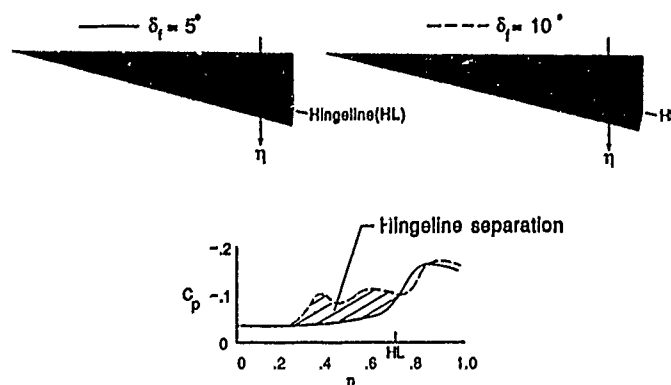
BECAUSE ATTACHED-FLOW WING DESIGN CONCEPTS EMPLOY WINGS WITH
CONSIDERABLE LEADING-EDGE RADIUS AND SEPARATED-FLOW CONCEPTS EMPLOY
WINGS WITH SHARP LEADING EDGES, CONCEPTS WHICH COMBINE BOTH TYPES OF
FLOW REQUIRE THAT THE MECHAISMS WHICH DETERMINE THE ONSET OF SEPARATION
BE UNDERSTOOD. TO ACCOMPLISH THIS AN EXPERIMENTAL/COMPUTATIONAL STUDY
OF INCIPIENT SEPARATION WAS INITIATED AND TYPICAL COMPUTATIONAL RESULTS
ARE SHOWN IN THE FIGURE. COMPUTED CROSSFLOW MACH NUMBER CONTOUR PLOTS
AND SPANWISE SURFACE-PRESSURE DISTRIBUTIONS ARE SHOWN AT $M = 1.6$ FOR A
65° DELTA WING WITH VARYING AMOUNTS OF LEADING-EDGE RADIUS AND CAMBER.

THE ALPHA = 4° RESULTS SHOW THAT LEADING-EDGE SEPARATION IS PRESENT FOR
THE SHARP LEADING EDGE, BUT THE ROUND LEADING-EDGE PRODUCES ATTACHED
FLOW. WHEN THE ANGLE OF ATTACK IS INCREASED TO 8°, THE FLOW IS
SEPARATED FOR THE ROUND LEADING EDGE AND A SPANWISE CAMBER OF 10° IS
REQUIRED TO MAINTAIN ATTACHED FLOW AT ALPHA = 8°.

IMPROVED UNDERSTANDING AND AN ABILITY TO PREDICT INCIPIENT SEPARATION AT
WING LEADING EDGES IS REQUIRED IN ORDER TO TAKE FULL ADVANTAGE OF
SUPERSONIC VORTEX FLAPS.

INCIPIENT SEPARATION COMPUTATIONAL STUDY

$M = 1.6, \lambda = 65°, Re = 2.0 \times 10^6/ft$
Turbulent Boundary Layer

Colored contour plots — Crossflow Mach number

Sharp Leading Edge

Rounded Leading Edge
No Camber

10° Camber

$\alpha = 4^o$

$\alpha = 8^o$
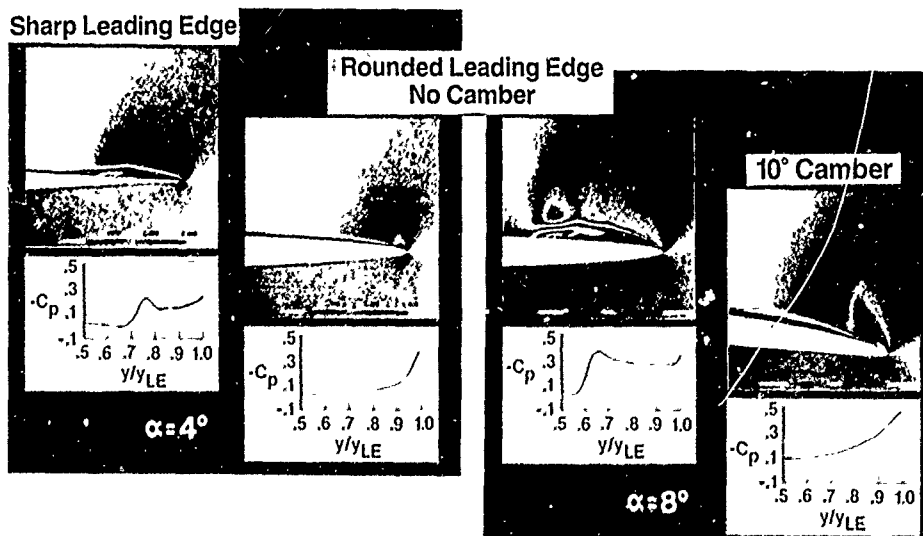
A TEST WAS CONDUCTED ON A WIND-TUNNEL MODEL OF A FIGHTER-TYPE FOREBODY WITH CANOPY AND STRAKES WITH SHARP LEADING EDGES TO DETERMINE THE AERODYNAMIC CHARACTERISTICS AT SUPERSONIC SPEEDS. AERODYNAMIC PREDICTIONS WERE ALSO PERFORMED USING A RECENTLY DEVELOPED EULER METHOD. AS SHOWN IN THE FIGURE AT $M = 1.8$ AND $A = 14^0$, A STRONG VORTEX DEVELOPS ON THE STRAKE LEADING EDGE.

THE RIGHT SIDE OF THE FIGURE SHOWS VAPOR-SCREEN PHOTOGRAPHS TAKEN ON THE LEESIDE OF THE MODEL LOOKING UPSTREAM. AS INDICATED IN THE FIGURE, THE VAPOR SCREENS WERE AT STREAMWISE STATIONS AT $X = 15.0$, 22.5, AND 30 INCHES. THE TOTAL LENGTH OF THE MODEL AS TESTED WAS 34.5 INCHES. CLEARLY SHOWN AT ALL THREE STATIONS IS A VORTEX FEEDING FROM THE STRAKE LEADING EDGE. AN EMBEDDED SHOCK TERMINATING ON THE LEADING-EDGE VORTEX IS CLEARLY EVIDENT AT LAST STATION, $X - 30.0$ INCHES.

THE LEFT SIDE OF THE FIGURE SHOWS A NUMERICAL REPRESENTATION OF THE FOREBODY/STRAKE ALSO SHOWING THE LEESIDE AND LOOKING UPSTREAM. ENTROPY CONTOURS COMPUTED BY THE EULER METHOD ARE SHOWN FOR STREAMWISE STATIONS CORRESPONDING TO THE VAPOR-SCREEN PHOTOGRAPHS. ENTROPY GRADIENTS ARE DIRECTLY RELATED TO VORTICITY THROUGH THE FUNDAMENTAL THEOREM OF CROCCO AND GIVE A CONVENIENT COMPUTATIONAL REPRESENTATION FOR VORTICIES WHEN DISPLAYED AS COLOR CONTOURS.

IT IS SEEN FROM THE FIGURE THAT THE EULER METHOD ACCURATELY PREDICTED THE LEADING-EDGE VORTICES. EXAMINATION OF CROSS-FLOW VELOCITY VECTOR AND SURFACE PRESSURES (NEITHER SHOWN IN THE FIGURE) INDICATE THAT THE EMBEDDED CROSSFLOW SHOCK WAS ACCURATELY PREDICTED; HOWEVER, THE SHOCK IS WEAK AND DOES NOT PRODUCE SIZABLE ENTROPY GRADIENTS.

EULER CODE PREDICTION FOR LEADING EDGE VORTEX FLOWS

Euler computation (Entropy)

Forebody with uncambered strake

Experiment (Vapor screen)

x = 15.0

x = 22.5

x = 30.0
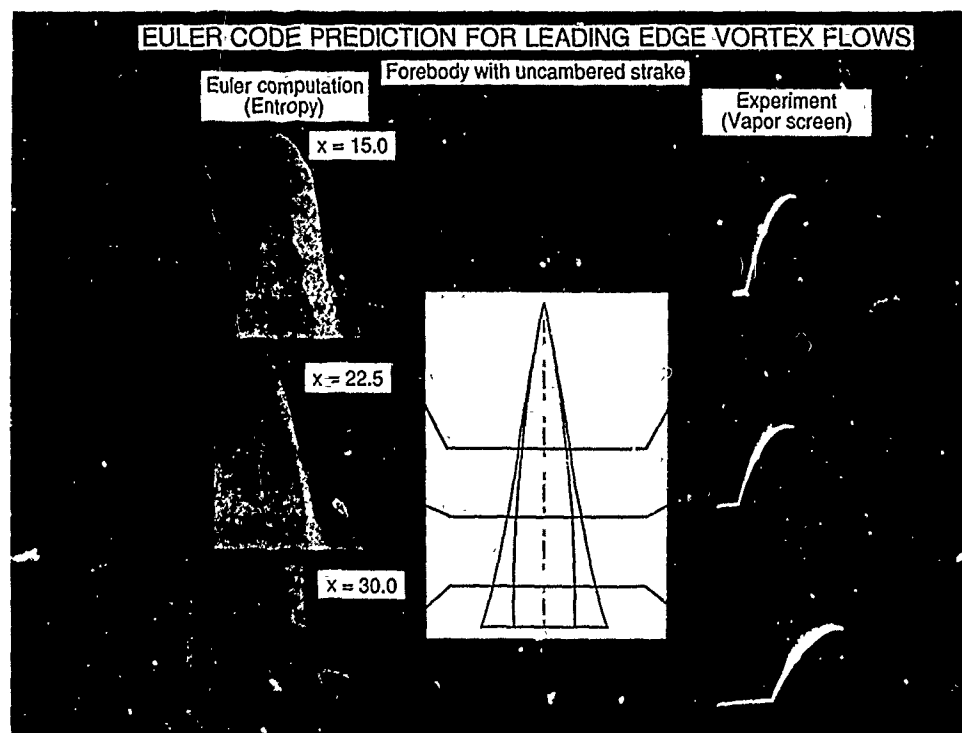
THE SUPERSONIC LEESIDE VORTEX FLOW ABOUT AN ELLIPTIC CROSS-SECTION
CONFIGURATION ARE SHOWN FOR AN ANGLE OF ATTACK OF 20^0 AND ROLL ANGLES OF
0^0 AND 45^0. THE FLOW FIELD SOLUTION WAS OBTAINED BY SOLVING REYNOLDS
AVERAGED NAVIER-STOKES EQUATIONS ON A GRID OF 33x51x57 (33 ALONG THE
BODY, 51 AROUND THE BODY, AND 57 POINTS NORMAL TO THE BODY). AT A ROLL
ANGLE OF 0^0 COLORED COMPUTER GRAPHICS FOR THE COMPUTED FLOWFIELD AT
THREE LONGITUDINAL STATIONS SHOW THE FORMATION OF A PAIR OF WELL DEFINED
SYMMETRICAL VORTICES IN THE LEEWARD FLOWFIELD. AT A ROLL ANGLE OF 45^0,
HOWEVER, THE COMPUTED FLOWFIELD OVER THE LEEWARD SURFACE OF THE BODY
SHOWS AN ASYMMETRIC VORTEX FORMATION WITH ONE VORTEX ATTACHED TO THE
BODY AND ONE DETACHED FROM THE BODY. THE HEIGHT OF THE DETACHED VORTEX
OFF THE BODY SURFACE INCREASES WITH INCREASING DISTANCE DOWNSTREAM.
SUCH AN ASYMMETRIC VORTEX FORMATION WOULD BE EXPECTED TO HAVE A LARGE
EFFECT ON THE BODY SURFACE LOADINGS. AS SHOWN ACROSS THE BOTTOM OF THE
FIGURE THE COMPUTED VORTEX FORMATIONS FOR BOTH ROLL ANGLES ARE IN GOOD
AGREEMENT WITH EXPERIMENTAL RESULTS OBTAINED FROM VAPOR SCREENS.

BODY VORTEX EFFECTS ON FLOW FIELD
Elliptic missile, $M_\infty = 2.5, \alpha = 20°$
$\phi = 0°$ $\phi = 45°$
Navier-Stokes computed flow field
Comparisons at $X/L \approx 1$
Vapor-screen data   Navier-Stokes computation   Vapor-screen data   Navier-Stokes computation
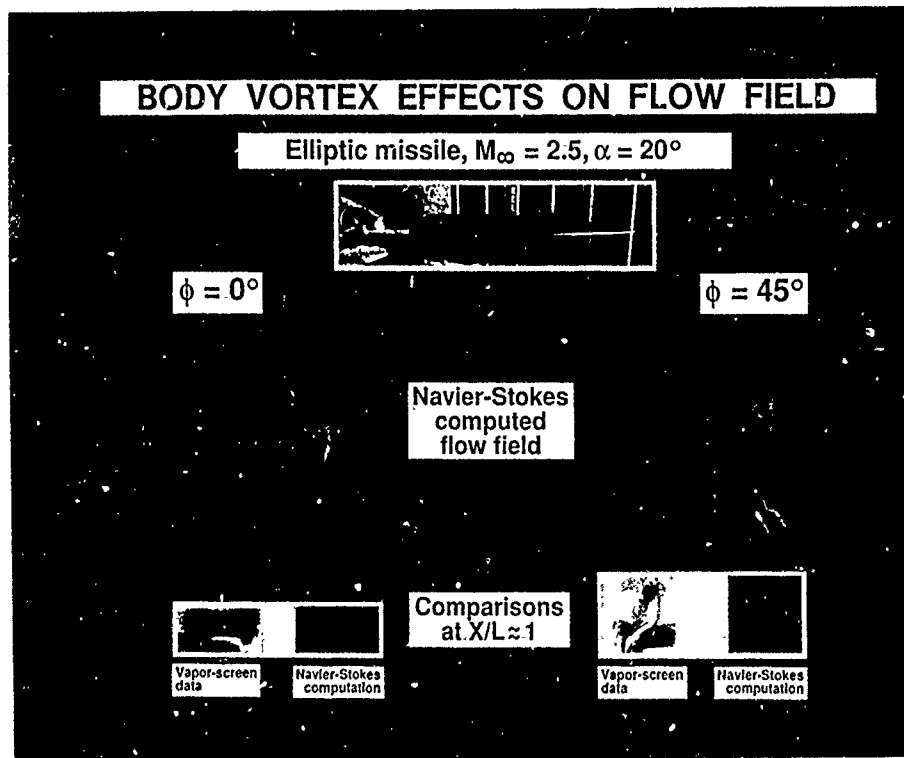
THE EFFECTS OF THE BODY VORTICES ON THE SURFACE PRESSURE DISTRIBUTIONS
ARE SHOWN AT APPROXIMATELY 60% BODY LENGTH. AT A ROLL ANGLE OF 0⁰ WHERE
AS SHOWN IN THE PREVIOUS SLIDE A PAIR OF SYMMETRIC VORTICES OCCURRED
OVER THE LEEWARD SURFACE, THE PRESSURE DISTRIBUTIONS SHOW SYMMETRICAL
SURFACE LOADINGS AROUND THE BODY. AT A ROLL ANGLE OF 45⁰ WHERE
ASYMMETRIC VORTICES OCCURRED OVER THE LEEWARD SURFACE, THE PRESSURE
DISTRIBUTIONS SHOW A HIGHLY ASYMMETRIC LOADING OVER THE BODY SURFACE AND
IN PARTICULAR OVER THE LEEWARD SURFACE. VERY GOOD AGREEMENT IS SHOWN
BETWEEN THE EXPERIMENTAL AND THEORETICAL PRESSURE DISTRIBUTIONS.

BODY VORTEX EFFECTS ON SURFACE PRESSURES
Elliptic missile, $M_\infty = 2.5$, $\alpha = 20°$

X/L = 0.6
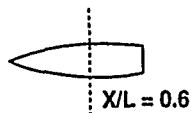
□ Experimental data
—— Navier-Stokes Theory

$\Phi = 0°$ $\Phi = 45°$

PREDICTION OF SOUND WAVES (OR NOISE) GENERATED BY SHOCK/VORTEX INTERACTION HAS A VARIETY
OF POTENTIAL APPLICATION SUCH AS THE DESIGN OF SUPERSONIC AND SUBSONIC JET ENGINES, DESIGN
OF HELICOPTER BLADES OPERATING IN SUPERCRITICAL RANGE, ETC. SEVERAL LINEAR THEORIES AND
SOME SHOCK-FITTED NUMERICAL TECHNIQUES HAVE BEEN USED IN THE PAST TO ANALYZE THE
SHOCK/VORTEX INTERACTION PROBLEM. HOWEVER, THESE METHODS CAN BE USED ONLY IN CASES OF
WEAK INTERACTIONS. UNDER STRONG INTERACTION, WHERE THE SHOCK DEFORMS SIGNIFICANTLY (MAY
EVEN BRANCH INTO SEVERAL SHOCKS), NEITHER LINEAR THEORY NOR SHOCK-FITTER NUMERICAL METHODS
ARE APPLICABLE. FURTHERMORE, THESE METHODS ARE NOT READILY EXTENDABLE TO MORE PRACTICAL
THREE-DIMENSIONAL INTERACTIONS. IN THE PRESENT ANALYSIS, A SHOCK-CAPTURING METHOD IS USED
TO STUDY THE SHOCK/VORTEX INTERACTION. NONLINEAR EULER EQUATIONS ARE SOLVED IN
CONSERVATION FORM BY A SECOND-ORDER ACCURATE UPWIND METHOD. CALCULATIONS ARE MADE FOR A
SUFFICIENTLY STRONG INTERACTION TO CREATE SHOCK BIFURCATON.

SHOWN IS AN EXPERIMENTAL INTERFEROGRAM ALONG WITH A SCHEMATIC FOR SUCH AN INTERACTION.
THE EXPERIMENTAL EQUIPMENT IS A DOUBLE SIDE SHOCK TUBE. IN THE LEFT-HAND HIGH PRESSURE
SIDE, A WEAK SHOCK WAVE IS EXCITED BY THE BURSTING OF A DIAPHRAGM; THE WAVE PRODUCES A
STARTING VORTEX AT THE TRAILING EDGE OF A MODEL IN THE TEST CHAMBER. THE INTERACTING
SHOCK WAVE IS GENERATED BY THE RIGHT-HAND HIGH PRESSURE PART AND RUNS FROM RIGHT TO LEFT
INTO THE PRECEDING VORTEX FIELD.

THE INTERFEROGRAM SHOWS THE FLOW FIELD AFTER THE SHOCK HAS INTERACTED WITH THE VORTEX.
THE SCHEMATIC OF THE FLOW FIELD IS SHOWN ON THE SIDE. THE INTERACTING POINT A BETWEEN THE
SHOCK FRONT (1) AND NOISE WAVE FRONT (4) AS WELL AS THE CONTACT POINT B BETWEEN THE FRONTS
(5) AND (3) DO NOT COINCIDE; BUT THERE IS A FRONT SECTION AB WHICH ENLARGES WITH TIME. AC
AND BC FORM THE CONTACT DISCONTINUIT.ES.

EXPERIMENTAL STUDY OF STRONG SHOCK VORTEX INTERACTION
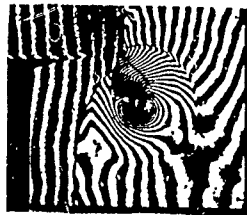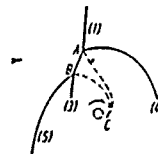
INTERFEROGRAM   SCHEMATIC

FLOW MACH NUMBER AND VALUES OF VARIOUS PARAMETERS IN THE VORTEX MODEL ARE LISTED ON THE FIGURE. THIS FIGURE ALSO SHOWS THE PRESSURE CONTOURS AS THE VORTEX MOVES DOWNSTREAM AND INTERACTS WITH THE SHOCK. THE CONTOURS AT T = 110 SHOW PRIMARY SHOCK, THE SECONDARY SHOCKS, AND THE TRIPLE POINTS WHICH ARE IN CLOSE AGREEMENT WITH THE EXPERIMENTALLY OBSERVED FEATURES SHOWN ON PREVIOUS SLIDE FOR THIS TYPE OF INTERACTION.

WORK IS IN PROGRESS TO PREDICT THE ACOUSTIC NOISE GENERATED IN THIS INTERACTION. EVEN THOUGH THE PRESENT ANALYSIS HAS BEEN ABLE TO PREDICT THE COMPLICATED FLOW WELL IN QUALITATIVE SENSE, ASSESSMENTS HAVE TO BE MADE TO FIND OUT WHETHER THE PRESENT SECOND-ORDER METHOD IS ADEQUATE OR HIGHER-ORDER METHODS ARE REQUIRED FOR QUANTIFICATION OF THE PHYSICS.

PRESSURE CONTOURS FOR STRONG VORTEX INTERACTION
(MACH NO. $\blacksquare$1.1, $\kappa = 3.07$, $\Omega = .0115$, $r_c = .075$, $u_c = .3$)

| Pressure T = 10 | Pressure T = 30 | Pressure T = 50 |

| Pressure T = 70 | Pressure T = 90 | Pressure T = 100 |
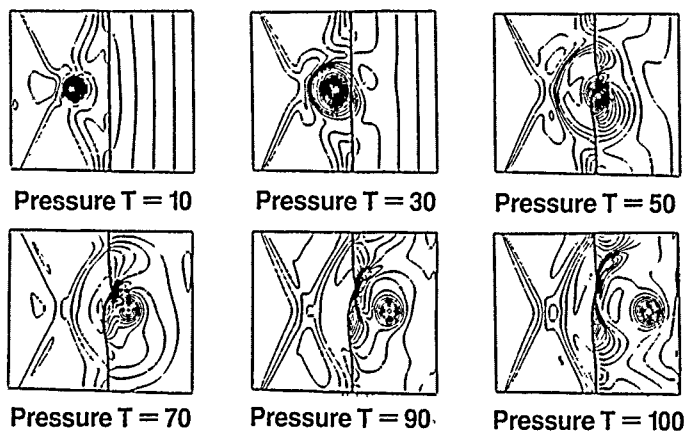
VII. TECHNOLOGY FOR AIRBREATHING

FLIGHT TO ORBIT

THE ENERGY AN OBJECT MUST HAVE TO BE IN A CIRCULAR ORBIT ABOUT THE EARTH IS COMPRISED OF TWO PARTS: KINETIC ENERGY AND POTENTIAL ENERGY. ON A SPECIFIC ENERGY OR ENERGY PER UNIT MASS BASIS, THE POTENTIAL ENERGY FOR AN ORBIT AT 500,000 FEET ALTITUDE IS ONLY ABOUT 5 PERCENT OF THE KINETIC ENERGY. THUS, THE ENERGY AN ORBITAL VEHICLE MUST HAVE IS ABOUT ALL KINETIC. KINETIC ENERGY VARIES WITH THE SQUARE OF THE SPEED OR WITH THE SQUARE OF THE MACH NUMBER SO THE AMOUNT OF WORK DONE ON THE ORBITAL MASS IS MUCH MORE AT THE HIGHER SPEEDS.

CONSIDER THE ENERGY A VEHICLE MUST HAVE TO GET TO ORBIT

E = KINETIC ENERGY + POTENTIAL ENERGY

$$E = \frac{V_0^2}{2} + g h_0$$

$$E = 3.38 \times 10^8 \ \frac{FT^2}{SEC^2} + 0.161 \times 10^8 \ \frac{FT^2}{SEC^2}$$

NOTE:

1. THE ENERGY A VEHICLE MUST HAVE TO OBTAIN ORBIT IS VIRTUALLY ALL KINETIC ENERGY

2. KINETIC ENERGY IS DIRECTLY PROPORTIONAL TO V^2 OR M^2

AT MACH 8, A VEHICLE HAS ABOUT 10 PERCENT OF THE SPECIFIC ENERGY (ENERGY PER POUND) REQUIRED FOR ORBIT AND AT MACH 15 IT HAS ABOUT 36 PERCENT OF THE SPECIFIC ENERGY REQUIRED FOR ORBIT.

REQUIRED ENERGY IS DIRECTLY PROPORTIONAL TO M^2

At M = 8: $\left(\frac{8}{25}\right)^2 = 0.10$

• 90% of the energy must be acquired above MACH 8

At M = 15: $\left(\frac{15}{25}\right)^2 = 0.36$

• 2/3 of the energy must be acquired above MACH 15

FOR AN AIRPLANE AT CRUISE WHERE ITS THRUST EXACTLY EQUALS DRAG, THERE IS NO CHANGE IN KINETIC ENERGY. NO USEFUL WORK IS DONE AND ALL OF THE ENERGY OF THE BURNED FUEL IS LEFT BEHIND IN THE ATMOSPHERE IN THE FORM OF HEAT.

CONSIDER AN AIRPLANE

- ENGINE THRUST DEPENDS ON ATMOSPHERIC DENSITY
- VEHICLE DRAG DEPENDS ON ATMOSPHERIC DENSITY
- NO CHANGE IN KINETIC ENERGY
- FOR CRUISE: T = D
- ALL THE ENERGY OF THE FUEL IS LEFT BEHIND IN THE ATMOSPHERE AS HEAT

THE THRUST OF A ROCKET IS ALMOST INDEPENDENT OF ATMOSPHERIC DENSITY YET THE DRAG OF A ROCKET-POWERED VEHICLE IS DIRECTLY PROPORTIONAL TO THE ATMOSPHERIC DENSITY. THEREFORE TO LEAVE AS LITTLE ENERGY BEHIND AS HEAT IN THE ATMOSPHERE AS POSSIBLE, A ROCKET-POWERED SPACE LAUNCH VEHICLE SHOULD CLIMB TO HIGH ALTITUDES BEFORE REACHING HIGH SPEEDS; MORE OF THE ENERGY OF THE ROCKETS FUEL CAN BE CONVERTED TO VEHICLE KINETIC ENERGY.

CONSIDER A ROCKET LAUNCH VEHICLE

- ROCKET THRUST IS INDEPENDENT OF ATMOSPHERIC DENSITY
- VEHICLE DRAG DEPENDS ON ATMOSPHERIC DENSITY
- HUGE CHANGE IN KINETIC ENERGY IS REQUIRED
- THE ROCKET VEHICLE WANTS TO LEAVE AS LITTLE ENERGY BEHIND IN THE ATMOSPHERE AS POSSIBLE
- THE ROCKET WANTS TO GO UP OUT OF THE ATMOSPHERE BEFORE ACCELERATING TO HIGH SPEED

FOR AN AERO-SPACE PLANE OR AN AIRBREATHING VEHICLE THAT IS TO ACCELERATE TO ORBITAL SPEEDS, BOTH THE ENGINE THRUST AND THE VEHICLE DRAG VARY DIRECTLY WITH ATMOSPHERIC DENSITY. IN FACT, FOR A SCRAMJET-POWERED VEHICLE, THE THRUST MINUS DRAG IS LESS AT HIGHER DENSITY. THEREFORE, AN AIRBREATHING LAUNCH VEHICLE, TO MINIMIZE FUEL USE, SHOULD ACCELERATE TO HIGH VELOCITIES WELL WITHIN THE ATMOSPHERE. WHAT IS THE BEST WAY TO DO THIS AND MINIMIZE THE AMOUNT OF ENERGY LEFT BEHIND IN THE ATMOSPHERE AS HEAT? WHAT ARE THE IMPORTANT GOVERNING PARAMETERS?

<u>CONSIDER THE AEROSPACE PLANE</u>

- ENGINE THRUST DEPENDS ON ATMOSPHERIC DENSITY

- VEHICLE DRAG DEPENDS ON ATMOSPHERIC DENSITY

- HUGE CHANGE IN KINETIC ENERGY IS REQUIRED

- IT MUST ACCELERATE WELL WITHIN THE ATMOSPHERE TO VERY HIGH SPEED

- IT MUST ALSO MINIMIZE THE AMOUNT OF ENERGY LEFT BEHIND
  IN THE ATMOSPHERE AS HEAT

What is required to do this?

What are the governing parameters?

A VERY SIMPLE APPROXIMATE ANALYSIS CAN BE MADE BY WRITING NEWTON'S
EQUATION OF MOTION IN TERMS OF SPECIFIC ENERGY.

S I M P L E   A N A L Y S I S   F O R

S I N G L E - S T A G E - T O - O R B I T

IF THE EQUATION:

$$F = mA$$

IS WRITTEN IN TERMS OF SPECIFIC ENERGY, THE KEY GOVERNING PARAMETERS
BECOME OBVIOUS AND THE EQUATION CAN BE EXPRESSED AS A PERFECT
DIFFERENTIAL AND INTEGRATED IN CLOSED FORM ASSUMING AVERAGE (OVER THE
SPECIFIC ENERGY RANGE) VALUES OF THE KEY PARAMETERS.

BY SUMMING THE FORCES ALONG THE FLIGHT PATH, AN EQUATION IS OBTAINED IN
WHICH THE LEFT SIDE IS THE POWER AVAILABLE TO DO WORK ON THE VEHICLE AND
THE RIGHT SIDE IS THE RATE OF CHANGE OF THE SPECIFIC ENERGY OF THE
VEHICLE.

SIMPLE ENERGY ANALYSIS
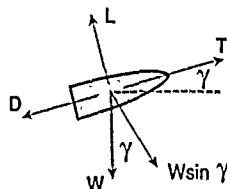
Summing forces along the flight path gives:
Thrust - Drag - Weight Component = Internal Force

$$T - D - W\sin\gamma = m\,\frac{dv}{dt}$$

From Which

$$\frac{VT}{m}\left(1 - \frac{D}{T}\right) = \frac{d}{dt}\left(\frac{V}{2} + gh\right)$$

↑Power available
to do work on
the vehicle

↑Rate of Change
of Vehicles
Specific Energy

THE EQUATION OF THE PREVIOUS FIGURE CAN BE EXPRESSED IN TERMS OF PERFECT DIFFERENTIALS AND INTEGRATED IN CLOSED FORM IF ONE ASSUMES THAT THE PARAMETERS THRUST TO DRAG RATIO (T/D) AND OVERALL PROPULSIVE EFFICIENCY $\left(\eta = \dfrac{VT}{Q}\Big/\dfrac{dm}{dt}\right)$ ARE BOTH INVARIENT WITH RESPECT TO SPECIFIC ENERGY.

FOR ROCKET-POWERED VEHICLES IT IS NORMAL TO ASSUME THAT THE SPECIFIC IMPULSE IS CONSTANT; BUT, SINCE SPECIFIC IMPULSE OF AN AIRBREATHING ENGINE VARIES WIDELY OVER THE SPEED RANGE FROM MACH 0 TO 25, IT WAS THOUGHT TO BE MORE APPROPRIATE TO ASSUME A CONSTANT OVERALL PROPULSIVE EFFICIENCY.

THE RESULT OF THIS SIMPLE APPROXIMATE ANALYSIS IS THE EQUATION SHOWN.

SIMPLE ENERGY ANALYSIS (Continued)

If a constant average value over the specific energy is assumed
for propulsion efficiency and thrust - to - drag ratio,
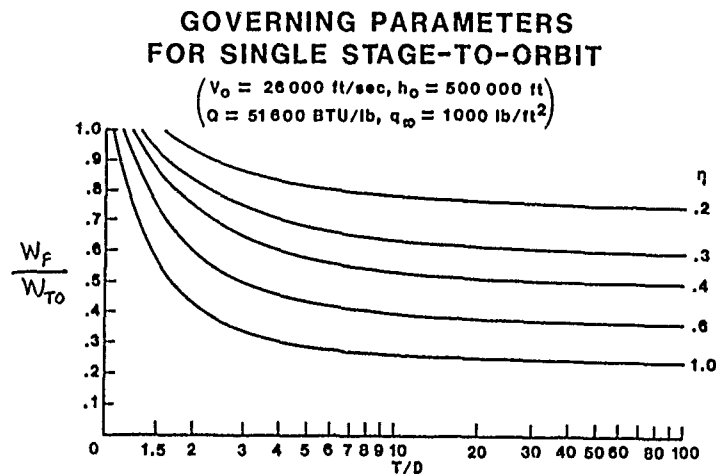then the equation can be solved

$$\frac{M_F}{W_T} = 1 - e - \frac{\left(\frac{V_o^2}{2} + gh_o\right)}{\eta Q\,(1 - D/T)}$$

RESULTS OF ANALYSIS

● THE THREE GOVERNING PARAMETERS THAT RESULT FROM THIS ANALYSIS ARE:

   (1) OVERALL PROPULSIVE EFFICIENCY: η_p

   (2) THRUST TO DRAG RATIO: T/D

   (3) FUEL WEIGHT FRACTION: $\dfrac{W_F}{W_{TO}}$

THIS FIGURE SHOWS THE VARIATION IN FUEL WEIGHT FRACTION (RATIO OF THE TOTAL WEIGHT OF FUEL TO THE TOTAL TAKE-OFF WEIGHT) WITH THRUST-TO-DRAG RATIO AND OVERALL PROPULSIVE EFFICIENCY. A HIGH FRACTION OF TOTAL TAKE-OFF WEIGHT MUST BE FUEL. FOR A PROPULSIVE EFFICIENCY OF 0.4 AND THRUST-TO-DRAG RATIO OF 3 ABOUT 65 PERCENT OF THE TAKE-OFF WEIGHT MUST BE FUEL.

GOVERNING PARAMETERS
FOR SINGLE STAGE-TO-ORBIT

$$\left(\begin{array}{l} V_0 = 26\,000 \text{ ft/sec, } h_0 = 500\,000 \text{ ft} \\ Q = 51\,600 \text{ BTU/lb, } q_\infty = 1000 \text{ lb/ft}^2 \end{array} \right)$$

THE DENSITY AND HEAT OF COMBUSTION OF TWO ROCKET PROPELLANTS, AMONIA-LIQUID OXYGEN AND HYDROGEN-LIQUID OXYGEN, AND TWO AIRBREATHER FUELS, JP-4 AND LIQUID HYDROGEN, ARE COMPARED IN THIS TABLE. THE DENSITY AND HEAT OF COMBUSTION ARE BASED ON THE VALUES OF BOTH PROPELLANTS FOR THE ROCKETS AND ON THE VALUES OF THE FUELS ALONE FOR THE AIRBREATHERS. OF COURSE, ROCKET PROPELLANTS AND JP-4 ARE MUCH MORE DENSE THAN LIQUID HYDROGEN SO IT IS EASIER TO DESIGN A ROCKET VEHICLE OR A JP-4 FUELED AIRCRAFT HAVING A HIGH FUEL WEIGHT FRACTION; BUT THERE IS ALSO MUCH LESS SPECIFIC ENERGY AVAILABLE.

LIQUID HYDROGEN IS SOMEWHAT UNIQUE IN THAT IT HAS ALMOST THREE TIMES THE SPECIFIC ENERGY OF MOST CONVENTIONAL AIRBREATHING FUELS. HOWEVER, IT IS ALSO UNIQUE IN ITS VERY LOW DENSITY. A MUCH LARGER VOLUME IS REQUIRED TO CARRY THE SAME AMOUNT OF ENERGY WITH LIQUID HYDROGEN THAN FOR JP-4. THIS LARGE VOLUME TAKES MORE STRUCTURE TO HOLD IT AND THUS MORE STRUCTURAL WEIGHT AND ALSO RESULTS IN HIGHER VEHICLE DRAG.

PROPERTIES OF PROPELLANTS

PROPERTY	ROCKETS		AIRBREATHERS	
	$NH_3 - O_2$	$H_2 - O^2$	JP4	LH_2
DENSITY, LB/FT^3	55.62	26.25	58.89	4.40
HEAT OF COMBUSTION, BTU/LB	2650	5700	18,700	51,600
HEAT OF COMBUSTION, BTU/FT^3	147,393	149,625	1,101,243	227,040
SPECIFIC ENERGY, FT^2/SEC^2	0.66×10^8	1.43×10^8	4.69×10^8	12.93×10^8

BASED ON THE SIMPLE ANALYSIS DISCUSSED PREVIOUSLY, THE MAXIMUM ATTAINABLE VELOCITY WITH THE FOUR PROPELLANTS OF THE PREVIOUS CHART ARE SHOWN AS A FUNCTION OF FUEL WEIGHT FRACTION FOR INFINITE THRUST-TO-DRAG RATIO. THE TOP OF EACH BAND REPRESENTS η = 0.3 AND THE BOTTOM REPRESENTS $\eta = 0.4$.

IT IS CLEARLY DIFFICULT TO REACH ORBITAL VELOCITY WITH A ROCKET HAVING A PROPULSIVE EFFICIENCY OF 0.4 OR LESS. IT IS PROBABLY SAFE TO SAY THAT ONLY HYDROGEN FUEL HAS ENOUGH SPECIFIC ENERGY TO PROVIDE ORBITAL CAPABILITY IN A PRACTICAL SINGLE-STAGE, AIRBREATHING VEHICLE.

ALSO SHOWN ON THE FIGURE ARE TWO DATA POINTS FOR THE ACCELERATION OF THE X-15. THE X-15 WAS PROPELLED BY AIR $NH_3 - O_2$ ROCKET, HAD A T/D OVER 5 AND AN η BETWEEN 0.3 AND 0.4. THE LOWER DATA POINT WAS THE MAXIMUM SPEED FLIGHT OF THE BASIC X-15 VEHICLE. THE HIGHER POINT WAS THE MACH 6.7 FLIGHT MADE USING EXTERNAL FUEL TANKS.

MAXIMUM ACHIEVABLE VELOCITY FOR VARIOUS PROPELLANTS

($T/D = \infty$)

Velocity in 1000's of ft/sec
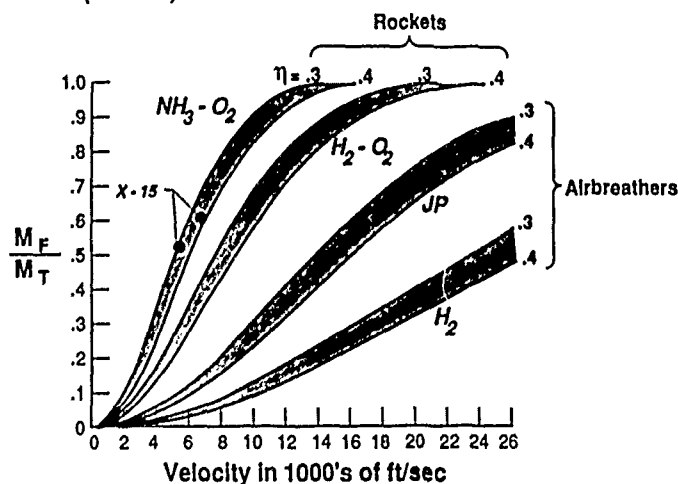
VIII. MODELING THE FLOW IN SCRAMJET COMBUSTORS

CONSIDERABLE RESEARCH HAS BEEN DONE AT NASA LANGLEY ON A HYDROGEN-FUELED SCRAMJET ENGINE CONCEPT WHICH IS INTENDED TO OPERATE OVER SPEEDS FROM MACH 4 TO MACH 10 WITH A FIXED GEOMETRY ENGINE. THIS CONCEPT USES STRUTS WHICH ACT TO SHORTEN THE INLET AND ALSO SERVE AS IN-STREAM FUEL INJECTORS. TO PROVIDE A VARIABLE DISTRIBUTION OF HEAT RELEASE WITHIN THE COMBUSTOR, TWO TYPES OF FUEL INJECTION ARE DISPLAYED. AT LOW MACH NUMBERS, THE FUEL IS INJECTED PARALLEL TO THE FLOW FROM THE BASE OF THE STRUTS AND MIXES AND REACTS SLOWLY WITH THE AIR. AS THE SPEED IS INCREASED, FUEL IS ALSO INJECTED FROM THE SIDES OF THE STRUTS TO ACHIEVE MORE RAPID MIXING. AT THE HIGHEST SPEEDS, IT IS DESIRABLE TO HAVE THE FUEL AND AIR MIX AND REACT AS RAPIDLY AS POSSIBLE.

AIRFRAME-INTEGRATED SUPERSONIC COMBUSTION RAMJET
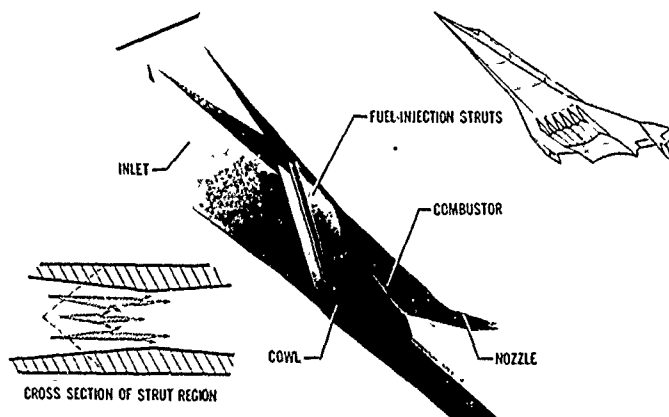
A SCHEMATIC OF A SCRAMJET ENGINE MODEL PROBLEM IS SHOWN. INLET AIR ENTERS THE ENGINE MODULE AT $M = 5$, $T = 325$ K, AND $P = 0.035$ ATM. GASEOUS HYDROGEN FUEL IS INJECTED FROM FOUR FUEL INJECTORS LOCATED ON THE STRUT SIDEWALLS AND ENGINE SIDEWALLS AT $M = 1.05$, $T = 246$ K, AND $P = 2.5$ ATM. THE FUEL INJECTORS ARE LOCATED 6 CM DOWNSTREAM OF THE ENGINE MINIMUM. THE DIMENSIONS OF THE ENGINE MODULE ARE GIVEN ON THE SLIDE. THE HYDROGEN FUEL AND AIR MIX DOWNSTREAM OF THE POINT OF INJECTION AND REACT IN THE COMBUSTOR.

THE EXPECTED SHOCK STRUCTURE IN THE INLET AND COMBUSTOR IS ALSO INDICATED ON THE FIGURE.

SCHEMATIC OF SCRAMJET ENGINE PROBLEM
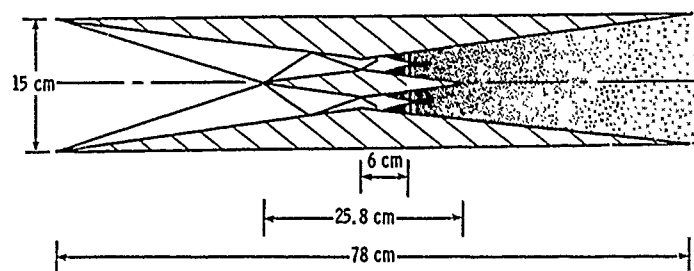
	M	T	P
INLET AIR	5.03	335 K	3546 Pa
HYDROGEN	1.05	246 K	254824 Pa

THIS FIGURE SHOWS THE VELOCITY VECTOR FIELD IN THE ENGINE ONCE STEADY STATE CONDITIONS HAVE BEEN REACHED. THE FLOW IS SEEN TO TURN THROUGH SHOCKS FROM THE INLET LEADING EDGES AND THE STRUT LEADING EDGE. THESE SHOCKS COALESE BEYOND THE STRUT LEADING EDGE AND REACH SUFFICIENT STRENGTH TO SEPARATE THE BOUNDARY LAYERS ON THE ENGINE SIDEWALLS AS CAN BE SEEN BY THE REVERSAL OF THE VELOCITY VECTORS. THE FLOW TAKES ON A HIGHLY PARABOLIC CHARACTER IN THE EARLY PORTION OF THE COMBUSTOR. THE STRONG JET INTERACTION REGION THAT OCCURS AT THE LOCATION OF FUEL INJECTION CAN BE SEEN JUST BEYOND THAT POINT. THE FLOW AGAIN SEPARATES ON EITHER SIDE OF THE FUEL INJECTORS PROVIDING LOCATIONS FOR FLAMEHOLDING.

MAGNIFIED VELOCITY VECTOR FIELD IN ENGINE

INLET   COMBUSTOR
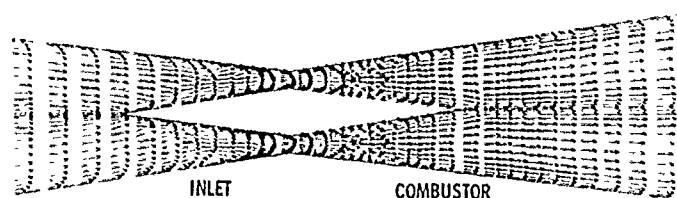
SHOWN ARE THE PRESSURE CONTOURS IN THE ENGINE. THE LEADING EDGE AND STRUT SHOCKS CAN BE SEEN IN THE SLIDE. THE STRONG INTERACTION REGION CONTAINING INJECTOR BOW SHOCKS CAN ALSO BE SEEN.

COMPUTED STATIC PRESSURE CONTOURS IN ENGINE
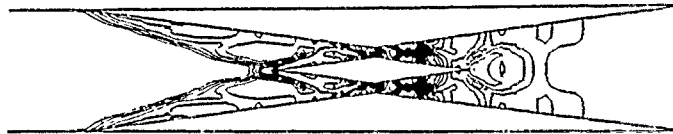
THE TEMPERATURE RISE DUE TO CHEMICAL HEAT RELEASE CAN BE SEEN FROM THE STATIC TEMPERATURE CONTOURS IN THE ENGINE. IT IS CLEAR IN THE SIMULATION THAT THE FUEL IS NOT COMPLETELY MIXING WITH AIR IN THE COMBUSTOR, RESULTING IN STRATIFIED REGIONS (MIXING LAYERS) OF ELEVATED TEMPERATURE ASSOCIATED WITH EACH FUEL INJECTOR. PEAK TEMPERATURES OF AROUND 2000 K ARE REACHED IN EACH MIXING LAYER.

COMPUTED STATIC TEMPERATURE CONTOURS IN ENGINE

T, K

SIMILAR RESULTS CAN ALSO BE SEEN IN THIS FIGURE WHICH SHOWS THE WATER MASS FRACTION DISTRIBUTION IN THE COMBUSTOR AS A RESULT OF CHEMICAL REACTION. CHEMICAL REACTION WAS MODELED IN THIS STUDY WITH EITHER AN EQUILIBRIUM CHEMISTRY MODEL OR A 9 SPECIES, 18 REACTION FINITE RATE CHEMISTRY MODEL. THE WATER DISTRIBUTION IS AGAIN STRATIFIED DUE TO INCOMPLETE MIXING.

COMPUTED WATER CONTOURS IN ENGINE

WATER MASS
FRACTION, %

INLET   COMBUSTOR
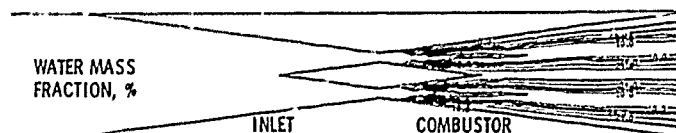
IN AN ATTEMPT TO IMPROVE MIXING, THE FUEL INJECTORS WERE MOVED UPSTREAM 4 CM TO ENHANCE THE FUEL-AIR INTERACTION. THE RESULTING VELOCITY VECTOR FIELD IN THE ENGINE IS SHOWN. FUEL-AIR MIXING WAS SIGNIFICANTLY IMPROVED, RESULTING IN CONSIDERABLY MORE HEAT RELEASE. THE INCREASED HEAT RELEASE DROVE THE FLOW SUBSONIC AND CAUSED THE FORMATION OF NORMAL SHOCKS AHEAD OF THE INJECTORS. THESE SHOCKS WERE NOT STABLE, AND THEY PROPOGATED INTO THE INLET CAUSING AN INLET-COMBUSTOR INTERACTION. LARGE SEPARATED REGIONS THEN FORMED IN THE INLET RENDERING AN UNACCEPTABLE DESIGN.

WITHOUT CHEMICAL REACTION, THE COMBUSTOR DID NOT CHOKE. THEREFORE, THE INLET-COMBUSTOR INTERACTION OCCURRED DUE TO THERMAL CHOKING RATHER THAN AERODYNAMIC CHOKING.

**COMPUTED VELOCITY VECTOR FIELD IN ENGINE
WITH CHOKED FLOW**
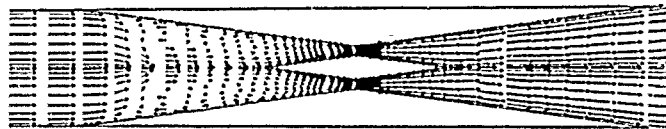
IX. AUGMENTATION OF MIXING IN SUPERSONIC

FREE-SHEAR LAYERS

MIXING AUGMENTATION

IN HIGH-SPEED SCRAMJET POWERED CONFIGURATIONS, ACHIEVING A HIGH MIXING AND COMBUSTION EFFICIENCY IS PARTICULARLY DIFFICULT. THIS IS A CONSEQUENCE OF THE FACT THAT WITH INCREASING VEHICLE MACH NUMBER, THE AVERAGE MACH NUMBER IN THE COMBUSTOR ALSO INCREASES. AS THE COMBUSTOR MACH NUMBER INCREASES, THE DEGREE OF FUEL AIR MIXING THAT CAN BE ACHIEVED THROUGH NATURAL CONVECTIVE AND DIFFUSIVE PROCESSES IS REDUCED LEADING TO AN OVERALL DECREASE IN COMBUSTION EFFICIENCY AND THRUST. BECAUSE OF THIS, IT IS NECESSARY TO INVESTIGATE MIXING ENHANCEMENT TECHNIQUES TO ACHIEVE INCREASED COMBUSTION EFFICIENCY. TECHNIQUES WHICH MIGHT BE USED FOR MIXING AUGMENTATION ARE LISTED. OF THESE, SOME OF THE TECHNIQUES HAVE BEEN STUDIED NUMERICALLY FOR TWO-DIMENSIONAL LOWS AND RESULTS ARE DISCUSSED IN SUBSEQUENT VIEWGRAPHS.

TYPICAL TECHNIQUES FOR MIXING AUGMENTATION

- PROVISION FOR INCREASED MIXING AREA, PARTICULARLY THROUGH SPANWISE CONVOLUTIONS

- IMPOSITION OF SWIRL OR LONGITUDINAL VORTEX MOTION

- COMBUSTOR DESIGN TO ENSURE TURBULENCE AUGMENTATION RATHER THAN DAMPING DUE TO COMBUSTION

- OPERATION IN THE NEAR FIELD OF THE MIXING ZONE WHERE INITIAL B.L. OR LOW Re NO. TURBULENCE STRUCTURES (AS OPPOSED TO ASYMPTOTIC FREE-MIXING STRUCTURES) ARE PRESENT

- INCREASED TURBULENCE PRODUCTION THROUGH PROVISION FOR MULTIPLE INFLECTION POINTS

- CONTROL OF INITIAL SHEAR-LAYER DYNAMIC VORTICITY PRODUCTION

- SHOCK INTERACTION

MIXING ENHANCEMENT BY TEMPERATURE CONTROL

SHOWN IS A SCHEMATIC OF A SPATIALLY DEVELOPING MIXING LAYER. A SPLITTER
PLATE ON THE LEFT SEPARATES THE INITIAL FUEL (TOP) AND AIR (BOTTOM)
STREAMS. THE AIR STREAM IS PRESUMED AT REST, WHEREAS THE FUEL STREAM
HAS A SPECIFIED MACH NUMBER M_∞ . THE RATIO OF THE AIR TO FUEL
TEMPERATURES IS DENOTED BY β_T . A FREE SHEAR LAYER DEVELOPS
DOWNSTREAM OF THE SPLITTER PLATE. THIS, OF COURSE, IS UNSTABLE AND
LINEAR STABILITY THEORY CAN DESCRIBE THE INITIAL STAGES OF THE
INSTABILITY.

MACARAEG & STREETT HAVE PERFORMED A PARAMETRIC STUDY OF THE TEMPORAL
STABILITY OF THE SELF-SIMILAR, NON-REACTING MIXING LAYER. THE
COMPRESSIBLE LINEAR STABILITY EQUATIONS WERE SOLVED WITH A SPECTRAL
METHOD USING ON THE ORDER OF 100 POINTS.
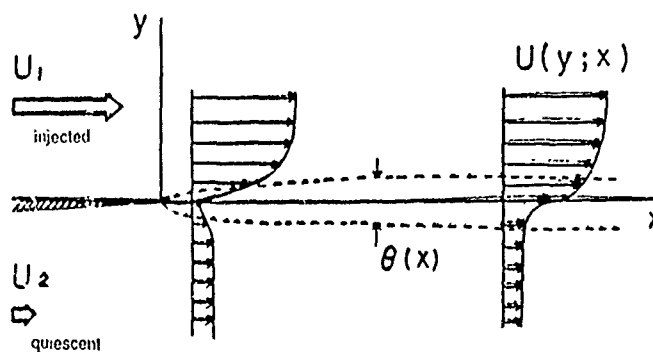
Sketch of spatially developing mixing layer.

$$\beta_T = T_{(quies)} / T_{(inject)}$$

TYPICAL DEPENDENCIES OF THE GROWTH RATES, DENOTED BY ω_i, UPON MACH
NUMBER, TEMPERATURE RATIO, AND REYNOLDS NUMBER RE ARE SHOWN. THE
DECREASE IN GROWTH RATE WITH INCREASING MACH NUMBER IS FAMILIAR AND
UNDERLIES THE NECESSITY O INCREASING THE MIXING AT HIGHER SPEEDS. THE
MODEST DEPENDENCE OF THE GROWTH RATE UPON REYNOLDS NUMBER REFLECTS THE
ESSENTIALLY INVISCID CHARACTER OF THE INSTABILITY. THE STRONG
DEPENDENCE OF THE GROWTH RATE UPON THE TEMPERATURE RATIO SUGGESTS THAT
MIXING CAN BE ENHANCED BY PROPER TUNING OF THE FUEL TEMPERATURE.
FORTUNATELY, THE GREATER INSTABILITY OF THE SHEAR LAYER WITH DECREASING
FUEL TEMPERATURE IS FAVORABLE TO HYPERSONIC COMBUSTORS: THE AIR
ENTERING THE COMBUSTOR WILL BE VERY HOT AND THE FUEL CAN BE RELATIVELY
COLD.

SHEAR LAYER LINEAR INSTABILITY
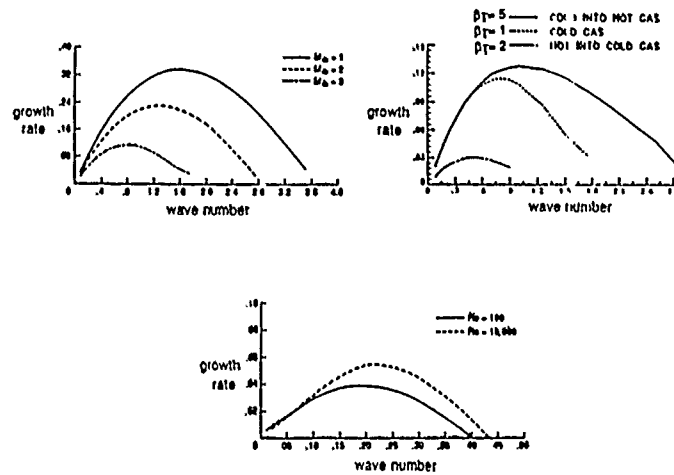
THIS FIGURE SHOWS THE RESULTS OF A CFD SOLUTION OF A MIXING AND REACTING
FLOW OF HYDROGEN AND AIR. THE TWO GASES ARE ESSENTIALLY SEPARATED BY A
THIN PLATE AND THEN TO MIX AND REACT ALONG THE FREE SHEAR LAYER THAT
FOLLOWS. THE COLORS INDICATE THE AMOUNT OF WATER VAPORS PRESENT IN THE
FLOW AND THUS SHOW THE DEGREE OF MIXING ACHIEVED WITH THE RED COLOR
INDICATING PRESSURE OF A SIGNIFICANT AMOUNT OF WATER. COMPARE THE VERY
SLOW MIXING SHOWN FOR THIS FLOW WITH THAT IN THE NEXT FEW FIGURES.

REACTING MIXING LAYER 1

CASE 1

$H_2 \rightarrow$
u = 2672 m/s
T = 2000K

Air →
u = 1729 m/s
T = 2000K

H2O MASS FRACTION
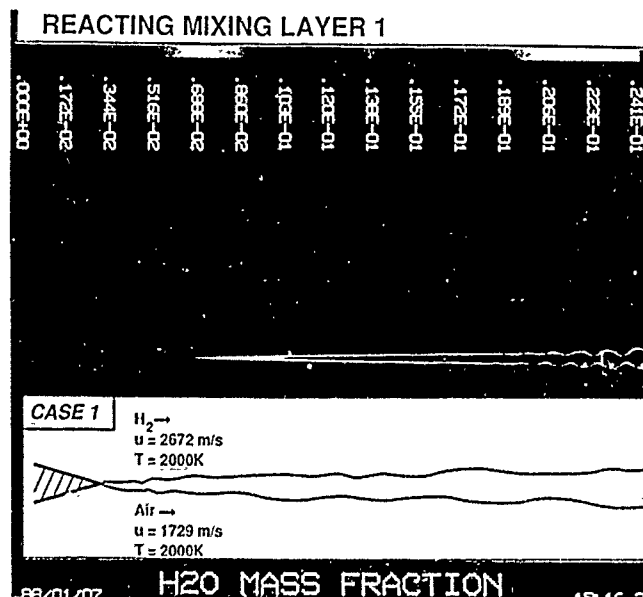
IN THIS CASE, TWO STATIONARY OBLIQUE SHOCK WAVES ARE POSITIONED SO THAT
THEY CROSS IN THE CENTER OF THE SEPARATED FREE SHEAR LAYER JUST
DOWNSTREAM OF THE PLATE. NOTE THAT MIXING AND REACTING ARE ONLY
SLIGHTLY ENHANCED BY THE SHOCKS.

REACTING MIXING LAYER 2

CASE 2

H2O MASS FRACTION
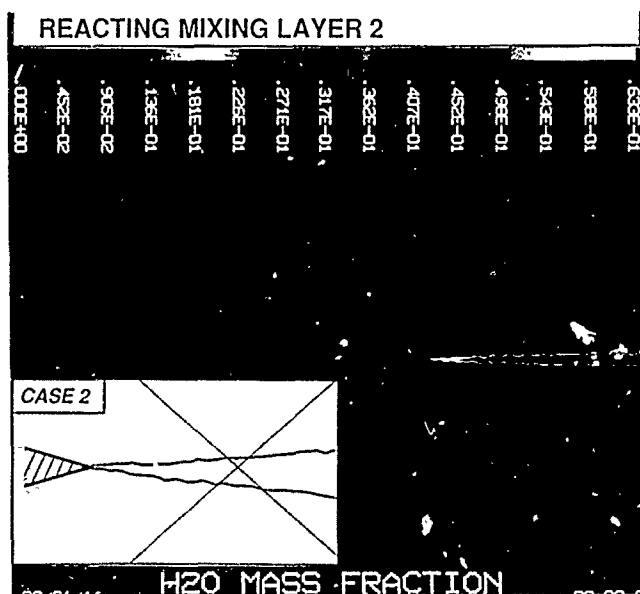
IN THIS CASE, A VERY SMALL BLUNT BODY IS POSITIONED JUST DOWNSTREAM OF
THE PLATE AND CAUSES A STRONGLY CURVED SHOCK IN THE FREE-SHEAR MIXING
LAYER. THIS CURVED BOW SHOCK PRODUCES VORTICITY AND GREATLY IMPROVES
MIXING OF THE TWO FLOWS.

REACTING MIXING LAYER 3

CASE 3

H2O MASS FRACTION
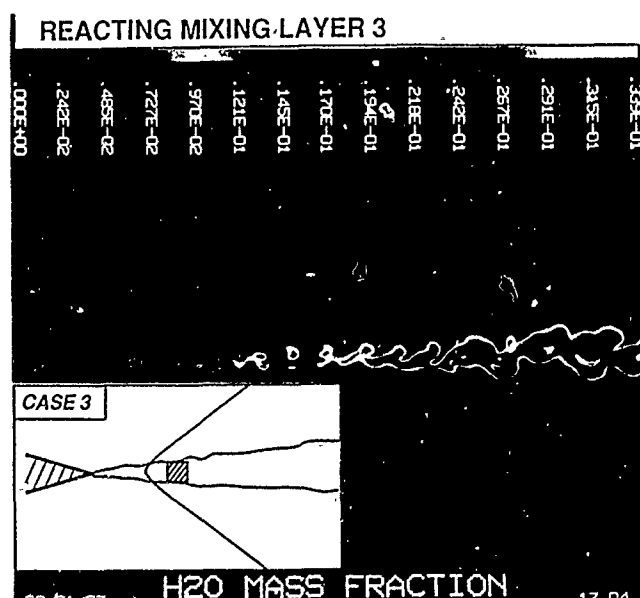
Of course, locating a blunt body in the mixing and reacting flow of a scramjet combustor is not practical. However, these mixing study results suggest that a different fuel injector arrangement might improve the mixing and reaction. Previously, the parallel and perpendicular fuel injectors were arranged on the struts as shown in the top left of the figure. By rearranging these fuel injectors as shown on the right, the fuel from the parallel injector now flows through the curved bow shock created by the perpendicular injector. Comparison of the CFD results for these two flows shows greatly increased mixing and reaction for the modified fuel injector.

STRUT MODIFICATION FOR IMPROVED COMBUSTION EFFICIENCY
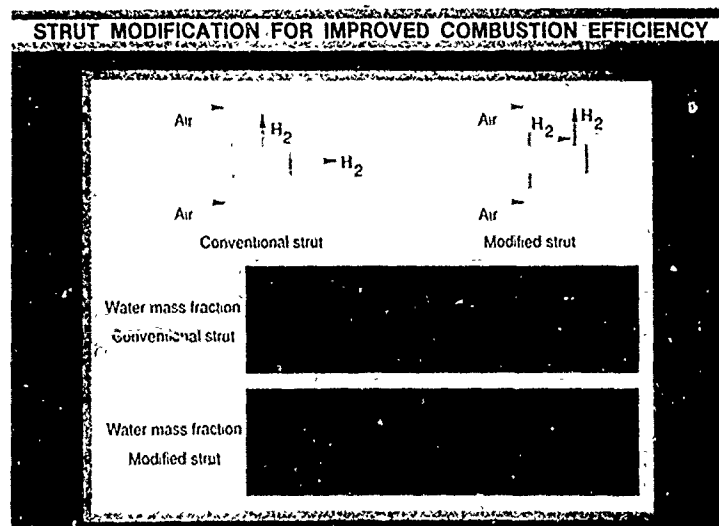
Proper integration of the scramjet engine with the airframe is required to obtain the high thrust-to-drag ratios desired at high speeds. Analyzing this complex flow required calculations of the forebody flow entering the inlet, the spillage from the multiple inlet module and the external nozzle flow.

HYPERSONIC ENGINE/AIRFRAME INTEGRATION

FOREBODY DESIGN

INLET INTERACTION

NOZZLE DESIGN
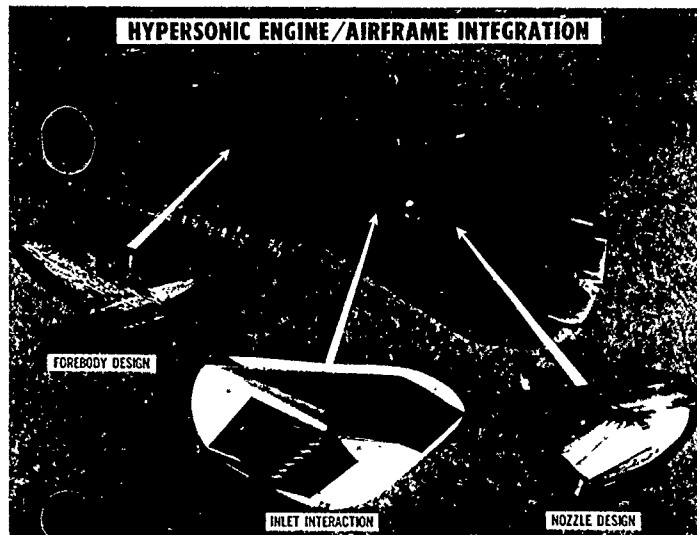
THIS FIGURE SHOWS LAMINAR FLOW PAST A HYPERSONIC LIFTING BODY AT MACH
19.2, ZERO ANGLE OF ATTACK, AND A UNIT REYNOLDS NUMBER OF 30,000/IN.
THE CALCULATIONS ARE MADE USING AN UPWIND THIN-LAYER-NAVIER-STOKES CODE
ON A GRID OF (45x65x65) UNDER EQUILIBRIUM AIR ASSUMPTION. THE FIGURE
SHOWS TEMPERATURE CONTOURS AT 4 CROSS SECTIONS. THICKENING OF BOUNDARY
LAYER IN THE LOWER SYMMETRY PLANE IS OBVIOUS FROM THIS FIGURE. THIS IS
NOT A DESIRABLE FEATURE OF THE FOREBODY FLOW SINCE THE FLOW ON THE LOWER
SURFACE IS CAPTURED BY THE SCRAMJET INLETS.

HYPERSONIC LIFTING BODY

TEMPERATURE

AOA=0.

M=19.2

Rc=30000/in

EQUILIBRIUM AIR
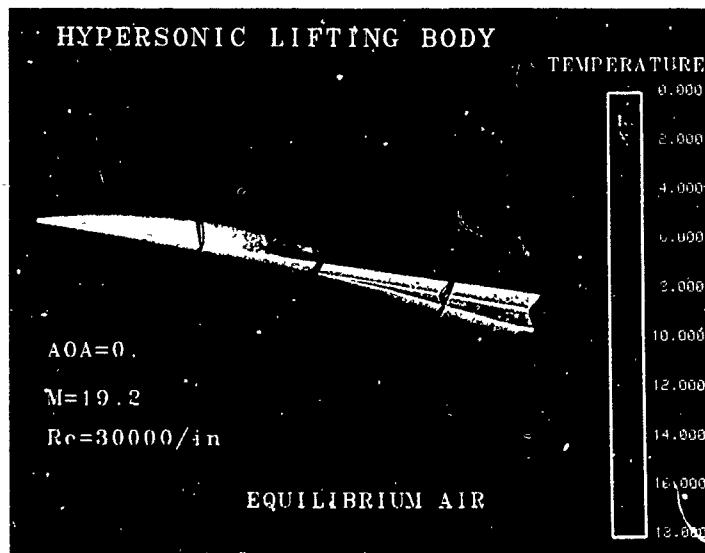
A THREE-MODULE SCRAMJET INLET CONFIGURATION IS SHOWN IN THIS FIGURE. IT
HAS SWEPT SIDEWALL COMPRESSION SURFACES WITH SWEEP ANGLE OF 30^0 AND
COMPRESSION ANGLE OF 10^0. ALTHOUGH NOT SHOWN IN THE FIGURE, THE COWL
CLOSURE STARTS AT THE THROAT. CALCULATIONS HAVE BEEN MADE FOR A MACH 4
TURBULENT FLOW THROUGH THESE INLETS USING A 3-D NAVIER-STOKES CODE.

Multiple module inlet
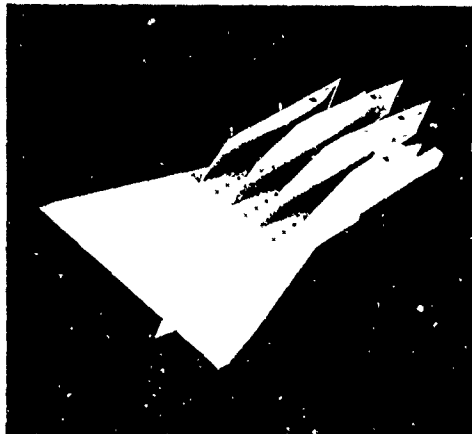
A GRID OF APPROXIMATELY 330,000 POINTS IS USED IN THE ANALYSIS FOR HALF
OF THE CONFIGURATION. THE FLOW IS CALCULATED FOR ZERO ANGLE OF ATTACK
AND A GEOMETRIC CONTRACTION RATIO OF 4. SHOWN IN THE FIGURE ARE THE
PARTICLE TRACES IN THE SYMMETRY PLANE OF THE CENTER MODULE. THIS FIGURE
CLEARLY SHOWS THE SPILLAGE OF THE FLOW FROM THE INLET DUE TO SWEPT
COMPRESSION SURFACES AND INTERACTION BETWEEN THE HIGH-PRESSURE INTERNAL
FLOW AND THE LOW-PRESSURE EXTERNAL FLOW. THIS INTERACTION IS CAUSED BY
THE AFT PLACEMENT OF THE COWL ON THE UNDERSURFACE OF THE MODULES.

Particle traces at mach 4
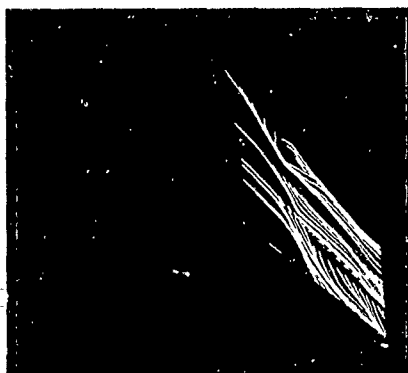
VALIDATION OF THE ENGINE-INSTALLED PERFORMANCE OF A SCRAMJET POWERED AIRCRAFT IN CONVENTIONAL AERODYNAMIC WIND TUNNELS CAN BEST BE DONE BY SIMULATION OF THE ENGINE EXHAUST WITH A SUBSTITUTE GAS. THE PROPER INVISCID SIMULATION OF SCRAMJET EXHAUST EFFECTS REQUIRES THE MATCHING OF COMBUSTOR EXIT (OR NOZZLE ENTRANCE) MACH NUMBER, STATIC PRESSURE, AND γ , THE RATIO OF SPECIFIC HEATS. THE ACTUAL CHEMISTRY OF THE SCRAMJET EXHAUST IS NOT A FIRST ORDER EFFECT FOR THIS APPLICATION. THE COMBUSTOR EXIT MACH NUMBER AND STATIC PRESSURE CAN BE MATCHED WITH AIR, BUT THE γ OF A SCRAMJET EXHAUST IS SIGNIFICANTLY DIFFERENT FROM THAT OF AIR.

THE BASIC CONCEPT OF A COLD GAS SIMULATION OF THE SCRAMJET EXHAUST IS ILLUSTRATED IN THE FIGURE. THE RANGE OF γ FOR A SCRAMJET EXHAUST AT MACH 8 IS PLOTTED VERSUS THE TEMPERATURE OF THE GAS. A SIMILAR PLOT FOR A PARTICULAR ARGON-FREON MIXTURE IS ALSO SHOWN. THE ENTIRE RANGE OF γ FOR THE SCRAMJET EXHAUST CAN BE MATCHED BY THE INERT GAS AT A TEMPERATURE THAT IS 5-10 TIMES LOWER THAN THAT OF THE SCRAMJET EXHAUST. THE INERT GAS IS ALSO SAFER AND MORE PRACTICAL FOR USE IN WIND TUNNELS THAN ARE COMBUSTION PRODUCTS.

SUBSTITUTE-GAS ENGINE EXHAUST SIMULATION CONCEPT (U)

70% F13B1 + 30% Ar

Range of γ for matching to scramjet exhaust at M = 8 flight condition

Scramjet exhaust (equilibrium)

γ

$T^{\circ}K$

(For Scramjet exhaust gas only)
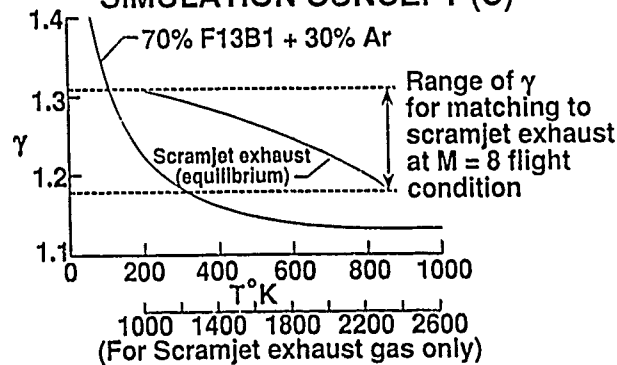
Unclassified

THE GRUMMAN DETONATION TUBE WAS USED TO EXPERIMENTALLY VERIFY THE COLD GAS SIMULATION TECHNIQUE. THIS FACILITY CAN OPERATE AT FLIGHT REYNOLDS NUMBER AND ENTHALPY VALUES IN THE MACH NUMBER RNGE BETWEEN 4 AND 10. A SMALL RECTANGULAR NOZZLE WAS PLACED IN THE TEST SECTION TO CREATE THE FLOW CONDITIONS THAT WOULD BE FOUND AT THE EXIT OF A SCRAMJET COMBUSTOR.

DETONATION TUBE TECHNIQUE FOR SIMULATING SCRAMJET EXHAUST

DIAPHRAGM
SCALE MODEL SCRAMJET NOZZLE
WINDOWS
DRIVER TUBE
DRIVEN TUBE
VACUUM CHAMBER
6 FT. DIAMETER
20 FT.
33 FT.
12 FT.

TIME

EXPANSION WAVE
INTERFACE
REFLECTED SHOCK WAVE
BURNED GAS
DETONATION WAVE
UNBURNED GAS
N_2O, H_2, N_2, A

DISTANCE

MAXIMUM TESTING TIME (5 MS)
GAS SIMULATING SCRAMJET STAGNATION PROPERTIES
• TOTAL ENTHALPY
• CHEMICAL CONSTITUENCY
NOZZLE-FLOW SIMULATION
• FINITE-RATE CHEMISTRY
• FULL-SCALE R_E

PHOTO OF MODEL IN DETONATION TUBE

SCALE 2-D SCRAMJET NOZZLE
MODEL IN DETONATION TUBE
VACUUM CHAMBER
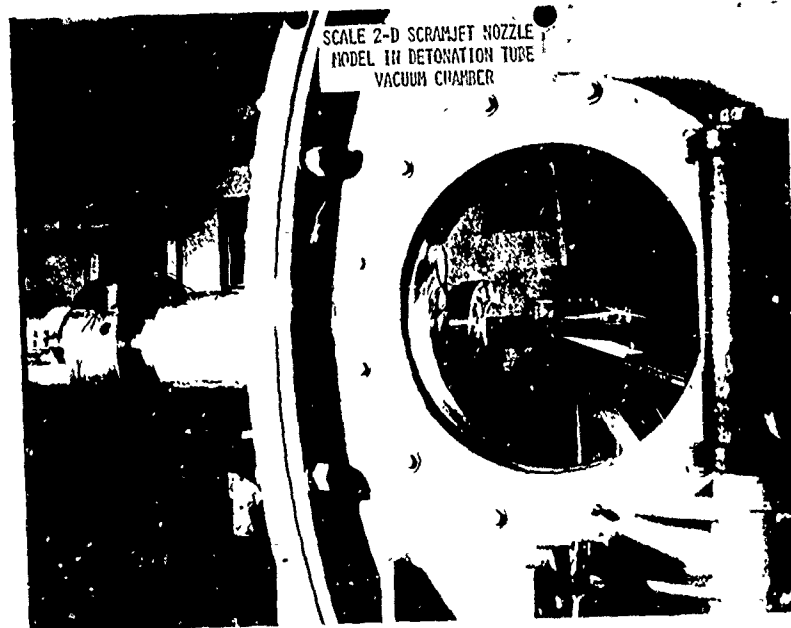
TESTS MADE IN THE DETONATION TUBE WITH HOT HYDROGEN-AIR COMBUSTION PRODUCTS AND COOL ARGON-FREON SUBSTITUTE GAS MIXTURES HAVE VALIDATED THE USE OF SUBSTITUTE GAS AS A WAY TO SIMULATE AN OPERATING SCRAMJET ENGINE IN CONVENTIONAL WIND TUNNEL TESTS.

NOZZLE PRESSURE DISTRIBUTIONS WITH AND WITHOUT SHOCKS
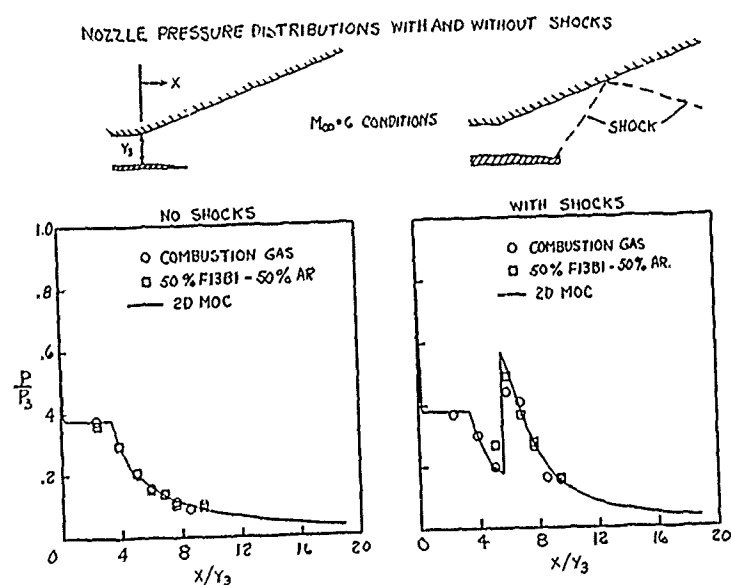
A Comparison of Air and Freon-Argon as the Simulant Gas

The simulant gas nozzle experiment was recently tested in the Langley 20-Inch Mach 6 Tunnel using air as the scramjet exhaust simulant gas. This test was for the purpose of requalifying the simulant gas supply system and to provide experimental data for CFD validation. This data can be used, however, to illustrate the difference in the nozzle flowfield that occur due to γ.

A sketch of the test article is shown. The wind-tunnel Reynolds number is about 7×10^6/ft at Mach 6 for a stagnation pressure of 365 psia and a stagnation temperature of 400° F. The conditions of the simulant gas at the combustor exit are Mach 1.70 and γ = 1.23.

Four cases are presented in the force and moment comparison below. Fence-on and fence-off cases are shown for Argon-Freon and air. The cross-hatched region indicates the force or moment increment due to the addition of the flow fence. All the cases are for β = 20°.

The pressure field and the characteristic lines are a function of γ, the effect of which is illustrated by the integrated surface pressures on the external nozzle. The magnitude of all the parameters is larger for the Freon-Argon simulant gas than for air. This trend indicates tha the surface pressures on the external nozzle are greater than for the Freon-Argon mixture than for air. The flow fence also increases the magnitude of the parameters.

SCRAMJET EXHAUST SIMULATION MODEL
Cold gas simulation
Mach 6
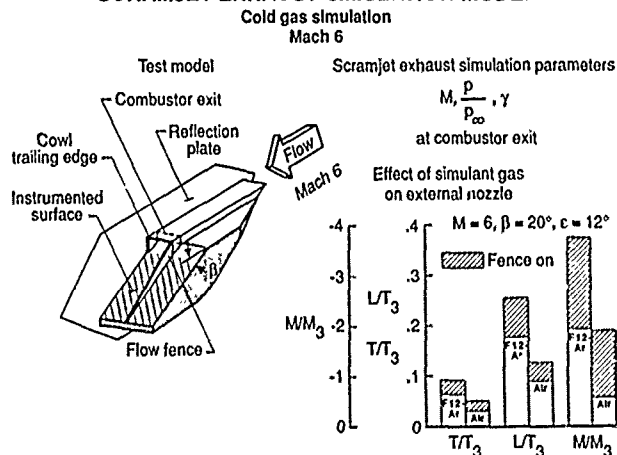
X. SUMMARY

• CURRENT INTEREST IN SUPERSONIC AND HYPERSONIC AIRCRAFT HAVE GENERATED A NEED FOR BETTER UNDERSTANDING OF THE FLOWS ABOUT SUCH VEHICLES

• NEW INSTRUMENTATION AND NEW TEST TECHNIQUES COMBINED WITH ADVANCES IN COMPUTATIONAL FLUID DYNAMICS GIVE US THE OPPORTUNITY TO OBTAIN A GREATLY IMPROVED UNDERSTANDING OF SUPERSONIC AND HYPERSONIC FLOWS

COMPUTATION OF COMPRESSIBLE VISCOUS FLOWS

by

D.Hänel
Aerodynamisches Institut
RWTH
Templergraben 55
D-5100 Aachen
Federal Republic of Germany

Abstract

This paper concerns with computational methods for the compressible Navier-Stokes equations with special consideration of hypersonic flows. In the first part the governing equations and relations for equilibrium flow are described, and their basic numerical approaches, in particular for the Euler terms are discussed. As a selected topic the application of the multigrid method to solutions of the Navier-Stokes equations is considered. As a further topic the influence of the numerical damping on the numerical solution of the conservation laws is discussed, and their influence on steady-state, and unsteady solutions of the Navier-Stokes equations is demonstrated. The special numerical problems arising in hypersonic, viscous flows are discussed by means of an upwind relaxation method , and modifications of the scheme to overcome these problems will be presented. Conclusions will be drawn for the specific requirements of hypersonic, viscous flows to the numerical methods.

1 Introduction

The computation of 3-D, supersonic flow around blunt bodies is of increasing interest for the development of spacecrafts and hypersonic airplanes. The physical and numerical problems to be solved cover a wide range of the fluid mechanics, ranging from rarefied gasdynamics, chemical non-equilibrium to problems of non-reactive, continuum flow. Rarefaction and chemical effects are of great importance, in particular for reentry vehicles and the consideration of that is of growing interest in the computational fluid dynamics. Nevertheless large portions of the flight path are governed by continuum flow, in particular for hypersonic planes in the Mach number-range of five to ten, but also for reentry bodies in the lower atmosphere. An overlook about these problems can be found e.g. in [1], [2].

The present paper concerns with the computation of viscous, hypersonic flow in the continuum flow regime. The viscous flow is of great importance for the prediction of the flight properties, in particular for the prediction of aerodynamical forces and heat flux rates. The vehicles considered are usually blunt bodies or planes with a low aspect ratio, thus the flow is three-dimensional and strong viscous/inviscid interactions can appear. The typical flow around blunt bodies is characterized by strong shock waves and expansions, embedded subsonic regions, and shock-boundary layer interactions with separation. To attack such flow problems the Navier-Stokes equations have to be solved. The numerical method required for such a problem must be powerful, should be sufficient accurate in viscous flow regions and should have the properties of high resolution schemes in the nearly inviscid flow portion.

From the numerical point of view an essential problem is to find in the structure of the Navier-Stokes equations, which involves different characterisic scale length to be resolved numerically. This fact requires much finer computational meshes than needed for the corresponding inviscid problem, and with that more computer storage and computational work is required. Besides of an necessary increase of computer capacity, the efficiency of numerical methods has to be improved. A close cooperation with the applied mathematics is necessary to utilize all the mathematical possibilities. A typical example for that is the developement of the multigrid methods and their application to hyperbolic and parabolic problems. The multigrid method, an useful concept for increasing the efficiency of numerical methods will be explained briefly is demonstrated by some results.

Another aim in the developement Navier-Stokes solvers is the improvement of the accuracy of viscous solutions, in particular for flows at high Reynolds numbers. In this case there is a very sensible balance between inertia and viscous terms. Physically the inertia terms have no dissipative contribution, but their numerical approximation generates a certain amount of numerical dissipation superposing the physical dissipation. Then the accuracy of the solution can be impaired, in particular in viscous layers where strong gradients are present. These problems, important in every numerical solution will be discussed in one section.

The special numerical problems arising in hypersonic, viscous flows will be discussed in a further section, and by means of an upwind relaxation method modifications of the scheme will be presented to reduce such problems. Finally conclusions will be drawn for the specific requirements to the numerical methods for hypersonic flow.

2 Governing Equations and Relations

From the gaskinetical point of view different flow ranges can be characterized by the Knudsen number Kn ,the ratio of the mean free path between the collision of two molecules, and of a characteristic macroscopic (body) length. Thus the flows can range from the nearly collision-free molecular flow (Kn=O(1)) to the collision-dominated continuum flow with $Kn \ll 1$. The latter is of interest in present consideration.

The governing equation for all these flow ranges is the Boltzmann equation, an integro-partial differential equation for the molecular distribution function. However the complexity of this equation is high, and a more general solution becomes very costly (e.g. Monte Carlo methods).

For the most situations encountered at ordinary densities in gas dynamics the Knudsen number is very small, the corresponding flows are continuum or near-continuum flows. Those the complexity of Boltzmann equation can be reduced by expanding the equation with respect to small Knudsen numbers (Chapman-Enskog expansion). By that a hierachy of flow equations can be derived with increasing order of Kn (e.g. see Vincenti,Kruger [3]). In this order it yields the Euler equations, the Navier-Stokes equations, and the Burnett equations. Equivalently, the hierachy describes the increasing deviation from the state of thermodynamical (translational) equilibrium. In this sense the Euler equations of inviscid flow can be considered as the conservation laws for thermodynamical equilibrium, whereas the Navier-Stokes equations describe small deviations from that. Both the Euler and Navier-Stokes equations are the most important tools for predicting technical relevant flow problems. The Burnett equations, although higher order equations have shown only small, if any improvement over the Navier-Stokes equations.

Theoretical and experimental investigations have shown that the Navier-Stokes equations describe sufficiently well the flow even in the near-continuum flow range (not to far from continuum). These equations although derived for nearly thermodynamical equilibrium are equally valid for flows with vibrational or chemical non-equilibrium, however, provided the thermodynamical variables are given in their extented definition appropriate the non-equilibrium situation.

2.1 Conservation Laws

The conservation laws for the specific mass (density ρ),the momentum ρV ,and the energy $\rho \bar{E}$ are formulated as the rate of change of the consesative variables Q in the volume τ balanced by the effect of the generalized fluxes $\vec{H}$ acting on the surface A. The conservation laws in the integral form read:

$$\int_{\tau} Q_t \, d\tau + \oint_A \vec{H} \cdot \vec{n} \, dA = 0 \tag{1}$$

The divergence form can be obtained by means of the integral theorem of Gauss:

$$Q_t + \nabla \cdot \vec{H} = 0 \tag{2}$$

Herein Q is the vector of the conservative variables

$$Q = (\rho, \rho\vec{v}, \rho E)^T$$

The generalized flux $\vec{H}$ can be split into a term for inviscid flow $\vec{H}_{inv}$ and one describing the viscous flow $\vec{H}_{visc}$. The inviscid term yields:

$$\vec{H}_{inv} = (\rho\vec{v}, \rho\vec{v}\,\vec{v} + p, \rho\vec{v}H_t)^T$$

The viscous part is

$$\vec{H}_{visc} = (0, \bar{\bar{\sigma}}, \bar{\bar{\sigma}} \cdot \vec{v} + \vec{q})^T$$

where $\bar{\bar{\sigma}}$ is the stress tensor, and $\vec{q}$ is the heat flux vector.

2.2 Equations of State

The equations of state define the thermodynamical, and calorical variables as function of conservative flow variables Q, for the assumption of thermodynamical equilibrium. The conservative quantity, the total energy $e = \rho E$ is connected with the internal energy by $e = \rho E = \rho(\varepsilon + \vec{v}^2/2)$

The internal energy ε is expressed by the *caloric equation of state* $\varepsilon = \varepsilon(\rho, T)$ as function of two thermodynamical variables, here ρ and T.

For a thermally perfect gas, an assumption for moderate density and temperature (e.g. air $T \leq 2000K$) the caloric equation reads $\varepsilon = \varepsilon(T) = \int c_v dT$. The additional assumption of calorically perfect gas (e.g. air $t \leq 500$) reduces the relation to $\varepsilon = c_v T$.

The *thermal equation of state* defines the pressure as function of two variables, e.g. of the internal energy ε, and of the density ρ:

$$p = p(\rho, \varepsilon) = Z(\rho, \varepsilon) \cdot \rho RT(\rho, \varepsilon) \tag{3}$$

where $Z(\rho, \varepsilon)$ is the compressibility factor. For a thermally perfect gas, Z=1, it yields $p = \rho RT$, and in addition for a calorically perfect gas it is $p = (\gamma - 1)\rho \varepsilon$.

With the equations of state, and with the thermodynamical laws the other quantities can be derived. For example the speed of sound at constant entropy $s = s(\rho, \varepsilon)$ becomes:

$$a^2 = \frac{dp}{d\rho}\big|_s = \frac{\partial p}{\partial \rho}\big|_\varepsilon + \frac{\partial p}{\partial \varepsilon}\big|_\rho \frac{p}{\rho^2} \tag{4}$$

which reduces for a perfect gas to $a^2 = \gamma p/\rho = \gamma RT$.

In general the equations of state for a real, non-perfect gas cannot be formulated in a closed form. Then the calculation of the state has to be carried out by an evaluation of the thermodynamical partition functions, from which Mollier diagrams can be constructed. For computational purposes the diagrams are often used in form of interpolation tables (e.g. Tannehill [4]).

2.3 Transport Quantities

Laminar flow requires the knowledge of the molecular transport of momentum and energy. The mostly used assumption for ordinary fluids is the linear relationship between shear stress and velocity gradient, and between heat flux and temperature gradient, which is in agreement with the gaskinetical consideration of the Navier-Stokes equations. Then it is for example: $\tau = \mu \frac{\partial u}{\partial y}$ and $q = \lambda\,grad\,T$ At moderate densities the coefficients of viscosity and heat conduction are usually functions of the temperature. For real multi-component gases the coefficients become functions of two variables, e.g. $\mu = \mu(\rho, \varepsilon)$, and have to be evaluated by means of mixing laws and the equations of state via the concentrations (see e.g. Bird, Stewart, Lightfoot [5]).

In *turbulent flow* the problem of closures is much more complicated than for laminar flow. Generally all turbulent flow simulations suffer under the lack of the correct physical modelling. Therefore the mostly used attempts are based on the Reynolds-averaged equations with any eddy viscosity assumption. Closures can be achieved by additional transport equations, like the $k - \varepsilon$ model, or by algebraic relations, like the mixing length assumption. All of these assumptions need parameters to be adapted empirically to the special flow problem. The most of these models are suited for boundary layer-like flows with small separation zones only (which motivates the use of the thin layer approximation).

In Navier-Stokes computations an additional difficulty arises for the evaluation of the boundary layer thickness, necessary for the scaling of the models. Therefore special turbulence models were derived for the requirements of Navier-Stokes solutions. At present the mostly used model for that is the two-layer algebraic model by Baldwin and Lomax [6].

2.4 Navier-Stokes Equations and their Approximations

2.4.1 Navier-Stokes Equations

In the following discussion the conservation equation will be refered to their formulation in a Cartesian system (x,y,t) and the gas is assumed to be perfect. Then the Cartesian components of the flux vectors may be $\vec{H}_{inv} = (F, G)^T$ and $\vec{H}_{vis} = (S, R)^T$. The integral form reads now

$$\int_\tau Q_t d\tau + \oint_A (F - S)dy - \oint_A (G - R)dx = 0 \tag{5}$$

, and the corresponding divergence form gives

$$Q_t + (F - S)_x + (G - R)_y = 0 \tag{6}$$

Herein is

$$Q = \begin{pmatrix} \rho \\ \rho u \\ \rho v \\ \rho E \end{pmatrix} \quad F = \begin{pmatrix} \rho u \\ \rho u^2 + p \\ \rho uv \\ \rho u H_t \end{pmatrix} \quad G = \begin{pmatrix} \rho v \\ \rho vu \\ \rho v^2 + p \\ \rho v H_t \end{pmatrix} \quad S = \begin{pmatrix} 0 \\ \tau_{xx} \\ \tau_{xy} \\ s_4 \end{pmatrix} \quad R = \begin{pmatrix} 0 \\ \tau_{xy} \\ \tau_{yy} \\ r_4 \end{pmatrix}$$

where $s_4 = q_x + u\tau_{xx} + v\tau_{xy}$ and $r_4 = q_y + u\tau_{xy} + v\tau_{yy}$. With the Stokes assumption $\mu_v = -2/3\mu$ the stress terms are expressed by Newtons assumption:

$$\tau_{xx} = 2\mu u_x + \mu_v \nabla \cdot \vec{v} \quad \tau_{yy} = 2\mu v_y + \mu_v \nabla \cdot \vec{v} \quad \tau_{xy} = \mu(u_y + v_x)$$

The components of the heat flux vector $\vec{q}$ are given by $q_x = \lambda \frac{\partial T}{\partial x}$ and $q_y = \lambda \frac{\partial T}{\partial y}$.

2.4.2 Thin Layer Approximation of the Navier-Stokes Equations

The thin layer approximation is a widely used approximation for the computation of viscous flows at high Reynolds numbers. In comparison to the complete Navier-Stokes equations in this approximation all the viscous terms with stream-wise derivatives are neglected in a similar way as done for the boundary layer equations. However, in contrast to those the thin layer approximation retains all the terms of the Euler equations, and in consequence the thin layer approximation preserves all the properties of the inviscid flow. Those upwind influence in viscous layers is given by the characteristic spreading in subsonic regions similar to higher order boundary layer concepts. For the equations in 2-D Cartesian coordinates, assuming the x-coordinate as the nearly streamwise direction, the thin layer approximation would read :

$$Q_t + F_x + (G - R)_y = 0 \tag{7}$$

where Q,F, and G have the meaning as before, but now the viscous term R contains only that stress terms wich have derivatives in normal (y-) direction.

There exists no rigorous theory for the derivation of this approximation, however its range of validity can be approximately considered to be the same as that of the higher order boundary layer theory. It means that local flow separation and small normal pressure gradients in viscous layers are covered by the approximation

From the computational point of view further motivations using this approximation are given from the fact that usually the step sizes in streamwise direction are much larger than normal to it, and those even when the complete equations are used the streamwise derivativies of the viscous terms are insufficiently resolved Furtheron most of the turbulence models used are suited only for boundary layer-like flows.

An important requirement for the application of the thin layer approximation is the use of streamline- (surface)- orientated, orthogonal meshes to grasp completely the remaining main stress terms.

2.4.3 Parabolized Navier-Stokes Equations

The parabolized Navier-Stokes equations correspond to the thin layer approximation if applied to steady-state, supersonic flow. For the example of 2-D flow the parabolized equations would read:

$$F_x + (G - R)_y = 0 \tag{8}$$

where the viscous terms R contain only terms with derivatives normal to the main flow, F, and G are the full Euler fluxes.

Now in stationary, supersonic flow all informations are transported downstream within the Mach cone, but in the subsonic layers upstream spreading can happen (along characteristics). Therefore the term "parabolic" is somewhat misleading. This property has to suppressed numerically to avoid instabilities of the solution if marching in space. The numerical suppressing is justified by the parabolic nature of the boundary layers. Therefore in commonly applied marching procedures either the pressure gradient normal to the wall is assumed to be zero across the subsonic layer, [7], or the contribution of the streamwise pressure gradient is is decreased in the subsonic layer as a function of the Mach number based on a stability analysis [8]. With that, very efficient, non-iterative marching methods (in streamwise direction) can be constructed for the computation of viscous, supersonic flow.

However per definition streamwise subsonic flow is excluded (e.g. near the stagnation point). Therefore, other solutions, e.g. taken from the Navier-Stokes equations, have to be used to update the initial conditions for the supersonic part.

Furtheron like the boundary layer equations the parabolic equations can not describe flow separation in streamwise direction. In normal direction where usually the flow is subsonic the parabolic equations allow the calculation of cross flow separation.

2.5 Boundary conditions

In this paper continuum flow at thermodynamical equilibrium is considered. Thus the boundary value problems correspond to that known for lower Mach numbers.

The boundary conditions at the wall for continuum flow are defined by the conditions of vanishing normal velocity, by the no-slip condition (vanishing tangential velocity v_t), and by the thermal conditions:

$$v_n = 0, \qquad v_t = 0, \qquad T = T_w \quad \text{or} \quad \frac{\partial T}{\partial n} = 0 \tag{9}$$

In the transition regime (not to far from the continuum) the flow is still sufficiently represented by Navier-Stokes equations. The influence of rarefaction effects can be restricted to the boundary conditions at the wall by using the so-called slip conditions (or incomplete accomodation of momentum and energy). Then the

boundary conditions for the temperature and the tangential velocity form a system of coupled equations for the value, and for the gradient at the wall. They can be written in a generalized form:

$$A\vec{V} + B\frac{\partial \vec{V}}{\partial n} = C \quad \text{with} \quad \vec{V} = \begin{pmatrix} v_t \\ T \end{pmatrix} \tag{10}$$

The coefficients in A,B, and C are given by the gaskinetical theory. An application of these slip conditions for viscous, near-continuum flow is given e.g. by Gökcen, Mac Cormack, Chapman [9]. In this paper it is shown that the Navier-Stokes equations are capable of describing the transition flow using appropriate slip boundary conditions. As an example from [9] Fig. 1 shows the computed skin friction drag versus Reynolds number on a flate plate using different wall conditions.
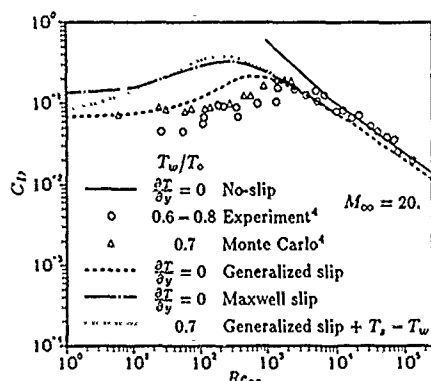

Fig.1 Skin friction drag of a flat plate versus Reynolds number. Influence of the slip conditions in near-continuum flow, taken from [9].

The *inflow and outflow boundary conditions* are less unique, since they depend strongly on the flow problem considered. The number of the boundary conditions (conditions from outside) and of the compatibility conditions (conditions from the interior integration domain) can be derived from the differential problem. For the complete Navier-Stokes equation such conditions are discussed e.g. in [10], [11]. For the thin layer approximation such additional conditions can be neglected. In the most cases the correct conditions cannot be satisfied, therefore the assumptions of nearly inviscid flow (characteristic updating of the conditions) and of the boundary layer concept (parabolic behaviour in space) are often used.

The *inflow boundary conditions* for hypersonic flow are usually well defined by the incoming supersonic flow forming the bow shock in front of a body. If the bow shock is captured the boundary conditions are represented by the supersonic inflow conditions. Since in usual Navier-Stokes computations the viscous shock structure is not resolved alternatively the shock can be fitted as a discontinuity like in inviscid flow. An example for the latter is given in a section below.

The *outflow boundary conditions* are more cumbersome. Usually the outflow boundary cuts an unknown flow field, and reasonable conditions have to be deduced from the physical problem. If the inviscid flow is supersonic and if the viscous portions at the outflow boundary is boundary layer-like, then the extrapolation of the boundary values from the interior is an reasonable conditions. In other cases additional conditions from outside (e.g. the pressure) have to be prescribed.

3 Basic Numerical Approximations

The complete Navier-Stokes equations form a system of quasi-linear partial differential equations, which is of parabolic-hyperbolic type in the time-space plane, and of elliptic-hyperbolic type in the space (steady-state). These different types of the equations demonstrate the complexity of the corresponding solutions.

However the main problems for the numerical solution of the Navier-Stokes equations essentially arise from the fact that very different length scales, and time scales are involved with the equations due to the different physical phenomena described by that. Typical characteristic lengths are for example the body length L, the boundary layer thickness $\delta \sim L/\sqrt{Re}$, and the viscous thickness of a shock wave $\delta \sim L/Re$, which differ by orders of magnitude in ordinary flows.

To achieve a sufficiently accurate numerical solution these scalings, at least the most important one, have to be resolved by the numerical method of solution. For the most of external, and internal flow problems the two essential flow regions are the viscous layers, and the nearly inviscid "outer" flow.

The viscous layers (boundary layers, wakes) are characterized by a small thickness δ normal to the main flow. Within the layer the Euler and viscous terms are nearly balanced. Thus the solution becomes continuous,

but shows large gradients and a strong curvature of the variables. This fact can lead to severe problems of accuracy of the numerical method if the layers are not resolved sufficiently well.

In the nearly inviscid regions the Euler terms are dominating and the properties of the solution correspond essentially to that of the hyperbolic Euler equations. Thus continuous (strong) ,and discontinuous (weak) solutions can appear, as well. The weak solution appears, since in general the viscous structure of a shock wave with the much-smaller scale length is not resolved. For capturing the discontinuous solutions the use of the conservative form of the Navier-Stokes equations is required, and a Navier-Stokes solver include an Euler solver with good shock capturing properties. Thus the Navier-Stokes solution includes all the numerical problems of the Euler solution, and much care has to be taken to avoid undesired interactions between the numerical dissipation of the Euler solver, and the physical disspation from the viscous terms in the Navier-Stokes equations.

In the following sections a brief summary of basic approaches for the discretization of the equations will be given and some examples for methods of solution will be presented.

3.1 Grid Arrangement and Conservative Discretization

The computation of the flow along curved shapes requires the correct treatment of the boundary conditions on the surfaces. An appropriate way is to orientate the computational mesh such that one coordinate line or plane coincides with the curved surface. This leads to a curvilinear coordinate systems, let's say (ξ, η) for 2-D, along that the grid nodes are counted.

The grid arrangement influences strongly the accuracy and efficiency of the numerical method. The essential requirements to the grid arrangement are:

- *clustering* of grid points in regions of high gradients (e.g. embedded shocks, viscous layers)

- *orthogonality* in particular in viscous regions

- *smooth distribution of step sizes* to reduce the truncation error

- *avoiding or at least reducing of mesh singularities*, e.g. by using subgrids or block structures

In general not all of the requierements can be satisfied sufficiently well, especially for complex problems.

The generation of grids is usually carried out by numerical grid generation methods. The most important tools for that are the conformal mapping, the algebraic generation, and the mesh generation based on the solution of elliptic and hyperbolic partial differential equations. A summary of such methods can be found e.g. in [12].

As a suitable procedure to improve the quality of an initial mesh a grid optimization procedure may be mentioned here. Such a procedure, based on [13], was used for the present computations [14]. The distribution of the grid points is calculated by a decision function F, which must be minimized.

$$F = \sum_i \sum_j \sum_k (\alpha \Theta_{i,j,k} + S_{i,j,k}) = \text{Min.} \tag{11}$$

where Θ is a measure for orthogonality and S for smoothness and volume control. The measures Θ and S are defined by the local vectors $\vec{r}$ to the neighbouring nodes, e. g.

$$\Theta_{i,j,k} = \sum_{m=1}^{6} \sum_{n=1}^{6} \frac{(\vec{r}_m \cdot \vec{r}_n)^2}{|r_m|^2 \cdot |r_n|^2} \quad , \qquad m \neq n \tag{12}$$

$$S_{i,j,k} = \sum_{m=1}^{6} |r_m|^2 \beta_m \tag{13}$$

The factors α and β are weighting factors. The solution is carried out by an iterative relaxation method

For conservative discretization in the discrete space a finite control volume has to be defined around or between the grid points. Within the volume the variables are represented as volume-averaged values, which are balanced by the values of the fluxes normal to the cell faces. For the conservative formulations the integral, and divergence form of the conservation laws can be used, as well.

The use of the integral form leads to the so-called "finite-volume" approach, where the surface integral is approximated by the sum over all pieces of the surface. Simplified written the discrete form reads in 2-D:

$$\frac{\Delta Q}{\Delta t} Vol + \sum_{k=1}^{4} (F \Delta y - G \Delta x) = 0 \tag{14}$$

Herein Q corresponds to its volume-averaged value, $(F\Delta y - G\Delta x)$ are the normal fluxes summed up over the single cell interfaces. The advantage of the "finite-volume" approach is the direct application to the physical (x,y) space, and the easy interpretation in curvilinear-meshes.

For using the divergence form, sometimes called "finite-difference" approach, first the differential equations have to be transformed in the curvilinear coordinate system and thereafter the equations are discretized in the transformed plane The advantage of this approach is given in-the more formal way of handling more complex terms.

For the 2-D example the transformed equations in the new coordinates (ξ, η) read:

$$\widehat{Q}_t + \widehat{F}_\xi + \widehat{G}_\eta = 0 \quad \text{with} \quad \widehat{Q} = QJ \quad \text{and} \quad \widehat{F} = Fy_\eta - Gx_\eta \quad \text{etc.} \tag{15}$$

Here J is the metric Jacobian, which can be interpreted as the volume, and x_η, etc. are parts of the surface normal vector The details can be found elsewhere. After the discretization in the transformed plane with the corresponding (properly discretized) metric formulation, the resulting discretized equations should agree with that derived by using the integral form.

It means both ways of the conservative discretization, the "finite-volume" and the "finite-difference" approach lead to the same discretized equations. Differences only can occur by different arrangements of the control volume, by the different numerical flux formulations, and by the different updating of the cell-interface fluxes.

There exists a number of possibilities for the arrangement of control volumes in a given grid. The basic requirement for all of the arrangements of the control volumes is that the volumes do not overlap, and that no gap is between.

The mostly used arrangements are the "node-centered" , the "cell-centered" , and the "cell-vertex" arrangements, which are sketched in Fig. 2.

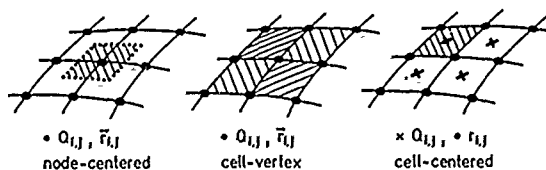| • $Q_{i,j}$, $\bar{r}_{i,j}$	• $Q_{i,j}$, $\bar{r}_{i,j}$	× $Q_{i,j}$, • $r_{i,j}$
node-centered	cell-vertex	cell-centered

Fig.2 Usual mesh-arrangements for conservative discretization.

For a Cartesian grid discretizations in these arrangements show nearly the same accuracy, but for a curvilinear grid different truncation errors can appear for a certain scheme. For example using a central scheme it could be shown that for a screwed grid the error from the "cell-centered" arrangement is larger than those for the "cell-vertex" arrangement [15]. Near a boundary the different grid arrangements require a different numerical treatment of the boundary conditions ,which can be important for the spatial accuracy near geometrical discontinuities, like the trailing edge [16]. The better geometrical flexibility have shown the "cell-centered" and the "cell-vertex" approaches, which also can be extented to triangulated, unstructured grids [17]].

3.2 Formulation of the Fluxes at the Cell Interfaces

The discretization of the conservation equations for the small control volume leads to the sytem of difference equations for the rate of change of the volume-averaged variables as function of the normal fluxes over the cell interfaces The projection of the variables to the cell interfaces and evolution of the fluxes determines essentially the quality of the solution.

In the following discussion the 1-D conservation equations will be used for the sake of simplicity. In the finite-difference form, they read for a grid point "i":

$$\frac{\Delta Q_i}{\Delta t} + \frac{F_{i+1/2} - F_{i-1/2}}{\Delta x} = \frac{R_{i+1/2} - R_{i-1/2}}{\Delta x} \tag{16}$$

Herein $\Delta Q_i/\Delta t$ is the discretized time derivative, defined by the method of solution, and $F_{i\pm1/2}$ and $R_{i\pm1/2}$ are the inviscid, and the viscous fluxes at the cell interfaces.

The viscous fluxes are usually updated by means of central differences $O(\Delta x^2)$, which corresponds to the elliptic nature of the viscous effects. Then a viscous term of the form $R = \mu\frac{\partial u}{\partial x}$ may be written as

$$R_{i+1/2} = \mu_{i+1/2}\frac{u_{i+1} - u_i}{\Delta x} \tag{17}$$

The formulation of the inviscid flux terms has a strong influence on the properties of the solution method and the various methods differ essentially by that.

In the *"projection-evolution"* approach (sometimes called MUSCL approach) [18]) first the basic variables (e.g. Q) are inter/extrapolated from both sides to the cell interface, and then a common numerical flux formulation is formed with both values.

In the *"evolution-projection"* approach the flux functions are formed on the grid points, where Q is given, and then the fluxes are projected to the cell interface. This approach is used e.g. for the "cell-vertex" schemes. Also combined forms of both may be possible.

Considering the *projection step* then the variables $Q_{i\pm1/2}$ at the cell interface are usually expressed by a polynomial of the variables of the neighbouring points. A general polynomial for the forward $Q^+_{i+1/2}$, and backward extra/interpolated values $Q^-_{i+1/2}$ may be written as:

$$Q^+_{i+1/2} = Q_i + 1/4\,\varphi_i\left((1+\kappa)\Delta^+Q + (1-\kappa)\Delta^-Q\right)_i$$
$$Q^-_{i+1/2} = Q_{i+1} - 1/4\,\varphi_{i+1}\left((1+\kappa)\Delta^-Q + (1-\kappa)\Delta^+Q\right)_{i+1} \qquad (18)$$

with $\Delta^+Q_i = Q_{i+1} - Q_i$ and $\Delta^-Q_i = Q_i - Q_{i-1}$.

Herein φ is a switching factor, and κ is the discretization factor. For $\varphi = 0$ it yields a first order upwind scheme $O(\Delta x)$, with $\varphi = 1$ the scheme becomes higher order accurate, at least second order. In more detail the scheme is then central $O(\Delta x^2)$ with $\kappa = 1$, upwind-biased $O(\Delta x^3)$ with $\kappa = 1/3$, upwind-biased $O(\Delta x^2)$ with $\kappa = 0$, and fully upwind $O(\Delta x^2)$ with $\kappa = -1$.

To avoid the oszillation of the numerical solution, in particular near captured shocks, the extrapolation has to be limited by a variable switching factor φ, which is controlled by the solution itself, i.e. $\varphi_i = \varphi(\Delta^+Q_i, \Delta^-Q_i)$. Such limiters, also called flux limiters can be constructed from the theory of almost monotonic solutions (TVD-theory) and transfered approximately to hyperbolic systems in multi-dimensions (see e.g. [19],[20]).

A number of formulations of such limiters can be found in the literature, e.g. in [21],[18],[22]. In the present work the limiter by van Albada et al.[21] $\varphi_{VA} = \frac{2r}{1+r^2}$ with $r = \frac{\Delta^+Q}{\Delta^-Q}$ is used. All these limiter formulations react on the local gradient and on the curvature of the variables, i.e. $\varphi \sim (1 - Q_{xx}/Q_x)$. Those in regions of weak changes of Q the limiter remains nearly one, but for strong changes the value decreases, the scheme reduces the accuracy, and stronger numerical dissipation is generated. The latter effect results in a sharp, non-oscillating resolution of embedded shocks. In viscous layers, however, where strong changes are also present, this numerical dissipation can significantly impair the solution.

In the *evolution step* of the MUSCL approach, the interpolated variables are used to calculate the fluxes at the cell interfaces.

Within each cell there exists an averaged value of the conservative variables, and thus the values show a jump at the interface to the neighbouring cell. According to the theory of the nonlinear hyperbolic Euler equations this jump of the values generates a local Riemann problem, where the information is transported forward and backward by the different gasdynamical waves and shocks. The solution of this local Rieman problem leads to Euler solvers of the Godunow-type [23],[24]. If the jump is considered to be weak, the Riemann problem can be solved approximately using the characteristic solution of the Euler equations. By means of this assumption a large number of existing flux formulations can be derived.

The consideration of the *approximate Riemann solvers* starts from the characteristic form of the Euler equations, which forms an uncoupled system of equations describing the information transport along the characteristic directions.

$$W_t + \Lambda W_x = 0 \qquad (19)$$

where $\Lambda = T^{-1}AT$, $T \cdot dW = dQ$, $T \cdot dQ = dF$, and $\Lambda = \mathrm{diag}(\lambda_i)$ with $\lambda_i = (u, u \pm a)$.

For subsonic flow $-a \leq u \leq a$ the eigenvalue matrix Λ may be split in a positive and a negative part.

$$\Lambda = \Lambda^+ + \Lambda^-$$

Then the characteristic form results in:

$$W_t + \Lambda^+ \delta_x W^+ + \Lambda^- \delta_x W^- = 0 \qquad (20)$$

In this semi-descrete version the space derivatives are discretized with the upwind differences corresponding the sign of the eigenvalues:

$$\delta_x W^\pm = \frac{W^\pm_{i+1/2} - W^\pm_{i-1/2}}{\Delta x} \qquad (21)$$

where $W^\pm$ are the backward or forward interpolated variables according Eq. (18).

The conservative form is achieved by multiplying the characteristic system with the eigenvector matrix T. Now by different splitting of the characteristic system, by different updating of the cell interface values, and by different approximate, conservative back transformations a large number of existing Euler flux formulations can be deduced by that.

In the following two typical approaches for classes of approximate Rieman solvers are demonstrated briefly.

The direct application of the conservative back transformation to Eq. (20) with $A^{\pm} = T \Lambda^{\pm} T^{-1}$, and $\delta_x F^{\pm} = A^{\pm} \delta_x Q$ leads to the class of *flux-vector splitting methods*, which read then:

$$Q_t + \delta_x(F^+ + F^-) = 0 \qquad (22)$$

The flux conservation requires that $F = F^+ + F^-$. The fluxes are computed from the correspondingly extrapolated values, i.e. $F_{i+1/2}^{\pm} = F^{\pm}(Q_{i+1/2}^{\pm})$.

The approximate formulation of the split fluxes is not unique.

The *flux-vector splitting by Steger, Warming* [25] makes use of the eigenvalue splitting $\Lambda^{\pm} = 1/2(\Lambda \pm |\Lambda|)$. Then the fluxes are defined by:

$$F = T(\Lambda^+ + \Lambda^-)T^{-1} Q = (A^+ + A^-)Q = F^+ + F^- \qquad (23)$$

An analysis of the formulation shows that the splitting error remains if one eigenvalue of A vanishes, leading to a finite dissipation for steady waves. Furtheron the eigenvalues change discontinuously near the sonic point, which reduces the rate of convergence, as found in test calculations.

The *flux-vector splitting by van Leer* [26] avoids the latter drawback of the Steger,Warming fluxes by defining the split fluxes as polynomials of the Mach number, which are smooth near the sonic point. Since one eigenvalue vanishes over a steady shock, its representation becomes very sharp. Furtheron this splitting if applied in implicit schemes results in very efficient, diagonal-dominant solution methods [27],[28]. However also this splitting formulation shows a remaining splitting error for steady tangential discontinuities, a drawback, influencing strongly the accuracy in viscous layers. In the modification of van Leer' splitting by Hänel,Schwane [29] the latter drawback could be esssentialy removed, and its application to viscous flow problems has shown an increased accuracy (results are given below).

The class of *flux-difference splitting methods* can be derived from Eq. (20) by using the eigenvalue splitting $\Lambda^{\pm} = \frac{1}{2}(\Lambda \pm |\Lambda|)$. Then the characteristic equations may be arranged to:

$$W_t + \frac{1}{2}\Lambda(\delta_x W^+ + \delta_x W^-) + \frac{1}{2}|\Lambda|(\delta_x W^+ - \delta_x W^-) = 0 \qquad (24)$$

Applying the back transformation the conservative form reads:

$$Q_t + \delta_x \tilde{F} = 0 \quad \text{with} \quad \delta_x \tilde{F} = \frac{\tilde{F}_{i+1/2} - \tilde{F}_{i-1/2}}{\Delta x} \qquad (25)$$

The numerical flux component $\tilde{F}_{i+1/2}$ may be defined then in different approximate ways, e.g. in the flux-difference splitting by Roe [30] the corresponding numerical flux reads:

$$\tilde{F}_{i+1/2} = \frac{1}{2}(F(Q^+) + F(Q^-)) + \frac{1}{2}|A(\bar{Q})|(Q^+ - Q^-) \qquad (26)$$

The matrix $|A|$ is determined such away that the averaged variables $\bar{Q}$ satisfies correctely the jump condition over a discontinuity parallel to the cell interface:

$$A(\bar{Q})(Q^+ - Q^-) = F(Q^+) - F(Q^-) \qquad (27)$$

This scheme shows a very sharp shock resolution and a small dissipation for steady tangential dicontinuities.The latter property is favourable for the computation of viscous flows.

A class of similar flux-difference splitting schemes are presented by H.Yee [31].

The *central schemes* likewise may be considered as a class of approximate Riemann solvers, where the characteristic range of influence is equally weighted independent of the Mach number. Assuming a symmetric interpolation polynomial for the cell interface values, which may be for example $Q_{i+1/2}^+ = Q_{i+1/2}^- = 1/2(Q_i + Q_{i+1})$, the conservative equations reduces to

$$Q_t + \delta_x F = 0 \quad \text{with} \quad F_{i+1/2} = F(\frac{Q_i + Q_{i+1}}{2}) \qquad (28)$$

Now the central formulation includes the correct eigenvalues of the Jacobian A, also the spatial discretization error does not include dissipative parts (even derivatives), in agreement with the wave character of the Euler solution However since this numerical approach ignores the characteristic range of influence, the numerical

solution shows a very poor shock capturing capability. Furtheron due to the missing dissipative parts of the numerical flux formulation any high-frequency error components of the solution can not be damped.Therefore in the practice artificial damping terms for high-frequency damping and shock capturing have to be added [32], which leads to similar problems of accuracy as for the other Euler solvers.

The preceding consideration of different Euler solvers covers only a small part of existing methods, which are so manifold as the authors are. The few number of schemes considered here will be used as a basis to discuss some aspects of solution methods for the Navier-Stokes equations.

As an important new tendency for Euler solvers the developement of _multi-dimensional Rieman solvers_ should be mentioned here. These schemes take into account multi-dimensional wave propagation and remove the drawback of mesh dependency of the usually one-dimensional Rieman solver. An example for that with further references is given e.g. in [33].

4   Methods of Solution

In general the time-dependent equations are used for solutions of unsteady, and stationary flow problems, as well. The advantage of using the time-dependent equations for steady-state computations, is that the initial value-boundary value problem remains independently from the Mach number range, and thus one single method can cover the whole ranges.

The computation of _time-dependent flows_ requires a discretization in time which is consistent and sufficiently accurate (at least $O(\Delta t)$). For time-accurate computations additional care has to be taken also the spatial discretization errors, which likewise influences the temporal accuracy.

For _steady-state computations_ the transient solutions have no meaning, as long as the steady-state solution will not be influenced by that. Therefore consistency and accuracy in time is not required, the method of solution (in time) can be chosen e.g. for a optimal rate of convergence. This leads to a class of pseudo time-dependent methods which correspond in principle to an iteration scheme. Herein known acceleration strategies for improving the convergence can be taken over like e.g. the Newton iteration with Gauss-Seidel relaxation,local time stepping or the multigrid methods.

An important decision for the selection of a method of solution is the decision to use an explicit or an implicit method. The _explicit methods_ have the simpler algorithm, only the steady-state operator has to be evaluated from the known initial state, the new state can be computed decoupled from grid point to grid point. Thus the explicit method is well suited for structured, and unstructured grids, as well. Vectorization and parallelization of the algorithm is much simpler to achieve. However the numerical time step of an explicit method is restricted by the numerical stability, which is proportional to the space step divided by the fastest gasdynamical wave speed. Additional restriction comes from the viscous terms, proportional to the cell Reynolds number.

If the steady-state solution is of interest only, the problem of time step restriction can be overcome by use of pseudo time-dependent methods with the corresponding acceleration strategies. Together with the simpler algorithmic structure very effective explicit methods for the solution of the Euler, and Navier-Stokes equations are available.

For time-accurate computations the explicit scheme results in a tolarable time advance, as long as in the physical problem only one time scale is present, e.g. the gasdynamical scaling in inviscid solutions, just defining the stability restriction. If however additional smaller scale lengths, like in viscous flows at high Reynolds numbers have to be resolved the time step becomes very small and the time accurate computation becomes too expensive. For this reason time accurate computations with an explicit scheme may be still efficient for inviscid flows and viscous flows at moderate Reynolds numbers, but for high Reynolds numbers some other ways, like implicit schemes or multigrid methods should be taken in consideration.

The _implicit schemes_ have the advantage of being unrestricted stable, or at least allow a much greater time step than an explicit scheme, but the computational work per time step due to the inversion of the large solution matrix is much larger. A handicap for vectorization of the implicit methods are the recursive structure of the inversion algorithms, but with a clever organization and sufficient computer storage the implicit algorithms can be vectorized in the same high degree as the explicit schemes.

The mostly used implicit scheme in the seventies was the Approximate Factorization (AF), [34]. This method allows the inversion per time step in a non-iterative way, which is an interesting aspect for time-accurate computations. Its efficiency for steady-state solutions, however, is restricted by the fact that the time step is limited to Courant numbers of $O(10)$ due to the factorization error. With the development of upwind schemes the relaxation schemes became an alternate, very efficient way of an implicit solution since by using that diagonal-dominant solution matrices can be achieved. These relaxation schemes make use of a iterative procedure to solve the equations each time step. If the solution matrix is sufficiently well-conditioned and diagonal-dominant the resulting solver becomes very robust and efficient for steady-state solutions since the time step is indeed unrestricted.An interesting aspect of the relaxation scheme is that the iterative procedure

per time step corresponds to a solution of a quasi-elliptic problem, which is challenging for the application of the multigrid methods.

The methods of solutions and their variants are numerous, therefore in the following section only two methods of solution for the Navier-Stokes equations will be discussed as typical examples for implicit and explicit methods.

The description of the methods is based on the time-dependent Navier-Stokes equations for a compressible fluid, written for a two dimensional curvilinear coordinate system, let's say (ξ, η, t). The equations in conservative form read:

$$\widehat{Q}_t + (\widehat{F} - \frac{1}{Re}\widehat{S})_\xi + (\widehat{G} - \frac{1}{Re}\widehat{R})_\eta = 0 \tag{29}$$

Details of the transformed equations can be found elsewhere.

With a conservative discretization in a way as described above the approximated Navier-Stokes equations (29) read:

$$\frac{\Delta\widehat{Q}}{\Delta t} + Res(\widehat{Q}) = 0 \tag{30}$$

where $\Delta\widehat{Q}/\Delta t$ is the discrete time derivative, and Res $(\widehat{Q})$ corresponds to the discretized steady-state operator:

$$Res(\widehat{Q})_{i,j} = \delta_\xi(\widehat{F} - \frac{1}{Re}\widehat{S}) + \delta_\eta(\widehat{G} - \frac{1}{Re}\widehat{T}) \tag{31}$$

$$\text{with} \quad \delta_\xi f = \frac{f_{i+\frac{1}{2},j} - f_{i-\frac{1}{2},j}}{\Delta\xi}; \quad \delta_\eta f = \frac{f_{i,j+\frac{1}{2}} - f_{i,j-\frac{1}{2}}}{\Delta\eta}$$

4.1 Implicit Relaxation Method

Starting from the discretized Navier-Stokes equations (30) the implicit backward Euler formulation is used for the time derivative. After the time linearization of the fluxes the difference equation reads

$$[\frac{1}{\Delta t} + \delta_\xi \widehat{A} + \delta_\eta \widehat{B} - \frac{1}{Re}(\delta_\xi \widehat{C} + \delta_\eta \widehat{D})]^n \Delta\widehat{Q}^n = -Res(\widehat{Q}^n) \tag{32}$$

with $\Delta\widehat{Q}^n = \widehat{Q}^{n+1} - \widehat{Q}^n$, where the superscript n denotes the time level, and $\widehat{A}, \widehat{B}, \widehat{C}, \widehat{D}$ are the Jacobian of the corresponding fluxes $\widehat{F}, \widehat{G}, \widehat{S}$ and $\widehat{T}$. Using for example the flux splitting concept the Jacobian of the Euler terms split up in two terms, like

$$\delta_\xi \widehat{A} = \delta_\xi (\widehat{A}^+ + \widehat{A}^-)$$

and are treated in the same way as the fluxes, using the MUSCL approach. For steady-state calculations, where time consistency is not required, the solution matrix of equation (32) is simplified using first order upwinding only. Thus the matrix to be inverted consists of tridiagonal block systems in each direction.

Even for this case the implicit scheme (32) requires the inversion of a large system of difference equations. Since the solution matrix is diagonally dominant resulting from the upwind differences, an iterative relaxation procedure is employed to the unfactored scheme allowing large time steps. Then the iterative procedure from time level n to n+1 reads

$$[\frac{1}{\Delta t} + \delta_\xi \widehat{A} + \delta_\eta \widehat{B} - \frac{1}{Re}(\delta_\xi \widehat{C} + \delta_\eta \widehat{D})]^n \Delta\widehat{Q}^\nu = -Res(\widehat{Q}^n) \tag{33}$$

where the superscript ν is the iteration index and $\Delta\widehat{Q}^\nu = \widehat{Q}^{n+1,\nu} - \widehat{Q}^n$. The iteration of equation (33) is performed by either a collective point or line Gauss-Seidel relaxation in alternating directions. The iterative procedure is stopped if $max|\Delta\widehat{Q}^{\nu+1} - \Delta\widehat{Q}^\nu| \leq \epsilon$ where ϵ is a small number. For more details see [28].

4.2 Runge-Kutta Time-Stepping Scheme

The second method which has been applied to the Navier-Stokes equations is the explicit Runge-Kutta method. Considering the equation (30) as a semi-discrete approximation of the time-dependent Navier-Stokes equations, the time discretization can be carried out as a sequence of intermediate steps in the sense of the classical Runge-Kutta method. At present a version of the Runge-Kutta method is used which has been successfully applied to Euler and Navier-Stokes equations e. g. by Jameson [35]. In contrast to the present work, central differencing with artificial damping was used in this paper.

For a N-step Runge-Kutta method the scheme for equation (30) reads

$$\begin{aligned} Q^{(0)} &= Q^n \\ &\vdots \\ \Delta Q^{(l)} &= -\alpha_l \Delta t \, Res(\widehat{Q}^{(l-1)}) / J \\ Q^{(l)} &= Q^{(0)} + \Delta Q^{(l)} \end{aligned} \left.\begin{aligned}\\ \\ \\ \end{aligned}\right\} \quad l = 1, \dots, N \tag{34}$$

$$\begin{aligned} &\vdots \\ Q^{n+1} &= Q^N \end{aligned}$$

In the present paper a 5-step Runge-Kutta scheme was adapted for a maximum Courant number which is 4.0 for the central and 3.5 for the upwind scheme. The upwind scheme shows the lower Courant number but the better high frequency damping, which is of advantage for the multigrid treatment.

To accelerate the convergence to the steady-state solution local time steps can be used which are dictated by the local stability limit and constant Courant number. The local time stepping allows a faster signal propagation, and thus faster convergence. A second acceleration technique is the implicit residual smoothing [35], for which a Runge-Kutta step of Eq (34) reads:

$$(1 - \varepsilon\,\delta_{\xi\xi})(1 - \varepsilon\,\delta_{\eta\eta})\,\Delta Q^{(l)} = -\alpha_l\,\Delta t\,Res(\widehat{Q}^{(l-1)})/J \tag{35}$$

with smoothing coefficients ε of $0(1)$ the CFL number can be increased by a factor of two to three.

5 Multigrid Formulations for the Solution of the Navier-Stokes Equations

The multigrid method is known to be the most efficient method for solving elliptic partial differential equations. The basic concepts of multigrid methods were formulated by Brandt [36],[37]. Encouraged by this success attempts were made to take up the multigrid concept in solution methods for time-dependent, parabolic or hyperbolic problems. Here, of very great interest are the numerical solutions of the conservation equations, which require a large amount of computational work for practical problems. Thus, to reduce the computational work, a number of investigations were made to incorporate the multigrid concept into existing methods of solution for the Euler- and Navier-Stokes equations, as well. Examples for multigrid applications in explicit and implicit Euler solutions are given by Chima, Johnson [38], Ni [39], Jameson [35], and by Hemker [41], Mulder [42] and others. Navier-Stokes applications can be found e. g. in the paper of Shaw, Wesseling [69], Thomas et al [44], Schröder, Hänel [28], and Radespiel,Swanson [40], Jameson,Siclari [46].

In the present paper the multigrid methods will be discussed for two basic solution concepts, an explicit scheme, and an implicit relaxation scheme.

Because of the different structures of the implicit and the explicit scheme the multigrid method is employed in different ways. In the present implicit relaxation method the multigrid method is used to accelerate the iterative matrix inversion each time step. Thus it is part of the relaxation procedure for each time step, and therefore called indirect multigrid method. For the explicit scheme the multigrid concept is applied in space and time, as well. It directly influences the solution in time and therefore is called direct method. A common requirement for the application of both multigrid formulations is the property of smoothing out the high frequency error components by the scheme. This requirement is satisfied in principle by the use of an upwind scheme. The common basic multigrid concept for both methods is the Full Approximation Storage concept (FAS) [37] which is employed in the present study and will be described briefly in the next section.

5.1 Full Approximation Storage Multigrid Concept

Brandt [37] has proposed the Full Approximation Storage (FAS) multigrid concept for the application to nonlinear equations. Therefore it was adopted in the present solution of the Navier-Stokes equations. Consider a grid sequence $G_k, k = 1, \ldots, m$ with the step sizes $h_k = 2h_{k+1}$ etc.

A finite difference approximation $L_m Q_m = 0$ on the finest grid G_m may be represented after some solution (smoothing) steps on a coarser grid G_{k-1} by a modified difference approximation:

$$L_{k-1}Q_{k-1} = \tau_{k-1}^m \tag{36}$$

where τ is the "fine to coarse defect correction" and refered to as the "discretization error" in the following. It maintains the truncation error of the fine grid G_m on the coarser grids G_{k-1} and is defined by

$$\tau_{k-1}^m = \tau_k^m + L_{k-1}(I_k^{k-1}Q_k) - II_k^{k-1}(L_kQ_k) \tag{37}$$

where I and II are restriction operators from grid G_k to G_{k-1} which are applied to the variable Q_k and the difference approximation L_kQ_k, as well. These operators can be used as injection or full weighting operators.

On the coarse grid G_{k-1} equation (36) is solved and the transfer (37) is repeated for the next coarser grid until the coarsest grid is reached. After some solution steps on the coarsest grid the solution is interpolated back to the finer grids with some solution steps in between.

According to the FAS scheme only the correction between the "old" fine grid solution Q_{k+1}^{old} and the "new" coarse grid solution Q_k is transfered to the fine grid e.g.·

$$Q_{k+1}^{new} = Q_{k+1}^{old} + I_k^{k+1}(Q_k - I_{k+1}^k Q_{k+1}^{old}) \tag{38}$$

Herein I_k^{k+1} is the interpolation operator, where so far only bilinear interpolation is used.

The described multigrid procedure corresponds to a typical cycle (V-cycle).

In a similar way as for the scheme, Eq. (36), the boundary conditions have to be corrected on the coarser grid. Let $\quad C_m Q_m + g_m = 0\quad$ be any boundary approximation on the finest grid, then the FAS correct approximation on the coarser grid is:

$$C_{k-1} Q_{k-1} + g_{k-1} = \tau_{B k-1}^m \tag{39}$$

$$\text{where} \quad \tau_{B k-1}^m = \tau_{B k}^m + C_{k-1}(I_k^{k-1} Q_k) + g_{k-1} - I_k^{k-1}(C_k Q_k + g_k) \tag{40}$$

For time-accurate computations this correct form should be used to avoid an larger truncation error. If the multigrid method is considered only for steady-state solutions, simplifications of the coarse grid boundary conditions can be used. One approach is to use frozen boundary conditions on the coarse grid while updating them only on the fine grid. This is a reasonable simplification, e. g. for a node-centered scheme, where the nodes (variables) are defined on the boundary itself. In schemes, like a cell-centered scheme [35], where the boundary is located between two nodes, the coarse grid boundary conditions can be used as for the fine grid (without correction), but then, only their change on the coarser grids is transfered to the fine grid using the FAS interpolation.

Different formulations are possible for the restriction operator (fine to coarse grid). The best way is to update the coarse grid values by the values of the fine grid cells that make up one coarse grid cell. This yields the full weighting restriction, e.g. for the residiual it is

$$II_k^{k-1} Res_k \widehat{Q}_k = \sum_{\text{fine cells}} \beta \, Res_k \widehat{Q}_k \tag{41}$$

where β is a weighting factor. In some cases (e.g. in node-centered meshes) the simple injection (point-to-point) can be used, which reads E.g. for the conservative variables $Q, (not \, \widehat{Q})$,

$$I_k^{k-1} Q_k = Q_k \tag{42}$$

The final formulation of the restriction depends on the mesh arrangement and on the degree of approximation of the multigrid scheme used.

5.2 Indirect Multigrid Method for a Relaxation Scheme

The purpose of multigrid is to reduce the large computational work of the matrix inversion each time step of a relaxation scheme Eq. (33). Similar concepts for the Euler equations were used e.g. in [41],[42]. In [28] this concept was applied to the iterative matrix inversion of the upwind relaxation method, according to Eq. (33). By use of the upwind discretization and flux-vector splitting the scheme becomes sufficiently dissipative and then the iterative procedure corresponds to a solution of a discrete quasi-elliptic system, which guarantees an efficient use of the multigrid method. On a coarser grid G_{k-1} the relaxation procedure, Eq. (33) is approximated by Eq. (36)

$$LHS_{k-1}^n \Delta \widehat{Q}_{k-1}^\nu + Res_{k-1}(\widehat{Q}_{k-1}^n) = \tau_{k-1}^m \tag{43}$$

with the discretization error

$$\tau_{k-1}^m = \tau_k^m + LHS_{k-1}^n(I_k^{k-1} \Delta \widehat{Q}_k^\nu) + Res_{k-1}(I_k^{k-1} \widehat{Q}_k^n) - II_k^{k-1}[LHS_k^n \Delta \widehat{Q}_k^\nu + Res_k \widehat{Q}_k^n] \tag{44}$$

After some relaxation sweeps on every grid level including the coarsest one, the correction $\Delta \widehat{Q}^\nu (not \, \widehat{Q}^{n+1,\nu})$ is interpolated back to the finer grids according to Eq. (38).

$$\Delta Q_{k+1}^\nu = \Delta Q_{k+1}^\nu + I_k^{k+1}(\Delta Q_k^\nu - I_{k-1}^k \Delta Q_{k+1}^\nu) \tag{45}$$

followed by one relaxation sweep on each grid to smooth the interpolation errors. The V-cycle is completed after the finest grid is reached and in general the next time step is carried out after one or two V-cycles.

The present scheme was developed for a node-centered mesh and therefore the simple point-to-point injection, Eq. (42), could be used for the restriction I of $\Delta \widehat{Q}^\nu$. The volume-weighted restriction II, Eq. (41), over the nine neighbouring fine grid cells is employed for the difference operator and the residual. Bilinear interpolation is used in Eq. (45). The boundary conditions were employed explicitly with respect to the iterative level on the finest grid only and remain unchanged on the coarser grid. The present method extended to 2-D, curvilinear grids is described by the authors in [28]. The method was applied and tested for different flow ranges. In the following the convergence behaviour of the multigrid method is demonstrated for two typical subsonic and supersonic solutions of the Navier-Stokes equations.
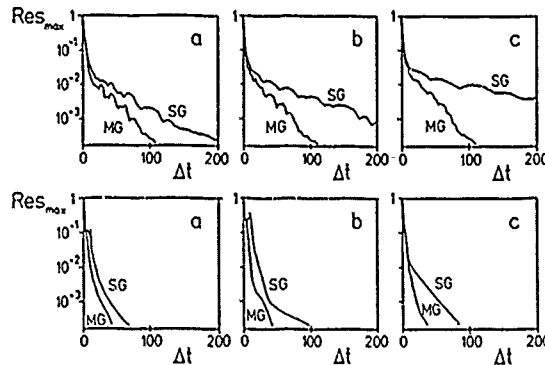
Fig. 3. Viscous subsonic flow past a flat plate
with $Re = 10^4, Ma = .9$

(N.-S.eq's,upwind relaxation method,
indirect MG)
Maximum residual versus time steps
for single-grid(SG) and multigrid(MG)
a) 2 grids, fine grid 17x17 points
b) 3 grids, fine grid 33x33 points
c) 4 grids, fine grid 65x65 points

Fig. 4. Viscous supersonic flow past a wedge
with $Re = 10^4, Ma = 2.0, \beta = 10°$

The subsonic boundary layer flow and the supersonic viscous flow over a wedge were computed to demonstrate the capability of the multigrid method. The history of convergence for different fine meshes as shown in Fig. 3, and Fig. 4 for the single grid (SG) and multigrid (MG) method. Always based on the same coarsest grid, two-, three-, and four-grid methods have been built up for the same integration domain. In general the rate of convergence of the single grid method decreases for both cases with increasing number of grid points, whereas for the multigrid method the rate is nearly independent of the number of grid points.

The present multigrid method was applied to different viscous, subsonic and supersonic flow problems, [28], [47], and has shown to be a reliable and effective method. In the different viscous flow cases computed with the present multigrid concept the estimated gain against single-grid methods was about a factor of two to twenty depending on the flow problem.

5.3 Direct Multigrid Method for Steady-State Solutions

For this method the multigrid procedure is employed directly on the time-dependent solution. In contrast to the indirect method the time advances also on the coarser grids. Applied to an explicit scheme the advantage of multigrid is twofold: first, computational time is saved because of the smaller number of grid points on the coarser grids and secondly, the time steps restricted by the numerical stability can be chosen larger on the coarser grids. In principle the direct method can be used for an implicit method as well.

Considering an explicit time-dependent algorithm as a solution method for steady-state solutions only, simplifications of the multigrid procedure are allowed as long as the steady-state solution is not impaired. The aim is the construction of an effective acceleration technique for explicit schemes to reduce the drawback of the time-step restriction. In this manner the multigrid method was succesfully used e. g. by Jameson [35] and other authors for accelerating the explicit Runge-Kutta time-stepping method.

In the present studies the behaviour of the direct multigrid procedure for the Runge-Kutta scheme with flux-vector splitting was investigated for different viscous flow problems.

Employing the FAS-multigrid procedure, Eq. (36), to the Runge-Kutta scheme, Eq. (34), an intermediate Runge-Kutta step on a coarser grid reads:

$$Q_{k-1}^{(l)} = Q_{k-1}^{(0)} - \alpha_l \Delta t_{k-1} \left(Res_{k-1} Q_{k-1}^{(l-1)} - \tau_{k-1}^m \right) / J_{k-1} \tag{46}$$

The discretization error τ between the fine grid "m" and the coarse grid "$k-1$" can be split in two terms:

$$\tau_{k-1}^k = (\tau_{k-1}^k)_{Res} + (\tau_{k-1}^k)_{time} \tag{47}$$

The first part of the discretization error corrects the spatial accuracy on the coarser grid and is defined by.

$$(\tau_k^{k-1})_{Res} = Res_{k-1}(I_k^{k-1} Q_k) - II_k^{k-1} Res_k(Q_k) \tag{48}$$

Approximating the time derivative of Q in the Runge-Kutta algorithm by $\Delta Q/\Delta t$ the second term can be written as:

$$
\begin{aligned}
(\tau_k^{k-1})_{time} &= \left[I_k^{k-1} \left(Q_k(t^{\tilde{n}}) - Q_k(t^{\tilde{n}} - \Delta t_{k-1}) \right) \right] \cdot J_{k-1}/\Delta t_{k-1} \\
&\quad - II_k^{k-1} \left[\left(Q_k(t^{\tilde{n}}) - Q_k(t^{\tilde{n}} - \Delta t_k) \right) \cdot J_k / \Delta t_k \right]
\end{aligned} \tag{49}
$$

where $t^{\tilde{n}}$ is the time when the grid level is changed. If the time steps Δt_k and Δt_{k-1} on the fine and on the coarse grid are different, then the variables on several fine grid levels have to be stored to establish time-accurate correction on the coarser grids.

One aim is to study the different multigrid influencing the convergence to steady-state. In a brief summary the important factors are:

- *high frequency damping properties of the basic solver* The Fig. 5. demonstrates, that different schemes with sufficient lead to similar rates of convergence.
- *grid arrangement* The Fig. 6 demonstrates similar convergence for cell-centered and node-centered grids, if the restriction operators and the coarse grid correction τ is appropriate chosen.
- *coarse grid boundary conditions* The investigations have shown that the more correct FAS formulation, Eq. (39) shows an advantage against simpler approximations, like frozen conditions. (see Fig. 7.).
- some other factors more, like multigrid cycle arrangement, number of smoothing steps, aspect ratio of grid cells, etc.
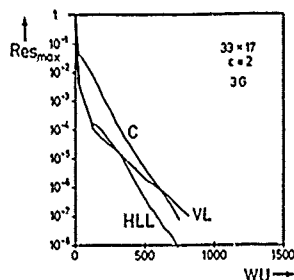
Fig. 5. Maximum residual versus work units.
Subsonic flow past a flat plate
with $Ma = .5, Re = 10^4$.
N.-S.eq's, Runge-Kutta method,
direct MG method.
Influence of different Euler solvers
VL flux-vector splitting, van Leer
HLL flux-difference splitting, Harten, Lax, Leer [45]
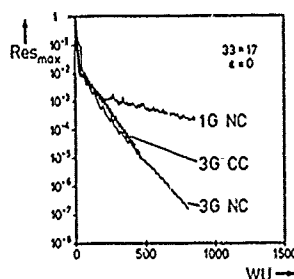C Central scheme + 4th order damping

Fig. 6. Influence of mesh configurations.
Legende see Fig. 5
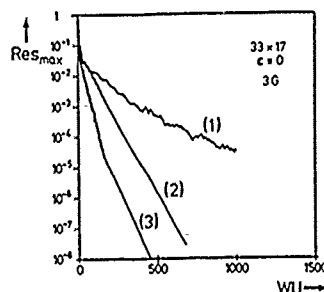NC node-centered mesh
CC cell-centered mesh

Fig. 7. Influence of coarse grid
boundary conditions.
Legende see Fig. 5.
(1) single grid solution
(2) MG, frozen boundary conditions
(3) MG, FAS- corrected
boundary conditions

The present studies were focused essentialy to subsonic, viscous flows. However in the literature multigrid application can be found for supersonic flow, too.

An explicit Runge-Kutta scheme with local time stepping and residual smoothing was presented by Siclari,Jameson [46]. A multigrid algorithm has been applied to the computation of both inviscid, and viscous supersonic/hypersonic conical flows. With the exception of one case, the multigrid algorithm reduced the computational time by at least a factor of two, whereby the multigrid gain was somewhat better for viscous flow (since the explicit non-multigrid scheme slows down due the viscous grid streching). Fig. 8, taken from [46], shows the convergence history for the multigrid and single grid time stepping method, applied to the calculation of the inviscid, and visccous flow over a circular cone.

The present investigations of the direct multigrid method and that in the literature have shown that the multigrid concept is a useful tool to reduce computational work, in particular for Navier-Stokes solutions. However the multigrid concept introduces a number of additional parameters to be adapted for succesful computations. To our experiences the largest gain even for steady-state calculations, was achieved when the multigrid elements were consequently formulated according the FAS concept.

Continuing investigations of the direct multigrid method concern with its use for unsteady solutions. Preliminary results are discussed in [49].
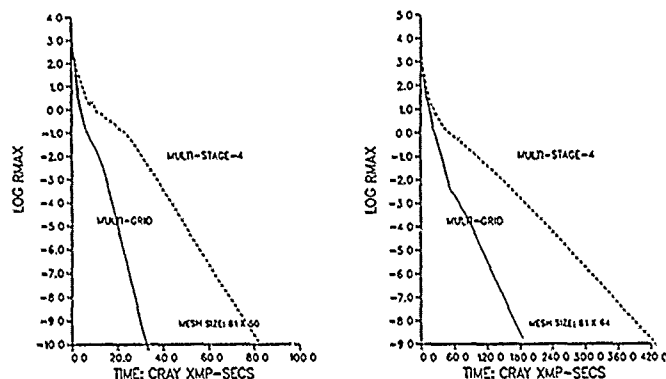
Fig. 8 Multigrid convergence of Runge-Kutta time stepping scheme solving the Euler equations(left), and the Navier-Stokes equations (right) for the flow over a circular cone at $Ma = 2.0, \alpha = 25°$ (Results taken from [46]).

6   On the Influence of Numerical Damping

The numerical damping summarizes the effects of dissipative, but also dispersive parts of the discretization error. In numerical solutions of the conservation equation the effects of numerical damping are essentially caused by the approximation of the Euler equations. Although the exact solution of the hyperbolic Euler equations is non-dissipative, a certain amount of numerical dissipation has to be included to capture shocks and to damp high frequency errors. This dissipation however impairs the accuracy of the solution. Since the Euler equations make an important part of the Navier-Stokes equations, the effects of numerical dissipation influence the viscous solution as well.

6.1   Numerical Damping in Solutions of the Euler Equations

The Euler equations form a nonlinear, hyperbolic system of partial differential equations, for which two classes of solution exist, the strong continuous solutions describing the non-dissipative wave transport along characteristics, and the weak, discontinuous solutions representing e.g. shocks. An efficient numerical method of solution has to capture both classes of solutions sufficiently well.

In numerical methods the differentials are approximated by differences (or elements) over finite step sizes. The truncation or discretization error, which is the difference between the differential and the corresponding difference approximation, consists of even and odd higher order derivatives, which are responsible for the dissipative and dispersive errors. Particularly the dissipative parts act viscosity-like and cause smearing of the solution or artificial vorticity production. Therefore the aim of the numerical approximation should be to minimize the amount of numerical dissipation.

On the other side a certain amount of numerical damping is necessary in the methods of solution to avoid the accumulation of randomly distributed small errors. Such errors can be external errors, like round-off errors, or can be caused internally by frequency amplification due to the nonlinear convection terms. In general, these errors are distributed with smallest resolvable wave length which is in the order of the step sizes. Therefore damping terms have to be included to filter these high frequency components without impairing the lower frequencies.

A widely used approach for such high frequency damping terms is to use fourth order differences, which have a sufficient filter effect and are small of $O(\Delta x^3)$ in smooth solutions. Such terms are internally generated by the scheme, e.g. in high resolution schemes, or have to be added artificially as in central schemes. These high frequency damping terms are efficient in smooth regions, but fail in regions of captured, stronger discontinuities. The finite difference methods treat such embedded discontinuities like continuous solutions, but due to the strong changes over a few grid points strong oscillations can be induced which are mainly caused by the frequency amplification of the nonlinear convection terms. Such solutions are not acceptable and therefore additional shock capturing terms have to be included into the Euler solver. Usually, such terms are based on second order differences with a nonlinear viscosity-like coefficient which produces a strong dissipation within the "shock layer" but vanishes outside in smooth regions. Again such terms can be added artificially as in central schemes, or are included into the scheme, as in high resolution upwind schemes.

Central Schemes for the Euler equations are a widely and very early used concept for the numerical solution of the Euler and Navier-Stokes equations. Examples for such schemes are the schemes by MacCormack [50],

by Beam and Warming [34] and by Jameson et al. [32]. These schemes use the averaging, Eq. (28), and thus lead to second order accurate solution methods in space. The truncation error has only dispersive part (odd derivatives) and therefore has no dissipative mechanism. Already in the early attempts artificial dissipative terms were added for this reason, e. g. in [51].

In the present state of art there exist formulations for the artificial damping terms which are commonly used. These damping formulations consist of a linear fourth order term $D^{(4)}$ and of a nonlinear term $D^{(2)}$. Then the one-dimensional Euler equations read:

$$\frac{\Delta Q_i}{\Delta t} + \frac{F_{i+\frac{1}{2}} - F_{i-\frac{1}{2}}}{\Delta x} + D_i^{(4)} - D_i^{(2)} = 0 \tag{50}$$

The high frequency damping term $D^{(4)}$, necessary to smooth errors of short wave lengths (e.g. round-off errors) has the form:

$$D^{(4)} = (\varepsilon^{(4)} \frac{\Delta x}{\Delta t}) \Delta x^3 \cdot Q_{xxxx} \tag{51}$$

where $\varepsilon^{(4)}$ is a user specified constant.

The shock capturing term $D^{(2)}$ has to suppress oscillations from the nonlinear terms in particular for shocks.

$$D^{(2)} = \varepsilon^{(2)} \frac{\Delta x}{\Delta t}) \Delta x \cdot Q_{xx} \tag{52}$$

The damping is controlled by the nonlinear coefficient $\varepsilon^{(2)}$, which is proportional to a constant, multiplied by the normalized curvature of the pressure. In smooth regions of pressure the term becomes very small, but is $O(\Delta x)$ in regions of strongly varying pressure. Refinements were given by various authors,

The effect of the damping terms becomes evident when considering the truncation error. Applying the numerical formulation Eq. (50) to the linear, hyperbolic model equation $Q_t + Q_x = 0$, the truncation error in space is:

$$\tau_s = (\varepsilon^{(2)} \frac{\Delta x}{\Delta t}) \Delta x \cdot Q_{xx} - \frac{1}{6} \Delta x^2 \cdot Q_{xxx} - (\varepsilon^{(4)} \frac{\Delta x}{\Delta t}) \Delta x^3 \cdot Q_{xxxx} + \ldots \tag{53}$$

Assuming the Courant number $\frac{\Delta x}{\Delta t}$ being O(1), then the artificial damping terms are of order $O(\Delta x)$, and $O(\Delta x^3)$, resp..

High resolution schemes (e.g. flux-vector or flux-difference splitting) are conservative like the central schemes, but take the advantage of the hyperbolic properties in form of discrete Riemann problems. In general they become higher order accurate by using upwind discretization. Nearly oscillation-free solutions and sharp shock representation is achieved making use of the total variation diminishing (TVD) principle [19] The development of these schemes is connected with Osher [52], Harten [19], van Leer [18] and many other authors. Because of the improved quality of the numerical solution, the high resolution schemes are used in the computational fluid dynamics with increasing tendency, although these schemes are more complicated and more costly than the central schemes.

The high resolution schemes do not use any added artificial damping terms, however since the high frequency smoothing and the shock capturing are necessary requirements, the corresponding mechanisms are implicitly included in the scheme.

A large number of high resolution schemes is existing with similar solution properties as discussed in the previous sections.

The damping properties of such an upwind scheme is strongly influenced by the extrapolation, Eq. (18), controlled by the discretization parameter κ, and by the limiter φ. This can be demonstrated by means of the spatial truncation error, derived by applying the extrapolation 18 to the linear model equation $Q_t + Q_x = 0$:

$$\tau_s = (1 - \varphi) \frac{\Delta x}{2} Q_{xx} - [1 - \frac{3}{2}\varphi(1 - \kappa)] \frac{\Delta x^2}{6} Q_{xxx} - [3(\varphi - \kappa) - (1 - \varphi)] \frac{\Delta x^3}{24} Q_{xxxx} + \ldots \tag{54}$$

The comparison with the truncation error for the central scheme with artificial damping in Eq. (53) reveals the similarity of the damping mechanisms in higher resolution schemes, which likewise generate two dissipative parts, a fourth order difference for high frequency damping, and an second order difference for shock capturing Assuming no limiting, $\varphi = 1$, the fourth order term in Eq. (54) becomes proportional to $(1 - \kappa)$ and damps as long as upwinding is used ($\kappa < 1$) but vanishes for central discretization ($\kappa = 1$). In regions of strong changes, where ($\varphi < 1$), the fourth order damping is reduced as in the blended damping formulation [32] in central schemes.

The second order term in Eq.(55) responsible for the sharp and oscillation-free solution of captured shocks, is completely controlled by the limiter φ and thus by the solution itself. The factor $(1 - \varphi)$ controls the amount of numerical viscosity added. If expanded in Taylor series, taking the limiters e.g. from [21], it yields

$$1 - \varphi \approx \frac{\Delta x^2}{2} (\frac{Q_{xx}}{Q_x})^2 \tag{55}$$

This value is very small in smooth regions, but becomes large, where $\frac{Q_{xx}}{Q_x} \gg 1$, e. g. near shock waves. Therefore the quality of the resolution of discontinuities is strongly determined by the formulation of the flux limiter φ.

The larger interest on the damping properties of high resolution schemes was concentrated on their effects in viscous flows [53],[54]. Thus further aspects are discussed in the next section.

6.2 Influence of Numerical Damping in Solutions of the Navier-Stokes Equations

A widely used way for developing a method of solution for the compressible Navier-Stokes equations is to add the viscous and heat conduction terms to a reliable working and stable Euler solver. This combination generally leads to efficient Navier-Stokes solvers, stable even for high Reynolds numbers. But in contrast to the inviscid solutions, the solutions of the Navier-Stokes equations contain very different characteristic scale length with correspondingly different types of solution. Typically are thin viscous layers with continuously, but strongly changing flow quantities, and large inviscid flow portions with discontinuous solutions, as well. Thus, the solution requires sufficient resolution and accuracy in all of these flow regimes. Computing the viscous flow at high Reynolds numbers the accuracy of the numerical solution is essentially influenced by numerical damping, caused by the discretization of the inviscid part (Euler terms) of the Navier-Stokes equations. In the solution of the Euler equations numerical dissipation is always present, and in viscous layers, where the strong gradients and curvatures occur, this dissipation becomes large and is superposed to the physical, viscous effects. Therefore the amount of the numerical dissipation in viscous flow solutions depends essentially on the type of the Euler solver used.

In the course of development and testing of methods of solutions for the Navier-Stokes equation the influence of the Euler damping on the viscous solution was found to be a crucial problem for accurate flow solutions. Therefore in the present investigation a number of different basic Euler solvers were used to study their influence on viscous steady-state flows. Results for the flux-vector-splitting scheme were published e. g. in [53]. More complicated and remarkable turned out to be the influence of the damping in viscous, unsteady flows as shown e.g. in [16]. A summary of these effects are presented in the following.

6.2.1 Viscous Steady-State Solutions

The accuracy of steady-state solutions is mainly governed by the spatial discretization and their damping properties.

Considering the classical central schemes, Eq. (50), with linear fourth order and nonlinear second order terms the investigations have shown a sufficient spatial accuracy for the boundary layer solution. The reason may be that the linear damping term can be held small per external parameters, and the nonlinear terms controlled by the curvature of the pressure, remain small in shear layers where the normal pressure changes are small. However in boundary layers with strong adverse pressure-gradients the deviations become stronger and require a careful analysis.

More attention has to be paid for the high-resolution Euler schemes within a Navier-Stokes solver. Such schemes are very well suited for capturing gasdynamical wave phenomena by using local approximate Riemann-solvers, higher order upwinding, and TVD flux limiters. These schemes achieve a sharp shock resolution by a controlled numerical dissipation which however is also generated in shear layers due to the curvatures of profiles. These aspects are discussed in several papers [53],[54]. The investigations have shown that the accuracy is influenced on the one hand by the different formulations of the Riemann solvers, and on the other by the way of constructing the higher order numerical fluxes, e. g. the flux limiter and discretization.

To show the essential influence of the different factors simplified test problems are considered in [53]. In the following some results of these investigations are shown.

The simplest problem studied was a numerical solution of the *nonlinear, scalar Burgers equation*:

$$Q_t \pm (Q^2/2)_x = (\nu Q_x)_x \qquad \nu > 0 \tag{56}$$

An exact steady-state solution of this equation is given by

$$Q(x) = Q_\infty \cdot tanh\left(\pm \frac{Q_\infty x}{2\nu}\right) \tag{57}$$

with the boundary conditions $Q(0,t) = 0$ and $Q(\infty,t) = Q_\infty$.

As a typical test problem for the full Navier-Stokes equation the *boundary layer flow* over a flat plate was considered. Since exact solutions for the problem are known, e.g. the solution by Blasius [55], numerical errors can be detected easily by comparison.
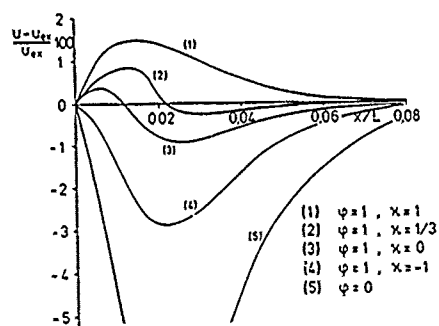
Fig. 9. Influence of the discretization on the relative error between numerical and exact solution of the scalar Burgers equation.
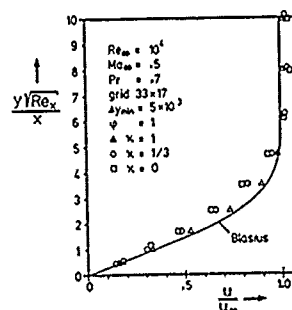
Fig. 10. Velocity distribution in the boundary layer over a flate plate (Navier-Stokes equations). Comparison of the computed results for different discretizations.

The influence of the upwind extrapolation was studied by applying Eq. (18) to both problems and varying the discretization parameter κ with $\varphi = 1$. The influence of different upwinding becomes apparently in Fig 9, where the relative error between the exact and the numerical solution of the scalar problem Eq. (56) is plotted over x. The tendency is that for smaller values of κ (i.e. more upwinding) the error becomes more negative, which means the solution tends to smear out more and more, although the schemes are higher order accurate. The Navier-Stokes solution for the boundary layer flow confirms this tendency. The Fig. 10 shows the boundary layer profiles for the flow over a flat plate using van Leer's flux splitting [26]. The different velocity profiles were achieved by varying only the extrapolation of $Q^{\pm}_{i+\frac{1}{2}}$, Eq. (18), from central to upwind discretization. Compared with the central discretization ($\kappa = 1$), which agrees well with the Blasius solution, all upwind formulations of second order accuracy ($\kappa = 0$) or even third order ($\kappa = 1/3$) tend to stronger dissipation.
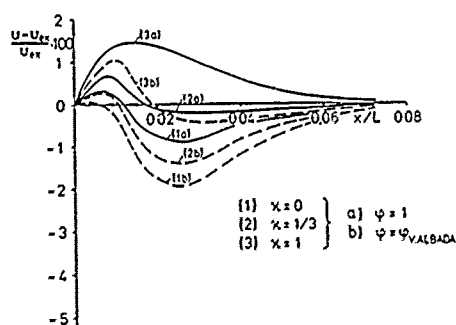

Fig. 11. Influence of a flux limiter on the relative error between numerical and exact solution of the scalar Burgers equation.
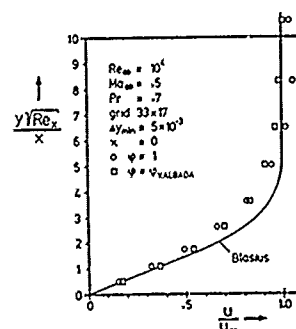
Fig. 12. Velocity distribution in the boundary layer over a flate plate (Navier-Stokes equations). Comparison of the computed results with limiter (van Albada et.al.) and without limiters.

The influence of the flux limiters is studied by applying additionally the limiter of Albada [21] to the preceding problems. The limiters control the higher order extrapolation, Eq. (18), for shock capturing. In principle they react upon the curvature by reducing the the higher order terms, which leads in smooth, viscous regoins to an undesired numerical dissipation. This tendency is clearly shown in Fig. 11 where the relative error of the scalar problem, Eq. (56), is plotted for different schemes without and with limiter. All the results with a limiter show a larger negative error, i.e. more dissipation. This behaviour is also reflected in the Navier-Stokes solution. In Fig. 12 the velocity profiles in the boundary layer are plotted for computations without limiters, $\varphi = 1$, and with a limiter (van Albada, [21]). The comparison shows that the limiters

suppress the overshooting in the outer part of the profile, but they increase the numerical diffusion in regions of high curvature. Concluding from that, limiter formulations are desired in viscous flows, which do not react so strongly to the curvature. Further investigations in [53] have shown indeed, that the different limiter formulations do it in a different strength.

The *formulation of the numerical Euler fluxes* has an essential influence on the accuracy in viscous layers. For example in Fig. 13, where the skin friction coefficient over a flat plate is plotted, the results with van Leer's flux vector splitting, [26], and with the flux difference splitting by Yee, Harten [56], in principle Eq. (26) are compared with the Blasius solution. In this case the flux difference splitting results in a more accurate solution. Both splitting schemes use similar discretization elements, only the way of constructing the approximate Riemann solver is different.
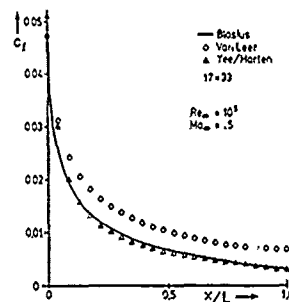

Fig. 13. Distribution of the skin friction
along a flat plate.
Solution
of the 2-D Navier-Stokes equations.
Comparison for different discretizations
of the Euler terms:

O   original van Leer flux- splitting
with upwind biased scheme $O(\Delta x^2)$

Δ   symmetric TVD scheme Yee/Harten $O(\Delta x^2)$

Deducing from that, an essential property of a Riemann solver if used within a Navier-Stokes solver should be the property that the eigenvalue along a tangential discontinuity vanishes. That is, since the boundary layer problem reduces to a tangential discontinuity in the limit $Re \to \infty$, with the no-slip condition fixed.

The flux-splitting scheme by van Leer [26] has not this property, and thus this scheme produces a large dissipation. To demonstrate this effect the boundary layer was calculated in one and the same mesh but for two Reynolds numbers $Re = 10^4$ and $Re = 10^{20}$. This physically unreasonable high Reynolds number was chosen in order to generate a practically inviscid flow with no-slip conditions. The resulting velocity profiles and the Blasius solution as a reference are plotted in Fig. 14. Although the physical boundary layer thickness for $Re = 10^{20}$ is much smaller than one step size, the numerical solution results in a thickness over several grid points.
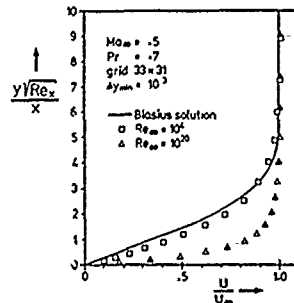

Fig. 14. Velocity distribution
in the boundary layer over a flat plate.
(Navier-Stokes solution with $\kappa = 0$
and limiter by van Albada et al.).
Comparison of the results for $Re = 10^4$
with the numerically generated boundary layer
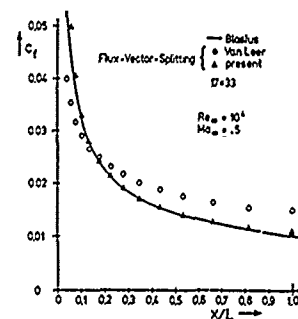for ($Re = 10^{20}$) computed in the same mesh.

Fig. 15. Distribution of the skin friction
along a flat plate.
Solution of the 2-D Navier- Stokes equations.
Comparison for different discretizations
of the Euler terms:
original by van Leer
present modification,[29]

To investigate this effect, and to improve the accuracy of van Leer's flux-vector splitting the behaviour in viscous regions was studied in more detail [29]. An analysis has shown that the upstream/downstream extrapolation for the split fluxes, Eq. (18), generates a flux defect in the case of the tangential momentum, which is strongly changing in a boundary layer profile. This defect could be essentially removed by applying one-sided upwinding in direction of the normal velocity to both split fluxes of the tangential momentum equation. It was found in test calculations, that the one-sided extrapolation of the tangential velocity reduces

the splitting error, and makes flux-vector splitting more consistent with the correct Riemann problem in particular for tangential discontinuities. The improved accuracy is demonstrated in Fig. 15 by comparison with the original formulation by van Leer. Further results are presented in [29].

6.2.2 Unsteady Viscous Flows

The temporal accuracy of a numerical solution of viscous flows is of the same importance as the spatial accuracy is, since many viscous flow problems become unsteady because of the strong interactions between viscous and inviscid flow. The computation of such flows requires sufficient accuracy in space and time. But the numerical error can hardly be estimated since both the spatial and the temporal discretization errors influence the time resolution. Furtheron due to the different scale lengths in time and space an analysis by means of scalar model equations is not sufficient to explain the numerical behaviour of a Navier-Stokes solution.

Therefore numerical experiments with solutions of the Navier-Stokes equations are necessary to detect the influence of the numerical errors. Such experiments were done recently. Results concerning with the numerical effects in time-dependent solutions of the Navier-Stokes equation are published in [16]. In this investigation the Navier-Stokes equations are solved with a Runge-Kutta time stepping scheme. Central discretization used in a cell-vertex grid system, results in a second order accurate algorithm in time and space. This method was used to study the time-dependent laminar flow over different airfoil geometries. As a typical result Fig. 16 shows the streak line patterns for the unsteady, separated flow around an NACA-0012 at high angle of attack. The periodical flow can be described quantitatively by the time history of the lift, which is a result of complex interactions between the inertia forces and separated flow. To achieve a good time accuracy about 2000 time steps per period were used. However, the numerical experiments revealed that beside of the time resolution the spatial discretization and its damping properties have a strong influence on the behaviour. To demonstrate this, the amount of the linear fourth order damping term, which is of $O(\Delta x^3)$ compared with the physical terms of the equations, was varied in a range commonly used in steady-state calculations. In Fig. 17 the history of the lift is plotted for different values of the coefficient $\varepsilon^{(4)}$ of the damping term. The results show a very different behaviour concerning the frequency and the amplitude for every case which is also reflected by the corresponding flow pattern. Similar large effects are also found by varying the grid spacing and grid arrangement.

These investigations have shown a very large influence of the numerical damping in unsteady solutions. Further work has to be done to achieve sufficiently time-accurate solutions.

Fig. 16. Instantaneous pattern of the velocity vectors for the separated flow over an NACA-0012 at high angle of attack $\alpha = 20^z$. Navier-Stokes solution from [16].
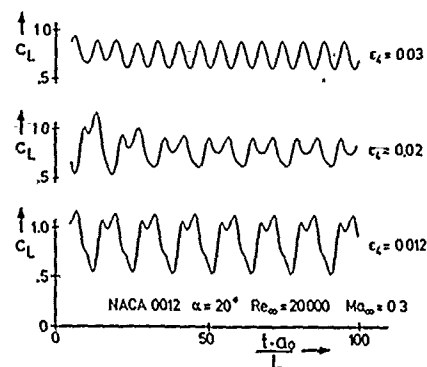
Fig. 17 Time histories of the lift coefficient for three values of the fourth order damping term (Legend see Fig. 16).

7 Applications to Hypersonic, Viscous Flows

7.1 Present upwind relaxation method by Schwane,Hänel

In this section an upwind relaxation method will be described, which is used by the authors for the computation of viscous, hypersonic flow. Some details of the method will be presented, and special features for adapting the method to the requirements of hypersonic flows will be discussed. This numerical method for solving the Navier-Stokes equations is a 3-D extension of the method published by the author in [28].

The governing equations are the 3-D thin layer approximation of the Navier-Stokes equations formulated for a curvilinear node-centered mesh. The 3-D mesh generation is carried out by the grid optimization procedure, Eq. (11), starting from an algebraic initial mesh. The method consists of an upwind high resolution scheme using flux-vector splitting for the Euler terms and central discretization for the viscous terms. The solution is carried out by an implicit relaxation procedure, as described by Eq. (33). The details of this method of solution for viscous, hypersonic flows can be found in [57],[58],[29].

Different to the former method [28] the present 3-D method uses a modified flux splitting formulation [29], [53], improved with respect to the accuracy and robustness in hypersonic, viscous flows. The improvements may be of general interest and will be explained in more next section.

7.1.1 Formulation of the flux-vector splitting for hypersonic viscous flows

Formulation of the original concept For the following discussion the 1-D Euler equations will be considered:

$$Q_t + F_x = 0 \tag{58}$$

According to the splitting concept the flux F is split into a forward flux F^+ and a backward flux F^- with $F = F^+ + F^-$. The original split fluxes by van Leer [26] read:

$$
\begin{aligned}
F_1^\pm &= \pm 1/4\rho a(u/a \pm 1)^2 \\
F_2^\pm &= F_1^\pm \cdot ((\gamma - 1)u \pm 2a)/\gamma \\
F_3^\pm &= F_1^\pm \cdot ((\gamma - 1)u \pm 2a)^2/(2(\gamma^2 - 1))
\end{aligned}
\tag{59}
$$

The split fluxes at a cell interface are updated by using forward/backward extrapolated variables $Q^\pm$ for $F^\pm(Q^\pm)$.

The favourable properties of this concept, that is smooth changes near the sonic point, and one zero eigenvalue, we want to preserve in our reformulation. However, these split fluxes are expressed by the density ρ, the velocity u and static speed of sound $a = \sqrt{\gamma p/\rho}$, which all are quantities changing strongly in high Mach number flows. Therefore they can cause stronger numerical errors, and reduce the convergence. Replacing these variables, at least partially, by less varying or even by invariant quantities an improvement in that flow regime can be expected.

Sonic Switching with the Critical Speed of Sound A drawback of the original splitting in hypersonic flows, but also of other Riemann solvers, is related to the use of the static speed of sound $a = \sqrt{\gamma p/\rho}$, which controls the eigenvalues, and thus the splitting. In strong expansions this quantity, but also p and ρ, become very small and their values can become faulty since they are calculated from the small difference between the large values of total and kinetic energy. As a consequence in implicit schemes the usual large time steps have to be reduced significantly to avoid negative thermodynamical quantities in the transient state. The scheme becomes inefficient in this case. To overcome these difficulties the splitting formulation, Eq. (60) was rearranged in this paper in order to avoid the use of the static speed of sound. Without impairing the essential properties of the original concept the splitting can be written as:

$$
\begin{aligned}
F_1^\pm &= \pm 1/4\rho\tilde{a}(u/\tilde{a} \pm 1)^2 \\
F_2^\pm &= F_1^\pm \cdot \left(u + \frac{p}{\rho\tilde{a}}(-u/\tilde{a} \pm 2)\right) \\
F_3^\pm &= F_1^\pm \cdot H_t
\end{aligned}
\tag{60}
$$

By this, the choice of the signal speed a does not influence the total flux $F = F^+ + F^-$. Therefore it can be appropriabely chosen with the only condition, that it approaches to the static speed of sound at the sonic points $Ma = \pm 1$. In van Leer's splitting a was chosen as $\tilde{a} = a = \sqrt{\gamma p/\rho}$ For our experience a more appropriate choice of $\tilde{a}$ is:

$$\tilde{a} = a^* = \sqrt{2(\gamma - 1)/(\gamma + 1) \cdot H_t} \tag{61}$$

where a^* is the critical speed of sound. The critical speed a^* is porportional to the square root of the total enthalpy and is therefore constant in isoenergetic (Euler-) flow (also in strong expansions) or only smoothly varying in viscous flows. For real gases the calculation of a^* is more complicated, but since the choice of $\tilde{a}$ is not unique an approximate relation for real gases can be found with the corresponding properties.

Split Energy Flux A further drawback of the original concept was noticed in supersonic blunt-body calculations where significant deviations of the computed wall temperature were found in regions of large Mach number gradients [53]. Investigations have shown that this effect is mainly caused by the non-preservation of the total enthalpy H_t using the original split energy flux of Eq. (60). This effect could be removed substantially by using an alternate split energy flux [53]:

$$F_3^\pm = F_1^\pm \cdot H_t \tag{62}$$

where the enthalpy H_t is transported as a whole by the split mass fluxes $F_1^\pm$. It has the advantage of being simpler and of being generally valid also in the case of real gases, where the original splitting has to be modified [59]. Since H_t is constant in isoenergetic flow, and weak varying in viscous flows smaller numerical errors are induced by this formulation. The improvement of the accuracy by this formulation is clearly demonstrated in Fig. 18 for the wall temperature distribution over an 3-D hemisphere-cylinder body.
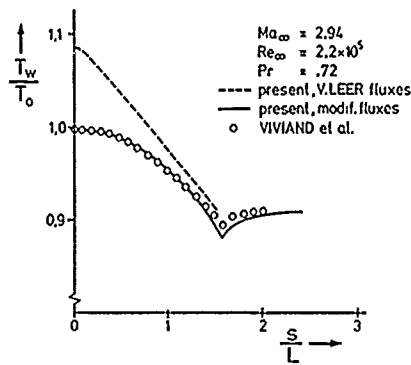

Fig.18 Wall temperature distribution related to the inflow stagnation temperature, over the arc length in the mid plane of a hemisphere-cylinder body. Influence of the modified split energy flux [53].

Modification of the Flux-Splitting for Viscous Flows Previous investigations [53], [54] have shown that van Leer's flux vector splitting used in a Navier-Stokes solver impairs the spatial accuracy in viscous regions more than other Euler schemes do. On the other hand the van Leer concept leads to reliable and efficient implicit solution methods and therefore attempts are made to improve the accuracy in viscous regions. Analysing the solution behaviour in a typical boundary layer flow the main source of inaccuracies beside of the effects of flux limiters etc. was found to be the splitting error of the tangential momentum equation at low Mach numbers. In such flows the tangential velocity u grows from zero at the wall to its large outer value u_e over a short distance δ, whereby the normal velocity v is small. Considering the Rieman problem in normal (y) direction, then the flux component $\rho v u$ of the tangential momentum is splitted according to van Leer's concept in

$$\rho v u = [\rho\bar{a}/4(1+v/\bar{a})^2 u]^+ + [-\rho\bar{a}/4(1-v/\bar{a}^2)u]^- \tag{63}$$

Assuming for simplicity $\rho a \approx const.$ and $v/a \ll 1$ it yields a remaining error

$$\rho v u \approx \rho\bar{a}/4(u^+ - u^-) \tag{64}$$

Since the curvature of u(y) in a boundary layer is large, the difference of the backward and forward extrapolated velocities $u^+ - u^-$ can become remarkable even with higher order extrapolation. This error was found to be responsible for the strong smearing using flux vector splitting in viscous layers.

This error, Eq. (64), can be completely removed if the tangential velocity u is extrapolated from one direction only i.e. either u^+ or u^-. This one-sided extrapolation is also motivated by the consideration of the Riemann problem at the cell interface. The characteristics updating in one dimension leads to a coupled system for the pressure p, the density ρ, and the normal velocity v along the characteristics $v, v \pm a$. In two and three dimensions the additional characteristic condition requires the transport of the tangential velocity (du=0) along the characteristic v, which is decoupled from the other conditions. This means that upwinding according to the direction of the normal velocity has to be used for tangential velocity (and not from both sides). Thus the one-sided extrapolation of the tangential velocity removes not only the essential splitting error, Eq. (64), but also makes the flux vector splitting more consistent with correct Riemann problem in particular for stationary tangential discontinuities.

For the implementation in existing algorithms the velocity tantential to a cell interface was set to

$$v_t = v_t^+ \quad \text{if} \quad v_n > 0 \quad , \text{and} \quad v_t = v_t^- \quad \text{if} \quad v_n < 0. \tag{65}$$

For the other variables the usual forward/backward extrapolation is remaining. The changes in the program for the steady-state operator were small, but for the implicit part rearrangements were necessary to achieve the same favourable convergence as before.

The improvement of accuracy in a boundary layer flow is demonstrated in Fig. 15, where the skin friction distribution over a flat plate, computed with the present formulation is compared with that, using the original van Leer's splitting.

The improvement of the spatial accuracy becomes more evidently in the computation of more complex, viscous flows as shown in an example below (Fig. 24 and 25).

Formulation of the Implicit Part at Hypersonic Speeds   In the original version of the algorithm the implicit operator (left hand side LHS(Q)) in Eq. (33) consists of the Jacobians of the split fluxes derived with respect to the conservative variables, e.g.:

$$\widehat{A}^{\pm} = \frac{\partial \widehat{F}^{\pm}}{\partial \widehat{Q}} \tag{66}$$

Herein most of the elements of the Jacobians are divided by the density ρ. For reasonable large values of the density no problems arise by that, but in hypersonic flows the density can approach zero, and the solution matrix becomes singular with the corresponding consequences for the convergence. Therefore in the present paper the implicit part was reformulated using non-conservative variables V with

$$V = (\rho, u, v, w, \varepsilon)^T \tag{67}$$

Then the implicit relaxation scheme, Eg. (3), reads:

$$\widetilde{LHS}(V^n) \cdot (V^{n+1} - V^n) = -Res\,Q^n \qquad \text{with} \quad Q^n = Q(V^n) \tag{68}$$

The new implicit operator $\widetilde{LHS}(V^n)$ contains the Jacobians derived with respect to the non-conservative variables, e.g.

$$\tilde{A}^{\pm} = \frac{\partial F^{\pm}}{\partial V} \tag{69}$$

which now are not divided by the density or by any other critical quantitity. Thus the good convergence properties of the scheme remain in hypersonic flow, even if strong expansions are present. Additionally, by this formulation the structure of the Jacobians becomes simpler.

7.1.2   Boundary Conditions and Shock Fitting

The present algorithm was applied to the computation of the viscous, super/hypersonic flow around blunt bodies. The domain of integration is bounded by three typical boundaries, which are formed by the bow shock, by the body contour and by the outflow boundary.

On the body the boundary conditions are given by the no-slip and thermal conditions at the wall, Eq. (9).

The outflow boundary conditions are less unique than the wall conditions, because a more or less arbitrary flow field is cutted by the boundary. As long as the outflow is supersonic and the boundary layer is attached a well-suited boundary condition is given by simple extrapolation of the boundary values from the interior. In the case of flow separation this condition becomes inaccurate, since information about the downstream state is necessary. However this state is unknown, more sophisticated conditions cannot be prescribed. The only way would be to shift the boundary in regions of more regular flows, where information are available (attached flow, known outflow pressure). In the present blunt body problem this way was not possible without significant increase of computational effort, therefore the simple extrapolation was used also in the case of separation. The result have shown to be reasonable despite of the cutted separation zone in some cases.

A shock-fitting procedure is applied at the outer boundary, so that the position of the detached bow shock is a result of the calculation. The state behind the shock is determined by the jump conditions over the shock, and the shock position by a simplified compatibility condition. Starting from a guessed shock position the variables behind the shock are calculated from the Rankine-Hugoniot relations and used as boundary conditions for the inner field. After one time step the solution is advanced and a corrected value of the pressure can be extrapolated from the interior flow field to the shock. From this pressure value and from the local shock slope a transient free stream Mach number $Ma_{n,\infty}^{\nu}$ in normal direction can be calculated, using the pressure relation over the shock. The difference of this Mach number and of the prescribed Mach number $Ma_{n,\infty}$ yields the local normal shift of the shock:

$$\overrightarrow{\Delta r}^{\nu} = a_{\infty}\Delta t \left(Ma_{n,\infty}^{\nu} - Ma_{n,\infty} \right) \tag{70}$$

3.36 The distribution of the normal shift vector $\Delta \vec{r}$ on the shock surface is not smooth in general, an effect which is amplified by the irregular grid point distribution resulting from the strongly stretched inner mesh with mesh singularities. The result would be an wriggled shock surface which again results in wrong inner shock conditions. Therefore the main problem for fitting is to achieve a very smooth new shock surface, which however should allow jumps in the slope due to secondary shocks coming from the inner domain. The smoothing of the shock surface was carried out in two steps. First the shift, Eq. (70), was interpolated in a new triangulated grid of the surface with regular cell size, which shows no singularities. The new shock position in the new grid is additionally smoothed by requiring locally minimum curvature. This was done in an iterative procedure. The final position is then redistributed to the original computational grid by interpolation. This fitting procedure avoids the problems near grid singularities and allows time steps as large as used in the inner scheme.

7.1.3 Results

As a typical hypersonic application of the present method results are shown for the flow around a double-ellipsoidal body. This problem, defined and experimentally studied in [60], is likewise used as a test case in the *HERMES R&D* program [61].
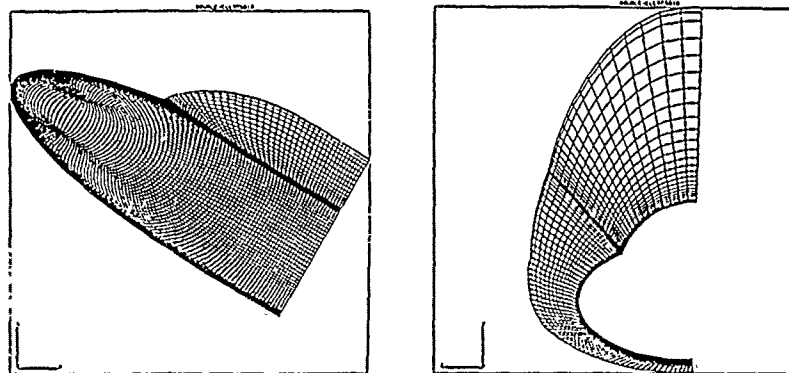

Fig.19 Computational mesh (250.000 grid points) on the surface of the body (left) and in the outflow plane (right) for the computation of the flow around a double-ellipsoidal body.
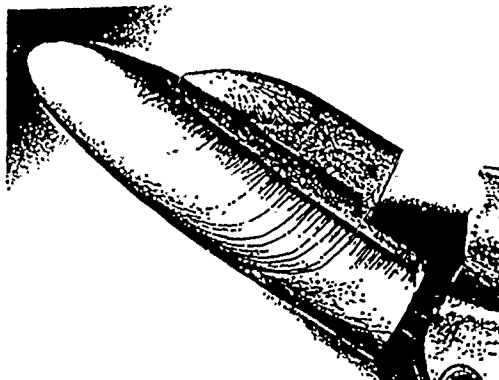

Fig.20 Experimentally observed oil-flow pattern for the double-ellipsoid with $(Ma = 8.15, Re = 2 \cdot 10^6, \alpha = 30°.)$
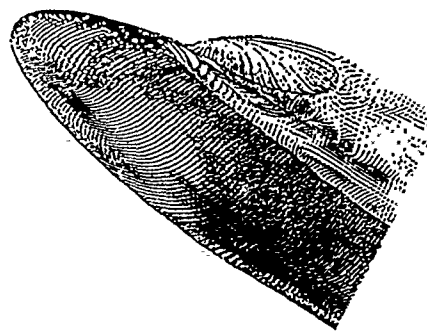
Fig.21 Vectors of the local skin friction on the body surface using a mesh of 250.000 grid points. $(Ma = 8.15, Re = 2 \cdot 10^6, \alpha = 30°.)$

The mesh used for this body is shown in Fig. 19 for the body surface and for the outflow plane. Herein an additional subgrid was used to avoid the strong singularity of a single mesh, the number of grid points in this example was 250.000. The following results refer to a flow with $Ma_\infty = 8.15$, $Re_\infty = 2 \cdot 10^6$, $T_0 = 800K$ and an angle of attack of $30°$.

This flow is characterized by distinct separation zones, which are demonstrated in Fig. 20 by means of

oilflow patterns taken from the experiment [60]. In this figure the complex flow structure on the lee-side becomes apparent with the primary separation enrolling to a vortex, and with a secondary reattachment and separation on the second ellipsoid ("canopy"). Using the fine mesh of 250.000 points the oilflow pattern of Fig. 20 was numerically simulated by plotting the shear stress vectors on the surface in Fig. 21. The comparison of Fig. 21 with the experimental picture, Fig. 20, shows a close agreement.

The isomach lines in the symmetry plane are plotted in Fig. 22. The patterns show the fitted bow shock, the "canopy" shock and a strong separation on the "canopy". A further separation is induced at the foot of the "canopy" shock. The main cross flow separation near the large axis of the first ellipsoidal is clearly demonstrated in Fig. 23, where the isomach lines are plotted in the outflow plane.
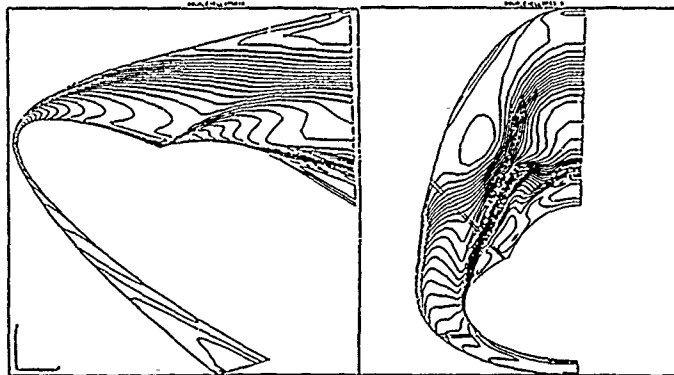

Fig.22 and Fig.23 Isomach lines in the symetry plane and in the outflow plane
(Legend see Fig.21)

These results were achieved with the algorithm, described above, including all the modifications for hypersonic flow, but with exception of the modification for viscous flow, Eq. (65), which was implemented later. Without this modification the Euler part generates a remarkable numerical dissipation due to the splitting error demonstrated in Eq. (63). This fact is demonstrated in Fig. 24, where the same problem is recomputed using a much coarser grid of 60.00 points only. Comparing the shear stress vectors in Fig. 24 with the fine grid solution, Fig. 21, and with the experiment, Fig. 20, a poor agreement on the lee-side can be stated which clearly is a result of the numerical dissipation due to the splitting error.
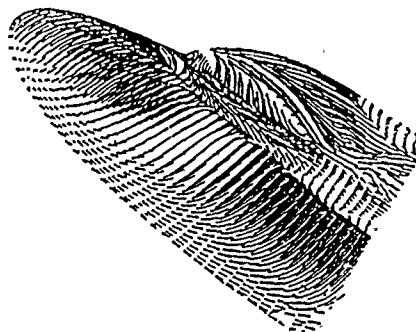

Fig.24   Vectors of the local skin friction
on the body surface using acoarse mesh
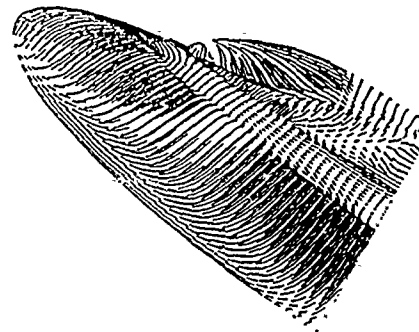of 60.000 grid points.
(Legerd see Fig.21)

Fig.25   Vectors of the local skin friction
on the body surface using acoarse mesh
of 60.000 grid points.
(Legend see Fig.21)
The comparison with Fig.24 demonstrates
the improvement of acurracy
by the new splitting [29].

Now this flow case was recomputed using the modification, Eq. (65), i.e. the one-sided extrapolation of tangential velocity in the splitting concept. Despite of the coarse mesh of 60.000 points used here as for Fig. 24, the shear stress vectors in Fig. 25 demonstrate, that nearly the same good agreement with the experiment

could be achieved as for the fine grid but without the improved numerical fluxes. This comparison and that for the simpler boundary layer in Fig. 15 have demonstrated the possibilities to improve the quality of an Navier-Stokes solver.

7.2 Selected Works for Hypersonic, Viscous Flows

In the past years the number of papers concerning with the computation of hypersonic flows is showing an increasing tendency as a consequence of the new hypersonic airplanes and space shuttle projects. Even restricting to solutions of viscous flows, the spectrum of methods and solutions is still very large. In principle most of the methods applied to the Euler equations are extentend in any way to the Navier-Stokes equations, and since many of them are sufficiently robust, they were also extented to hypersonic flows. An evaluation of the quality and efficiency becomes very difficult sinces the approaches and problems, solved are too different. Additionally a number of uncertaincos are existing with respect to the description of the physical phenomena, like laminar-turbulent transition, chemical reaction rates, and rarefaction effects. Therefore a successful development of the computational methods for reliable flow prediction requires a critical comparison of numerical, analytical and experimental results. A useful tool for that are workshops, where well-defined and validated problems have to be solved by the different methods and the solutions have to be compared. A promising workshop for hypersonic flows is the one proposed for January, 1990 in Antibes [61]. This workshop will consist of a number of well-defined 2-D and 3-D hypersonic flow problems validated by corresponding experiments.

In the present paper a selection of works concerning with hypersonic/supersonic, viscous flows will be presented to demonstrate the variety of possbile approaches for h_ personic, viscous flows, however without claiming completeness.

A possible classification can be made with respect to the degree of approximation for the governing equations of viscous flow. There are solutions for the

full Navier-Stokes equations (NS) (including Reynolds-averageu equations)

thin layer approximation (TL)

parabolized Navier-Stokes equations (PNS)

The most complete description can provide the full equations, including all the inviscid and viscous effects, also the interactions between. The thin layer approximation, although streamwise derivatives of the viscous terms are neglected, has nearly the same validity in high Reynolds number flows where viscous effects are concentrated in thin layers.

Mostly the NS or TL equations are used in a time-dependent formulation, also for steady-state solutions.

The parabolized Navier-Stokes equations correspond to the stationary thin layer equations. They allow very economical space marching methods, if applied to steady-state, supersonic flow with (in streamwise direction) attached viscous layers. In the cross flow planes flow separation is provided.

In the following some typical methods for solving the NS and TL equations will be discussed.

A first example for that was explained in more detail in the preceding chapter. This upwind relaxation method by Hänel,Schwane [29], [58] uses flux-vector splitting and is coupled with a shock fitting procedure.

An upwind relaxation scheme is applied to complex hypersonic viscous flow by Schmatz, [62]. The spatial discretization is based on the characteristic flux extrapolation approach by Eberle [63]. To increase the robustness for hypersonic flows, this approach was combined with with flux-vector splitting by Steger and Warming.

Mac Cormack in [64] follows a similar concept with line relaxation and flux-vector splitting (of Steger-Warming type). This concept was prefered for the extension to the stiff chemical equations. Preliminary results were given for simple body contours showing e.g. species conc ntrations and the different temperatures at non-equilibrium.

Likewise a fully implicit method is used by Bardina,Lombard [65], based on flux-difference splitting and on a strongly diagonal-dominant factorization and relaxation method. The bow shock is completely captured. The method was proposed to be very appropriated for chemical reactions and adaptive grid technique.

An example of an relaxation scheme, applied to the stationary Navier-Stokes equations is presented by Rieger and Jameson, [66]. In this scheme the steady-state operator is by central finite-volume discretization with artificial dissipation added. The implicit part is developed in the sense of a Newton iteration, the flux Jacobian are splitted in a simplified manner using the spectral radius of the eigenvalues. The solution is carried out with a LU-decomposition scheme. In this paper the flow around a HERMES space shuttle was computed for viscous, and inviscid flow,as well. As an interisting example, the Fig. 26 shows the iso-mach lines in a certain cross section of the shuttle for both types of flow. The comparison reveals the different formation of the vortical flow in particular in the vincinity of the body.
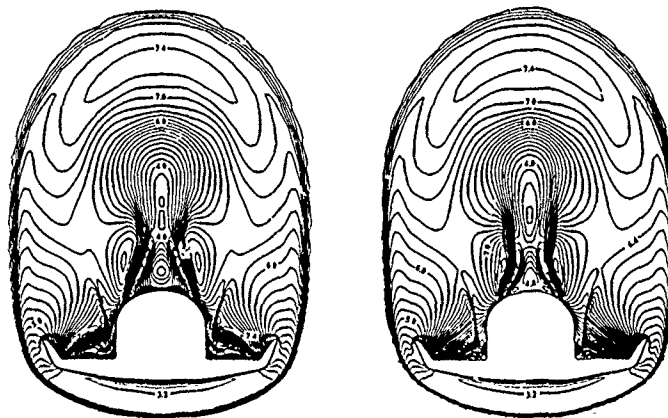
Fig.26 Computation of the 3-D flow around a space shuttle (HERMES) with $Ma = 8, Re/m = 10^6, \alpha = 30°$
Implicit LU scheme for Euler and Navier-Stokes eq's (Results from [66]).
Isomach lines in the cross section $x = 12.7m$ for viscous (left) and inviscid (right) flow

Computations using a hybrid explicit-implicit difference scheme including shock-fitting is published by Kordulla et.al. [67]. Herein a central scheme is used with the corresponding artificial damping terms. To overcome the severe time step restriction in meshes with cells of high aspect ratios the scheme is explicit in the two-direction tangential to the body, but is implicit normal to it. The equations of state for equilibrium flow are included. Results were presented for different 3-D configuration, likewise for the double-ellipsoidal test body. Similar results were shown as in Fig 20 to 25.

An example for using an explicit scheme for hypersonic flows is the "historical" paper by Mac Cormack, 1969, [68], where the well-known predictor-corrector method was applied to the Navier-Stokes equations. Also nowadays this method is in use as a reliable and cheap method of solution. A very complex application for that is given by Shang, Scherr [69], where the hypersonic flow around a complete aircraft was computed ($Ma = 5.95, Re = 1.64 \cdot 10^7/m$) with an algebraic turbulence model included.

Furtheron a large number of solutions may be mentioned presented by H. Yee [31], based on symmetric and upwind TVD-schemes.

Another class of methods of solution are based on the finite-element approach in triangulated, unstructured grids additionally using adaptive meshes.

INITIAL MESH (1071 KNOTS)

ADAPTED-MESH (2 REFINEMENT LEVELS, 2938 KNOTS)

P/Pin

• FEM-CALCULATION
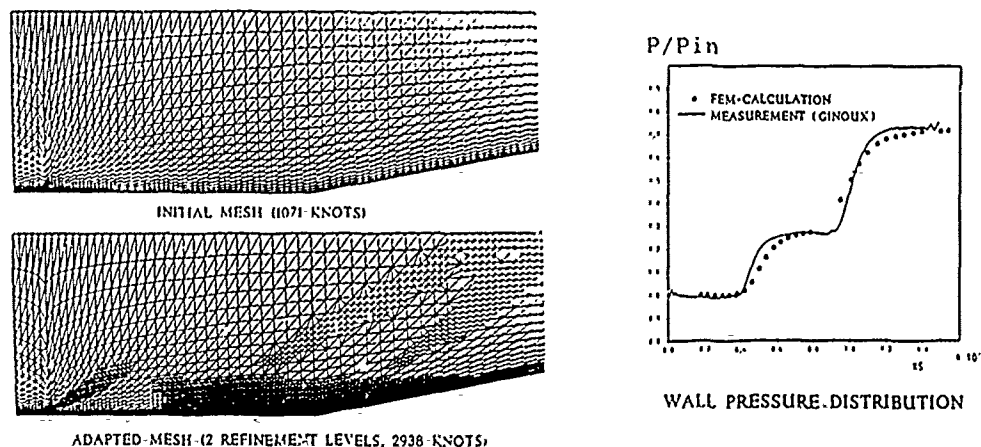— MEASUREMENT (CINOUX)

WALL PRESSURE DISTRIBUTION

Fig.27 Computation of the flow over a 10° compression ramp with $Ma = 2.25$ using a finite element
Navier-Stokes solver with adaptive mesh enrichment (Results from [71]).Initial and final mesh (left)
and comparison of the computed pressure distribution with experiment (right).

An example for the possibilities of adaptive grid enrichment in viscous, supersonic flow is taken from Koschel,Vornberger [71]. As a demonstration Fig. 27 shows the initial and final mesh and the computed pressure distribution for supersonic flow over a compression ramp. Here a two step explicit Taylor-Galerkin

finite-element method is applied to the full Navier-Stokes equations.

An application of an upwind finite-element method using unstructured triangular meshes with several layers of quadrilateral elements near solid walls is presented by Prabhu,Stewart,Thareja [72] to high speed viscous equilibrium flow. Fig. 28 shows the adapted meshes and the temperature contours for ideal, and real equilibrium gas.
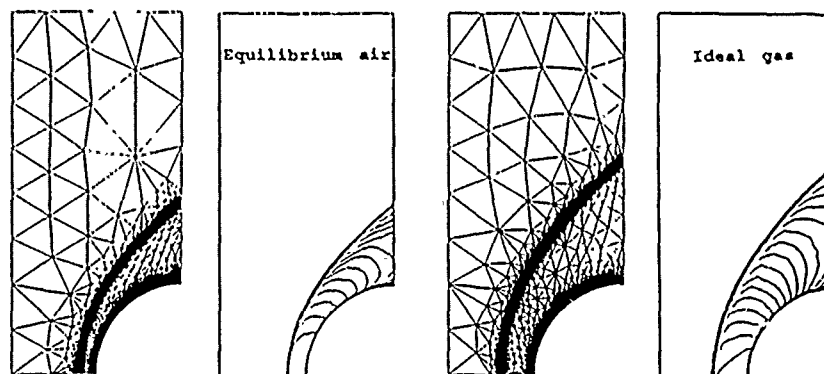

Fig.28   Adapted finite element meshes and temperature contours of ideal gas and equilibrium air
for the viscous flow past a cylinder at $Ma = 16$.
(Results taken from [72]).

A large number of 2-D and 3-D hypersonic applications of finite-element methods for reacting and non-reacting flows were presented by Periaux [70], summarizing the works of INRIA and AMD-BA in France. For the Navier-Stokes equations a Petrow-Galerkin finite-element method is used with streamline upwinding and entropy variables.

The parabolized Navier-Stokes equations (PNS) allow computations in a very economical way for flows which satisfy the presumptions. Applications can be found for the computation of supersonic, and hypersonic flow over complex geometries or complex physical flows. An example for the latter may be the paper by Prabhu,Tannehill [73], where a PNS-code is presented, solving the conservation equations for a multi-component, chemically reacting gas mixture.
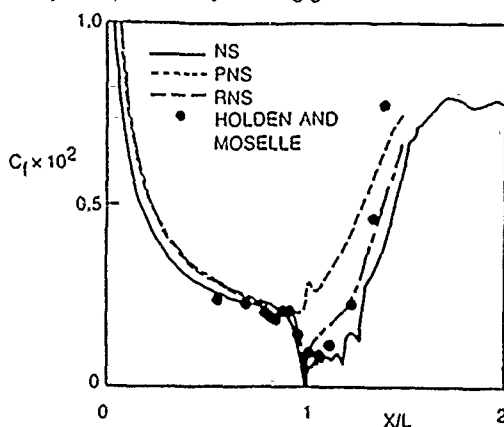

Fig.29   Comparison of the skin friction
over a compression ramp calculated
using the NS, PNS, and RNS
equations.
(Results taken from [74]).

In interesting contribution is given by Power,Barber [74], where a comparison is made between solutions of the Navier-Stokes equations (NS), the parabolized equations (PNS), and the so called reduced Navier-Stokes equations (RNS). The RNS equations correspond in their form the PNS equations, but the streamwise pressure gradient term was modified to account for the upstream propagation of pressure waves within the subsonic layers. The RNS solution is somewhat more expensive than the PNS solution, but much cheaper than the NS solution. Results are given for strong viscous/inviscid interactions on a compression ramp at Ma=14. Fig. 29 shows a comparison of the skin friction distribution using NS,PNS, and RNS procedures. The results confirm that the PNS equations are not able to describe strong interactions, even without separation, whereas the

results from the RNS equations are closer to that of the full equations.

A similar comparison was presented by Ng,Ajmani,Taylor,Brock [75] using upwind schemes for high speed viscous flow. Comparative studies were made for the PNS, TL and full NS equations. Typical factors of the CPU time were reported with 1 for PNS and 3 to 20 for the TL and NS equations depending strongly on the problem studied.

An interesting new attempt was made by Taylor,Ng,Walters [76], where the favourable properties of the PNS and NS methods was tried to combine. The algorithm depends on a decomposition of the global domain into sub-domains, where a small "elliptic" region is identified, and the remainder of the flow is identified as a single larger "hyperbolic" region. A direct solver is applied to the elliptic region, and then coupled to a Gauss-Seidel relaxation in the hyperbolic region marching in streamwise direction.

8   Conclusions

The preceding survey about some typical approaches to hypersonic, viscous flows has shown the variety of the numerical methods applicable to these problems. Despite of the variety some conclusions can be drawn or at least tendencies can be shown.

1. All the Navier-Stokes solutions for hypersonic flow require a robust, and a highly resolving Euler solver to handle the strong gasdynamical wave phenomena. The great majority of methods uses the upwind and symmtric high resolution Euler schemes, based on the TVD principle.

2. The strongest shock, the bow shock, should be treated as a discontinuity by a shock fitting procedure, this leads to a correct treatment and saves grid nodes in comparison to the capturing. The embedded shocks are usually weaker and can be captured. But examples have demonstrated that capturing of the bow shock can also be used with the advantage of avoiding the more complicated fitting procedure. Then the shock is resolved over several grid points, the number of points depends on the properties of scheme used, and on the grid arrangement (shock surface orientation). This "smearing" of the shock can be a disadvantage if smaller scale lengths, e.g. through chemical reactions, have to be resolved. Of similar importance are the strong expansions in which the thermodynamical quantities approach very small values. This can cause incorrect solutions and a loss of convergence, as stated in the preceding chapter.

3. The thin viscous layers require a fine resolution and a very accurate algorithm, since here strong gradients and curvatures are present. Special attention has to be given to the numerical dissipation of the Euler solver which is superposed the physical dissipation and impairs the viscous flow solution.

4. The survey has shown that explicit and implicit schemes are used, as well. Both types are able to capture the gasdynamical waves. However for flows at high Reynolds numbers where one spatial stepsize becomes much smaller than the others the stability restriction of the explicit schemes reduces significantly the efficiency. This restriction can be partially reduced by some acceleration techniques for steady-state computations (e.g. local time steps, multigrid etc.) With the increasing difference of the characteristic scale lentgth to be resolved (increasing stiffness), the implicit methods become more efficient since they are not restricted by the numerical stability. In particular, in chemical reacting flows where additional small scale lengths have to be resolved, this fact should be taken into account.

5. Among the implicit schemes, the number of schemes using an iterative procedure for the matrix inversion each time step (relaxation schemes), shows an increasing tendency, compared with that using non-iterative methods like approximate factorization methods. The advantage of the unfactored relaxation schemes is that the time step is really unrestricted and that different appropriate relaxation techniques can be applied (e.g. point or line relaxations, multigrid). Furtheron the most of the relaxation schemes allow a more flexible organization of the algorithm, either minimizing the storage requirement to one set of the variables plus geometry per grid point, or if sufficient storage is available CPU time can be saved by storing the quantities which are constant during the iteration loop, (doing the latter an estimation for present relaxation scheme [58] would give an gain in CPU time of five to ten).

6. Parallel to solutions on structured grids using finite difference/volume methods a large number of calculations are carried on unstructured grids mainly using finite element methods. The primary advantage of the latter is the geometrical flexibility, avoiding the mesh singularities of the structured grids, and the more economical mesh arrangement. Adaptive grid refinement by mesh enriching allows an increased accuracy in critical regions. Drawbacks of the unstructured formulation is the more expensive calculation and the increased storage requirement per grid node. The unstructured algorithm makes the vectorization more difficult. The solution method is usually restricted to (decoupled) explicit schemes,

thus the schemes may become inefficient for high Reynolds numbers due to the stability restriction. A significant difference in the quality of the computed results seems not to exist. In future developments the advantages of unstructured and structured grids, and of finite element and finite difference/volume methods should be combined.

7. A further important point is the utilization of the computer architecture, i.e. high rates of of vectorization and parallelization are required for the very expensive Navier-Stokes computations. Hereby the explicit structures are of advantage. However also the most of implicit schemes are highly vectorizable with some more efforts (and storage), in particular for threedimensional algorithms. Parallelization on mult' n ocessor machines becomes increasingly simpler with the improved software of the supercomputer manu'ic ·rers.

References

[1] First Joint Europe-US Short Course on Hypersonics. Org. by GAMNI-SMAI and Univers. of Texas at Austin, Paris, Dec. 1987, (1987). Published in: Bertin, J.J (Ed.): Hypersonic Flow. Birkhauser Boston, Inc. (1989).

[2] Second Joint Europe-US Short Course on Hypersonics. Org. by GAMNI-SMAI, Univers. of Texas at Austin, and U.S. Air Force Academy, Colorado Springs, Jan. 1989, (1989). To be published by Birkhauser Boston, Inc.

[3] Vincenti, W., Kruger, C.: Introduction to Physical Gasdynamics. Wiley and Sons, Inc., New York, (1967).

[4] Scrinivasan, S., Tannehill, J.C., Weilmuenster, K.J.: Simplified curve fits for the thermodynamic properties of equilibrium air. NASA RP 1181, (1987).

[5] Bird, R.B., Stewart, W.E., Lightfoot, E.N.: Transport Phenomena. Wiley and Sons, Inc., New York, (1960).

[6] Baldwin, B ; Lomax, H.: Thin Layer Approximation and Algebraic Model for Separated Turbulent Flows. AIAA-paper, No. 78-257, (1978).

[7] Schiff, L.B., Steger, J.L.: Numerical simulation of steady supersonic viscous flow. AIAA-paper, No. 79-0130, (1979).

[8] Vigneron, Y.C., Rakich, J.V., Tannehill, J.C.: Calculation of supersonic viscous flow over delta wings with sharp supersonic leading edges. AIAA-paper, No. 78-1137, (1978).

[9] Gokcen, T., Mac Cormack, R W., Chapman, D.R.. Computational fluid dynamics near the continuum limit. AIAA paper, No. 87-1115, (1987).

[10] Dutt P : Stable boundary conditions and difference schemes for Navier-Stokes equations. ICASE report No. 85-37, (1985).

[11] Nordström, J.: Energy absorbing boundary conditions for the Navier-Stokes equations. In. Lecture Notes in Physics, vol 264, Springer Verlag, (1986).

[12] Weatherill, N.P.: Mesh Generation in Computational Fluid Dynamics. VKI Lecture Series on Comp. Fluid Dynamics, von Karman Institut for Fluid Dynamics, Rhode-Saint-Genese, March 1989, (1989).

[13] Carcaillet, R., Kennon, S. R. Dulikravitch, G. S.. Generation of Optimum Three-dimensional Computational Grids. Notes on Numerical Fluid Mechanics, 13, pp. 38-46, Vieweg-Verlag, Braunschweig, (1985).

[14] Schwane, R., Hänel, D.: Computation of Viscous Supersonic Flow around Blunt Bodies. 7th GAMM Conf. on Num. Math. in Fluid Mech., Louvain-La Neuve, 1987.

[15] Rossow C.. Comparison of Cell Centered and Cell Vertex Finite Volume Schemes. In: Deville, M. (Ed.), Notes on Numer. Fluid Mech., vol 20, pp. 327-334, Vieweg Verlag (1988).

[16] Dortmann, K.. Computation of viscous unsteady compressible flow about airfoils, to be published in: Proc. of the IC 11 NMFD, Lecture Notes in Physics, Stinger Verlag, 1989.

[17] Jameson, A., Baker, T.J.: Euler Calculations for a Complete Aircraft. Lecture Notes in Physics, vol. 264, Springer-Verlag-Berlin, (1986).

[18] van Leer, B. Towards the ultimate conservative difference scheme V. A second order sequel to Godunov's method. J. Comp. Phys. vol.32, pp.101-136, (1979).

[19] Harten, A.: High resolution schemes for hyperbolic conservation laws, J. Comp. Phys., vol. 49, pp. 357-393, (1983).

[20] Sweby, P.K . High resolution schemes using the flux limiter for hyperbolic conservation laws, SIAM J. Numer. Analyt., vol. 21, pp.995-1011, (1984).

[21] van Albada, G. D., van Leer, B., Roberts, W. W.: A comparative study of computational methods in cosmic gas dynamics. Astron. Astrphys. vol. 108, pp.76-84, (1982).

[22] Roe, P.L., Baines, M.J. Algorithms for advection and shock problems. Proc. of 4th GAMM Conf. on Num Meth in Fluid Mech., Notes on Num. Fluid Mech., vol 5, Vieweg Verlag (1982).

[23] Godunov, S.K.: Finite-Difference method for computation of discontinuous solutions. (in Russian), Math. Sbornik vol.47, pp 271, (1959).

[24] Collela, P., Glaz, H.M.:. Efficient solution algorrithms for the Riemann problem for real gases. J. Comp. Phys., vol 59,pp 264, (1985).

[25] Steger, J.L., Warming, R.F.: Flux-vector splitting of the inviscid gas dynamic equations with applications to finite-difference methods. J. Comp. Phys., vol 40, pp 263-293, (1981).

[26] van Leer, B.: Flux-vector splitting for the Euler equations. Lecture Notes in Physics vol. 170, pp. 507-512, (1982).

[27] Thomas, J.L., Walters, R.W.. Upwind relaxation algorithms for the Navier-Stokes equations. AIAA-paper No. 85-1501, (1985).

[28] Schröder, W., Hänel, D.: An unfactored implicit scheme with multigrid acceleration for the solution of the Navier-Stokes equations. Comp. & Fluids, vol 15, p$_{p}$. 313-336, (1987).

[29] Schwane, R., Hänel, D.. An implicit flux-vector splitting scheme for the computation of viscous hypersonic flow. AIAA-paper No. 89-0274, (1989).

[30] Roe, P.L.: Approximate Rieman solvers, parameter vectors and difference schemes. J. Comp. Phys., vol 22, pp 357, (1981).

[31] Yee, H.C.: A class of high-resolution explicit and implicit shock-cpturing methods for hyperbolic conservation laws. VKI Lecture Series on Comp. Fluid Dynamics, von Karman Institut for Fluid Dynamics, Rhode-Saint-Genese, March 1989, (1989).

[32] Jameson, A., Schmidt, W., Turkel, E.: Numerical solution of the Euler equations by finite-volume methods using Runge-Kutta time-stepping schemes. AIAA-paper 81-1959, (1981).

[33] Powell, K., van Leer, B.. A genuinely multi-dimensional upwind cell-vertex scheme for the Euler equations. AIAA-paper 89-0095, (1989).

[34] Beam, R. M., Warming, R.F.: An implicit factored scheme for the compressible Navier-Stokes equations. AIAA J. vol. 16, pp. 393-402, (1978).

[35] Jameson, A.: Solution of the Euler equations for two dimensional transonic flow by a multigrid method. Presented at the International Multigrid Conference, Copper Mountain, (1983).

[36] Brandt, A.. Multi-level adaptive solutions to boundary-value problems. Mathematics of Computation, vol 31, No. 138, pp. 333-390, (1977).

[37] Brandt, A.: Guide to multigrid development. In: Lecture Notes in Mathematics vol 960., pp. 220-312, Springer Verlag Berlin, (1981).

[38] Chima, R. V., Johnson, G. M.: Efficient solution of the Euler and Navier-Stokes equations with a vectorized multiple-grid algorithm, AIAA Journal, vol. 23, No. 1, pp. 23-32. (1985).

[39] Ni, R. H.. A multiple grid scheme for solving the Euler equations, AIAA Journal, vol. 20, No. 11, pp. 1565-1571 (1982).

[40] Radespiel, R., Swanson, R.C.. An investigation of cell centered and cell vertex multigrid schemes for the Navier-Stokes equations. AIAA paper 89-0548, (1989).

[41] Hemker, P. W., Spekreijse, S. P.: Multigrid solution of the steady Euler equations. Notes on Numerical Fluid Mechanics, vol 11, Vieweg Verlag, (1985).

[42] Mulder, W. A.: Multigrid relaxation for the Euler equations. J. Comp. Phys., vol 60, pp.235-252, (1985).

[43] Shaw, G., Wesseling, P.: Multigrid method for the compressible Navier-Stokes equations. Rep. of the Dep. of Math. and Inf., Nr. 86-13, Univ. Delft, (1986).

[44] Anderson, W. K., Thomas, J.L., Rumsey, C. L.: Extension and application of flux-vector splitting to calculation on dynamic meshes, AIAA paper 87-1152 CP (1987).

[45] Harten, A., Lax, D., van Leer, B.: On upstream differencing and Godunov schemes for hyperbolic conservation laws. SIAM Review, vol 25, (1983).

[46] Siclari, M.J., Del Guidice, P., Jameson, A.: A multigrid finite volume method for solving the Euler and Navier-Stokes equations for high speed flow. AIAA paper 89-0283 1989).

[47] Schröder, W.. Numerische Integration der Navier-Stokes Gleichungen unter Verwendung des Mehrgitter-[48] Konzeptes. Thesis, RWTH Aachen (1987).

[49] Hänel, D., Meinke, M., Schröder, W.. Application of the multigrid method in solutions of the compressible Navier-Stokes equations. Fourth Copper Mountain Conf. on Multigrid Meth., Copper Mountain, Col., April 9-13, (1989).

[50] Mac Cormack, R.W.: A numerical method for solving the equations of compressible viscous flow. AIAA J., vol 20, pp. 1275-1281, (1982).

[51] von Neumann, J., Richtmyer, R. D.: A method for the numerical calculation of hydrodynamic shocks. J. of Appl. Physics, vol 21 pp. 285-288, (1950).

[52] Osher, S., Chakravarthy, S.: High resolution schemes and entropy condition. SIAM J. Num. Anal., vol 21 pp. 955-984, (1984).

[53] Hänel, D.: On the accuracy of the upwind schemes in solutions of the Navier-Stokes equations, AIAA paper 87-1105 CP (1987).

[54] van Leer, B., Thomas, J. L., Roe, P. L., Newsome, R. W.: A comparison of numerical flux formulas for the Euler and Navier-Stokes equations. AIAA paper 87-1104 CP (1987).

[55] Schlichting, H.: Boundary-Layer Theory. Mac Graw-Hill, Inc., New York, (1968).

[56] Yee, H. C., Harten, A.: Implicit TVD schemes for hyperbolic conservation laws. AIAA paper 85-1513 CP (1985).

[57] Hänel, D.. On the numerical solution of the Navier-Stokes equations for commpressible fluids. VKI Lecture Series on Comp. Fluid Dynamics, von Karman Institut for Fluid Dynamics, Rhode-Saint-Genese, March 1989, (1989).

[58] D. Hänel, R. Schwane: On the computation of hypersonic viscous flows. In: J. J. Bertin (Ed.): Hypersonic Flow, vol. II, Birkhauser Boston, Inc., (1989).

[59] Vinokur, M., Montagne, J.-L.: Generalized flux-vector splitting for a real gas. In preparation (see also YEE, H., NASA Memo 8964, (1987)).

[60] de Costa, J. L., Aymer de la Chevalerie, D., Alziry de Roquefort, T.: Ecoulement tridimensional hypersonique sur une combinaison d'ellipsoides. Rapport N.4RDMF 86, UniversitBe de Poitieres, France (1987).

[61] Workshop on Hypersonic Flows for Reentry Problems. To be organized by INRIA and GAMNI-SMAI, Jan. 1990, Antibes, France, (1990).

[62] Schmatz, M A.. Three-dimensional viscous flow simulation using an implicit relaxation scheme. Notes on Num. Fluid Mech., vol. 22, pp. 226-243, Vieweg Verlag, Braunschweig (1988).

[63] Eberle, A.. 3-D Euler calculations using characteristic flux extrapolation. AIAA-paper 84-0119, (1985).

[64] Mac Cormack. The numerical computation of the equations of hypersonic flow. Contribution on the 2nd Joint Europe/US Short Course in Hypersonics, Colorado Springs, (1989).

[65] Bardina, J., Lombard, C.K.:Three dimensional hypersonic flow simulations with the CSCM upwind Navier-Stokes Method. AIAA paper 87-1114 CP, (1987).

[66] Rieger, H., Jameson, A.. Solution of steady three-dimensional compressible Euler and Navier-Stokes equations by an implicit LU scheme. AIAA-paper 88-0619 (1988).

[67] Riedelbauch, S.,Müller, B., Kordulla, W.: Semi-implicit finite difference simulation of laminar flow over blunt bodies. Proc. of 11th ICNMFD, Williamsburg, (1988). To appear in Springer Verlag.

[68] Mac Cormack, .W.. The effect of viscosity in hypervelocity impact cratering. AIAA paper 69-354, (1969).

[69] Shang, J.S., Scherr, S.J.: Numerical simulation of the flowfield around a complete aircraft. AGARD Conf. Proc. 412, (1986).

[70] Periaux, J. Finite element simulations of three-dimensional hypersonic reacting flows around Hermes. Contrib. on Second Joint Europe-US Short Course on Hypersonics. Org. by GAMNI-SMAI, Univers. of Texas at Austin, and U.S. Air Force Academy, Colorado Springs, Jan. 1989,1989).

[71] Koschel, W , Vornberger, A.. Turbomachinery flow calculation on unstructured grids using finite element methods. To appear in. Notes on Numerical Fluid Mechanics, Vieweg Verlag, Braunschweig, (1989).

[72] Prabhu, P.K., Stewart, J.R., Thareja, R.R.: A Navier-Stokes solver for high speed equilibrium flows and application to blunt bodies. AIAA paper 89-0668, (1989).

[73] Prabhu, D K., Tannehill, J.C., Marvin, J.G.: A new PNS code for chemical nonequilibrium flows. AIAA-J.,vol 26, No. 7, pp. 808-815, (1988).

[74] Power, G D.,.Barber, T.J.. Analysis of complex hypersonic flows with strong viscous/inviscid interaction. AIAA-J., vol. 26, No. 7, pp 832-840, (1988).

[75] Ng, W.F., Mitchell, C.R., Ajmani, K., Taylor, A.C., Brock. J.S.: Viscous analysis of high speed flows using an upwind finite volume technique. AIAA paper 89-0001, (1989).

[76] Taylor, A.C., Ng, W.F., Walters, R.W.: An improved upwind finite volume relaxation method for high speed viscous flows. AIAA paper 89-0549, (1989).

TURBULENCE MODELS FOR COMPRESSIBLE FLOWS

J. COUSTEIX - B. AUPOIX

Office National d'Etudes et de Recherches Aérospatiales (ONERA)
Centre d'Etudes et de Recherches de TOULOUSE
Département d'Aérothermodynamique

2 avenue E. Belin - 31055 TOULOUSE Cedex (FRANCE)

SUMMARY

The main objective of this paper is the presentation and the discussion of turbulence models devoted to calculate aerodynamic flows characterized by high speeds and heat exchanges.

The basic equations of the average flow are obtained from the NAVIER-STOKES equations. After a discussion of various possible ways for defining the averaging process, the equations are written by using the mass weighted averages.

A general background of turbulence models is presented in incompressible flow and several models applied in compressible flow are described. This includes mixing length models, one-equation models, two-equation models and REYNOLDS stress models. The effects of compressibility and the development of turbulent heat flux equation models are also presented.

Finally a few comparisons between computed and experimental data are given.

1 - INTRODUCTION

The main objective of this paper is the presentation and the discussion of turbulence models devoted to calculate aerodynamic flows characterized by high speeds and heat exchanges.

In boundary layers at high speeds, the dissipation (due to the deformation work of viscous stresses which transforms mechanical energy into heat) is significant and leads to subsequent heat exchanges within the fluid.

Very often, the high speed flows are associated with a strong shock wave in front of the body. This shock wave produces a strong compression and high temperatures in the flow. Therefore, it is often necessary to maintain the wall at a low temperature in order to avoid any damage ; consequently, the wall heat flux is very strong.

The role of turbulence models is not only to enable us to calculate these heat fluxes but also the influence of high speeds and heat exchanges on the velocity field and on the skin friction.

Unfortunately, there is no theory of turbulence. This means that turbulence models are techniques devoted to predict or reproduce the main characteristics of the flow as far as possible. This also means that experiments are necessary for the elaboration of turbulence models and for the control of their validity. To illustrate this point, two examples are given below.

The first example is the rather unexpected reduction of the spreading rate of the mixing layer in supersonic flow (fig. 1). This result forced modellers to serious adaptations of models and, in fact, this problem is not yet properly solved.

The second example concerns the effect of Mach number on the skin friction of the flat plate. As shown in figure 2, due to D. BUSHNELL (1980-81 STANFORD Conference), there was a large scatter in the predictions until the sixties. Later, experimental data have been obtained and all the "predictions" collapsed onto the same curve.

In the following sections, a review of available models will be presented. It is assumed that the fluid is air which behaves as a perfect gas. Reactive flows such as flames or dissociated air flows are excluded and mixtures of fluids with different density are also excluded.

2 - GENERAL IDEAS ON THE CALCULATION OF TURBULENT INCOMPRESSIBLE FLOWS

2.1. The various approaches of calculation

There is not a unique strategy to calculate a turbulent flow.

For simple flows, such as the boundary layer on a flat plate, correlations between the main boundary layer characteristics have been determined empirically. This is for example the law for the evolution of the skin friction coefficient as a function of the REYNOLDS number. At the other extreme, when the flow is complex, it can be useful to have correlations between the desired result and a few important parameters.

The calculation of boundary layers is often done by using integral methods. The principle of these methods is to solve the boundary layer equations integrated normal to the wall, between the wall and the outer edge ; the set of global equations is closed with more or less elaborated relationships between the boundary layers characteristics (skin friction, displacement thickness, momentum thickness, ...). The most sophisticated of these integral methods are very efficient and are still in use nowadays.

Another way for calculating a boundary layer is to solve the local equations. The equations are obtained from a decomposition of the flow into an average flow and a fluctuating flow. In incompressible, two-dimensional, steady flow, the averaged equations are :

$$\frac{\partial U}{\partial x} + \frac{\partial V}{\partial y} = 0 \tag{1a}$$

$$\rho U \frac{\partial U}{\partial x} + \rho V \frac{\partial U}{\partial y} = -\frac{dP}{dx} + \frac{\partial}{\partial y}\left(\mu \frac{\partial U}{\partial y} - \rho \langle u'v' \rangle\right) \tag{1b}$$

The pressure gradient $\frac{dP}{dx}$ being assumed to be known, the solution of equations (1) requires a model which expresses the REYNOLDS stress $-\rho \langle u'v' \rangle$ which represents the effect of turbulence on the mean flow.

For standard boundary layers, specific models have been developed such as mixing length schemes. For more complex flows, other techniques involving transport equations describing the evolution of turbulence characteristics are available.

These models are devoted to engineering applications. For more fundamental studies of turbulence, various approaches are used : direct numerical simulations, large eddy simulations, two-point closures, stochastic models, ... It should be noticed that these approaches are also useful for improving the hypotheses introduced in transport equation models.

2.2. General background of turbulence modelling

Let us recollect now the general background of one-point closure models.

2.2.1. Turbulence scales - Eddy viscosity

In equation (1b), the apparent turbulent stress is combined with the viscous stress and contributes to the diffusion of momentum. This analogy is often advocated to introduce the concept of eddy viscosity to express the REYNOLDS stresses as a function of the mean velocity gradient in the same way as the viscous stresses ; the reasoning is based on a hypothetical resemblance between the molecular motion and the turbulent motion and it leads to the mixing length scheme. In fact, it is better to introduce these concepts as resulting from a dimensional necessity (TENNEKES-LUMLEY, 1972). Let us consider a shear flow in which the velocity gradient has a predominant component, let us say $\frac{\partial U}{\partial y}$. On the other hand, it is assumed that the energy-containing eddies can be characterized by a velocity scale u and a length scale l. The mixing length hypothesis consists of assuming that the mean flow imposes its time scale to the turbulent flow. So, we get :

$$\frac{u}{l} = \frac{\partial U}{\partial y} \tag{2}$$

The mixing length model is deduced from eq. (2) and assuming a good correlation between the fluctuations u' and v' :

$$- \langle u'v' \rangle \sim u\, l\, \frac{\partial U}{\partial y} \quad \text{or} \quad - \langle u'v' \rangle \sim l^2 \left(\frac{\partial U}{\partial y}\right)^2 \tag{3}$$

This simple example shows the importance of scales in turbulence modelling. Indeed, turbulence is modelled by assuming two types of structures characterized by their scales. On the one hand, we have the energy-containing eddies, the scales of which are u (velocity), l (length), $\theta = l/u$ (time) and, on the other hand, we have the dissipative eddies, the scales of which are v, η, $\tau = \eta/v$.

2.2.2. Dissipation

The dissipation process is an important characteristic of turbulence which represents the transformation of kinetic energy into heat due to the work performed by the viscous stresses. This point can be shown from the comparison between the kinetic energy equation and the enthalpy equations. In compressible flow, the equations for the instantaneous flow are :

$$\rho \frac{D}{Dt} \left(\frac{u_i u_i}{2} \right) = p \frac{\partial u_i}{\partial x_i} + \frac{\partial}{\partial x_j} (t_{ij} \, u_i) - \mu \, \varphi_D \tag{4}$$

$$\rho \frac{Dh}{Dt} = \frac{\partial}{\partial x_i} \left(\frac{\lambda}{C_p} \frac{\partial h}{\partial x_i} \right) + \frac{\partial p}{\partial t} + u_j \frac{\partial P}{\partial x_j} + \mu \, \varphi_D \tag{5}$$

with $t_{ij} = - p \, \delta_{ij} + 2\mu \left(s_{ij} - \frac{\delta_{ij}}{3} \frac{\partial u_\ell}{\partial x_\ell} \right)$; $s_{ij} = \frac{1}{2} \left(\frac{\partial u_i}{\partial x_j} + \frac{\partial u_j}{\partial x_i} \right)$

φ_D is the dissipation function :

$$\varphi_D = 2 \, s_{ij} \left(s_{ij} - \frac{\delta_{ij}}{3} \frac{\partial u_\ell}{\partial x_\ell} \right)$$

From equations (4) and (5), it is clear that the work $\mu \, \varphi_D$ of viscous stresses represents an exchange between kinetic energy and heat. In addition, $\varphi_D \geq 0$ because :

$$\varphi_D = \left(\frac{\partial u}{\partial y} + \frac{\partial v}{\partial x} \right)^2 + \left(\frac{\partial v}{\partial x} + \frac{\partial w}{\partial y} \right)^2 + \left(\frac{\partial w}{\partial x} + \frac{\partial u}{\partial z} \right)^2 + \frac{2}{3} \left[\left(\frac{\partial u}{\partial y} - \frac{\partial v}{\partial y} \right)^2 + \left(\frac{\partial v}{\partial y} - \frac{\partial w}{\partial z} \right)^2 + \left(\frac{\partial w}{\partial z} - \frac{\partial u}{\partial x} \right)^2 \right]$$

Returning now to the case of an *incompressible flow*, we have :

$$\varphi_D = 2 \, s_{ij} s_{ij}$$

The average value of the total kinetic energy is :

$$\frac{\langle u_i u_i \rangle}{2} = K + k = \frac{U_i U_i}{2} + \frac{\langle u_i' u_i' \rangle}{2}$$

The dissipation rate of the kinetic energy K of the mean flow (for a unit mass) is :

$$D = 2 \, \nu \, S_{ij} S_{ij} \quad ; \quad S_{ij} = \frac{1}{2} \left(\frac{\partial U_i}{\partial x_j} + \frac{\partial U_j}{\partial x_i} \right) \tag{6}$$

and the dissipation rate of the turbulent kinetic energy k (for a unit mass) is :

$$\epsilon = 2\nu \langle s_{ij}' s_{ij}' \rangle \quad ; \quad s_{ij}' = \frac{1}{2} \left(\frac{\partial u_i'}{\partial x_j} + \frac{\partial u_j'}{\partial x_i} \right) \tag{7}$$

The origin of dissipation ϵ is the work performed by the fluctuations of viscous stresses. When the REYNOLDS number is large, as required to have a fully developed turbulence, it can be shown that ϵ is much larger than D.

2.2.3. Energy cascade - Dissipative scales

The dissipation ϵ plays a central role in the description of turbulence which can be summarized as follows.

Let us consider a shear flow with a dominant velocity gradient component $\frac{\partial U}{\partial y}$. The source of turbulence is the shear $\frac{\partial U}{\partial y}$ which imposes its time scale to the energy-containing eddies.

On considering the equations for k and K (obtained from the NAVIER-STOKES equation), it is shown that an exchange of energy takes place between the mean motion and the turbulent motion at a rate $- \langle u'v' \rangle \frac{\partial U}{\partial y}$; generally, this term contributes to a production of turbulent kinetic energy and therefore to a destruction of mean kinetic energy. This energy feeds the energy-containing eddies. If the REYNOLDS number $u\ell/\nu$ characterizing these eddies is large, an inviscid process takes place, in which the eddies become smaller and smaller due to a vortex stretching mechanism. In the same time, energy is transferred to smaller eddies. This process continues until the REYNOLDS number characterizing the smaller eddies is of order unity ; at this stage, the viscosity is effective and the energy is transformed into heat through the viscous dissipation. The scales of these dissipative eddies are obtained from a dimensional consideration of eq.(7). The characteristic time of s'_{ij} is τ, so that :

$$\epsilon \sim \frac{\nu}{\tau^2} \tag{8}$$

On the other hand, the hypothesis that the REYNOLDS number characteristic of the dissipative eddies is of order unity gives :

$$\frac{\nu\,\eta}{\nu} = 1 \tag{9}$$

Then, the KOLMOGOROV scales which are typical of the dissipative eddies are :

$$\eta = \left(\frac{\nu^3}{\epsilon}\right)^{1/4} \quad ; \quad \upsilon = (\epsilon\nu)^{1/4} \quad ; \quad \tau = \left(\frac{\nu}{\epsilon}\right)^{1/2} \tag{10}$$

2.2.4. Single time scale hypothesis

The dissipative scales are related to those characterizing the energy-containing eddies.

To show this, let us consider the fully developed flow in a pipe (FAVRE et al, 1972). It is easy to demonstrate that the dissipation rate of (K + k) averaged over the pipe section is :

$$D = \lambda \frac{\bar{U}^3}{4R}$$

where λ is the pressure drop coefficient, $\bar{U}$ is the velocity averaged over the pipe section, R is the pipe radius. As said before, if the REYNOLDS number is large, the dissipation rate D is nearly equal to the average of ϵ over the pipe section.

In the case of a smooth wall, λ varies as $(\bar{U}R/\nu)^{-1/4}$ and in the case of a fully rough wall, λ is independent of the REYNOLDS number. Let us notice that in the case of the smooth wall, the viscous stresses are larger than the apparent turbulent stresses in a thin layer near the wall ; therefore the flow is not fully turbulent over the entire pipe cross section. On the contrary, in the case of the fully rough wall, the flow can be considered as fully turbulent everywhere. Then, it appears that in a fully turbulent flow, the non dimensional dissipation rate is independent of the REYNOLDS number and, in particular, of the viscosity ν. The paradox is that from eq.(7), ϵ seems to be proportional to ν. The solution is to assume that the dissipation rate is ruled by the energy-containing eddies.

From a dimensional analysis, the following crucial relationship results :

$$\epsilon = \frac{u^3}{\ell} \tag{11}$$

In fact, the consideration of the spectral energy equation leads to assume that the dissipation

rate ϵ is nearly equal to the rate of energy transfer from the large to the small eddies. As this process takes place between eddies characterized by a large REYNOLDS number, the viscosity is not involved and the relationship (11) seems natural.

The relationship (11) can also be deduced from the hypothesis that turbulence is ruled by a single-time scale. Let t_D be the time needed to dissipate an amount of energy u^2. We have :

$$t_D = \frac{u^2}{\epsilon}$$

The single-time scale hypothesis tells that :

$$t_D = \theta \quad \text{that is} \quad \epsilon = \frac{u^3}{\ell}$$

The relationship (11) can be used to determine the length ℓ in the mixing length model (3). We get :

$$- \langle u'v' \rangle \sim \frac{u^4}{\epsilon} \frac{\partial U}{\partial y} \tag{12}$$

This is the basic relationship used in a k-ϵ model (the velocity scale u is given as $u = k^{1/2}$).

The comparison between eq.(8) and (11) shows that the dissipative eddies have to adjust their time scale τ in order that ϵ is independent of ν. Precisely, τ is proportional to $\nu^{1/2}$.

Using eq.(11), the ratios of energy-containing scales and dissipative scales are :

$$\frac{\nu}{u} = R_\ell^{-1/4} \quad ; \quad \frac{\eta}{\ell} = R_\ell^{-3/4} \quad ; \quad \frac{\tau}{\theta} = R_\ell^{-1/2} \tag{13}$$

with

$$R_\ell = \frac{u \ell}{\nu}$$

These expressions show that the gap between the two families of eddies increases as the REYNOLDS number R_ℓ increases ; the structure of the dissipative eddies becomes independent of the structure of the large eddies at high REYNOLDS number. The dissipative eddies become isotropic due to a scrambling effect of turbulence.

2.2.5. Mathematical tools

Besides this description of turbulence, a few mathematical tools are used. In the transport equations governing the evolution of REYNOLDS stresses or of the dissipation rate, many terms are unknown and require a modelling. These terms have a tensorial form and it is very suitable to model them by a tensor which has the same properties as the original term. These properties are for example : symmetry, galilean invariance, objectivity. Very often, the original tensor has special properties when its contraction is taken or in the case of isotropic or homogeneous turbulence. It is also suitable that the model respects these properties.

Another requirement should be the realizability (LUMLEY, 1978 ; REYNOLDS, 1987). For example, the kinetic energy k or the dissipation rate ϵ cannot be negative ; the correlation coefficient $|\langle u'v' \rangle|/(\langle u'^2 \rangle \langle v'^2 \rangle)^{1/2}$ should be less than unity ; other conditions such as the limit behaviour of one-dimensional or two-dimensional turbulence can be useful guides for turbulence modelling. Very often, the realizability conditions are not examined thoroughly because they are considered as extreme cases which are rare in practice.

Finally, another useful tool is the invariant representation of tensors as function of other tensors. From physical considerations, the main quantities which influence the unknown term are guessed. Then the invariant representation theorems enable us to find the modelled form of the unknown term taking into account the properties of the original tensor (symmetry, invariance, ...). From dimensional argument, it is possible to express coefficients of the modelled form as function of turbulence scales and finally comparisons with experiments help in fixing the values of numerical constants.

2.3. Examples of turbulence models

It is not possible to present all the turbulence models published in the literature. Here, we give first the REYNOLDS stress transport equation model developed by LAUNDER et al, 1975.

The REYNOLDS stress equations are derived from the NAVIER-STOKES equations. For high REYNOLDS num-

ber, these equations are :

$$\frac{D}{Dt} \langle u_i' u_j' \rangle = P_{ij} - D_{ij} + \varphi_{ij} + \frac{\partial}{\partial x_\ell} J_{ij\ell} \qquad (14)$$

We have :

1) $P_{ij} = - \left(\langle u_i' u_\ell' \rangle \frac{\partial U_j}{\partial x_\ell} + \langle u_j' u_\ell' \rangle \frac{\partial U_i}{\partial x_\ell} \right)$ is the production term (generally this term contributes to a production of the corresponding REYNOLDS stress, but it is not always the case).

2) $D_{ij} = 2\nu \left\langle \frac{\partial u_i'}{\partial x_\ell} \frac{\partial u_j'}{\partial x_\ell} \right\rangle$ is the destruction term. Its contraction D_{ii} represents the dissipation rate of two times the turbulent kinetic energy.

3) $\varphi_{ij} = \left\langle \frac{p'}{\rho} \left(\frac{\partial u_i'}{\partial x_j} + \frac{\partial u_j'}{\partial x_i} \right) \right\rangle$ is the velocity-pressure correlation. The incompressibility condition of velocity fluctuation shows that the trace φ_{ii} is zero. This means that this term contributes to a redistribution of energy between the components $\langle u'^2 \rangle$, $\langle v'^2 \rangle$, $\langle w'^2 \rangle$.

4) $J_{ij\ell} = - \langle u_i' u_j' u_\ell' \rangle - \left\langle \frac{p'}{\rho'} \left(u_i' \delta_{j\ell} + u_j' \delta_{i\ell} \right) \right\rangle$ is the diffusion term. The diffusion is due to the interaction between the velocity components and to the interaction between pressure and velocity.

The modelled form of the REYNOLDS stress equations is given by the following formulae :

$$D_{ij} = \frac{2}{3} \delta_{ij} \, \epsilon \qquad (15)$$

$$\varphi_{ij} = \varphi_{ij,1} + \varphi_{ij,2} \qquad (16)$$

$$\varphi_{ij,1} = - C_1 \, \epsilon \left(\frac{\langle u_i' u_j' \rangle}{k} - \frac{2}{3} \delta_{ij} \right) \qquad (16a)$$

$$\varphi_{ij,2} = - \frac{C_2 + 8}{11} \left(P_{ij} - \frac{2}{3} P\delta_{ij} \right) - \frac{30 C_2 - 2}{55} k \left(\frac{\partial U_i}{\partial x_j} + \frac{\partial U_j}{\partial x_i} \right) - \frac{8 C_2 - 2}{11} \left(Q_{ij} - \frac{2}{3} P\delta_{ij} \right) \qquad (16b)$$

with $Q_{ij} = - \langle u_i' u_\ell' \rangle \frac{\partial U_\ell}{\partial x_j} - \langle u_j' u_\ell' \rangle \frac{\partial U_\ell}{\partial x_i}$; $P = - \langle u_m' u_\ell' \rangle \frac{\partial U_m}{\partial x_\ell}$.

Another form of $\varphi_{ij,2}$ often used by LAUNDER is :

$$\varphi_{ij,2} = - C_2' \left(P_{ij} - \frac{2}{3} P\delta_{ij} \right) \qquad (16c)$$

$$J_{ij\ell} = C_s' \frac{k}{\epsilon} \langle u_\ell' u_m' \rangle \frac{\partial}{\partial x_m} \langle u_i' u_j' \rangle \qquad (17)$$

The REYNOLDS stress equations are completed with a transport equation for the dissipation rate :

$$\frac{D\epsilon}{Dt} = - C_{\epsilon 1} \frac{\epsilon}{k} \langle u_m' u_\ell' \rangle \frac{\partial U_m}{\partial x_\ell} - C_{\epsilon 2} \frac{\epsilon^2}{k} + \frac{\partial}{\partial x_\ell} \left(C_\epsilon' \frac{k}{\epsilon} \langle u_m' u_\ell' \rangle \frac{\partial \epsilon}{\partial x_m} \right) \qquad (18)$$

The values of the constants are :

$$C_1 = 1.8 \; ; \; C_2' = 0.6 \; ; \; C_{\epsilon 1} = 1.44 \; ; \; C_{\epsilon 2} = 1.92 \; ; \; C_s' = 0.22 \; ; \; C_\epsilon' = 0.15$$

The model for D_{ij} comes from the hypothesis that the dissipative eddies are isotropic.

The model for $J_{ij\ell}$ comes from a crude modelling of the transport equations for the triple correlation $\langle u_i' u_j' u_\ell' \rangle$.

The modelling of the velocity-pressure correlation is one of the most difficult problems. The formulae (16) are obtained by assuming that φ_{ij} is function of the turbulent stresses and by taking into account the properties of the original terms.

Another difficulty is the equation for the dissipation rate ϵ which is used to describe the length

scale. This equation is subjected to many discussions and is a weakness of the model.

Another problem is the modelling of the flow near a wall. Low REYNOLDS number versions of REYNOLDS stress equations taking into account the proximity of the wall (in particular, in the expression of φ_{ij}) have been proposed but they are not very satisfactory. A simple approach is to calculate the near wall flow with a mixing length model and the outer flow is calculated with a transport equation model. Another possibility is to use, near the wall, an equation for the turbulent kinetic energy in which the dissipation is calculated with a prescribed dissipation length.

Very often, the complete REYNOLDS stress model is not used as such. Algebraic formulae can be obtained if assumptions on the convection and diffusion terms are made.

For example, RODI, 1972, proposed that :

$$\frac{D}{Dt} \langle u_i' u_j' \rangle - \text{Diff} \langle u_i' u_j' \rangle = \frac{\langle u_i' u_j' \rangle}{k} \left(\frac{Dk}{Dt} - \text{Diff}(k) \right)$$

Using eq.(16c) for $\varphi_{ij,2}$, we get :

$$\langle u_i' u_j' \rangle - \frac{2}{3} \delta_{ij} k = \frac{1 - C_2'}{C_1 - 1 + P/\epsilon} \frac{k}{\epsilon} \left(P_{ij} - \frac{2}{3} \delta_{ij} P \right) \tag{19}$$

In fact, the most widely used transport equation model is the k-ϵ model in which the turbulent stresses are expressed as :

$$\rho \langle u_i' u_j' \rangle - \frac{2}{3} \rho k \delta_{ij} = \mu_t \left(\frac{\partial U_i}{\partial x_j} + \frac{\partial U_j}{\partial x_i} \right)$$

with $\mu_t = C_\mu \, \rho \, \frac{k^2}{\epsilon}$.

The k and ϵ equations are :

$$\rho \frac{Dk}{Dt} = \rho P - \rho \epsilon + \frac{\partial}{\partial x_\ell} \left(\frac{\mu_t}{\sigma_k} \frac{\partial k}{\partial x_\ell} \right) \tag{20}$$

$$\rho \frac{D\epsilon}{Dt} = \rho \frac{\epsilon}{k} (C_{\epsilon 1} P - C_{\epsilon 2} \epsilon) + \frac{\partial}{\partial x_\ell} \left(\frac{\mu_t}{\sigma_\epsilon} \frac{\partial \epsilon}{\partial x_\ell} \right) \tag{21}$$

$$C_{\epsilon 1} = 1.44 \; ; \; c_{\epsilon 2} = 1.92 \; ; \; C_\mu = 0.09 \; ; \; \sigma_k = 1 \; ; \; \sigma_\epsilon = 1.3$$

3 - EQUATIONS FOR A COMPRESSIBLE FLOW

3.1. Various types of averages

3.1.1. Conventional decomposition

The calculation of turbulent flows is approached by using a statistical treatment. In *incompressible flow*, this leads to decompose the velocity as :

$$u_i = \langle u_i \rangle + u_i'' \quad ; \quad \langle u_i'' \rangle = 0 \tag{22}$$

where u_i is the instantaneous velocity ; $\langle u_i \rangle$ is the ensemble average velocity ; u_i'' is the turbulent fluctuation.

The fluctuation is noted u_i'' ; this is to avoid a confusion between the fluctuation defined from eq.(22) and the fluctuation u_i' defined from a mass-averaged velocity which will be introduced later. In incompressible flow, $f' = f''$.

The pressure is decomposed as :

$$p = \langle p \rangle + p' \tag{23}$$

In *incompressible flow*, the average of the continuity and momentum equations gives :

$$\frac{\partial U_i}{\partial x_i} = 0 \tag{24a}$$

$$\rho \frac{\partial U_i}{\partial t} + \rho U_j \frac{\partial U_i}{\partial x_j} = -\frac{\partial P}{\partial x_i} + \frac{\partial}{\partial x_j} \left(2\mu\, S_{ij} - \rho \langle u_i'' u_j'' \rangle \right) \tag{24b}$$

with

$$U_i = \langle u_i \rangle \; ; \; P = \langle p \rangle \; ; \; S_{ij} = \frac{1}{2}\left(\frac{\partial U_i}{\partial x_j} + \frac{\partial U_j}{\partial x_i} \right)$$

Let us notice that the difference between the instantaneous and average continuity equations tells us that the velocity fluctuations are incompressible :

$$\frac{\partial u_i''}{\partial x_i} = 0 \tag{25}$$

In eq.(24b), the average process introduces a new unknown, the REYNOLDS stress tensor $\rho \langle u_i'' u_j'' \rangle$, the determination of which is called the closure problem. This problem has been discussed in section 2.

In *compressible flow*, the existence of density fluctuations adds a freedom in the definition of average quantities. Indeed, the average continuity and momentum equations are :

$$\frac{\partial \langle \rho \rangle}{\partial t} + \frac{\partial \langle \rho u_i \rangle}{\partial x_i} = 0 \tag{26}$$

$$\frac{\partial}{\partial t} \langle \rho u_i \rangle + \frac{\partial}{\partial x_j} \langle \rho u_i u_j \rangle = -\frac{\partial \langle p \rangle}{\partial x_i} + \frac{\partial}{\partial x_j} \langle f_{ij} \rangle \tag{27}$$

$$f_{ij} = 2\mu \left(s_{ij} - \frac{\delta_{ij}}{3} \frac{\partial u_\ell}{\partial x_\ell} \right)$$

The main question is to choose how to decompose $\langle \rho u \rangle$ and $\langle \rho u_i u_j \rangle$. The decomposition of $\langle f_{ij} \rangle$ is less important because the viscous stresses are negligible in turbulent flow. A discussion of this problem has been done by CHASSAING, 1985.

If the velocity is decomposed according to eq.(22), we have :

$$\langle \rho u_i \rangle = \langle \rho \rangle \langle u_i \rangle + \langle \rho' u_i'' \rangle \; ; \; \rho = \langle \rho \rangle + \rho'$$

$$\langle \rho u_i u_j \rangle = \langle \rho \rangle \langle u_i \rangle \langle u_j \rangle + \langle \rho' u_i'' \rangle \langle u_j \rangle + \langle \rho' u_j'' \rangle \langle u_i \rangle + \langle \rho \rangle \langle u_i'' u_j'' \rangle + \langle \rho' u_i'' u_j'' \rangle$$

Many additional terms appear and the formulation of equations is very complicated.

3.1.2. Mass-weighted averages

Most of the works use a mass-weighted velocity $\tilde{U}_i$. This type of average has been introduced by FAVRE, 1958, in turbulence studies. Let us notice that this type of average is also used in statistical mechanics of fluids and in the studies of gas mixtures with chemical reactions, for example. The mass-weighted velocity $\tilde{U}_i$ is :

$$\tilde{U}_i = \frac{\langle \rho u_i \rangle}{\langle \rho \rangle} \; ; \; u_i = \tilde{U}_i + u_i' \; ; \; \langle \rho u_i' \rangle = 0 \tag{28}$$

In this way, we have :

$$\langle \rho u_i \rangle = \langle \rho \rangle \tilde{U}_i \tag{29a}$$

$$\langle \rho u_i u_j \rangle = \langle \rho \rangle \tilde{U}_i \tilde{U}_j + \langle \rho u_i' u_j' \rangle \tag{29b}$$

and the average equations are :

$$\frac{\partial \langle \rho \rangle}{\partial t} + \frac{\partial}{\partial x_i} \left(\langle \rho \rangle \tilde{U}_i \right) = 0 \tag{30a}$$

$$\langle \rho \rangle \frac{\partial \tilde{U}_i}{\partial t} + \langle \rho \rangle \tilde{U}_j \frac{\partial \tilde{U}_i}{\partial x_j} = -\frac{\partial \langle p \rangle}{\partial x_i} + \frac{\partial}{\partial x_j} \left(F_{ij} - \langle \rho u_i' u_j' \rangle \right) \tag{30b}$$

with $F_{ij} = \langle 2\mu\, s_{ij} - \dfrac{2}{3}\mu\, \dfrac{\partial u_\ell}{\partial x_\ell}\, \delta_{ij}\rangle$.

These equations have an "usual" form.

The concept of average stream surface has the same meaning as in incompressible flow. In addition, the equations for $\langle \rho u_i' u_j'\rangle$ are obtained in a natural way and not too many additional terms are introduced.

The danger is that the equations are too close to the incompressible case and it is tempting to apply them an "incompressible" closure, which is not always justified.

3.1.3. Other decompositions

Another way to decompose $\langle \rho u_i u_j\rangle$ is to make a distinction between the quantity which is transported (i.e. the momentum) and the velocity which is responsible for the transport (BAUER et al, 1968 ; HA MINH et al, 1981). This leads to write :

$$\langle \rho u_i u_j\rangle = G_i \langle u_j\rangle + \langle g_i^{\cdot}\, u_j^{\cdot\cdot}\rangle$$

or

$$\langle \rho u_i u_j\rangle = G_j \langle u_i\rangle + \langle g_j^{\cdot}\, u_i^{\cdot\cdot}\rangle$$

with

$$G_i = \langle \rho u_i\rangle \quad ; \quad \rho u_i = G_i + g_i^{\cdot}$$

$$\langle g_i^{\cdot} u_j^{\cdot\cdot}\rangle = \langle \rho u_i^{\cdot\cdot} u_j^{\cdot\cdot}\rangle + \langle \rho' u_j^{\cdot\cdot}\rangle \langle u_i\rangle$$

Another decomposition has been proposed by CHASSAING, 1985 :

$$\langle \rho u_i\rangle = \langle \rho\rangle \langle u_i\rangle + \langle K_i\rangle \tag{31a}$$

$$\langle \rho u_i u_j\rangle = \langle \rho\rangle \langle u_i\rangle \langle u_j\rangle + \langle \rho u_i^{\cdot\cdot} u_j^{\cdot\cdot}\rangle + \langle K_i\rangle \langle u_j\rangle + \langle K_j\rangle \langle u_i\rangle \tag{31b}$$

with $\langle K_i\rangle = \langle \rho u_i^{\cdot\cdot}\rangle$.

The average continuity and momentum equations are :

$$\frac{\partial \langle \rho\rangle}{\partial t} + \frac{\partial}{\partial x_j}\left(\langle \rho\rangle \langle u_j\rangle\right) + \frac{\partial}{\partial x_j}\langle K_j\rangle = 0 \tag{32a}$$

$$\frac{\partial}{\partial t}\left(\langle \rho\rangle \langle u_i\rangle\right) + \frac{\partial}{\partial x_j}\left(\langle \rho\rangle \langle u_i\rangle \langle u_j\rangle\right) + \frac{\partial}{\partial x_j}\langle \rho u_i^{\cdot\cdot} u_j^{\cdot\cdot}\rangle + \langle A_i\rangle = -\frac{\partial \langle p\rangle}{\partial x_i} + \frac{\partial}{\partial x_j} F_{ij} \tag{32b}$$

with

$$\langle A_i\rangle = \frac{\partial}{\partial t}\langle K_i\rangle + \frac{\partial}{\partial x_j}\left(\langle K_i\rangle \langle u_j\rangle + \langle K_j\rangle \langle u_i\rangle\right)$$

In this formulation, the velocity is decomposed according to eq.(22) ; this has the advantage that the classical kinematic concepts of vorticity and strain rate have the same interpretation for the instantaneous velocity field as for the average and fluctuating velocity fields.

The contribution of turbulence appears through two types of terms $\langle \rho u_i^{\cdot\cdot} u_j^{\cdot\cdot}\rangle$ and $\langle \rho u_i^{\cdot\cdot}\rangle$. The evolution of $\langle \rho u_i^{\cdot\cdot} u_j^{\cdot\cdot}\rangle$ is described by a transport equation.

The contribution of turbulence through the term $\langle \rho u_j^{\cdot\cdot}\rangle$ is specific of variable density flows. As argued by CHASSAING, it could be useful for the modelling not to group this term with the other contributions of turbulence, because this term represents a specificity of these flows.

It should be noticed that the correlation $\langle \rho u_i^{\cdot\cdot}\rangle$ constitutes a source term in the continuity equation and it is not possible to follow a system of fluid particles closed by a stream surface.

The evolution of the correlation $\langle \rho u_i^{\cdot\cdot}\rangle$ is not determined by a transport equation but $\langle \rho u_i^{\cdot\cdot}\rangle$ can be expressed by using the state law. In the case of a mixture of two non reacting gases, the density ρ of the mixture and the mass fraction C of one species are related by a law of the form :

$$\rho = a\rho C + b$$

where a and b are determined constants.

Then, we have :

$$\langle \rho u_j^{"} \rangle \, (1 - a\langle c \rangle) = a \, \langle \rho c^{"} u_i^{"} \rangle$$

Therefore $\langle \rho u_j^{"} \rangle$ is not an additional unknown because this term is related to the flux $\langle \rho c^{"} u_i^{"} \rangle$ which is in the equation for the average concentration.

If the fluid follows the perfect gas law ($p = \rho RT$), the expression of $\langle \rho u_i^{"} \rangle$ is more complicated :

$$\langle \rho u_i^{"} \rangle = - \frac{\langle \rho u_i^{"} T^{"} \rangle}{\langle T \rangle} + \frac{\langle p^{"} u_i^{"} \rangle}{R \langle T \rangle}$$

For the study of mixtures of non reacting gases, this procedure is viable although it is unusual to work with open systems.

Up to now, the application to compressible high speed flow has not been performed. Therefore, we will use the mass-weighted averages.

3.2. Mass-weighted averages

The velocity is decomposed into a mass-weighted average $\tilde{u}_i$ and a fluctuation u_i'. The same decomposition is used for the enthalpy and the internal energy :

$$u_i = \tilde{u}_i + u_i' \quad ; \quad \tilde{u}_i = \frac{\langle \rho u_i \rangle}{\langle \rho \rangle} \quad ; \quad \langle \rho u_i' \rangle = 0 \tag{33a}$$

$$h = \tilde{h} + h' \quad ; \quad \tilde{h} = \frac{\langle \rho h \rangle}{\langle \rho \rangle} \quad ; \quad \langle \rho h' \rangle = 0 \tag{33b}$$

$$e = \tilde{e} + e' \quad ; \quad \tilde{e} = \frac{\langle \rho e \rangle}{\langle \rho \rangle} \quad ; \quad \langle \rho e' \rangle = 0 \tag{33c}$$

The pressure and the density are decomposed into a classical average and a fluctuation :

$$p = P + p' \quad ; \quad P = \langle p \rangle \quad ; \quad \langle p' \rangle = 0 \tag{34}$$

$$\rho = \langle \rho \rangle + \rho' \quad ; \quad \langle \rho' \rangle = 0$$

Let us notice that the averaged velocity fluctuation $\langle u_i' \rangle$ is not zero :

$$\langle u_i' \rangle = - \frac{\langle \rho' u_i' \rangle}{\langle \rho \rangle} \tag{35}$$

In a general way, the classical averages and mass-weighted averages are linked. If we define :

$$f = F + f' \qquad F = \frac{\langle \rho f \rangle}{\langle \rho \rangle}$$
$$f = \langle f \rangle + f''$$

We have :

$$F - \langle f \rangle = f'' - f' = - \langle f' \rangle = \frac{\langle \rho' f' \rangle}{\langle \rho \rangle} = \frac{\langle \rho' f'' \rangle}{\langle \rho \rangle} \tag{36a}$$

$$\langle \rho f_1' f_2' \rangle = \langle \rho f_1' f_2'' \rangle = \langle \rho f_1'' f_2' \rangle \tag{36b}$$

$$\langle \rho f_1' f_2' \rangle = \langle \rho f_1'' f_2'' \rangle - \frac{\langle \rho' f_1'' \rangle \langle \rho' f_2'' \rangle}{\langle \rho \rangle} \tag{36c}$$

Such relationships enable us to transform the equations written with the classical averaged velocities to the equations written with the mass-weighted velocities.

3.3. Equations with mass-weighted averages

To simplify the writing of the averaged equations, $\langle \rho \rangle$ is written ρ. For example, we have :

$$\rho \tilde{u}_i = \langle \rho \rangle \, \tilde{u}_i$$

but when ρ is combined with a random function inside a sign $\langle\rangle$, the same convention does not apply :

$$\langle\rho u_i' u_j'\rangle \neq \langle\rho\rangle\langle u_i' u_j'\rangle$$

When no confusion is expected, the sign $(\sim)$ is omitted :

$$U_i = \tilde{u}_i$$
$$h = \tilde{h}$$

Continuity equation

$$\frac{\partial\rho}{\partial t} + \frac{\partial\rho U_k}{\partial x_k} = 0 \tag{37}$$

Momentum equation

$$\rho\frac{DU_i}{Dt} = \frac{\partial}{\partial x_k}\left(- P\delta_{ik} + F_{ik} - \langle\rho u_i' u_k'\rangle\right) \tag{38}$$

with :

$$\frac{D\bullet}{Dt} = \frac{\partial\bullet}{\partial t} + U_k\frac{\partial\bullet}{\partial x_k}$$

$$F_{ik} = \langle 2\mu\left(s_{ik} - \frac{\delta_{ik}}{3}\frac{\partial u_\ell}{\partial x_\ell}\right)\rangle$$

$$s_{ik} = \frac{1}{2}\left(\frac{\partial u_i}{\partial x_k} + \frac{\partial u_k}{\partial x_i}\right)$$

At high REYNOLDS number, the viscous stress F_{ik} is negligible compared with the turbulent stress $-\rho\langle u_i' u_k'\rangle$. Near a wall, this is no longer true. Even if the fluctuations of viscosity are neglected, the expression of F_{ik} is not simple because :

$$\langle\frac{\partial u_i}{\partial x_k}\rangle = \frac{\partial U_i}{\partial x_k} - \frac{\partial}{\partial x_k}\left(\frac{\langle\rho' u_i'\rangle}{\rho}\right)$$

Kinetic energy equations

The mean value of the kinetic energy is decomposed as :

$$\frac{1}{2}\langle\rho u_i u_i\rangle = \frac{1}{2}\rho\,U_i U_i + \frac{1}{2}\langle\rho u_i' u_i'\rangle = \rho K + \rho k \tag{39}$$

The first part K corresponds to the averaged motion and the second part k to the fluctuations.

The corresponding equations are :

$$\rho\frac{DK}{Dt} = P\frac{\partial U_i}{\partial x_i} - F_{ik}\frac{\partial U_i}{\partial x_k} + \langle\rho u_i' u_k'\rangle\frac{\partial U_i}{\partial x_k} + \frac{\partial}{\partial x_k}\left[U_i\left(- P\delta_{ik} + F_{ik} - \langle\rho u_i' u_k'\rangle\right)\right] \tag{40a}$$

$$\rho\frac{Dk}{Dt} = \langle p'\frac{\partial u_i'}{\partial x_i}\rangle - \langle f_{ik}\frac{\partial u_i'}{\partial x_k}\rangle - \langle\rho u_i' u_k'\rangle\frac{\partial U_i}{\partial x_k} + \frac{\langle\rho' u_i'\rangle}{\rho}\frac{\partial P}{\partial x_i} + \frac{\partial}{\partial x_k}\left(- \langle u_i' p'\rangle\delta_{ik} + \langle f_{ik} u_i'\rangle - \frac{1}{2}\langle\rho u_k' u_i' u_i'\rangle\right) \tag{40b}$$

with $f_{ik} = 2\mu\left(s_{ik} - \frac{\delta_{ik}}{3}\frac{\partial u_\ell}{\partial x_\ell}\right)$; $s_{ik} = \frac{1}{2}\left(\frac{\partial u_i}{\partial x_k} + \frac{\partial u_k}{\partial x_i}\right)$

$$F_{ik} = \langle f_{ik}\rangle$$

The dissipation rate of the instantaneous kinetic energy is $\varphi = f_{ik}\frac{\partial u_i}{\partial x_k}$. Its averaged value is decomposed as :

$$\langle\varphi\rangle = \Phi + \langle\varphi'\rangle \tag{41}$$

with

with

$$\varphi = f_{ik} \frac{\partial u_i}{\partial x_k}$$

$$\Phi = F_{ik} \frac{\partial U_i}{\partial x_k}$$

$$\langle \varphi' \rangle = \langle f_{ik} \frac{\partial u_i'}{\partial x_k} \rangle$$

Φ is the dissipation rate of the kinetic energy of the averaged motion which appears in eq.(40a). $\langle \varphi' \rangle$ is the dissipation rate of the averaged kinetic energy of the fluctuating motion which appears in eq.-(40b). The exchange of energy between K and k is represented by the work of the REYNOLDS stresses $- \langle \rho u_i' u_k' \rangle \frac{\partial U_i}{\partial x_k}$.

In the k-equation, the compressibility appears explicitly through two terms : $\langle p' \frac{\partial u_i'}{\partial x_i} \rangle$ and $\frac{\langle \rho' u_i' \rangle}{\rho} \frac{\partial P}{\partial x_i}$. This does not mean however that the compressibility cannot influence other terms.

REYNOLDS stress equations

We define T_{ij} as :

$$T_{ij} = \langle \rho u_i' u_j' \rangle / \rho$$

The REYNOLDS stress equation is :

$$\rho \frac{DT_{ij}}{Dt} = \rho P_{ij} - \rho D_{ij} + \rho \Phi_{ij} + \rho C_{ij} + \frac{\partial}{\partial x_k} (\rho J_{ijk}) \tag{42}$$

with :

$$\rho P_{ij} = - \rho T_{ik} \frac{\partial U_j}{\partial x_k} - \rho T_{jk} \frac{\partial U_i}{\partial x_k}$$

$$\rho D_{ij} = \langle f_{ik} \frac{\partial u_j'}{\partial x_k} \rangle + \langle f_{jk} \frac{\partial u_i'}{\partial x_k} \rangle$$

$$\rho \Phi_{ij} = \langle p' \left(\frac{\partial u_i'}{\partial x_j} + \frac{\partial u_j'}{\partial x_i} \right) \rangle$$

$$\rho C_{ij} = \frac{\langle \rho' u_i' \rangle}{\rho} \frac{\partial P}{\partial x_j} + \frac{\langle \rho' u_j' \rangle}{\rho} \frac{\partial P}{\partial x_i}$$

$$\rho J_{ijk} = - \langle \rho u_k' u_i' u_j' \rangle + \langle f_{ik} u_j' \rangle + \langle f_{jk} u_i' \rangle - \langle u_i' p' \rangle \delta_{jk} - \langle u_j' p' \rangle \delta_{ik}$$

The interpretation of this equation is nearly the same as in incompressible flow. ρP_{ij} is the production term ; ρD_{ij} is the destruction term ($\rho \frac{D_{ii}}{2}$ is the dissipation of k) ; $\rho \Phi_{ij}$ is the velocity-pressure correlation ; ρJ_{ijk} is the diffusion due to interactions between velocity fluctuations, due to viscosity and due to interactions between pressure and velocity.

The compressibility appears explicitly only through the term C_{ij} but, once again, the modelled form of the other terms can be influenced by compressibility. For example, the modelling of Φ_{ij} is based on the POISSON equation for p' which is obtained by taking the divergence of the momentum equation. In this equation, many additional terms appear due to the compressibility of the flow :

$$- \frac{\partial^2 p'}{\partial x_i \partial x_i} = 2 \frac{\partial^2}{\partial x_\ell \partial x_m} (\langle \rho \rangle u_\ell' U_m) + 2 \frac{\partial^2}{\partial x_\ell \partial x_m} (\rho' u_\ell' U_m) + \frac{\partial^2}{\partial x_\ell \partial x_m} (\rho' U_\ell U_m) + \frac{\partial^2}{\partial x_\ell \partial x_m} ((\langle \rho \rangle + \rho') u_\ell' u_m' - \langle \rho u_\ell' u_m' \rangle) \tag{43}$$

$$- \frac{\partial^2 \rho'}{\partial t^2} - \frac{\partial^2}{\partial x_\ell \partial x_m} (f_{\ell m} - F_{\ell m})$$

Energy equation

The enthalpy h and the internal energy e are related by the equation :

$$\rho h = \rho e + p \tag{44}$$

Taking the average, we obtain :

$$\langle \rho \rangle \, \tilde{h} = \langle \rho \rangle \, \tilde{e} + \langle p \rangle \tag{45}$$

The fluctuations are related by :

$$h' = e' + \frac{p}{\rho} - \frac{\langle p \rangle}{\langle \rho \rangle}$$

The total energy E is :

$$E = e + \frac{u_i u_i}{2}$$

The mass averaged total energy $\tilde{E}$ is defined by :

$$\langle \rho \rangle \, \tilde{E} = \langle \rho \rangle \, \tilde{e} + \frac{\langle \rho u_i u_i \rangle}{2} = \langle \rho \rangle \, \tilde{e} + \langle \rho \rangle \, \frac{\tilde{u}_i \tilde{u}_i}{2} + \frac{\langle \rho u_i' u_i' \rangle}{2}$$

or

$$\tilde{E} = \tilde{e} + K + k \tag{46}$$

We also have :

$$E' = e' + \tilde{u}_i u_i' + \frac{1}{2} u_i' u_i' - \frac{1}{2} \frac{\langle \rho u_i' u_i' \rangle}{\langle \rho \rangle}$$

In the same way, the mass-averaged total enthalpy $\tilde{h}_i$ is :

$$\tilde{h}_i = \tilde{h} + K + k \; ; \; K = \frac{\tilde{u}_i \tilde{u}_i}{2} \; ; \; k = \frac{1}{2} \frac{\langle \rho u_i' u_i' \rangle}{\langle \rho \rangle} \tag{47}$$

and :

$$h_i' = h' + \tilde{u}_i u_i' + \frac{1}{2} u_i' u_i' - \frac{1}{2} \frac{\langle \rho u_i' u_i' \rangle}{\langle \rho \rangle}$$

BUSHNELL et al, 1976, mentioned that at high MACH numbers, the velocity fluctuations intensity can represent a significant fraction of the static enthalpy because h/h_i becomes very small and h_i is close to $U^2/2$. Now, if, in a calculation method, the turbulence intensity is not well known, it can result in an error on the static enthalpy and hence on the density.

The energy equation can be written for the internal energy $\tilde{e}$ or for the enthalpy $\tilde{h}$ or for the total enthalpy $\tilde{h}_i$ or for the total energy $\tilde{E}$.

In the following equations, when there is no possible confusion, the signs (~) and <> are omitted.

$$\rho \, \frac{De}{Dt} = \Phi + \langle \varphi' \rangle - P \, \frac{\partial U_i}{\partial x_i} - \langle p \, \frac{\partial u_i'}{\partial x_i} \rangle - \frac{\partial}{\partial x_i} \left(Q_i + \langle \rho u_i' e' \rangle \right) \tag{48}$$

where Φ and $\langle \varphi' \rangle$ are the dissipation rates of K and k (eq.41). In equations (40a) and (40b), Φ and $\langle \varphi' \rangle$ appear with an opposite sign.

$\bar{Q}$ is the averaged value of the molecular heat flux :

$$Q_i = - \langle \lambda \, \frac{\partial T}{\partial x_i} \rangle$$

and $\langle \rho u_i' e' \rangle$ is the turbulent flux of internal energy.

The equation for the mass-averaged enthalpy is :

$$\rho \, \frac{Dh}{Dt} = \Phi + \langle \varphi' \rangle + \frac{\partial P}{\partial t} + U_i \, \frac{\partial P}{\partial x_i} - \frac{\langle \rho' u_i' \rangle}{\rho} \, \frac{\partial P}{\partial x_i} + \langle u_i' \, \frac{\partial p'}{\partial x_i} \rangle - \frac{\partial}{\partial x_i} \left(Q_i + \langle \rho u_i' h' \rangle \right) \tag{49a}$$

The equation for the mass-averaged total enthalpy is :

$$\rho \frac{Dh_1}{Dt} = \frac{\partial P}{\partial t} - \frac{\partial}{\partial x_k} \left(- \langle f_{jk} u_j \rangle + Q_k + \langle \rho u_k' h_1' \rangle \right) \tag{49b}$$

The equation for the mass-averaged total energy is :

$$\rho \frac{DE}{Dt} = \frac{\partial}{\partial x_k} \left(\langle f_{ik} u_i \rangle - \langle \rho u_i \rangle \delta_{ik} - Q_k - \langle \rho u_k' E' \rangle \right) \tag{50}$$

Equations (48), (49) and (50) can be deduced one from each other. In particular, the turbulent fluxes are linked by the formulae :

$$\langle \rho u_k' e' \rangle = \langle \rho u_k' h' \rangle - \langle \rho u_k' \rangle \tag{51a}$$

$$\langle \rho u_k' E' \rangle = \langle \rho u_k' e' \rangle + \langle \rho u_k' u_j' \rangle U_j + \frac{1}{2} \langle \rho u_k' u_j' u_j' \rangle \tag{51b}$$

$$\langle \rho u_k' h_1' \rangle = \langle \rho u_k' h' \rangle + \langle \rho u_k' u_j' \rangle U_j + \frac{1}{2} \langle \rho u_k' u_j' u_j' \rangle \tag{51c}$$

Generally, the turbulent heat flux is used. Its evolution is described by the following equation for $Q_{t_i} = \langle \rho u_i' h' \rangle$:

$$\frac{\partial Q_{t_i}}{\partial t} + \frac{\partial}{\partial x_k} \left(Q_{t_i} U_k \right) = - \langle \rho u_k' h' \rangle \frac{\partial U_i}{\partial x_k} - \langle \rho u_k' u_i' \rangle \frac{\partial h}{\partial x_k} - \langle f_{ik} \frac{\partial h'}{\partial x_k} \rangle - \langle \lambda \frac{\partial T}{\partial x_k} \frac{\partial u_i'}{\partial x_k} \rangle + \langle u_i' \phi \rangle \tag{52}$$

$$+ \langle p' \frac{\partial h'}{\partial x_i} \rangle - \frac{\langle \rho' h' \rangle}{\rho} \frac{\partial P}{\partial x_i} + \langle u_i' \frac{\partial p}{\partial t} \rangle + \langle u_i' u_k \frac{\partial p}{\partial x_k} \rangle + \frac{\partial}{\partial x_k} \left(- \langle \rho u_k' u_i' h' \rangle - \langle h' p' \rangle \delta_{ik} + \langle h' f_{ik} \rangle + \langle u_i' \lambda \frac{\partial T}{\partial x_k} \rangle \right)$$

3.4. Boundary layer equations

In a two-dimensional steady flow, the boundary layer assumptions lead to the following equations :

$$\frac{\partial \langle \rho \rangle \tilde{u}}{\partial x} + \frac{\partial \langle \rho \rangle \tilde{v}}{\partial y} = 0 \tag{53a}$$

$$\langle \rho \rangle \tilde{u} \frac{\partial \tilde{u}}{\partial x} + \langle \rho \rangle \tilde{v} \frac{\partial \tilde{u}}{\partial y} = - \frac{\partial \langle p \rangle}{\partial x} + \frac{\partial}{\partial y} \left(\langle \mu \frac{\partial u}{\partial y} \rangle - \langle \rho u' v' \rangle \right) \tag{53b}$$

$$\frac{\partial \langle p \rangle}{\partial y} = - \frac{\partial}{\partial y} \left(\langle \rho v'^2 \rangle \right) \tag{53c}$$

$$\langle \rho \rangle \tilde{u} \frac{\partial \tilde{h}_i}{\partial x} + \langle \rho \rangle \tilde{v} \frac{\partial \tilde{h}_i}{\partial y} = \frac{\partial}{\partial y} \left(\langle u \mu \frac{\partial u}{\partial y} \rangle - U \langle \rho u' v' \rangle + \langle \lambda \frac{\partial T}{\partial y} \rangle - \langle \rho v' h' \rangle \right) \tag{53d}$$

It is useful to give an order-of magnitude of certain terms. The state equation gives :

$$\frac{\rho'}{\langle \rho \rangle} = - \frac{T'}{\tilde{T}} + \frac{p'}{\langle p \rangle} - \frac{\rho' T'}{\langle \rho \rangle \tilde{T}}$$

For external Mach numbers less than 5, the velocity fluctuations are subsonic and the terms $\frac{p'}{\langle p \rangle}$ and $\frac{\rho' T'}{\langle \rho \rangle \tilde{T}}$ are negligible, so that :

$$\frac{\rho'}{\langle \rho \rangle} \simeq - \frac{T'}{\tilde{T}}$$

and we have :

$$\frac{\tilde{T} - \langle T \rangle}{\tilde{T}} = \frac{\langle \rho' T' \rangle}{\langle \rho \rangle \tilde{T}} \simeq \frac{\langle T'^2 \rangle}{(\tilde{T})^2}$$

$$\frac{|\tilde{u} - \langle u \rangle|}{\tilde{u}} = \frac{|\langle \rho' u' \rangle|}{\langle \rho \rangle \tilde{u}} = \frac{|\langle \rho' u' \rangle|}{(\langle \rho'^2 \rangle \langle u'^2 \rangle)^{1/2}} \frac{\langle \rho'^2 \rangle^{1/2}}{\langle \rho \rangle} \frac{\langle u'^2 \rangle^{1/2}}{\tilde{u}}$$

Now, $\dfrac{\langle \rho'^2 \rangle^{1/2}}{\langle \rho \rangle} \simeq \dfrac{\langle T'^2 \rangle}{\tilde{T}}$ and the correlation coefficient between ρ' and u' is less than 1. Then, we have :

$$\frac{|\tilde{u} - \langle u \rangle|}{\tilde{u}} = \frac{|\langle \rho' u' \rangle|}{\langle \rho \rangle \, \tilde{u}} \leq \frac{\langle T'^2 \rangle^{1/2}}{\langle T \rangle} \frac{\langle u'^2 \rangle^{1/2}}{\tilde{u}}$$

In the same way, we have :

$$\frac{|\tilde{v} - \langle v \rangle|}{\tilde{v}} = \frac{|\langle \rho' v' \rangle|}{\langle \rho \rangle \, \tilde{v}} \leq \frac{\langle T'^2 \rangle^{1/2}}{\langle T \rangle} \frac{\langle v'^2 \rangle^{1/2}}{\tilde{u}} \frac{\tilde{u}}{\tilde{v}}$$

An order of magnitude of $\dfrac{\langle T'^2 \rangle^{1/2}}{\tilde{T}}$ is often obtained by assuming that for boundary layers on an adiabatic wall with an external Mach number less than 5, the fluctuations of total enthalpy are negligible, so that :

$$\frac{T'}{\tilde{T}} \simeq - (\gamma - 1) \, M^2 \, \frac{u'}{\tilde{u}}$$

For the considered case, $\dfrac{\langle T'^2 \rangle^{1/2}}{\tilde{T}}$ is at most of the order of 0.2 and $\dfrac{\langle u'^2 \rangle^{1/2}}{\tilde{u}}$ is at most of the order of 0.1.

Then, we can assume that $\tilde{T} \simeq \langle T \rangle$ and $\tilde{u} \simeq \langle u \rangle$, but $\tilde{v}$ can be very different from $\langle v \rangle$ because $\tilde{v}/\tilde{u}$ is small. These orders of magnitude also show that $\dfrac{|\langle u' \rangle|}{\tilde{u}} = \dfrac{|\langle \rho' u' \rangle|}{\langle \rho \rangle \, \tilde{u}}$ is at most of the order of 0.02.

An estimation of the turbulence induced normal pressure gradient can also be performed (BUSHNELL et al, 1976). Equation (53c) shows that :

$$\langle p \rangle + \langle \rho v'^2 \rangle = \text{cst}$$

This expression is evaluated between the region of peak $\langle v'^2 \rangle$ located around $y/\delta \approx 0.1$ (the pressure is nearly equal to $\langle p \rangle_e$) and the wall :

$$\langle p \rangle_w \simeq \langle p \rangle_e + \frac{\langle \rho \rangle_p}{\langle \rho \rangle_e} \rho_e U_e^2 \frac{\langle v'^2 \rangle_p}{U_e^2}$$

or

$$\langle p \rangle_w \simeq \langle p \rangle_e + \frac{\langle \rho \rangle_p}{\langle \rho \rangle_e} \gamma M_e^2 \frac{\langle v'^2 \rangle_p}{U_e^2}$$

Taking $\dfrac{\langle \rho \rangle_p}{\langle \rho \rangle_e} \approx 0.2$ and $\dfrac{\langle v'^2 \rangle_p}{U_e^2} \approx 5 \ 10^{-3}$, an order of magnitude of the variation of the static pressure within the boundary layer is :

$$\frac{\langle p \rangle_w}{\langle p \rangle_e} \approx 1 + 10^{-3} M_e^2$$

The induced normal pressure gradient can be significant if the Mach number is large. However, even in these conditions, this is not a first order effect.

Now let us examine the term $\langle \mu \dfrac{\partial u}{\partial y} \rangle$. If μ is decomposed as $\mu = \langle \mu \rangle + \mu'$, we have :

$$\langle \mu \frac{\partial u}{\partial y} \rangle = \langle \mu \rangle \frac{\partial \tilde{u}}{\partial y} + \langle \mu \rangle \frac{\partial \langle u' \rangle}{\partial y} + \langle \mu' \frac{\partial u'}{\partial y} \rangle$$

It has been shown that $\langle u' \rangle \ll \tilde{u}$. The term $\langle \mu' \dfrac{\partial u'}{\partial y} \rangle$ can be neglected by arguing that μ depends on T and the range of frequencies concerning μ' and $\dfrac{\partial u'}{\partial y}$ is very different (μ' belongs to the energy containing scales whereas $\dfrac{\partial u'}{\partial y}$ belongs to the dissipative scales). Finally the viscous term becomes :

$$\langle \mu \frac{\partial u}{\partial y} \rangle = \langle \mu \rangle \frac{\partial \tilde{u}}{\partial y}$$

The same analysis can be performed with the terms $\langle u \mu \dfrac{\partial u}{\partial y} \rangle$ and $\langle \lambda \dfrac{\partial T}{\partial y} \rangle$ in the energy equation.

Therefore, equations (53) are often simplified as :

$$\frac{\partial \rho U}{\partial x} + \frac{\partial \rho V}{\partial y} = 0 \tag{54a}$$

$$\rho U \frac{\partial U}{\partial x} + \rho V \frac{\partial U}{\partial y} = -\frac{\partial P}{\partial x} + \frac{\partial}{\partial y} \left(\mu \frac{\partial U}{\partial y} - \langle \rho u'v' \rangle \right) \tag{54b}$$

$$\frac{\partial P}{\partial y} = 0 \tag{54c}$$

$$\rho U \frac{\partial h_i}{\partial x} + \rho V \frac{\partial h_i}{\partial y} = -\frac{\partial}{\partial y} \left(U\mu \frac{\partial U}{\partial y} - \langle \rho u'v' \rangle U + \lambda \frac{\partial T}{\partial y} - \langle \rho v'h' \rangle \right) \tag{54d}$$

With the above simplifications, the total enthalpy is related to the static enthalpy by :

$$h_i = h + \frac{U^2}{2}$$

Let us notice that the boundary layer equations can also be written with the classical averages (instead of the mass-weighted averages as above). In this case, the equations have exactly the same form as equations (54) but the vertical velocity is replaced by $\langle v \rangle + \frac{\langle \rho'v'' \rangle}{\rho}$.

4 - PECULIARITIES OF TURBULENT COMPRESSIBLE FLOWS

4.1. Variations of density and temperature

The flows under consideration are characterized by a high Mach number and very often by a heat transfer at walls. Therefore heat is produced by direct dissipation and transferred by the turbulent fluctuations.

These phenomena imply a non uniform averaged temperature and density, which influence the velocity field.

In a boundary layer developing on an adiabatic wall, the large amount of dissipation near the wall leads to a large static temperature in this region. Then the kinematic viscosity is larger than near the external edge of the boundary layer and the local REYNOLDS number is smaller. Compared with an incompressible boundary layer, the viscous sublayer is thicker.

The variation of density in itself does not imply a modification of the turbulence structure. For example, the study by BROWN and ROSHKO of a low-speed mixing layer with a mixing of gases with different densities showed that the spreading rate of the layer is not affected by the variation of density. On the contrary, the spreading rate of a mixing layer of air is significantly reduced in supersonic flow. This means that there is a genuine compressibility effect in this case. It is not clear however if this is due to an effect on the turbulence structure. At least partly, the reduction of the spreading rate can be attributed to an effect of compressibility on the stability properties of the flow which are at the origin of the large scale structures. PAPAMOSCHOU-ROSHKO studied ten configurations of free shear layers obtained by using the flow of various gases (N_2, Ar, He) at various MACH numbers (between 0.2 and 0.4). These authors introduced a convective MACH number which is defined in a coordinate system moving with the convection velocity of the dominant waves and structures of the shear layers. The theoretical analysis is performed by studying the stability of a compressible inviscid vortex sheet. PAPAMOSCHOU-ROSHKO showed that the growth rates of the various free shear layers fall nearly onto a single curve. This result indicates that the shear layer question is more related to a stability problem than to a turbulence problem.

4.2. Decomposition of the fluctuating field in three modes

Another feature of compressible flows is that all the flow characteristics are fluctuating : velocity, temperature, density and pressure.

KOVASZNAY showed that these fluctuations can be expressed as a function of three basic modes (see FAVRE et al) : fluctuations of vorticity, entropy and pressure (acoustic fluctuations) and when the level of fluctuations is low, the equations describing the evolution of vorticity and pressure are separated. (The correlation coefficients between the various modes are not necessarily low).

When the fluctuations are no longer low, a second-order theory predicts various possible interactions between modes. In supersonic flows, a strong interaction is the vorticity-vorticity interaction which is at the origin of the aerodynamic noise.

These flows are also characterized by the pressure fluctuations (which are isentropic) which can

be transmitted over long distances as MACH-waves. The loss of turbulent energy by sound radiation is low but the radiated energy can have a strong effect on the laminar-turbulent transition. In supersonic and hypersonic wind tunnels, the transition on a flat plate or on a cone is strongly dependent on the noise generated by the turbulent boundary layers developing on the test section walls. The transition location is correlated with the test section-size because the noise affecting the transition depends on the distance between the model and the tunnel walls.

The role played by the pressure fluctuations in the turbulence modelling can be very different in compressible or incompressible flows. For example, the influence of compressibility on the $\langle p' \frac{\partial u_i'}{\partial x_i} \rangle$ term appears through the POISSON equations (43) for the pressure which contains much more terms in a compressible flow.

The averaged pressure gradient can also modify the processes of turbulence generation or destruction in supersonic flows. The pressure gradient can be very strong (through a shock wave or an expansion fan) and the interaction with the term $\frac{\langle p'u_i' \rangle}{\rho}$ in the turbulent kinetic energy equation can be significant. This also means that the wall curvature is an important parameter because it implies the existence of a normal pressure gradient and an effect on the turbulence.

4.3. The MORKOVIN hypothesis

Let us go back to the decomposition of the turbulent field into three modes : vorticity, entropy and acoustic pressure. At low Mach numbers in an isothermal flow, only the vorticity mode remains. In a compressible flow, if the vorticity generation by interactions between modes is negligible, the turbulence structure is unaffected by compressibility (the possible vorticity generation interactions are vorticity-entropy, vorticity-acoustic pressure, entropy-acoustic pressure).

From experimental data, MORKOVIN, 1961 showed that the acoustic mode and the entropy mode are negligible in boundary layers with usual rates of heat transfer and $M_e < 5$.

According to MORKOVIN, these flows are such as :

$$\frac{p'}{P} \ll 1 \quad ; \quad \frac{T_i'}{T_i} \ll 1$$

Using the state law and assuming that the velocity fluctuations u'/U are not too large, we have :

$$\frac{\rho'}{\rho} \simeq - \frac{T'}{T} \simeq (\gamma - 1) M^2 \frac{u'}{U}$$

The following relationships are deduced :

$$\frac{\langle \rho'^2 \rangle^{1/2}}{\rho} = \frac{\langle T'^2 \rangle^{1/2}}{T} = (\gamma - 1) M^2 \frac{\langle u'^2 \rangle^{1/2}}{U} \qquad (55a)$$

$$r_{u'T'} = \frac{\langle u'T' \rangle}{\left(\langle u'^2 \rangle \langle T'^2 \rangle \right)^{1/2}} = - 1 \qquad (55b)$$

This is the so-called strong REYNOLDS analogy. In fact, the basic hypotheses presented above are not very well founded and improvements of the analysis have been proposed by GAVIGLIO, 1987. Nevertheless, practical results such as formulae (55) can give reasonable orders of magnitude. For example, in a boundary layer on an adiabatic wall in supersonic flow, $r_{u'T'}$ is of order - 0.8.

The use of the strong REYNOLDS analogy must be done with care, in particular when the flow undergoes rapid variations.

It should also be noticed that some of the formulae deduced from the strong REYNOLDS analogy are not galilean invariant ; this is the case of the formula (55a) because M^2/U is not galilean invariant.

BRADSHAW, 1977, associated the validity of the MORKOVIN hypothesis with low values of $\frac{\langle \rho'^2 \rangle^{1/2}}{\rho}$. For boundary layers with an external MACH number lower than 5, the condition is fulfilled as $\frac{\langle \rho'^2 \rangle^{1/2}}{\rho}$ is smaller than 0.1. BRADSHAW noticed that at higher MACH numbers, the total temperature fluctuations are no longer negligible but when the wall is cooled, the level of temperature and density fluctuations increases only slowly with the MACH number. At these higher MACH numbers, the pressure fluctuations increase and the

turbulence structure can be affected (pressure-vorticity and pressure-entropy interactions can generate vorticity fluctuations).

BRADSHAW also noticed that in free mixing layers, the level of velocity fluctuations $\langle u'^2 \rangle^{1/2}/U$ can reach 0.3 so that the density fluctuations are larger. This implies that the limit of validity of the MORKOVIN hypothesis ($\langle \rho'^2 \rangle^{1/2}/\rho < 0.1$) is limited to external MACH numbers less than 1.5. This is in rough agreement with experimental data but as already said, it is not clear that the effect of MACH number on the spreading rate of the mixing layer is due to an alteration of the turbulence structure or to an effect on the stability of the flow (which is at the origin of the large structures).

The "incompressible" behaviour of boundary layers in supersonic flow can be illustrated by examining shear stress profiles (figure 3). MAISE and McDONALD, 1968, determined the evolution of the shear stress in a flat plate boundary layer at $M_e = 0$ and $M_e = 5$ for a REYNOLDS number $R_\theta = 10^4$ and an adiabatic wall. The comparison of the profiles - $\langle \rho u'v' \rangle / \tau_w$ shows that the effect of compressibility is small. Similar results have been obtained by SANDBORN up to $M_e = 7$. In the same way, quantities like $\langle \rho u'^2 \rangle / \tau_w$ are not affected by compressibility (SANDBORN, 1974).

MAISE and McDONALD also showed that the mixing length distribution is nearly independent of MACH number. This means that the turbulent shear stress is expressed as :

$$- \langle \rho u'v' \rangle = \rho \ell^2 \left(\frac{\partial U}{\partial y}\right)^2 \tag{56}$$

where ℓ/δ has the same evolution of y/δ as in incompressible flow (figure 4). This formula can be used to calculate equilibrium or near equilibrium boundary layers, but no shock wave-boundary layer interaction for example.

Many features of supersonic boundary layers are close to the incompressible case but some effects of compressibility on turbulence structure can be noticed. For example, the intermittency function defined as the fraction of time that the flow is turbulent is sharper in supersonic flow ; this means that the region with intermittent turbulence is narrower in supersonic flow (figure 5).

The entrainment coefficient is also affected by the MACH number. Compared to an equivalent boundary layer in incompressible flow, the entrainment coefficient of a boundary layer on an adiabatic wall is approximately doubled at $M_e = 5$.

4.4. Compressibility transformations

The idea that compressible flows behave like incompressible flows leads many authors to look for transformations which reduce the study of compressible flows to that of an equivalent incompressible flow.

In fact, there is no method which enables us to transform exactly the equations of a compressible boundary layer into incompressible equations.

Among the various problems, we can cite the presence of large temperature gradients normal to the wall, the dissipation effects, the fluctuating density terms, ... which have no counterpart in incompressible flow.

The idea of compressibility transformation is however used for specific purposes. Let us give two examples : i) the study of the law of the wall and ii) the construction of a skin friction law.

4.4.1. Compressibility transformation for the law of the wall

The law of the wall is obtained by assuming that, near the wall, the shear stress is constant :

$$- \langle \rho u'v' \rangle = \tau_w$$

Assuming that the mixing length is $\ell = \chi y$, a transformation of velocity is defined :

$$U^* = \int_0^U \left(\frac{\rho}{\rho_w}\right)^{1/2} dU \tag{57}$$

which leads to the law of the wall :

$$\frac{U^*}{U_\tau} = \frac{1}{\chi} \ln \frac{y U_\tau}{\nu_w} + C \quad ; \quad U_\tau = (\tau_w/\rho_w)^{1/2} \tag{58}$$

If compressibility effects are negligible, χ and C have the same values as in incompressible flow : $\chi = 0.41$, $C = 5$.

The law of the wall can be explicited for the physical variables if a velocity-temperature relationship is available. A general law is not known and a reliable formulation of the law of the wall only exists for a boundary layer developing on an adiabatic wall, for moderate pressure gradients and an external MACH number less than 5.

Using the CROCCO relationship :

$$T_i = T_w + (T_{i_e} - T_w) \frac{U}{U_e}$$

or

$$\frac{\rho_w}{\rho} = \frac{T}{T_w} = 1 + \left(\frac{T_{i_e}}{T_w} - 1\right) \frac{U}{U_e} - \left(\frac{T_{i_e}}{T_w} - \frac{T_e}{T_w}\right) \left(\frac{U}{U_e}\right)^2$$

We obtain the solution proposed by VAN DRIEST, 1951 :

$$\frac{U^*}{U_e} = \frac{1}{A} \sin^{-1} \left[\frac{2A^2 \frac{U}{U_e} - B}{(B^2 + 4A^2)^{1/2}}\right] + \frac{1}{A} \sin^{-1} \frac{B}{(B^2 + 4A^2)^{1/2}} \qquad (59)$$

with :

$$A^2 = \frac{\gamma - 1}{2} M_e^2 \frac{T_e}{T_w}$$

$$B = \left(1 + \frac{\gamma - 1}{2} M_e^2\right) \frac{T_e}{T_w} - 1$$

4.4.2. Compressibility transformation for the skin friction law

In compressible flow, the flat plate skin friction law has been derived with success from the concept of reference enthalpy.

Using a density ρ^* and a viscosity μ^* evaluated at a reference enthalpy h^*, the skin friction law of the flat plate boundary layer in compressible flow is assumed to follow the same law as in incompressi-

$$\frac{\tau_w}{\rho^* U_e^2} = \frac{0.0184}{\left(\frac{\rho^* U_e x}{\mu^*}\right)^{1/6}} \qquad (60)$$

where x is the distance from the flat plate leading edge.

Formula (60) can be written as :

$$\frac{C_f}{2} = \frac{\tau_w}{\rho_e U_e^2} = \frac{0.0184}{R_x^{1/6}} f \quad ; \quad R_x = \frac{\rho_e U_e x}{\mu_e} \qquad (61)$$

where :

$$f = \left(\frac{\mu^*}{\mu_e}\right)^{1/6} \left(\frac{\rho^*}{\rho_e}\right)^{5/6}$$

The compressibility function f is evaluated from the reference enthalpy given by the MONHAGAN formula :

$$h^* = h_e + 0.54 (h_w - h_e) + 0.16 (h_{ad} - h_e)$$

where h_{ad} is the recovery enthalpy :

$$h_{ad} = h_e \left(1 + r \frac{\gamma - 1}{2} M_e^2\right) \quad ; \quad r = 0.9$$

It should be noticed that this simple method gives the right evolution of skin friction with MACH number and wall temperature.

4.5. Transition and low REYNOLDS number effects

To study this problem, BUSHNELL et al, 1975, characterized the boundary layer with the parameter δ^*

based on the thickness δ :

$$\delta^* = \frac{\delta \, (\tau_{max}/\rho_w)^{1/2}}{\nu_w}$$

where the index "max" refers to the maximum shear τ in the boundary layer.

Qualitatively, the importance of low REYNOLDS numbers are given in a (δ^*, R_x) plane (figure 6).

This diagram shows that the effects of low REYNOLDS numbers can be important even if the REYNOLDS number $R_x = \frac{\rho_e U_e x}{\mu_e}$ is large. BUSHNELL et al observed that the level of the mixing length in the outer region can be doubled or more when δ^* is of order 100 (figure 7a). However this increase is a function of distance downstream of transition (compare figures 7a and 7b) ; it takes about a distance of 30-50 δ to wash out the low REYNOLDS number effects.

BUSHNELL et al also insist on the "precursor transition" effect. This effect is characterized by the existence of large scale disturbance in the outer region of compressible boundary layers far upstream of the nominal transition point. In practice, this effect implies that the outer boundary layer (velocity profile, ...) departs from the laminar state well upstream of the nominal wall transition location. BUSHNELL et al mentioned a possible further manifestation of this effect which is the increase in surface heating upstream of the conventional transition point (figure 8).

The transition onset is greatly affected by compressibility effects : influence of MACH number, influence of wall to boundary layer edge temperatures ratio. ARNAL used the e^n-transition criterion to evaluate these effects. Let us recollect the principle of this technique. The stability properties of laminar boundary layers are determined by solving the ORR-SOMMERFELD equations. These solutions indicate whether small perturbations are stable or unstable (the perturbation are waves characterized by their frequency and wave length). Another result of these solutions is the amplification rate of the unstable waves. Then, it is possible to calculate the total amplification rate A/A_0 of the most amplified waves. The transition criterion introduced by VAN INGEN, 1956, and SMITH-GAMBERONI, 1956, tells that transition occurs when A/A_0 reaches a critical level e^n. The factor n is an empirical input which characterizes the quality of the external flow : when the external flow is noisy, the value of n is small (in noisy supersonic or hypersonic wind tunnels, $n = 2-4$) ; in a clean environment, n is of order 8-10 (BUSHNELL et al, 1988).

The calculated effects of MACH number (adiabatic wall) and of the wall to edge temperature ratios are shown in figures 9 and 10. Let us notice that these results are at least in qualitative agreement with experimental data. For a boundary layer developing on an adiabatic wall, an increase in MACH number stabilizes the transition (the transition REYNOLDS number is larger) except in the range $2 < M < 3.5$, where the opposite effect is observed (figure 9). Figure 10 shows that, for a given MACH number, a cooling of the wall increases the transition REYNOLDS number compared to the case of an adiabatic wall at the same MACH number. It is also noted that the beneficial effect of wall cooling is less pronounced as the MACH number increases.

4.6. Turbulent heat flux

The diffusion of heat in a turbulent boundary layer is due to the molecular diffusivity and to the transport by turbulence. The corresponding fluxes are :

$$Q_\ell = - \lambda \frac{\partial T}{\partial y} \quad \text{and} \quad Q_t = \langle \rho v' h' \rangle$$

When the flow is fully turbulent, the ratio Q_t/Q_ℓ is large and the thermal transfer is mainly due to turbulence.

As already seen, the correlation between velocity and temperature fluctuations is good. The coefficient $|\langle v'T'\rangle|/(\langle v'^2\rangle\langle T'^2\rangle)^{1/2}$ can be of the order 0.6. Then, the order of magnitude of Q_t/Q_ℓ is :

$$\frac{Q_t}{Q_\ell} \sim \frac{u \, \ell}{\nu} \, \mathcal{P} \, \frac{\langle T'^2 \rangle^{1/2}}{\Delta T}$$

where $\mathcal{P}$ is the PRANDTL number and ΔT is a characteristic temperature difference within the boundary layer.

Thus the thermal turbulence is characterized by the PECLET number :

$$\mathcal{P}_t = R_\ell \mathcal{P}$$

For air, the PRANDTL number is close to unity so that the thermal field is fully turbulent for the same range of REYNOLDS numbers as the velocity field.

Then, the turbulent heat fluxes are often analyzed by using the turbulent PRANDTL number $\mathscr{P}_t$ defined as :

$$\mathscr{P}_t = \frac{\langle\rho u'v'\rangle}{\dfrac{\partial U}{\partial y}} \left/ \frac{\langle\rho v'T'\rangle}{\dfrac{\partial T}{\partial y}} \right. \tag{62}$$

In certain analyses, the value $\mathscr{P}_t = 1$ is taken. This is the so-called REYNOLDS analogy (which is different from the strong REYNOLDS analogy).

For flat plate boundary layers in air, the turbulent PRANDTL number is of order $\mathscr{P}_t = 0.8$-0.9 with a tendency to increase near the wall and to decrease near the outer edge.

No systematic effects of MACH number, low REYNOLDS number or blowing have been observed (BUSHNELL et al, 1976).

The data of BLACKWELL et al show a decrease in $\mathscr{P}_t$ when the pressure gradient is positive (see LAUNDER, 1976).

The value of the PRANDTL number can be influenced by boundary conditions. For example, on a rough wall compared with a smooth wall, the increase in heat flux is less than the increase in the skin friction.

On the other hand, the value of the PRANDTL number depends on the type of flow. In free flows, $\mathscr{P}_t$ is significantly less than unity in the central part of the flow. For round jets, $\mathscr{P}_t$ is of order 0.7. For wakes, values of order 0.5 have been measured. This means that calculating a compressible turbulent flow with a turbulent PRANDTL number is a simple solution but not the best.

The analogy between the fluctuations of velocity and temperature has been extensively studied by FULACHIER and ANTONIA. They found that there is a good analogy for the energy-containing part of the spectra of the temperature fluctuations and of the total velocity fluctuations ; this result has been obtained for different types of flows.

These authors also showed that the spectral distribution of the PRANDTL number is not at all uniform. The analogy between velocity and temperature fluctuation is analyzed by using the parameter B :

$$B = \frac{\langle q'^2\rangle^{1/2}}{\langle T'^2\rangle^{1/2}} \frac{\dfrac{\partial T}{\partial y}}{\dfrac{\partial U}{\partial y}}$$

where q' is the fluctuation of the total velocity.

FULACHIER and ANTONIA observed that B varies from flow to flow but is nearly constant within a given flow. In addition, the spectral distribution of B is nearly uniform (except for high values of frequency).

4.7. Other problems

As already seen, the compressibility of the flow adds many complexities as compared to the incompressible flow. The list of problems discussed in this section is not complete and many other effects could be cited.

The hypersonic vehicles often have a blunt shape so that a bow shock wave exists in front of them. Then, the streamlines which cross this shock wave do not have the same entropy jump and the boundary layer is fed with variable entropy streamlines ; the associated variations of free stream characteristics normal to the wall can be large. The influence on the turbulence structure is not known.

Instability like GÖRTLER vortices can develop in supersonic or hypersonic flow. This has been observed in the flow on a compression ramp for example.

The shock wave-boundary layer interaction is obviously a problem of prime importance in transonic, supersonic and hypersonic flow. This topic has been reviewed by DELERY, 1988 in great details.

5 - TURBULENCE MODELS

Most of the turbulence models used in compressible flows are based on the eddy viscosity formulation. Accordingly, the turbulent shear stresses are expressed as :

$$- \langle \rho u_i' u_j' \rangle + \frac{2}{3} \rho k \delta_{ij} = 2\mu_t \left(S_{ij} - \frac{\delta_{ij}}{3} \frac{\partial U_\ell}{\partial x_\ell} \right) \quad ; \quad S_{ij} = \frac{1}{2} \left(\frac{\partial U_i}{\partial x_j} + \frac{\partial U_j}{\partial x_i} \right) \tag{63}$$

One drawback of this model is that the principal axes of the REYNOLDS stress tensor are aligned with the principal axes of the rate of strain tensor. To take into account the possible non alignment between stresses and rates of strain, SAFFMAN and, later, WILCOX and RUBESIN proposed a more complex constitutive relationship. These latter authors used :

$$- \langle \rho u_i' u_j' \rangle + \frac{2}{3} \rho k \delta_{ij} = 2\mu_t \left(S_{ij} - \frac{\delta_{ij}}{3} \frac{\delta U_\ell}{\partial x_\ell} \right) + \frac{8}{9} k \frac{(S_{im} R_{mj} + S_{jm} R_{mi})}{(\beta^* \omega^2 + 2 S_{nm} S_{mn})} \tag{64}$$

with $R_{ij} = \frac{1}{2} \left(\frac{\partial U_i}{\partial x_j} - \frac{\partial U_j}{\partial x_i} \right)$; $\beta^* = 0.09$.

WILCOX and RUBESIN used this formulation in a $k-\omega^2$ two-equation model where ω is the rate of dissipation per kinetic energy unit ($\omega = \epsilon/k$).

The constitutive relationship (63) or (64) is not sufficient to express the REYNOLDS stresses because μ_t is not known. The eddy viscosity is determined either by a zero-equation model (mixing length model) or by a one-equation model (generally the k-equation) or by a two-equation model ($k-\epsilon$ or $k-\omega^2$ model for example).

In addition, the solution of the mean energy equation requires the modelling of the turbulent heat flux $\langle \rho u_i' h' \rangle$ which is generally expressed via a PRANDTL number :

$$\langle \rho u_i' h' \rangle = - \frac{\mu_t}{\mathcal{P}_t} \frac{\partial h}{\partial y} \tag{65}$$

The solution of the energy equation also requires the modelling of the triple correlation term $\langle \rho u_i' u_j' u_j' \rangle$ (eq. 51). This term is the main contribution of the diffusion term in the k-equation (eq.40b). The formulation used in incompressible flow is generally retained :

$$- \frac{1}{2} \langle \rho u_i' u_j' u_j' \rangle = \frac{\mu_t}{\sigma_k} \frac{\partial k}{\partial x_j} \tag{66}$$

where σ_k looks like a PRANDTL or SCHMIDT number. (In the $k-\epsilon$ model of LAUNDER et al, $\sigma_k = 1$).

The expression (66) shows that it is necessary to know the evolution of the turbulent kinetic energy k. In the one-equation or two-equation model, the k-equation is included. If a mixing length model is used, the calculation of k from the constitutive law (63) is not possible but the application of this model is generally restricted to boundary layer type flow, in which case the triple correlation is neglected involving the boundary layer assumptions.

5.1. Mixing length scheme

5.1.1. Model of MICHEL et al

The mixing length scheme developed by MICHEL et al, 1969, has been used in compressible flow. The extension is very straightforward and consists of using the local density as in formula (56).

This model is used for boundary layers where the expression of the turbulent stress $- \langle \rho u'v' \rangle$ is :

$$- \langle \rho u'v' \rangle = \rho F^2 \ell^2 \left(\frac{\partial U}{\partial y} \right)^2 \tag{67a}$$

In this expression, ℓ is the mixing length which is given as a function of the distance from the wall y/δ reduced by the boundary layer thickness. The formula is the same as in incompressible flow :

$$\frac{\ell}{\delta} = 0.085 \tanh \left(\frac{\chi}{0.085} \frac{y}{\delta} \right) ; \chi = 0.41 \tag{67b}$$

The damping function F is given as a function of $\tau = \mu \dfrac{\partial U}{\partial y} - \langle \rho\, u'v' \rangle$ by the relationship :

$$F = 1 - \exp\left[-\frac{\ell}{26\chi\mu}(\tau\rho)^{1/2}\right] \tag{67c}$$

This formula is a modified form of the VAN DRIEST damping function (the VAN DRIEST formula is obtained by taking the values of τ, ρ and μ at the wall in eq.67c).

The turbulent heat flux is calculated with a constant PRANDTL number ($\mathscr{P}_t = 0.89$) :

$$\langle \rho v' h' \rangle = -\frac{1}{\mathscr{P}_t} \rho\, F^2 \ell^2\; \frac{\partial U}{\partial y}\frac{\partial h}{\partial y} \tag{67d}$$

Although this model is a very crude extension of the incompressible scheme, it enables us to reproduce correctly the compressibility effects in supersonic boundary layers not too far from equilibrium. This model has also been used to construct self-similar solutions which produced the closure relationships of an integral method (COUSTEIX et al, 1974). This integral method also gives good agreement with experimental data for compressible boundary layers not too far from equilibrium.

5.1.2. CEBECI-SMITH model

A more complex model has been developed by CEBECI-SMITH, 1974. This is also a mixing length scheme where the eddy viscosity is expressed by a two-layer formulation.

In the outer region of the boundary layer, μ_t is :

$$\mu_{t_o} = \alpha\, \rho\, U_e\, \delta_{11} \tag{68a}$$

with $\delta_{11} = \displaystyle\int_0^\infty \left(1 - \frac{U}{U_e}\right) dy$; $\alpha = 0.0168$.

In the inner region, μ_t is given by :

$$\mu_{t_i} = \rho\, \kappa^2 y^2\, (1 - e^{-y/A})^2\, \frac{\partial U}{\partial y} \tag{68b}$$

The two formulae are matched at the point where $\mu_{t_i} = \mu_{t_o}$.

The damping function is obtained by extending the VAN DRIEST proposal taking into account the effects of pressure gradient and wall blowing (or suction) :

$$A = A^* \frac{\mu}{\rho N}\left(\frac{\tau_w}{\rho_w}\right)^{-1/2}\left(\frac{\rho}{\rho_w}\right)^{1/2} \tag{68c}$$

$$N^2 = \frac{\mu}{\mu_e}\left(\frac{\rho_e}{\rho_w}\right)^2 \frac{p^*}{V_w^*}\left[1 - \exp\left(11.8\,\frac{\mu_w}{\mu}\,V_w^*\right)\right] + \exp\left(11.8\,\frac{\mu_w}{\mu}\,V_w^*\right) \tag{68d}$$

$$p^* = \nu_e U_e\, \frac{dU_e}{dx}\left(\frac{\rho_w}{\tau_w}\right)^{3/2}$$

$$V_w^* = V_w\left(\frac{\rho_w}{\tau_w}\right)^{1/2}$$

In these formulae, the index w means that a quantity is calculated at the wall and the index e refers to the outer edge of the boundary layer. The quantities without index are calculated at the point where A is evaluated. The quantity V_w is the wall transpiration velocity.

The coefficients κ and A^* are function of the REYNOLDS number :

$$\kappa = 0.4 + \frac{0.19}{1 + 0.49\, Z_2^2} \tag{68e}$$

$$A^* = 26 + \frac{14}{1 + Z_2^2} \tag{68f}$$

with $Z_2 = R_\theta 10^{-3} > 0.3$; $R_\theta = \frac{\rho_e U_e \theta}{\mu_e}$; $\theta = \int_0^\infty \frac{\rho u}{\rho_e u_e} \left(1 - \frac{u}{u_e}\right) dy$.

The turbulent heat flux is also given by a two-layer model :

$$\langle \rho v' h' \rangle = - \rho a_t \frac{\partial h}{\partial y}$$

In the outer region, the eddy diffusivity is :

$$a_{t_o} = \frac{\alpha_1}{\mathcal{P}_t} U_e \delta_{1i} ; \quad \alpha_1 = \alpha = 0.0168 \tag{69a}$$

In the inner region, the eddy diffusivity is :

$$a_{t_i} = \kappa\kappa_h y^2 \frac{\partial U}{\partial y} (1 - e^{-y/A}) (1 - e^{-y/B}) \tag{69b}$$

where A is given by eq. 68c and B is :

$$B = B^* \frac{\mu}{\rho N} \left(\frac{\tau_v}{\rho_v}\right)^{-1/2} \left(\frac{\rho}{\rho_v}\right)^{1/2} \tag{69c}$$

where N is given by eq. 68d.

The coefficients κ_h and B^* are function of the REYNOLDS number. For air, the formulae are :

$$\kappa_h = 0.44 + \frac{0.22}{1 + 0.42 Z_2^2} \tag{69d}$$

$$B^* = 35 + \frac{25}{1 + 0.55 Z_2^2} \tag{69e}$$

with $Z_2 = R_\theta 10^{-3} > 0.3$.

In the case of a fluid with constant properties ($\rho = $ cst, $\mu = $ cst), the turbulent PRANDTL number in the inner region as given by the CEBECI-SMITH model is :

$$\mathcal{P}_t = \frac{\nu_t}{a_t} = \frac{\kappa}{\kappa_h} \frac{1 - e^{-y^*/A^*}}{1 - e^{-y^*/B^*}}$$

At the wall, we have :

$$\mathcal{P}_t = \frac{\kappa}{\kappa_h} \frac{B^*}{A^*}$$

and in the fully turbulent region ($y^* \to \infty$) :

$$\mathcal{P}_t = \frac{\kappa}{\kappa_h}$$

For high REYNOLDS number, $\mathcal{P}_t = 1.22$ for $y = 0$ and $\mathcal{P}_t = 0.91$ for $y^* \to \infty$.

The experimental data show that, near the wall, the turbulent PRANDTL number $\mathcal{P}_t$ depends on the molecular PRANDTL number $\mathcal{P}$. Away from the wall, in the fully turbulent region, it can be assumed that the characteristics of turbulence (for velocity and temperature fluctuations) are independent of the fluid properties so that it seems reasonable to assume that $\mathcal{P}_t$ is not influenced by $\mathcal{P}$.

NA and HABIB, 1973, using experimental data obtained with fluids of different PRANDTL number ($0.02 < \mathcal{P} < 15$), proposed to take into account the effect of $\mathcal{P}$ on B^* :

$$B^* = B^{**}/\mathcal{P}^{1/2}$$

$$B^{**} = \sum_{i=1}^{5} C_i (\log \mathcal{P})^{i-1}$$

$C_1 = 34.96$; $C_2 = 28.79$; $C_3 = 33.95$; $C_4 = 6.33$; $C_5 = -1.186$.

Let us notice that in the outer region, ν_t and a_t are sometimes multiplied by an intermittency function γ :

$$\gamma = (1 + 5.5 \ (y/\delta))^6)^{-1}$$

At high REYNOLDS number, the influence of its inclusion is small.

5.1.3. BALDWIN-LOMAX model

The CEBECI-SMITH model has been modified by BALDWIN-LOMAX, 1978, for applications to NAVIER-STOKES solutions. A difficulty with the CEBECI-SMITH model is that the thickness δ_{11} is ill-defined in separated flows. In the BALDWIN-LOMAX model, the length scale y_M is obtained from the vorticity distribution. It is claimed that this length is well defined and easily computed for a wide class of flows.

The BALDWIN-LOMAX model is also a two-layer model. The expressions of μ_{t_1} and μ_{t_0} are :

$$\mu_{t_1} = \rho \ (0.41 \ y \ d)^2 \ \sqrt{\omega_i \omega_i} \tag{70a}$$

$$\mu_{t_0} = 0.0269 \ \rho \ F_w \gamma \tag{70b}$$

ω_i is the i-th component of the vorticity vector. γ is the intermittency function :

$$\gamma = \left[1 + 5.5 \left(0.3 \ \frac{y}{y_M} \right)^6 \right]^{-1}$$

d is the VAN DRIEST damping function and y_M is the length scale defined as the outermost value of y where the function $F = (y \ \sqrt{\omega_i \omega_i} \ d)$ has a local maximum F_M. F_w is given by :

$$F_w = y_M \ \min \left(F_M, \ 0.25 \ \frac{(\Delta U)_{max}^2}{F_M} \right)$$

where $(\Delta U)_{max}$ is the maximum velocity difference in the boundary layer at a given x-station.

The BALDWIN-LOMAX model has been mainly used for solving the averaged NAVIER-STOKES equations with the thin layer approximation (in this approximation, the longitudinal diffusion is neglected but no assumption is made about the pressure gradient which is normal to the wall). It seems that this model has not been widely tested for flows with strong heat transfer.

MARVIN and COAKLEY indicate that the CEBECI-SMITH and BALDWIN-LOMAX models give similar predictions of both attached and separated boundary layer flows for low to moderate supersonic flows. The predictions of attached flows are usually in good agreement with experiment but the predictions of separated flows are frequently deficient. At hypersonic speeds, the models also tend to give similar predictions although there is some evidence that the BALDWIN-LOMAX model may be more sensitive to MACH number than the CEBECI-SMITH model.

In a general manner it can be said that the zero equation models are able to give rather accurate results even at high MACH number as far as boundary layers not too far from equilibrium are concerned. It should be noticed that these flows are common in supersonic and hypersonic flows and that is why these simple models are attractive ; in addition, they are easy to use and economic. As mentioned by BUSHNELL et al, 1976, it is interesting to notice that the adjustment of constants (for example in the CEBECI-SMITH model, the effects of low REYNOLDS number or of pressure gradients or of wall blowing) is essentially obtained from incompressible data.

The calculations of shock wave-boundary layer interactions with the above models are not very good. Ad hoc modifications have been proposed to handle these flows with more or less success (see DELERY, 1988).

5.2. One-equation models

Most of one equation models in use today are based on the solution of the turbulent kinetic energy. Among the first authors to develop this type of procedure, we can cite GLUSHKO, 1965, and BRADSHAW et al,

1967. This type of model has been used in particular at the 1968 STANFORD Conference (BRADSHAW-FERRIS, BECKWITH-BUSHNELL) for the calculation of incompressible boundary layers.

5.2.1. BRADSHAW et al model in incompressible flow

Let us recollect the main features of the BRADSHAW et al model.

This is a model for the outer part of the boundary layer only ; this characteristic is very common when transport equations are used.

In incompressible flow, three hypotheses are introduced to close the system formed by the momentum equation and the k-equation. The first hypothesis is to assume a constant ratio between the shear stress and the kinetic energy :

$$\tau_t = -\langle \rho u'v' \rangle = 2a_1 \rho k \qquad a_1 = 0.15 \tag{71a}$$

The second hypothesis consists of expressing the dissipation rate by means of a dissipation L :

$$\epsilon = \frac{(\tau_t/\rho)^{3/2}}{L} \tag{71b}$$

where L is a prescribed function of y/δ (figure 11). This closure relationship is close to the basic formula (eq. 11).

The third hypothesis concerns the diffusion term (in the y-direction) which is given as :

$$\text{Diff}_y(k) = \frac{\partial}{\partial y} \left[G \, \tau_t \, \left(\frac{\tau_t}{\rho}\right)_{max}^{1/2} \right] \tag{71c}$$

where G is a prescribed function of y/δ (figure 11).

The weakness of the model is the prescription of the dissipation length but this length seems to be more invariant than the mixing length.

5.2.2. RUBESIN model

Another way for the closure of the k-equation is to express the turbulent shear stress by the eddy viscosity model (eq. 63). Then, the dissipation rate is given by $\epsilon \sim k^{3/2}/L$ and the diffusion term is given by eq. 66. In such a model, the eddy viscosity μ_t is expressed by a PRANDTL-KOLMOGOROV formula $\mu_t \sim \rho \sqrt{k} \, L$. Obviously the length scale remains unknown and has to be prescribed.

These hypotheses are the basis of the model developed by RUBESIN, 1976 who extended the GLUSHKO model to compressible flows.

In this model, the turbulent shear stress is calculated from the eddy viscosity formulation (63) with :

$$\mu_t = F(R_t) \tag{72}$$

where R_t is a turbulence REYNOLDS number defined as :

$$R_t = \frac{\rho \sqrt{k} \, L}{\mu} \tag{73a}$$

The function F is given by :

$$F(R_t) = \alpha \, \mu \, R_t \begin{cases} \bar{R}_t & \text{if } \bar{R}_t < 0.75 \\ \bar{R}_t - (\bar{R}_t - 0.75)^2 & \text{if } 0.75 \leq \bar{R}_t < 1.25 \\ 1 & \text{if } 1.25 < \bar{R}_t \end{cases} \tag{73b}$$

where $\bar{R}_t = R_t/R_0$. α and R_0 are constants.

The length scale L is a function of $\bar{y} = y/\delta$:

$$L = \delta \begin{cases} \bar{y} & \text{if } \bar{y} < 0.23 \\ (\bar{y} + 0.37)/2.61 & \text{if } 0.23 \leq \bar{y} < 0.57 \\ (1.48 - \bar{y})/2.52 & \text{if } 0.57 \leq \bar{y} < 1.48 \end{cases} \tag{73c}$$

The turbulent heat flux is given by :

$$\langle \rho v'h' \rangle = -\rho a_t \frac{\partial h}{\partial y} \tag{74}$$

with $\rho a_t = F(\Gamma R_t)$.

The dissipation rate and the diffusion term of the k-equation are :

$$\epsilon = \frac{\mu_k Ck}{L^2} \tag{75a}$$

$$\text{Diff}(k) = \frac{\partial}{\partial x_j} \left(\mu_k \frac{\partial k}{\partial x_j} \right) \tag{75b}$$

with $\mu_k = \mu + F(\lambda R_t)$.

The constants of the models are : $\alpha = 0.22$, $C = 4.69$, $R_0 = 120$, $\lambda = 0.4$, $\Gamma = 1.1$.

5.2.3. Compressibility terms

The complete modelling of the k-equation requires the knowledge of the compressibility terms $\dfrac{\langle \rho' u_i' \rangle}{\rho}$ and $\langle p' \dfrac{\partial u_i'}{\partial x_i} \rangle$.

At NASA AMES, RUBESIN, 1976, proposed expressions given below.

First assuming that the fluctuations of total temperature are negligible and that the velocity fluctuations are small compared with the mean velocity, one obtains :

$$T' = -\frac{U_i}{C_p} u_i' \tag{76}$$

In addition, it is assumed that within an eddy, the fluid has a polytropic behaviour, that is :

$$\frac{P'}{P} = n \frac{\rho'}{\rho} = \frac{n}{n-1} \frac{T'}{T} \tag{77}$$

Combining eq. (76) and (77), one gets :

$$\rho' = -\frac{\rho}{(n-1) C_p T} U_i u_i' \tag{78}$$

From this expression, the correlation $\langle \rho' u_j' \rangle$ is deduced :

$$\frac{\langle \rho' u_j' \rangle}{\rho} = -\frac{U_i}{(n-1) C_p T} \langle u_i' u_j' \rangle \tag{79}$$

The correlation $\langle u_i' u_j' \rangle$ is approximated by $\langle \rho u_i' u_j' \rangle / \rho$ and, using the eddy viscosity model, the correlation $\langle \rho' u_j' \rangle$ is given by :

$$\langle \rho' u_j' \rangle = \frac{U_i}{(n-1) C_p T} \left[2\mu_t \left(S_{ij} - \frac{\delta_{ij}}{3} \frac{\partial U_\ell}{\partial x_\ell} \right) - \frac{2}{3} \rho k \delta_{ij} \right] \tag{80}$$

where $(n-1)$ appears as a modelling constant.

If the mean velocity is larger in one direction (let us say $i = 1$), eq. (79) can be written as :

$$\frac{\langle \rho' u_j' \rangle}{\rho} = - \frac{U_i}{(n-1) C_p T} \langle u_i'^2 \rangle \tag{81a}$$

or, approximately, as :

$$\frac{\langle \rho' u_j' \rangle}{\rho} = \alpha \, U_i \, \frac{k}{a^2} \quad ; \quad a^2 = (\gamma - 1) \, C_p T \tag{81b}$$

where α is a model constant.

In this expression, a MACH number $k^{1/2}/a$ formed with the turbulent kinetic energy appears. Let us notice that expressions (81) are not galilean invariant.

Another possible model for $\langle \rho' u_j' \rangle$ is to use eq. (77) directly to deduce :

$$\frac{\langle \rho' u_j' \rangle}{\rho} = \frac{1}{(n-1) T} \langle T' u_j' \rangle \tag{82}$$

Then a model for the turbulent heat flux can be used to express $\langle \rho' u_j' \rangle$.

The various models for $\langle \rho' u_j' \rangle$ do not seem to have been largely tested. In most of the published work from NASA AMES, this term has been neglected.

The modelling of the other compressibility term $\langle p' \frac{\partial u_i'}{\partial x_i} \rangle$ is based on the assumption of a polytropic behaviour of the fluid (eq. 77) :

$$\langle p' \frac{\partial u_i'}{\partial x_i} \rangle = n \, \frac{p}{\rho} \, \langle \rho' \frac{\partial u_i'}{\partial x_i} \rangle$$

Using the continuity equation and assuming a slow variation of the turbulence intensity along a streamline, RUBESIN arrived at :

$$\langle \rho' \frac{\partial u_i'}{\partial x_i} \rangle = \frac{\langle \rho'^2 \rangle}{\rho^2} \, \rho \, \frac{\partial U_i}{\partial x_i}$$

The quantity $\frac{\langle \rho'^2 \rangle}{\rho^2}$ can be estimated from (eq. 78). VIEGAS-HORSTMAN, 1978, used the expression :

$$\langle p' \frac{\partial u_i'}{\partial x_i} \rangle = \xi \, \frac{C_v}{C_p} \, \rho k M^2 \, \frac{\partial U_i}{\partial x_i} \tag{83}$$

where M is the local MACH number of the averaged flow ; C_p and C_v are constant pressure and constant volume specific heats. ξ is a model constant ($\xi = 0.73$).

To summarize, the turbulent kinetic energy as used by VIEGAS-HORSTMAN is :

$$\frac{\partial}{\partial t} (\rho k) + \frac{\partial}{\partial x_j} (\rho U_j k) = - \langle \rho u_i' u_j' \rangle \frac{\partial U_i}{\partial x_k} + \xi \, \frac{C_v}{C_p} \, \rho k M^2 \, \frac{\partial U_i}{\partial x_i} - \mu_x \, \frac{Ck}{L^2} + \frac{\partial}{\partial x_j} \left(\mu_x \, \frac{\partial k}{\partial x_j} \right) \tag{84}$$

Let us also notice that the energy equation of the averaged flow (for example the equation for the total enthalpy) can be solved by using eq.74 to express the turbulent heat flux and the triple velocity correlations can be expressed by eq. (66).

5.3. Two-equation models

Basically, the two-equation models are eddy viscosity models in which the REYNOLDS stresses are expressed by eq. 63 and the turbulent heat fluxes are obtained from a turbulent PRANDTL number.

The eddy viscosity coefficient involves the use of a velocity scale u and a length scale l. The idea of two-equation models is to calculate these scales from transport equations. Instead of using equations for u and l, it is possible to form transport equations for any two combinations of these basic quantities. Several couples of variables are possible, for example $(k-\epsilon)$, $(k-\omega^2)$, (q, ω), ... (ω is the dissipation rate of kinetic energy per unit of kinetic energy ($\omega = \epsilon/k$) and q is the square root of kinetic

energy $(q = k^{1/2})$. Then the eddy viscosity is :

$$\mu_t \sim \frac{k^2}{\epsilon} \quad ; \quad \mu_t \sim \frac{k}{\omega} \quad ; \quad \mu_t \sim \frac{q^2}{\omega}$$

Very often, the transport equations are extended from the incompressible case by simply using the local averaged density where it is required.

5.3.1. q-ω model (COAKLEY, 1983)

Among the various models tested by COAKLEY, 1983, for calculating shock wave/boundary layer interactions in transonic flow, it seems that the (q-ω) model has some advantages ; in particular, this model is claimed to be easier to incorporate in the solution of the averaged NAVIER-STOKES equations. The numerical aspect of a turbulence model is very important ; a good physical model is not useful if it leads to untractable numerical difficulties. It is probably one of the reasons why zero-equation models remain popular in the solution of NAVIER-STOKES equations and why more elaborated models have not yet known the same success.

The (q-ω) model proposed by COAKLEY consists of the following set of equations :

$$\frac{\partial}{\partial t}(\rho q) + \frac{\partial}{\partial x_j}(\rho q U_j) = H_q + \frac{\partial}{\partial x_j}\left[\left(\mu + \frac{\mu_t}{\sigma_q}\right)\frac{\partial q}{\partial x_j}\right] \tag{85a}$$

$$\frac{\partial}{\partial t}(\rho \omega) + \frac{\partial}{\partial x_j}(\rho \omega U_j) = H_\omega + \frac{\partial}{\partial x_j}\left[\left(\mu + \frac{\mu_t}{\sigma_\omega}\right)\frac{\partial \omega}{\partial x_j}\right] \tag{85b}$$

$$\mu_t = C_\mu \frac{D\rho q^2}{\omega}$$

$$H_q = \frac{1}{2}\left(C_\mu D \frac{S}{\omega^2} - \frac{2}{3}\frac{\mathcal{D}}{\omega} - 1\right)\rho \omega q$$

$$H_\omega = \left[C_1\left(C_\mu \frac{S}{\omega^2} - \frac{2}{3}\frac{\mathcal{D}}{\omega}\right) - C_2\right]\rho \omega^2$$

$$S = \left(\frac{\partial U_i}{\partial x_j} + \frac{\partial U_j}{\partial x_i} - \frac{2}{3}\delta_{ij}\frac{\partial U_k}{\partial x_k}\right)\frac{\partial U_i}{\partial x_j} \quad ; \quad \mathcal{D} = \frac{\partial U_k}{\partial x_k}$$

$$D = [1 - \exp(-\alpha R_t)]/(1 + \beta \chi)$$

$$\chi = \left(C_\mu \frac{S}{\omega^2}\right)^{1/2} - 1$$

$$C_\mu = 0.09 \quad ; \quad C_1 = 0.405\ D + 0.045 \quad ; \quad C_2 = 0.92$$

$$\mathcal{P}_t = 0.9 \quad ; \quad \sigma_q = 1 \quad ; \quad \sigma_\omega = 1.3$$

R_t is a turbulence REYNOLDS number which is defined as $R_t = qy/\nu$ (with $\alpha = 0.0065$) or as $R_t = q^2/\nu\omega$ (with $\alpha = 0.0018$). Various values of β have been tested ($0 < \beta < 1$).

At the wall, the boundary conditions are : $q = 0$; $\frac{\partial \omega}{\partial y} = 0$.

It is interesting to notice that this model is valid throughout the boundary layer, between the wall and the outer edge, without the need for additional terms in order to have a correct behaviour of q near the wall. This is in contrast with the k-ε models presented below.

5.3.2. k-ε model (JONES-LAUNDER)

The low REYNOLDS number version of the (k-ε) model by JONES-LAUNDER, 1972, is :

$$\frac{\partial}{\partial t}(\rho k) + \frac{\partial}{\partial x_j}(\rho k U_j) = H_k + \frac{\partial}{\partial x_j}\left[\left(\mu + \frac{\mu_t}{\sigma_k}\right)\frac{\partial k}{\partial x_j}\right] \qquad (86a)$$

$$\frac{\partial}{\partial t}(\rho \epsilon) + \frac{\partial}{\partial x_j}(\rho \epsilon U_j) = H_\epsilon + \frac{\partial}{\partial x_j}\left[\left(\mu + \frac{\mu_t}{\sigma_\epsilon}\right)\frac{\partial \epsilon}{\partial x_j}\right] \qquad (86b)$$

$$\mu_t = C_\mu\, D\rho\, \frac{k^2}{\epsilon}$$

$$H_k = \left[C_\mu\, DS\, \frac{k^2}{\epsilon} - \frac{2}{3}\, \Im k - \epsilon - 2\nu\left(\frac{\partial q}{\partial y}\right)^2\right]\rho$$

$$H_\epsilon = \left[C_{\epsilon_1}\left(C_\mu\, D\, S\, \frac{k^2}{\epsilon} - \frac{2}{3}\, \Im k\right) - C_{\epsilon_2}\, E\epsilon + 2C_\mu D\nu\, \frac{k^3}{\epsilon^2}\left(\frac{\partial^2 U}{\partial y^2}\right)^2\right]\rho\,\frac{\epsilon}{k}$$

$$D = \exp\left(-\frac{3.4}{(1 + 0.02R_t)^2}\right) \;;\; E = 1 - \frac{2}{9}\exp\left(-\frac{R_t^2}{36}\right) \;;\; R_t = \frac{k^2}{\nu\epsilon}$$

$$C_\mu = 0.09 \;;\; C_{\epsilon_1} = 1.45 \;;\; C_{\epsilon_2} = 1.92 \;;\; \mathcal{P}_t = 0.9 \;;\; \sigma_k = 1 \;;\; \sigma_\epsilon = 1.3$$

The model proposed by CHIEN, 1982, is a modified version of the JONES-LAUNDER model. In the expression of H_k, the term $-2\nu\left(\frac{\partial q}{\partial y}\right)^2$ is replaced by $-2\nu\frac{k}{y^2}$; in H_ϵ, the term $2C_\mu D\nu\frac{k^3}{\epsilon^2}\left(\frac{\partial^2 U}{\partial y^2}\right)^2$ is replaced by $-2\nu\frac{k}{y^2}F$. The expressions of D, E and F are :

$$D = 1 - \exp(-\,0.0115\,y^*) \;;\; y^* = \frac{y}{\nu_w}\sqrt{\frac{|\tau_w|}{\rho_w}}$$

$$E = 1 - \frac{2}{9}\exp\left(-\frac{R_t^2}{36}\right) \;;\; R_t = \frac{k^2}{\nu\epsilon}$$

$$F = \exp(-\,0.5\,y^*)$$

$$C_\mu = 0.09 \;;\; C_{\epsilon_1} = 1.35 \;;\; C_{\epsilon_2} = 1.8$$

$$\mathcal{P}_t = 0.9 \;;\; \sigma_k = 1 \;;\; \sigma_\epsilon = 1.3$$

These (k-ε) models are neither better nor worse than the (q-ω) model, but the numerical experience reported by COAKLEY, 1983, is that the (q-ω) model has essentially the same degree of numerical compatibility as the zero-equation model of CEBECI-SMITH.

5.3.3. k-ω model (WILCOX, 1988)

Recently, WILCOX, 1988, examined the performances of three two-equation models : the k-ε JONES-LAUNDER model, the k-ω² WILCOX-RUBESIN model and a new WILCOX k-ω model where the REYNOLDS stresses are given by eq. 63 and the eddy viscosity is :

$$\mu_t = \rho\,\frac{k}{\omega}$$

The k-ω equations are :

$$\frac{\partial}{\partial t}(\rho k) + \frac{\partial}{\partial x_j}(\rho U_j k) = -\langle\rho u_i' u_j'\rangle\frac{\partial U_i}{\partial x_j} - \beta^*\rho\omega k + \frac{\partial}{\partial x_j}\left[\left(\mu + \frac{\mu_t}{\sigma_k}\right)\frac{\partial k}{\partial x_j}\right] \qquad (87a)$$

$$\frac{\partial}{\partial t}(\rho\omega) + \frac{\partial}{\partial x_j}(\rho U_j \omega) = -\gamma\,\frac{\omega}{k}\,\langle\rho u_i' u_j'\rangle\,\frac{\partial U_i}{\partial x_j} - \beta\rho\omega^2 + \frac{\partial}{\partial x_j}\left[\left(\mu + \frac{\mu_t}{\sigma_\omega}\right)\frac{\partial\omega}{\partial x_j}\right] \tag{87b}$$

with $\beta = \dfrac{3}{40}$; $\beta^* = \dfrac{9}{100}$; $\gamma = \dfrac{5}{9}$; $\sigma_k = 2$; $\sigma_\omega = 2$.

This model is also used in compressible flow. In this case, the turbulent heat flux is obtained from a turbulent PRANDTL number.

The model is used near a wall without any additional term and the wall boundary conditions are : $k = 0$; $\omega \rightarrow \dfrac{6\upsilon}{\beta y^2}$ (balance between molecular diffusion and dissipation in eq. 87b). In a boundary layer, this model gives $k \sim y^{3.23}$ near the wall.

The comparison of the three tested two-equation models to equilibrium and non equilibrium boundary layers with and without pressure gradient indicates a superiority of the k-ω model. It is also interesting to notice that no wall functions are required.

5.3.4. Compressibility terms

In general, the authors who tried to include compressibility effects in a two-equation model observed that any additional term in the kinetic energy equation requires a modification in the second equation (the ε-equation, let us say). The additional terms in the two equations have a similar form but the characteristic time is different. This is in accordance with the idea that a modification in the production of turbulent kinetic energy also affects the dissipation rate after a time of the order of k/ε. Then, in the ε-equation, a term is included which is proportional to the term added in the k-equation ; the coefficient of proportionality is of order ε/k (GALMES et al, 1983).

GALMES et al, 1983, modified the JONES-LAUNDER model to include compressibility terms in the calculation of two-dimensional boundary layers. In the k-equation, the additional terms are :

$$-\langle\rho u'^2\rangle\,\frac{\partial U}{\partial x} - \langle\rho v'^2\rangle\,\frac{\partial V}{\partial y} + \frac{\langle\rho' u'\rangle}{\rho}\,\frac{\partial P}{\partial x}$$

First it is assumed that the normal stress are proportional to the kinetic energy :

$$\langle\rho u'^2\rangle = \rho k \quad ; \quad \langle\rho v'^2\rangle = 0.4\rho k$$

It is also assumed that the strong REYNOLDS analogy is valid (this is acceptable for boundary layers not too far from equilibrium on adiabatic walls). Then the velocity density correlation is :

$$\frac{\langle\rho' u'\rangle}{\rho} = R_{\rho u}(\gamma - 1)\,M^2\,\frac{\langle\rho u'^2\rangle}{\rho U}$$

where $R_{\rho u}$ is the velocity density correlation coefficient. Let us notice that this formula is not galilean invariant.

Finally, inviscid fluid approximations are used to simplify the numerical procedure :

$$\text{div}U = M^2\,\frac{\partial U}{\partial x}$$

$$\rho U\,\frac{\partial U}{\partial x} = -\frac{\partial P}{\partial x}$$

The compressibility terms become :

$$-\langle\rho u'^2\rangle\,\frac{\partial U}{\partial x} - \langle\rho v'^2\rangle\,\frac{\partial V}{\partial y} + \frac{\langle\rho' u'\rangle}{\rho}\,\frac{\partial P}{\partial x} = \rho\,\frac{kU}{\gamma P}\,\frac{\partial P}{\partial x}\left(b_k + \frac{C_k}{M^2}\right) \tag{88a}$$

with :

$$b_k = 0.4 + R_{\rho u}(\gamma - 1) \quad ; \quad C_k = 0.6$$

The correlation coefficient $R_{\rho u}$ has been taken as $R_{\rho u} = 0.8$.

In the ε-equation, GALMES et al add to the right hand side terms similar to those expressed by eq.87. The additional term in the ε-equation is :

$$C_{\epsilon_3}\,\frac{\epsilon}{k}\,\frac{\rho k U}{\gamma P}\,\frac{\partial P}{\partial x}\left(b_k + \frac{C_k}{M^2}\right) \tag{88b}$$

The value taken for C_{ϵ_3} is $C_{\epsilon_3} = 3$.

Most of the calculations performed by GALMES et al adopt a standard expression for $- \langle \rho u'v' \rangle$:

$$- \langle \rho u'v' \rangle = C_\mu \ f u \ \rho \ \frac{k^2}{\epsilon} \ \frac{\partial U}{\partial y} \ ; \ C_\mu = 0.09$$

$$f\mu = \exp \left[\frac{-3.4}{\left(1 + \left(\frac{R_t}{50} \right) \right)^2} \right] \ ; \ R_t = \frac{k^2}{\nu \epsilon}$$

GALMES et al also mentioned that the eddy viscosity could have to be modified. They suggest the following expression :

$$\mu_t = C_\mu \ \frac{\rho k^2}{\epsilon (1 - A.T./\epsilon)} \tag{89}$$

where A.T. represents the additional terms in the k-equation.

Eq. 89 is based on the balance between production and dissipation terms in the k-equation but the additional hypothesis which is introduced namely in the ratio $- \langle u'v' \rangle / k$ is unaffected and is not certain.

DUSSAUGE-QUINE, 1988, proposed a model for the pressure-velocity correlation in which they include some compressibility effects (this model will be discussed in section 5.4.). They do not add compressibility terms in the k- and ϵ-equations, but use a modified eddy viscosity which is obtained by simplifying the REYNOLDS stress equations. The result is :

$$- \langle \rho u'v' \rangle = C_\mu \rho \ \frac{k^2}{\epsilon} \ \frac{1}{\left(1 - \frac{3}{2} \ \beta \ k(2) \ M^2 \right)^2} \ ; \ C_\mu = 0.09 \tag{90}$$

where M is the local MACH number and β is :

$$\beta = \frac{\alpha \ (\gamma - 1)}{(C_1 - 1) + P/\epsilon} \ ; \ C_1 = 1.5 \ ; \ k(2) = 1.5 \ ; \ \gamma = \frac{C_p}{C_v} = 1.4$$

where P is the production term in the k-equation.

α is a model constant. Various values have been tested ($-1.35 \leq \alpha \leq -0.8$).

DUSSAUGE-QUINE applied this model to the calculation of a supersonic free shear layer. The results are encouraging as this model predicts a decrease in the spreading rate of the shear layer when the MACH number increases, whereas the standard k-ϵ model indicates practically no influence of MACH number.

To end this section on compressibility terms, let us mention the work of HORSTMAN, 1987, who performed calculations using a JONES-LAUNDER model modified by the inclusion of compressibility terms. Three modifications have been tested :

MOD A : in the right hand side of the ϵ-equation, the term $- C_{\epsilon_1} \ \frac{2}{3} \ \rho \epsilon \ \frac{\partial U_k}{\partial x_k}$ is replaced by $\left(1 - \frac{2}{3} \ C_1'' \right) \rho \epsilon \ \frac{\partial U_k}{\partial x_k}$ with $C_1'' = 4.5$.

MOD B : the compressibility terms in the k-equation are modelled using the following relationships :

$$\langle u_i' \rangle = - \frac{\langle \rho' u_i' \rangle}{\rho} = C_{\kappa_1} \ U \ \frac{\gamma - 1}{n - 1} \ \frac{k}{U_\ell U_\ell} \ M^2$$

$$\langle p' \ \frac{\partial u_i'}{\partial x_i} \rangle = C_{\kappa_2} \ \frac{n}{\gamma} \ \left(\frac{\gamma - 1}{n - 1} \right)^2 \ \rho k M^2 \ \frac{\partial U_k}{\partial x_k}$$

with $n = 1.2$; $C_{\kappa_1} = 0$; $C_{\kappa_2} = 0.12$.

Additional terms are also included in the ϵ-equation. They have the same form as those added in the k-equation but they are multiplied by $C_\epsilon \ \frac{\epsilon}{k}$ with $C_\epsilon = 0.3$.

MOD C : using the identity :

$$- \langle \rho u_i' u_j' \rangle = - \rho \langle u_i'' u_j'' \rangle - \langle \rho' u_i' u_j' \rangle - \frac{\langle \rho' u_i' \rangle \langle \rho' u_j' \rangle}{\rho}$$

it is argued that the model gives the quantity $- \rho \langle u_i'' u_j'' \rangle$. Neglecting the triple correlations and making assumptions like those used in eq. 79-81, the eddy viscosity coefficient is multiplied by :

$$\frac{1}{1 - C \left(\frac{\gamma - 1}{n - 1}\right)^2 \frac{k}{a^2} M^2} \quad ; \quad C = 1$$

5.4. REYNOLDS stress transport equation models

As for the lower order models, the most straightforward method to obtain a model with transport equations for the various components of the REYNOLDS stress tensor is to use the incompressible model in which the local averaged density is placed where necessary. The basis of the equations has been given in paragraph 2.3..

The compressibility appears explicitely only in the term :

$$\rho C_{ij} = \frac{\langle \rho' u_i' \rangle}{\rho} \frac{\partial P}{\partial x_j} + \frac{\langle \rho' u_j' \rangle}{\rho} \frac{\partial P}{\partial x_i} \tag{91}$$

The velocity density correlation can be modelled as given in paragraph 5.3. (eq. 79-82).

5.4.1. "Incompressible" model for the pressure-strain term

Compressibility can also affect other terms. Let us examine the pressure-strain correlation $\langle p' \left(\frac{\partial u_i'}{\partial x_j} + \frac{\partial u_j'}{\partial x_i}\right) \rangle$. An incompressible modelling of this term implies that $\langle p' \frac{\partial u_i'}{\partial x_i} \rangle = 0$; this means that the velocity fluctuations behave like an incompressible field. If this hypothesis is retained, the pressure-velocity correlation can be expressed as (VANDROMME-HA MINH, 1987) :

$$\rho \Phi_{ij} = \langle p' \left(\frac{\partial u_i'}{\partial x_j} + \frac{\partial u_j'}{\partial x_i}\right) \rangle = \rho \Phi_{ij,1} + \rho \Phi_{ij,2} \tag{92}$$

$$\rho \Phi_{ij,1} = - C_1 \frac{\epsilon}{k} \left(\langle \rho u_i' u_j' \rangle - \frac{2}{3} \delta_{ij} \rho k\right)$$

$$\rho \Phi_{ij,2} = - \frac{C_2 + 8}{11} \left(\rho P_{ij} - \frac{2}{3} \delta_{ij} \rho P\right) - \frac{8C_2 - 2}{11} \left(\rho Q_{ij} - \frac{2}{3} \delta_{ij} \rho P\right) - \frac{30C_2 - 2}{55} \rho k \left(2S_{ij} - \frac{2}{3} \delta_{ij} \frac{\partial U_\ell}{\partial x_\ell}\right)$$

$$\rho P_{ij} = - \left(\langle \rho u_i' u_\ell' \rangle \frac{\partial U_j}{\partial x_\ell} + \langle \rho u_j' u_\ell' \rangle \frac{\partial U_i}{\partial x_\ell}\right)$$

$$\rho P = - \langle \rho u_\ell' u_m' \rangle \frac{\partial U_m}{\partial x_\ell}$$

$$\rho Q_{ij} = - \left(\langle \rho u_i' u_\ell' \rangle \frac{\partial U_\ell}{\partial x_j} + \langle \rho u_j' u_\ell' \rangle \frac{\partial U_\ell}{\partial x_i}\right)$$

$$S_{ij} = \frac{1}{2} \left(\frac{\partial U_i}{\partial x_j} + \frac{\partial U_j}{\partial x_i}\right)$$

This modelling is valid at high REYNOLDS number. Near the wall, the model has been completed by GIBSON-LAUNDER, 1978, to take into account the effects of wall reflexion term which appears when the POISSON equation for the pressure is solved. A term $\rho \Phi_{ij,w}$ is added to $\rho \Phi_{ij,1} + \rho \Phi_{ij,2}$ in eq. 92 :

$$\rho \Phi_{ij,w} = \frac{\rho k^{3/2}}{2.5 \epsilon x_n} \left(g_{km} n_k n_m \delta_{ij} - \frac{3}{2} g_{ki} n_k n_j - \frac{3}{2} g_{kj} n_k n_i\right)$$

$$g_{\alpha\beta} = C_{1v} \frac{\epsilon}{k} \frac{\langle \rho u_\alpha' u_\beta' \rangle}{\rho} + C_{2v} \Phi_{\alpha\beta,2} \quad ; \quad C_{1v} = 0.5 ; C_{2v} = 0.3$$

In these formulae, x_n is the distance normal to the wall and x_i are the components of a unit vector normal to the wall.

5.4.2. Models for the pressure-strain terms with compressibility effects

STRAHLE, 1988, starts with the POISSON equation for the pressure and tries to follow the same reasoning as in an incompressible flow, but he was led to introduce several approximations ; for example, it is assumed that the density fluctuations are small ($\rho'/\rho \ll 1$). However certain of these approximations are not consistently applied all along the development. The final result is :

$$\rho \Phi_{ij} = -\frac{(C_2 + 8)}{11}\left(P^*_{ij} - \frac{2}{3}P^*\delta_{ij}\right) - \frac{(30C_2 - 2)}{55}k\left(\frac{\partial \rho U_i}{\partial x_j} + \frac{\partial \rho U_j}{\partial x_i}\right) - \frac{(8C_2 - 2)}{11}\left(Q^*_{ij} - \frac{2}{3}P^*\delta_{ij}\right) \quad (93)$$

$$- C_1 \rho \frac{\epsilon}{k}\left(\frac{\langle \rho u'_i u'_j \rangle}{\rho} - \frac{2}{3}\delta_{ijk}\right)$$

$$P^*_{ij} = -\left[\langle u'_i u'_\ell \rangle \frac{\partial \rho U_j}{\partial x_\ell} + \langle u'_j u'_\ell \rangle \frac{\partial \rho U_i}{\partial x_\ell}\right]$$

$$P^* = -\langle u'_i u'_\ell \rangle \frac{\partial \rho U_j}{\partial x_\ell}$$

$$Q^*_{ij} = -\left(\langle u'_i u'_\ell \rangle \frac{\partial \rho U_\ell}{\partial x_j} + \langle u'_j u'_\ell \rangle \frac{\partial \rho U_\ell}{\partial x_i}\right)$$

It should be noticed that this model introduces additional unknowns which are the terms $\langle u'_i u'_j \rangle$. In addition, this formulation has not yet been tested in a calculation method.

J.P. BONNET, 1981, also tried to include compressibility terms in the modelling of the pressure-velocity correlation term. He argued that the pressure equation in a steady compressible two-dimensional thin shear flows suggests that compressibility affects mainly the return-to-isotropy term ($\Phi_{ij,1}$) through the following contribution :

$$[\Phi_{ij,c}]_B = \frac{1}{4\pi}\int 2\left(\frac{\partial U}{\partial x_j}\right)_A \left\langle \left(\frac{\partial^2 \rho' u'_i}{\partial x_i \partial x_j}\right)_A \left(\frac{\partial u'_i}{\partial x_j} + \frac{\partial u'_j}{\partial x_i}\right)_B\right\rangle \frac{dvol}{|\vec{r}|} \quad (94)$$

with $\overrightarrow{BA} = \vec{r}$.

Then, assuming that the pressure fluctuations are small ($p'/\rho \ll \rho'/\rho$), the density fluctuations are such that $\frac{\rho'}{\rho} = -\frac{T'}{T}$. The strong REYNOLDS analogy is also used (negligible total temperature gradient and fluctuations), so that $\frac{T'}{T} = (\gamma - 1)M^2 \frac{u'}{U}$. With these two assumptions, the return-to-isotropy term becomes :

$$\Phi_{ij,1} + \Phi_{ij,c} = -C_1\left(1 + C_A(\gamma - 1)M^2\right)\frac{\sqrt{2k}}{\Lambda}\left(\langle \rho u'_i u'_j \rangle - \frac{2}{3}\delta_{ij}\rho k\right) \quad (95)$$

where Λ is a turbulence length associated with the modelling developed by DONALDSON.

BONNET proposed an alternative form to eq. 95 :

$$\Phi_{ij,1} + \Phi_{ij,c} = -C_1\left(1 + C_B\frac{\langle \rho u'^2 \rangle}{\rho a^2}\right)\frac{\sqrt{2k}}{\Lambda}\left(\langle \rho u'_i u'_j \rangle - \frac{2}{3}\delta_{ij}\rho k\right) \quad (96)$$

where a is the sound celerity.

This model was applied to the calculation of the free shear layer. With $C_A = 1$ or $C_B = 8$, the model gives a rapid decrease in the spreading rate of the shear layer as the MACH number increases in agreement with the experimental results.

DUSSAUGE-QUINE, 1988, also consider the compressibility effects on the pressure-strain terms. They describe the pressure equation in the case of an incompressible fluctuating field with non constant density as :

$$-\frac{\partial^2 p'}{\partial x_\ell \partial x_\ell} = 2\rho \frac{\partial U_j}{\partial x_i} \frac{\partial u_i'}{\partial x_j} + \rho \frac{\partial u_i'}{\partial x_j} \frac{\partial u_j'}{\partial x_i} + \frac{\partial \rho'}{\partial x_i} \left(\frac{\partial u_i'}{\partial t} + U_j \frac{\partial u_i'}{\partial x_j} + u_j' \frac{\partial U_i}{\partial x_j} \right) + \text{higher order terms} \qquad (97)$$

The terms involving the density fluctuations are modelled by analogy with the classical return-to-isotropy ROTTA model.

In a thin shear flow with a preferred direction, the contribution to the pressure-velocity correlation $\rho\phi_{ij,1}$ is an additional term $\pi_{ij,\rho}$, the form of which is :

$$\pi_{ij,\rho} = U \frac{\epsilon}{k} T_{ij}^1 \qquad (98a)$$

where T_{ij}^1 is a function of the arguments $\langle \rho' u_i' \rangle$, $\langle \rho' u_i' u_j' \rangle$ ... Only the argument of lowest order $\langle \rho' u_i' \rangle$ is retained. Arguing the incompressibility of the velocity fluctuations, the condition $\pi_{ii,\rho} = 0$ is used. Then, the expression of T_{ij}^1 is :

$$T_{ij}^1 = \alpha \left[\langle \rho' u_i' \rangle \delta_{ij} - \frac{3}{2} \left(\langle \rho' u_j' \rangle \delta_{i1} + \langle \rho' u_i' \rangle \delta_{j1} \right) \right] \qquad (98b)$$

The density-velocity correlations are obtained from :

$$\frac{\langle \rho' u_i' \rangle}{\rho} = k(i) \ (\gamma - 1) \ M^2 \ \frac{\langle u_i' u_i' \rangle}{U} \qquad (98c)$$

with $k(1) = 0.8$; $k(2) = 1.5$.

Relationships (98a-b-c) are used in an algebraic stress model as proposed by RODI. The result is :

$$\frac{\langle u_i' u_j' \rangle}{k} = \left(\frac{\langle u_i' u_j' \rangle}{k} \right)_0 K_{ij} \qquad (99)$$

where the index 0 represents the model without compressibility effects. Then K_{ij} is a correction function given by :

$$K_{11} = \frac{1}{1 - 2\beta k(1) M^2}$$

$$K_{22} = 1 - \frac{\beta k(1) M^2}{1 - 2\beta k(1) M^2} \left(\frac{\langle u_1' u_1' \rangle}{\langle u_2' u_2' \rangle} \right)_0$$

$$K_{12} = \frac{1}{1 - \frac{3}{2} \beta k(2) M^2}$$

with :

$$\beta = \frac{\bar{\alpha} \ (\gamma - 1)}{(C_1 - 1) + P/\epsilon} \quad ; \quad C_1 = 1.5$$

where P is the production per unit mass of turbulent kinetic energy.

This model has been used with the k-ϵ equations. The shear stress is :

$$- \langle u_1' u_2' \rangle = C_\mu \frac{k^2}{\epsilon} \frac{\partial U}{\partial y} \qquad (100)$$

with : $C_\mu = C_{\mu 0} (K_{12})^2$; $C_{\mu 0} = 0.09$.

A value α between $- 1.35$ and $- 0.8$ gives satisfactory predictions of the behaviour of the supersonic free shear layer.

5.4.3. REYNOLDS stress equation model

Let us examine the modelling of the other terms of the REYNOLDS stress equation :

$$\rho \frac{DT_{ij}}{Dt} = \rho P_{ij} - \rho D_{ij} + \rho \phi_{ij} + \rho C_{ij} + \frac{\partial}{\partial x_k} (\rho J_{ijk}) \qquad (101)$$

Neglecting the pressure-velocity correlation $\langle p'u_i' \rangle$, the turbulent diffusion term is obtained from the modelling of the triple velocity correlation :

$$- \langle \rho u_k' u_i' u_j' \rangle = C_s' \frac{k}{\epsilon} \langle \rho u_k' u_\ell' \rangle \frac{\partial}{\partial x_\ell} \left(\frac{\langle \rho u_i' u_j' \rangle}{\rho} \right) \tag{102a}$$

At high REYNOLDS number, the viscous diffusion term is neglected but near a wall, this term must be retained. To obtain a simple expression, many hypotheses are needed : the correlations between viscosity fluctuation and fluctuations of velocity or density are negligible, the velocity fluctuations are incompressible, ... Then the viscous part of ρJ_{ijk} is approximated by :

$$\mu \frac{\partial}{\partial x_k} \left(\frac{\langle \rho u_i' u_j' \rangle}{\rho} \right) \tag{102b}$$

The compressibility term ρC_{ij} involves the modelling of the term $\langle \rho u_i' \rangle$. One of the expressions given in paragraph 5.2. (eq. 79-82) can be used.

Finally the destruction term ρD_{ij} is assumed to be isotropic at high REYNOLDS number. This means that :

$$\rho D_{ij} = \frac{2}{3} \rho \delta_{ij} \epsilon \tag{102c}$$

To take into account the non isotropy of ρD_{ij} at low REYNOLDS number, the following expression can be used (DALY-HARLOW, DONALDSON) :

$$\rho D_{ij} = \frac{\epsilon}{k} \left(\langle \rho u_i' u_j' \rangle \, fs + (1 - fs) \frac{2}{3} \delta_{ij} \rho k \right)$$

with $fs = \frac{1}{1 + R_t/10}$; $R_t = \frac{k^2}{\nu \epsilon}$.

Very often the REYNOLDS stress transport equations are not used as such. They are simplified in order to obtain the algebraic stress models. Symbolically the REYNOLDS stress equations have the form :

$$\rho \frac{DT_{ij}}{Dt} = S_{ij} + \frac{\partial}{\partial x_\ell} (\rho J_{ij\ell}) \tag{103}$$

where S_{ij} represents the source and sink terms of the T_{ij}-equation. S_{ij} are functions of T_{ij}.

A possible way to derive an algebraic stress model is to use the hypothesis proposed by RODI, 1972 :

$$\rho \frac{DT_{ij}}{Dt} - \frac{\partial}{\partial x_k} (\rho J_{ijk}) = \frac{T_{ij}}{k} \left[\rho \frac{Dk}{Dt} - \frac{\partial}{\partial x_\ell} \left(\frac{\rho J_{mm\ell}}{2} \right) \right] \tag{104}$$

or, using eq. 103 :

$$S_{ij} = \frac{T_{ij}}{k} \frac{S_{mm}}{2} \tag{105}$$

Equations (105) form a set which can be solved to express the stresses T_{ij} as a function of the velocity gradient, k and ϵ. This means that the turbulence model involves only the solution of two partial differential equations (k-ϵ for example) and a set of algebraic equations.

5.5. Turbulent heat flux equations

Very few models have been proposed for the closure of the turbulent heat flux transport equations at least for compressible flows as they are considered here. If the heat is taken as a passive contaminant, models are available (LAUNDER, 1976, EL GOBASHI-LAUNDER, 1983, NEWMAN et al, 1981, JONES-MUSONGE, 1988). This is obviously a first approach of the problem which can give very useful information. It is also interesting to consider models devoted to calculate mixtures of gases of different density ; when these models involve transport equations for the flux of concentration (CHASSAING-HERARD, 1987, JONES-PASCAU, 1988), a few results can be useful for the modelling of turbulent heat flux transport equations.

5.5.1. FINSON-WU model

Among the very few attempts towards including turbulent heat flux equations in a calculation method, the work by FINSON-WU, 1979, can be cited. Their model involves transport equations for the REYNOLDS stress components. This model has been applied with the boundary layer approximation and the fluctuations of density are neglected. FINSON-WU proposed the following equations for $\langle h'^2 \rangle$, $\langle v'h' \rangle$ and $\langle u'h' \rangle$:

$$\rho \frac{D\langle h'^2 \rangle}{Dt} = -2\rho \langle v'h' \rangle \frac{\partial h}{\partial y} - C_{T_1} \rho \frac{\epsilon}{k} \langle h'^2 \rangle + 0.4 \frac{\partial}{\partial y} \left(\rho \frac{k\langle v'^2 \rangle}{\epsilon} \frac{\partial \langle h'^2 \rangle}{\partial y} + \frac{\mu}{\mathcal{P}} \frac{\partial \langle h'^2 \rangle}{\partial y} \right)$$

$$\rho \frac{D\langle v'h' \rangle}{Dt} = -\rho \langle v'^2 \rangle \frac{\partial h}{\partial y} - 0.09835 \rho \langle u'h' \rangle \frac{\partial U}{\partial y} - C_{T_2} \rho \frac{\epsilon}{k} \langle v'h' \rangle + 0.8 \frac{\partial}{\partial y} \left(\rho \frac{k\langle v'^2 \rangle}{\epsilon} \frac{\partial}{\partial y} \langle v'h' \rangle + \frac{\mu}{\mathcal{P}} \frac{\partial}{\partial y} \langle v'h' \rangle \right)$$

$$\rho \frac{D}{Dt} \langle u'h' \rangle = -0.3989 \rho \langle v'h' \rangle \frac{\partial U}{\partial y} - \rho \langle u'v' \rangle \frac{\partial h}{\partial y} - C_{T_2} \rho \frac{\epsilon}{k} \langle u'h' \rangle + 0.4 \frac{\partial}{\partial y} \left[\rho \frac{k\langle v'^2 \rangle}{\epsilon} \frac{\partial}{\partial y} \langle u'h' \rangle + \frac{\mu}{\mathcal{P}} \frac{\partial \langle u'h' \rangle}{\partial y} \right]$$

with :

$$C_{T_1} = \frac{0.8 + 7.5 \, \pi/R_\Lambda}{1 + 12.5 \, \pi/R_\Lambda} \quad ; \quad C_{T_2} = \frac{1.165 + 12.5 \, \pi/R_\Lambda}{1 + 12.5 \, \pi/R_\Lambda} \quad ; \quad R_\Lambda = \frac{\sqrt{k} \, \Lambda}{\nu}$$

The length scale Λ is related to the dissipation rate ϵ by :

$$\epsilon = 0.4 \frac{k^{3/2}}{\Lambda} (1 + 12.5 \, \pi/R_\Lambda)$$

5.5.2. JONES-MUSONGE model (incompressible flow)

In incompressible flow, several models have been proposed for calculating a scalar field with scalar flux equations. The scalar is often the temperature and it is probably possible to extend these models to compressible flows.

One of these models has been given by JONES-MUSONGE. The equations are :

$$\frac{D}{Dt} \langle u_i' u_j' \rangle = P_{ij} + A_{ij} - \frac{2}{3} \delta_{ij} \epsilon + C_s \frac{\partial}{\partial x_\ell} J_\ell \left(\langle u_i' u_j' \rangle \right)$$

$$\frac{D\epsilon}{Dt} = \frac{\epsilon}{k} \left(C_{\epsilon_1} P - C_{\epsilon_2} \epsilon \right) + C_\epsilon \frac{\partial}{\partial x_\ell} J_\ell (\epsilon)$$

$$\frac{D}{Dt} \langle u_i' \varphi' \rangle = P_{i\varphi} + B_i + C_s \frac{\partial}{\partial x_\ell} J_\ell \left(\langle u_i' \varphi' \rangle \right)$$

$$\frac{D}{Dt} \langle \varphi'^2 \rangle = P_\varphi - 2\epsilon_\varphi + C_s \frac{\partial}{\partial x_\ell} J_\ell \left(\langle \varphi'^2 \rangle \right)$$

$$\frac{D}{Dt} \epsilon_\varphi = -C_{D_1} \frac{\epsilon_\varphi^2}{\langle \varphi'^2 \rangle} - C_{D_2} \frac{\epsilon \epsilon_\varphi}{2k} - C_{D_3} \frac{\epsilon}{k} \langle u_i' \varphi' \rangle \frac{\partial \Phi}{\partial x_i} - C_{D_4} \frac{\epsilon_\varphi}{k} \langle u_i' u_j' \rangle \frac{\partial U_i}{\partial x_j} + C_s \frac{\partial}{\partial x_\ell} J_\ell (\epsilon_\varphi)$$

with :

$$J_\ell(f) = \frac{k}{\epsilon} \langle u_j' u_\ell' \rangle \frac{\partial f}{\partial x_j}$$

$$P_{ij} = -\langle u_j' u_\ell' \rangle \frac{\partial U_i}{\partial x_\ell} - \langle u_i' u_\ell' \rangle \frac{\partial U_j}{\partial x_\ell}$$

$$Q_{ij} = -\langle u_j' u_\ell' \rangle \frac{\partial U_\ell}{\partial x_i} - \langle u_i' u_\ell' \rangle \frac{\partial U_\ell}{\partial x_j}$$

$$P = -\langle u_i' u_j' \rangle \frac{\partial U_i}{\partial x_j}$$

$$P_{i\varphi} = -\langle u_j' \varphi' \rangle \frac{\partial U_i}{\partial x_j} - \langle u_i' u_j' \rangle \frac{\partial \Phi}{\partial x_j}$$

$$P_\varphi = -2 \langle u_i' \varphi' \rangle \frac{\partial \Phi}{\partial x_j}$$

$$b_{ij} = \frac{\langle u_i' u_j' \rangle}{2k} - \frac{\delta_{ij}}{3}$$

$$A_{ij} = -2C_1\epsilon\, b_{ij} - C_2\,\delta_{ij}\,P - C_3 P_{ij} + C_4 k\left(\frac{\partial U_i}{\partial x_j} + \frac{\partial U_j}{\partial x_j}\right) + C_5\,\langle u_i'u_j'\rangle\,\frac{\partial U_\ell}{\partial x_\ell} - C_6 Q_{ij} + C_7\,k\delta_{ij}\,\frac{\partial U_\ell}{\partial x_\ell}$$

$$B_i = -C_{\varphi_1}^*\,\frac{\epsilon}{k}\,\langle u_i'\varphi'\rangle + 2C_{\varphi_2}\,b_{ij}k\,\frac{\partial\Phi}{\partial x_j} + C_{\varphi_3}\,\langle u_i'\varphi'\rangle\,\frac{\partial U_i}{\partial x_j} + C_4\,\langle u_j'\varphi'\rangle\,\frac{\partial U_j}{\partial x_i}$$

$$C_{\varphi_1}^* = C_{\varphi_1}\Big/\left(1 + c_{\varphi_1}'\sqrt{b_{ij}b_{ij}}\right)$$

The model constants are :

$$C_s = 0.22 \quad C_1 = 1.5 \quad C_2 = -0.53 \quad C_3 = 0.67 \quad C_4 = -0.12$$
$$C_\epsilon = 0.18 \quad C_{\epsilon_1} = 1.4 \quad C_{\epsilon_2} = 1.9$$
$$C_{\varphi_1} = C_{\varphi_1}' = 3 \quad C_{\varphi_2} = 0.12 \quad C_{\varphi_3} = 1.09 \quad C_{\varphi_4} = 0.51$$
$$C_{D_1} = 2 \quad C_{D_2} = 1.8 \quad C_{D_3} = 1.7 \quad C_{D_4} = 1.4$$

It should be noted that the pressure correlation terms (pressure-strain and pressure-scalar) have not been modelled as in the LAUNDER-REECE-RODI model. These terms are not decomposed into a rapid part and a return-to-isotropy part, but are globally considered. In particular, the exact result obtained when an isotropic turbulent field is suddenly submitted to a mean strain field is not verified. As a counterpart, it seems that better agreement is obtained for homogeneous sheared flows even in the case of strong shear.

6 - EXAMPLES OF APPLICATIONS

6.1. Flat plate boundary layers

An integral method has been used (COUSTEIX et al. 1974) to determine the effects of MACH number and wall temperature on the skin friction of the flat plate boundary layer. The integral method is based on the solution of the global equations of continuity, momentum and energy. The closure relationships are obtained from self-similarity solutions calculated with a mixing length scheme.

Figures 12 and 13 show the comparisons of numerical results with the VAN DRIEST II results. These latter results are in good agreement with the experimental data and are recommended as references at the 1980-81 STANFORD Conference. The integral method gives right trends in the range of parameters investigated ($M_e < 5$; $0.2 < T_v/T_{ad} < 1.$).

CEBECI-SMITH also presented comparisons of experimental skin friction coefficients for adiabatic flat plate boundary layers by using results obtained with their method. In the range $0.4 < M_e < 5$, $1\,600 < R_\theta < 702\,000$, figure 14 shows that the calculations reproduce the experiments very well.

Another application of the integral method proposed by COUSTEIX et al is shown on figure 15. In the experiments performed by HASTINGS-SAWYER, the MACH number is nearly constant ($M_e = 4$) and the wall is adiabatic. Good results are obtained on boundary layer thickness and skin friction.

The following application concerns a flat plate boundary layer with heat transfer (COLEMAN et al). The calculations have been first performed in turbulent flow with a mixing length scheme given by eq. 67 (figure 16). It seems that the quality of results is poor as the MACH number increases. Calculations have also been performed by ARNAL by taking into account transition effects. In the transition region, the shear stress is calculated by :

$$-\langle\rho u'v'\rangle = \hat{\epsilon}\,\mu_t\,\frac{\partial U}{\partial y}$$

The eddy viscosity is given by a mixing length scheme. In incompressible flow, the intermittency function $\hat{\epsilon}$ is prescribed according to figure 17 (θ is the momentum thickness calculated at the current point and θ_T is the value determined at the transition point). In compressible flow, the intermittency function $\hat{\epsilon}$ is expressed by the same function but $\frac{\theta}{\theta_T} - 1$ is replaced by $\left(\frac{\theta}{\theta_T} - 1\right)\Big/\left(1 + 0.02\,M_e^2\right)$ to take into account the lengthening of the transition region at high speeds. In the application shown on figure 18, the transition point is prescribed according to the experiments. Qualitatively, well behaved computational results are obtained but the level of heat fluxes is slightly overestimated in the turbulent region.

6.1. Boundary layer with pressure gradient

In the experiments of CLUTTER-KAUPS, the boundary layer is studied along a body of revolution with different conditions of velocity, pressure gradient and wall temperature. In the example presented, the MACH

number is around 2.5, the pressure gradient is slightly negative and the ratio T_w/T_{ad} is around 0.6.

The calculations have been performed using three methods : the integral method proposed by COUSTEIX et al, a mixing length scheme (eq. 67) and the k-ϵ JONES-LAUNDER model. This case does not pose special difficulties and all the methods are in good agreement with experiments.

In the experiments of LEWIS et al. 1972, the boundary layer is studied along the inner wall of a cylinder and a centerbody placed along the axis generates the pressure gradient. The wall is adiabatic. The calculations shown in figure 20 have been performed by CEBECI. The calculated results reproduce the effects of adverse and favorable pressure gradient very well.

6.3. Boundary layer with variable wall temperature

Extensive studies of boundary layers with pressure gradient, heat fluxes and blowing and suction have been performed by MORETTI-KAYS, MOFFAT-KAYS. The case presented in figure 21 deals with a negative pressure gradient and a variable wall temperature. The calculations by CEBECI-SMITH follow the experimental data remarkably well.

6.4. Effects of wall blowing

BUSHNELL et al, 1975, analysed the effects of wall blowing on the skin-friction coefficient of flat plate boundary layers. They studied the ratio C_f/C_{fo} of the skin friction with and without blowing at the same value of the REYNOLDS number Re_x as a function of the blowing parameter $2F/C_{fo}$ ($F = \dfrac{\rho_w v_w}{\rho_e u_e}$). It is found that the MACH number has a small effect on this curve (figure 22). Calculations were performed using a mixing length scheme in which the outer level of the mixing length is function of δ^* to take into account low REYNOLDS effects just downstream a transition region (figure 7a). In the range $M_e < 6.6$, the calculations are in good agreement with experiments (figure 22). Calculations by RUBESIN and SQUIRE with a conventional mean field closure also showed that there is a small influence of MACH number, REYNOLDS number and wall temperature.

6.5. Calculations with heat flux transport equations

FINSON-WU used the model presented in paragraph 5.5.1. to calculate boundary layer on rough wall. To do this, they added roughness functions in the momentum equation, in the turbulent kinetic energy equation and in the dissipation equation.

Figures 23 and 24 show the results of their calculation at low speed and comparisons with measurements by HEALZER et al. The calculations reproduce the increase in the skin friction coefficient and in the STANTON number (St = $\varphi_w/\rho_e u_e (h_{i_e} - h_w)$). It is interesting to notice that the increase in the heat flux is less than the increase in skin friction. This means that the REYNOLDS analogy is not preserved. This case illustrates the interest in using a model with heat flux transport equations.

FINSON-WU also applied their model to the data obtained during the "Passive Nosetip Technology (PANT) program" (JACKSON-BAKER). An example of comparisons is shown in figure 25 which gives the heat transfer coefficient on the nose of the body with and without roughness. At least qualitatively, the calculated results indicate the right trend of the experimental data.

Figure 26 shows the application of the model proposed by JONES-MUSONGE (paragraph 5.5.2.) to the experimental data obtained by TAVOULARIS and CORRSIN in a nearly homogeneous shear flow with a linear temperature gradient. The results represented in figure 26 are the turbulent PRANDTL number and the ratio of heat fluxes. Here again, this case illustrates the value of a model with heat flux transport equations.

JONES-MUSONGE applied their model with the same success to a thermal mixing layer downstream of a turbulence grid and to a slightly heated plane jet in stagnant surrounds.

6.6. Shock wave-boundary layer interactions

BENAY et al, 1987, performed a critical study of various turbulence models applied to the calculation of shock wave-boundary layer interaction in transonic flow. This study has been performed by using the boundary layer equations solved in the inverse mode (the displacement thickness distribution is introduced as a datum in this calculation method). The authors verified the validity of this approach by comparison with NAVIER-STOKES solutions. They tested mixing length models (from MICHEL, ALBER and BALDWIN-LOMAX) and models with transport equations (the JOHNSON-KING model which includes an equation for the maximum shear

stress, the k-ϵ JONES-LAUNDER model, the Algebraic Stress Model which is obtained from the RODI proposal applied to the HANJALIC-LAUNDER three equation model). In a general way, the authors concluded that the models with transport equations behave better than the other models. The best results are obtained with the Algebraic Stress Model (figures 27b-c-d). It is noticed that the mean velocity profiles are well calculated with this model whereas the turbulence characteristics are not. However the experiment reveals that the flow is not strictly steady and the unsteadiness can interact with turbulence ; on the other hand, the experimental data are not analysed by taking into account this unsteadiness.

Another example is provided by calculations performed at NASA with NAVIER-STOKES equations (see MARVIN-COAKLEY). The experimental configuration is depicted in figure 28a. The results obtained with three models are compared with the experimental data : the CEBECI-SMITH model, the BALDWIN-LOMAX and a q-ω model has been proposed by COAKLEY, 1983 (eq. 85) ; this model has been modified to take into account compressibility corrections (the term $-\frac{2}{3} C_1 \mathcal{D} \rho \omega$ is replaced by $-2.4 C_1 \mathcal{D} \rho \omega$ in the expression of H_ω) and finally a heat transfer correction is included (in the eddy viscosity, the length scale becomes $\ell = \min(2.4y, q/\omega)$ in order to reduce the heat transfer in the region of reattachment). The results are given in figures 28b and 28c for two angles of the corner : $\theta = 15°$ and $\theta = 38°$. A reasonable agreement is obtained with the three models for $\theta = 15°$; for the case $\theta = 38°$, the results obtained with the CEBECI-SMITH model have not been given because of the difficulties in computing the displacement thickness distribution. It should also be noticed that the overshoot of the heat flux near the reattachment is not predicted by any model.

6.7. Calculation of the free shear layer

The free shear layer is a flow where the inadequacy of "incompressible" models has been attributed to compressibility terms. Indeed the models extended from the incompressible case without compressibility effects predict practically no effect of the MACH number on the rate of expansion of the free shear layer whereas the experimental results indicate a decrease in the expansion as the MACH number increases. The results shown in figure 29 are concerned with a shear layer with a zero velocity on one side and a non zero velocity U_e on the other side. The thickness δ is defined as the distance between the points where the velocity is $\sqrt{0.1} U_e$ and $\sqrt{0.9} U_e$. The computed results have been produced by BONNET for the 1980-81 STANFORD Conference according to eq. 96. Improvements of the same quality have been obtained by VANDROMME and by DUSSAUGE-QUINE (eq. 100). These compressibility corrections lead to improved results (as compared with experimental data) but it is not sure if the effects of MACH number are attributable to modifications of the turbulence structure or to a problem of stability which modifies the large structures of the shear layer in which case it is not justified to accuse the turbulence model.

7 - CONCLUSIONS

The calculations of classical compressible turbulent boundary layers not too far from equilibrium have often been approached with rather simple models extended in a straightforward manner from the incompressible case. For these cases, this approach is justified even at MACH numbers as high as 10 except perhaps for the calculation of wall heat flux where some uncertainty is still present. Indeed, in most of the calculations, the turbulent heat flux is evaluated by using a turbulent PRANDTL number which is assumed essentially to be a constant. This hypothesis influences directly the calculation of the wall heat fluxes. In many situations, the value of the PRANDTL number is not the value determined in a flat plate boundary layer. Therefore, it is certainly valuable to try to develop transport equations for the turbulent heat fluxes. This work is performed when the temperature can be considered as a passive scalar which is a first approach to the more general problem of compressible flow. Useful information can be gained from the studies of the mixing of non reactive gases and from the study of homogeneous compressed turbulence (REYNOLDS, 1987).

The question of including compressibility corrections in the transport equations is not solved because these terms have been used for flows such as the free shear layer or shock wave-boundary layer interaction. It seems that the inclusion of such terms has often been beneficial but it is not clear if these compressibility terms are completely justified or if they mask other problems. In the case of the shock wave-boundary layer interaction, models are available which give reasonable agreement on pressure distribution for example, but none of them give the viscous parameters with the required accuracy.

A third important problem is the near wall treatment (which is not specific of the compressible flows). In most of the applications, a simple model is used (for example a mixing length or a one-equation model) but efforts are devoted to develop more general models valid in the fully turbulent region and in the near wall region (LAUNDER-TSELEPIDALIS, 1988).

Indeed the near wall model is very important because not only it influences the prediction of the skin friction for example, but also it has an important effect on the numerical behaviour of the model. The numerical properties of the models are rather rarely studied, although they are of great practical relevance ; indeed it is not very useful to have a well physically funded model which leads to untractable numerical difficulties.

Acknowledgements

REFERENCES

ARNAL D. "Laminar-turbulent transition problems in supersonic and hypersonic flows" AGARD FDP VKI Special Course on Aerothermodynamics of Hypersonic Vehicles (30 May-3 June 1988)

BALDWIN B.S., LOMAX H. "Thin layer approximation and algebraic model for separated turbulent flows" AIAA Paper n° 78-0257 (1978)

BALDWIN B.S., LOMAX H. "Thin layer approximation and algebraic model turbulent flows" AIAA Paper N° 78-0257 (1978)

BAUER P.T., ZUMWALT G.W., FILA L.J. "A numerical method and an extension of the Korst jet mixing theory for multispecies turbulent jet mixing" AIAA Paper N° 68-112 (1968)

BECKWITH I.E., BUSHNELL D.M. "Calculation of mean and fluctuating properties of the incompressible turbulent boundary layer - Computation of turbulent boundary layers" 1968 AFOSR-IFP-STANFORD Conference, Ed. S.J. KLINE, M.V. MORKOVIN, G. SOVRAN, D.J. COCKRELL (1968)

BENAY R., COET M.C., DELERY J. "Validation de modèles de turbulence appliqués à l'interaction onde de choc-couche limite transsonique" La Rech. Aérosp. N° 1987-3 (1987)

BLACKWELL B.F., KAYS W.M., MOFFAT R.J. Rept. HMT-16, Mech. Eng. Dept., STANFORD University (1972)

BONNET J.P. "Comparison of computation with experiment" 1980-81 AFOSR-HTTM STANFORD Conference on Complex Turbulent Flows, Ed. S.J. KLINE, B.J. CANTWELL, G.M. LILLEY

BONNET J.P. "Comparison of computation with experiment - Summary report" AFOSR-HTTM STANFORD Conference 1980-81 on Complex Turbulent Flows, Ed. S.J. KLINE, B.J. CANTWELL, G.M. LILLEY

BRADSHAW P., FERRIS D.H., ATWELL N.P. "Calculation of boundary layer development using the turbulent energy equation" J.F.M. 28, 593 (1967)

BRADSHAW P., FERRISS D.H. "Deviation of a shear stress transport equation from the turbulent energy equation - Computation of turbulent boundary layers" 1968 AFOSR-IFP STANFORD Conference, Ed. S.J. KLINE, M.V. MORKOVIN, G. SOVRAN, D.J. COCKRELL (1968)

BRADSHAW P. "Compressible turbulent shear layers" Annual Review of Fluid Mechanics (1977)

BROWN G.L., ROSHKO A. "On density effects and large structures in turbulent mixing layers" J.F.M. Vol. 64 Part 4 (1974)

BUSHNELL D.M., WATSON R.D., HOLLEY B.B. "MACH and REYNOLDS number effects on turbulent skin friction reduction by injection" J. Spacecraft Vol. 12 N° 8 (1975)

BUSHNELL D.M., CARY A.M., HOLLEY B.B. "Mixing length in low REYNOLDS number compressible turbulent boundary layers" AIAA Journal Vol. 13 N° 8 (1975)

BUSHNELL D.M., CARY A.M., HARRIS J.E. "Calculation methods for compressible turbulent boundary layers" VKI Lecture Series LS86 (1976) NASA SP-422 (1977)

BUSHNELL D.M., MALIK M.R., HARVEY W.D. "Transition prediction in external flows via linear stability theory" IUTAM Symp. Transonicum III, GÖTTINGEN (May 1988)

CEBECI T., SMITH A.M.O. "Analysis of turbulent boundary layers" Academic Press (1974)

CHASSAING P. "Une alternative à la formulation des équations du mouvement d'un fluide à masse volumique variable" Journal de Mécanique Théorique et Appliquée Vol. 4 N° 3 (1985)

CHASSAING P., HERARD J.M. "Second order modelling of variable density turbulent mixing" Sixth Symp. on Turbulent Shear Flows, TOULOUSE (1987)

CHIEN J.Y. "Predictions of channel boundary layer flows with a low REYNOLDS number turbulence model" AIAA Journal, Vol. 20, pp. 33-38 (1982).

CLUTTER D.W., KAUPS K. "Wind tunnel investigations of turbulent boundary layers on axially symmetric bodies at supersonic speeds" DOUGLAS Aircraft Division Rep. N° LB 31425 (1964)

COAKLEY T.J. "Turbulence modelling methods for the compressible NAVIER-STOKES equations" AIAA 83 1693, DAN-VERS, MA (July 1983)

COLEMAN G.T., ELESTROM G.M., STOLLERY J.L. "Turbulent boundary layers at supersonic and hypersonic speeds" AGARD CP 93 (1971)

Conf. AFOSR-IFP STANFORD 1968 "Computation of turbulent boundary layer" Vol. I, ed. S.J. KLINE, M.V. MORKOVIN, G. SOVRAN, D.J. COCKRELL - Vol. II, Ed. D. COLES, C. HIRST STANFORD Univ. Press, STANFORD, CALIFORNIA (1968)

COUSTEIX J., HOUDEVILLE R., MICHEL R. "Couches limites turbulentes avec transfert de chaleur" La Rech. Aérosp. N° 1974-6 (1974)

DALY B.J., HARLOW F.H. "Transport equations in turbulence" Phys. Fluids 13, 2634 (1970)

DELERY J. "Shock/shock and shock wave/boundary layer interactions in hypersonic flows" AGARD FDP VKI Special Course on Aerothermodynamics of Hypersonic Vehicles (1988)

DONALDSON C.P. "A progress report on an attempt to construct an invariant model of turbulent shear flows" AGARD CP 93 (1971)

DUSSAUGE J.P., QUINE C. "A second order closure for supersonic turbulent flows - Application to the supersonic mixing" Workshop on "The Physics of Compressible Turbulent Mixing" PRINCETON, N.J. (1988) To be published in "Lecture notes in engineering" Springer Verlag

EL GOBASHI S.E., LAUNDER B.E. "Turbulent time scales and the dissipation rate of temperature variance in the thermal mixing layer" Phys. Fluids 26 (9), pp. 2415-2419 (1983)

FAVRE A. "Equations statistiques des gaz turbulents" C.R. Ac.Sci. 246, pp. 2576, 2723, 2839, 3216 (1958)

FAVRE A., KOVASZNAY L.S.G., DUMAS R., GAVIGLIO J., COANTIC M. "La turbulence en mécanique des fluides" Ed. GAUTHIER-VILLARS (1976)

FINSON M.L., WU P.K.S. "Analysis of rough wall turbulent heating with application to blunted flight vehicles" AIAA Paper 79-0008 (1979)

FULACHIER L., ANTONIA R.A. "Spectral relationships between velocity and temperature fluctuations in turbulent shear flows" Phys. Fluids 26(8) pp. 2105-2108 (1983)

GALMES J.M., DUSSAUGE J.P., DEKEYSER I. "Couches limites turbulentes supersoniques soumises à un gradient de pression : calcul à l'aide d'un modèle k-ϵ" Journal de Mécanique Théorique et Appliquée, Vol. 2 N° 4, pp.539-558 (1983)

GAVIGLIO J. "REYNOLDS analogies and experimental study of heat transfer in the supersonic boundary layer" Int. J. Heat Mass Transfer Vol. 30 N° 5, pp. 911-926 (1987)

GIBSON M.M., LAUNDER B.E. "Ground effects on pressure fluctuations in the atmospheric boundary layer" J.F.M., Vol. 86 (1978)

GLUSHKO G.S. "Turbulent boundary layer on a flat plate in an incompressible fluid" Bull. Acad. Sci. USSR, Mech. Ser., N° 4, pp. 13-23 (1965)

HA MINH H., LAUNDER B.E., MacINNES H. "A new approach to the analysis of turbulent mixing in variable density flows" Third Symp. on Turb. Shear Flows, DAVIS (1981)

HANJALIC K., LAUNDER B.E. "A REYNOLDS stress model of turbulence and its application to thin shear flows" J.F.M. Vol. 52, Part 4 (1972)

HANJALIC K., LAUNDER B.E. "Contribution towards a REYNOLDS stress closure for low REYNOLDS number turbulence" J.F.M. Vol. 74 N° 3 (1976)

HASTINGS R.L., SAWYER W.G. "Turbulent boundary layers on a large flat plate at M = 4" RAs TR 70040

HEALZER J.M., MOFFAT R.J., KAYS W.M. "The turbulent boundary layer on a rough porous plate : experimental heat transfer with uniform blowing" Thermosciences Division, Dept. of Mech. Eng., STANFORD University Report N° HMT-18 (1974)

HORSTMAN C.C. "Prediction of hypersonic shock wave-turbulent boundary layer interaction flow" AIAA Paper N° 87-1367 (June 1987)

JACKSON M.D., BAKER D.L. "Passive Nosetip Technology (PANT) Program Interim" Report Vol. III, Part I SAMSO-TR-74-86, ACUREX Corp., MOUNTAIN VIEW, CALIFORNIA (1974)

JONES W.P., LAUNDER B.E. "The prediction of laminarization with a two-equation model of turbulence" Int. J. of Heat Mass Transfer Vol. 15 (1972)

JONES W.P., MUSONGE P. "Closure of the REYNOLDS stress and scalar flux equations" Phys. Fluids 31 (12) pp. 3589-3604 (1988)

JONES W.P., PASCAU A. "Calculation of variable density flows with a second moment closure" EUROMECH 237 (1988)

LADERMAN A.J., DEMETRIADES A. "Measurements of the mean and turbulent flow in a cooled wall boundary layer at MACH = 9.37" AIAA Paper n° 7273 (1972)

LAUNDER B.E., REECE G.J., RODI W. "Progress in the development of a REYNOLDS stress turbulence closure" J.-F.M. Vol. 68, Part 3 (1975)

LAUNDER B.E. "Heat and mass transport" in "Turbulence" Ed. P. BRADSHAW - Topics in Applied Physics - Vol. 12 Springer Verlag, BERLIN-HEIDELBERG-NEW YORK (1976)

LAUNDER B.E. "An introduction to single-point closure methodology" in "Introduction to the modelling of turbulence" VKI Lecture Series 1987-06 (May 1987)

LAUNDER B.E., TSELEPIDAKIS D.P. "Contribution to the second-moment modelling of sublayer turbulent transport" Zoran Zaric Memorial, BELGRAD (1988)

LEWIS J.E., GRAN R.L., KUBOTA T. "An experiment in the adiabatic compressible turbulent boundary layer in adverse and favorable pressure gradients" J. Fluid Mech. 51 (1972)

LUMLEY J.L. "Computational modelling of turbulent flows" Adv. Appl. Mech. 18 (1978)

MAISE G., McDONALD M. "Mixing length and kinematic eddy viscosity in a compressible boundary layer" AIAA J. 6, 73 (1968)

MARVIN J.G., COAKLEY T.J. "Turbulence modelling of hypersonic flows" The Second Joint EUROPE/US Short Course in Hypersonics - COLORADO SPRINGS (1989)

MICHEL R. "Couches limites - Frottement et transfert de chaleur" Cours de l'Ecole Nationale Supérieure de l'Aéronautique (1967)

MICHEL R., QUEMARD C., DURANT R. "Application d'un schéma de longueur de mélange à l'étude des couches limites d'équilibre" ONERA N.T. N° 154 (1969)

MICHEL R., QUEMARD C., COUSTEIX J. "Solutions de similitude pour les couches limites turbulentes avec gradient de pression en fluide compressible" La Rech. Aérosp. N° 1971-6 (1971)

MOFFAT R.J., KAYS W.M. "The turbulent boundary layer on a porous plate ; experimental heat transfer with uniform blowing and suction" Int. J. Heat Mass Transfer 11 (1968)

MORETTI B.M., KAYS W.M. "Heat transfer to a turbulent boundary layer with varying free stream velocity and varying surface temperature : an experimental study" Int. J. Heat Mass Transfer 8 (1965)

MORKOVIN M.V. "Effects of compressibility on turbulent flows" Coll. Intern. CNRS n° 108, Mécanique de la Turbulence, Editions CNRS (1961)

NA T.Y., HABIB I.S. "Heat transfer in turbulent pipe flow based on a new mixing length model" Appl. Sci. Res. 28 (1973)

NEWMAN G.R., LAUNDER B.E., LUMLEY J.L. "Modelling the behaviour of homogeneous scalar turbulence" J.F.M. Vol. 111, pp. 217-232 (1981)

PAPAMOSCHOU D., ROSHKO A. "The compressible turbulent shear layer : an experimental study" J.F.M. Vol. 197, pp. 453-477 (1988)

REYNOLDS W.C. "Fundamentals of turbulence for turbulence modelling and simulation" AGARD Report n° 755 (1987)

RODI W. "The prediction of free boundary layers by use of a two-equation model of turbulence" Ph.D.Thesis, University of LONDON (1972)

RUBESIN M.W. "The influence of surface injection on heat transfer and skin friction associated with the high speed turbulent boundary layer" NACA RM A 55L13 (1956)

RUBESIN M.W. "A one-equation model of turbulence for use with the compressible NAVIER-STOKES equations" NASA TM X-73-128 (1976)

SAFFMAN P.G. "Development of a complete model for the calculation of turbulent shear flows" DUKE Turb. Conf., DUKE Univ., DURHAM (1976)

SANDBORN V.A. " A review of turbulence measurements in compressible flow" NASA TM X-62, 337 (1974)

SMITH A.M.O., GAMBERONI N. "Transition, pressure gradient and stability theory" DOUGLAS Aircraft Co. Report ES26 388, EL SEGUNDO, CALIFORNIA (1956)

SQUIRE L.C., VERMA V.K. "The calculation of compressible turbulent boundary layers with fluid injection" ARC CP N° 1265 (1973)

STANFORD Conference "1980-81 AFOSR-HTTM-STANFORD Conference on Complex Turbulent Flows" Ed. S.J. KLINE, B.J. CANTWELL, G.M. LILLEY

STRAHLE W.C. "Pressure-strain and pressure-scalar gradient correlations in variable-density turbulent flows" AIAA Journal Vol. 26 N° 8, pp. 969-973 (1988)

TAVOULARIS S., CORRSIN S. "Experiments in nearly homogeneous turbulent shear flow with a uniform mean temperature gradient" J.F.M. Vol. 104 (1981)

TENNEKES H., LUMLEY J.L. "A first course in turbulence" The MIT-Press (1972)

VAN DRIEST E.R. "Turbulent boundary layer in compressible fluids" J. Aeron. Sci. 18, 145 (1951)

VANDROMME D. "Contribution à la modélisation et la prédiction d'écoulements turbulents à masse volumique variable" Doctorat d'Etat - Université de LILLE (1983)

VANDROMME D., HA MINH H. "Turbulence modelling for compressible flows" in "Introduction to the modelling of turbulence" VKI Lecture Series 1987-06 (May 1987)

VAN INGEN J.L. "A suggested semi-empirical method for the calculation of the boundary layer transition region" Univ. of Technology, Dept. of Aero. Eng., Rept. UTH-34, DELFT (1956)

VIEGAS J.R., HORSTMAN C.C. "Comparison of multiequation turbulence models for several shock separated boundary layer interaction flow" AIAA Paper 78-1165 (July 1978)

VIEGAS J.R., HORSTMAN C.C. "Comparison of multi-equation turbulence models for several shock separated boundary layer interaction flows" AIAA Journal Vol. 17, N° 8 (1979)

WILCOX D.C., RUBESIN M.W. "Progress in turbulence modelling for complex flow fields including the effects of compressibility" NASA TP 1517 (1980)

WILCOX D.C. "Reassessment of the scale-determining equation for advanced turbulence models" AIAA Journal Vol. 26, N° 11, pp. 1299-1310 (1988)
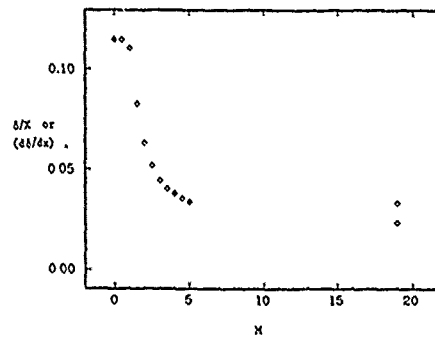
1

Spreading rate of the mixing layer in supersonic
flow ($U_{1e} = 0$ $U_{2e} \neq 0$ $\delta =$
thickness of the layer between $U/U_{2e} = \sqrt{0.1}$ and
$\sqrt{0.9}$) From P. Bradshaw – 1980-81 Stanford Conference
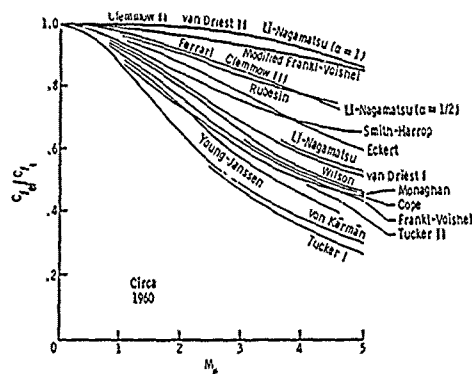
2a

Flat plate boundary layer. Effect of Mach
number on the skin friction (insulated wall)
as predicted by various authors. State of the
art circa 1960. From D. Bushnell 1980-81
Stanford Conference.

2b

Flat plate boundary layer. Effect of Mach number on the
skin friction and Nusselt number. State of the art
circa 1970. From D. Bushnell 1980-81 Stanford Conference.

3

Effect of Mach number on the shear stress
distribution in a flat plate boundary layer.
Figure taken from MARVIN-COAKLEY
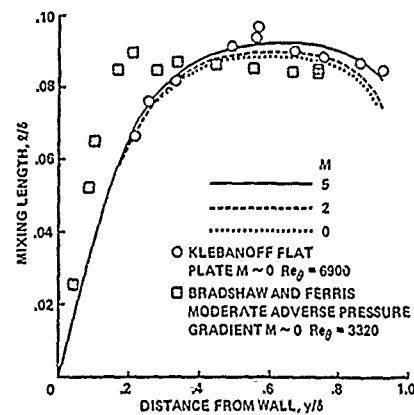
4

Effect of Mach number on the mixing length
distribution from MAISE and Mc DONALD
Figure taken from MARVIN-COAKLEY
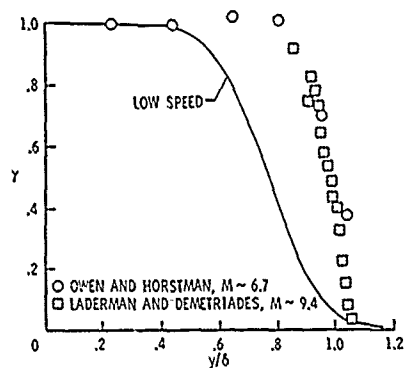
5

Effect of Mach number on the intermittency function from SANDBORN
(figure taken from BUSHNELL et al, 1976)
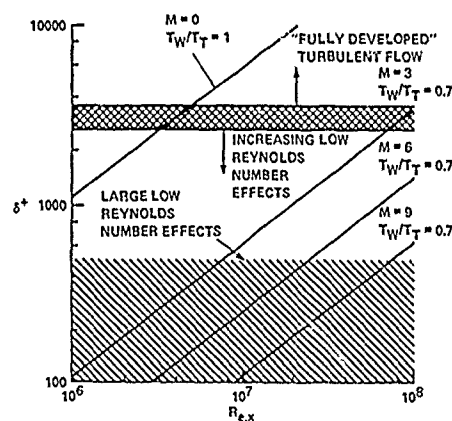
6

Importance of low Reynolds number effects at high Mach number from BUSHNELL et al, 1976
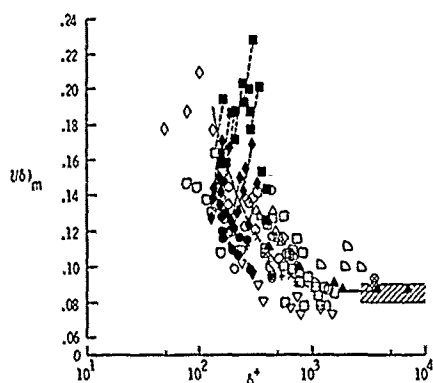
7a

Variation of the outer level of the mixing length downstream of natural transition on plates, cones and cylinders from BUSHNELL et al.
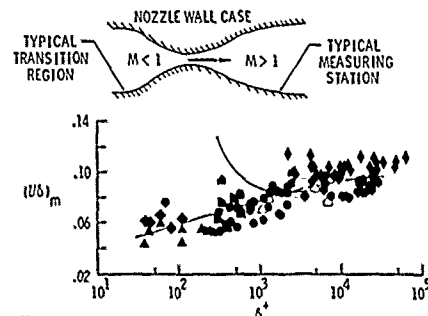
7b

Effects of low boundary layer Reynolds number on the outer level of the mixing length for flows on nozzle walls without laminarization-retransition from BUSHNELL et al.
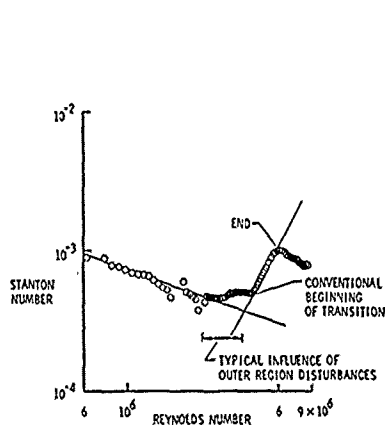
8

Precursor transition effect on wall heat flux from LADERMAN-DEMETRIADES
(figure taken from BUSHNELL et al, 1976)
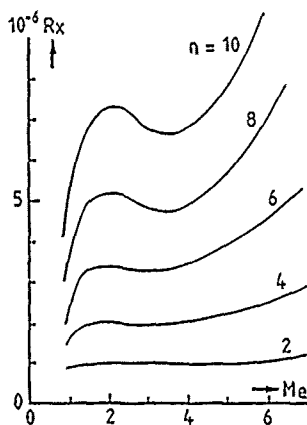
9

Application of the e^n method to the boundary layer transition on a sharp cone with an adiabatic wall from ARNAL, 1988
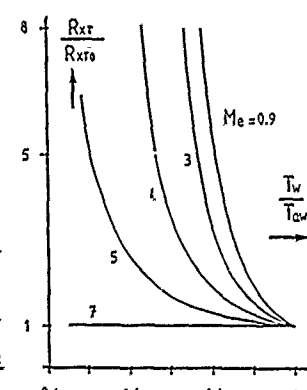
10

Theoretical effect of wall cooling on the flat plate transition Reynolds number as calculated by the e^n method $(n = 9)$ from ARNAL, 1988. R_{xto} is the transition Reynolds number for $Tw/Taw = 1$ (adiabatic wall). R_{xto} depends on the value of the Mach number.
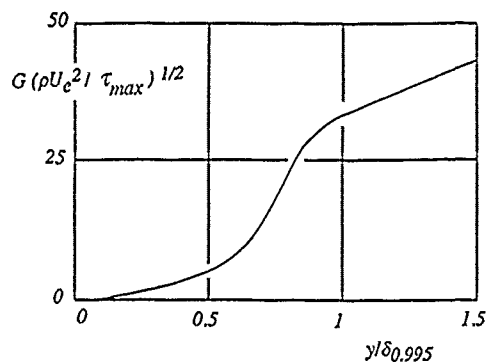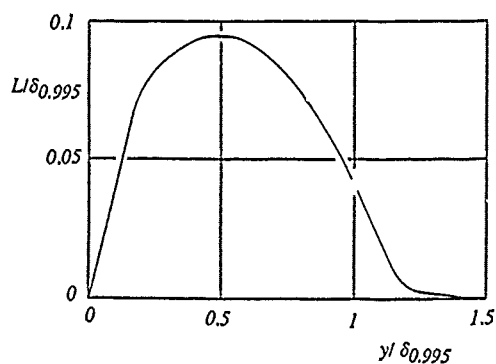
11

Empirical function describing the dissipation and diffusion terms in the BRADSHAW et al model.
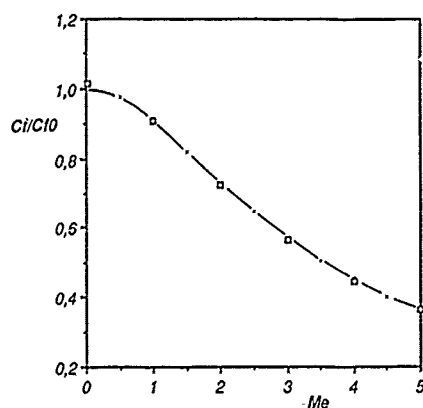
12

Effect of Mach number on the skin friction of a flat plate boundary layer (insulated wall).
Free flight at 15000 m
$R\theta = 10\ 000$ $Cf_o = 2.634\ 10^{-3}$
Van DRIEST II applied to Karman-Schönherr equation .

☐ Integral method
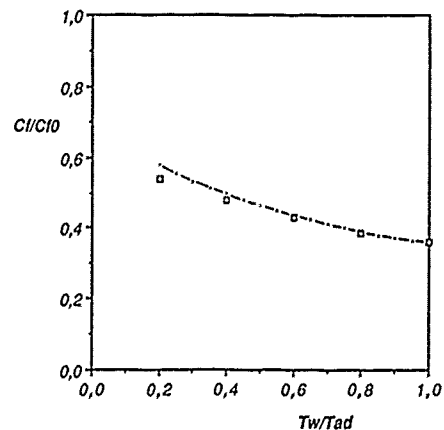
13

Effect of wall temperature on the skin friction of a flat plate boundary layer ($M_e = 5$) – T_w = wall temperature – T_{ad} = adiabatic wall temperature
Free flight at 15000 m – $R\theta = 10\ 000$
$Cf_o = 2.634\ 10^{-3}$
Van DRIEST II applied to Karman – Schönherr

☐ Integral method

3-49
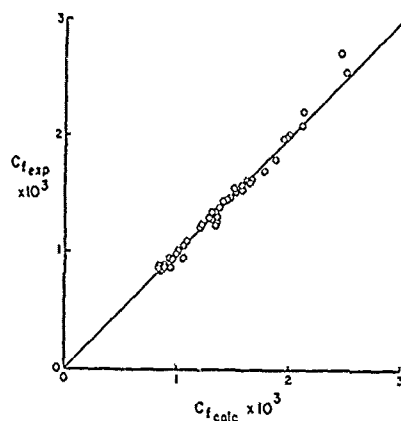
14
Comparison of calculated and experimental
local skin friction values for adiabatic
flat plates. Calculations from CEBECI-SMITH
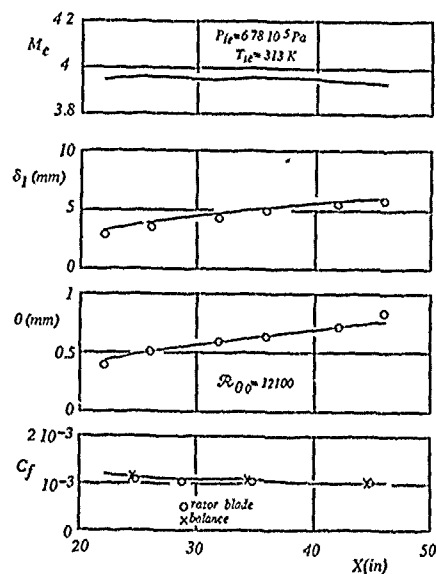
15
Calculation of the experiments of HASTINGS-SAWYER
with an integral method.

$P_{i_e}=678\,10^5\,Pa$
$T_{i_e}=313\,K$
$\mathcal{R}_{\theta\,0}=12100$
o rotor blade
x balance
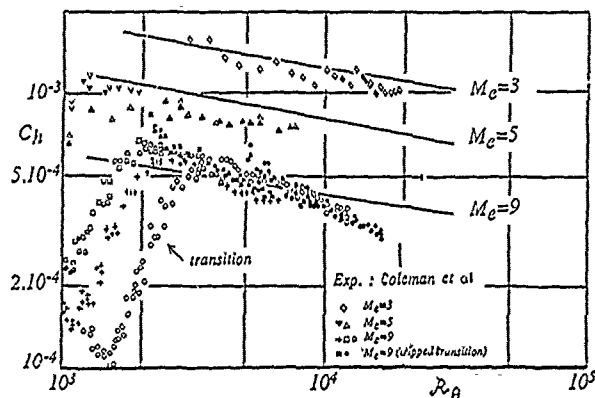
16 Calculations of COLEMAN et al. Experiments with a mixing
length scheme.

Exp. : Coleman et al
$M_e=3$
$M_e=5$
$M_e=9$
$M_e=9$ (tripped transition)
transition

$10^{-5}\,R_e/cm$
5.5
2.76
1.46 } Experiments : Coleman , Elfstrom and Stollery
—— Calculations

$M_e = 9$
$T_i = 1070\,K$
$T_w = 295\,K$
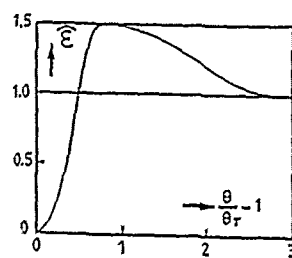
17 Intermittency function used by
ARNAL in incompressible flow.

$\frac{\theta}{\theta_T}-1$
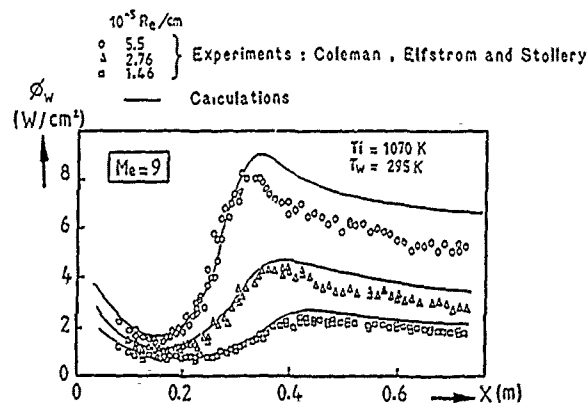
18 Calculations of COLEMAN et al. Experiments taking into
account the transition region (from ARNAL)
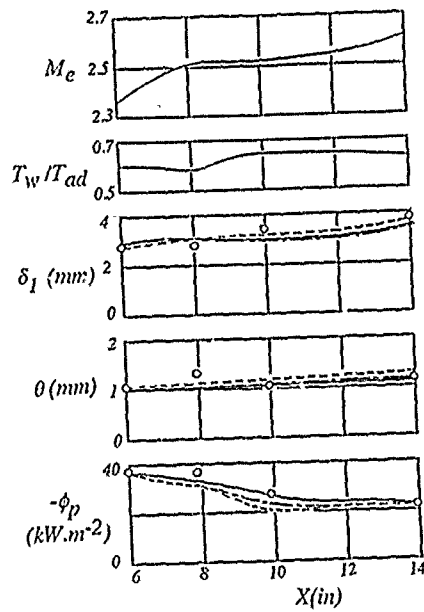
19
Calculation of CLUTTER-KAUPS experiments
— integral method
—·— mixing length
---- k - ε model (JONES-LAUNDER)
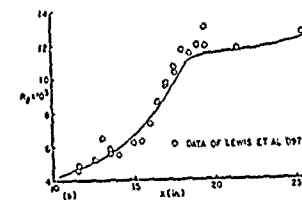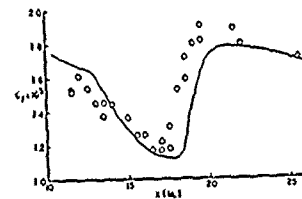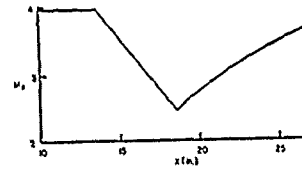
20
Calculations of LEWIS et al
experiments by CEBECI-SMITH
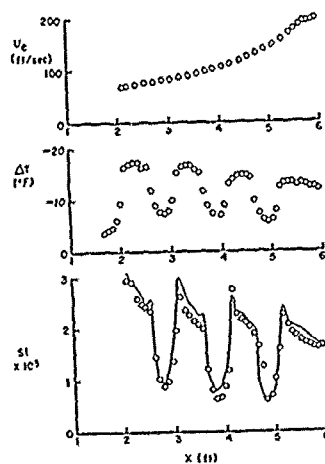
21
Boundary layer with variable wall
temperature

∘∘∘ Experiments : MORETTI - KAYS
— Calculations : CEBECI-SMITH
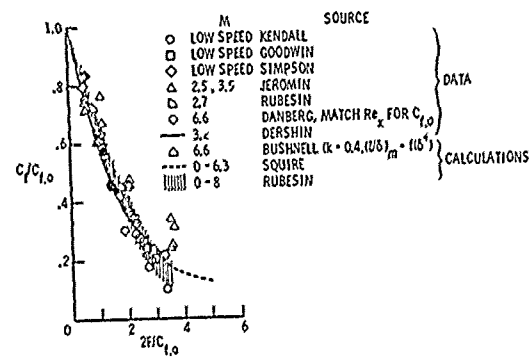
22
Effects of wall blowing on turbulent skin friction
(from BUSHNELL et al)
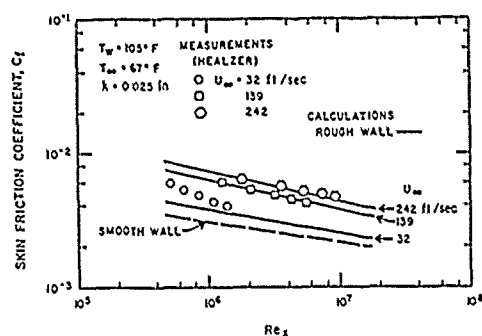
23
Calculation of the skin friction
coefficient on a roughened flat plate
by FINSON-WU
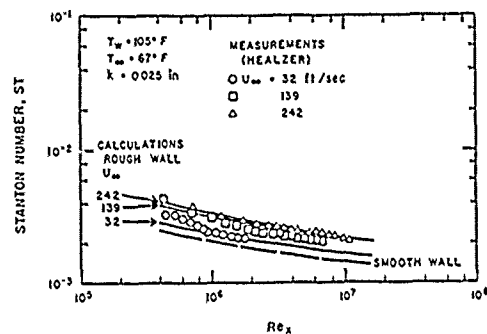
24
Calculation of the heat transfer
coefficient on a roughened flat plate
by FINSON-WU
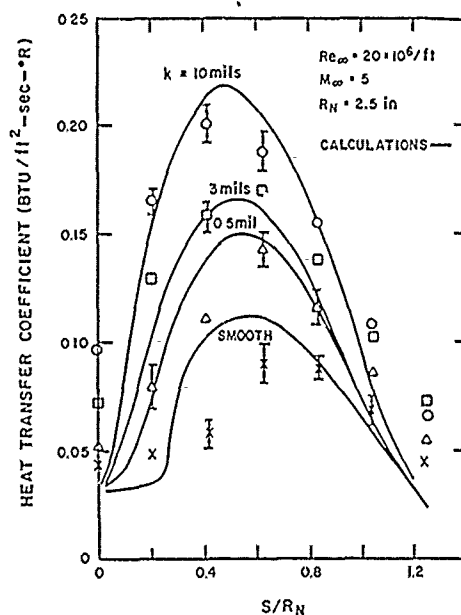
25
Comparison of the FINSON-WU model with
PANT heat transfer data
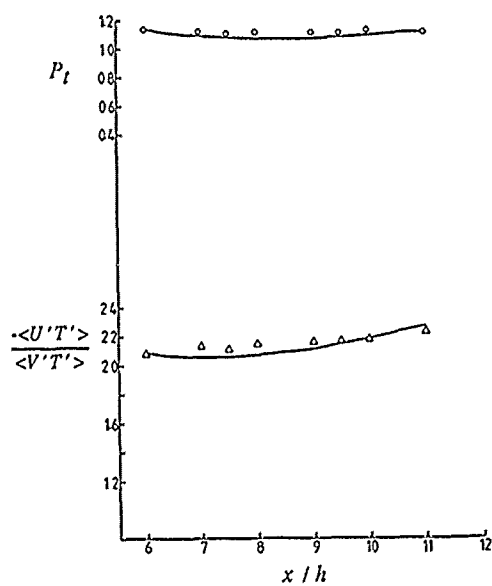
26
Scalar turbulence in a nearly homogeneous
shear flow with a linear mean temperature
gradient o△ Experiment : TAVOULARIS - CORRSIN

——— Calculations : JONES-MUSONGE
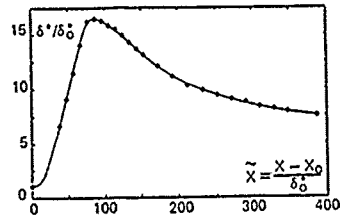
27a
Calculations of a boundary layer/
shock-wave interaction with an
inverse boundary layer method – $M_{e_0} = 1.36$
The experimental displacement thickness
distribution is used as an input of the
method (from BENAY et al)

27b
Comparison between calculated and
experimental pressure distributions
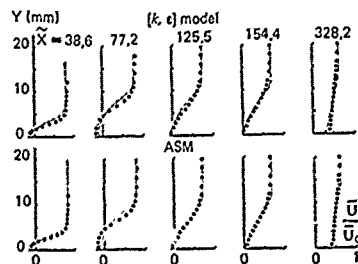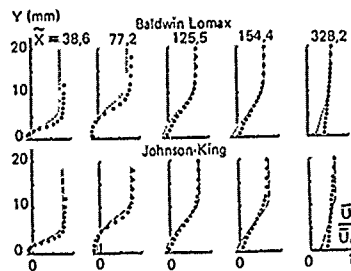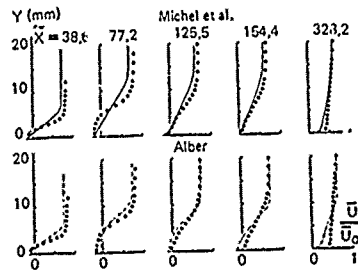
27c
Comparisons between calculated
and experimental boundary layer
velocity profiles.
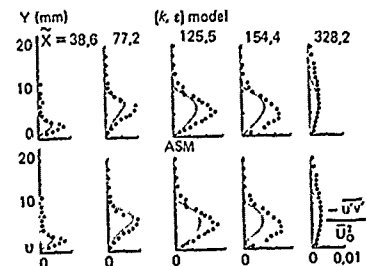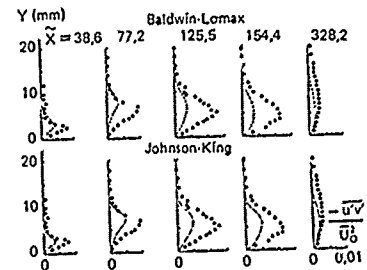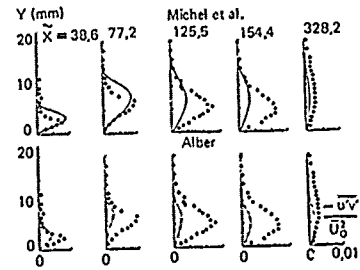
27d
Comparisons between calculated and
experimental boundary layer shear
stress profiles.

M = 9.2
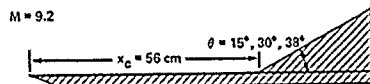
28a
Study of a compression corner flow
(from MARVIN-COAKLEY)
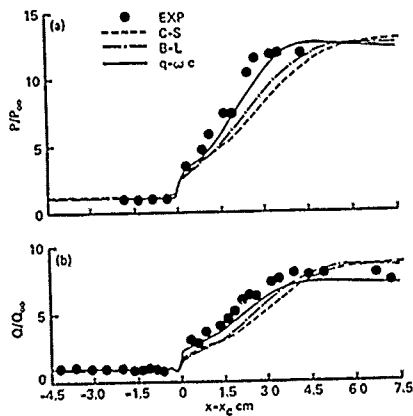
28b
Comparison between calculated and
experimental data on a compression
corner flow - θ = 15° - Pressure and
heat transfer distributions
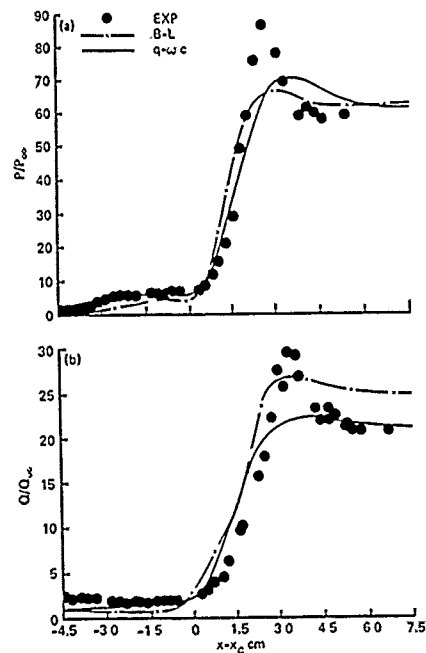
28c
Comparison between calculated and
experimental data on a compression
corner flow - θ = 38° - Pressure and
heat transfer distributions
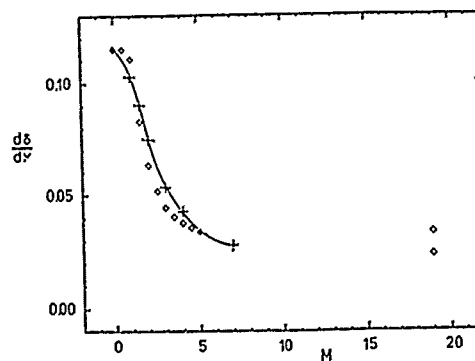
29
Calculation of the free shear layer expansion
rate
◊ experimental data

——— + ——— Calculations (J.P. BONNET)

SHOCK-SHOCK BOUNDARY LAYER INTERACTIONS

by

Michael S.Holden
Calspan/UB Research Center
P.O. Box 400
Buffalo, New York 14225
United States

SUMMARY

A study is presented of the aerothermal characteristics of shock/shock boundary layer interactions generated by single and multiple shocks. A review is presented of experimental studies which have been conducted over the Mach number range from Mach 2 to 19 in the continuous and short duration test facility. The results of recent experimental studies in which detailed measurements of the distribution of heat transfer and pressure were made for Types III and IV interactions in laminar flows at Mach 6 and 19 are discussed in detail. In these studies measurements at Mach 6 to 19 indicated that the severity of the interaction increased with transition and increasing Mach number, as suggested from simple models. Some Type IV interactions where maximum heating occurs can also be unstable and, therefore, may be difficult to predict with accuracy. The studies of multiple shock interaction demonstrated that the largest heat loads are generated on the cylinder if the shocks coalesce before they are incident on the cylinder. While the flow fields and aerothermal loads generated by multiple shock impingement provide test cases for code prediction, the peak heating loads are significantly less than for a single shock of the same strength. Because of the low Reynolds numbers at which transition occurs in the free shear layers developed from either single or multiple shock/shock interactions, coupled with the occurrence of flow instabilities for Type IV interactions, it will be difficult to accurately predict the maximum heating in such flows over a large and important part of the flight regime. However, the major feature of the flow field and pressure distributions have been predicted with good accuracy with finite difference and finite element schemes for the solutions of the Navier-Stokes equations.

TABLE OF SYMBOLS

CH or St	-	Stanton Number
A	-	Constant used in peak heating correlation
N	-	Constant used in peak heating correlation
P	-	Pressure
U	-	Velocity
q or q	-	Heat Transfer (Btu/ft^2)
H	-	Enthalpy
M	-	Mach number
R	-	Gas constant (1717.91 ft-lbslug R)
C_p	-	Pressure coefficient
T	-	Temperature (R)
Y, y	-	Normal distance measured away from surface
X, x	-	Normal distance measured into surface
C(t)	-	Transient specific heat
k(t)	-	Transient heat conductivity
r	-	Non-dimensional time
Pr	-	Prantl number
J	-	778.26 ft-lb/Btu
ρ	-	Density
μ	-	Viscosity
α	-	Reattachment angle
U_R	-	Width of reattachment region
δ	-	Width of the shear layer
$\dot{q}$	-	Heat transfer rate (Btu/(ft^2·sec))
γ	-	Specific heat ratio
τ	-	Time constant
λ	-	Wave length
η	-	Non-dimensional distance
ξ	-	Non-dimentional temperature
ω	-	Radial frequency (2 π f) or jet width
$\bar{R}$	-	Cross flow Reynolds number
$\sqrt{\alpha\omega}$ or η	-	Characteristic length scale
θ	-	Shock generator angle
$\bar{\chi}$	-	Swept Angle
ν	-	Kinematic viscosity

TABLE OF SYMBOLS (cont.)

ℓ	-	Length of shear layer
R_b	-	Body Radius
Re	-	Reynolds Number
V	-	Characteristic velocity
c	-	Chord length
ϵ	-	$(\gamma-1)/(\gamma+1)$
γ	-	Specific heat ratio, c_p/c_v
T_*	-	$T_o \left[1 + 3 (T_w/T_o)\right]/6$
C^*	-	$(\mu_*/\mu_\infty)(T_\infty/T_*)$
d	-	Depth of substrate
t	-	Thickness of blunt leading edge or nose
k	-	$D_N/(\frac{1}{2}\rho_\infty U^2 t)$
D_N	-	Nose drag
h	-	Heat transfer coefficient (Btu/(hr·R^o))
P'_o	-	Undisturbed stagnation pressure
ϕ	-	Orbitor angle

SUBSCRIPTS

max	-	Peak value
o	-	Undisturbed value
w	-	Wall values
R	-	Reattachment region
s	-	Shear layer
STAG	-	Stagnation region
REAL	-	Real value
IDEAL	-	Ideal value
*	-	Reference value
LAM	-	Laminar value
aw	-	Adiabatic wall value
∞	-	Free stream
e	-	Edge conditions
b	-	Body
A	-	At attachment line
d	-	Diameter
i	-	Initial value
LE	-	Leading edge

1. INTRODUCTION

The heating rates generated on blunt bodies by a shock incident on the bow shock in the stagnation region can be orders of magnitude greater than the stagnation value in the absence of the interaction and, therefore, are of considerable interest to designers of hypersonic vehicles. Initial studies by Edney[1] of flowfields and large heating loads generated in shock/shock interaction regions demonstrate that for certain incident shock/bow shock configurations, the pressure recovered on the body can be orders of magnitude larger than the pitot pressure, which, in turn, causes a corresponding heat transfer rate increase in the stagnation region. Edney and, later,

others(2,3) showed that six different flow configurations can be generated depending on the strength of the incident shock and its point of intersection with the bow shock. Figure 1 shows the flow patterns defined by Edney in terms of Types I through VI interactions, and the relative incident/bow shock configurations. Types I, II, and V are interactions where the shock propagates to the surface of the body, resulting in a shock/boundary layer interaction. A Type VI interaction results in an expansion fan boundary layer interaction which does not cause significant aerothermal load enhancement. However, Types III and IV interactions result in large heating and pressure loads and are of greatest interest to researchers.

A Type III interaction (shown in Figure 2) is defined as one generated when the oblique shock is incident on the bow shock slightly below the stagnation region, resulting in a shear layer with subsonic stagnation region flow on one side and supersonic flow on the other. The heating rates generated in such a flow are very similar to the reattachment heating developed in reattaching shear layers and studied extensively in laminar and turbulent hypersonic flows by Holden(4). The levels of heating developed at the reattachment point of the separated shear layer are strongly dependent on the laminar, transitional characteristics of the shear layer. The correlations assembled by Birch and Keyes(5) demonstrate that such a shear layer is highly unstable and transition Reynolds numbers in the order of 10^4 can be anticipated, as shown in Figure 4.
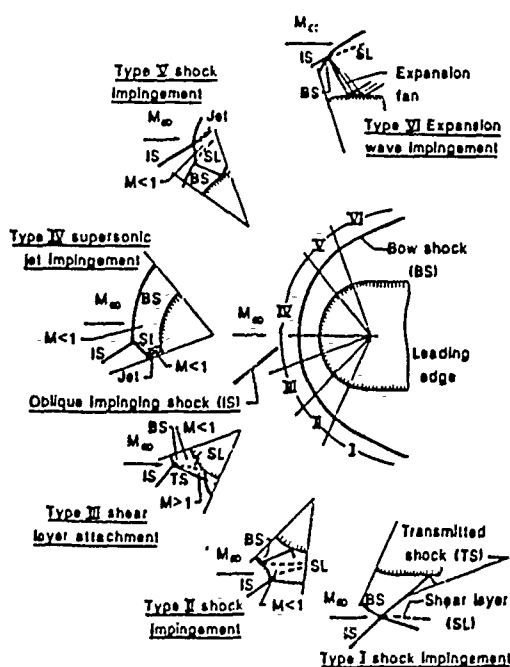
Figure 1   SIX TYPES OF SHOCK WAVE INTERFERENCE PATTERNS

(Keyes and Hains)

BOW SHOCK

M < 1

③

BODY

SHEAR LAYER

P

②

IMPINGING SHOCK

R

①

⑤

Q

④

S

T
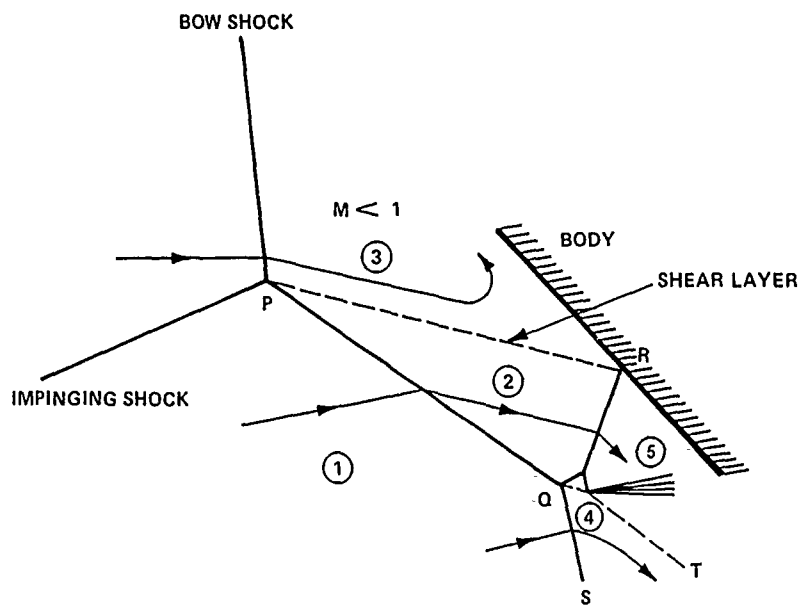
Figure 2   TYPE III INTERFERENCE, M = 4.6, θ = 10°

Bow Shock

Cylinder

Mach > 1   Mach < 1

Jet Bow Shock

Mach < 1

Jet, Mach > 1

Impinging Shock

Mach > 1

Mach < 1

——— Shock Wave
— · Expansion Wave
- - - Shear Layer

Bow Shock
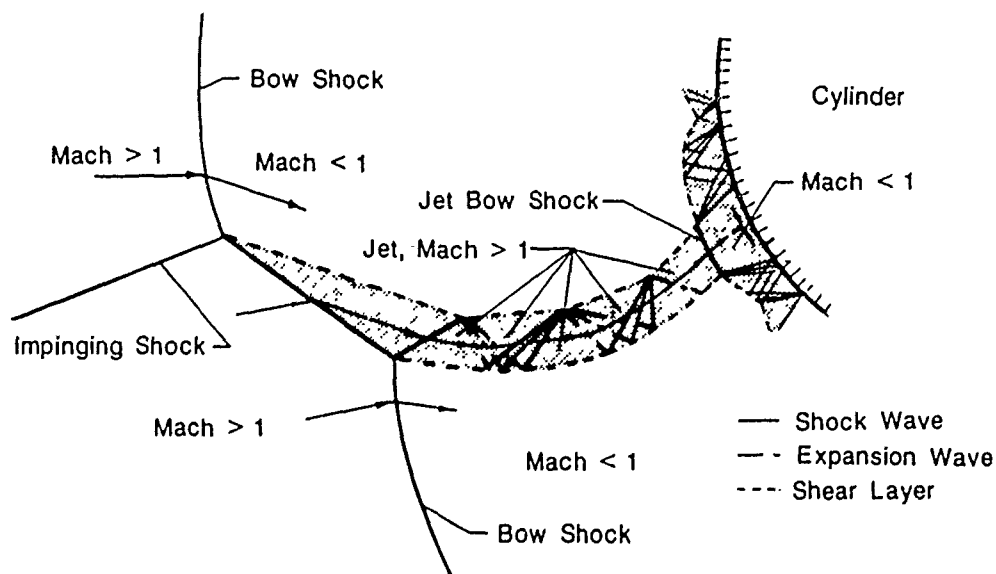
Figure 3   SCHEMATIC OF A TYPE IV INTERFERENCE PATTERN IMPINGING ON A
CYLINDER
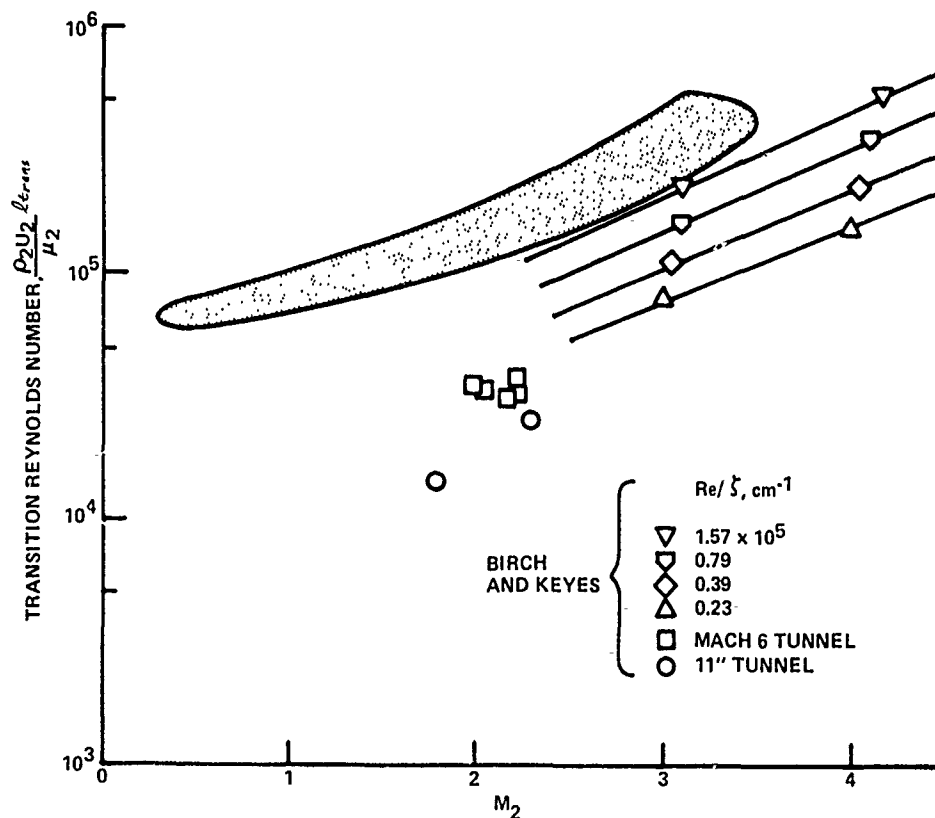
Figure 4 VARIATION OF TRANSITION REYNOLDS NUMBER WITH MACH NUMBER

Chapman, D.R., Kuenn, D.M., and Larson, H.K., "Investigation of Separated Flows in Supersonic and Subsonic Streams with Emphasis on the Effects of Transition," Rept. 1356, 1958, NACA.

When the oblique shock is incident close to the normal region of the bow shock, the flow is processed by a series of shocks and expansions (shown in Figure 4) which create a narrow supersonic jet. This jet, which is bounded on either side by shear layers, is terminated by a normal shock just ahead of the surface, forming a narrow stagnation region. The relatively efficient compression in the Type IV interaction, coupled with the large local velocity gradients in this small stagnation region, are responsible for the large local heating rates generated in this type of interaction. The pressure recovery (relative to the pitot pressure) increases with increasing Mach number, and so the interference heating (relative to stagnation point heating) can be expected to increase in severity with increasing Mach number. Also, Edney suggests that if significant dissociation occurs, lowering the effective specific heat ratio will result in a compression process that has higher pressure, and correspondingly higher heat transfer rates. This prediction, based on a highly simplified (constant) model, has yet to be verified for high-temperature, non-equilibrium flows.

In the first segment of this report a review has been presented of the aerothermal characteristics of shock-shock boundary layer interactions generated by single and multiple shock. Experimental studies have been conducted over the Mach number range from 2 to 19 in the continuous and short duration test facilities. The severity of the heating loads requires the use of insulated models and short test times to prevent distortion from lateral heat conduction. The results of recent experimental studies in which detailed measurements of the distribution of heat transfer and pressure were made for Types III and IV interactions in laminar flows at Mach 6 to 19 are then presented and the results discussed in detail.

2.   REVIEW OF EARLIER STUDIES

The studies of the aerothermal loads generated by shock/shock boundary layer interaction or "interference heating" began shortly after the advent of supersonic flight and construction of supersonic wind tunnels. Most of the earlier studies were concerned with the pressure loads generated by shock/shock interaction. However the thermal failure of the pylon supporting a dummy ramjet engine in X-15 flights tests, as well as in a sled test conducted by Air Force(6,7) provide a graphic demonstration (Figures 5, 6) of the searing heating loads that can be generated in these regions. While one of the most definitive studies of shock/shock interaction resulted from an investigation of "anomolous heating rates" by Edney (1), the major studies of interference heating have been formulated to investigate the aerothermal loads (i) from the shock incident on a fin, wing or pylon (ii) the nosetip/body shock interaction on indented nosetips and spiked bodies, and (iii) the impingement of shocks onto inlet cowl lips and injector struts. A chronological summary of various investigations is given in Table 1.

Investigations of "shock impingement" heating began in the early 60's with studies of the oblique shock incident on swept and unswept fins. These early studies were motivated by observations of unusually high heating rates generated during the flow visualization studies of various uninstrumented supersonic aircraft configurations at NASA Langley. The first definitive investigation of shock interaction heating were wind tunnel and free-flight studies conducted in supersonic flows up to Mach 5.5 to measure the heating in regions of shock impingement on unswept cylinders by Newlander(8) and Carter and Car(9). A typical model configuration of Newlander's investigation along with the associated heating rates is shown in Figure 7. Similar material is shown in Figure 8 for the free flight investigation of Carter and Carr. These studies revealed the heating enhancements were 5 to 10 times higher than the reference stagnation heating value when a shock/shock interaction occured. Measurements on similar configurations were conducted in hypersonic flows by Francis(10). At NASA Langley, Beckwith(11) and Bushnell(12,13) measured the

interference heating on a swept cylinder close to its junction with a wedge, while Jones(14) studied a fin-plate interference at Mach 6. Bushnell's earlier work (12) focused on the interfering heating problem caused by the root region of wedge-swept cylinder configuration and initially the analysis of localized effects of shock/shock interactions was not pursued. However, in a subsequent study, Bushnell(13), conducted studies in which he isolated both effects of shock/shock interactions and effects of
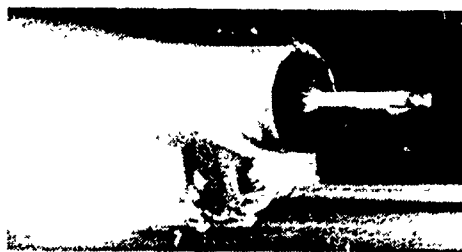
Figure 5a   SLED ON TEST TRACK AT HOLLOMAN AFB IN MOTION AT 7000 fps

Figure 5b   SLED ON TEST TRACK AT HOLLOMAN AFB RESULTING INTERACTION HEATING DAMAGE
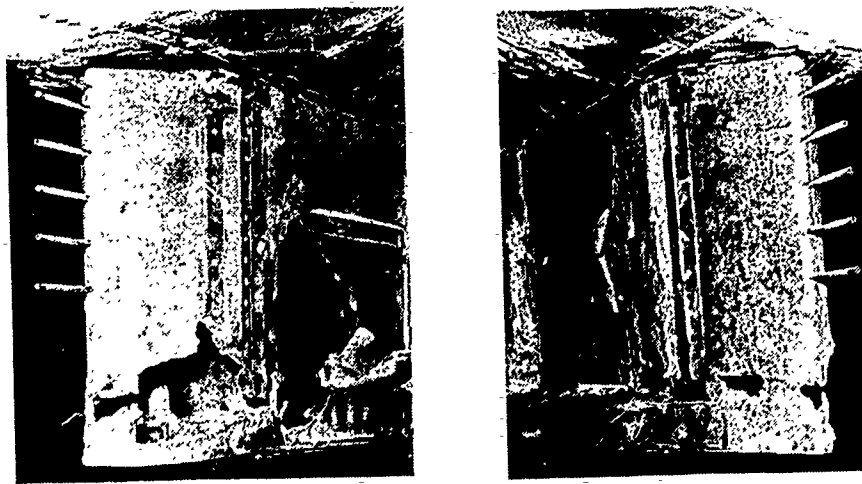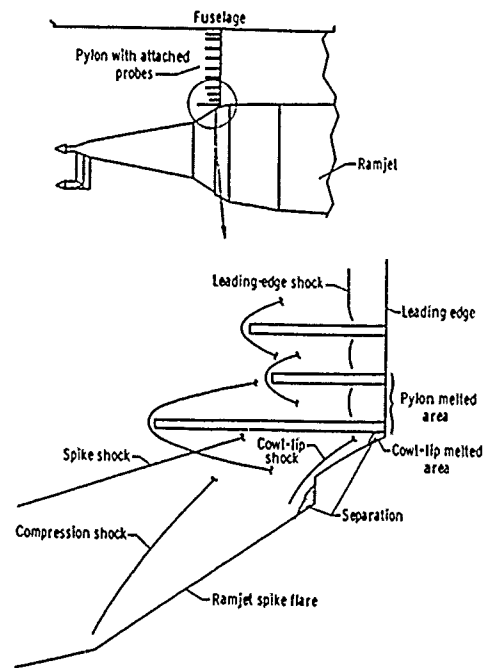
Figure 6   DAMAGE TO X-15 PYLON RESULTING FROM SHOCK-SHOCK
INTERACTIONS

Table I. SUMMARY OF SHOCK INTERFERENCE INVESTIGATIONS

Author and Date	Reference number	M_∞	Re_∞ /ft	Fin diameter, d, in.	Shock general angle, θL, deg	Fin sweep, λ, deg	Static Pressure	Heat Transfer	Schlieren	Oil	$\dfrac{q_{max}}{q_{ref}}$	Remarks
Newlander (1961)	15	2.65, 3.51, 4.44	1.32×10^6 to 4.56×10^6	2.706	16.25	0		x		x	1.8, 2.0, 3.1	Wedge and fin mounted on flat plate. Partially immersed in boundary layer. Thermocouple/Stainless Steel Model
Carter and Carr (1961)	16	2.0	15.96×10^6 to 30.01×10^6	.75	-	0		x	x			*Not applicable. Shock generated by hemisphere/cylinder.
		2.53 to 5.5	0.7145×10^5 to 8.76×10^6	.32	-	0					0.1 to 0.5 (M=3) 1.5 to 2	Free flight to 10,500 ft. altitude. Thermocouple/Thinwall Stainless Steel Cylinder
Beckwith (1964)	18	4.15	17.28×10^6 43.21×10^6	1.00	0	90	x	x	x		2.5	Thermocouple/Stainless Steel Model
Jones (1964)	21	6.0	0.7145×10^5 to 8.76×10^6	1.00	-	60	*x	x		x	1 to 3	*Only at R /ft = 10×10^5. Model yawed up to 30°.
Siler and Deskins (1964)	22	19.0	0.287×10^6	2.00	0 to 40	0 to 60	x	x	x		2.5 to 5	34 Stainless Steel, Calorimeter Type transducer based on a thermocouple.
Bushnell (1965)	19	8.0	0.924×10^6 to 1.05×10^6	1.00	12	45 and 60	x	x	x		3 to 5	Thin thermocouple/thin wall model.
Francis (1965)	17	9.0	1.757×10^6 to 1.15×10^6	1.00	*6,34	0	x	x	x		1 to 4	*Cone and wedge with one cylinder and one wedge fin, both flued.
Ray and Palko (1965)	28	6,*8,10	0.56×10^6 to 3.6×10^6	5.00	0 to 60	0 to 60	x	x	x	x	2.5 to 5	*Data not presented for M = 8.
Jones and Hurt (1967)	46	8	5.7×10^5	-	0	0	x	x	o		9	Phase changing paint "Tension Shell" mc~?
Heirs and Loubsky (1967)	27	14	0.095×10^6	1.00	0 to 15	0, 22.5, 45	x	x	x	x	10	Luminous photographs supplement schlieren photographs. Chromel-con stanian thermocouples, thin wall leading edge model.
Edney (1968)	1	4.6, 7	1.24×10^6 to 14.42×10^6 0.335×10^6 to 2.334×10^6		0 to 15, 0 to 5	0	x	x	x		10	Axisymmetric blunt bodies and fins. Thin film gauges.
Bushnell (1968)	20	8	0.503×10^6 to 5.03×10^6	.75	12	0.76	x	x	x		x	Mica/Glass Model, Temp. sensitive paint.
Watts (1968)	14	8	0.5396×10^6 to 1.418×10^6	.75	12	0	x	x	x			Flight data only. Pressure data later reported by Burcham and Nugent (1970).
Young, Kaufman, Korkegi (1968)	38	3, 5	0.5396×10^6 to 1.418×10^6		0	0	x	x	x	x	4	1/80 Scale straightwing shuttle model thin film H/T gauges.
Rogers (1971)	30	8, 10	10^6	-	0	0	x	x	x			Thin film H/T gage
Holden (1972)	51	6.5 to 13	10×10^6 to 100×10^6	.394	0 to 20	0	x	x	x		50	Only pressures reported.
Kaufman, Korkegi, and Morton (1972)	39	2.5, 3.0	0.6×10^6	-	0	0	x	+x	*x			*Shadowgraphs also. *Thermocouple and phase-change coating data.
Haslett et al. (1972)	40	8	$.360 \times 10^6$ to 3.59×10^6	1.00	1.5 to 15		x	x	x		1.15	347 Stainless steel models pressure model temp paint/epoxy model.
Keyes and Hains (1973)	29	6-20	1 to 7.8×10^6	1.92	30°	0	x	x	x		7.5 to 17	Copper/Constantian thermocouple-hollow cylinder.
Ginoux et. al. (1973)	42	2.25	.405 to $.87 \times 10^6$	1.78	6°	0	x	x	x		3	Computational solution to N.S. comparaed to
Tannehill (1976)	35	5.95	185×10^6	1.92	-							*Diameter of model?
Holden (1988)	1	11, 13	5×10^5 to 10×10^6	12"	10 to 15°		x	x	x		5 to 18	Thin film gauges
Witing and Holden (1988)	6	6, 8	.5 to 4.9×10^6	3.00	10 to 15°		x	x	x		5 to 28	Thin film gauges
Holden and Wieting (1985)	36	6-18	20×10^6 to 0.5×10^6	3.00	10 to 15°		x	x	x			Thin film gauges
Glass, Holden and Wieting (1989)	52	8	1.5×10^6	3	10 to 15, 10 to 30°		x	x	x		5 to 18	*Swept angles

holden = szard_tab1

M	$R\left(=\frac{\mathcal{V}_\infty L}{\nu_\infty}\right)$	$h_L=\left(\frac{\dot{q}}{T_{AW}-T_W}\right)$
2.65	3.95×10^6	0.01661
2.65	2.65	.01356
2.65	1.60	.00959
3.51	3.95	.01472
3.51	2.75	.01231
3.51	1.60	.00938
4.44	4.50	.01282
4.44	3.20	.01071
4.44	2.15	.00871
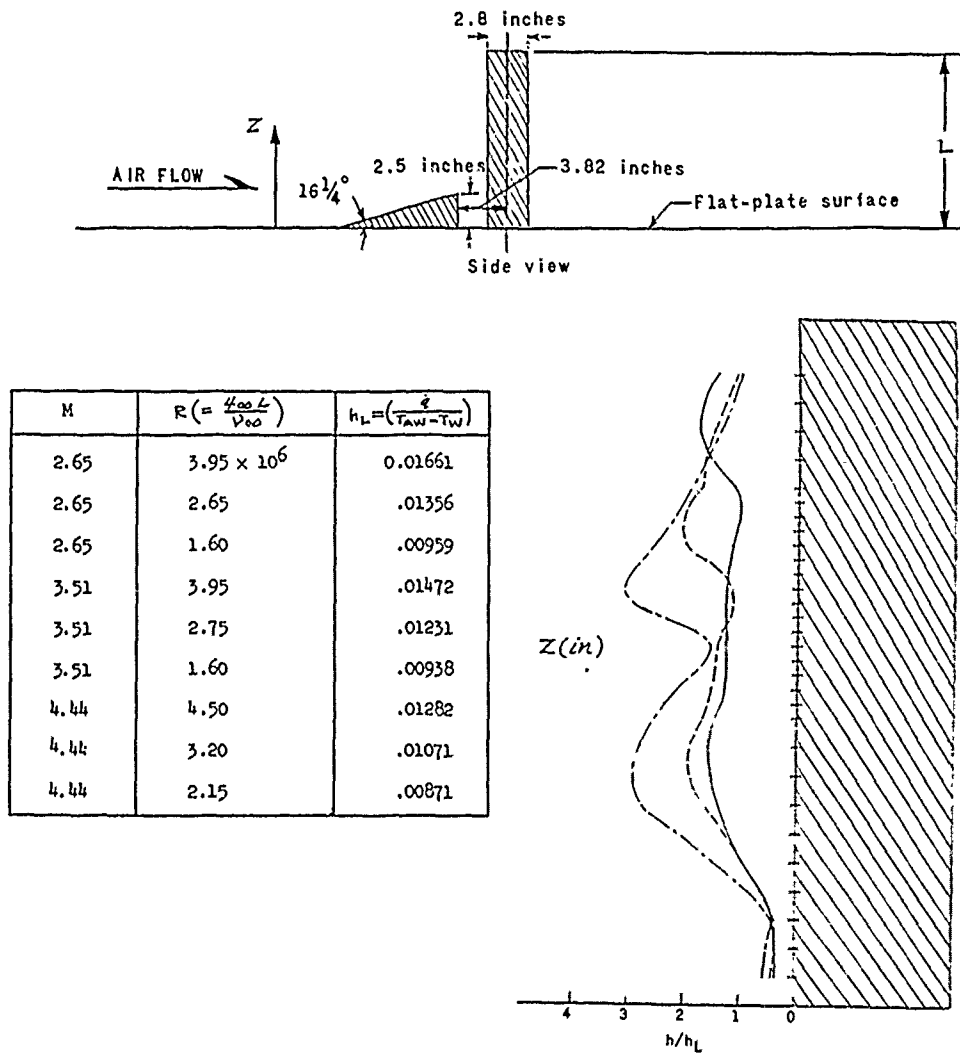
Figure 7 SHOCK IMPINGEMENT HEATING ON A RIGHT CIRCULAR CYLINDER AT A MACH NUMBER OF 2.65 TO 4.44. INVESTIGATION OF NEWLANDER (REF. 8)

$M_\infty = 5.50; \; R_D = 1.87 \times 10^6.$
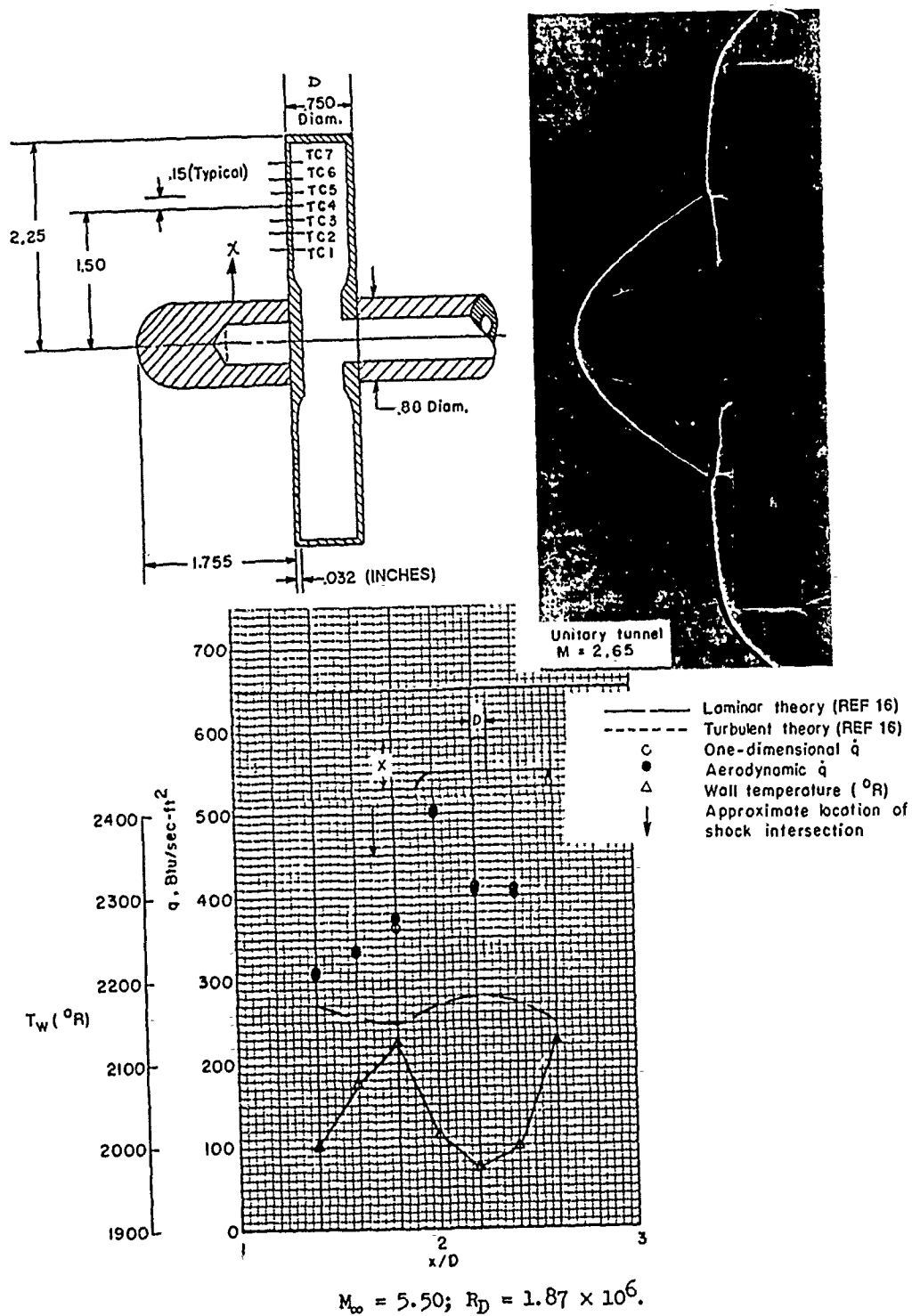
Figure 8   FREE FLIGHT SHOCK INTERFERENCE MEASUREMENTS OF HEAT TRANSFER ON UNSWEPT CYLINDER AT MACH NUMBERS UP TO 5.5 (REF 16)

separated root region. By supporting the cylinder away from the shock generator, he removed the separated region at the wedge/cylinder junction. The effects of leading edge transitions were also investigated (Figure 9(a)). A typical result of peak heating expectations based on Bushnell's work, and others, and their typical model configuration is given in Figure 9(b).

Also during the mid-sixties studies were being conducted for AFFDL in the AEDC facilities by Siler et al(15), Gulbran et al(16) and (17), Knox(18) Ray and Palko(19) and Uselton(25). Again, the emphasis in this work was on leading edge shock impingement and was a direct result of AFFDL's experience with high heat loading observed during their supersonic aircraft testing programs. Siler's investigation of leading edge surface heat transfer yielded heating enhancements of 5 times the values without shock impingement. The high heat rates caused by the shock/shock interaction are illustrated in Figure 10. This test was conducted in AEDC's tunnel F, using nitrogen as the test gas at Mach 19. The investigation(s) of Ray and Palko were conducted in AEDC Tunnels B and C, again with a wedge/cylinder model configuration. These studies were conducted in air at Mach 6 to 10. The peak heat transfer rates observed here were from 3 to 4 times the undisturbed rate.

At NASA Ames, Heirs and Loubsky (20) also studied the effects of shock impingement on the heat transfer to a cylindrical leading edge in the Ames 6 foot Shock Tunnel at Mach 5 to 14. This latter study highlighted a number of problems associated with the measurement of the large transfer rates and gradients generated in the interaction regions. More specifically, in the experiments of Heirs and Loubsky, and in many of the other earlier studies, the conductivity of the model surfaces were such that the peak heating and the distribution of heating rates were significantly reduced by heat conduction along the model surface. Although a correction procedure can be used, it can be highly inaccurate, particularly if the actual heat transfer distribution is as complex as it is in shock/shock interaction regions. Also the large response time of the instrumentation used made it impossible to resolve unsteady movement in the interaction region. Even with these conduction losses, the measured peak heat rates on an unswept cylinder impinged by externally generated shock wave was measured to be 10 times that of the undisturbed values. This study also concluded that increasing the swept angle of the cylinder will alleviate the heat loading. At larger swept angles, the heat transfer rates could be adequately analyzed by the application of the two dimension boundary layer transformed to a swept cylinder

HEAT TRANSFER TO LEADING EDGE WITH AND WITHOUT GROOVES

$M_\infty = 8$; $x/D \approx 12$

$$N_{NU} = \left[\frac{q/(T_{Aw}-T_w)}{K_\infty} \right] D$$

THEORY

TURBULENT

LAMINAR

○ GROOVED
□ SMOOTH

600
400

100

60

40

10^4

10^5

10^6

LOW $R_{\infty,D}$ HIGH $R_{\infty,D}$

$R_{\infty,D}$
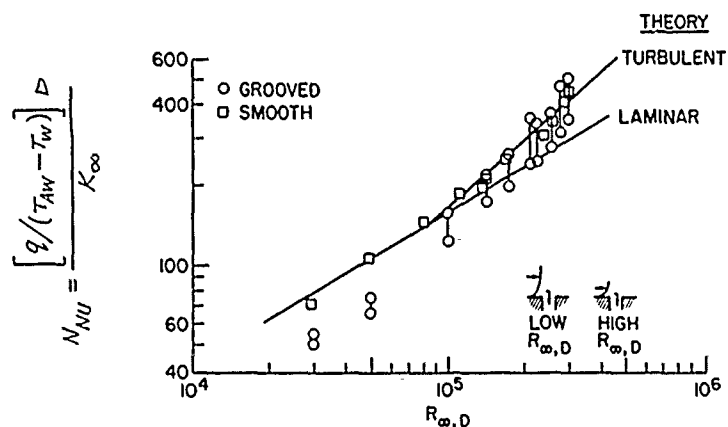
RESULTS OF SURVEY OF TRANSITION DATA ON SWEPT LEADING EDGES

$2.5 \leq M_\infty \leq 8$; $\Lambda > 40°$

"DELTA-WING" CONFIGURATIONS

$(R_{\infty,D})_{transition} > 8 \times 10^5$

CONFIGURATIONS HAVING END CONTAMINATION

$(R_{\infty,D})_{transition} \approx 2 \times 10^5$
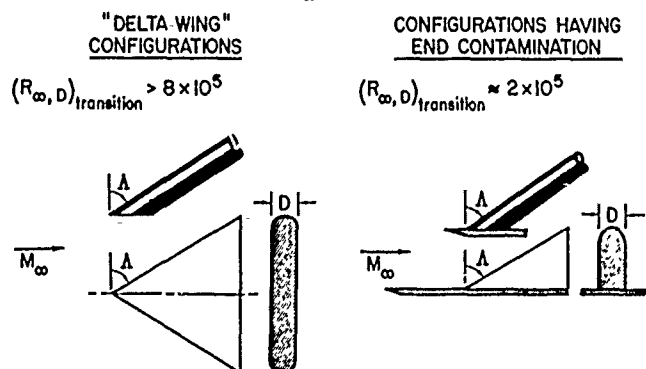
Figure 9a   EFFECTS OF SHOCK IMPINGEMENT ON PEAK HEATING INVESTIGATION OF BUSHNELL (REF. 12,13)

FLOW FIELD
ASSOCIATED WITH LEADING-EDGE SHOCK IMPINGEMENT

SEPARATED-FLOW
REGION

IMPINGING
SHOCK

BOW SHOCK

M_∞

VORTEX-
SHEET IMPINGEMENT

VORTEX SHEET

LEADING EDGE

EFFECT OF SHOCK IMPINGEMENT ON MAXIMUM HEATING
CYLINDRICAL LEADING EDGE; $\Lambda = 0°$

⊠ SEPARATION AND IM-
PINGEMENT IN CLOSE
PROXIMITY

▨ SOME ROOT SEPARATION,
IMPINGEMENT IN DE-
VELOPING BOW-SHOCK
REGION

○ NO ROOT SEPARATION,
IMPINGEMENT IN DE-
VELOPED BOW-SHOCK
REGION

$M_\infty = 14$

$M_\infty = 2.5$ TO 19

$\dfrac{h_{max}}{h_1}$

$M_\infty = 10$ $M_\infty = 10$ $M_\infty = 8$

h_2/h_1

P_2/P_1

MAXIMUM HEATING AS A FUNCTION OF DISTANCE
FROM TIP OF CYLINDER
$\Lambda = 0°$; $M_\infty = 8$

$\dfrac{h_{max}}{h_1}$

Δ/D

SHOCK STAND OFF DISTANCE

Figure 9b   ILLUSTRATION OF INTERFERENCE PATTERN GENERATED BY A
HYPERSONIC AIRCRAFT AND A TYPICAL WIND TUNNEL MODEL USED
(REF. 12, 13)
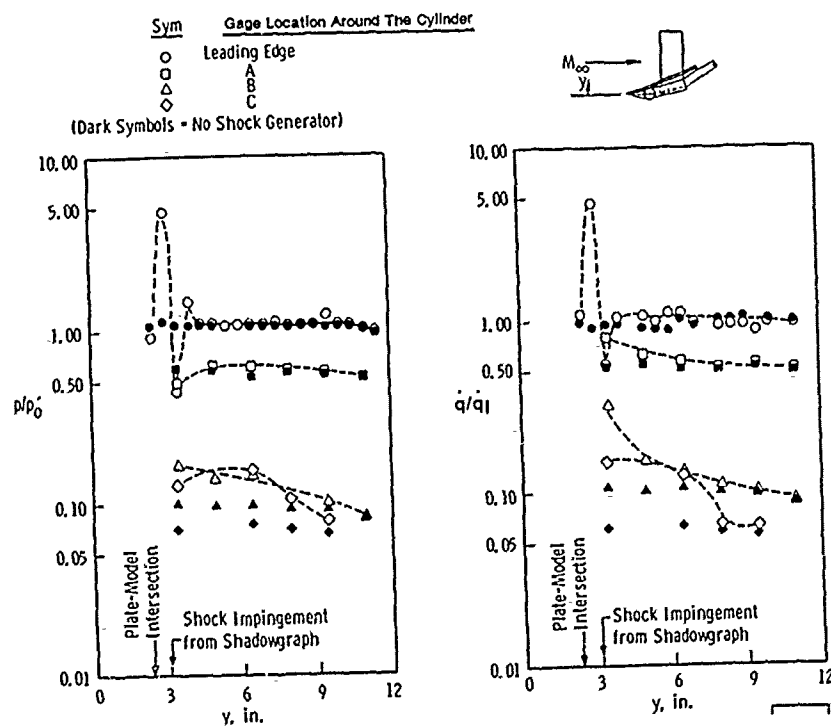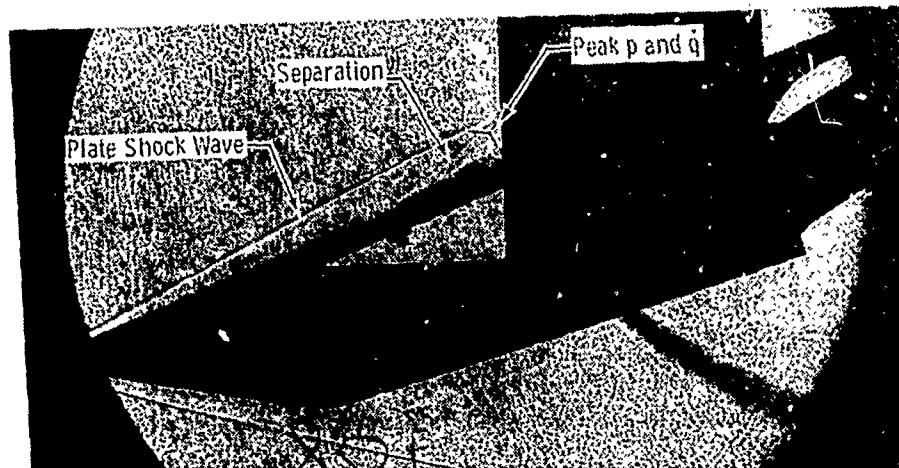
Figure 10   PRESSURE AND HEAT TRANSFER DISTRIBUTION ON STAGNATION LINE
OF LEADING EDGE. INVESTIGATION OF SILER AND DESKIN (REF 15.)

configurations. A typical prediction of unswept configuration as compared with an experimental result at Mach 14 is illustrated in Figure 11.

In one of the most significant investigations of shock/shock interaction phenomena, Edney[1] identified the basic flowfield structure in regions of shock/shock interaction for a number of shock geometries, and suggested simple prediction methods to estimate the aerothermal loads generated by them. The work of Edney provided valuable insights to various types of inviscid and viscous interaction problems and will be discussed further in detail. Following this major work, a series of studies were initiated by NASA Langley to develop more accurate methods for predicting shock interaction heating with application to the design of the Shuttle project. The work of Hains and Keyes[2] and later Morris and Keyes[22] and Bushnell[12] and Bushnell and Weinstein[45] extended the experimental work of Edney and provided some simple but reasonably accurate prediction techniques with which to estimate the aerodynamic loads, as well as some accurate peak heating rate measurements. The work of Hain and Keyes, in particular, focused on various types of interactions which could possibly occur on the surface of the shuttle/tank configurations. It concluded that a Type IV interaction could occur on the shuttle/tank configuration, increasing the local heating rate up to 20 times that of undisturbed freestream heating rate. The test result, model configuration, as well as a typical location of this type of interaction is illustrated in Figure 12(a-b)[2]. The computer program written by Morris and Keyes[21] provides useful information in this regard. Measurements of the shock impingement heat loads on the Shuttle were also made in a number of other studies with the models of the orbitor [23] or the orbitor/tank (24,33) configuration.

During the mid-sixties to early seventies, the Air Force, motivated by their experiences with the X-aircraft testing program, supported work on shock impingement on blunt fins (25,26) and inlets (3), as well as (at the Von Karman Institute) shock impingement on conical bodies and cylinders. The works of Kaufman(31,32) were directed to the study of detail structure of separation and interaction regions of the blunt fin mounted on a flatplate. The focus of these works was to study detailed flow structure by various means of flow visualization and to perform detailed pressure measurements. Although the abnormal peak heat rates were observed, no heat transfer data was reported. The later works of Haslett and Kaufman focused more heavily on the heat load measurements, but in a more complex geometrical configuration. The tested configurations included various combinations of the orbital model with flat
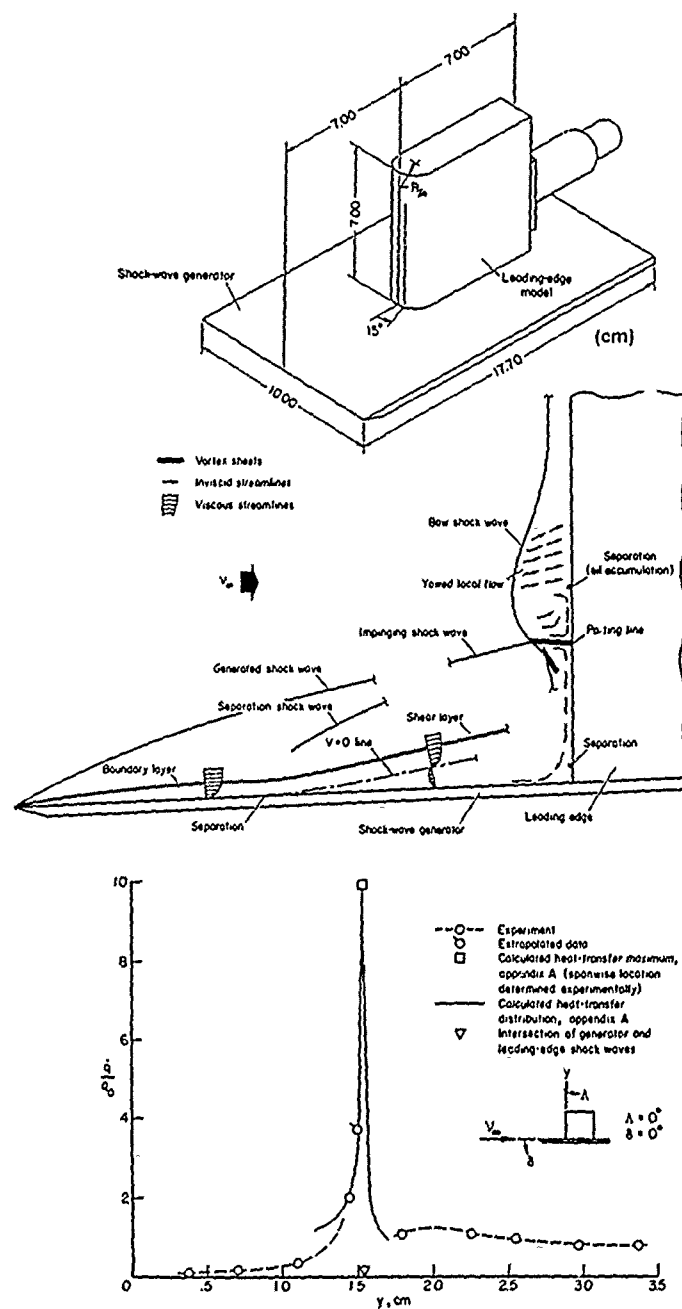
Figure 11   SPANWISE HEAT–TRANSFER DISTRIBUTION ON STAGNATION LINE OF
THE LEADING EDGE INVESTIGATION OF HEIRS AND LOUBSKY (REF. 20)
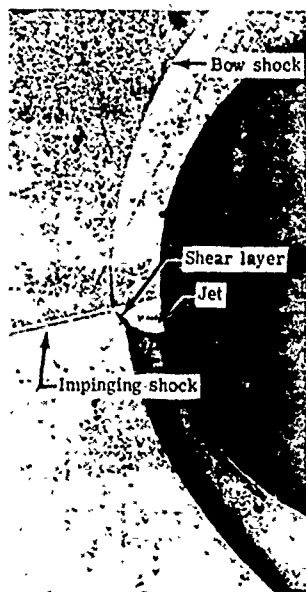
L-73-254
(a) Schlieren photograph.
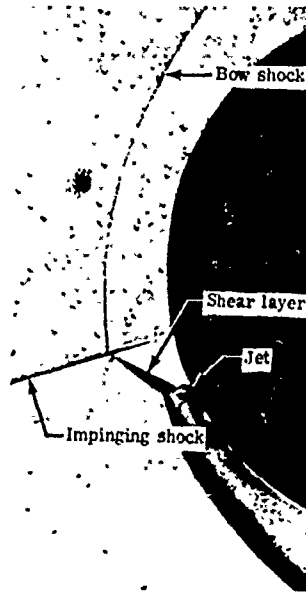
L-73-255
(a) Schlieren photograph.
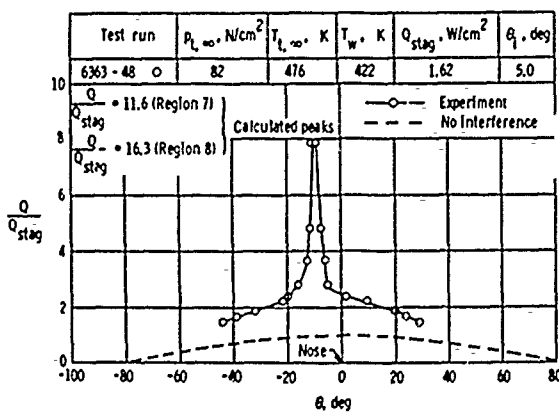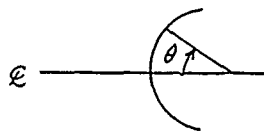
(c) Heat-transfer distribution.
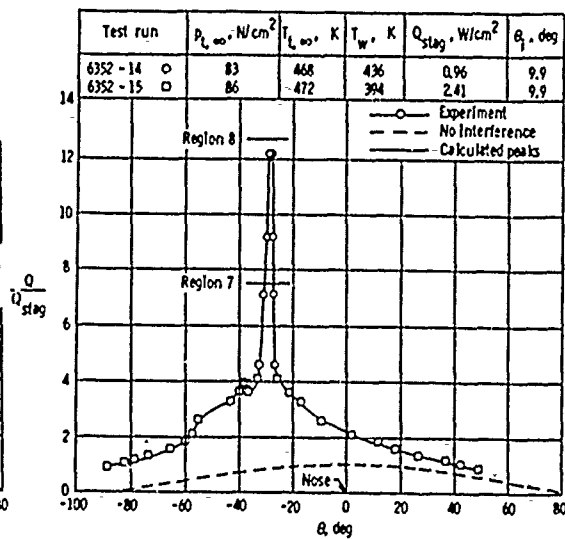
(c) Heat-transfer distribution.

Figure 12a   TYPE IV INTERACTION(S) PRESSURE/HEAT TRANSFER DISTRIBUTION
ON A HEMISPHERE AT MACH NO. 5.94. INVESTIGATION OF KEYES
AND HAINS (REF. 2)
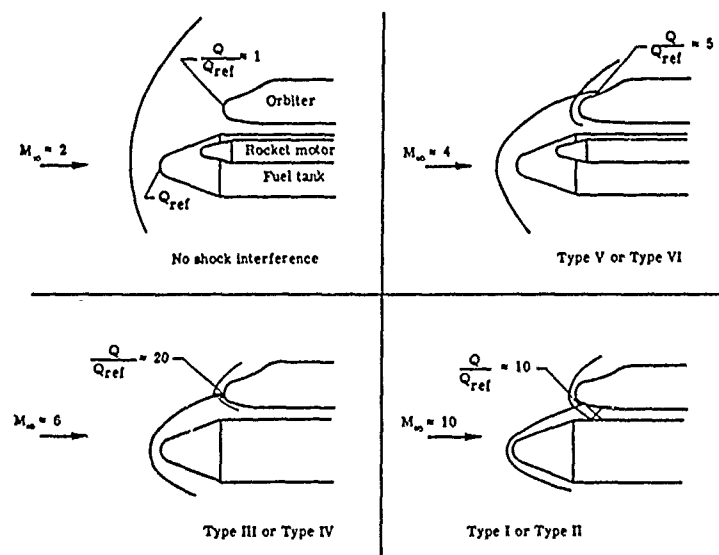
Shock interference heating during ascent of a mated shuttle configuration.
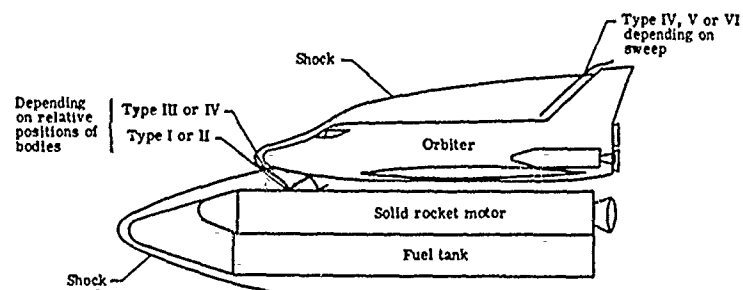
Figure 80.- Locations of types of interference heating on mated configuration at $M_\infty \approx 20$.

Figure 12b   TYPES III AND IV SHOCK INTERFERENCE PATTERN GENERATED DURING ASCENT OF A MATED SHUTTLE CONFIGURATION

receiver plates as well as an orbital model with tank (receiver) model combination (Figure 13). The first combination, along with surface mounted heat transfer gages, was used to validate a typical empirical heat load amplification correlation function. A typical comparison of the results are illustrated in Figure 14. The later configuration, the combination of orbit/tank along with heat sensitive paint was used to predict residual heat loading on the shuttle fuel tank system during the separation stage. A typical result is illustrated in Figure 14, where peak heating is showed to be as high as 30 times the undisturbed values. The work of Craig and Ortwerth was directed specifically toward cowl lip heating, which currently is of major interest in the design of NASP. Studies by Gulbran et al(16,17), and work by Ginoux and Matthews provided further measurements and analysis.

The studies of cavity induced shear layer on a conical model along with shear impingement caused by Types III and IV shock/shock interactions on a cylinder were performed at von Karman Institute (VKI) by Ginoux and Matthews(34,35). The investigation of reattachment of cavity induced shear layer on a conical model was performed at Mach 5.3 in the VKI's continous supersonic wind tunnel. Figure 15 illustrates the analogy drawn by Edney(2) between Type III interaction and a cavity flow. In a later work, Ginoux(35), studied the Types III and IV shock/shock interaction produced on a wedge/cylinder configuration. Only small peak heat rates were observed because of the low freestream Mach number (2.25), which was used in this investigation. Typical geometrical configurations and distributions of heat transfer are shown in Figure 16.

The heating loads developed in regions of shear layer impingements were measured in a number of studies of spiked bodies (Holden(36)), indented noseshapes (Holden(37,38)) and Tension Shells(39). In these studies, the interaction regions were generated by the interaction between the nose tip shock and body shock as illustrated by Figures 17, 18, and 19. In most cases the basic mechanism for heating enhancement is the reattachment of a free shear layer, although there are a number of cases where a free jet is formed. Figures 18 and 19 show some of the typical heat transfer distributions developed along the body surfaces. The investigation of flowfield around a tension shell by Jones and Bushnell utilized phase changing paint to measure heat transfer rate. The test gas of tetrafluoromethane was used in order to attempt to evaluate the effects of γ on the interaction.

1-UPSTREAM OF SHOCK   2-DOWNSTREAM OF REFLECTED SHOCK
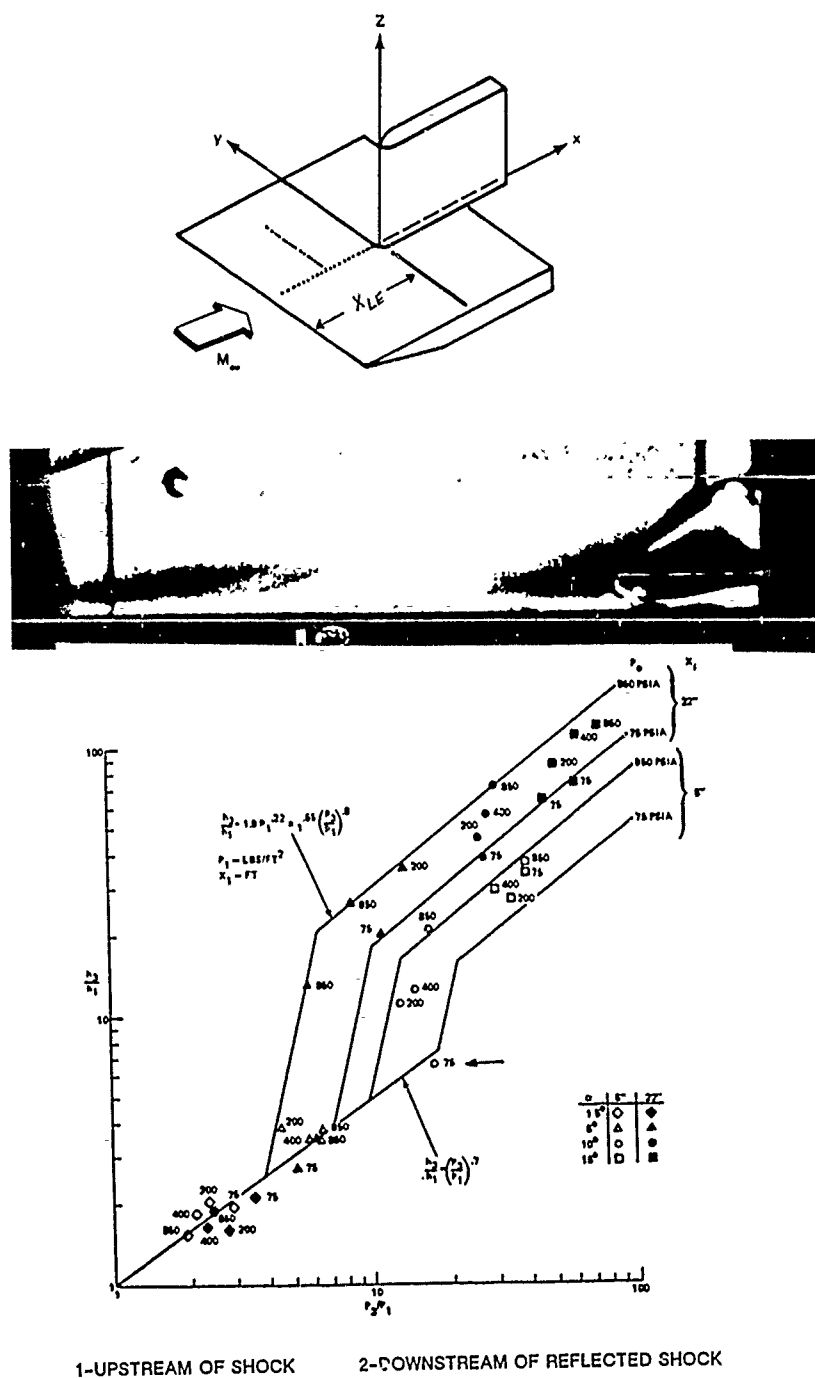
Figure 13   SHOCK INTERFERENCE HEATING ON BLUNT CYLINDER AT MACH 3.
INVESTIGATION OF KAUFMAN (REF. 32, 33)
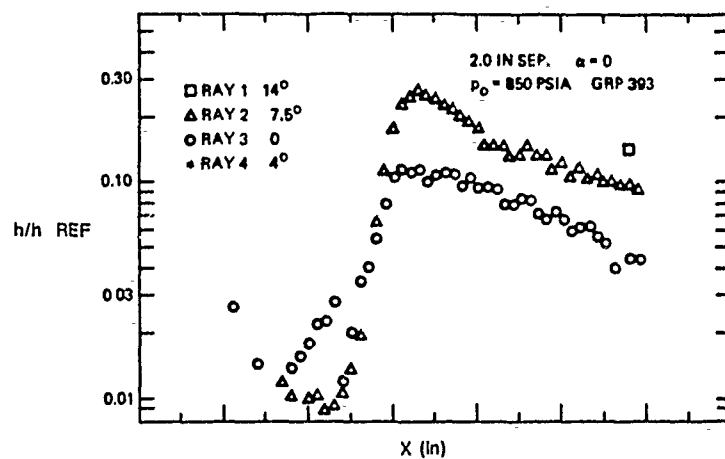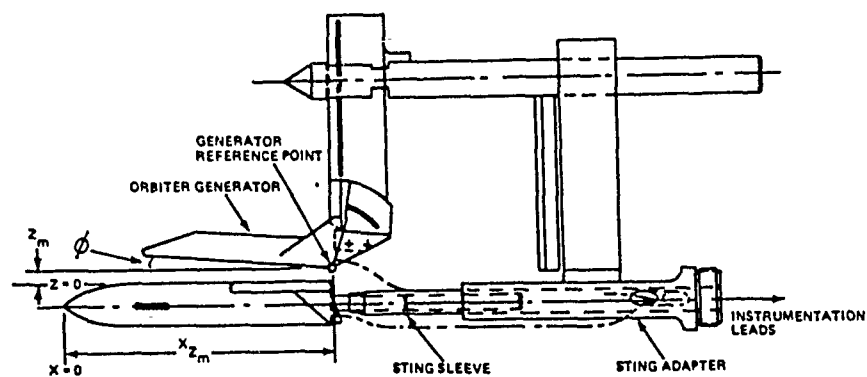
Figure 14   INTERFERENCE HEATING DISTRIBUTION ON ORBITER CAUSED BY
BOOSTER (REF. 33)

P – SEPARATION LINE
R – REATTACHMENT LINE
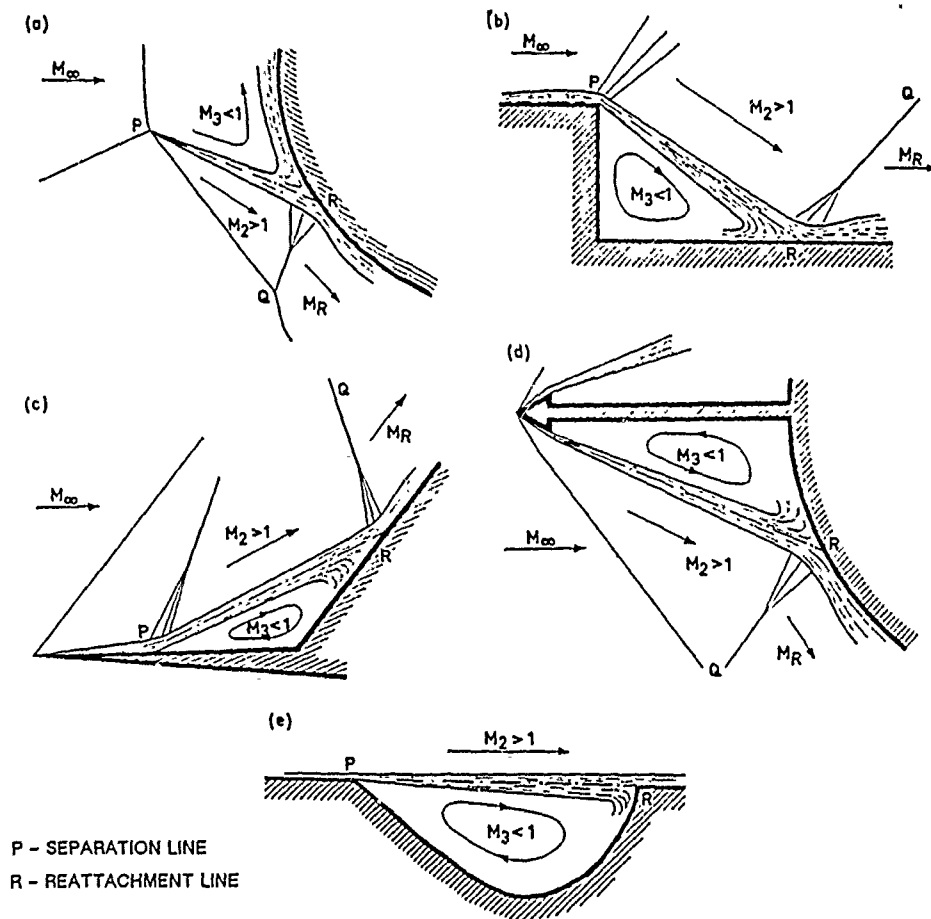
Figure 15   ANALOGY BETWEEN TYPE III AND CAVITY FLOW (REF. 1)

$M_\infty = 2.25$

o $P_0 = 80$ mm Hg laminar shearlayer
a $P_0 = 130$ mm Hg transitional
+ $P_0 = 175$ mm hg turbulent
— — shock layer distribution

$\dfrac{h}{h_{0_{STAG}}}$

θ (DEGREES)
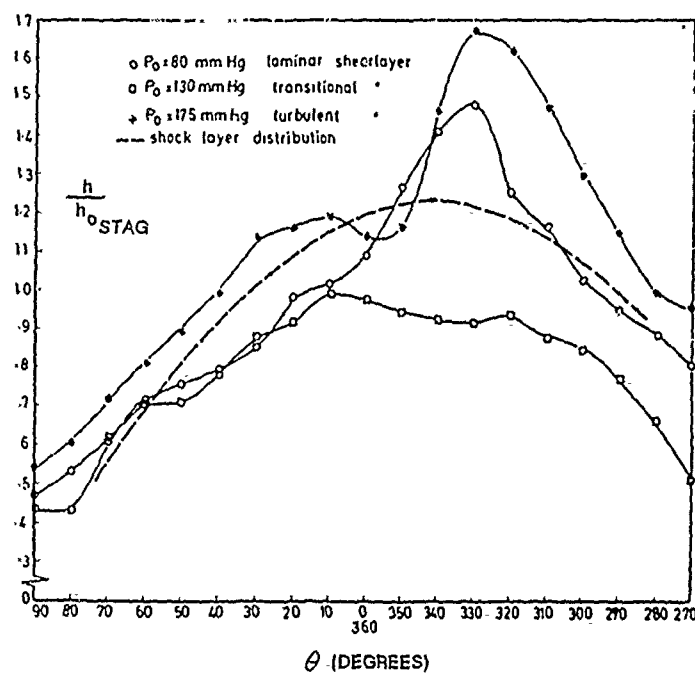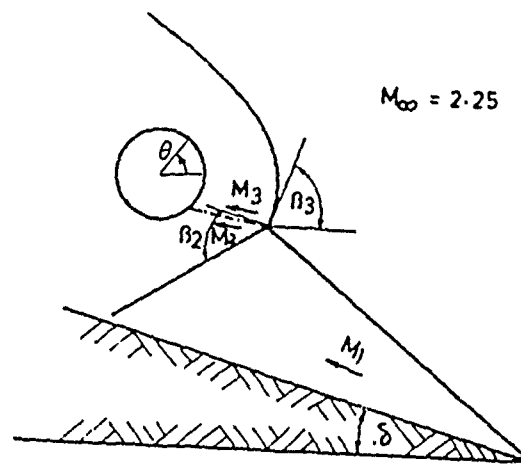
Figure 16   INTERFERENCE HEATING ON RIGHT CIRCULAR CYLINDER AT MACH 3.
INVESTIGATION OF GINOUX (REF. 34)
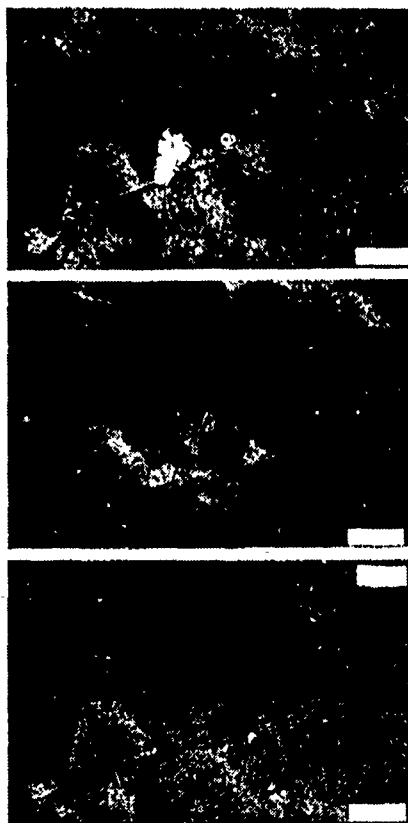
Figure 17   INTERFERENCE HEAT ON SPIKED BODY AT CALSPAN (Ref. 36)
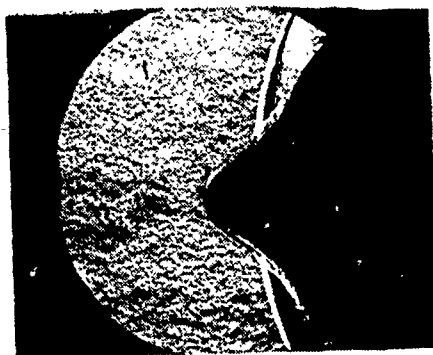
(a) MACH 11

(b) MACH 13
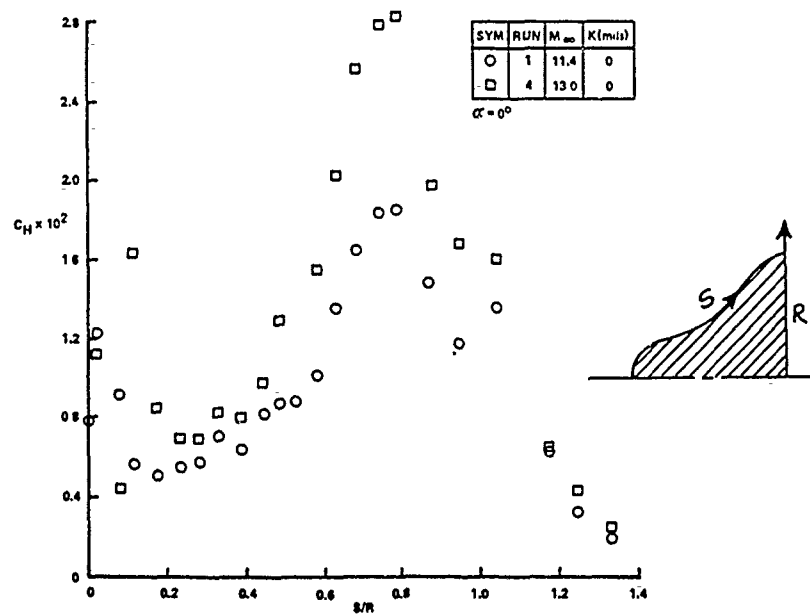
Figure 18 SHOCK/SHOCK INTERACTION HEATING ON INDENTED NOSE
TIP (Ref. 38)
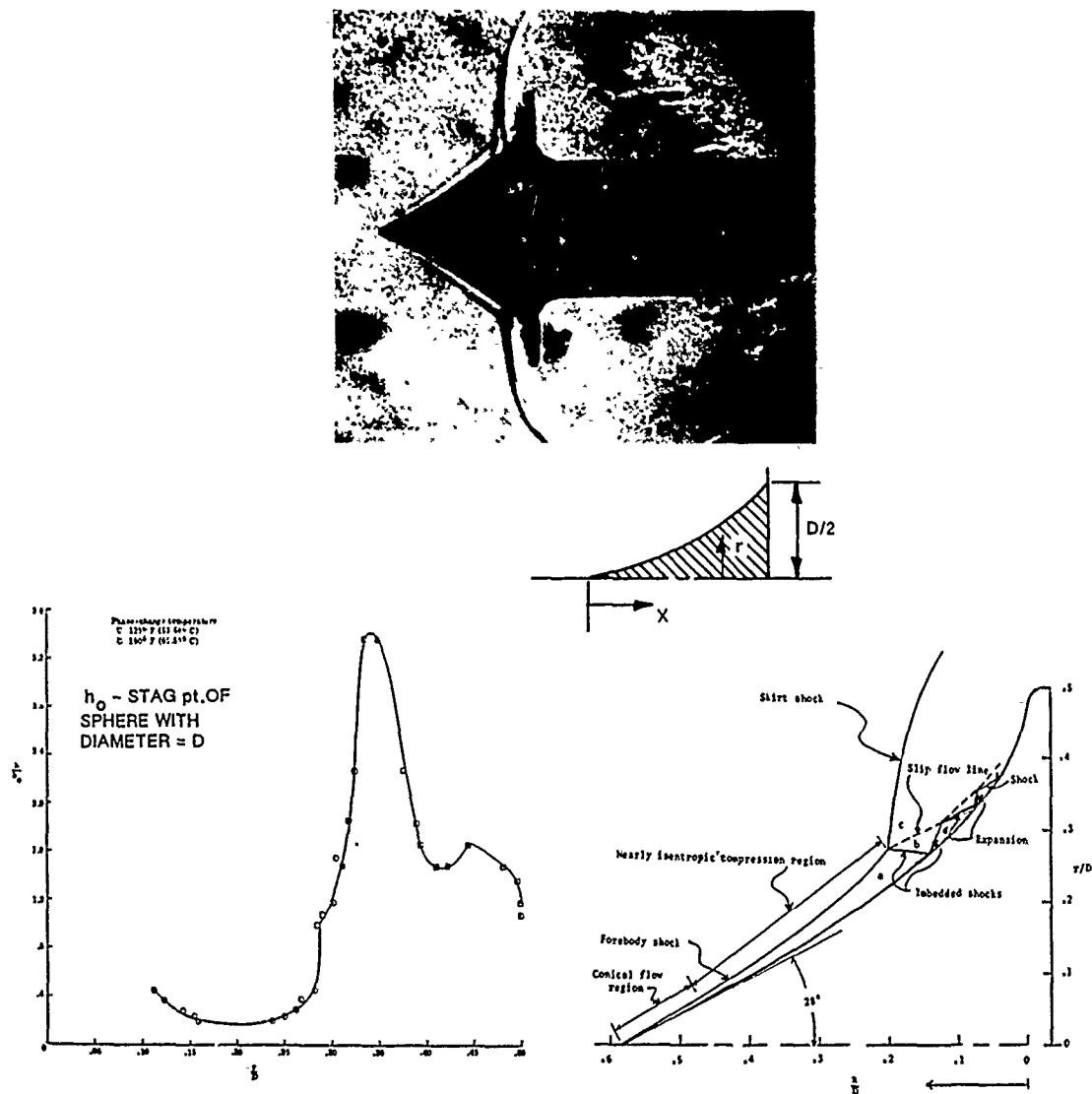
Figure 19 SHOCK–SHOCK INTERACTION HEATING ON "TENSION SHELLS." IN-
VESTIGATION OF JONES AND BUSHNELL (Ref. 39)

Both investigations of spiked bodies and indented nose tips used high-frequency thin-film instrumentation to measure heat transfer distribution. These studies were part of a more extensive program to study the transient behaviors associated with the aerodynamics of ballistic and maneuverable re-entry vehicles (MRVs). Again a graphic illustration of the damage caused by the heating in reattachment regions on spiked bodies was provided by sled tests conducted at Holloman. As shown in Figure 6 the shock from spike induced heating loads caused significant damage to the sled and its runners.

Following the experiments and analysis of Keyes and Hains, Tannehill, Hoist and Rakich[27] and later Tannehill, Holst, Rakich and Keyes[28] performed a number of numerical studies of shock/shock interaction induced by an oblique shock impinging on the shock layer ahead of a circular cylinder. Solutions were obtained to the time-dependent Navier Stokes equations for a number of cases with different shock strengths for laminar flow at Mach 4.6 and 5.96. While substantial grid refinement was required to obtain meaningful solutions, the numerical solutions were in good agreement with shock shape, and pressure and heat transfer distributions. Figure 20 illustrates a typical comparison of the numerical prediction to that of measurement by Edney[1].

Following a period during which there was little new experimental or theoretical research interest in the aerothermal loads generated in shock/shock interactions, efforts were renewed to design airbreathing hypersonic vehicles. Large aerothermal loads resulting from shock/shock interaction are generated on the control surfaces, the cowl lip and on the injection struts of these vehicles.

Experimental studies by Holden et al[29] and Wieting and Holden[40] provided detailed heat transfer and pressure distributions in regions of single and multiple shock/shock interaction at Mach 6 to 19. A key feature of these later studies is that very highly resolved measurements were made on surfaces with little lateral heat conduction. Detailed numerical solutions were obtained for comparison with these studies using finite difference and finite element techniques by Klopfer and Lee[41] and Stewart et al[42]. In the following section we review some of the features of flow fields of single and multiple regions of shock/shock interaction and the aerothermal loads that are developed in them.

Comparison of shock shapes.

Comparison of wall pressures.

Comparison of surface heat transfer rates.
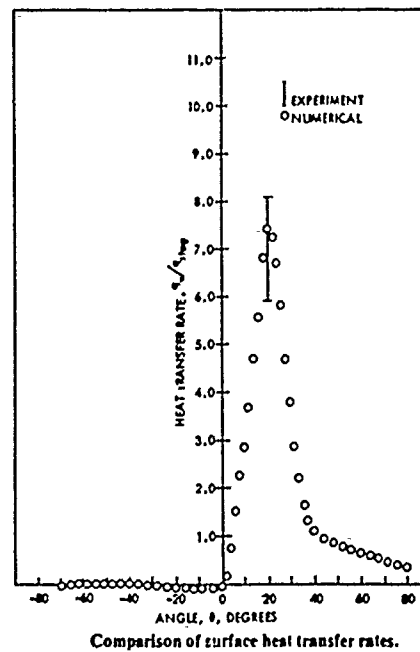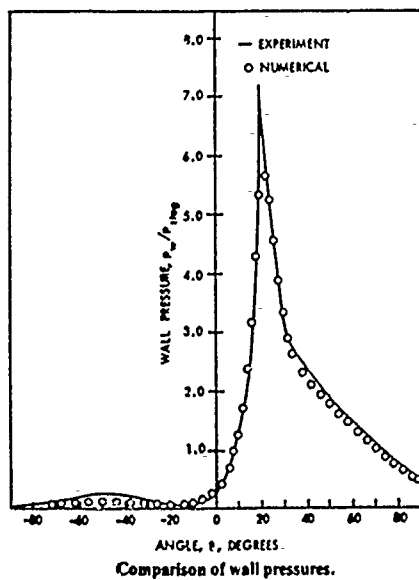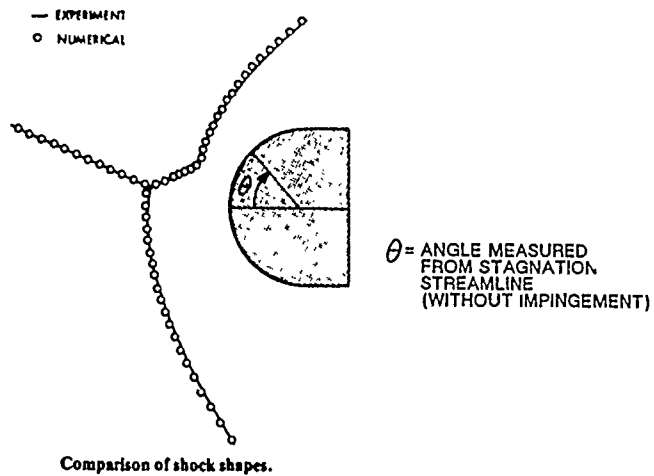
Figure 20 COMPARISON BETWEEN NUMERICAL PREDICTION OF EQUATIONS AND MEASUREMENTS OF KEYES. INVESTIGATION OF TANNEHIL ET AL (Ref. 27, 28)

3. REVIEW OF FLOWFIELD STRUCTURE AND SIMPLE PREDICTION
    TECHNIQUES

As discussed in the introduction, Edney(1) identified six types of shock
wave interference. Each type depends upon the orientations and strengths of the
interacting shock waves, the freestream Mach number, and the ratio of specific heats.
These interactions can induce increases in local heat transfer rates through the following
viscous/inviscid interaction mechanisms: (1) shock/boundary layer interaction, (2) free
shear-layer attachment, and (3) supersonic jet impingement. These flow mechanisms
are capable of producing large localized increases in heat transfer rate which can
exceed the undisturbed value by more than one order of magnitude. To successfully
design an air breathing hypersonic vehicle, it is important to develop prediction
techniques for defining the likely types of interference and the magnitude of the heat
transfer rates developed in the interactions. For each of the six types of interference,
simple methods to predict the interference patterns and calculate the heat transfer
rates have been developed. Here we review these techniques, which in most cases
have been embodied in various simple codes.

3.1 Type I Interference

A Type I interference occurs when both shock waves are weak, and the
flow behind each is supersonic. Such interactions would occur with the attached shock
waves on wedges or cones, or for the case of a blunt body, if the interaction occurred
below the sonic point. Typical Type I interference patterns are shown in Figure 21.
Since the flowfield associated with Type I interference is supersonic throughout, it can
be calculated in some detail.

Type I interference results in the formation of a shear layer which is
bounded by the transmitted bow and impinging shock waves. Across the shear layer
the pressures must be equal and the flow velocities parallel. Interactive procedures
can be utilized to obtain the strength of the transmitted shocks and the orientation of
the shear layer relative to the freestream direction which satisfies these conditions.

From the strengths of the impinging and bow shocks, which are either
input or calculated from the Rankine-Hugoniot relations, it is possible to determine
flow conditions in regions 2 and 3. To start the iterative procedure, a value of the

(a) CYLINDER/PLATE LE

(b) WEDGE

(c) SWEPT CYLINDER
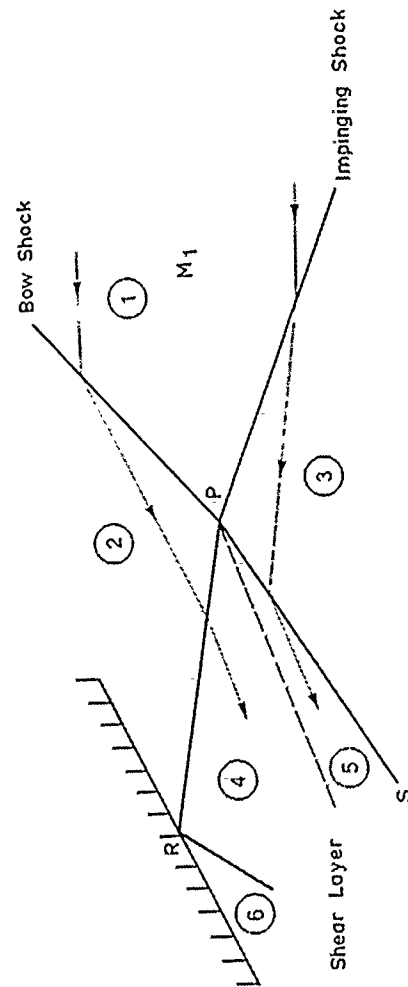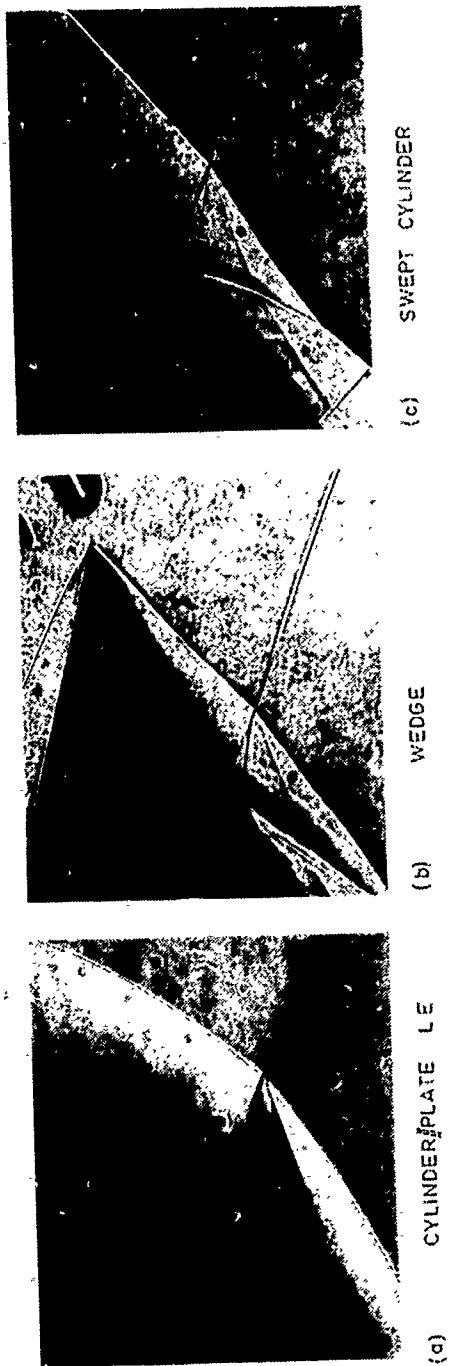
Figure 21   TYPE I INTERFERENCE, M = 4.6, θ = 10°

flow deflection is assumed, and conditions in regions 4 and 5 are computed, using the Rankine-Hugoniot equations. If the pressures are equal, within a specified tolerance, the calculation is terminated. If they are not equal, the shear layer deflection angle is incremented toward the region with the lower pressure, and the procedure is repeated. From the strength of the transmitted impinging shock and the orientation of the body surface at the impingement point, it is possible to calculate conditions in region 6, once again utilizing the Rankine-Hugoniot equations. Two cases of regular and Mach reflection must be considered. Regular reflection occurs for Mach numbers sufficiently high and impingement angles sufficiently low to ensure an attached shock system. The latter case occurs if this condition is not satisfied and the pressure rise is then calculated based upon normal shock relations.

The increase in heat transfer at the point of impingement of the transmitted shock is, of course, the result of viscous-inviscid shock/boundary layer interaction. This interaction is probably the best understood of all the viscous-inviscid interactions possible. Several attempts have been made to develop computational techniques which will predict both the pressure and heat transfer distributions through the interaction region. The best known of the simple methods for laminar flows are based on the work of Lees and Reeves[43], and Holden[44]. Detailed solutions to the Navier Stokes equations for laminar interaction regions has also been shown to provide a powerful and accurate prediction technique when used with sufficient grid resolution (see Appendix A).

Probably the most useful simple approach is to employ empirical correlations for laminar, transitional and turbulent shock/boundary layer interactions. These correlations are based upon the inviscid pressure rise across the interaction region, and are of the form:

$$\frac{CH_{max}}{CH_0} = A \left[\frac{p_{max}}{p_0} \right]^N$$

where CH is the Stanton number based on freestream conditions and p is the pressure. The subscripts MAX and o denote maximum and undisturbed values. A and N are constants which depend upon whether the interaction is laminar, transitional or turbulent. For planar shocks impinging on flat surfaces, Holden's[4] studies suggest $N = 0.5$ for laminar flows and $N = 0.85$ for turbulent flow.

To predict peak heating rates require a knowledge of the undisturbed heating rates ahead of the interaction. The reference temperature method of Van Driest is probably the most accurate for hypersonic flows.

3.2   Type II Interference

As the strength of the impinging or bow shock increases, a condition is eventually reached where Type I interference is no longer possible, and the flow transitions to Type II interference. Typical Type II patterns are shown in Figure 22. The existence of subsonic regions at present precludes a detailed analysis of the interference. However, with the Type I analysis it is possible to predict when Type II interference will occur. Schlieren photographs, from which the length scale is found, together with Type I analysis can be used to estimate the peak heating rates in these flows.

3.3   Type III Interferences

Type I and II interference patterns involve the interaction of two weak oblique shock waves. When one of the shocks is strong, (i.e., followed by subsonic flow) interference patterns designated Types III and IV will occur. The type of interaction generated depends upon the orientation of the flowfield at the impingement point. Typical Type III interference patterns are shown in Figure 23. As in the case of Type I interference, the interaction is characterized by the formation of a shear layer. However, for the Type III interaction, one side of shear layer is bounded by a subsonic region.

The procedure to predict the flowfield are the same for Type I and Type III, except that the bow shock strength is computed. The Rankine-Hugoniot relations are used in going from region 1 to region 2. Results from this exact analysis may then be used in an approximate analytic technique which calculates the shock stand-off distance, shock shape, shear layer length and shear layer impingement point.

The peak heating in regions of Type III interference results from the reattaching shear layer. An analogous problem, that of separation induced by a compression ramp, has received considerable attention. Bushnell and Weinstein(45) have

(a) CYLINDER/PLATE LE

(b) WEDGE

(c) SWEPT CYLINDER

(d) HEMISPHERE

(e) FLAT FACED CYLINDER
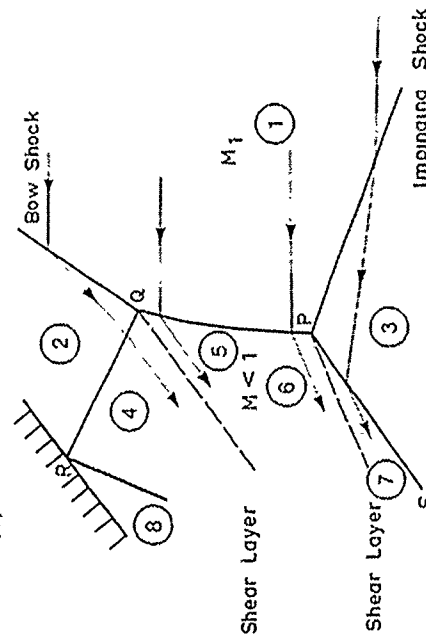
Figure 22   TYPE II INTERFERENCE, M = 4.6, θ = 10°

(a) CYLINDER & PLATE L E

(b) WEDGE

(c) SWEPT CYLINDER

(d) HEMISPHERE

(e) FLAT FACED CYLINDER
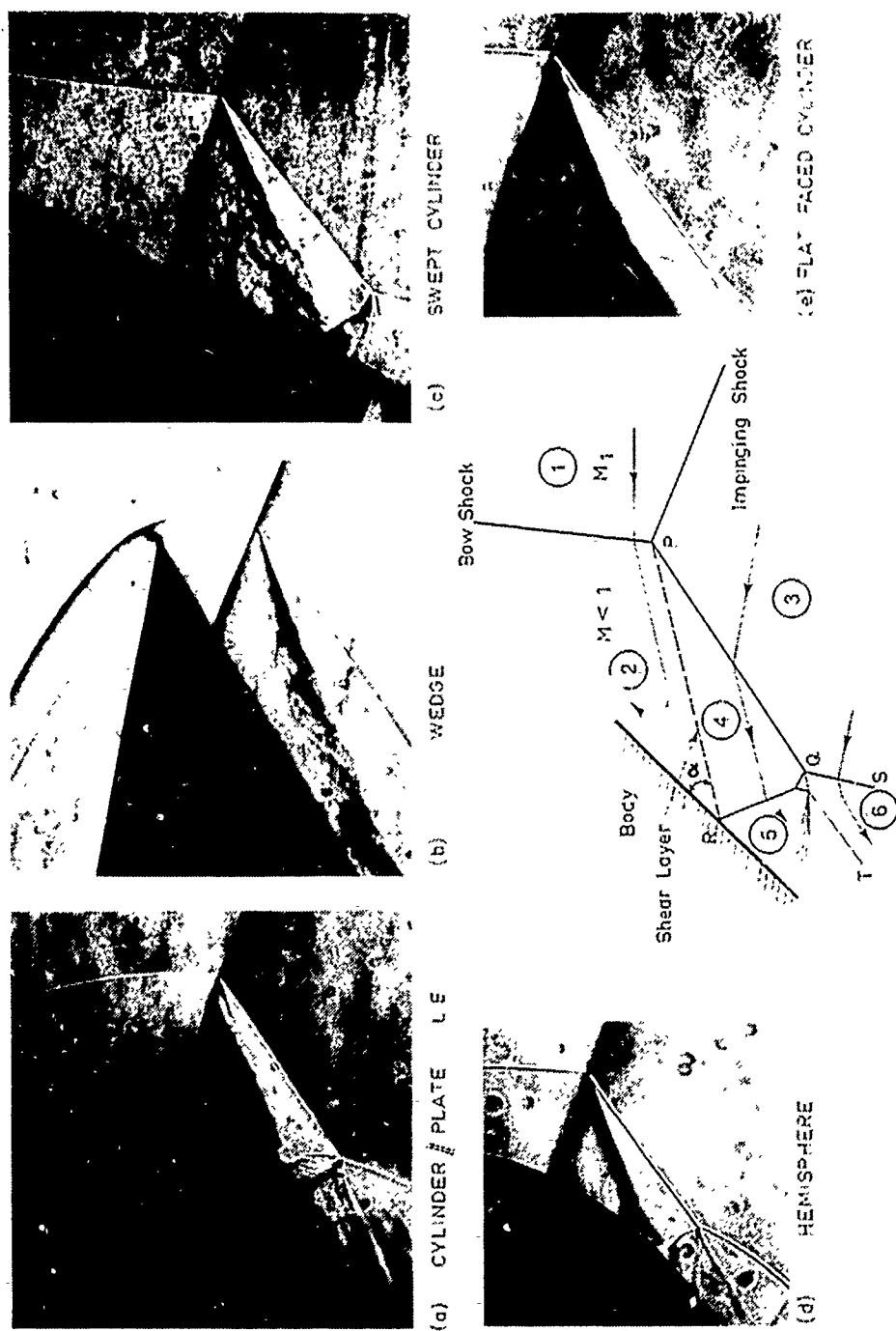
Figure 23 TYPE III INTERFERENCE, M = 4.6, $\theta = 10°$

proposed a correlation for separated boundary layer reattachment which has been adapted to Type III interference. The correlation is of the form

$$\frac{q_{max}}{\rho_{W5} u_S (H_{AW} - H_W)} = A \left[\frac{\rho_{W5} u_5 \delta_{SL}}{\mu_W \sin\alpha} \right]^{-N}$$

where A and N depend on whether the flow is laminar or turbulent; ρ_W and μ_W are the wall density and viscosity, respectively; u_5 is the velocity behind the reattachment shock; δ_{SL} is the shear layer width at reattachment; and α is the reattachment angle.

Suggested values for A and N are (see Reference 45)

Interaction	A	N
Laminar	.19	0.5
Turbulent	.021	0.2

The wall density, ρ_W, depends, through the equation of state, on the wall temperature and the pressure in region 5, which is computed from the known approaching Mach number and angle. For impingement on a two-dimensional body, the two-dimensional Rankine-Hugoniot relations are used to compute the pressure; for three-dimensional bodies, conical flow results are used. The same is true for the calculation of the velocity u_5. The shear layer width δ_{SL} is computed from (45).

Interaction

$$\text{Laminar} \quad \delta_{SL})_{LAM} = 5.0 \left[\frac{\ell_{SL} u_4}{\rho_4 u_4} \right]^{0.5}$$

$$\text{Turbulent} \quad \delta_{SL})_{TURB} = 1.6 \, \ell_{SL} / 13$$

where ℓ_{SL} is the shear layer length, and is obtained from the approximate solution discussed earlier.

This method appears to give reasonably accurate results for large attachment angles, but has the disadvantage of predicting zero heat transfer for grazing incidence of the shear layer (i.e., = 0).

3.4 Type IV Interference

Type IV interference can occur when the impinging shock intersects the bow shock between the sonic line and the body axis. The resultant flow configuration is shown in Figures 24 and 25. The impinging shock causes a displacement of the body shock and the formation of a supersonic jet that is embedded in a subsonic region. A jet shock is produced by the jet as it impinges on the body surface. Intense heating, which can be many times that of the stagnation point region is generated by the impinging jet.

The location of the jet bow shock within the jet will depend on the stand-off distance of the shock configuration. This distance is obtained from experimental data.

The impingement region of the jet with the body surface is shown in Figure 25. The jet width and Mach number are obtained from the particular region, in the jet, where the bow shock is assumed to occur. The bow shock is assumed to be a circular arc that intersects the jet boundary and sonic line at one point. The inclination of the wall is such that the impingement is not too far from normal.

The stagnation point heat transfer is computed from the heat transfer relation for a blunt nosed body given by Kemp[46] is

$$q_{STAG} = 0.76 \left(P_r \right)^{-0.6} \left(\rho_w \mu_w \right)^{0.1} \left(\rho_{STAG} \, \mu_{STAG} \right)^{0.4} \left(\frac{d u_w}{dx} \right)_{STAG}^{1/2} \left(H_0 - H_w \right) \quad \text{(II.20)}$$

where

$$\frac{d u_w}{dx} \Big|_{STAG} = \frac{u_\infty}{R_b} \left\{ \frac{(\gamma - 1)}{\gamma} \left[1 + \frac{2}{(\gamma - 1) M_\infty^2} \right] \left(1 - \frac{1}{\gamma M_\infty^2} \right) \right\}^{0.5}$$

This expression is used to obtain the heat transfer with and without shock interaction. Using these expressions for the jet impingement flow Edney suggests the expression

$$\frac{q_{PR}}{q_{STAG}} = 1.03 \left(\frac{R_b}{\overline{W}} \, \frac{P_{MAX}}{P_{STAG}} \right)^{0.5}$$

Where R_b and $\overline{W}$ are the body radius and jet width respectively and subscripts PR and $STAG$ are values at the peak stagnation point, respectively.
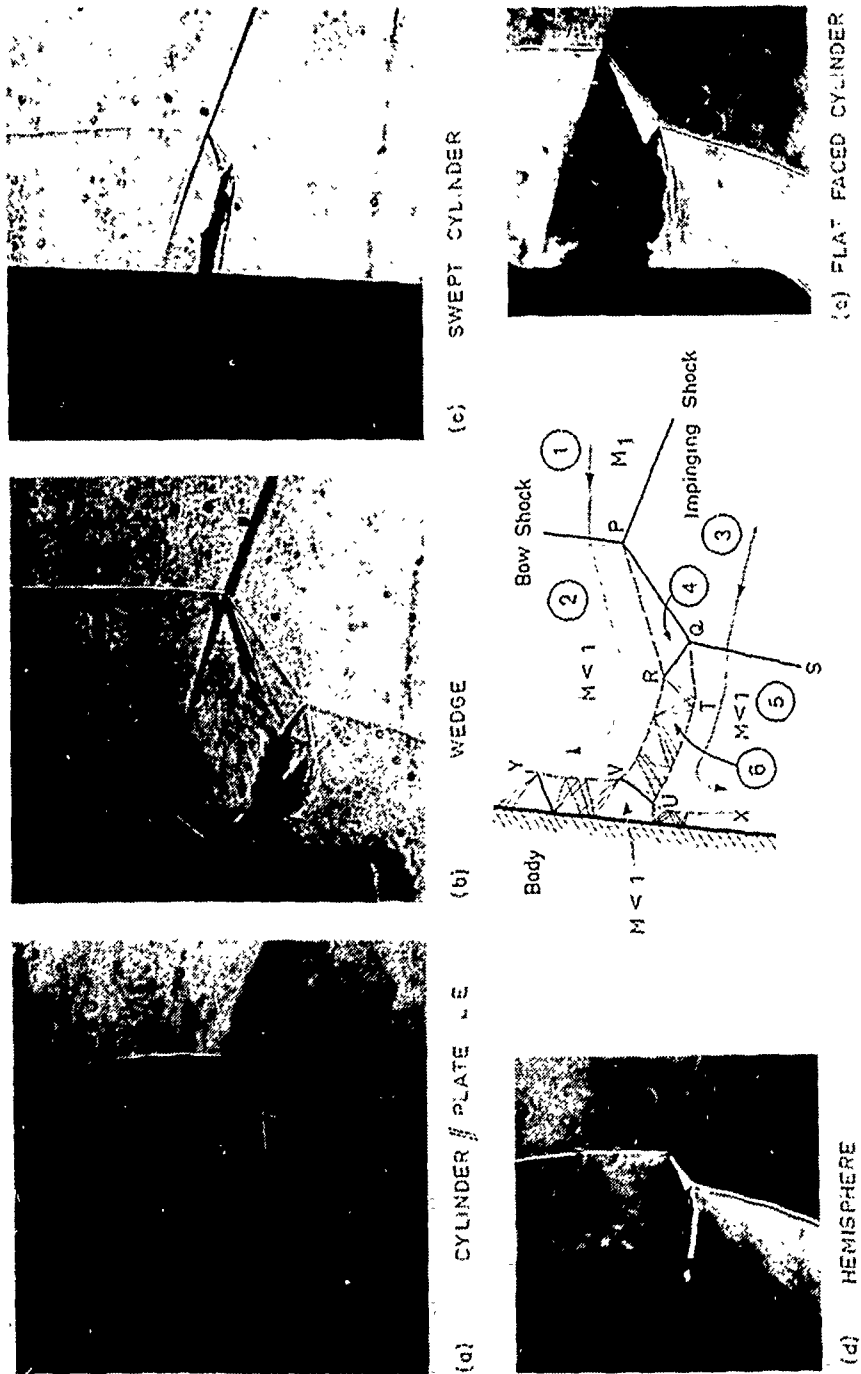
Figure 24 TYPE IV INTERFERENCE, M = 4.6, θ = 10°

(a) CYLINDER / PLATE

(b) WEDGE

(c) SWEPT CYLINDER
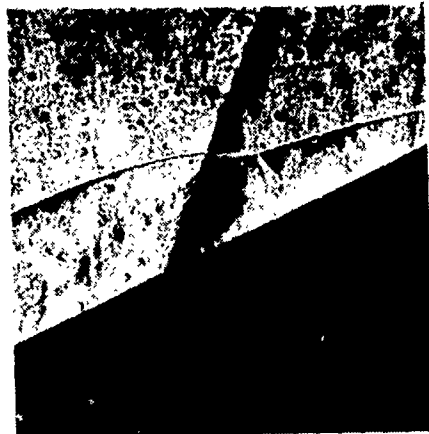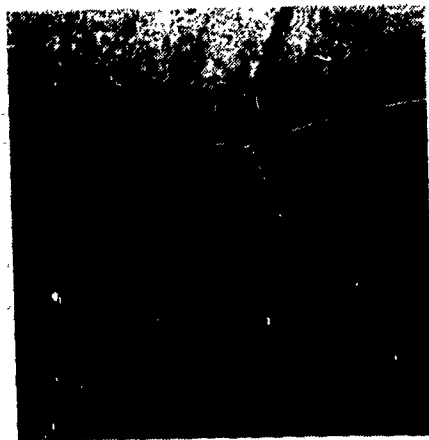
(d) HEMISPHERE
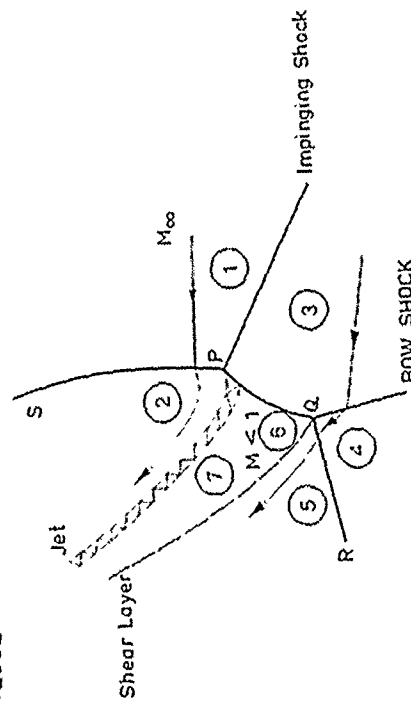
Figure 25   TYPE V INTERFERENCE, M = 4.6, θ = 10°

3.5 Type V Interference

Types V and VI interference result when two weak shock waves of the same family interact. This type of interference would be expected, for example, on the leading edges of fins with moderate to high sweep.

A typical Type V interference pattern, which would occur for moderate fin sweep, is shown in Figure 25. Note that in this case the interaction produces a transmitted shock, a shear layer and a supersonic jet. Impingement of each of these with the body may lead to increased heating. Although quite important from a practical standpoint, Type V interference is difficult to analyze because of the existence of a subsonic region. However, it is possible to predict when Type V interference will occur. From the schlieren photographs and pressure and heat transfer data it is possible to devise correlation suitable for engineering calculations.

3.6 Type VI Interference

Type VI interference, shown in Figure 26, occurs when the impinging shock interacts with the bow shock associated with a highly swept fin. In this case, the flow is supersonic throughout, and consequently, can be calculated in detail.

The prediction computational scheme is similar to that for Type I, differing only in that a Prandtl-Meyer expansion is used to get from region 4 to region 5.

Type VI interference provides a favorable pressure gradient for the boundary layer, and thus does not lead to an increase in local heating. However, study of this type of interference is important, since it provides a means for predicting the onset of Type V interference, which does lead to significant increases in local heat transfer rates. The Type VI program is capable, through the use of an interactive procedures, to predict the occurrence of Type V interference for various values of freestream Mach numer, specific heat ratio and strength of impinging shock. Figure 27 shows varying interference pattern which occur when a cylinder upon which a shock is incident is swept through a series of angles. The heating level generated in the interaction region varies from those associated with the Type IV interference to the Type VI interference.

(a) CYLINDER ⫽ PLATE

(b) WEDGE

(c) SWEPT CYLINDER

Shear Layer

Expansion

S

②

⑤

P

①

M₁

③

④

Impinging Shock

Bow Shock
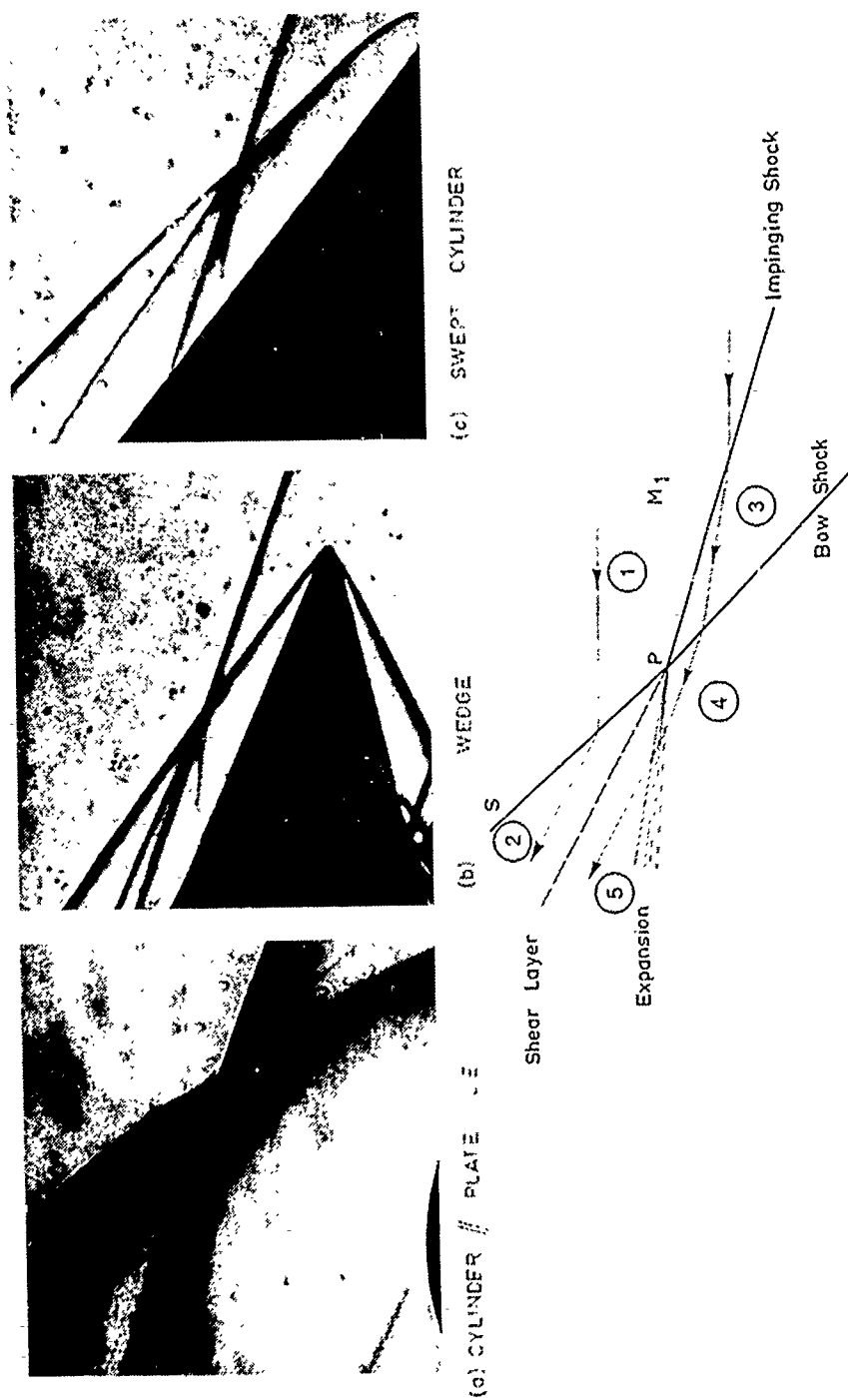
Figure 26   TYPE VI INTERFERENCE, M = 4.6, θ = 10°
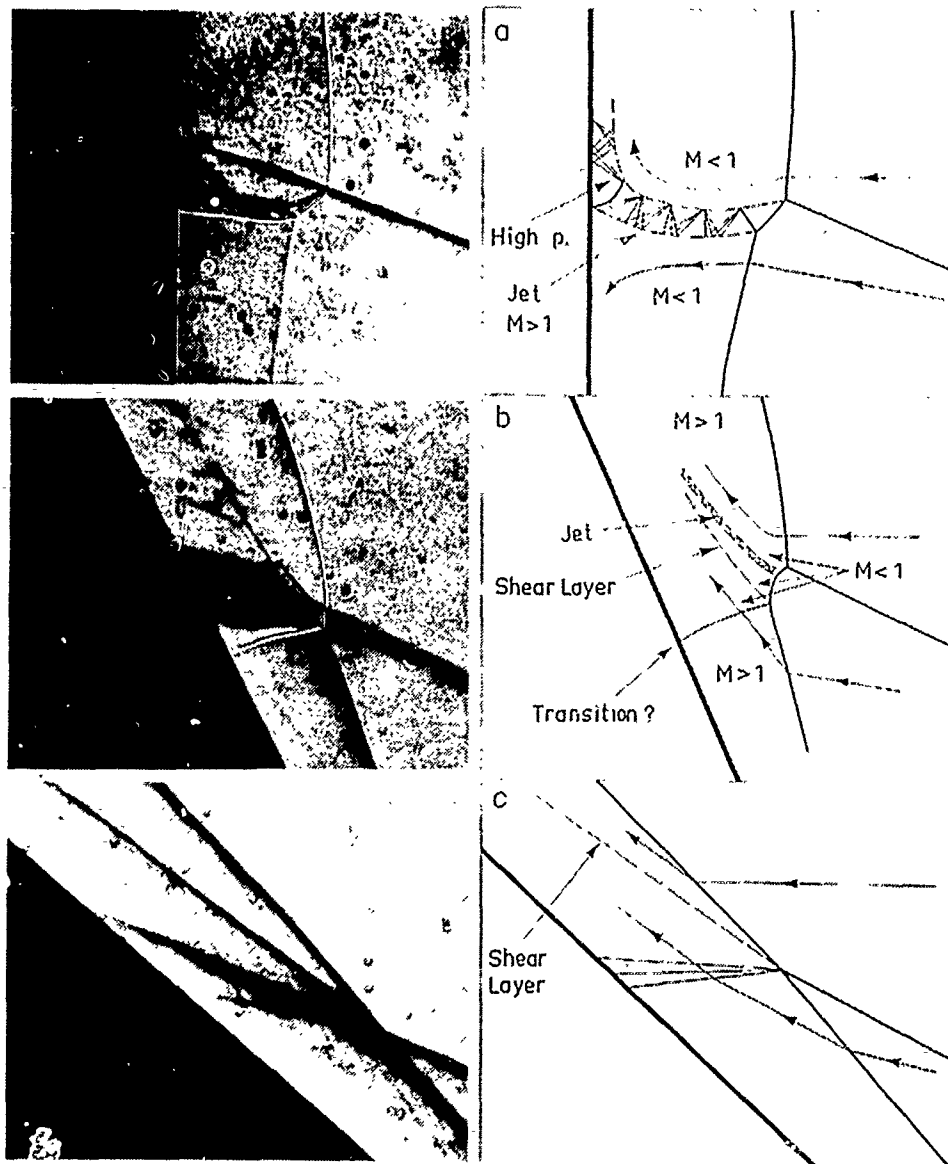
Figure 27 EFFECT OF VARYING SWEEP ANGLE OF CYLINDRICAL FIN
a. Type IV interference.
b. Type IV interference.
c. Type VI interference. $M = 4.6$. $\xi = 5^{0}$.
(from Reference 1)

4.   EXPERIMENTAL PROGRAM

4.1   Program Objective and Design

The objectives of these recent studies was to provide detailed pressure and heat transfer measurements as well as Schlieren photographs to define the structure and properties of regions of shock/shock interaction at Mach numbers from 6 to 19. The emphasis in these studies was placed on the study of Type III and IV interactions, for these provided the largest aerothermal loads. Studies were performed over a range of Reynolds numbers to explore the effects of transition on the heating rates. Measurements were performed for fully laminar conditions to provide a data set which could be compared with theory without transition or turbulence modeling problems.

The first group of studies was designed to explore the aerothermal characteristics of the interaction between a planar shock and the shock layer ahead of a circular cylinder supported perpendicular to the flow. The objectives of this study were to investigate the effects of Mach number on the magnitude and distribution of heating in the interaction region on the cylinder for a numbr of different types of interactions. The Mach number range from 6 to 19 was selected, and the emphasis was placed on an examination of Type III and IV interactions because of the large aerothermal loads associated with these configurations. The other major factor which controls the peak heating levels in regions of shock/shock interaction is the condition of the shear layer (laminar/turbulent) generated by Type III interaction and surrounding the jet for the Type IV interaction. The Reynolds number in the shock layer adjacent to the shear layer is believed to be the most important parameter controlling transition of the shear layer, which is in turn controlled by the Mach number and Reynolds number of the free stream. Measurements were made at Mach 6, 8 and 16 for Reynolds number large enough for turbulent shear layers to be generated. The majority of the studies at Mach numbers from 11 to 19 were conducted for Reynolds numbers where the shear layers were fully laminar.

The second series of studies was conducted to examine the effects of sweeping the interaction region on the peak heating generated in the interaction region. In addition to problems in obtaining two-dimensional flows over the models, questions associated with transition of the boundary layer on the swept cylinder in the absence of the shock/shock interaction is an important issue. The tests that were conducted

in this series were a preliminary set designed principally to aid in the formulation of a subsequent, more extensive, investigation.

The third and final series of studies was designed to investigate the aerothermal loads associated with the impingement of two oblique shocks in the stagnation region of a transverse cylinder. The objective of this set of studies was to determine whether the heating levels generated by the impingement of two oblique shocks incident on bow shock would generate heating loads significantly less than a single shock of the same overall strength. This investigation stemmed from questions associated with the impingement of multiple shocks from the compression ramp of ramjet inlets on the cowl lip. In these experiments, the effects of the relative strengths of the two incident shocks and their positions relative to the bow shock were investigated. In particular, attempts were made to determine whether the heating loads would be substantially reduced by preventing the two ramp shocks from coalescing before they are incident on the bow shock. Measurements were made to determine the relative magnitude of the heating loads developed for a single impinging shock and a pair of focused shocks with the same overall turning angle.

There are a number of key problems that must be solved before a meaningful experimental study of shock/shock interaction at hypersonic speeds can be conducted. First is to obtain a blockage-free flow between the shock generator and the cylinder while at the same time preventing expansion at the trailing edge of the shock generator influencing the shock/shock interaction. Also, to accurately define the characteristics of the interaction regions, consistent with the 0.010-inch gage spacing attainable with our thin-film instrumentation, a 3-inch cylinder is required. These constraints require typical shock generator lengths of 4 feet, with 18 inch model widths to attain two-dimensional flow over the center of the models. Large experimental facilities are required for such experimental studies. We designed models with shock generator angles between 10 and 15 degrees based on Edney's prediction technique, to give the maximum interference heating enhancement. In the multiple shock interaction investigation, two shock generator angles were selected so that the total turning angle was always between 10 and 15 degrees.

4.2   Experimental Facilities, Models, Instrumentation and Data Reduction

4.2.1   Experimental Facilities

The experimental studies were conducted in the Calspan 48-inch and 96-inch Shock Tunnels at Mach numbers of 6.5, 8, 11.7, 15.6, and 18.9. The facilities and their performance are described in Reference 50. The free stream conditions at which the current experimental program was conducted are plotted on the Mach number versus unit Reynolds number map shown in Figure 28(a). At Mach numbers of 6 and 8 the Reynolds numbers were sufficiently large that the interactions were turbulent. At Mach 11, 15 and 18 the flows were completely laminar with the exception of one condition at Mach 15 where we believe the Type III and IV interactions were turbulent.

The operation of the shock tunnel in the reflected shock mode is shown with the aid of the diagram shown in Figure 28(b). The tunnel is started by rupturing a double diaphragm that permits high-pressure helium in the driver section to expand into the driven section. This generates a normal shock which propagates through the low pressure air. A region of high-temperature, high-pressure air is produced between this normal shock front and the gas interface (often referred to as the contact surface) between the driver and driven gas. When the primary or incident shock strikes the end of the driven section, it is reflected, leaving a region of almost stationary, high-pressure, heated air. This air is then expanded through a nozzle to the desired free stream conditions in the test section.

The duration of the flow in the test section is controlled by the interactions between the reflected shock, the interface, and the leading expansion wave generated by the nonstationary expansion process occurring in the driver section. We normally control the initial conditions of the gases in the driver and driven sections so that the gas interface becomes transparent to the reflected shock interaction. This is known as operating under "tailored-interface" conditions. Under these conditions, the test time is controlled by the time taken for the driver/driven interface to reach the throat, or the leading expansion wave to deplete the reservoir of pressure behind the reflected shock. The flow duration is either driver-gas-limited or expansion-limited, respectively. Figure 28(c) shows the flow duration in the test section as a function of the Mach number of the incident shock. Here, it can be seen that for operation at low M_is, running times of over 25 milliseconds can be obtained with a long driver section. When

(a) PERFORMANCE MAP

(b) WAVE DIAGRAM FOR TAILORED-INTERFACE SHOCK TUBE

(c) TEST TIME AVAILABLE FOR TAILORED INTERFACE
OPERATION OF THE SHOCK TUNNEL
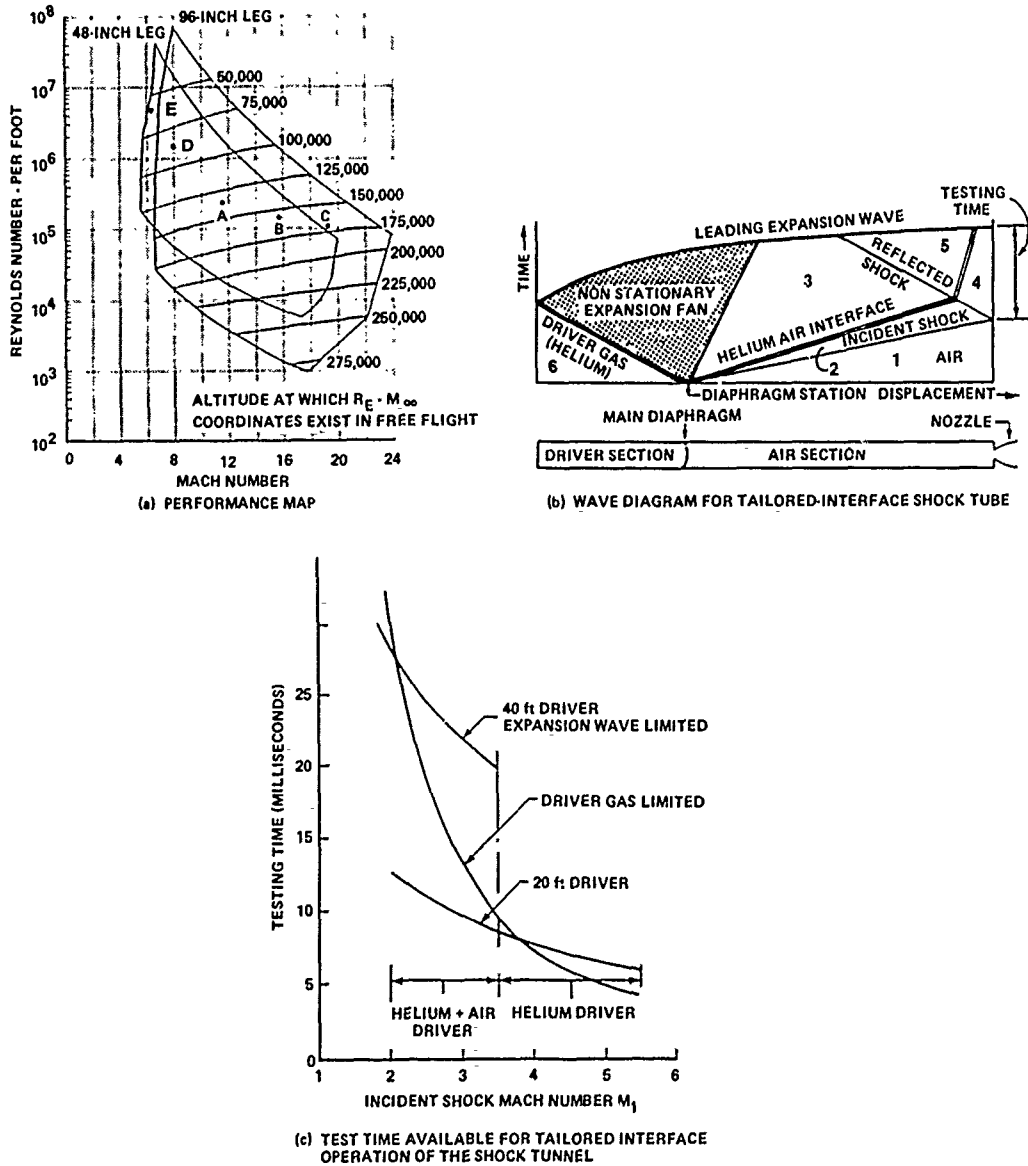
Figure 28   PERFORMANCE CHARACTERISTICS OF CALSPAN'S SHOCK TUNNEL

performed under these latter conditions at high pressures and high Reynolds numbers, the test running times are of the same magnitude or longer than for piston-driven tunnels (48, 4) with comparable stagnation temperatures, and the reservoir conditions and flow quality are superior to those of piston-driven tunnels. This results from the fact that the test gas is processed by a simple reflected shock rather than by the multiple shocks of piston-driven tunnels. A further consequence is that the free stream conditions can be calculated far more accurately in a shock tunnel. Note that when sensitive high-frequency instrumentation is used in the very severe heating conditions encountered in interaction regions in hypersonic flow, running times longer than 20 milliseconds can result in damage to, or destruction of, the sensing element.

4.2.2 Models

Three basic models used in these experimental studies, each associated respectively with the single shock/bow shock interaction studies, the investigation of sweep on the shock/shock interaction, and finally the studies of multiple shock/bow interaction.

The model used in the studies of the planar single shock/bow shock interactions is shown in Figure 29. The highly instrumented 3-inch diameter cylinder is supported by two side arms, so it can be translated both parallel and perpendicular to the back of the shock generator and rotated. The length of the shock generator and its position relative to the circular cylinder is adjustable. In general, the position of shock impingement is controlled by adjusting the position of both the cylinder and the shock generator. The cylinder was heavily instrumented with heat transfer and pressure instrumentation as shown in Figure 30. As shown, the instrumentation is concentrated in a high density region on the cylinder to provide the resolution needed to define the peak heating and the large heat transfer gradients which are generated in Type III and IV interaction regions. In almost all of the experiments the cylinder was rotated so that this high density segment was positioned in the interaction region. A listing of the gage positions on the cylinder is given in Table 2.

A schematic diagram for the model used in this study is shown in Figure 31. For this study new shock generators and ramps were constructed to provide a range of shock strengths and relative positions for the two incident shocks. The angles of the shock generator plate and the ramp were varied to change the strengths of the
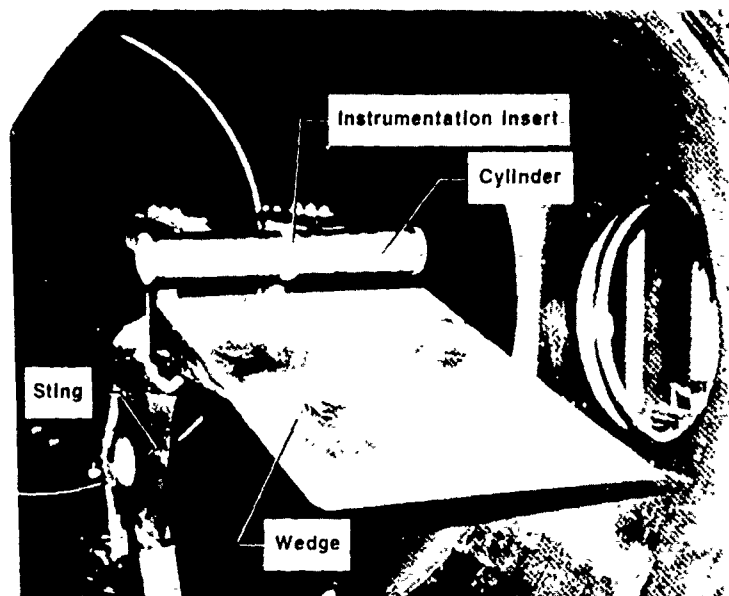
Figure 29   SHOCK INTERFERENCE MODEL MOUNTED IN CALSPAN'S 48-INCH
HYPERSONIC SHOCK TUNNEL
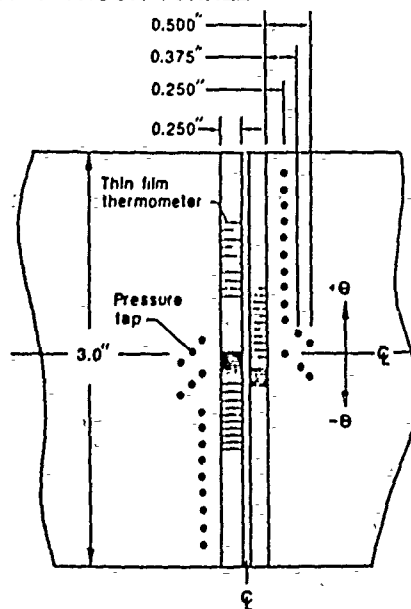
Figure 30   INSTRUMENTATION SCHEMATIC OF CALSPAN'S 48-INCH HYPERSONIC
SHOCK TUNNEL

TABLE 2
GEOMETRIC CONFIGURATION OF CYLINDER

SHOCK INTERACTION CYLINDER GAUGE POSITIONS

GAUGE	DEGREES FROM P 30	INCHES FROM P 30
P 30	0.000	0.0000
P 28	14.324	0.3750
P 26	28.648	0.7500
P 25	35.810	0.9375
P 24	42.972	1.1250
P 23	50.134	1.3125
P 22	57.296	1.5000
P 21	64.458	1.6875
P 20	69.232	1.8125
P 15	71.620	1.8750
P 19	74.007	1.9375
P 14	76.394	2.0000
P 18	78.782	2.0625
P 13	81.169	2.1250
P 17	83.556	2.1875
P 12	85.944	2.2500
P 16	88.331	2.3125
P 11	90.718	2.3750
P 10	95.493	2.5000
P 9	102.655	2.6875
P 7	116.979	3.0625
P 5	131.303	3.4375
P 3	145.627	3.8125
P 1	159.951	4.1875
HT 42	22.208	0.5814
HT 41	25.428	0.6657
HT 40	28.648	0.7500
HT 39	31.868	0.8343
HT 38	35.088	0.9186
HT 37	38.308	1.0029
HT 36	41.524	1.0871
HT 35	44.744	1.1714
HT 32	48.128	1.2600
HT 34	48.128	1.2600
HT 31	51.184	1.3400
HT 33	51.184	1.3400
HT 30	54.240	1.4200
HT 72	55.386	1.4500
HT 73	56.341	1.4750
HT 29	57.296	1.5000

GAUGE	DEGREES FROM P 30	INCHES FROM P 30
HT 74	57.296	1.5000
HT 75	58.251	1.5250
HT 76	59.206	1.5500
HT 77	60.161	1.5750
HT 28	60.352	1.5800
HT 78	61.115	1.6000
HT 79	62.070	1.6250
HT 80	63.025	1.6500
HT 27	63.407	1.6600
HT 81	63.980	1.6750
HT 26	66.463	1.7400
HT 25	69.519	1.8200
HT 11	70.833	1.8544
HT 12	71.627	1.8752
HT 13	72.422	1.8960
HT 24	72.575	1.9000
HT 14	73.216	1.9168
HT 15	74.011	1.9376
HT 16	74.805	1.9584
HT 17	75.600	1.9792
HT 23	75.630	1.9800
HT 18	76.394	2.0000
HT 63	76.394	2.0000
HT 19	77.189	2.0208
HT 64	77.349	2.0250
HT 20	77.983	2.0416
HT 65	78.304	2.0500
HT 21	78.778	2.0624
HT 66	79.259	2.0750
HT 22	79.572	2.0832
HT 101	79.572	2.0832
HT 67	80.214	2.1000
HT 102	80.367	2.1040
HT 103	81.161	2.1248
HT 68	81.169	2.1250
HT 104	81.956	2.1456
HT 69	82.121	2.1500
HT 105	82.750	2.1664
HT 70	83.079	2.1750
HT 10	83.537	2.1870

GAUGE	DEGREES FROM P 30	INCHES FROM P 30
HT 106	83.556	2.1875
HT 71	84.034	2.2000
HT 9	84.339	2.2080
HT 107	84.351	2.2083
HT 8	85.142	2.2290
HT 108	85.145	2.2291
HT 109	85.940	2.2499
HT 7	85.944	2.2500
HT 6	86.734	2.2707
HT 110	86.734	2.2707
HT 111	87.529	2.2915
HT 5	87.533	2.2916
HT 112	88.323	2.3123
HT 4	88.331	2.3125
HT 113	89.118	2.3331
HT 3	89.129	2.3334
HT 114	89.916	2.3540
HT 43	89.916	2.3540
HT 2	89.928	2.3543
HT 62	90.730	2.3753
HT 1	90.730	2.3753
HT 44	93.102	2.4374
HT 61	93.786	2.4553
HT 45	96.287	2.5208
HT 60	96.841	2.5353
HT 46	99.469	2.6041
HT 59	99.897	2.6153
HT 47	102.655	2.6875
HT 58	102.953	2.6953
HT 48	105.841	2.7709
HT 57	106.009	2.7753
HT 49	109.026	2.8543
HT 56	109.064	2.8553
HT 55	112.120	2.9353
HT 50	112.208	2.9376
HT 54	115.176	3.0153
HT 51	115.394	3.0210
HT 53	118.232	3.0953
HT 52	118.579	3.1044

two incident shocks. The positions of the intersection of the incident shocks with the bow shock ahead of the cylinder were controlled by translating the ramp and the shock generator plate relative to the support system and each other as well as adjusting the elevation and streamwise location of the cylinder. Again the cylinder was rotated to place high density instrumentation segments in the interaction region.

4.2.3 Heat Transfer Instrumentation

The large heat transfer gradients that are generated in the interaction regions on the cylinder can be significantly distorted by lateral heat conduction unless the heat transfer instrumentation is mounted on an insulating surface. Because our platinum thin-film gages are mounted on a pyrex substrate, they are well suited for this application. However, with heating rates up to 1000 Btu/ft^2/sec, the rise in surface temperature during the shock tunnel's short run times can also lead to problems with data analysis and interpretation. As shown in Figure 30, the platinum films were deposited on cylindrical glass inserts forming a continuous circumferential surface. Two sets of circumferential inserts were employed with overlapping gage positions to check the accuracy of the measurements. These gages have a microsecond response time and can easily follow the instabilities which can occur in shock/shock interaction regions.

4.2.4 Pressure Instrumentation

We used both flush-mounted and orifice pressure gages in these studies to obtain measurements of the mean and fluctuating pressure levels through the interaction regions. Calspan piezoelectric pressure gages were connected to a series of short, closely spaced orifices to obtain the mean pressure distribution around the model. Larger high-frequency PCB quartz transducers were flush-mounted beneath a thin insulating skin to the surface of the model in key areas of the flow.

4.2.5 Flow Visualization

We used a single-pass schlieren system with a focal length of 10 feet for flow visualization in this study. The knife edge was set parallel to the conical segment which precedes the concave section of the model, and adjusted to give a 15% cut-off. A single microsecond spark is triggered close to the end of the steady runtime. The tunnel windows have a 16 inch diameter.
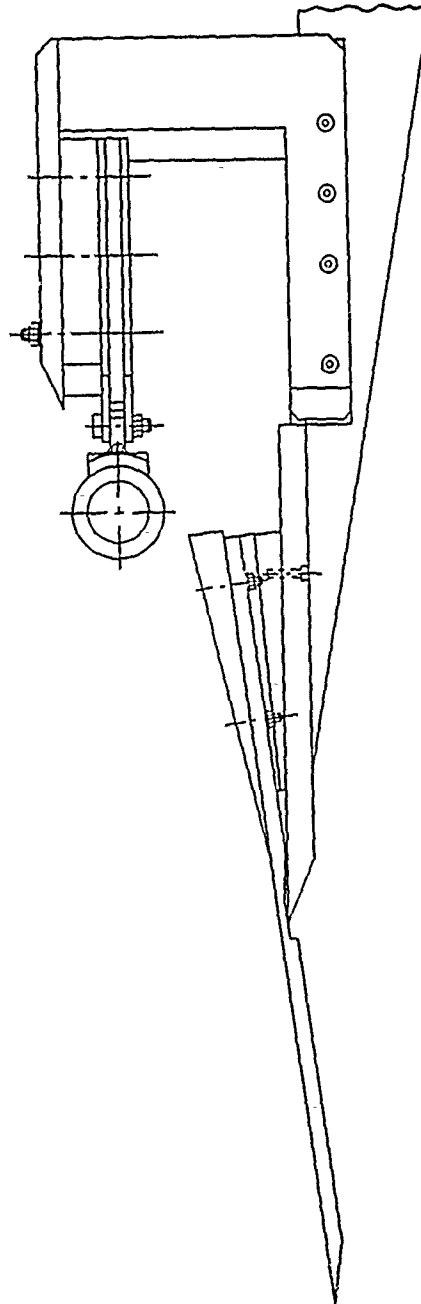
Figure 31   SCHEMATIC OF MULTIPLE SHOCK INTERACTION MODEL

5. TEST PROCEDURES

5.1 Introduction

Two aspects of this experimental program make the reduction of the measurements relatively unique. First, for some test configurations, the heat transfer rates were so large that gage temperature increases of over 500°F were not uncommon for the 15 millisecond run times, generated in the 48-inch Shock Tunnel fitted with a 40-foot-long driver. Second, in a significant number of cases with Type IV interactions, unsteady oscillations were observed in the jet impingement region. Large flow instabilities were observed for typical frequencies of 2 to 5 kHz. In some cases, we also experienced spurious flow transients resulting from the interaction between the bow shock and wedge support system which were mounted close to each other. These problems, coupled with the large number of measurements recorded on the two separate data systems with significantly different characteristics, stimulated the development of a new, faster and more complete data reduction capability. This new reduction and presentation system provides on-line reduction, plotting and analysis capabilities for measurements in unsteady flows with very large heat transfer rates.

Analyzing HST voltage time histories acquired by the PDP-11/73 (also known as the DDAS II) or NAVCOR facilities is an integral part of Calspan's data reduction process. Until recently, the software did not provide a convenient means for merging time histories from the two independent data collection systems. Program CUBRED[1] was designed to permit the integration of raw voltage files for subsequent analysis of temporal and frequency-related phenomena. Additionally, the program was extended to include some new features and offline processes. The Rae-Taulbee algorithm, which accounts for variable thermal properties, is now an alternative to the Cook-Felderman numerical technique for computing heat transfer profiles. The detailed development of the Rae-Taulbee algorithm is in Appendix A. CUBRC's COMPAQ 386 computer, an IBM PC-AT clone, was chosen for the new software design because of its simplicity, computational speed and portability.

The architectures of the data collection devices differed greatly. The sample spacing, number of samples, and test duration in DDAS II acquired files may

---

1. Developed under internal research.

vary. NAVCOR files, on the other hand, have 300 samples spaced 50 microseconds apart over 14.95 milliseconds. A separate program (NCTODD) is used to accomplish the merger of NAVCOR and PDP files. NAVCOR raw voltage time histories on merged files are altered to conform to the DDAS II run specifications. Potentially, a total of 177 channels (128 from DDAS II, 49 from NAVCOR) may be examined and archived efficiently.

5.2 Evaluation of Stagnation and Freestream Test Conditions

The stagnation and freestream test conditions were based on measurements of the incident shock wave speed, U_i, the initial temperature of the test gas (in the driven tube), T_1, the initial pressure of the test gas, p_1, and the pressure behind the reflected shock wave, p_0. The incident shock wave Mach number, $M_i = U_i/a_1$, was calculated where the speed of sound, a_1, was a function of p_1 and T_1. The freestream Mach number, M_∞, was determined from correlations of M_∞ with M_i and p_0. These correlations were based on previous airflow calibrations of the D nozzle.

Freestream test conditions of pressure, temperature, Reynolds number, etc., were computed, assuming isentropic expansion of the test gas from the conditions behind the reflected shock wave to the freestream Mach number. Real gas effects were taken into account for this expansion under the justified assumption that the gas was in the thermochemical equilibrium. In the freestream, the static temperature, T_∞, was sufficiently low that the ideal gas equation of state, $p_\infty = \rho R T$ was applicable where R was the gas constant for the test gas.

The stagnation enthalpy, H_0, and temperature T_0, of the gas behind the reflected shock wave were calculated from:

$$H_0 = \frac{H_5}{H_1} T_1 \text{ and } T_0 = \frac{T_5}{T_1} T_1$$

where (H_5/H_1) and (T_5/T_1) are functions of U_i (or M_1) and p_1 and are given in Reference 4 for air. H_1 was obtained from Reference 5 for air, knowing p_1 and T_1.

The freestream static temperature was found from the energy equation, knowing H_0 and M_∞,

$$T_\infty = \frac{H_0}{c_p} \left(\frac{1}{1 + \frac{(\gamma-1)}{2} M_\infty^2} \right)$$

where C_p = 6006 ft-lb/slug R° and γ = 1.40.

The freestream static pressure was calculated from

$$p_{\infty} = \frac{p}{p_{\flat}} p_0 \left(1 + \frac{(\gamma - 1)}{2} M_{\infty}^2 \right)^{\frac{\gamma_{\infty}}{(\gamma_{\infty}-1)}}$$

where

$$\frac{p}{p_{Ideal}} = \frac{(p_{\infty}/p_0)_{Real}}{(p_{\infty}/p_0)_{Ideal}}$$

is the real gas correction to the ideal gas static-to-total pressure ratio as described in Reference 6. The sources for the real gas data used in this technique were References 7 and 8.

The freestream velocity was determined from

$$U_{\infty} = M_{\infty} a_{\infty} \qquad \text{where}$$
$$a_{\infty} = \sqrt{(\gamma_{\infty} R T_{\infty})} \quad , \text{ the speed of sound.}$$

The freestream dynamic pressure was found from

$$q_{\infty} = \frac{1}{2} \gamma_{\infty} p_{\infty} M_{\infty}^2$$

and the freestream density than was calculated from the ideal gas equation of state

$$\rho_{\infty} = p_{\infty} / R T_{\infty}$$

where R = 1717.91 ft-lb/slug R° for air. Values of the absolute viscosity, μ, used to compute the freestream Reynolds number per foot were obtained from Reference 5.

The test section pitot pressure, p_0', was determined from q_{∞} and the ratio (p_0'/q_{∞}). This ratio has been correlated as a function of M_{∞} and H_0 for normal shock waves in air in thermodynamic equilibrium.

5.3 Reduction of Measurements of Pressures and Heat Transfer

5.3.1 Measurement Time Selection

Measurements were made during the current studies for a number of different test conditions and tunnel configurations. While in all cases the basic flowfield had stabilized within several milliseconds, we observed flow instabilities which we believe were an intrinsic feature of these flows for some model configurations. For example, a Type IV interaction (where the jet tries to impinge normal to the cylinder surface) we observe a movement in the peak heating and presure which suggests that the jet oscillates, deflecting above and below the normal impingement point. Under such conditions the data was read just preceeding the schlieren photograph of the flow, to avoid electrical interference from the spark source. In cases where there was some degree of flow unsteadiness, the selection of the time and duration over which the data was averaged was based on an exhaustive analysis of all the measurements and flow visualization made in this program, together with experience gained in many earlier experimental studies. The summary of test times are tabulated in Table 3.

5.3.2 Pressure Measurements

The measured voltages from the pressure transducers were reduced to engineering units (psi) by applying the amplifier gains and the transducer calibration factors. The pressures were then converted to absolute pressures (psia) by adding the measured initial vacuum pressure in the test section. The latter was the reference pressure for the transducers. The pressures were then averaged over the time interval of steady flow to obtain an average value for each case. The values of the pressure coefficients, C_p, were calculated from

$$C_p = (p - p_\infty)/q_\infty$$

where p was the measured model pressure (psia).

The pressure ratio was also calculated by dividing the pitot pressure, p_o', into the model pressure.

RUN	Mach†	Re†	STGN GAGE	T†** (ms)	Ts** (ms)	V* (in)	H* (in)	S/G ANGLE (deg)	S/G LENGTH (in)	RAMP ANGLE (deg)	RAMP LENGTH (in)	B* (in)	MODEL SWEEP (deg)	TEST TYPE
9	6.35	4.5E+06	P18	7	2	N/A	N/A	N/A	N/A	N/A	N/A	N/A	0.00	SINGLE SHOCK
10	6.35	4.4E+06	P18	7	2	3.20	0.09	10.0	26.5	N/A	N/A	N/A	0.00	SINGLE SHOCK
11	6.35	4.4E+06	P18	7	2	3.50	0.05	10.0	26.5	N/A	N/A	N/A	0.00	SINGLE SHOCK
12	6.35	4.3E+06	P21	7	2	3.34	0.06	10.0	26.5	N/A	N/A	N/A	0.00	SINGLE SHOCK
13	6.35	4.4E+06	P18	7	6	3.34	0.09	10.0	26.5	N/A	N/A	N/A	0.00	SINGLE SHOCK
14	6.36	4.7E+06	P18	7	6	3.55	0.09	10.0	26.5	N/A	N/A	N/A	0.00	SINGLE SHOCK
15	6.33	2.4E+06	P23	6	6	3.55	0.06	10.0	26.5	N/A	N/A	N/A	0.00	SINGLE SHOCK
16	8.02	1.4E+06	P23	6	4.5	2.95	0.06	10.0	26.5	N/A	N/A	N/A	0.00	SINGLE SHOCK
17	8.06	1.5E+06	P23	6	3.5	2.95	0.50	10.0	26.5	N/A	N/A	N/A	0.00	SINGLE SHOCK
18	8.03	1.5E+06	P21	6	3.5	2.86	0.50	10.0	26.5	N/A	N/A	N/A	0.00	SINGLE SHOCK
19	8.03	1.5E+06	P21	6	3.5	2.78	0.59	10.0	26.5	N/A	N/A	N/A	0.00	SINGLE SHOCK
20	7.94	7.6E+05	P21	6	3.5	2.78	0.59	12.5	26.5	N/A	N/A	N/A	0.00	SINGLE SHOCK
21	8.03	1.6E+06	P21	6	3.5	2.89	0.59	12.5	26.5	N/A	N/A	N/A	0.00	SINGLE SHOCK
24	7.95	7.7E+05	P21	6	N/A	2.89	0.59	12.5	26.5	N/A	N/A	N/A	0.00	SINGLE SHOCK
26	8.14	3.8E+06	HT39	6	1.5	3.36	0.63	15.0	26.5	N/A	N/A	N/A	0.00	SINGLE SHOCK
27	8.03	1.5E+06	P21	6	3.5	2.95	0.31	15.0	26.5	N/A	N/A	N/A	0.00	SINGLE SHOCK
28	7.93	7.2E+05	P21	6	3.5	2.95	0.31	15.0	26.5	N/A	N/A	N/A	0.00	SINGLE SHOCK
29	8.03	1.5E+06	P23	6	3.5	3.19	0.31	15.0	26.5	N/A	N/A	N/A	0.00	SINGLE SHOCK
30	8.15	1.8E+06	P11	6	3.5	2.31	0.75	15.0	26.5	N/A	N/A	N/A	0.00	SINGLE SHOCK
31	8.03	1.5E+06	P18	6	3.5	N/A	N/A	N/A	26.5	N/A	N/A	N/A	0.00	SINGLE SHOCK
32	6.38	5.0E+06	P18	7	2	2.00	0.44	10.0	26.5	N/A	N/A	N/A	0.00	SINGLE SHOCK
33	11.00	4.4E+06	P21	4	2	2.25	0.44	10.0	26.5	N/A	N/A	N/A	0.00	SINGLE SHOCK
34	11.01	4.3E+06	P21	4	2	2.72	1.81	10.0	26.5	N/A	N/A	N/A	0.00	SINGLE SHOCK
35	11.01	4.5E+06	P21	4	2	2.41	1.50	10.0	26.5	N/A	N/A	N/A	0.00	SINGLE SHOCK
36	11.00	4.2E+06	P21	4	4	2.41	2.10	10.0	26.5	N/A	N/A	N/A	0.00	SINGLE SHOCK
37	11.00	4.3E+06	P18	4	4	N/A	N/A	N/A	N/A	N/A	N/A	N/A	0.00	SINGLE SHOCK
38	12.97	4.7E+06	P18	3	N/A	N/A	N/A	N/A	N/A	N/A	N/A	N/A	0.00	SINGLE SHOCK
39	16.50	1.2E+06	P21	3	N/A	2.94	0.16	10.0	48.0	N/A	N/A	N/A	0.00	SINGLE SHOCK
40	19.14	3.7E+05	P23	3	N/A	3.63	0.09	10.0	48.0	N/A	N/A	N/A	0.00	SINGLE SHOCK
41	16.31	1.0E+06	P25	3	N/A	3.94	-0.25	10.0	48.0	N/A	N/A	N/A	0.00	SINGLE SHOCK
42	16.33	1.0E+06	P21	10	5	2.83	-2.76	12.5	26.5	N/A	N/A	N/A	0.00	SINGLE SHOCK
43	16.27	9.4E+05	.21	10	3	3.19	1.81	12.5	26.5	N/A	N/A	N/A	0.00	SINGLE SHOCK
44	8.04	1.4E+06	P18	10	3	3.08	0.35	12.5	26.5	N/A	N/A	N/A	0.00	SINGLE SHOCK
59	8.05	1.5E+06	P23	10	5	3.08	0.35	12.5	26.5	N/A	N/A	N/A	0.00	SINGLE SHOCK
60	8.05	7.3E+05	P24	10	3	3.08	0.35	12.5	26.5	N/A	N/A	N/A	0.00	SINGLE SHOCK
61	7.97	7.1E+05	P24	10	3	3.19	1.81	12.5	26.5	N/A	N/A	N/A	0.00	SINGLE SHOCK
62	7.75	3.7E+05	P21	10	3	3.19	1.81	12.5	26.5	N/A	N/A	N/A	0.00	SINGLE SHOCK
63	7.94	1.8E+06	P24	10	3	3.43	1.43	12.5	26.5	N/A	N/A	N/A	0.00	SINGLE SHOCK
64	8.06	7.0E+05	P21	10	3	3.63	1.43	12.5	26.5	N/A	N/A	N/A	0.00	SINGLE SHOCK
66	7.94	1.8E+06	P21	10	3	3.19	1.81	12.5	26.5	N/A	N/A	N/A	15.00	SWEPT SHOCK
67	8.03	1.5E+06	P24	10	3	3.43	1.43	12.5	26.5	N/A	N/A	N/A	15.00	SWEPT SHOCK
68	8.05	1.5E+06	P21	10	3	3.63	1.43	12.5	26.5	N/A	N/A	N/A	15.00	SWEPT SHOCK
69	8.04	1.5E+06	P24	10	3	3.63	1.43	12.5	26.5	N/A	N/A	N/A	15.00	SWEPT SHOCK
70	8.05	1.4E+06	P24	10	3	3.63	-0.33	12.5	26.5	N/A	N/A	N/A	15.00	SWEPT SHOCK
71	8.06	1.9E+06	P24	10	3	3.31	-0.33	12.5	26.5	N/A	N/A	N/A	15.00	SWEPT SHOCK
72	7.97	7.1E+05	P24	10	3	3.31	-0.33	12.5	26.5	N/A	N/A	N/A	15.00	SWEPT SHOCK
73	7.97	1.4E+06	P24	10	3	3.31	-0.33	12.5	26.5	N/A	N/A	N/A	15.00	SWEPT SHOCK
74	8.05	1.4E+06	P24	10	3	N/A	N/A	N/A	N/A	N/A	N/A	N/A	15.00	SWEPT SHOCK
75	8.03	1.5E+06	P21	10	3	3.44	1.34	12.5	26.0	N/A	N/A	N/A	30.00	SWEPT SHOCK
76	8.03	1.5E+06	P21	10	3	3.09	1.34	12.5	26.0	N/A	N/A	N/A	30.00	SWEPT SHOCK
77	8.04	1.5E+06	P21	10	3	3.44	-0.25	12.5	26.0	N/A	N/A	N/A	30.00	SWEPT SHOCK
78	8.03	1.5E+06	P21	10	3	3.24	1.34	12.5	26.0	N/A	N/A	N/A	30.00	SWEPT SHOCK

TABLE 3
SUMMARY OF TEST CONDITIONS

RUN	Mach†	Re†	STGN GAGE	T*** (ms)	TS** (ms)	V* (in)	H* (in)	S/G ANGLE (deg)	S/G LENGTH (in)	RAMP ANGLE (deg)	RAMP LENGTH (in)	B* (in)	MODEL SWEEP (deg)	TEST TYPE
79	8.05	1.8E+06	P21	10	3	3.44	1.34	12.5	26.0	N/A	N/A	N/A	30.00	SWEPT SHOCK
80	7.99	7.1E+05	P21	10	3	3.44	1.34	12.5	26.0	N/A	N/A	N/A	30.00	SWEPT SHOCK
81	8.04	1.5E+06	P21	10	3	N/A	N/A	N/A	35.0	N/A	N/A	N/A	30.00	SWEPT SHOCK
82	8.04	1.5E+06	P21	10	3	3.90	1.58	7.5	35.0	N/A	N/A	N/A	0.00	MULTI SHOCK
83	8.04	1.4E+06	P21	10	3	3.97	1.32	7.5	36.0	5.0	14.00	0.05	0.00	MULTI SHOCK
84	8.04	1.4E+06	P21	10	3	3.97	1.32	7.5	36.0	5.0	14.00	1.05	0.00	MULTI SHOCK
85	8.04	1.4E+06	P21	10	3	3.97	1.32	7.5	36.0	5.0	14.00	1.05	4.00	MULTI SHOCK
86	8.04	1.4E+06	P21	10	3	3.97	1.32	7.5	36.0	5.0	12.03	-1.00	0.00	MULTI SHOCK
87	8.04	1.5E+06	P21	10	3	3.97	1.32	7.5	36.0	5.0	14.00	-1.00	0.05	MULTI SHOCK
88	8.05	1.7E+06	P21	10	3	3.97	1.32	7.5	36.0	5.0	14.00	1.05	0.50	MULTI SHOCK
89	8.04	1.5E+06	P21	10	3	4.12	1.32	7.5	36.0	N/A	N/A	N/A	0.00	MULTI SHOCK
90	8.04	1.5E+06	P21	10	3	4.00	1.32	7.5	36.0	6.0	11.00	-1.44	0.00	MULTI SHOCK
91	8.04	1.5E+06	P21	10	3	4.00	1.32	7.5	36.0	6.0	11.00	-1.44	0.00	MULTI SHOCK
92	8.04	1.5E+06	P21	10	3	4.00	1.32	7.5	36.0	6.0	13.25	-2.69	0.00	MULTI SHOCK
93	8.04	1.5E+06	P21	10	3	4.00	1.32	7.5	36.0	6.0	13.25	-3.44	0.00	MULTI SHOCK
94	8.04	1.5E+06	P24	10	3	4.25	1.32	7.5	36.0	6.0	11.00	-0.25	0.00	MULTI SHOCK
95	8.03	1.5E+06	P21	10	3.5	3.41	1.22	12.5	36.0	6.0	13.25	-0.25	0.00	MULTI SHOCK
98	8.03	1.5E+06	P21	10	3	2.79	0.22	12.5	26.0	N/A	N/A	N/A	30.00	SWEPT SHOCK
99	8.30	2.3E+06	P21	10	5	2.79	0.22	12.5	26.5	N/A	N/A	N/A	0.00	SINGLE SHOCK
100	8.29	2.2E+06	P21	10	5	2.89	0.22	10.0	26.5	N/A	N/A	N/A	0.00	SINGLE SHOCK
101	8.31	2.5E+06	P22	5	1.2	3.35	1.86	12.5	26.5	N/A	N/A	N/A	0.00	SINGLE SHOCK
102	11.70	2.0E+05	P22	5	1.2	4.15	-1.40	10.0	46.3	N/A	N/A	N/A	0.00	SINGLE SHOCK
103	11.63	2.0E+05	P22	4.5	1.2	4.52	-0.62	10.0	46.3	N/A	N/A	N/A	0.00	SINGLE SHOCK
104	11.55	1.7E+05	P24	4.5	1.2	3.69	-1.40	10.0	44.0	N/A	N/A	N/A	0.00	SINGLE SHOCK
106	15.62	1.6E+05	P22	4.5	1.2	3.39	-1.40	10.0	46.3	N/A	N/A	N/A	0.00	SINGLE SHOCK
107	15.61	1.6E+05	P22	3.2	2.4	3.30	-1.40	10.0	46.3	N/A	N/A	N/A	0.00	SINGLE SHOCK
108	15.58	1.5E+05	P22	3.2	2.4	3.42	-1.60	10.0	46.3	N/A	N/A	N/A	0.00	SINGLE SHOCK
109	18.86	1.9E+05	P22	3.2	2.4	3.85	-1.54	10.0	46.3	N/A	N/A	N/A	0.00	SINGLE SHOCK
110	18.80	1.8E+05	P24	3.2	2.4	3.75	-0.34	10.0	46.3	N/A	N/A	N/A	0.00	SINGLE SHOCK
112	18.84	1.9E+05	P24	3.2	2.4	3.94	-1.40	10.0	46.3	N/A	N/A	N/A	0.00	SINGLE SHOCK
113	11.63	2.0E+05	P21	5	1.2	3.99	1.40	10.0	44.0	N/A	N/A	N/A	0.00	SINGLE SHOCK
114	15.67	1.6E+05	P22	4.5	1.2	3.93	1.10	12.5	44.0	N/A	N/A	N/A	0.00	SINGLE SHOCK
115	15.68	1.7E+05	P21	4.5	1.2	3.93	2.10	12.5	44.0	N/A	N/A	N/A	0.00	SINGLE SHOCK
116	18.92	2.1E+05	P21	2	2.4	3.99	1.10	12.5	44.0	N/A	N/A	N/A	0.00	SINGLE SHOCK

* REFER TO MODEL DIAGRAM
** MEASURED FROM START OF STEADY STATE
*** TOTAL TEST TIME

CYLINDER

FLOW DIRECTION

RAMP S.G.PLATE

H - DISTANCE FROM BASE OF MODEL TO BASE OF PLATE (NON TO GAP)
M - HORIZONTAL DISTANCE BETWEEN CYLINDER
V - VERTICAL DISTANCE BETWEEN CYLINDER ABS AND TOP OF PLATE
A - MODEL GAUGE LOCATED AT HORIZONTAL PLANE (GENERATOR FORE)
C - SHOCK GENERATOR PLATE ANGLE
U - RAMP ANGLE
W - RAMP LENGTH
P - SHOCK GENERATOR PLATE LENGTH
SWEEP ANGLE IS THE ANGLE OF S.G PLATE AND CYLINDER RELATIVE TO THE PERPENDICULAR TO FLOW DIRECTION

TABLE 3 (Cont'd)
SUMMARY OF TEST CONDITIONS

5.3.3   Heat Transfer Measurements

The thin-film heat transfer gage is a resistance thermometer which reacts to the local surface temperature of the model. The first step of the data reduction was to convert the measured voltage time history for each gage to a temperature time history, taking into account the gage resistance, the current through the gage, the gage calibration factor, and the amplifier gain. The theory of heat conduction was used to relate the surface temperature to the rate of heat transfer. Because the platinum resistance element has negligible heat capacity and, hence, negligible effect on the Pyrex substrate surface temperature, the substrate can be characterized as being homogeneous and isotropic. Furthermore, because of the short duration of the shock tunnel test, the substrate can be treated as a semi-infinite body. The one-dimensional heat conduction equation is

$$\rho c(t) \, \frac{\partial T}{\partial y} = \frac{\partial}{\partial y} \left(k(T) \, \frac{\partial T}{\partial y} \right)$$

where ρ, C, and k are the substrate density, specific heat, and thermal conductivity, respectively; y is the distance normal to the substrate surface; and T(t) is the transient surface temperature rise (T(0)=0). Final data reduction was done using the Raw-Taulbee method to solve the heat conduction equation numerically as described in Appendix wever for a quick look at the data the Cooke Felderon method was used

$$q\,(t_m) = 2 \sqrt{\left(\rho \, \frac{Ck}{\tau} \right)} \sum_{i=1}^{m} \frac{T(t_i) - T(t_{i-1})}{(t_m - t_i)^{1/2} + (t_m - t_{i-1})^{1/2}}$$

where m is the number of time interval steps from t = 0 to t_m. In as much as the heat transfer gage outputs were sampled at constant time intervals of 50 or 100 usec and were digitized by the DDAS, this equation provided a straightforward method for calculating the heat transfer rates. The heat transfer rates, $\dot{q}\,(t)$, were averaged over the steady-flow portion of each test run to obtain a value of $\dot{q}$ for each gage. Initially, the heat-transfer rates were calculated with time t = 0 taken just before the arrival of the airflow. It was found that because the heat transfer gages responded to the nozzle cooling flow, which was initiated before the airflow, the heat transfer rates had to be recalculated with the time t = 0 taken prior to onset of the cooling flow.

The equation above is valid for constant values of $(\eta C k)$, whereas and k are functions of the substrate temperature. A correction for the variation of $(\eta C k)$ with temperature was applied using the method of Reference 54.

The Stanton number, CH, based on the freestream conditions, was calculated from the following

$$CH = J \frac{\dot{q}}{\rho_\infty U_\infty (H_o - H_w)}$$

where $J = 778.26$ ft-lb/BTU, and H_w is the enthalpy at the measured wall temperature.

5.3.4 Measurement Recording System

All data were recorded on a 128-channel Calspan Digital Data Acquisition System II (DDAS II). This system consists of 128 Marel Co. Model 117-22 amplifiers, an Analogic ANDS 5400 data acquisition and distribution system and a Digital Equipment Corp. LSI 11/73 computer. The Analogic system functions as a transient event recorder in that it acquires, digitizes and stores the data in real time. Immediately after each test run the data is transferred to the DEC computer for processing.

The Marel amplifiers provide gains up to 1000 for low level signals, can be AC or DC coupled to the transducers, and have selectable low-pass filters with cut-off frequencies of 300, 1000 or 3000 Hz. The Analogic system contains a sample-and-hold amplifier, a 12-bit analog-to-digital converter and 4096 sample memory for each channel.

After the data are transferred to the DEC computer, plots of the analog voltage time histories are generated to determine the overall quality of the data and to select the steady-flow time interval. The data are then reduced to engineereing units (psi or °F) and, in the case of pressures, averaged over the selected steady-flow time interval. The calculation of heat transfer rate from the temperature time history requires an additional data reduction step that is described in Section 5.3.3.

The raw data (voltage) time histories are transferred to magentic tape for archival storage while temporary storage of raw and reduced data is on one of the three disk drives of the DEC computer. Tabulations and time history plots of raw and/or reduced data are generated using the computer's printer.

6. RESULTS AND DISCUSSION

6.1 Introduction

The studies discussed here provide detailed experimental measurements and insight into the key mechanisms associated with the aerothermal loads induced by shock/shock interaction in high Mach number (6 to 19) hypersonic flows, where little such detailed information exists. In each study, our investigation centered on flow configurations that generate the largest heating loads and were of greatest interest in terms of developing simple flow models and detailed code validation. In the first study, we investigated the effects of Mach number on aerothermal loads generated by Types III, IV and VI interaction regions for Mach numbers between 6 and 19 a small part of this latter study was devoted to examining sweep effects. In the second study, which was conducted at Mach 8, we examined the flow structure and aerothermal loads in the shock/shock interaction regions induced by multiple incident shock/bow shock interaction to determine if heating loads induced by two separate shocks incident on a bow shock in the stagnation region induce heating loads greater than if the shocks had coalesced before incidence.

6.2 Mach Number Effects on Single Shock/Bow Shock Interaction

Edney's earlier studies suggest that Mach numbers between 10 and 19 and flow deflection between 11 and 14 degrees produce the maximum heating enhancement. Based on this, we selected a 12.5 degree shock generator angle for our studies. Measurements of the distribution of heat transfer and pressure in the interaction regions were made at Mach 8, 11.2, 15.6 and 18.8. At each Mach number, a series of runs were made at various incidence shock positions to obtain a series of flows between Types III and IV interactions. Test conditions, heat transfer and pressure measurements, plots of these quantities and Schlieren photographs for each test condition are provided in Appendix B. The cylinder was rotated to place the high-density region of the instrumentation in the region of maximum heat transfer. Measurements of the distributions of pressure and heat transfer to the cylinder in the absence of the incident shock were made at Mach 8 and 16 and are shown compared with theory in Figures 32 and 33. The measurements are in good agreement with the Fay and Riddel[49] stagnation value and the Rose, Kemp and Detra[46] distribution. The variation of the distribution of pressure and heat transfer with the shock impingement point at Mach 8 are shown for
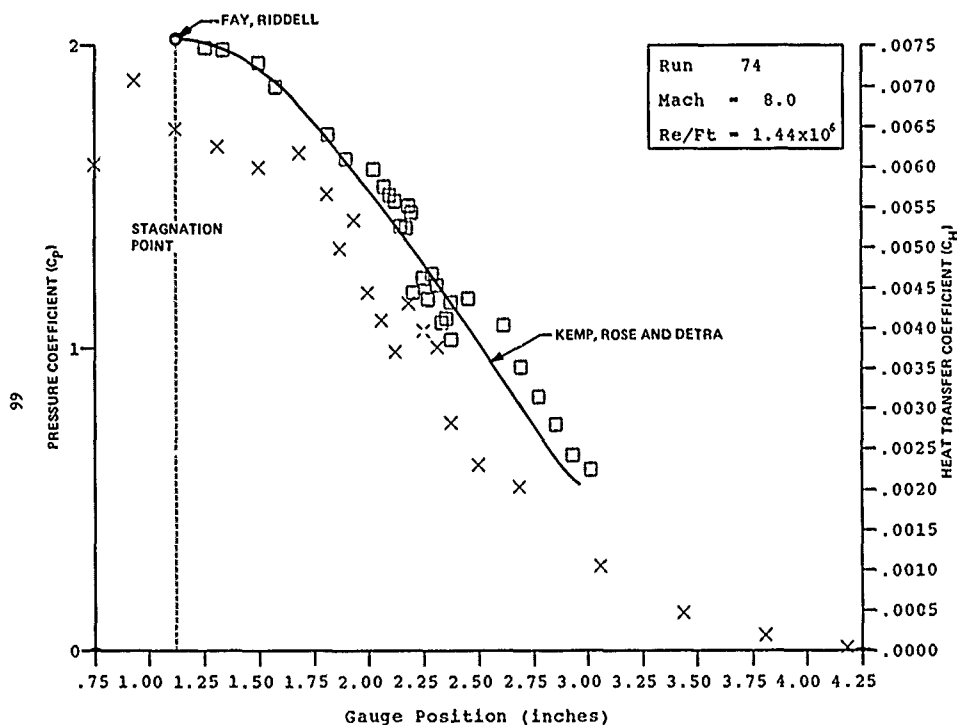
Figure 32 COMPARISONS BETWEEN MEASURED AND PREDICTED HEAT
TRANSFER AROUND A CIRCULAR CYLINDER AT MACH 8
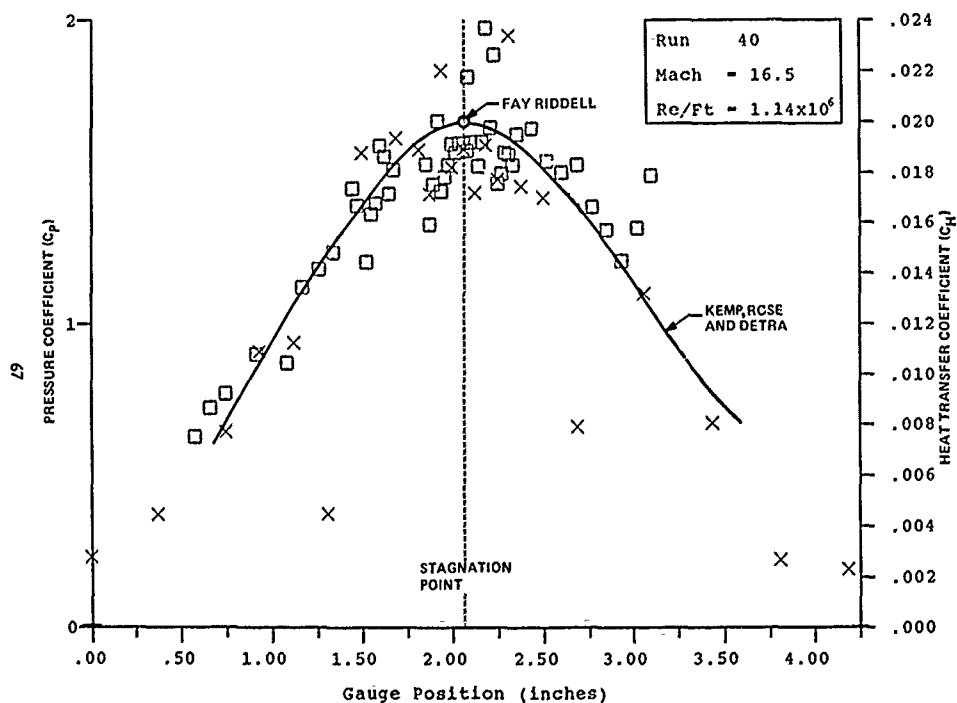
Figure 33 COMPARISON BETWEEN MEASURED AND PREDICTED HEAT TRANSFER
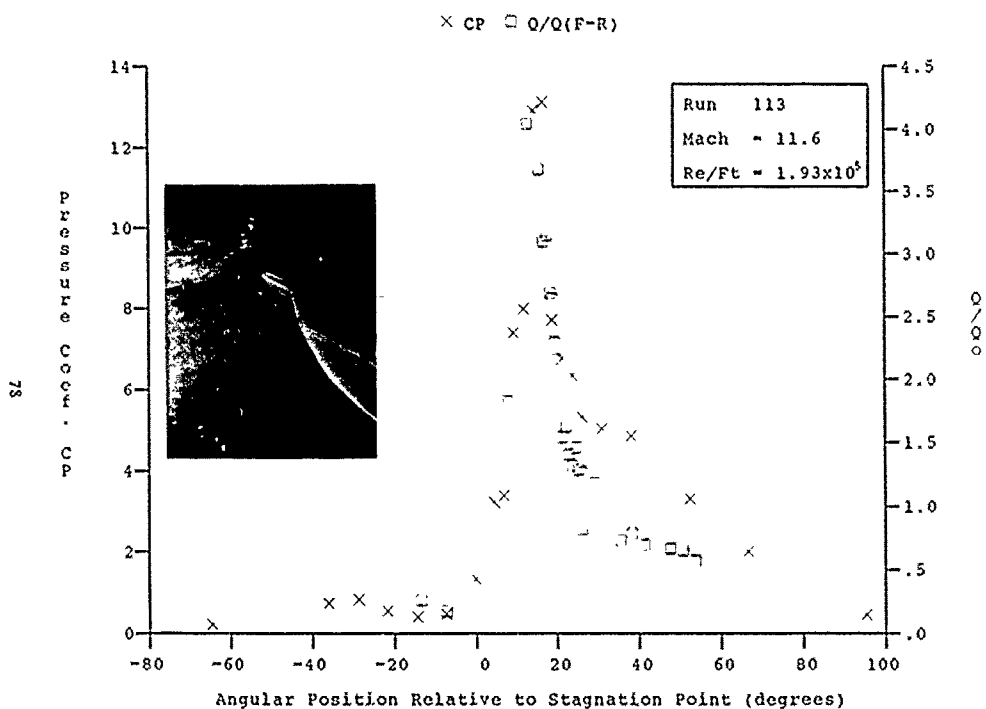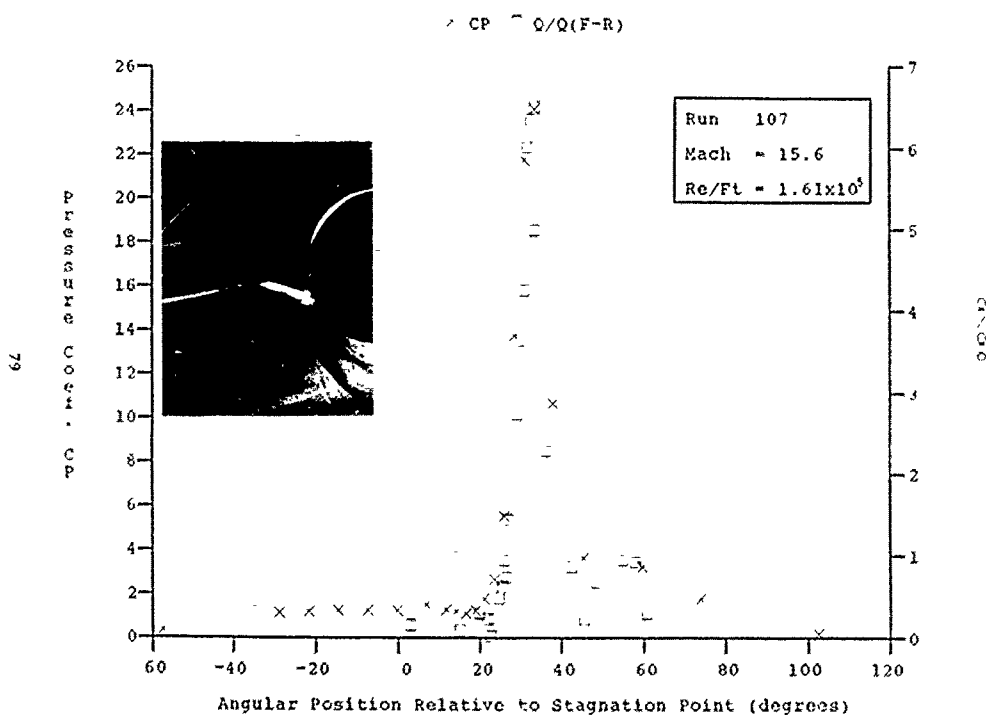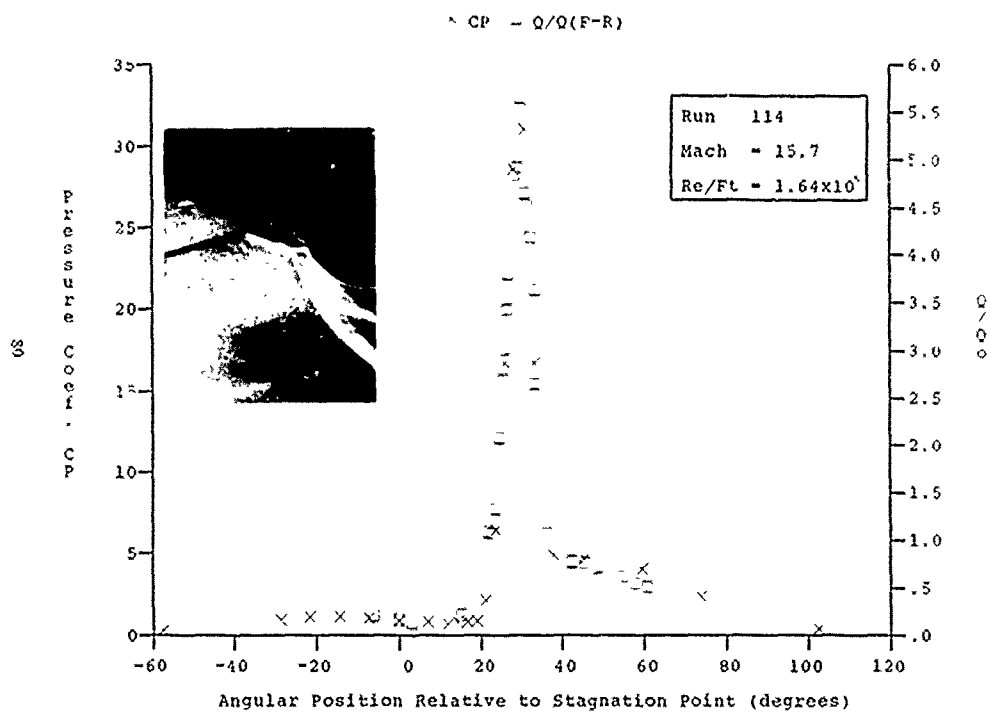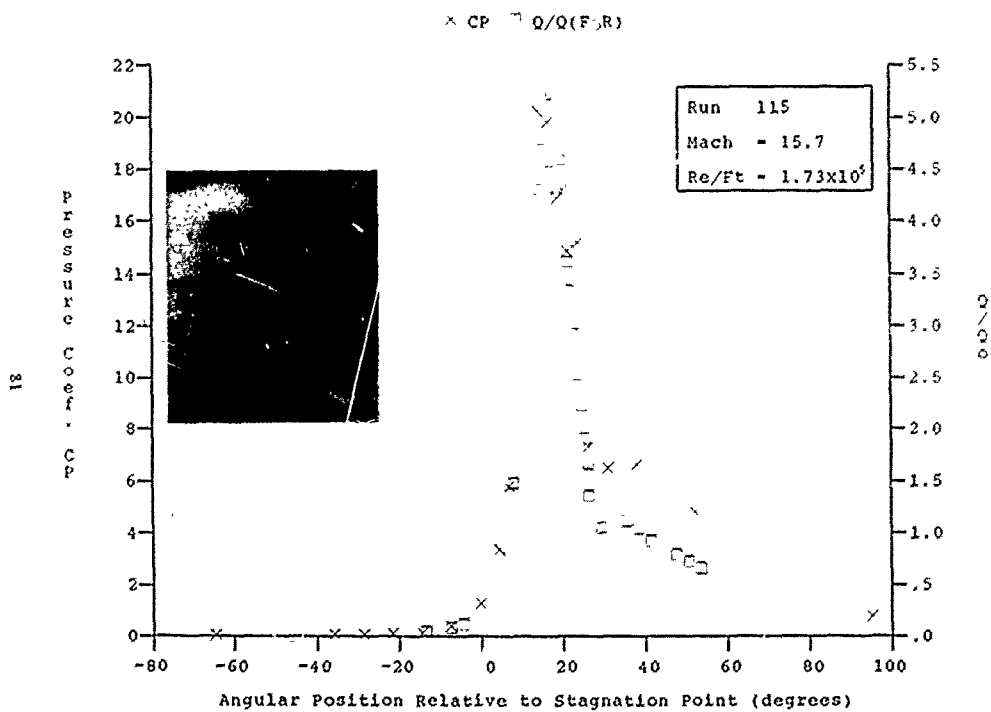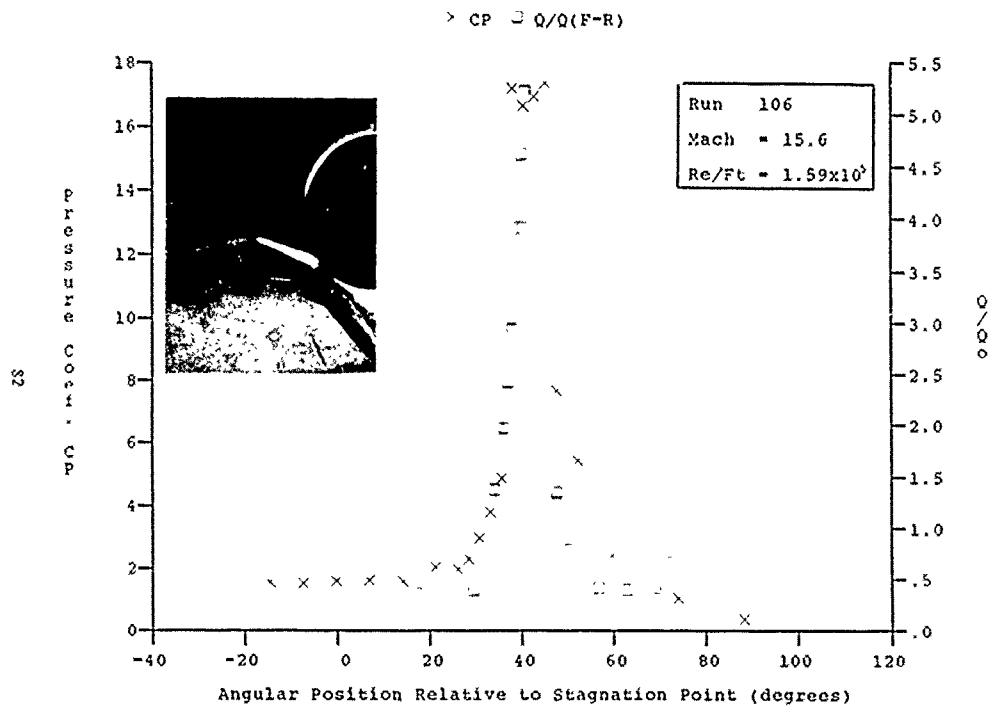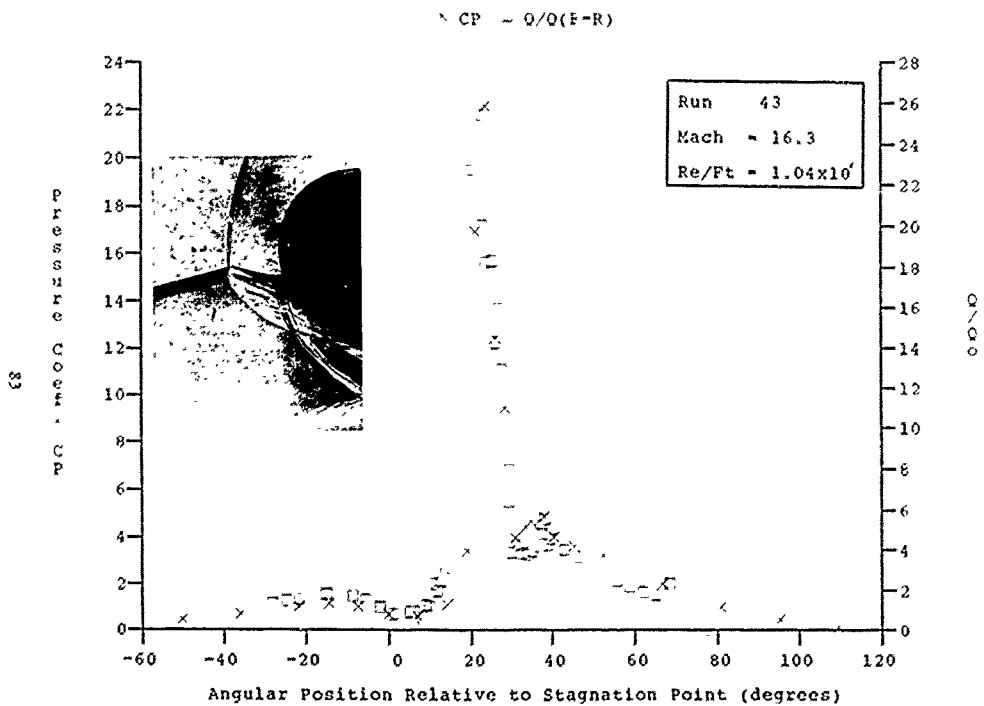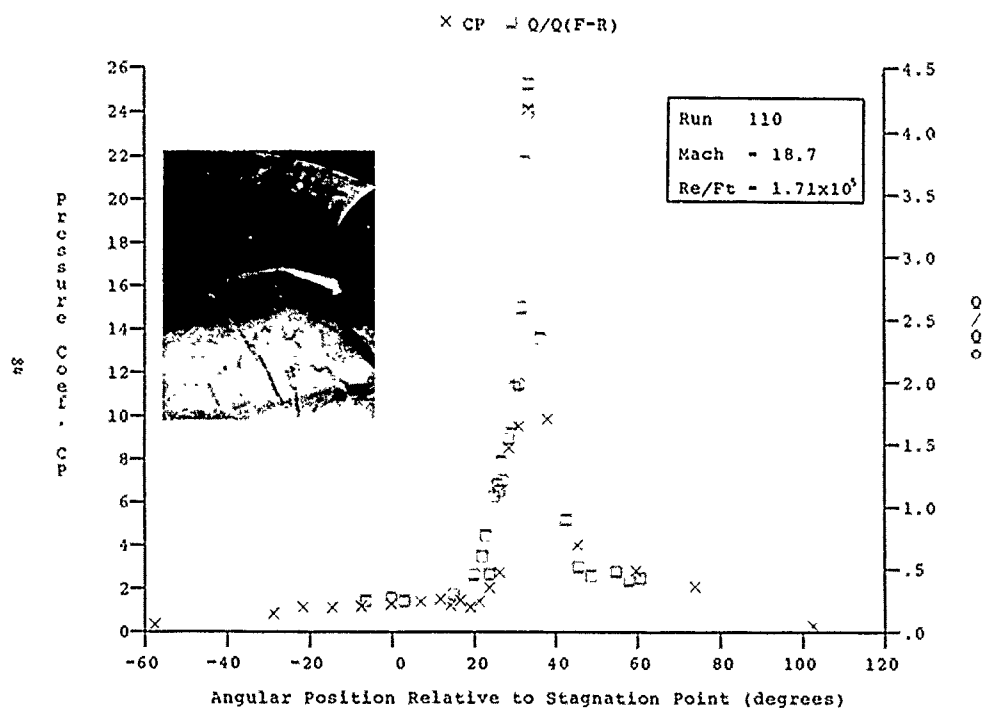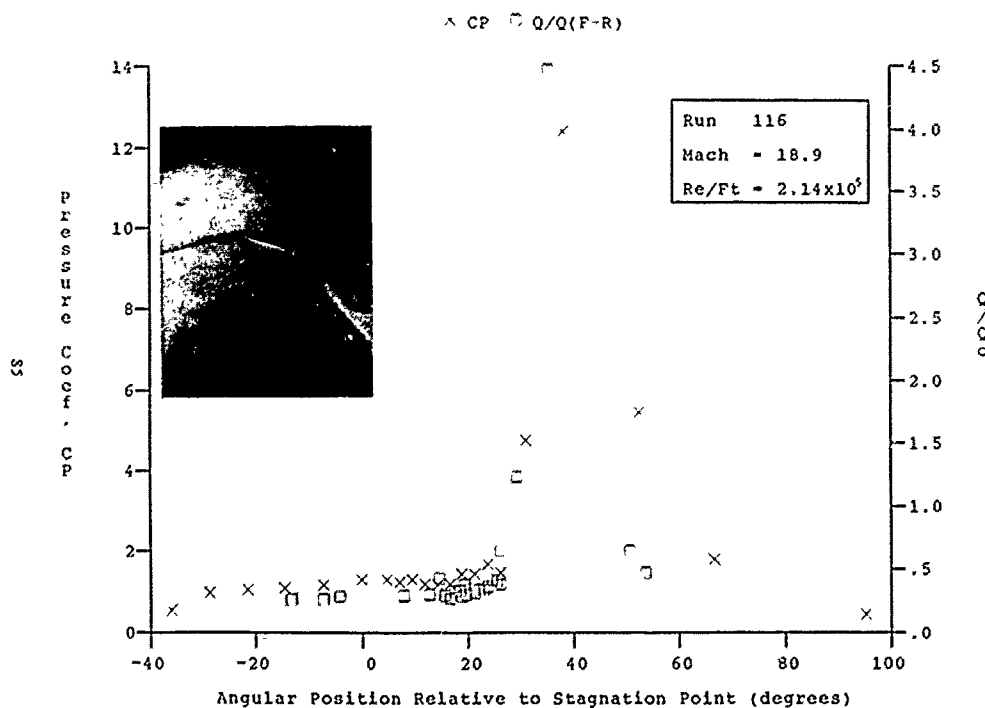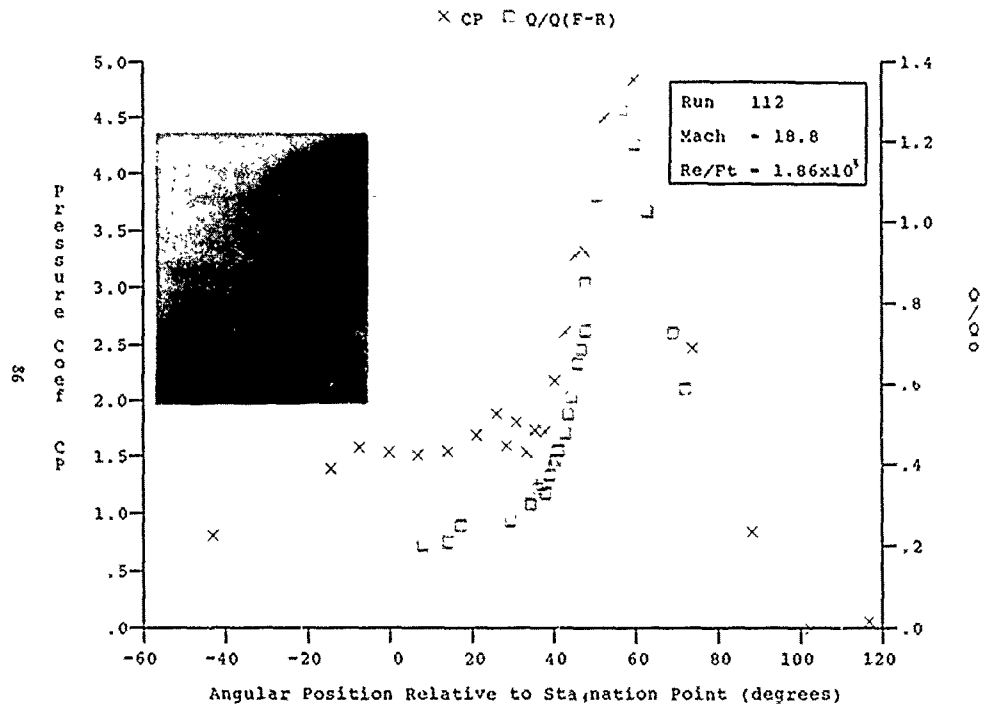AROUND A CIRCULAR CYLINDER AT MACH 16
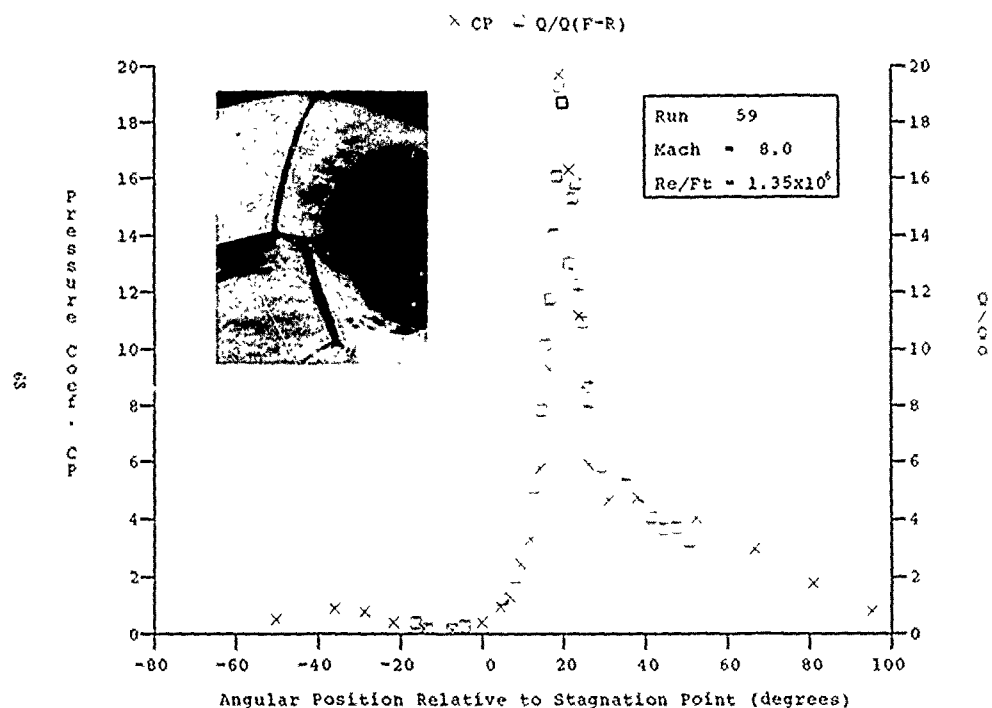
Figure 34a   HEAT AND PRESSURE DISTRIBUTION IN SHOCK/SHOCK INTERACTION
REGIONS INDUCED BY A 12.5° SHOCK GENERATOR OVER A 3-INCH
DIAMETER CYLINDER AT MACH 8 FOR RUN 59
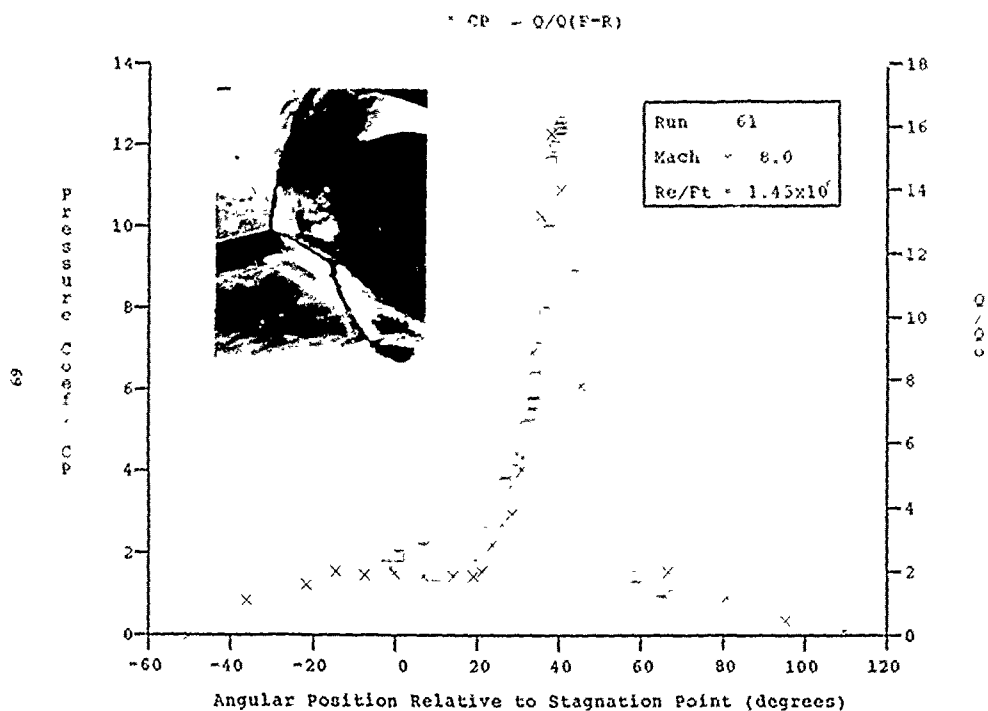
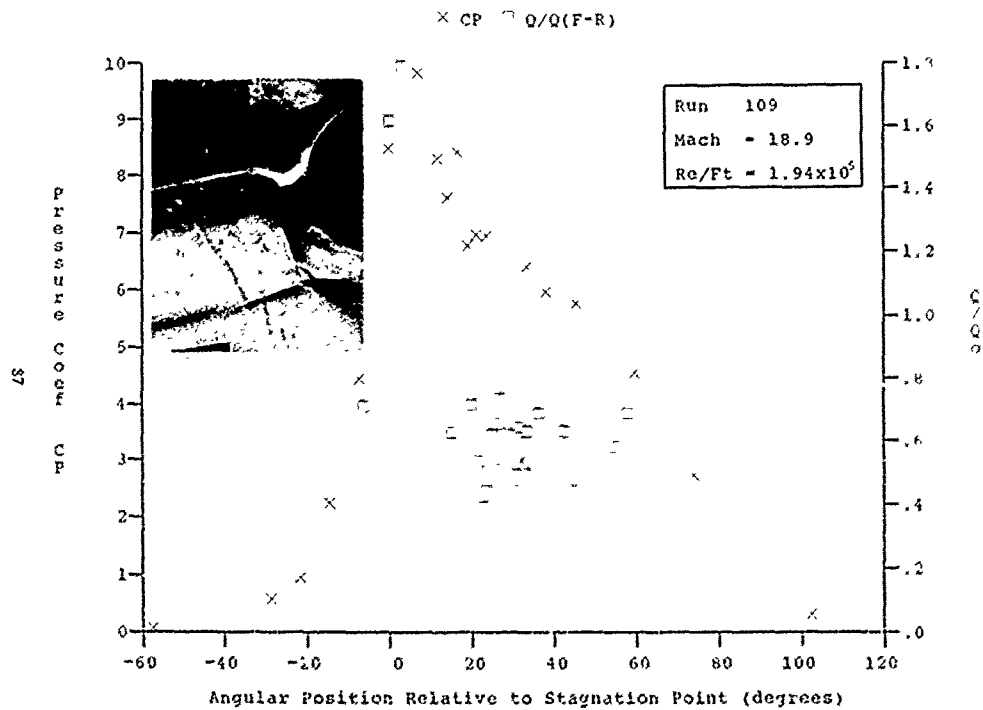Figure 34b   HEAT AND PRESSURE DISTRIBUTION IN SHOCK/SHOCK INTERACTION
REGIONS INDUCED BY A 12.5° SHOCK GENERATOR OVER A 3-INCH
DIAMETER CYLINDER AT MACH 8 FOR RUN 61

< CP   - Q/Q(F-R)
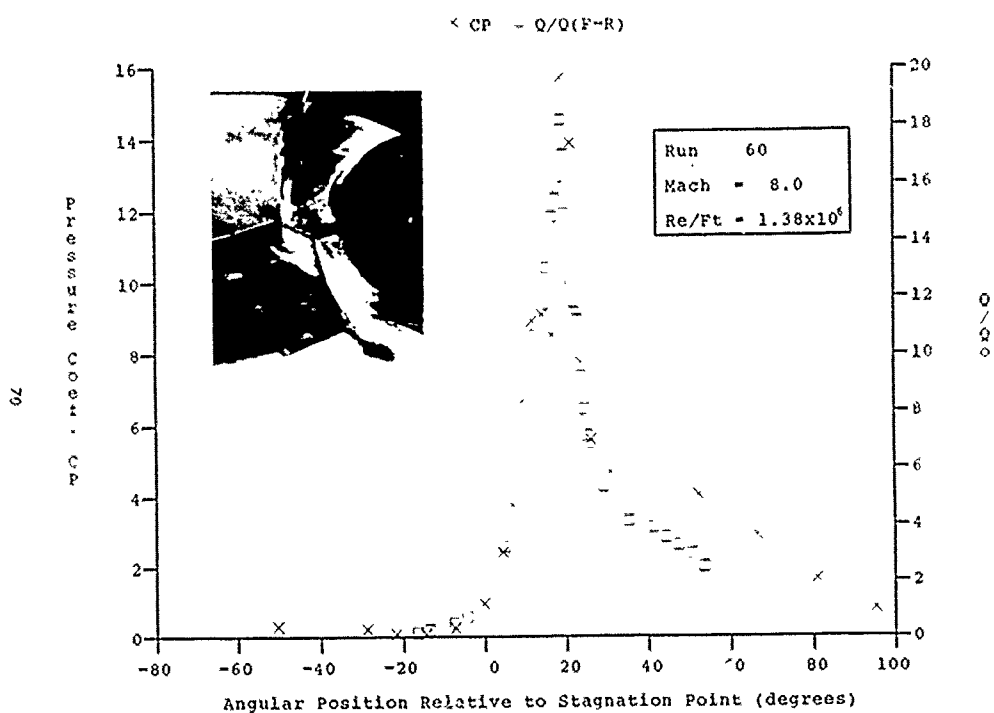
Figure 34c   HEAT AND PRESSURE DISTRIBUTION IN SHOCK/SHOCK INTERACTION
REGIONS INDUCED BY A 12.5° SHOCK GENERATOR OVER A 3-INCH
DIAMETER CYLINDER AT MACH 8 FOR RUN 60

× CP   ◡ Q/Q(F-R)
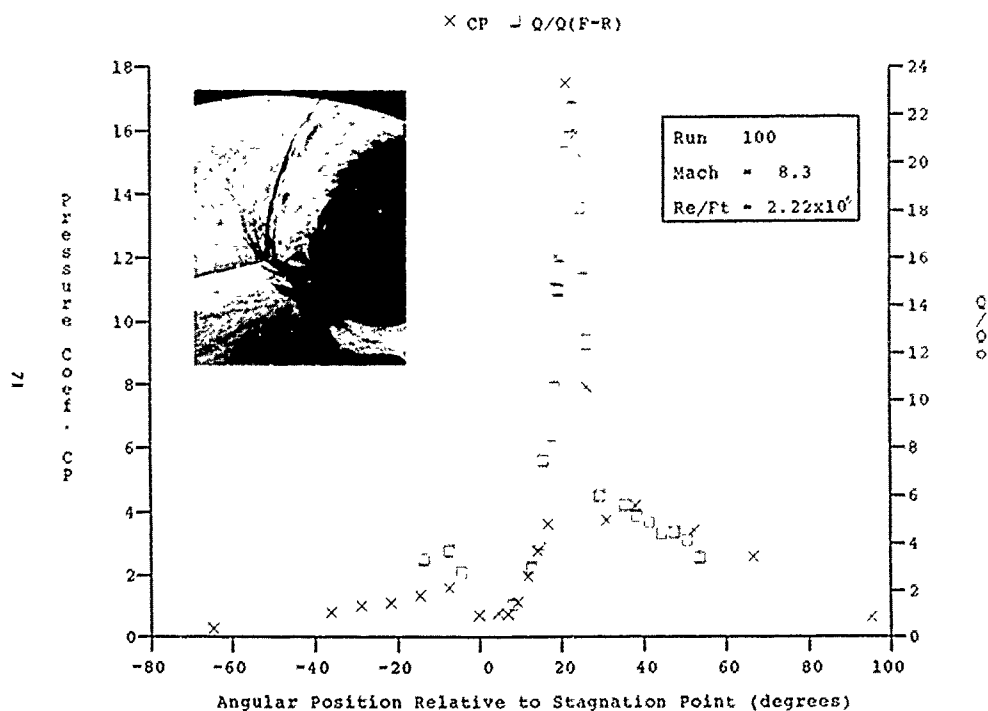
Figure 34d   HEAT AND PRESSURE DISTRIBUTION IN SHOCK/SHOCK INTERACTION
REGIONS INDUCED BY A 12.5° SHOCK GENERATOR OVER A 3-INCH
DIAMETER CYLINDER AT MACH 8 FOR RUN 100
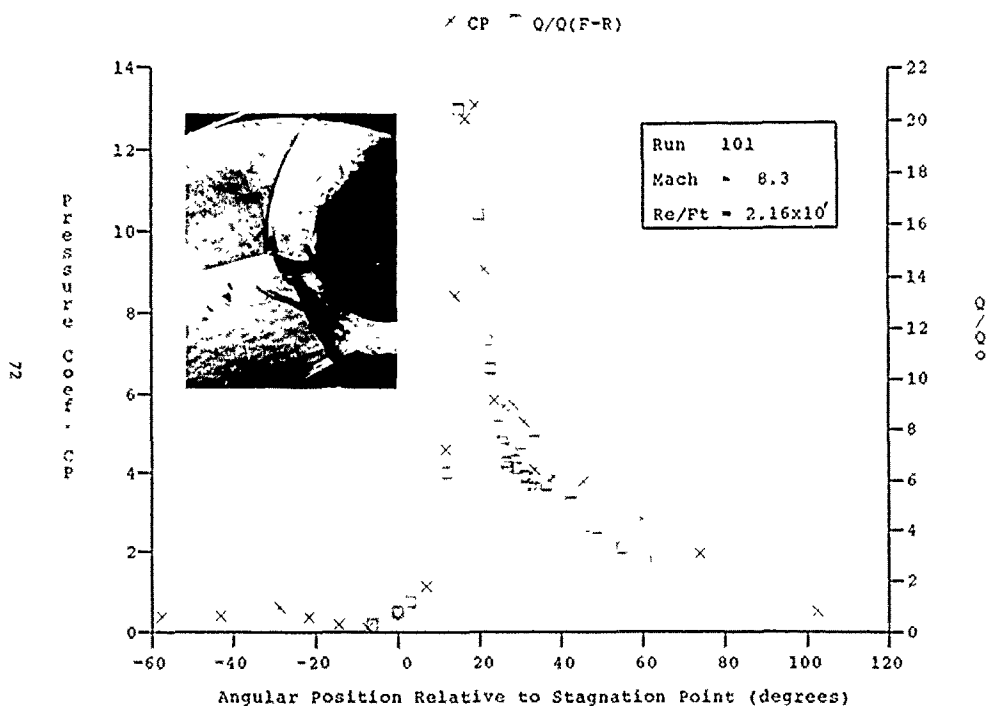
Figure 34e HEAT AND PRESSURE DISTRIBUTION IN SHOCK/SHOCK INTERACTION
REGIONS INDUCED BY A 12.5° SHOCK GENERATOR OVER A 3-INCH
DIAMETER CYLINDER AT MACH 8.3 FOR RUN 101
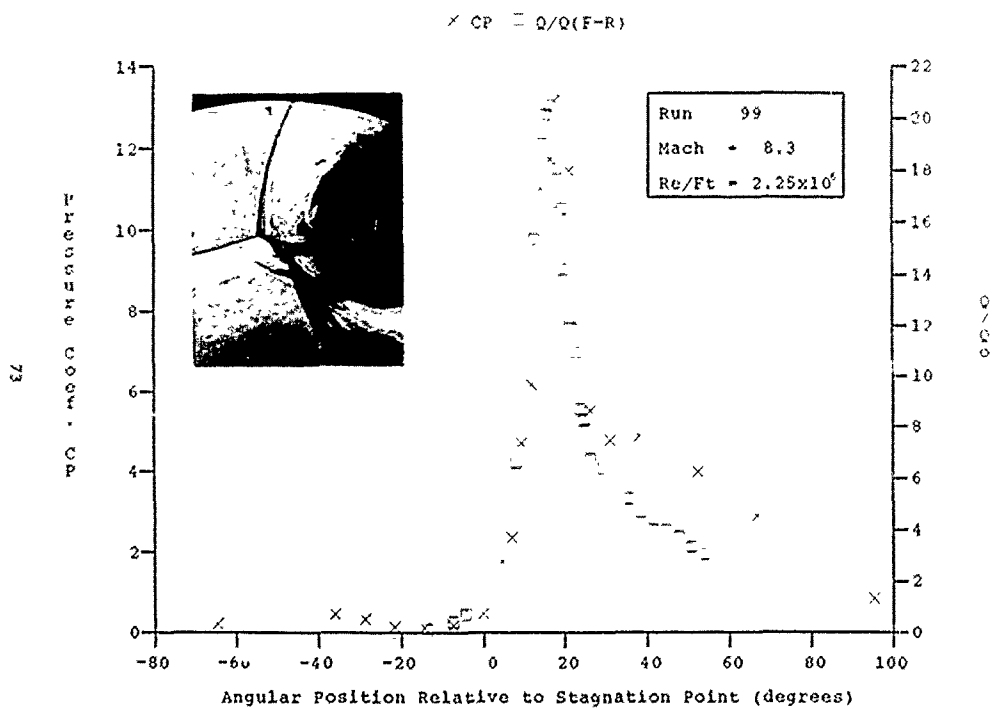
Figure 34f HEAT AND PRESSURE DISTRIBUTION IN SHOCK/SHOCK INTERACTION
REGIONS INDUCED BY A 12.5° SHOCK GENERATOR OVER A 3-INCH
DIAMETER CYLINDER AT MACH 8 FOR RUN 99

a series of measurements in Figures 34a through 34f. For the Type IV interaction, an extremely rapid rise in heat transfer and pressure at the base of the jet was observed. However, we did not observe a local plateau in the maximum heating across the jet width. Instead, a local point maximum, whose position responded to the unsteady movement of the jet, was observed over a fraction of the jet width.

Our measurements show that for interactions where the jet is almost normal to the surface, a small flow unsteadiness (shown in the heat transfer and pressure records in Figure 35) causes the jet to fluctuate between flowing upward or downward. We observed typical oscillation frequencies of between 3 and 10 kHz for some Type IV interactions. As the impingement position was moved away from the stagnation region and the interaction changed to a Type III interaction, initially we observed little decrease in the peak heating or the pressure and heat transfer distributions. With the peak being so narrow and the gradient so steep, selecting a meaningful peak value is difficult, if not impossible. In addition, lowering the impingement point results in a rapid decrease in the overall level of heating and pressure in the interaction region. The same basic trends appear at Mach 11, as shown in the distributions of Figures 36a through 36c. In Figure 36a, we see a Type IV interaction with jet impingement slightly below the stagnation point where the heating level is less than when the interaction is moved away from the stagnation point (Figure 36b). Moving the interaction further around the body again reduces the overall heating levels, although again, the gradients are so steep that a maximum in the pressure and heat transfer is difficult to accurately define. The measurements at Mach 16 (Figures 37a through 37e) show the sensitivity of the aerothermal loads in the Type IV interaction to the position of the jet impingements. We also observe that for these totally laminar interactions, there is no dramatic change in the pressure and heat transfer distribution when there is a change from a Type IV to a Type III interaction. In the Mach 18 studies, we captured a Type IV flow configuration where the jet was deflected well above the centerline (Figures 38a through 38d), with a resultant significant drop in peak aerothermal loads relative to the Type IV interaction where the jet impinges below the centerline. Again, as the interaction is moved lower on the cylinder, the loads diminish. While defining a peak heating load is difficult, the general trend of peak heating and pressure with the position of jet impingement is shown in Figure 39. Figure 39 shows that peak loads occur when the interaction is approximately 20 degrees below the stagnation point, regardless of the Mach number. Plotting the peak heating and pressure enhancement against peak pressure ratio (Figure 40), we see that the interactions become more severe when

HEAT TRANSFER
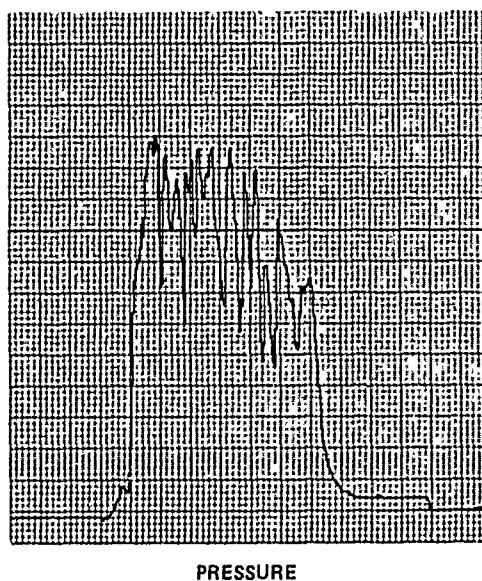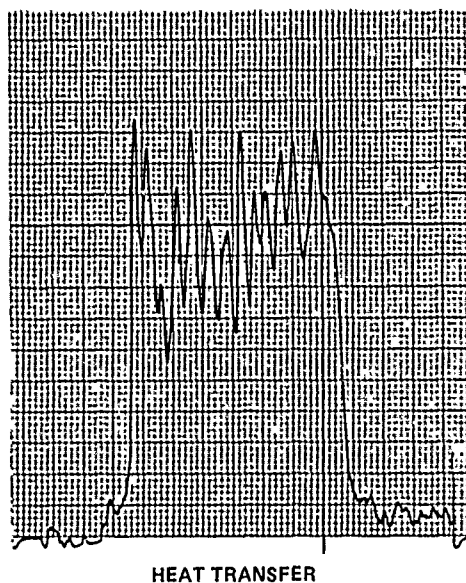
PRESSURE

Figure 35   TIME HISTORIES FOR HEAT AND PRESSURE IN TYPE IV INTERACTION
REGION AT MACH 8
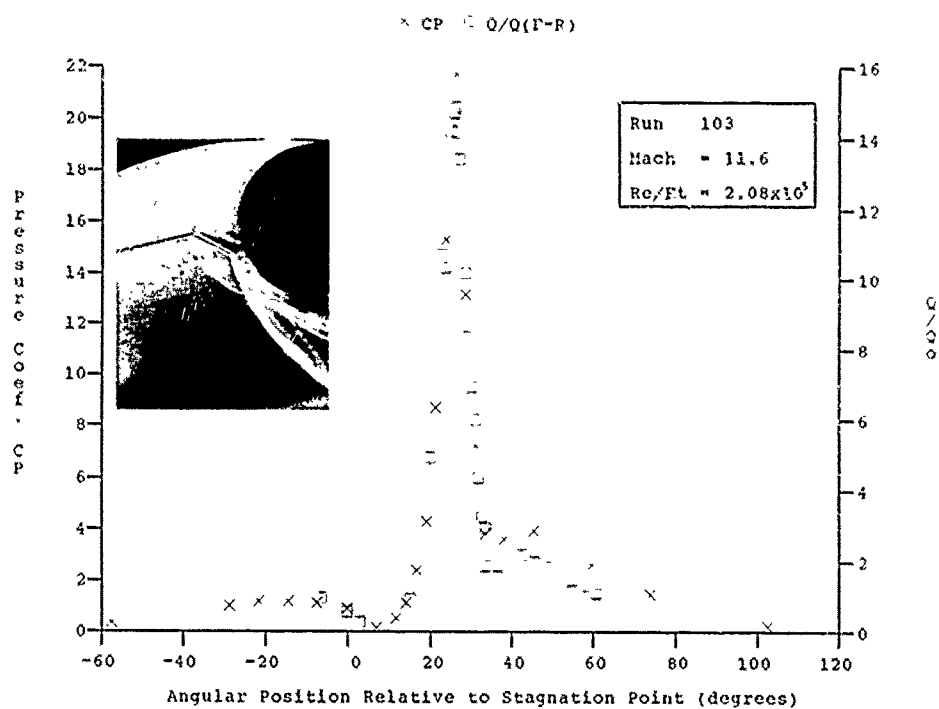
Figure 36a HEAT AND PRESSURE DISTRIBUTION IN SHOCK/SHOCK INTERACTION
REGIONS INDUCED BY A 12.5° SHOCK GENERATOR OVER A 3-INCH
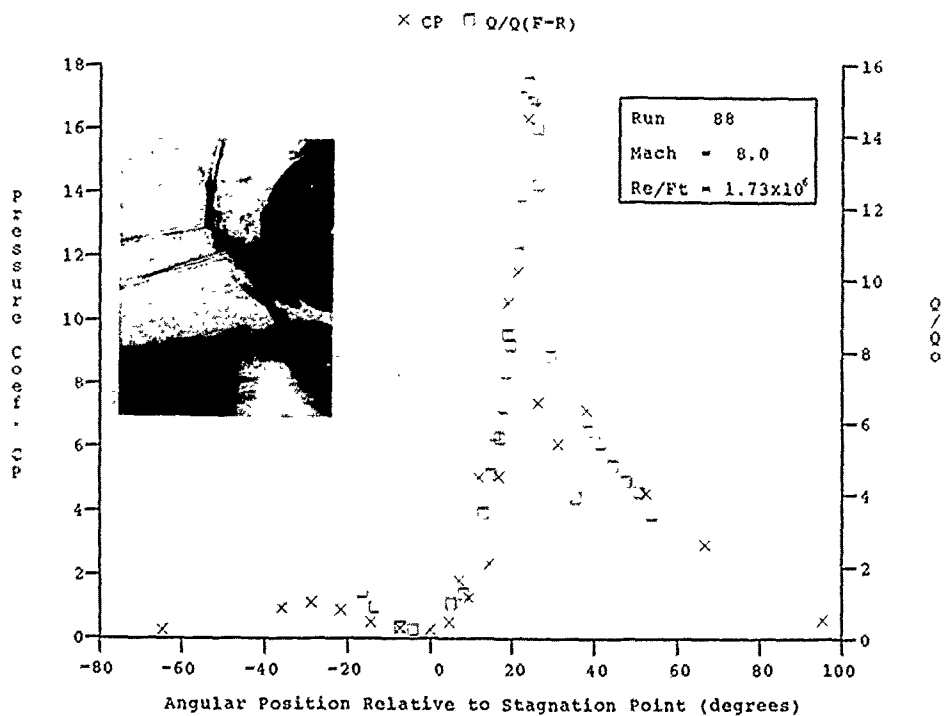DIAMETER CYLINDER AT MACH 11.6 FOR RUN 103
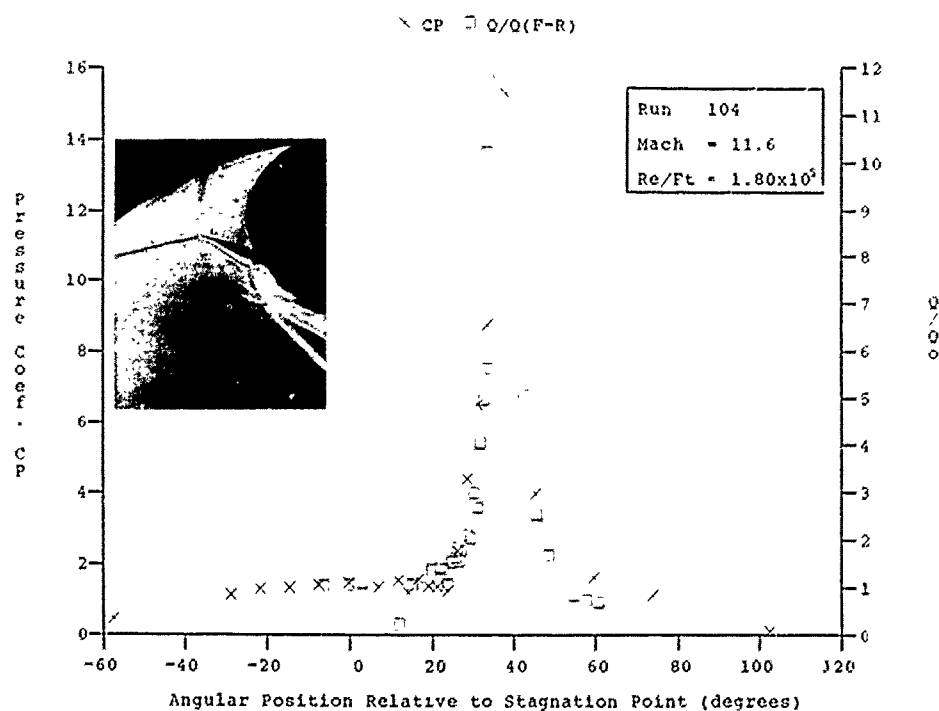
Figure 36b HEAT AND PRESSURE DISTRIBUTION IN SHOCK/SHOCK INTERACTION
REGIONS INDUCED BY A 12.5° SHOCK GENERATOR OVER A 3-INCH
DIAMETER CYLINDER AT MACH 11.6 FOR RUN 104

78

$\times$ CP $\quad\square$ Q/Q(F-R)

Figure 36c HEAT AND PRESSURE DISTRIBUTION IN SHOCK/SHOCK INTERACTION
REGIONS INDUCED BY A 12.5° SHOCK GENERATOR OVER A 3-INCH
DIAMETER CYLINDER AT MACH 11.6 FOR RUN 113
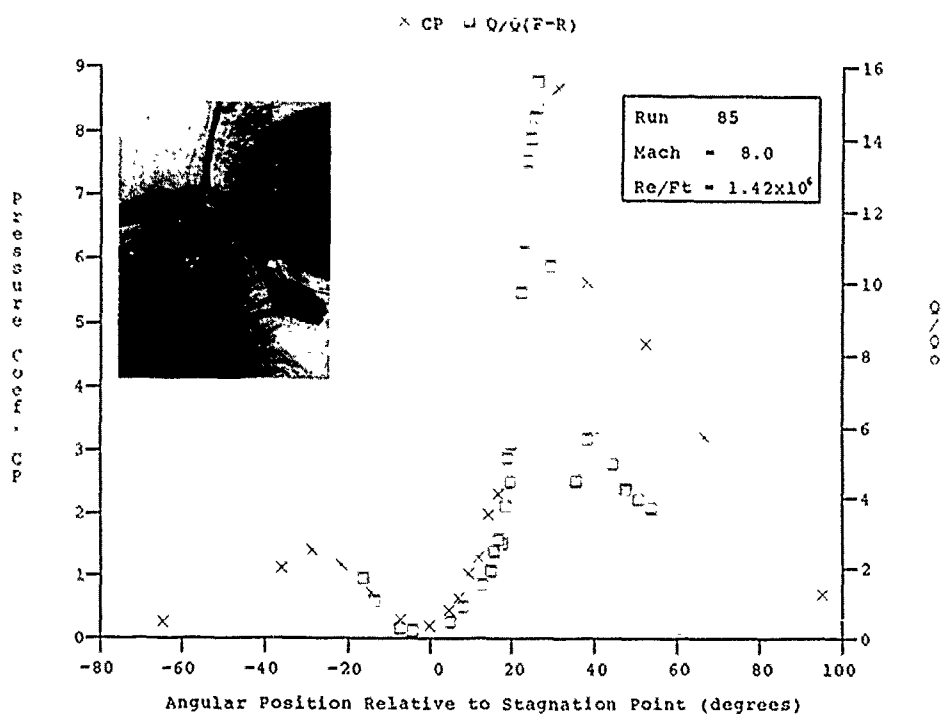
79

$\times$ CP $\quad\sim$ Q/Q(F-R)

Figure 37a HEAT AND PRESSURE DISTRIBUTION IN SHOCK/SHOCK INTERACTION
REGIONS INDUCED BY A 12.5° SHOCK GENERATOR OVER A 3-INCH
DIAMETER CYLINDER AT MACH 15.6 FOR RUN 107

CP — Q/Q(F-R)
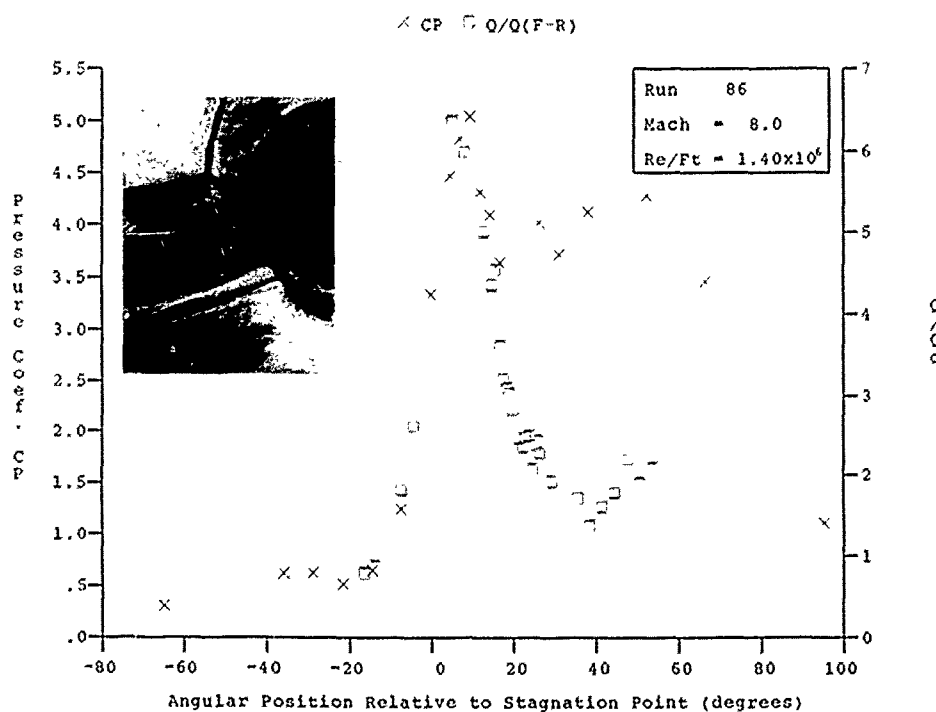

Angular Position Relative to Stagnation Point (degrees)

Figure 37b   HEAT AND PRESSURE DISTRIBUTION IN SHOCK/SHOCK INTERACTION
REGIONS INDUCED BY A 12.5° SHOCK GENERATOR OVER A 3-INCH
DIAMETER CYLINDER AT MACH 15.7 FOR RUN 114

CP   Q/Q(F-R)

Angular Position Relative to Stagnation Point (degrees)

Figure 37c   HEAT AND PRESSURE DISTRIBUTION IN SHOCK/SHOCK INTERACTION
REGIONS INDUCED BY A 12.5° SHOCK GENERATOR OVER A 3-INCH
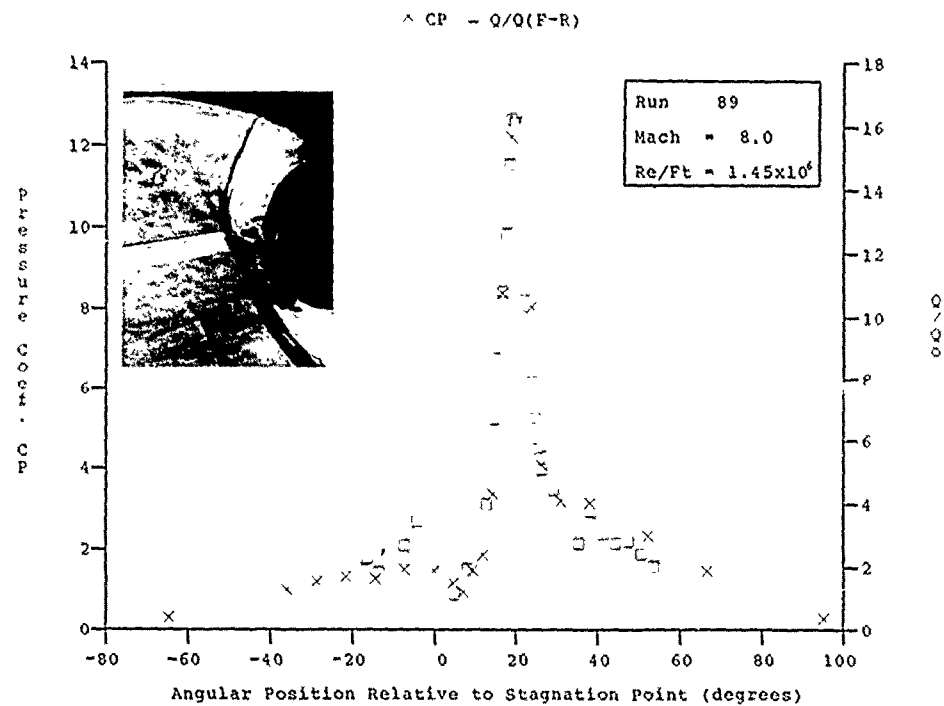DIAMETER CYLINDER AT MACH 15.7 FOR RUN 115

> CP ⊃ Q/Q(F-R)

Figure 37d   HEAT AND PRESSURE DISTRIBUTION IN SHOCK/SHOCK INTERACTION
REGIONS INDUCED BY A 12.5° SHOCK GENERATOR OVER A 3-INCH
DIAMETER CYLINDER AT MACH 15.6 FOR RUN 106

` CP – Q/Q(F-R)

Figure 37e   HEAT AND PRESSURE DISTRIBUTION IN SHOCK/SHOCK INTERACTION
REGIONS INDUCED BY A 12.5^ SHOCK GENERATOR OVER A 3-INCH
DIAMETER CYLINDER AT MACH 16.3 FOR RUN 43

Figure 38a HEAT AND PRESSURE DISTRIBUTION IN SHOCK/SHOCK INTERACTION
REGIONS INDUCED BY A 12.5° SHOCK GENERATOR OVER A 3-INCH
DIAMETER CYLINDER AT MACH 18.7 FOR RUN 110

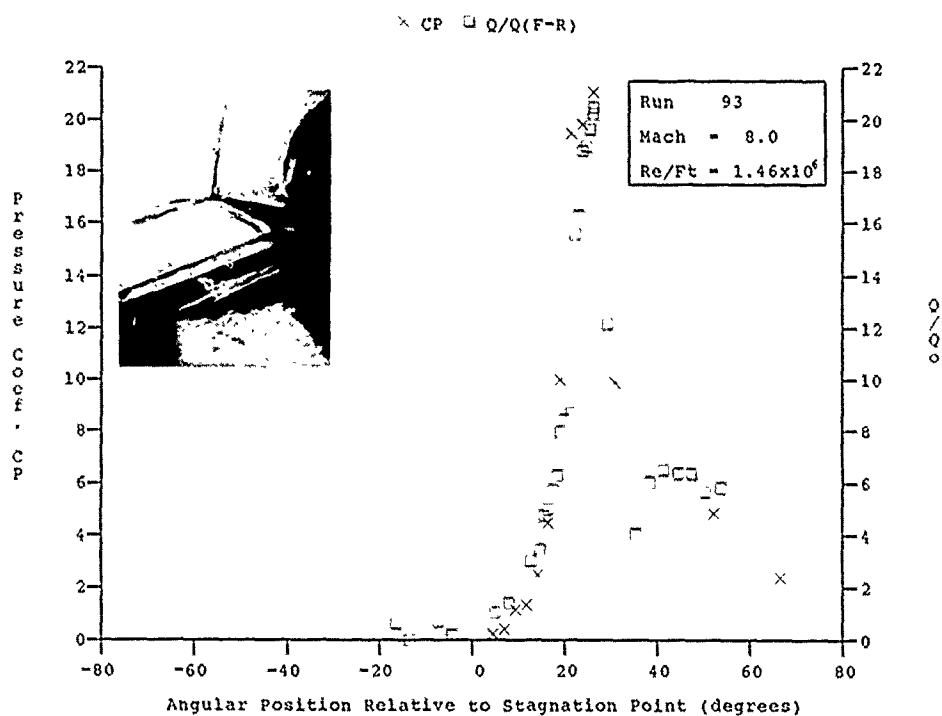

Figure 38b HEAT AND PRESSURE DISTRIBUTION IN SHOCK/SHOCK INTERACTION
REGIONS INDUCED BY A 12.5° SHOCK GENERATOR OVER A 3-INCH
DIAMETER CYLINDER AT MACH 18.9 FOR RUN 116

Figure 38c HEAT AND PRESSURE DISTRIBUTION IN SHOCK/SHOCK INTERACTION REGIONS INDUCED BY A 12.5° SHOCK GENERATOR OVER A 3-INCH DIAMETER CYLINDER AT MACH 18.8 FOR RUN 112

Figure 38d HEAT AND PRESSURE DISTRIBUTION IN SHOCK/SHOCK INTERACTION REGIONS INDUCED BY A 12.5° SHOCK GENERATOR OVER A 3-INCH DIAMETER CYLINDER AT MACH 18.9 FOR RUN 109
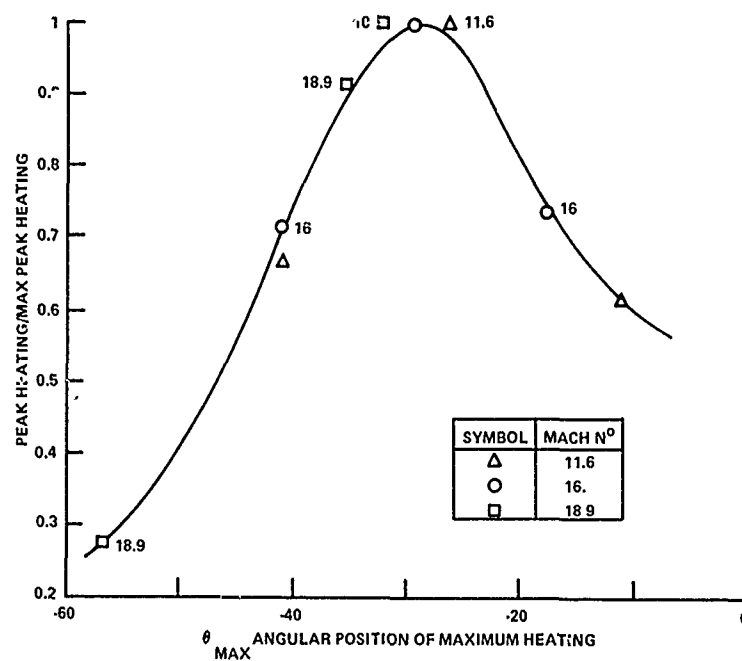
Figure 39 ANGULAR POSITION OF THE POINT OF MAXIMUM HEATING FOR SINGLE SHOCK/SHOCK INTERACTION STUDY
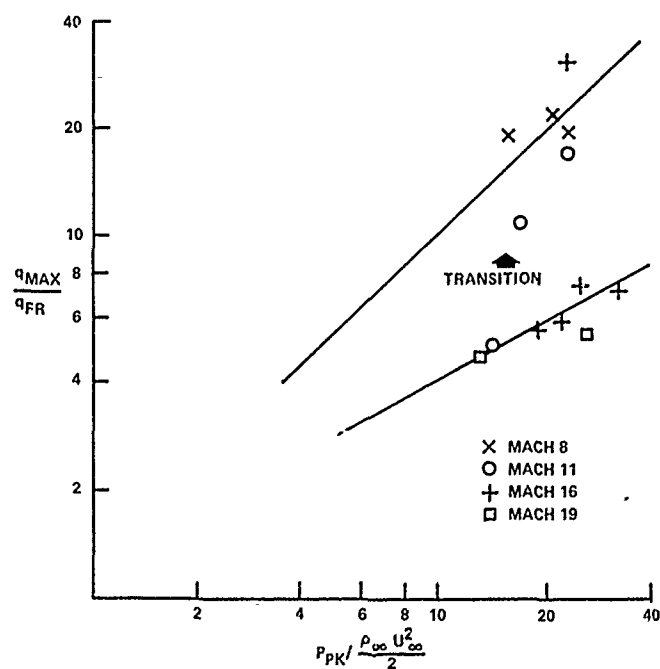
Figure 40a CORRELATION OF PEAK HEATING AND PRESSURE MEASUREMENTS
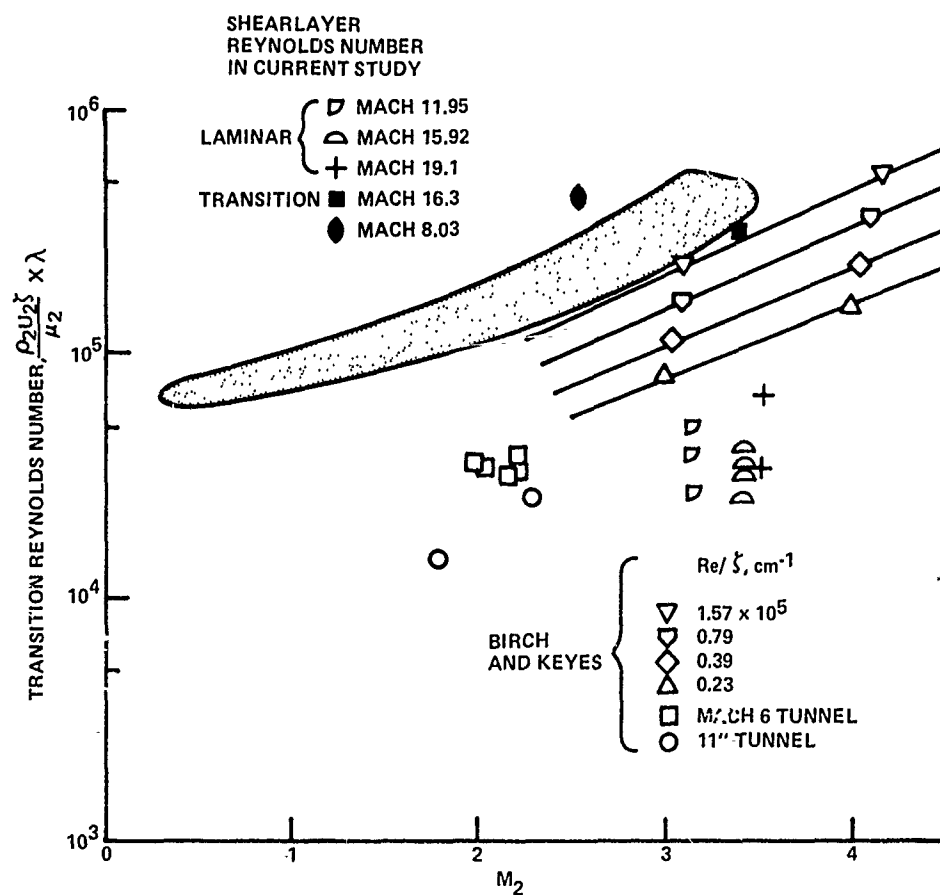
Figure 40b   VARIATION OF TRANSITION REYNOLDS NUMBER WITH MACH NUMBER

Chapman, D.R., Kuenn, D.M., and Larson, H.K., "Investigation of Separated Flows in Supersonic and Subsonic Streams with Emphasis on the Effects of Transition," Rept. 1356, 1958, NACA.

transition occurs. For Types III and IV interactions, the peak heating enhancement is plotted against the pressure enhancement as suggested by Edney. Keeping in mind the intrinsic problems in preparing this correlation, the ½-power law relationship appears to be as useful as any other. In support of our contention that #6 larger heating augmentations are asociated with transitional shear layers for the type III interaction we have plotted in Figure 40b the Reynolds number based on the length of the free shear layers measured in our studies on the Burch compilation of shear layer transition measurements shown in Figure 4. We observe that the measurements at Mach 8 and 16 which exhibit the large heating augmentations are those with shear layer Reynolds int he range of 10^5 to 10^6.

6.3   Studies of Multiple Shock/Shock Interaction

The severity of the aerothermal loads induced by shock/shock interaction has led to speculation on techniques that can be used to reduce loads for configurations such as inlets, where the compression must be captured. Preventing the formation of a single bounding shock and allowing multiple shock impingement on the inlet lip may significantly reduce the peak heating and pressure loads. Here, we briefly discuss the results of a preliminary study to examine such an approach. We selected two configurations that generated total flow turning angles of 12.5 and 13.5 degrees in 7.5/5 degree and 7.5/6 degree two-shock-generation configurations. These configurations were selected to match the interaction strengths developed in the earlier studies. We examined configurations where the two shocks coalesced before the bow shock to one, when the shocks impinged on either side of the stagnation line. All the measurements were made at Mach 8 and a Reynolds number of 1.5×10^6. Test conditions, heat transfer and pressure measurements, plots of these quantities and schlieren photographs for each test condition are provided in Appendix C. The pressure and heat transfer distributions for the 7.5/5 studies are shown in Figures 41a through 41e. Starting with the flow configuration where the incident shocks combine ahead of the bow shock (Figure 41a) and translating the shocks relative to the cylinder and each other, we observe the following results. First, the peak heating loads are significantly reduced by allowing multiple impingements. Spreading the shocks about the stagnation line results in the greatest reduction, as shown in Figure 41b. Even very small relative displacements, as shown in Figures 41c and 41d, can cause significant loading reductions. The flow configuration in Figure 41d is of particular interest because a jet and shear layer are formed in this flow. For completeness, we also show the measurements for
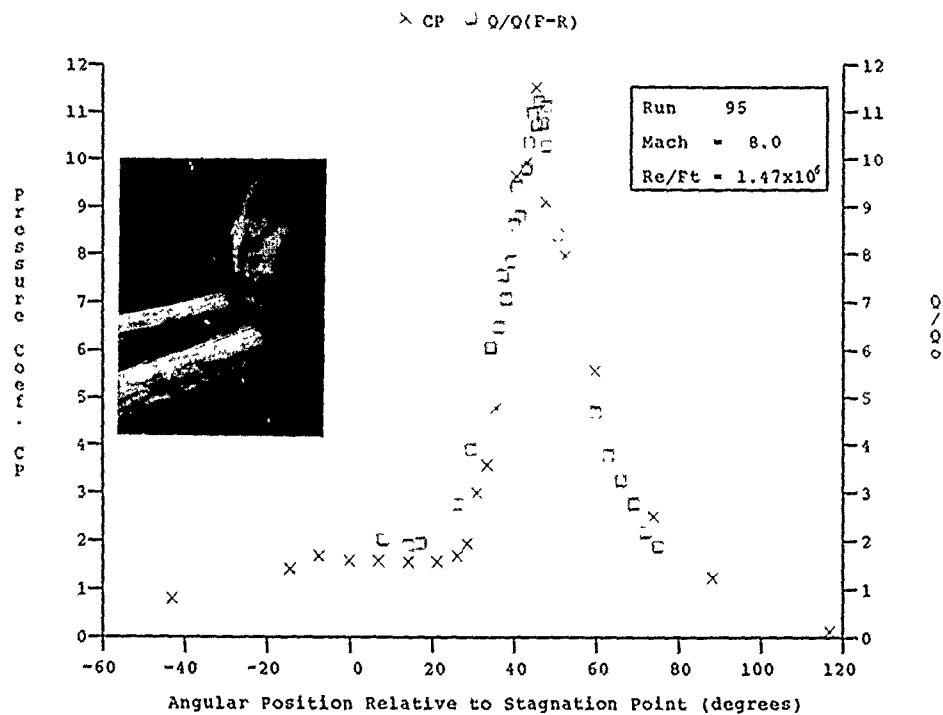
92

$\times$ CP $\sim$ Q/Q(F-R)
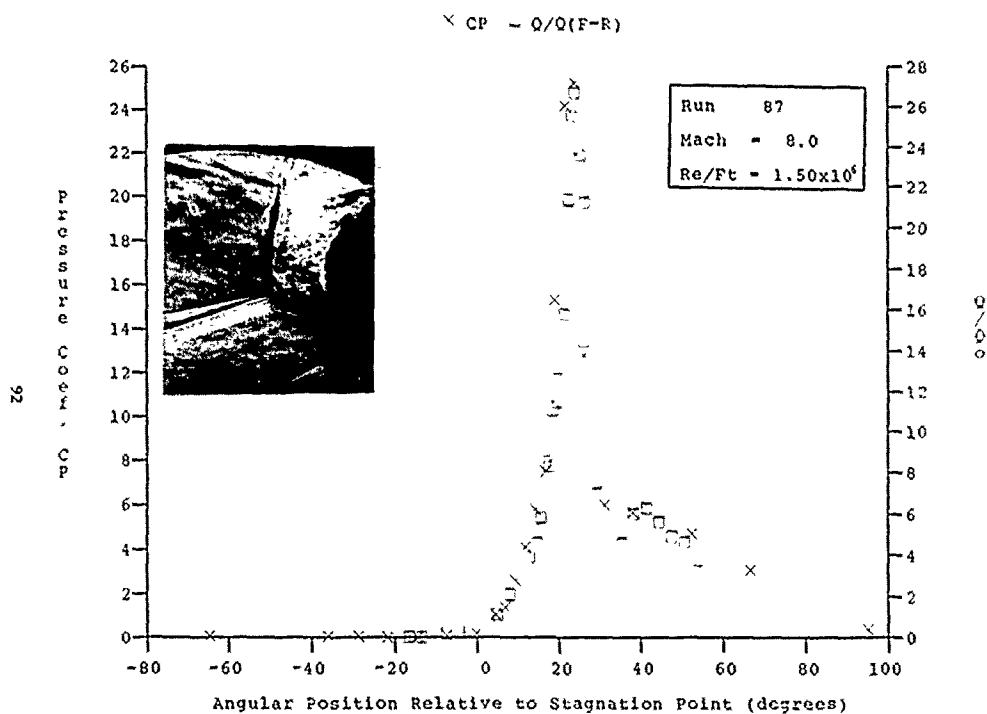
Figure 41a   HEAT AND PRESSURE DISTRIBUTION IN MULTIPLE SHOCK
INTERACTION REGIONS INDUCED BY A 7.5/5° SHOCK GENERATOR
OVER A 3-INCH DIAMETER CYLINDER AT MACH 8 FOR RUN 87

$\times$ CP $\square$ Q/Q(F-R)

Figure 41b   HEAT AND PRESSURE DISTRIBUTION IN MULTIPLE SHOCK
INTERACTION REGIONS INDUCED BY A 7.5/5° SHOCK GENERATOR
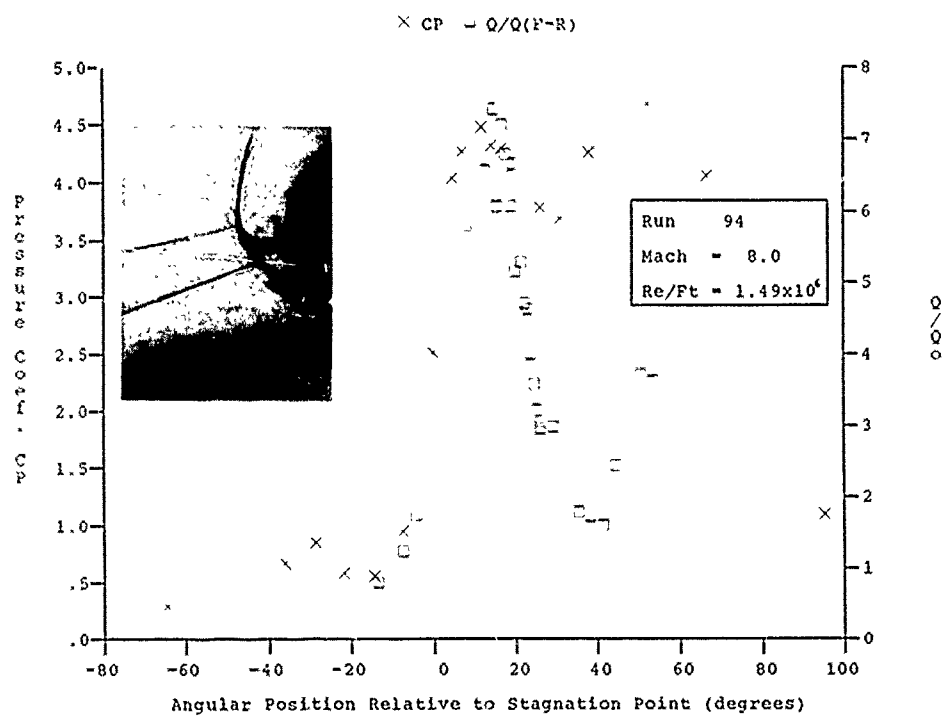OVER A 3-INCH DIAMETER CYLINDER AT MACH 8 FOR RUN 88

X CP ⊔ Q/Q(F-R)

Figure 41c HEAT AND PRESSURE DISTRIBUTION IN MULTIPLE SHOCK
INTERACTION REGIONS INDUCED BY A 7.5/5° SHOCK GENERATOR
OVER A 3-INCH DIAMETER CYLINDER AT MACH 8 FOR RUN 85

X CP ⊓ Q/Q(F-R)

Figure 41d HEAT AND PRESSURE DISTRIBUTION IN MULTIPLE SHOCK
INTERACTION REGIONS INDUCED BY A 7.5/5° SHOCK GENERATOR
OVER A 3-INCH DIAMETER CYLINDER AT MACH 8 FOR RUN 86

Figure 41e HEAT AND PRESSURE DISTRIBUTION IN MULTIPLE SHOCK
INTERACTION REGIONS INDUCED BY A 7.5/5° SHOCK GENERATOR
OVER A 3-INCH DIAMETER CYLINDER AT MACH 8 FOR RUN 89

the 7.5 shock generator only in Figure 34e. A similar flow of interest is shown in Figures 42a through 42e from the 7.5/6 studies. However, the enhancements occur when the shock coalesces ahead of the bow shock. Notice that in this series, separating the shocks does not cause as great a reduction as in the 7.5/5 configuration.

Figure 42a   HEAT AND PRESSURE DISTRIBUTION IN MULTIPLE SHOCK INDUCED
INTERACTION REGIONS INDUCED BY A 7.5/6° SHOCK GENERATOR
OVER A 3-INCH DIAMETER CYLINDER AT MACH 8 FOR RUN 93
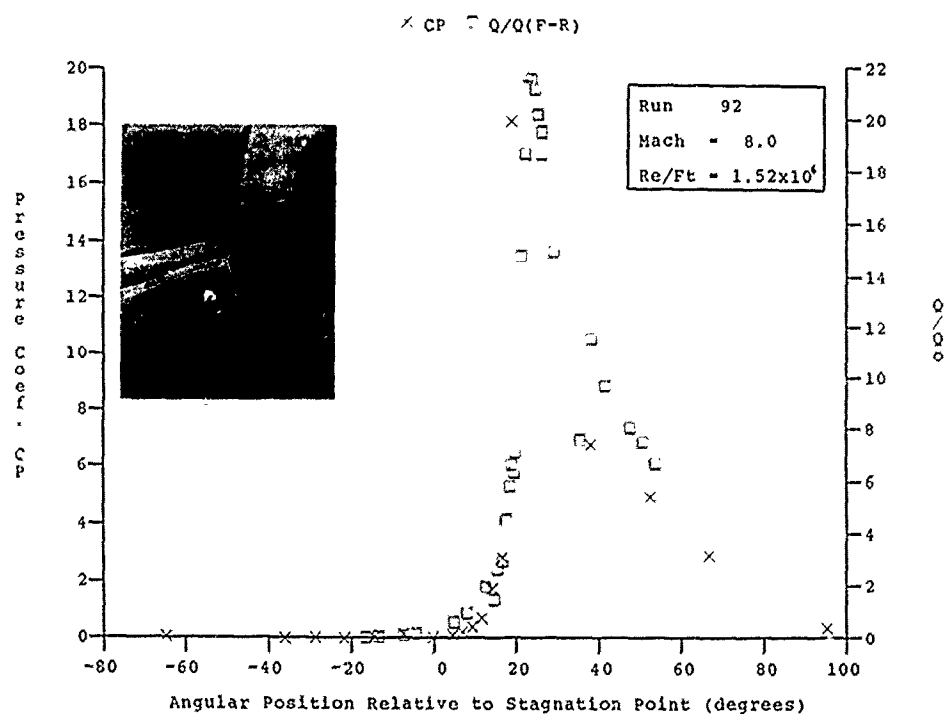
Figure 42b   HEAT AND PRESSURE DISTRIBUTION IN MULTIPLE SHOCK INDUCED
INTERACTION REGIONS INDUCED BY A 7.5/6° SHOCK GENERATOR
OVER A 3-INCH DIAMETER CYLINDER AT MACH 8 FOR RUN 92
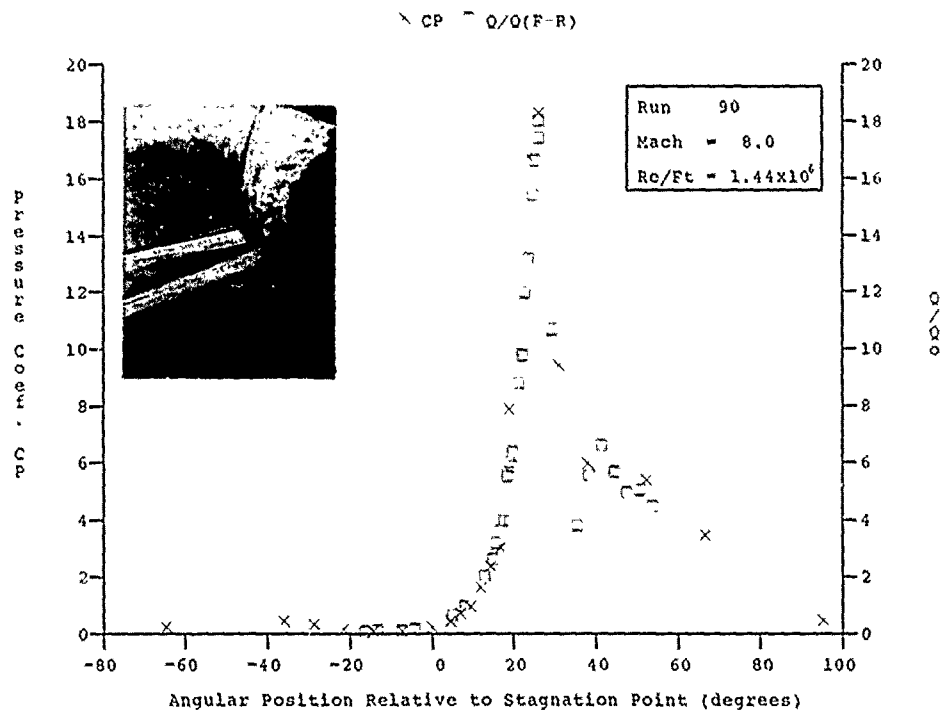
Figure 42c HEAT AND PRESSURE DISTRIBUTION IN MULTIPLE SHOCK INDUCED INTERACTION REGIONS INDUCED BY A 7.5/6° SHOCK GENERATOR OVER A 3-INCH DIAMETER CYLINDER AT MACH 8 FOR RUNS 90 AND 91

Figure 42d HEAT AND PRESSURE DISTRIBUTION IN MULTIPLE SHOCK INDUCED INTERACTION REGIONS INDUCED BY A 7.5/6° SHOCK GENERATOR OVER A 3-INCH DIAMETER CYLINDER AT MACH 8 FOR RUN 95

Figure 42e HEAT AND PRESSURE DISTRIBUTION IN MULTIPLE SHOCK INDUCED
INTERACTION REGIONS INDUCED BY A 7.5/6° SHOCK GENERATOR
OVER A 3-INCH DIAMETER CYLINDER AT MACH 8 FOR RUN 94

## 7. PRELIMINARY STUDIES OF SWEEP EFFECTS ON REGIONS OF SHOCK/ SHOCK INTERACTION

7.1 Introduction

Regions of shock/shock interaction are seldom two-dimensional in most practical situations. Therefore a knowledge of the effects of crossflow is important. One controlled way of studying this effect is to sweep the interaction region creating a quasi-two-dimensional flow. Practically, this can create problems with end effects and introduce an additional fundamental phenomena-attachment line transition. At large Reynolds numbers, the absence of an incident shock sweeping the cylinder introduces a crossflow instability at the attachment line which if large enough can result in transition and turbulent heating along the attachment line. With a shock incident on the swept cylinder we therefore have the potentially interesting situation of a shear layer or jet incident on a turbulent attachment line. While, as discussed later there are criteria for predicting turbulent heating on sweep cylinders clearly no such information is available for shock/shock interaction regions. Therefore the results from these studies must be carefully interpreted to distinguish between sweep and transition effects.

7.2 Experimental Studies

This was an intrisincially difficult experiment to conduct because we were attempting to place the incident at the same radial station on the bow shock along the entire length of the cylinder. To achieve this we fabricated inserts which fit between the support system and shock generator which rolled and yawed the shock generator to place its leading edge in the same plane as the stagnation line of the cylinder. Because we have only one set of schlieren window stations we were unable to align the optics with the axis of the swept cylinder therefore, as shown in Figure 43 the flow visualization does not provide definitive information on the structure of the flow field.

Figure 43   TYPICAL SCHLIEREN OF 15° SWEPT CYLINDER AT MACH 8

Measurements of heat transfer and pressure around the cylinder were made for sweep angles of 15 and 30 degrees with a shock generator angle of 12.5 degrees. At each sweep angle the position of the incident shock was varied to search for the maximum heating rates generated by type III and IV interation regions. The measurements made in this segment of the program are plotted and tabulated in Appendix D.

7.3   Discussion of Measurements

The distribution of heat transfer and pressure for the two sweep angles without an incident shock are shown in Figure 44(a-b). While the measurements on the 15' swept cylinder are in good agreement with laminar theory, the heating levels for the 30' sweep exceed the laminar case. As discussed earlier there is a strong likelihood that attachment line transition has occurred in the latter case.

The boundary layer along the attachment line of a swept cylinder has been examined in a number of earlier studies concentrated principally in subsonic and low supersonic flows. In supersonic compressible flows the characteristic of attachment line boundary layer can be described in terms of the parameters M_e, $\bar{R}$, T_w/T_e, V_A and Pr. Here the crossflow Reynolds number is by

$$\bar{R} = V_A \, \frac{\bar{\eta}}{V_A}$$

Where $\bar{\eta}$ is the characteristic scale length of the attachment line boundary layer   depends on the chordwise velocity gradient $dU/dx_{x=0}$ and the kinematic viscosity selecting

$$\bar{\eta} = \sqrt{\left(\frac{u_A}{\left(\frac{dU_A}{dx} \right)_{x=0}} \right)}$$

then $$\bar{R} = \sqrt{\left(\frac{V_A^2}{V_A} \left(\frac{dU_A}{dx} \right)_{x=0} \right)}$$

or $$\bar{R} = \sqrt{\left(V_A^2 \, \frac{c}{(V_A U - U_1)} \right)}$$
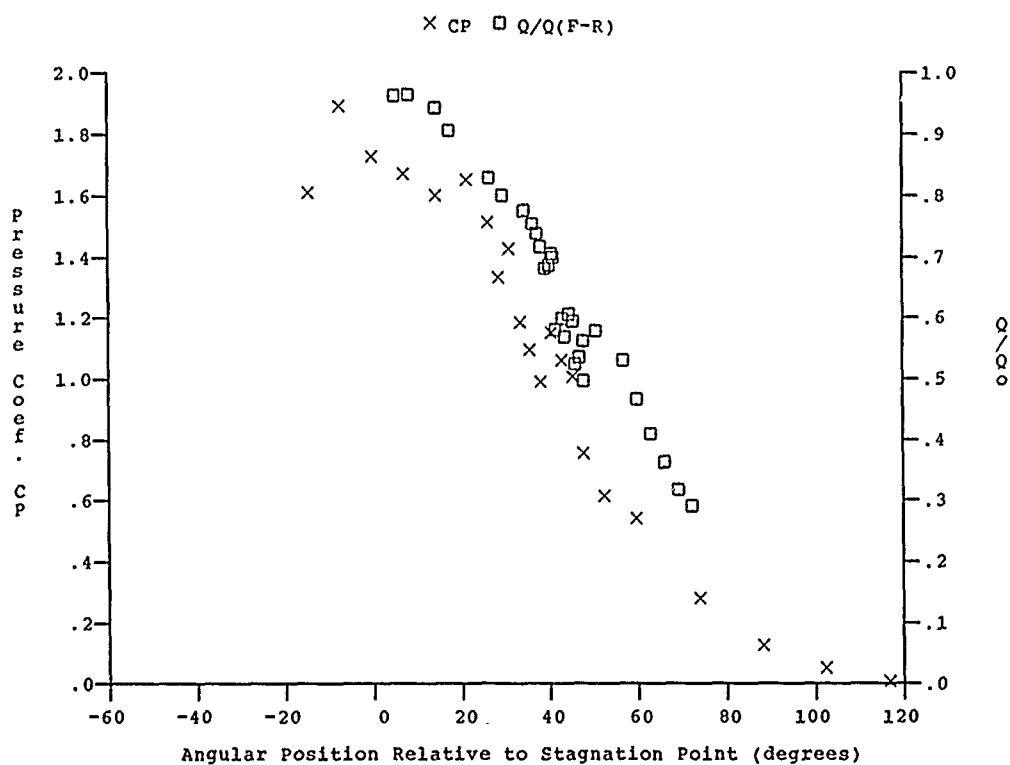
Figure 44a   PRESSURE AND HEAT TRANSFER TO SWEPT CYLINDER Ψ = 15°
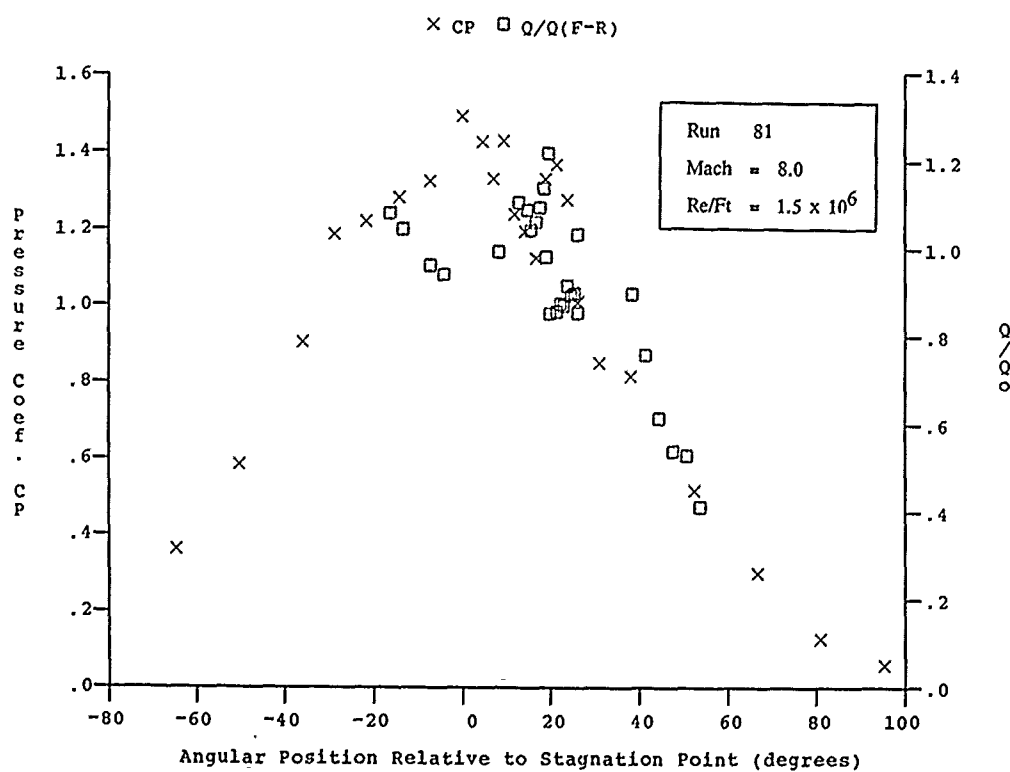
Figure 44b   PRESSURE AND HEAT TRANSFER TO SWEPT CYLINDER ψ = 30°

where

$$U_1 = \left(\frac{c}{U_\infty} \frac{dU_{\infty,o}}{dx} \right)_{x=0}$$

For incompressible laminar flow, it can be shown that the heating rate to the attachment line is given by

$$St_A = \frac{0.571}{\overline{R}} \frac{1}{Pr^{2/3}}$$

For uncompressible turbulent flows the attachment line heating can be expressed as

$$St_A = \frac{0.0689}{2Pr^{2/3}} \frac{1}{\overline{R}^{0.42}}$$

To account for compressibility effects employing a reference temperature at which the properties of the flow are evaluated, has been used successfully for flat plate and cone flow. Poll[53] has suggested that for the attachment line a reference temperature defined by the relationship

$$T_A = 0.1 T_w + 0.69 T_{aw} + 0.3 T_e$$

is the most appropriate for attachment line flows.

The expressions for laminar and turbulent attachment line heating in compressible flow then become

$$St_A = \frac{q}{\rho_\infty U_\infty (h_{aw} - h_w)} = \frac{0.571}{Pr^{2/3}} \sqrt{\left(\frac{\rho_A T_A}{\rho_\infty T_*} \right)} \sqrt{\left(\left(\frac{\mu_*}{\mu_\infty} \right) \frac{U_1}{Re_{d_\infty}} \right)} \sin \lambda \cos^{1/2} \lambda$$

for laminar flows and

$$St_A = \frac{q}{\rho_\infty U_\infty (h_{aw} - h_w)} = \frac{0.0689}{2Pr^{2/3}} \left(\frac{\rho_A T_A}{\rho_\infty T_*} \right)^{0.79} \left(\left(\frac{\mu_*}{\mu_\infty} \right) \frac{U_1}{Re_{d_\infty}} \right)^{0.21} \sin^{1.58} \lambda \cos^{0.21} \lambda$$

With the above discussion in mind it is interesting to compare the pressure and heating levels for the type IV/III interactions for sweep angles of 0, 15 and 30 degrees shown in Figures 36, 45a and 45b respectively. We see that there is reduction
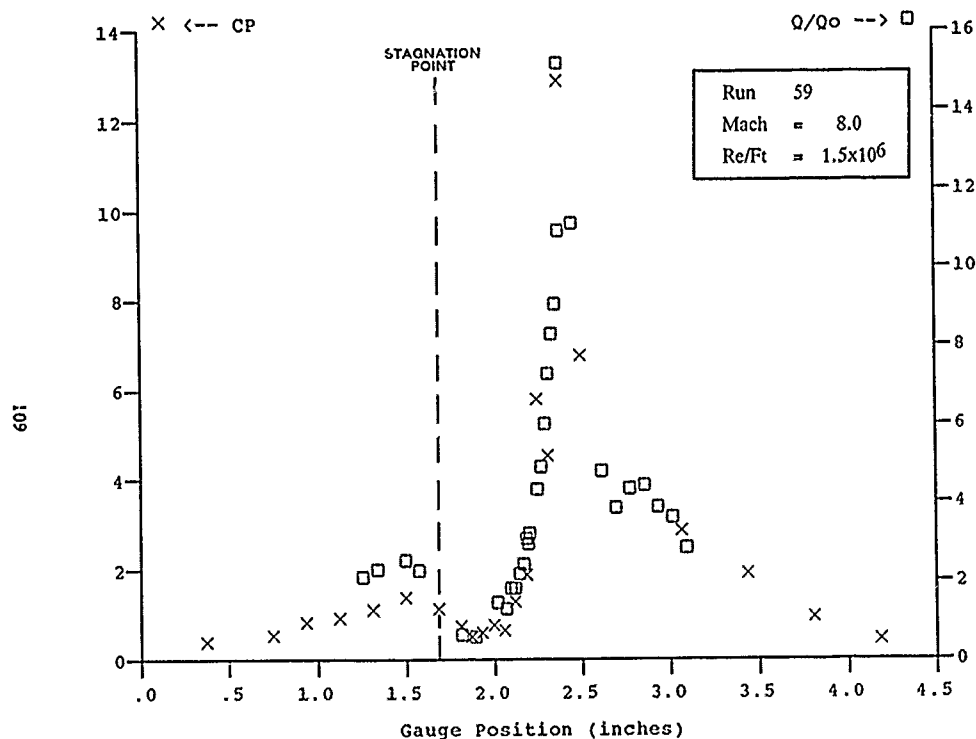
Figure 45A HEAT AND PRESSURE DISTRIBUTION IN SHOCK/SHOCK INTERACTION
REGIONS INDUCED BY A 12.5° SHOCK GENERATOR SWEPT AT 15°
OVER A 3-INCH DIAMETER CYLINDER AT MACH 8 FOR RUN 59
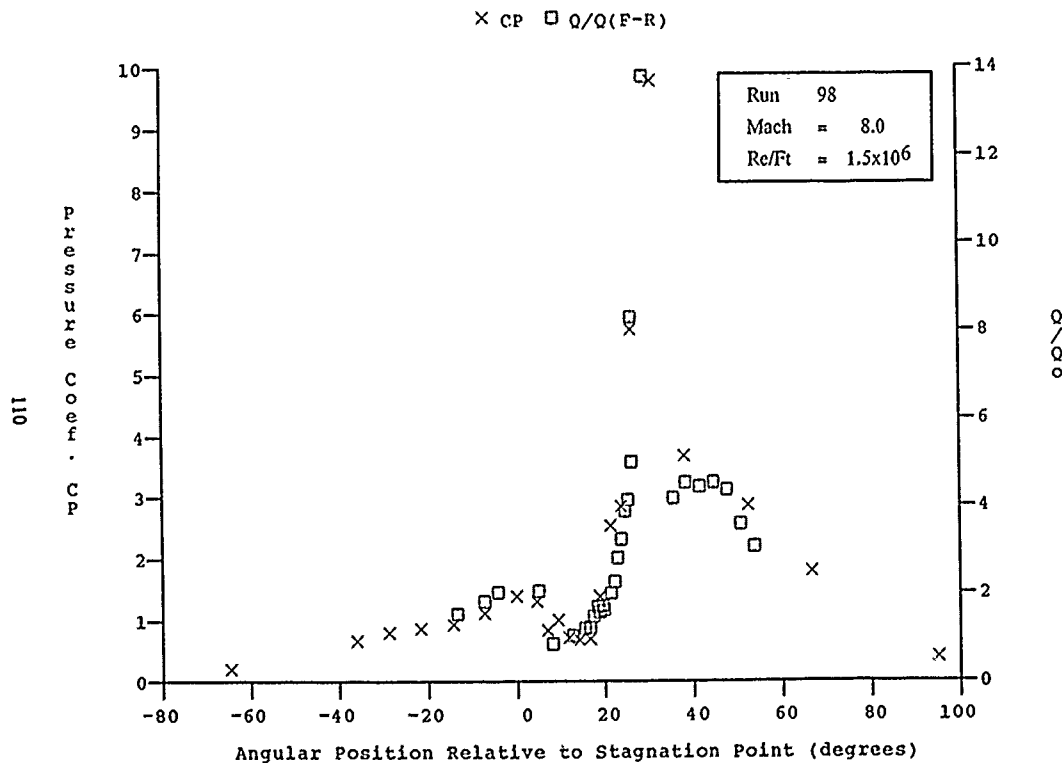
Figure 45b HEAT AND PRESSURE DISTRIBUTION IN SHOCK/SHOCK INTERACTION
REGIONS INDUCED BY A 12.5° SHOCK GENERATOR SWEPT AT 30°
OVER A 3-INCH DIAMETER CYLINDER AT MACH 8 FOR RUN 98

in heating of between 20 and 30 percent when the cylinder is swept 30 degrees. More definitive and detailed measurements are required however before we can define the changes in flow field and aerothermal loads in swept interaction regions. In particular, experiments are required in higher Mach numbers flow were the interactions are completely laminar.

8.   CONCLUSIONS

A study has been presented of the aerothermal characteristics of two-dimensional shock/shock interactions generated by single and multiple shock incidence on a cylindrical bow shock. These studies were conducted at Mach 8 to 19 in the Calspan 48-inch Shock Tunnel. The severity of the heating loads requires the use of insulated models and short test times to prevent distortion from lateral heat conduction. In the first of two studies reported here, the detailed measurements of the distribution of heat transfer and pressure were made for Types III and IV interactions in laminar flows at Mach 8 to 19. The measurements at Mach 11 to 19 indicated that the severity of the interaction increased with transition and increasing Mach number, as suggested from simple models. The measurements at Mach 8 are believed influenced by shear layer transition. The laminar measurements should provide a detailed data base for code validation. However, some Type IV interactions where maximum heating occurs can also be unstable and, therefore, may be difficult to predict with accuracy. The studies of multiple shock interaction demonstrated that the largest heat loads are generated on the cylinder if the shocks coalesce before they are incident on the cylinder. While the flow fields and aerothermal loads generated by multiple shock impingement will provide excellent test cases for code prediction, the peak heating loads are significantly less than for a single shock of the same strength. Due to the low Reynolds numbers at which transition occurs in these flow fields from either single or multiple shock/shock interactions, coupled with the occurrence of flow instabilities for Type IV interactions, it will be difficult to accurately predict such flows over a large and important part of the flight regime.

9. REFERENCES

1. Edney, B., "Anomalous Heat Transfer and Pressure Distributions on Blunt Bodies at Hypersonic Speeds in the Presence of an Impinging Shock," FFA Report 115, Aeronautical Research Institute of Sweden, 1968.

2. Keyes, J.W. and Hains, F.D., "Analytical and Experimental Studies of Shock Interference Heating in Hypersonic Flow," NASA Report TN D-7139, May 1973.

3. Craig, R.R. and Ortwerth, P.J., "Experimental Study of Shock Impingement on a Blunt Leading Edge with Application to Hypersonic Inlet Design," AFAPL Report TR-71-10, April 1971.

4. Holden, M.S., "A Review of Aerothermal Problems Associated with Hypersonic Flight," AIAA 24th Aerospace Sciences Meeting, Reno, Nevada, AIAA Paper 86-0207, January 1986.

5. Birch, S.F. and Keyes, J.W., "Transition in Compressible Free Shear Layers," AIAA Journal Spacecraft, Vol. 9, No. 8, August 1972.

6. Watts, Joe D., "Flight Experience with Shock Impingement and Interference Heating on the X-15-2 Research Airplane", NASA TM X-1669, 1968.

7. Korkegi, R., "Survey of Viscous Interactions Associated with High Mach Number Flight," AIAA J. Vol. 9, No. 5, May 1971.

8. Newlander, R.D., "Effects of Shock Impingement on the Distribution of Heat-Transfer Coefficients on a Right Circular Cylinder at Mach Numbers of 2.65, 3.51 and 4.44." NASA TN D-642, 1961.

9. Carter, H.S. and Carr, R.E., "Free-Flight Investigation of Heat Transfer to an Unswept Cylinder Subjected to an Incident Shock and Flow Interference From an Upstream Body at Mach Number Up to 5.50." NASA TN D-9908.

10. Francis, W. Leon, "Experimental Heat-Transfer Study of Shock Impingement on Fins in Hypersonic Flow," J. Spacecraft and Rockets, Vol. 2, No. 4, July-Aug. 1965, pp. 630-632.

11. Beckwith, I.E., "Experimental Investigation of Heat Transfer and Pressures on a Swept Cylinder in the Vicinity of its Intersection with a Wedge and Flat Plate at Mach Number 4.15 and High Reynolds Numbers." NASA TN D-2020, 1964.

12. Bushnell, D.M., "Interference Heating on a Swept Cylinder in Region of Intersection with a Wedge at Mach Number 8," NASA TN D-3094, 1965.

13. Bushnell, D.M., "Effects of Shock Impingement and Other Factors on Leading-Edge Heat Transfer," NASA TN D-4543, 1968.

14. Jones, R.A., "Heat-Transfer and Pressure Investigation of a Fin-Plate Interference Model at a Mach Number of 6," NASA TN D-2028, 1964.

15. Siler, L.G. and Deskin, H.E., "Effect of Shock Impingement on the Heat-Transfer and Pressure Distributions on a Cylindrical-Leading Edge Model at Mach Number 1911," AEDC-TDR-64-228, 1964.

16. Gulbran, C.E. et al, "Heating in Regions of Interfering Flow Fields. Part II - Leading Edge Shock Impingement," AFFDL TRG5-49, Jan. 1967, PT II, Air Force Flight Dynamics Lab.

17. Gulbran, C.E. et al, "Heating in Regions of Interfering Flow Fields Part I - Twc- and Three-Dimensional Laminar Interactions at Mach 8," AFFDL TR 65-49, Part I, 1965, Air Force Flight Dynamics Lab.

18. Knox, C.E., "Measurements of Shock-Impingement Effects on the Heat-Transfer and Pressure Distributions on a Hemicylinder Model at Mach Number 19", AEDC-TR-65-245, U.S. Air Force, Nov. 1965.

19. Ray, A.D. and Palko, R.L., "An Investigation of the Effects of Shock Impingement on a Blunt Leading Edge." AEDC-TR-65-153, July 1965.

20. Hiers, R.S. and Loubsky, W.J., "Effects of Shock-Wave Impingement on the Heat Transfer on a Cylindrical Leading Edge," NASA TN D-8859, Feb. 1967.

21. Morris, D.J. and Keyse, W.J., "Computer Programs for Predicting Supersonic and Hypersonic Interference Flow Fields and Heating," NASA TM X-2725, May 1973.

22. Keyes, J.W. and Morris, D.J., "Correlations of Peak Heating in Shock Interference Regions at Hypersonic Speeds," Journal of Spacecraft and Rockets, Vol. 9, No. 8, Aug. 1972, pp. 621-623.

23. Rogers, C.E., "Experimental Investigation of Leading-Edge Shock Impingement and Interaction Heating on a 1/80 Scale Model of a NASA Straight Wing Orbiter Configuration at Mach Numbers 8 and 16", CAL No. AA-2977-V-1, Aug. 1971.

24. Lanning, W.D. and Hung, F.T., "Shuttle Ascent and Shock Impingement Aerodynamic Heating Studies (Aerodynamic Heating Data from Shock Impingement Studies Simulating Space Shuttle Ascent)," NASA CR 123538, 1971.

25. Uselton, J.C., "Fin Shock/Boundary-Layer Interaction Tests on a Flat Plate with Blunted Fins at M = 3 and 5." AEDC-TR-113, U.S. Air Force, June 1967.

26. Kaufman II, L.G. and Korkegi, R.M., "Shock Impingement Caused by Boundary Layer Separation Ahead of Blunt Fins," ARL 72-118, Aug. 1972.

27. Tannehill, J.C., Holst, T.L., and Rakich, J.V., "Numerical Computation of Two-Dimensional Viscous Blunt Body Flows with an Impinging Shock," AIAA J., Vol. 14, No. 2, Feb. 1976.

28. Tannehill, J.C., Holst, T.L., Rakich, J.F. and Keyes, J.W., "Comparison of a Two-Dimensional Shock Impingement Computation with Experiment," AIAA J. Vol. 14, No. 4, April 1976.

29. Holden, M.S., Weiting, A.R., Moselle, J.R., and Glass, C., "Studies of Aerothermal Loads Generated in Regins of Shock/Shock Interaction in Hypersonic Flow," AIAA 08-0477, Jan. 1988.

30. Holden, M.S., et al, "Studies of Aerothermal Loads Generated in Regions of Shock/Shock Interaction in Hypersonic Flow," AIAA 87-0477, Jan. 1988.

31. Young, F., Kaufman, L. II, and Korkegi, R., "Experimental Investigation of Interactions Between Blunt Fin Shock Waves and Adjacent Boundary Layer at Mach Numbers 3 and 5," ARL 68-0214, Dec. 1968.

32. Kaufman, L.II and Korkegi, R., "Shock Impingement Caused by Boundary Layer Separation Ahead of Blunt Fins," ARL 72-0118, Aug. 1972.

33. Haslett, R.A. and Kaufman, L. II, et al, "Interference Heating Due to Shock Impingement," AFFDL TR-72-66, July 1972.

34. Ginoux, J.J. and Matthews, R.D., "Effects of Shock Impingement on Heat Transfer," VKI TN 87, May 1973.

35. Ginoux, J.J. and Matthews, R.D., "Effects of Shock Impingement on Heat Transfer, Part II. Effect of Shear Layer Impingement on Pressure and Heat Transfer Rate Distribution Around a Cylinder," AFOSR-TR-74-0714, Feb. 1974.

36. Holden, M.S., "Accurate Vehicle Experimental Dynamics Program - Final Report," SAMO-TR-79-47, Aug. 1979.

37. Holden, M.S., "Maneuvering Vehicle Aerodynamics Experiment Program," BMO-TR-82-16, Nov. 1981.

38. Holden, M.S., "Studies of Heat-Transfer and Flow Characteristics of Rough and Smooth Indented Nose Shapes, Part I," AIAA 86--384, Jan. 1986.

39. Jones, R.A., Bushnell, D.M. and Hunt, J.L., "Experimental Flow Field and Heat Transfer Investigation of Several Tension Shell Configurations at Mach Number of 8," NASA TN D-3800, Jan. 1967.

41. Klopfer, G.H. and Yee, H.C., "Viscous Hypersonic Shock-on-Shock Interaction on Blunt Cowl Lips," AIAA Paper 88-0233, January 1988.

42. Stewart, J.R., Thareja, R.R., Wieting, A.R., and Morgan, K., "Application of Finite Element and Remeshing Technique to Shock Interference on a Cylindrical Leading Edge," AIAA Paper 88-0368, January 1988.

40. Wieting, A.R. and Holden, M.S., "Experimental Study of Shock Wave Interference Heating on a Cylindrical Leading Edge at Mach 6 and 8," AIAA 22nd Thermophysics Conference, Honolulu, Hawaii, AIAA Paper 87-1511, June 1987.

43. Lees, L., Reeves, G.L., "Supersonic Separated and Reattaching Laminar Flows," I. General Theory and Application to Adiabatic Boundary Layer/Shock-Wave Interactions, AIAA J., 2, 1907, (1964).

44. Holden, M.S., "Theoretical and Experimental Studies of the Shock Wave-Boundary Layer Interaction on Curved Compression Surfaces," Proceedings of the Symposium on Viscous Interaction Phenonema in Supersonic and Hypersonic Flow, Hypersonic Research Laboratory, Aerospace Research Laboratories, 7-8 May 1969.

45. Bushnell, D. and Weinstein, L., "Correlation of Peak Heating for Reattachment of Separated Flows," J. Spacecraft and Rocket 5, 1111, 1968.

46. Kemp, N., Rose, P., and Detra, R., "Laminar Heat Transfer Around Blunt Bodies in Disassociated Air", JAS, Vol. 26, July 1959, pp. 421-430.

47. Needham, D.A., Elfstrom, G.M., and Stollery, J.L., "Design and Operation of the Imperial College Number 2 Hypersonic Gun Tunnel," I.C. Aero Report 70-04, May 1970.

48. Enkenhus, K.R. and Parazzoli, C., "The Longshot Free-Piston Cycle, Part I - Theory," von Karman Inst. for Fluid Dynamics, Technical Note 51, November 1968.

49. Fay, J.A. and Riddell, F.R., "Theory of Stagnation Point Heat Transfer in Dissociated Air," Journal of the Aeronautical Sciences, Vol. 25, No. 2, February 1958.

50. "Calspan Hypersonic Shock Tunnel, Description and Capabilities Brochure," 1975.

51. Holden, M.S., "Shock-Wave Turbulent Boundary Layer Interactions in Hypersonic Flow," AIAA 72-74, Jan. 1972.

52. Glass, C.E., Holden, M.S., Wieting, A.R., "Effect of Leading Edge Sweep on Shock-Shock Interference at Mach 8", AIAA-89-0271, January 1989.

53. Poll, D.I.A., "The Development of Intermittent Turbulence on a Swept Attachment-Line Incluidng the Effects of Compressibility," The Aeronautical Quarterly, Vol. XXXIV, Feb. 1983, pp. 1-23.

54. Seymour, P.J., "Techniques for Evaluation of Unsteady Heat Flux From Film Gauges," Master of Science Thesis at University of Buffalo, 1982.

Appendix A
A REVIEW OF THE CHARACTERISTIC OF REGIONS OF SHOCK WAVE/
BOUNDARY INTERACTION FOR LAMINAR AND TURBULENT HIGH SPEED FLOWS
WITH HEAT TRANSFER

1.   INTRODUCTION

In both laminar and turbulent flows, the aerothermal loads associated with viscous/inviscid interaction or shock/boundary layer interaction present the most serious design problems, and at the same time are the most difficult to compute with accuracy. In supersonic flows, regions of shock wave/boundary layer interaction have the largest impact on aerodynamic load. In hypersonic flow, the large thermal loads and gradients generated in turbulent shock interaction regions are of the greatest concern. However, the large dynamic loads associated with intrinsic unsteadiness of these flows, of course, also remain a principal concern. Although the aerothermal heating loads associated with regions of shock wave/turbulent boundary layer interaction will present significant problems in hypersonic flight at low altitudes, it may be the laminar viscous/inviscid interaction and flow separation, which occurs in high altitude hypervelocity flight, which provides fundamental limitations on the performance of maneuvering hypersonic vehicles, and in particular those employing airbreathing propulsion systems. The effectiveness of jet interaction and flap control systems and intakes and combustors of hypersonic ramjets may be seriously reduced as the compression surfaces are in essence "faired in" by viscous/inviscid interaction and flow separation in the high altitude regime. The use of boundary layer control to alleviate such problems is made difficult in hypersonic flow because the major portion of the mass and momentum in a laminar boundary layer over a cooled wall is contained at its outer edge. Since the severe heating loads in shock/boundary layer on certain key components may mandate the use of ablative- or transpiration-cooled thermal protection systems, the effects of surface roughness and blowing on the characteristics of shock/boundary layer interaction over such components can constitute important and, as yet, unresolved problems.

Over the past 15 years, there has been a massive increase in computational capabilities with which to make a direct assault on the Navier-Stokes equations, and in particular, the problem of describing regions of shock wave/boundary layer interaction with embedded regions of recirculating flows. Such methods have met with great success in describing regions of shock wave/laminar boundary layer interaction in

hypersonic flow, as described in Section 2. Some questions for flows with large embedded separated regions have been resolved by three-dimensional computation of these flows. For turbulent flows, predictions based on Navier-Stokes code have met with little real success when attempting to describe separated interaction regions in hypersonic flow and, as discussed in Section 3, it is not clear whether the problem lies in the turbulence modeling, compressibility effects, or in the intrinsically unsteady characteristics of these flows.

In this brief review of laminar and turbulent shock wave/boundary interaction phenomenon with heat transfer, we focus on the salient characteristics of two classes of interaction phenomena. The first is generated by flows over compression surfaces where the shock waves are developed "internally" and the upstream influence and flow separation are developed by "free interaction" between the viscous and inviscid flow. The second is induced by the impingement of a shock wave onto the boundary layer. We first discuss the general features and prediction of laminar interaction flows. We then describe the corresponding, but significantly different fluid mechanic mechanisms, associated with turbulent boundary layer subjected compression corners and incident shocks, and the simple and advanced computational methods which have been used to predict the characteristics of these flows.

2.   SHOCK WAVE/LAMINAR BOUNDARY LAYER INTERACTION

2.1   INTRODUCTION

While predicting the detailed structure of turbulent separated regions of shock wave/boundary layer interactions is one of the most difficult tasks in the design of control systems and inlets on airbreathing vehicles, it is the occurrence of large separated regions induced in laminar viscous/inviscid interactions which may present the greatest problems. Closely coupled with the viscous/inviscid phenomena are the effects of leading edge bluntness and boundary layer displacement, which are always a factor in realistic designs for high altitude hypersonic vehicles. The viscous/inviscid interaction at the leading edges of flat plates and cones have been studied extensively for both sharp and blunt tips. The reduction in density and momentum close to the wall induced by bluntness effects, coupled with the intrinsic feature of the laminar hypersonic boundary layer (concentrating the mass and momentum at its outer edge) may make it very difficult (but nevertheless important) to employ boundary layer control. For continuum flows in the absence of real gas effects, the prediction methods developed by Cheng[1] and subsequently verified in a number of experimental studies provide a very simple way of predicting the distribution of pressure and heat transfer to sharp and blunted bodies. Typical correlations for leading edge interaction measurements are shown in Figures 1, 2 and 3. For gross design purposes, prediction based on these models would be more than adequate. However if the leading edges are transpiration or ablatively cooled and if the detailed structure of the shock layer is required, more sophisticated codes must be employed. The predictions on the Navier-Stokes equations, which have carefully handled in the shock/viscous layer very close to the leading edge, should therefore provide accurate predictions.

2.2   GENERAL FEATURES OF LAMINAR INTERACTION REGIONS

Maintaining a fully laminar region of shock wave/boundary layer interaction in supersonic flows has proved difficult. However, the increased stability of the laminar boundary in hypersonic flow coupled with lower Reynolds numbers associated with high altitude flight has made laminar regions of viscous/inviscid interaction of significant practical importance. A number of important features are observed in laminar interaction regions which are associated with the extensive nature of the interaction regions, and the effects of nose tip bluntness, and surface curvature. In hypersonic

flows, the pressure rise along a region of viscous/inviscid interaction can extend over twenty boundary layer thicknesses downstream of the interaction, as illustrated in Figure 4, for both attached and separated flows. Pressure rises of over two orders of magnitude occur through the almost isentropic expansion in the reattachment compression region, and in contrast to turbulent interactions, large overshoots in heat transfer and pressure are observed in this region. Correlations of the pressure rise to induce incipient separation and the plateau pressure in the separated regions of these flows are presented in Figures 5 and 6. Employing a blunt leading edge can significantly reduce the pressure recovery on the compression surface, as illustrated in Figure 7. It is clear that maintaining thin leading edges is an important feature of an inlet design. It is interesting to note, as illustrated in Figure 7, that while the pressure and heat transfer through the interaction region are strongly influenced by nose tip bluntness, boundary separation occurs at approximately the same wedge angle, although at a significantly lower overall pressure rise. Correlations of bluntness effects on the characteristic of these flows are given in Figures 8 and 9. The effects of surface curvature on boundary layer separation was studied in References 2 and 3. It has also been found that, while in turbulent flows, introducing small surface curvature dramatically increased the pressure rise to induce incipient separation, as illustrated in Figures 10 and 11, surface curvature has little influence on separation in laminar hypersonic flows.

2.3 PREDICTION TECHNIQUES

There have been two basic approaches to predict size and properties of laminar attached and separated interaction regions in separated flows. The first is to employ the first or second order boundary layer equations, coupled through equations describing a displacement surface to the outer inviscid flow-viscous/inviscid interaction flow models. The second is to employ the full (or slightly reduced) Navier-Stokes equations; here there is no need to include the interaction modeling. While the first approach is now virtually obsolete, it is interesting to review its conceptual aspects. Most of the viscous interaction models have their roots in the early studies of Howarth[4], Lighthill[5], and Owatitsch and Weighardt[6] who attempted to understand and model the mechanism of upstream influence. While it was initially believed that upstream influence could be described in terms of upstream propagation through the subsonic region of the boundary layer, experimental studies demonstrated significantly larger upstream influence in laminar flow than predicted from such models. For laminar flows it was shown that upstream influence and flow separation could be described with good accuracy

by a model in which the viscous layer grew by mutual interaction with the outer inviscid flow. Using a semi-empirical modification of the Crocco-Lees[7] method based on this "free interaction" model, Glick[8] was able to successfully describe the properties of a complete shock-induced separated region. To eliminate some of the semi-empirical features of Glick's method, Honda[9] and later Lees and Reeves[10], added a third equation, the moment of momentum equation, and obtained a generally good agreement with measurements in supersonic separated flows over adiabatic walls. To predict laminar viscous interaction regions under highly-cooled wall conditions and the associated reattachment heating, Holden[11] added the integral form of the energy equation to the equations for mass, momentum, and moment of momentum employed by Honda, using Cohen and Reshotko's[12] similar solutions as proposed by Lees and Reeves. Reasonably good agreement was found between theory and experiment at Mach numbers in the low hypersonic range. At high Mach numbers, Holden showed that the normal pressure gradients must be included in the description of hypersonic interaction regions to describe such flows. A comparison between Holden's theory and the measurements of skin friction, pressure and heat transfer made on the flat-plate, $18°$-wedge is shown in Figure 12. Incorporating $\partial p / \partial y$ into the formulation enabled a solution to be obtained where previously artifices, such as the super-subcritical jump, would have to be employed to overcome the problems inherent in conventional boundary layer theory for cooled wall hypersonic flows. Such approaches have been made obsolete by the conduction of computer and algorithms successfully capable of efficiently solving the Navier-Stokes equation. However, a rapid prediction of the occurrence of separation and heat transfer in the reattachment regions of shock and wedge induced interaction regions can be made with the aid of the correlations shown in Figures 5, 6, 13, 14.

The explosive development of computing power and the numerical techniques for the direct solution of the Navier-Stokes equations for laminar flows has virtually eliminated contemporary efforts to model or correlate the characteristics of laminar separated flows. Beginning twelve years ago with explicit Navier-Stokes solutions by McCormack[13] for laminar separation in supersonic and hypersonic flow, there has been a continuing and rapid development which in 1989 is typified by the calculations by Rudy et al.[14] with a series of both explicit and upwind implicit Navier-Stokes codes. Examples of comparisons between the results of such computations and measurements in laminar shock- and wedge-interactions are shown in Figures 15 and 16. Here we see, as shown in earlier computations, that the solutions are capable of accurately predicting

the detailed surface and flow properties and the timewise develop of separated flow induced by incident shocks and compression corners.

These solutions, and those obtained in earlier numerical studies demonstrate that correctly gridding these flows, especially in the reattachment compression region, is an important factor in attaining accurate solutions. However, when a grid with adequate resolution is employed these solutions can accurately predict not only the distribution of flow and surface properties of two- and three-dimensional interaction but also the timewise development of these flows. An important next step is to provide guidelines to specify the grid spacing for the flows. Once this has been accomplished, it would appear that experimental studies of laminar viscous/inviscid interaction would be best concentrated on high temperature flows with chemistry and those bordering the noncontinuum flow regime. Understanding the flow mechanisms in shock wave/turbulent boundary layer interaction represents a far more fruitful area for experimental research.

3.   SHOCK WAVE/TURBULENT BOUNDARY LAYER INTERACTION IN HYPERSONIC FLOW

3.1   INTRODUCTION

Regions of shock wave/turbulent boundary layer interaction, in which large pressure gradients, flow separation and turbulent nonequilibrium flows are generated have traditionally been the testing ground of prediction techniques, particularly those based on the solution of the full Navier-Stokes equations where the recirculating flow can be handled "more exactly". However, despite the significant advances in computational techniques during the past decade, there remain significant gaps in our understanding and ability to model and predict regions of shock wave/boundary interactions in supersonic and hypersonic flows. At the heart of the problem lies the difficulty of describing the generation and development of turbulence in the extremely large pressure gradients developed across shock wave which penetrate the boundary layer and the associated problems of flow unsteadiness and compressibility. Also, many problems which have been ascribed to poor turbulence modeling may, in fact, stem from the grid selection or nature of the numerical scheme.

Much of the current experimental database on shock-induced turbulent separated flows comes from studies in which the time averaging characteristics of the instruments and recording equipment can provide a distorted view of the phenomena being examined. For example, if the separation shock is continuous in low frequency motion in a streamwise direction as suggested by earlier studies[42,43], the instantaneous pressure distribution for mean position of the separation shock might look as shown in Figure 17(a), whereas the time average pressure distribution would be as shown in Figure 17(c). The time-averaged measurements do not provide a meaningful picture of the violent shock-induced separation process. It is also debatable whether the time- or mass-averaged Navier-Stokes equation should be compared with the instantaneous distribution at the mean separation shock location, or the measurements averaged over a time period longer than the characteristic movements of the separation shock. The validity of using the time averaged Navier-Stokes equation to describe these flows is also in question.

3.2 STRUCTURE AND CHARACTERISTICS OF SHOCK WAVE/BOUNDARY LAYER INTERACTIONS

The mechanism of shock wave/turbulent boundary layer interaction and flow separation in hypersonic flows differs significantly from that in laminar flows particularly in the mechanism of upstream disturbance propagation. While in laminar flow, it is the interaction between the high momentum flow at the edge of the boundary layer and the incident shock wave or model surface (see Figure 4) which is the most important element in generating the adverse gradients leading to flow separation; in turbulent flows, the incident shock or wedge shock penetrates to the base of the boundary layer where a viscous/inviscid interaction takes place (see Figure 18). The series of photographs showing the development of a turbulent separated region with increased interaction strength are shown in Figure 18 and Figure 19.

The initial development of the separation region takes place by an elongation into the laminar sublayer, with the separation and reattachment shocks combining within the boundary layer to form a single shock. Only when the separation point has fed well forward of the junction is a well-defined plateau region formed. Then, in contrast to laminar interaction regions, the separation shock originates at the bottom of the boundary layer and is contained within the boundary layer until it coalesces with the reattachment compression process. In separated regions induced by

an externally generated shock, separation first takes place in the region where the incident shock strikes the laminar sublayer (see Figure 20). The separation point moves forward with increasing strength of the incident shock until the separation shock becomes visible in the inviscid flow downstream of the incident shock; as yet, separation is still downstream of the point where the incident shock passes through the edge of the boundary layer. For large incident shocks, boundary thickening occurs ahead of the incident shock when a large separated region is induced. However, as in wedge-induced separated regions, viscous/inviscid interaction takes place almost entirely within the original boundary layer. The structure wedge and shock-induced turbulent interaction regions at Mach 13 are very similar to those at Mach 8; however, as we might anticipate the viscous interaction region and the associated shocks are even more firmly embedded within the original boundary layer. We find little or no upstream influence ahead of the separation shock in hypersonic turbulent shock wave/boundary layer interactions.

Surface measurements with high frequency instrumentation indicated that turbulent separated regions were highly unsteady, and typically the separation point would oscillate in a streamwise direction with an amplitude of approximately one-quarter to one-third of the local boundary layer thickness, at frequencies in the range from 1 to 10 kHz (see Figure 21). While it is difficult to define separation for the general case of three-dimensional turbulent separated regions, for two-dimensional steady flow, we can define incipient separation as the condition where the mean skin friction is positive everywhere in the interaction region, but at one point is vanishingly small. Unfortunately, turbulent interaction regions in hypersonic flow are far from steady and the problem in these regions becomes how to define incipient separately in an unsteady flow. In the experimental studies by Holden[15], where dynamic measurements of the skin friction in turbulent interaction regions were made, the separation conditions were defined when the time average of surface shear at one point only on the surface was zero (see Figure 21). The unsteady character of the records from transducers in the recirculation region indicated it would be unrealistic to assume that a laminar sublayer model, in the conventional sense, could be used to describe the lower part of the recirculating region, as is done in some of the triple deck calculations. Surprising because of the very different flow field characteristics of the wedge incident shock interactions, the pressure rise to induce incipient separation was found to be independent of the mechanism inducing separation from Mach 6 to 13 as demonstrated in Figure 22. The mean distribution of skin friction, heat transfer and pressure to the wall's bounding, both shock- and wedge-induced interaction regions were similar for well separated flows

with identical total pressure rises. Both the pressures and heat transfer distributions are characterized by well-defined plateaus in the recirculation region and large gradients in the separation and reattachment regions. Again the plateau pressure was found to be independent of the type of interaction as shown in Figure 23. The maximum heat transfer rates generated in the reattachment regions of these flows is of considerable importance. It has been observed that for separated interaction regions the peak pressure and heat transfer in the reattachment region could be correlated in the form shown in Figure 24 for Mach numbers from 2 to 13. Figure 25 shows a correlation of incipient separation conditions determined in the studies at hypersonic speeds together with the measurements on adiabatic walls at supersonic speeds. With the exception of Kuehn's measurements, the effect of Reynolds number is weak. However, the studies of Kuehn,[16] Sterrett and Emery,[17], Holden[18], Elfstrom[19] and Appels[20] indicate that for $Re_\delta = 7 \times 10^5$ increasing the Reynolds number decreases the angle to promote separation or decreases the length of a separated region. Roshko and Thomke,[21] Law,[22] and Appels[23] find that increased Reynolds number increases the angle to promote separation or decreases the length of a separated region. However, Settles, et al[24] finds incipient separation remains uninfluenced by Reynolds number, while the scale of a separated interaction region decreases with increased Reynolds number. It remains to be determined how the method used to define incipient separation can be influenced by the trend observed. The reader is referred to the original papers by Roshko and Thomke[21], Law,[22] Settles, Bogdonoff and Vas[24] for a detailed debate on the validity of each other's techniques and data interpretation.

The influence of Reynolds number on occurrence of turbulent boundary layer separation and the size of two-dimensional separated regions remains weak and influenced principally by the characteristics of the upstream boundary layer. Most of the early studies of shock wave-turbulent boundary layer interaction were made in the turbulent boundary layer over a tunnel wall. The measurements of Green[25], Roshko and Thomke[21], Law[22], Settles, Bogdonoff and Vas[24], and Appels[23], all made under adiabatic wall conditions, indicate that increasing Reynolds number decreases the size of a turbulent separated region. In contrast, the studies of Chapman, Kuehn, and Larson[26], Kuehn[16], and Holden[18], Elfstrom and Appels[19] at hypersonic speeds, all conducted on "highly cooled" models mounted in the test section, have shown the opposite trend. As in the case of incipient separations, the answer may lie in changes in the equilibrium structure of a turbulent boundary layer with Reynolds number.

From the experimental studies of turbulent separation in hypersonic flows, it appears that turbulent separation may be a two-stage process. First, separation occurs in the sublayer with a very small recirculation region forming at the base of the turbulent boundary layer. This region is highly unsteady. As the strength of the interaction is increased, a larger turbulent recirculation region is formed and the size of this region increases rapidly with interaction strength. Thus, of the turbulent separation process, the occurrence of separation must depend upon the method chosen to detect it and the relative thickness of the laminar sublayer. For example, the relatively small thickness of the laminar sublayer in high Reynolds number, highly cooled flow should make the laminar separation harder to detect and of less importance than in slightly supersonic flows over adiabatic surfaces. The studies of Holden[18], Elfstrom, and Appels[19] in hypersonic flows over lightly cooled walls have demonstrated an abrupt change in the characteristics of upstream influence when a turbulent boundary layer "separates." In contrast, measurements by Spaid and Frishett[27], Appels[20], Roshko and Thomke[21], and Settles et al[24] made under conditions where the laminar sublayer exerts a far greater influence on the development of separation, demonstrate a less definitive separation process.

3.3 COMPARISONS WITH NAVIER-STOKES SOLUTIONS

The complexity of the flow field in regions of shock wave/turbulent boundary layer interaction is such that it is unrealistic to expect to describe such regions in any detail within the framework of the boundary layer equations. As discussed above, there are questions as to whether the time or mass averaged Navier-Stokes equations capture the basic fluid mechanics associated with the intrinsically unsteady nature of separated regions. In hypersonic flows the effects of compressibility on the structure and development of turbulence must also be considered.

In the rush to demonstrate that the Navier-Stokes codes can be successfully applied to describe a variety of interaction problems, very little emphasis has been placed on the demonstration that the numerical schemes are indeed an accurate representation of the equations upon which they are based. At a minimum, the sensitivity to grid size should be examined, and particularly for turbulent interacting flows, an analysis of the characteristic scale lengths, as that employed in triple deck theory, should be performed to aid in grid positioning. The complexity of turbulent interaction regions makes it essential that detailed information from experiments be used to

construct realistic models of the turbulent transport mechanisms. The aerothermal environment in hypersonic turbulent interacting flows makes delicate probing of these flows difficult, and because the typical natural frequencies in these flows are of the order of 500 kHz, the instrumentation and recording requirements are highly complex. While skin friction and heat transfer measurements are useful in the evaluation of turbulence modeling techniques, employing comparisons with pressure data to support the models used in a Navier-Stokes code is a weak "verification."

While there have been strenuous efforts to obtain predictions of two-dimensional and three-dimensional turbulent interaction regions, it is currently recognized that "successes" with "Navier-Stokes" code in describing some three-dimensional turbulent interactions regions is a result of the dominance of the pressure and inertial terms in these flows. In these latter comparisons (References 30 & 43) it was found that the modeling of turbulence could be changed without significantly changing the numerical solution. For two-dimensional interactions it appears the modeling of turbulence is more critical. To obtain good agreement for these latter flows, some very gross assumptions must be made in the turbulence model. Shang and Hankey[28], for example, chose to apply an empirical relationship (selected by matching the length of the separated region) to rapidly decrease the turbulent scale size through the interaction region. Horstmann[29], however, found the best agreement with Settles'[30] measurements in wedge-induced separated regions using a two equation model for turbulence scale size and vorticity. Working with this same turbulence model, however, Horstmann[29] was unable to predict the occurrence of separation on two incident shock/turbulent boundary layer configurations studied by Holden at Mach 11.2. As shown in Figures 26 and 27, both these flow fields are clearly separated and yet the numerical solution fails to predict the characteristic plateaus in either the heat transfer or pressure distributions. The modeling of turbulence in separated interaction regions at hypersonic Mach numbers should account for the effects of compressibility and the generation of turbulence by the unsteady movement of the incident and induced shocks as they traverse and interact with a major region of the turbulent boundary layer. Clearly, further detailed experimental work on insightful theoretical modeling is required to develop numerical prediction techniques which are capable of describing turbulent interaction regions in detail.

3.4   SWEPT WEDGE AND SKEWED SHOCK/BOUNDARY LAYER INTERACTION

In many practical situations the oblique shock would be swept thereby introducing crossflow into the interaction region. Experimental studies of this type have been conducted by Ericsson, Reding and Guenther[31], Settles and Perkins[32], and Settles and Teng[33]. Settles, who studied the interaction region over swept and unswept flat plate/wedge configurations in an adiabatic Mach 3 airflow, found that introducing crossflow increased the scale of the separated interaction region. Considerable effort was expended in this latter study to determine the Reynolds number scaling, and the length from the upstream tip of the wedge for the flow to become quasi-two-dimensional. However, the effect of changing the overall spanwise scale of the model on the scale of the interaction was not examined explicitly. The measurements of surface and pitot pressure through the interaction regions were in good agreement with solutions to the Navier-Stokes equations obtained by Horstmann[29]. More recently Holden[34] performed studies of crossflow effects on the size and properties of the interaction region induced by a swept-oblique-shock incident on a turbulent boundary layer over a flat plate at Mach 11 and $R_{e_L} = 30 \times 10^6$. Experiments were conducted for two strengths of incident shock, the first ($\theta SG = 12.5^\circ$) to generate a separated condition close to incipient separation, and the second ($\theta SG = 15^\circ$) to generate a well-separated flow. Distributions of heat transfer and pressure as well as schlieren photographs of the unswept or two-dimensional flow condition and the 30 degree swept condition are shown in Figures 28 and 29. It is clear from the well defined plateau regions in the distributions of pressure and heat transfer, as well as the well defined separation shock in the schlieren photograph, that a well separated region, extending two inches in length, is induced beneath the stronger incident shock. The measurements made of the distribution of heat transfer and pressure beneath the well separated flow induced by both the 12.5 degree and the 15 degree shock generators swept at angles of 0 and 30 (shown in Figures 28 and 29) indicated that the induced crossflow has little effect on the size and characteristics of the interaction regions. If there is a perceptible effect, it is a decrease in the length of the separated region with increased crossflow. The significant differences between Holden's and Settles' measurements of the variation of interaction length with sweep angle and those obtained in these studies are shown in Figure 30. While Settles finds an almost threefold increase in separation length at sweep angles of 40 degrees, Holden found 10 percent reduction in this length. Further studies are required to resolve this issue.

Section 4

REFERENCES

1. Cheng, H.K., Hall, J.G., Golian, T.C. and Hertzberg, A., "Boundary-Layer Displacement and Leading-Edge Bluntness in High Temperature Hypersonic Flow," J. Aero/Space Sci., Vol. 28, No. 5, May 1961.

2. Sterrett, J.R. and Emery, J.C., "Experimental Separation Studies of Two-Dimensional Wedges and Curved Surfaces at Mach Numbers of 4.8 to 6.2," NACA TND-1014.

3. Holden, M.S. and Moselle, J.R., "Theoretical and Experimental Studies of the Shock-Wave Boundary Layer Interaction on Compression Surfaces in Hypersonic Flow," Calspan Report No. AF-2410-A-1, October 1969. Also ARL 70-0002, January 1970.

4. Howarth, L., "The Propagation of Steady Disturbances in a Supersonic Stream Bounded on One Side by a Parallel Subsonic Stream," Proc. Camb. Phi. Soc. 1947, p. 44, Part 3.

5. Lighthill, M.J., "On Boundary-Layers and Upstream Influence. Part II. Supersonic Flows Without Separation," P.R.S.A., 1953, pp. 217 and 478.

6. Oswatitsch, K. and Wieghardt, K., "Theoretical Analysis of Stationary Potential Flows and Boundary-Layers at High-Speed, German Wartime Report, 1941." Translated as N.A.C.A. TM 1189.

7. Crocco, L. and Lees, L., "A Mixing Theory for the Interaction between Dissipative Flows and Nearly Isentropic Streams," J. Aero. Sci., Vol. 19, No. 10, pp. 649-676, October 1972.

8. Glick, H.S., "Modified Crocco-Lees Mixing Theory for Supersonic Separated and Reattaching Flows," J. Aero. Sci., Vol. 29, No. 10, pp. 1238-1244, October 1962.

9. Honda, M., "A Theoretical Investigation of the Interaction Between Shock Waves and Boundary Layers," J. Aero/Space Sci. 25, pp. 667-678, November 1958, Japan Tokyo Univ. Rep. Inst. High-Speed Mech. 8 1957, pp. 109-130.

10. Lees, L. and Reeves, B.L., "Supersonic Separated and Reattaching Laminar Flows: I. General Theory and Application to Adiabatic Boundary Layer-Shock Wave Interactions," GALCIT Tech. Report No. 3, October 1963.

11. Holden, M.S., "An Analytical Study of Separated Flow Induced Shock Wave-Boundary Layer Interaction," Calspan Report No. AI-1972-A-3, December 1965.

12. Cohen, C.B. and Reshotko, E., "Similar Solutions for the Compressible Laminar Boundary Layer with Heat Transfer and Pressure Gradient," NACA Report No. 1293, 1956.

13. Hung, C.M. and MacCormack, R.W., "Numerical Solutions of Supersonic and Hypersonic Laminar Flows Over a Two-Dimensional Compression Corner," AIAA Paper 75-2, January 1975.

14. Rudy, D.H., Thomas, J.L., Kumar, A., Gnoffo, P.A. and Chakravarthy, S.R., "A Validation Study of Four Navier-Stokes Codes for High-Speed Flows," AIAA Paper AIAA-89-1838, Buffalo, NY, June 12-14, 1989.

15. Holden, M.S., "Shock Wave Turbulent Boundary Layer Interaction in Hypersonic Flow," AIAA 10th Aerospace Sciences Meeting, San Diego, CA, 17-19 January 1972, AIAA-72-74.

16. Kuehn, D.M., "Experimental Investigation of the Pressure Rise Required for the Incipient Separation of Turbulent Boundary Layers in Two-Dimensional Supersonic Flow," NASA Memo 1-21-59A, Feb. 1959.

17. Sterrett, J.R. and Emery, J.C., "Experimental Separation Studies of Two-Dimensional Wedges and Curved Surfaces at Mach Numbers of 4.8 to 6.2," NACA TND-1014.

18. Holden, M.S., "Shock Wave-Turbulent Boundary Layer Interaction in Hypersonic Flow," AIAA 77-45.

19. Elfstrom, G.M., Coleman, G.T. and Stollery, J.L., "Turbulent Boundary Layer Studies in a Hypersonic Gun Tunnel," 8th Annual International Shock Tube Symposium, London, England, July 1971.

20. Appels, C. and Richards, B.E., "Incipient Separation of a Compressible Turbulent Boundary Layer," AGARD Conference Pre-Print No. 168 on Flow Separation.

21. Roshko, A. and Thomke, G. J., "Flare-Induced Separation Lengths in Supersonic, Turbulent Boundary Layers," AIAA Aerospace Sciences Meeting, Paper No. 75-6, 1975.

22. Law, C.H., "Supersonic Turbulent Boundary Layer Separation Measurements at Reynolds Numbers of 10^7 and 10^8, AIAA Journal, Vol. 12, No. 6, June 1974, pp. 794-797.

23. Appels, C., "Incipient Separation of a Compressible Turbulent Boundary Layer," von Karman Institute Technical Note 99, April 1974.

24. Settles, G.S., Bogdonoff, S.M. and Vas, I.E., "Incipient Separation of a Supersonic Turbulent Boundary Layer at Moderate to High Reynolds Numbers," AIAA Paper 75-7, 1975.

25. Green, J.E., "Interactions Between Shock Waves and Turbulent Boundary Layers," Progress in Aerospace Sciences, Vol. 11, pp. 235-340, Pergamon Press, Oxford, 1970.

26. Chapman, D.R., Kuehn, D.M. and Larson, H.G., "The Investigation of Separated Flows in Supersonic and Subsonic Streams with Emphasis on the Effects of Transition," NACA Report No. 1356, 1958.

27. Spaid, F. W. and Frishett, J.C., "Incipient Separation of a Supersonic Turbulent Boundary Layer Including the Effects of Heat Transfer", AIAA Paper, 1971.

28. Shang, J.S., Hankey, W.L. and Petty, J.S., "Three-Dimensional Supersonic Interacting Turbulent Flow Along a Corner," AIAA Paper 78-1210, July 1978; also AIAA Journal, Vol. 17, No. 7, July 1979, pp. 706-713.

29. Horstmann, C.C. and Hung, C.M., "Computations of Three-Dimensional Turbulent Separated Flows at Supersonic Speeds," AIAA Paper 79-2, January 1979.

30. Settles, G.S. and Horstmann, C.C., "Flowfield Scaling of a Swept Compression Corner Interaction--A Comparison of Experiment and Computation," AIAA-84- 0096, 22nd Aerospace Sciences Meeting, January 9-12, 1984.

31. Ericsson, L.E., Reding, J.P. and Guenther, R.A., "Effects of Shock-Induced Separation," Lockheed Missiles and Space Co., Sunnyvale, CA, L-87-69-1, July 1969.

32. Settles, G.S. and Perkins, J.J., "Upstream Influence Scaling of 2D & 3D Shock/Turbulent Boundary Layer Interactions at Compression Corners," AIAA-81-0331 19th Aerospace Sciences Meeting, January 12-15, 1981.

33. Settles, G.S. and Teng, H.Y., "Flow Visualization of Separated 3D Shock Wave/Turbulent Boundary Layer Interactions," AIAA-82-0229, 20th Aerospace Sciences Meeting, January 11-14, 1982.

34. Holden, M.S. "Experimental Studies of Quasi-Two-Dimensional and Three-Dimensional Viscous Interaction Regions Induced by Skewed-Shock and Swept- Shock Boundary Layer Interactions," Calspan Report No. 7018-A-2 Report Covering Period 15 January 1982 - 31 July 1984, July 1984.

35. Hall, J.G. and Golian, T.C., "Shock-Tunnel Studies of Hypersonic Flat-Plate Airflows," CAL Report No. AD-1052-A-10, AFOSR TR 60-142; AD 251084, December 1960.

36. Vidal, R.J. and Wittliff, C.E., "Hypersonic Low Density Studies of Blunt and Slender Bodies," Rarefied Gas Dynamics Third Symposium, Vol. II, Academic Press, 1962.

37. Vidal, R.J. and Bartz, J.A., "Surface Measurements on Sharp Flat Plates and Wedges in Low-Density Hypersonic Flow," CAL Report No. AF-2041-A-2, February 1968.

38. Holden, M.S., "Theoretical and Experimental Studies of Laminar Flow Separation on Flat-Plate Wedge Compression Surfaces in the Hypersonic Strong Interaction Regime," ARL 67-0112 (May 1967).

39. Holden, M.S., "Boundary Layer Displacement and Leading-Edge Bluntness Effects on Attached and Separated Laminar Boundary Layers in a Compression Corner, Part II: Experimental Study", AIAA J. Vol. 9, No. 1, pp. 84-93, January 1971.

40. Cheng, H.K. and Pallone, A.J., "Inviscid Leading-Edge Effect in Hypersonic Flows," Readers' Forum, J. Aerospace Sci., Vol. 23, No. 7, p. 700, July 1956.

41. Holden, M.S., "Experimental Studies of Quasi-Two-Dimensional and Three-Dimensional Viscous Interaction Regions Induced by Skewed-Shock and Swept-Shock Boundary Layer Interaction," Paper presented at the AIAA 19th Thermophysics Conference Snowmass, Colorado 25-27 June 1984, AIAA Paper AIAA-84-1677.

42. Dolling D.S. and Murphy, M., "Wall Pressure Fluctuations in a Supersonic Separated Compression Ramp Flowfield," AIAA-82-0986, AIAA/ASME 3rd Joint Thermophysics, Fluids, Plasma and Heat Transfer Conference, June 7-11, 1982.

43. Holden, M.S., "Shock Wave-Turbulent Boundary Layer Interaction in Hypersonic Flow," AIAA 10th Aerospace Sciences Meeting, San Diego, California, 17-19 January 1972, AIAA-72-74.

44. Knight, D., Horstmann, C.C., Shapey, B. and Bogdonoff, S., "The Flowfield Structure of the 3-D Shock Wave Boundary Layer Interaction Generated by a 20 Degree Sharp Fin at Mach 3" AIAA-86-343.

SYM	M	Re/IN	TW/To	
▼	11.7	14,100	0.179	
★	15.6	11,300	0.157	HOLDEN (Ref. 39)
✦	18.9	15,100	0.134	
⬦	16.1	28,000	0.122	
▷	14.6	37,000	0.122	HALL & GOLIAN
ᛒ	12.0	79,000	0.137	(Ref. 35)
⬢	11.4	16,000	0.118	
⊖	9.0	80,000	0.118	
○	14.7	11,400	0.079	VIDAL & WITTLIFF
△	14.4	4,800	0.078	(Ref. 36)
□	24.0	2,720	0.060	
⊞	20.2	4,270	0.064	
⊕	20.3	4,000	0.063	VIDAL & BARTZ
⊕	19.5	2,040	0.063	(Ref. 37)
▽	19.4	2,090	0.064	
△	20.3	1,130	0.064	
◁	13.6	2,200	0.099	
◊	14.4	5,500	0.099	HOLDEN (Ref. 38)
◇	14.8	14,000	0.099	
△	16.0	2,420	0.048	
▷	20.0	8,050	0.056	

$$\chi_{\in_x} = \in \left[0.664 + 1.73 \left(H_w/H_o \right) \right] M^3 \sqrt{C^*/R_{e_x}}$$

Figure 1   Correlation of pressure data on sharp flat plates

SYM	M	Re/IN	TW/To	
▼	11.7	14,100	0.179	
★	15.6	11,300	0.157	HOLDEN (Ref.39)
✦	18.9	15,100	0.134	
◈	16.1	28,000	0.122	
▶	14.6	37,000	0.122	HALL & GOLIAN (Ref. 35)
⊟	12.0	79,000	0.137	
⬤	11.4	16,000	0.118	
⊖	9.0	80,000	0.118	
○	14.7	11,400	0.079	VIDAL & WITTLIFF (Ref. 36)
△	14.4	4,800	0.078	
□	24.0	2,720	0.060	
⊞	20.2	4,270	0.064	
⊕	20.3	4,000	0.063	VIDAL & BARTZ (Ref. 37)
⦶	19.5	2,040	0.063	
▽	19.4	2,090	0.064	
⌂	20.3	1,130	0.064	
◁	13.6	2,200	0.099	
◊	14.4	5,500	0.099	HOLDEN (Ref. 38)
◇	14.8	14,000	0.099	
⬦	16.0	2,420	0.048	
▷	20.0	8,050	0.056	

y-axis: $\left[\in (0.664 + 1.73\, T_w / T_o)\, M^2 C_w \right] \times 10^{-1}$

STRONG INTERACTION THEORY (CHENG, Ref. 1)

FIRST ORDER WEAK INTERACTION THEORY $T_w/T_o = 0.04 - 0.15$

$$\chi_{\in_x} = \in \left[0.664 + 1.73 \left(H_w / H_o \right) \right] M^3 \sqrt{C^* / R_{e_x}}$$

Figure 2 Correlation of heat transfer data on sharp flat plates

$$\epsilon\left(0.664+1.73\ T_w/T_o\right)\left[K_\epsilon/\chi_{\epsilon_x}^2\right]M^3\,1/2\,C_f/\sqrt{\gamma_\infty'}\ x\ 10'$$

SYM.	t (IN)	M	RE/IN	
▯	0.200	19.8	8050	
⬡	0.710	19.8	8050	
◗	0.030	19.8	8050	CYLINDRICAL
◇	1.200	19.8	8050	LEADING EDGE
▽	0.080	19.8	8050	
⬗	0.080	19.8	2054	
△	0.710	19.8	8050	FLAT LEADING EDGE
⬡	0.007	19.8	8050	

CHENG'S ZERO ORDER THEORY (Ref. 1)

CHENG AND PALLONE (Ref. 40)

$$\left[\frac{K_\epsilon}{\chi_{\epsilon_x}^2}\right]\frac{p}{\gamma p_\infty}\ x\ 10^{-1}$$

$$\epsilon\left(0.664+1.73\ T_w/T_o\right)\left[K_\epsilon/\chi_{\epsilon_x}^2\right]M^3 C_H/\sqrt{\gamma_\infty'}$$

$$\chi_\epsilon/K_\epsilon^{2/3}=\frac{\epsilon\left[0.664+1.73\left(H_w/H_o\right)\right]M^3\sqrt{c^*/Re_x}}{\left[M^3 k\epsilon\left(t/\chi\right)\right]^{2/3}}$$
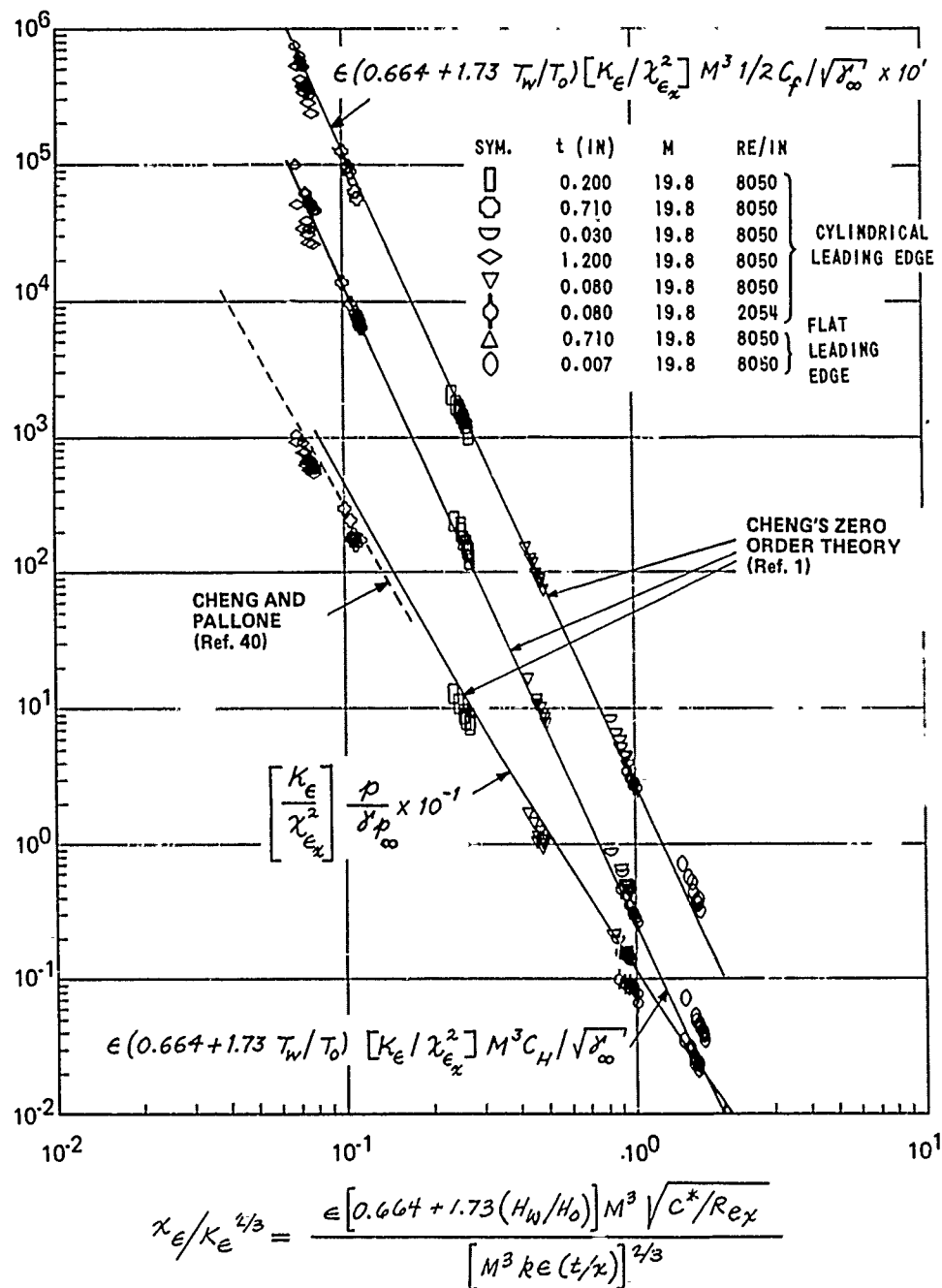
Figure 3   Correlation of skin friction, heat transfer, and pressure data on blunted flat plates (from Reference 1)
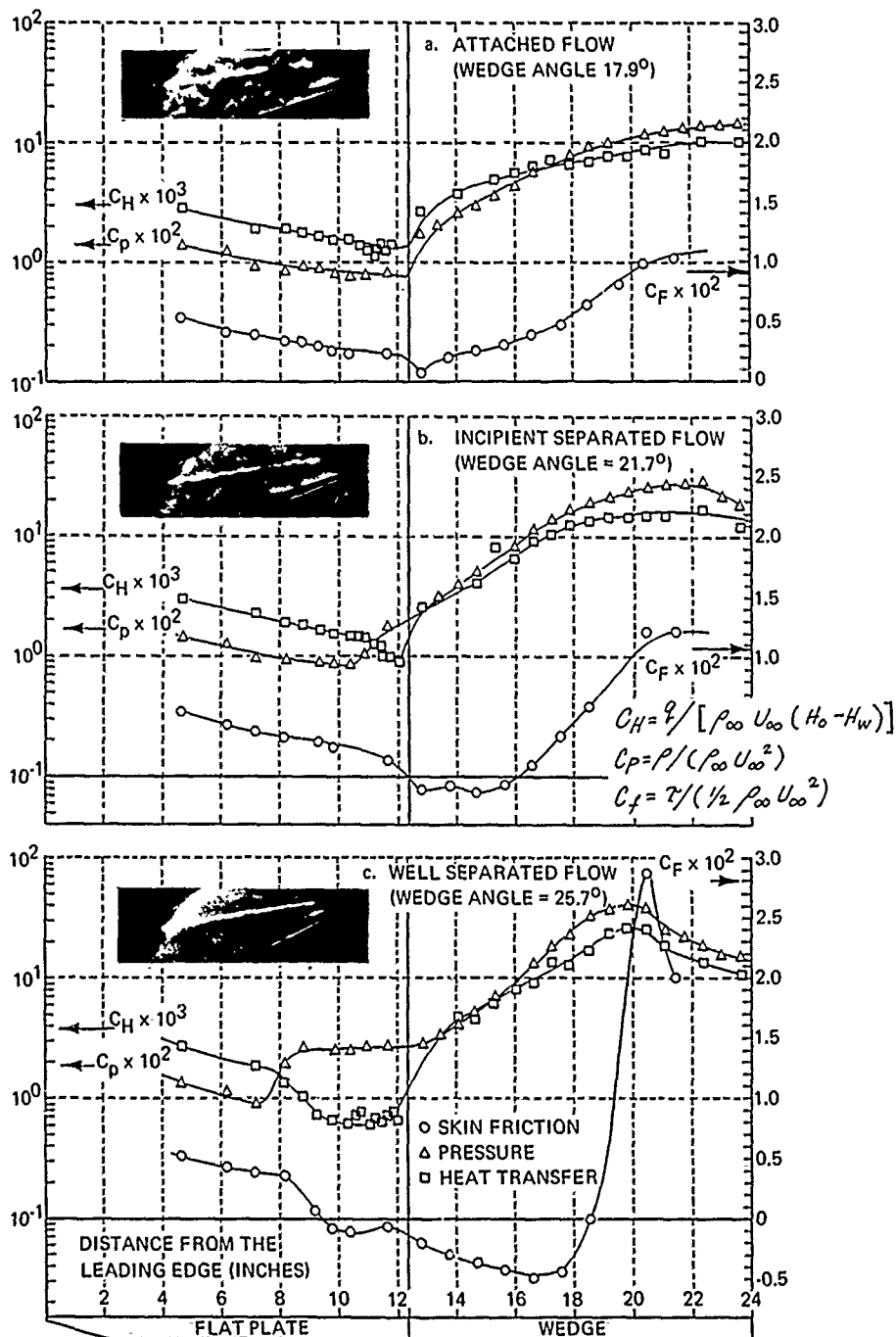
Figure 4   The distribution of skin friction, pressure and heat transfer on the 0.080" diameter blunt flat plate–wedge model ($M_\infty = 19.8$, Re/IN = 8.70 x 10^3)
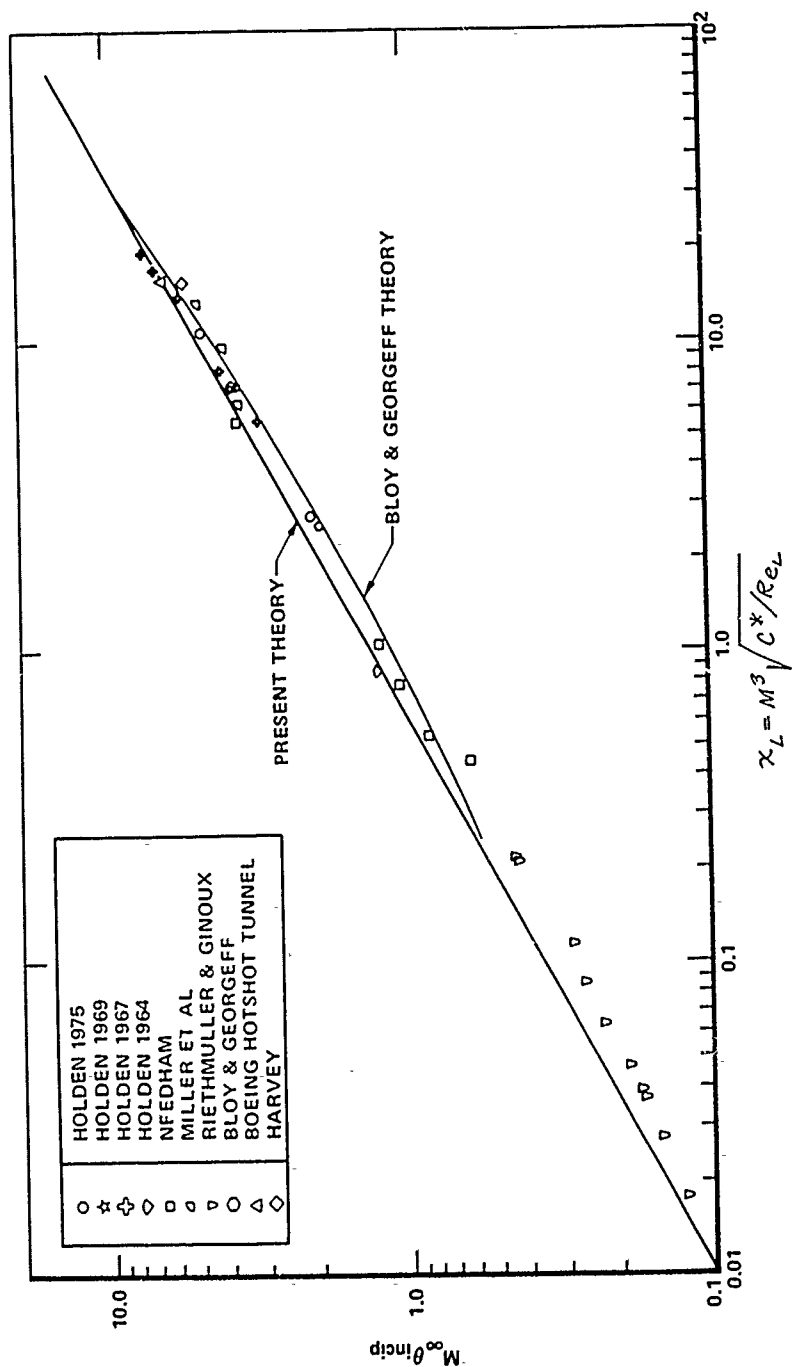
Figure 5   Correlation of incipient separation conditions for wedge-induced interactions
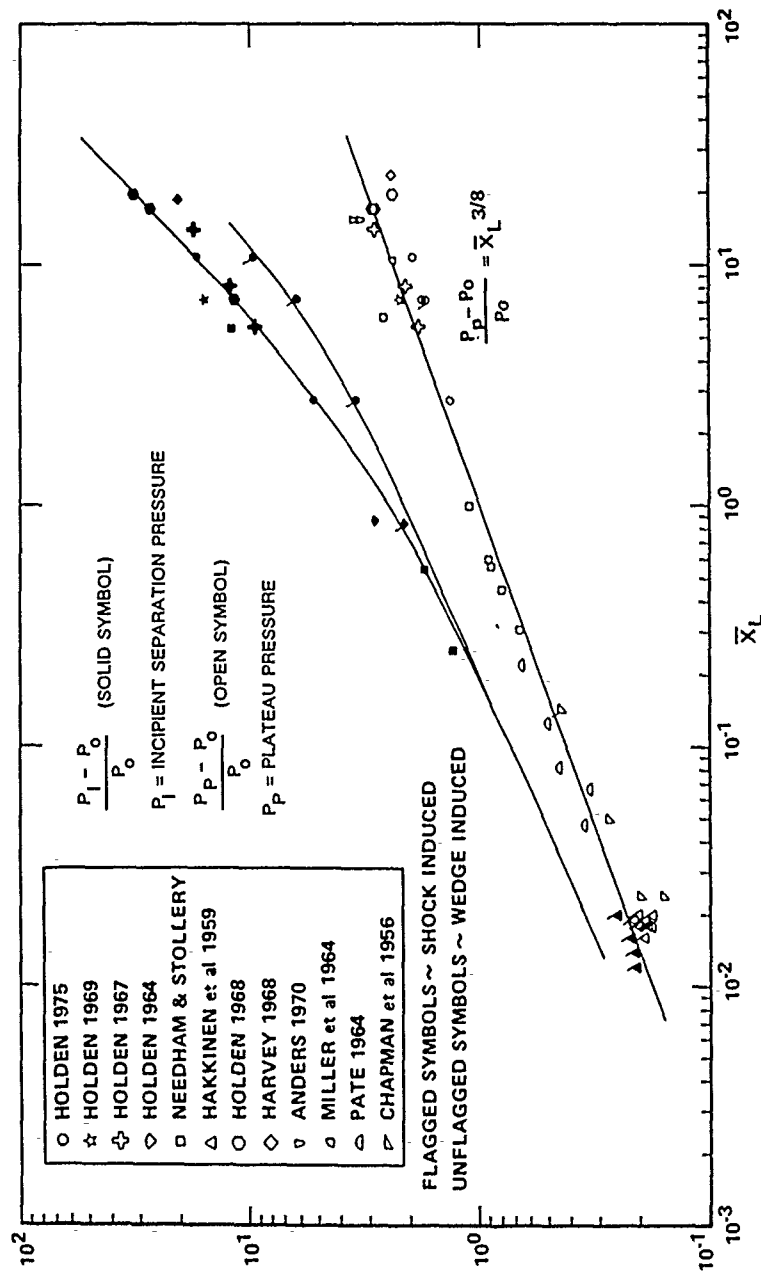
Figure 6 Correlation of the pressure rise to induce incipient separation
and the plateau pressure in shock and wedge–induced interactions
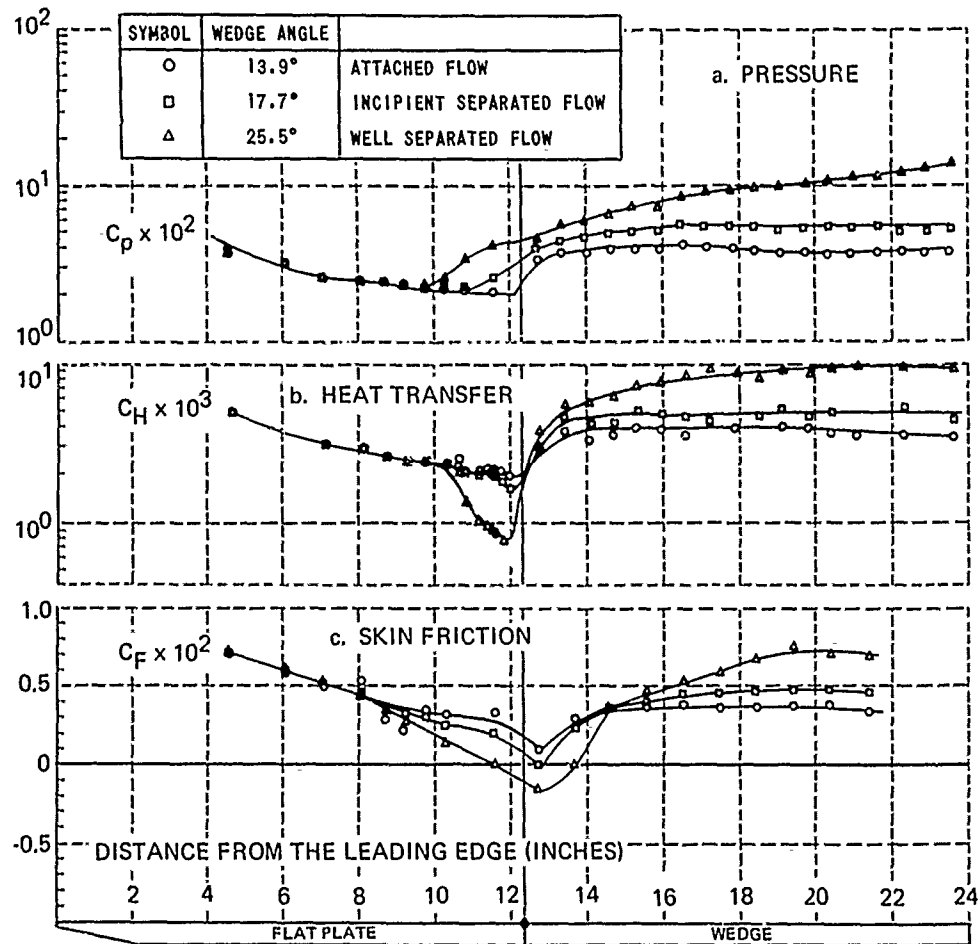
Figure 7 The distribution of skin friction, pressure and heat-transfer on the
0.71" flat-ended blunt flat plate-wedge model conditions
$(M_\infty = 19.8, Re/IN = 8.70 \times 10^3)$ (REF. 39)

SYM	t(IN)	Re/IN	M_∞
○	1.2D	8700	19.8
△	1.71F	8700	19.8
○	0.71D	8700	19.8
▽	0.80D	8700	19.8
◇	0.080D	8700	19.8
△	0.30D	8700	19.8
◊	0.080D	2055	19.8
◗	0.007F	8700	19.8

$$M_\infty \, \theta_{incip}\left(\frac{K_{\epsilon_L}}{\chi^2_{\epsilon_L}}\right) \qquad M_\infty \, \theta_{incip}\Big| = 4.32 \, \chi^{1/2}_{\epsilon_L}$$

$$\frac{p_{plateau}}{p_0}\left(\frac{K_{\epsilon_0}}{\chi^2_{\epsilon_0}}\right)^2$$

$$\chi_{\epsilon_L}\Big/K^{2/3}_{\epsilon_L} = \frac{\epsilon\left[0.664 + 1.73\left(H_w/H_0\right)\right]M^3\sqrt{C^*/Re_{\epsilon_L}}}{M^3 \, \epsilon \, k\left(t/L\right)}$$
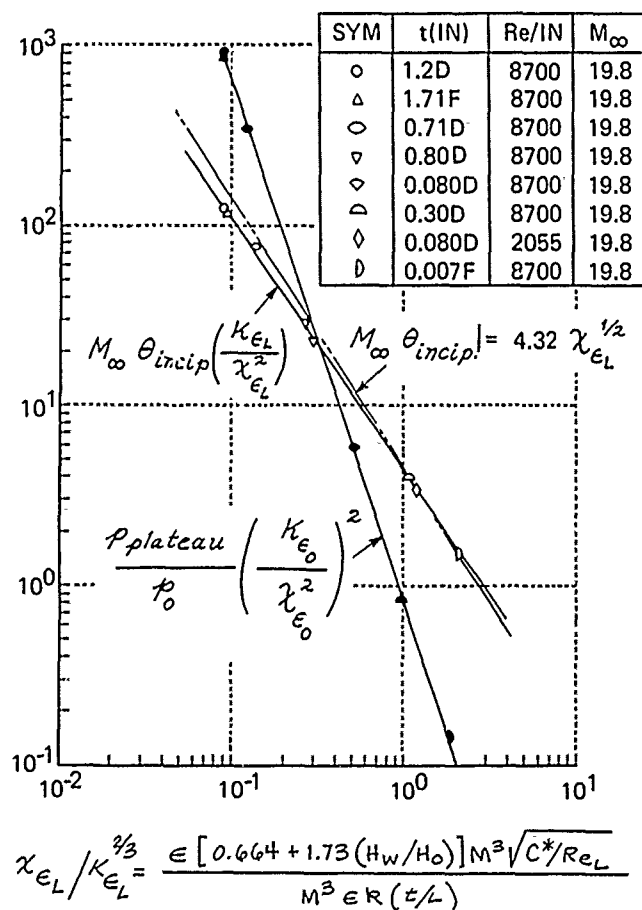
Figure 8   Correlation of the incipient separation and plateau pressure
on blunt flat plate-wedge compression surfaces

The data plotted show the legend:

o	1.20″ DIA.	◇	0.08″ DIA.
△	0.71″ FLAT	▷	0.03″ DIA.
□	0.71″ DIA.	○	0.007″ FLAT
◊	0.20″ DIA.	▽	0.0005″ DIA.

$M_\infty = 19.8$, $\theta = 25.7^\circ 40''$, $Re/IN = 8.70 \times 10^3$
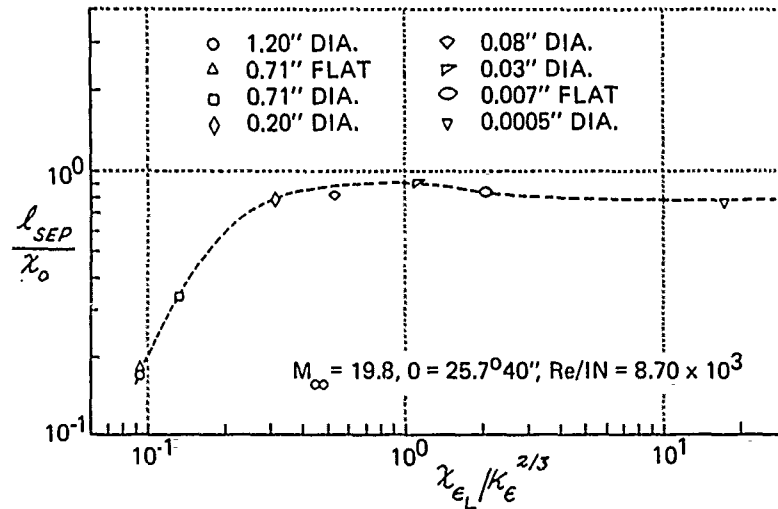
ℓ_{SEP} = LENGTH OF THE SEPARATED REGION

χ_o = DISTANCE TO THE BEGINNING OF THE INTERACTION

$$\frac{\in (0.664 + 1.73\, T_W/T_0)\, M^3\, (c^*/Re_L)^{1/2}}{(\in K\, M^3\, t/\chi)^{2/3}}$$

Figure 9 Variation of the length of well separated regions with the bluntness–viscous interaction parameter $X_\epsilon/K^{2/3}$ (REF. 39)
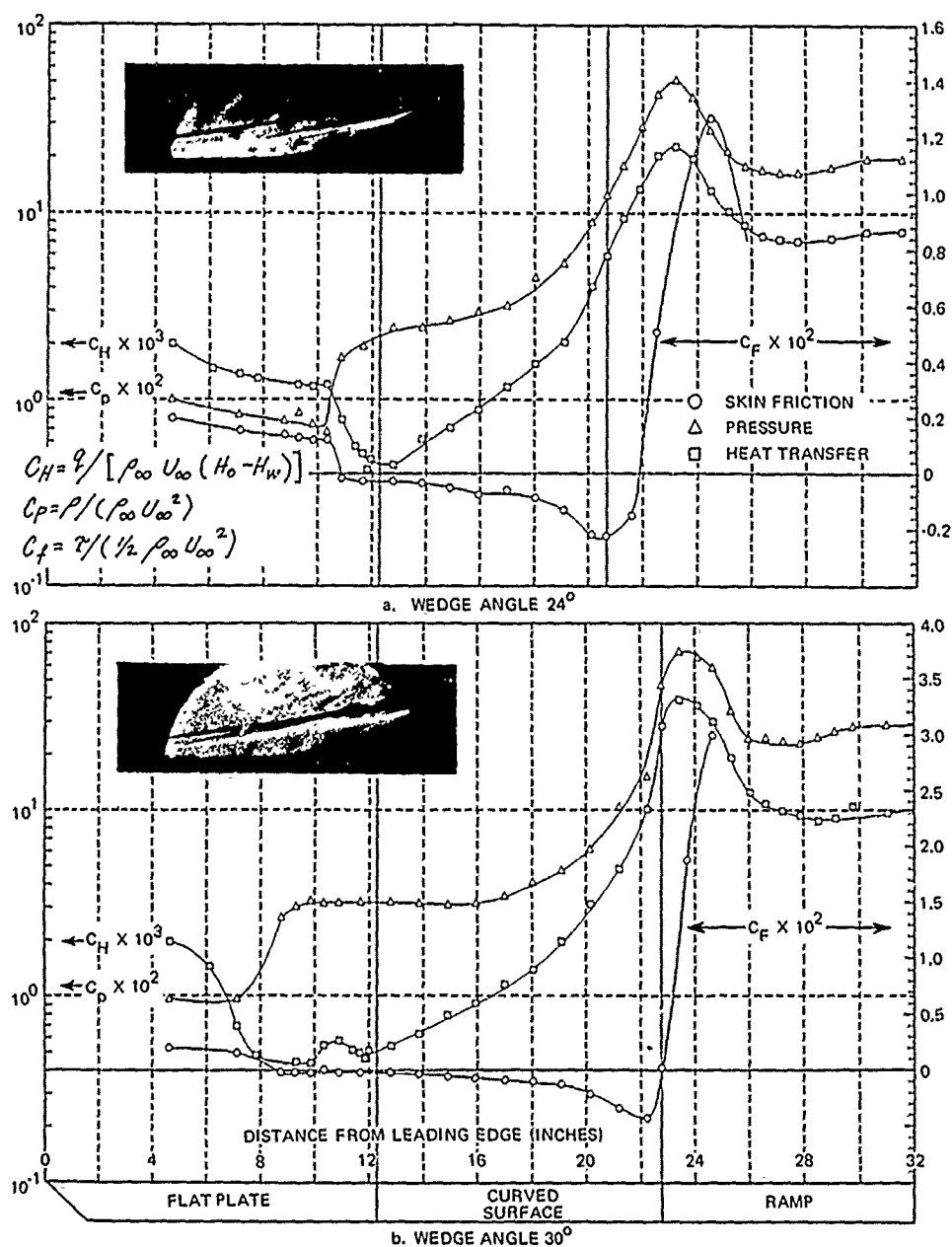
Figure 10 Skin friction, heat transfer and pressure distributions
on the flat plate–20"R cylindrical arc–wedge models
(M_∞=14.0, Re/FT = 7.2 x 10^4)
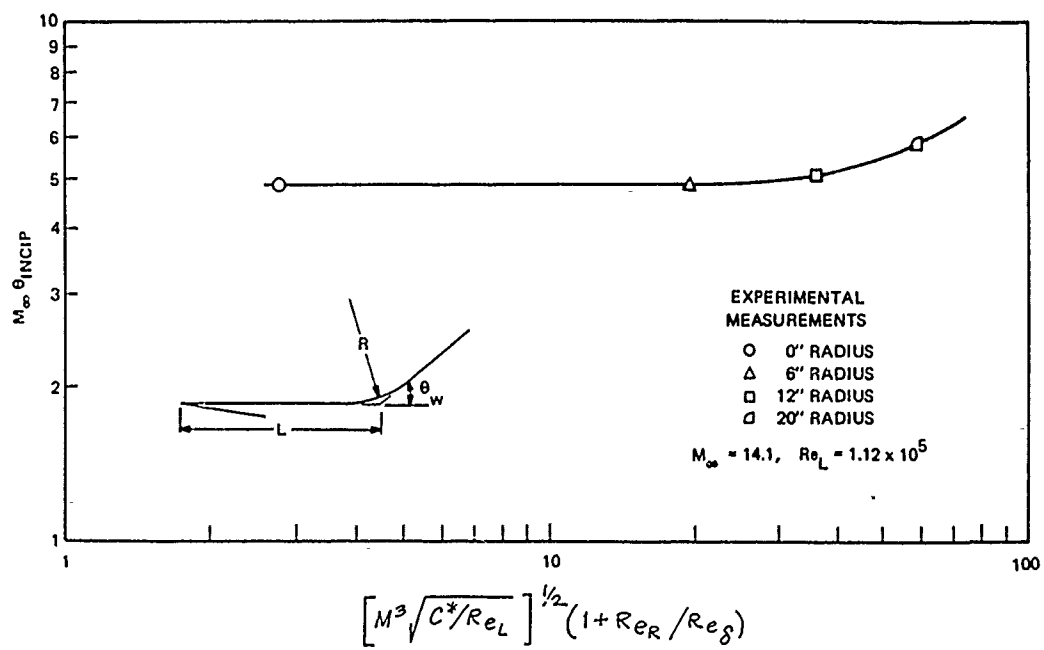
Figure 11 Incipient separation conditions for curved surfaces
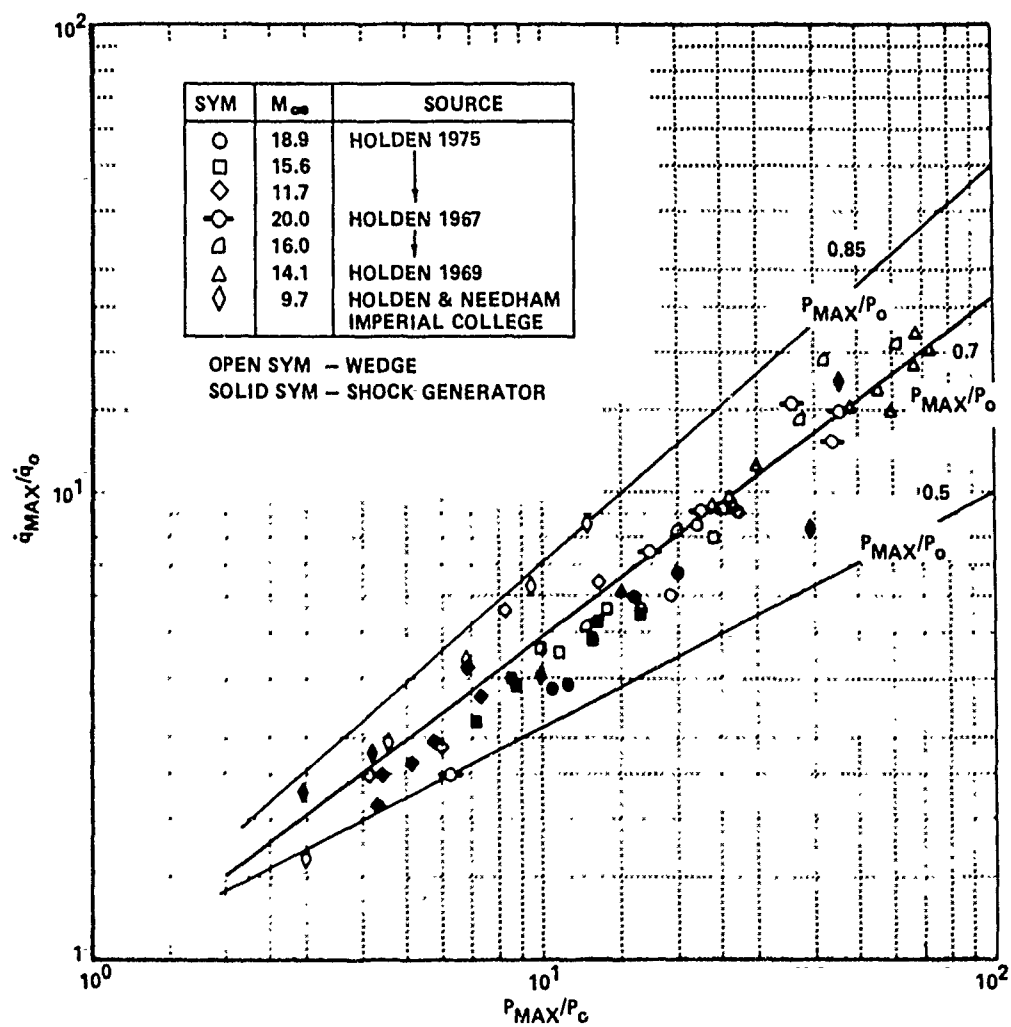
Figure 12 Heat transfer in shock and wedge-induced interaction regions
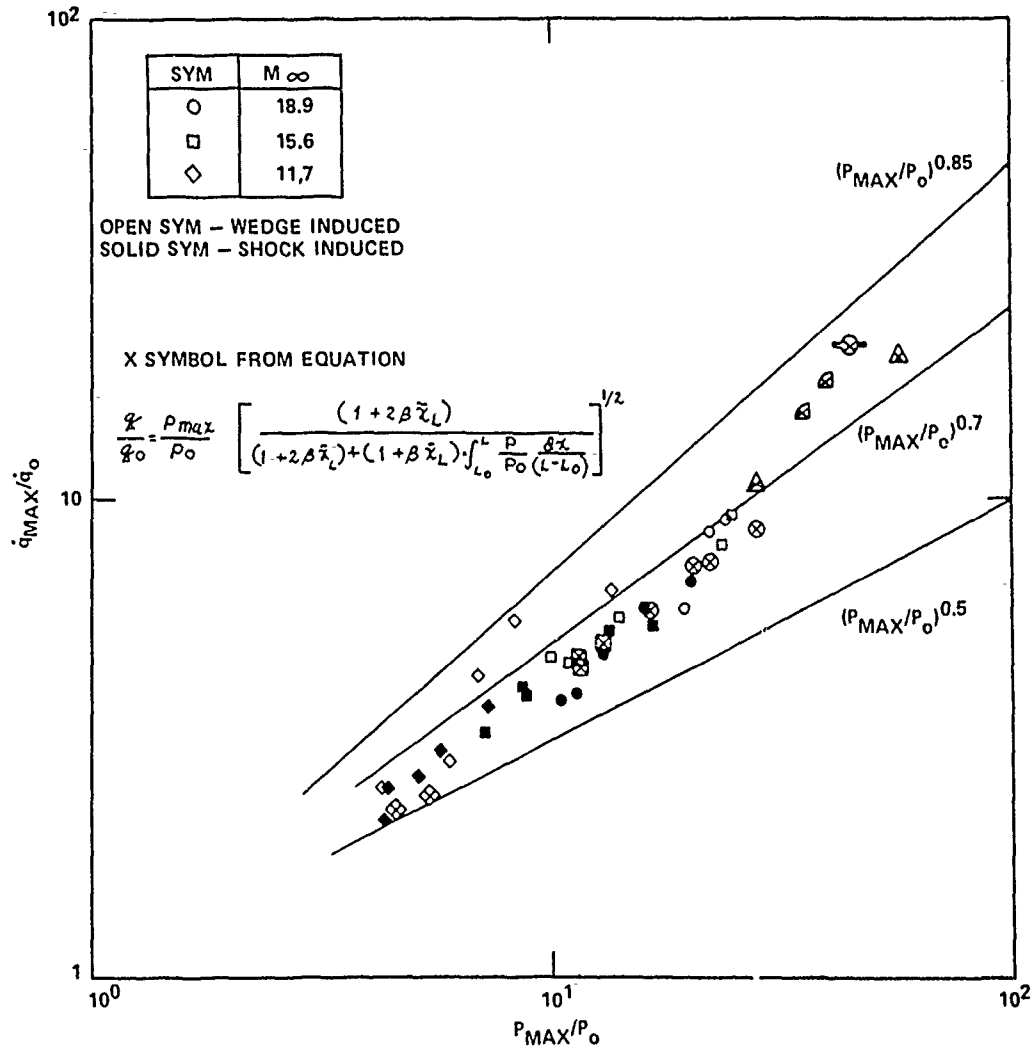
Figure 13 Comparison between simple correlation and prediction method
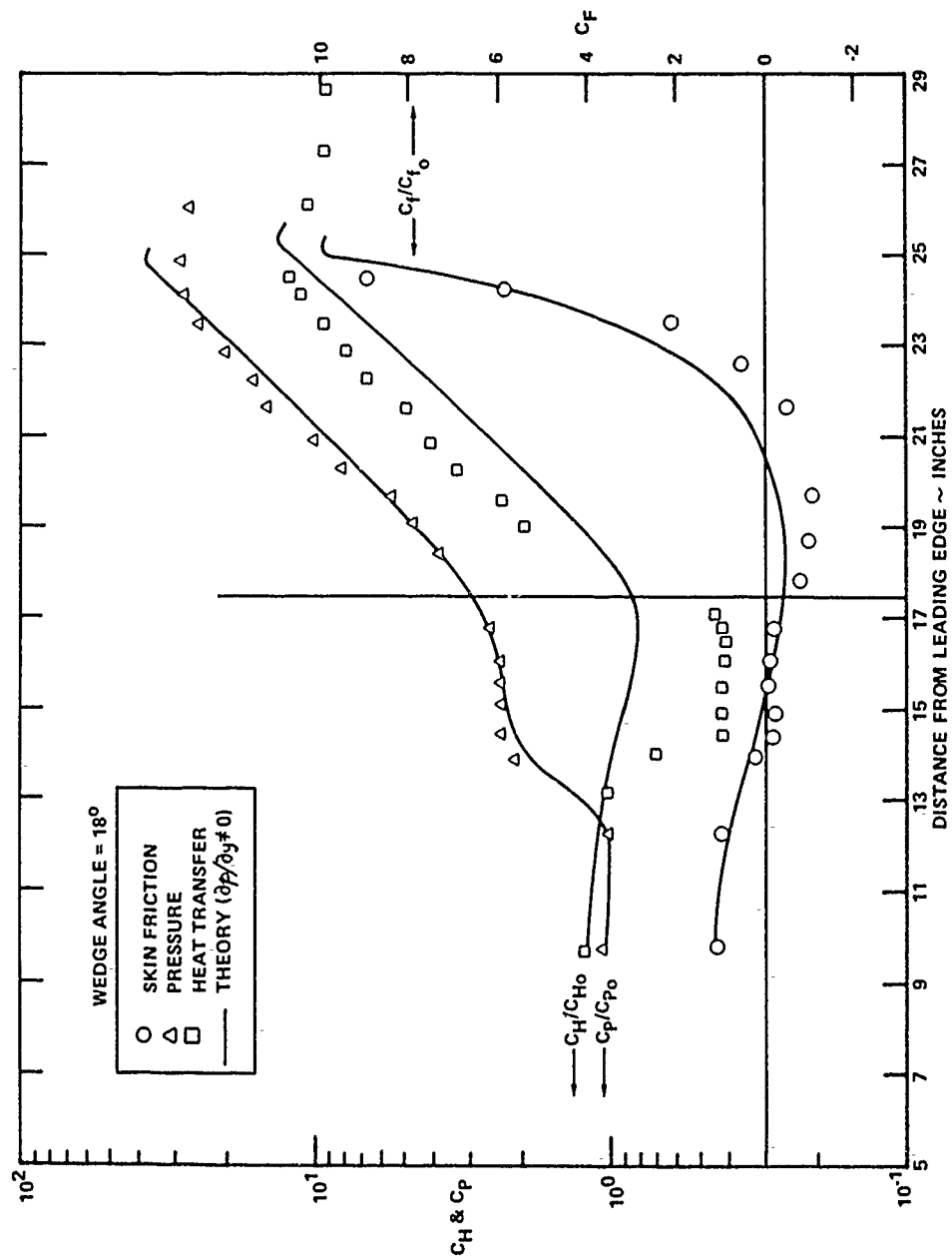
Figure 14 Comparison between the integral solution and experimental measurements in a well separated wedge-induced interaction region

(a) 3-D solution for 24°wedge. CFL3D.

(b) Surface pressure

(c) Surface heat transfer

(d) Skin friction
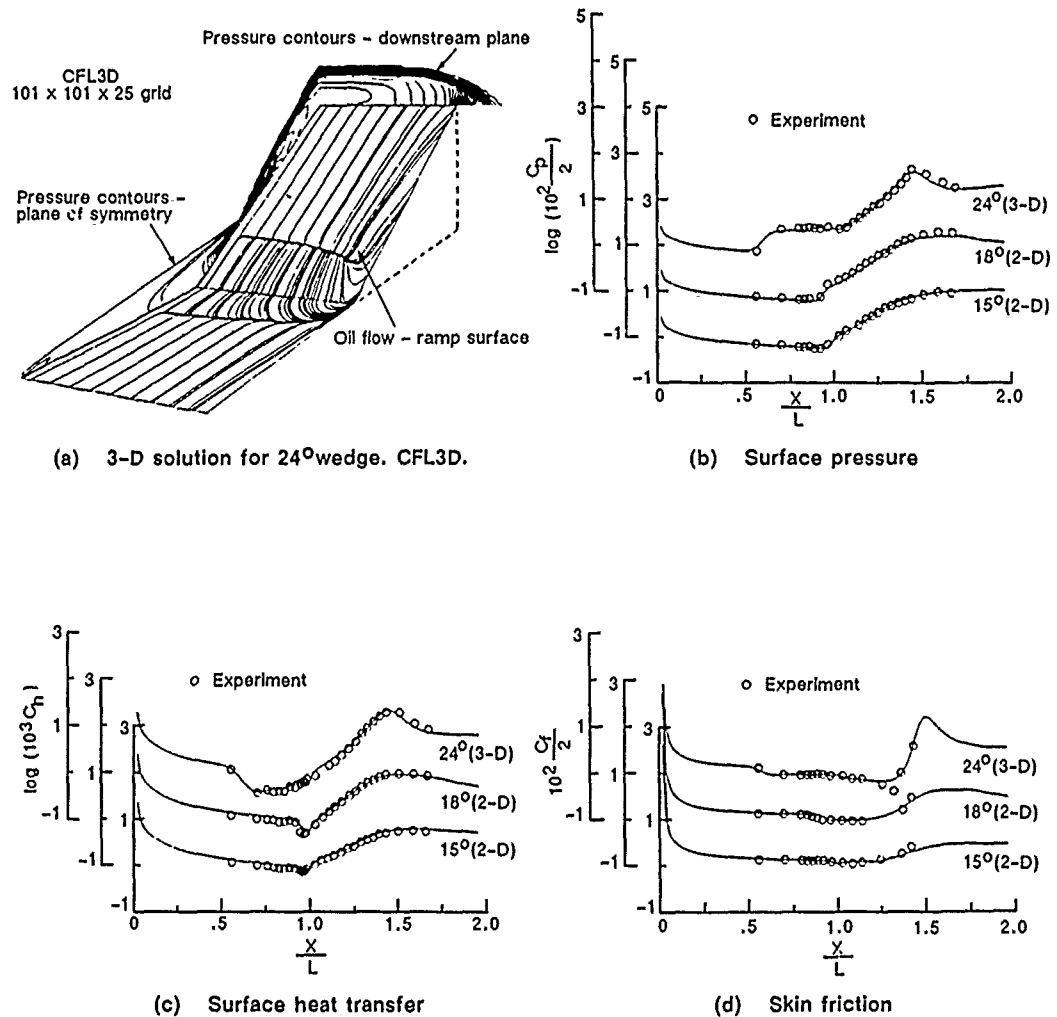
Figure 15 Comparisons between surface measurements and the results of the CFL3D Navier-Stokes Solutions for flows over a compression ramp. (Ref.14)

(a) Pressure

(b)　θ = 6.45°

(c)　θ = 6.45°
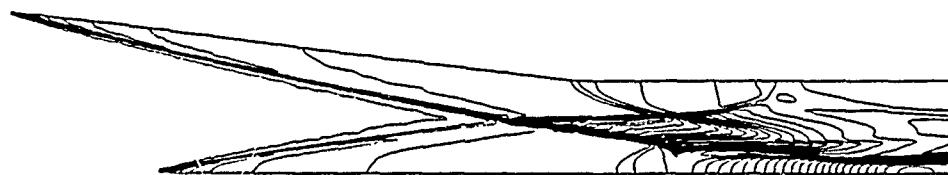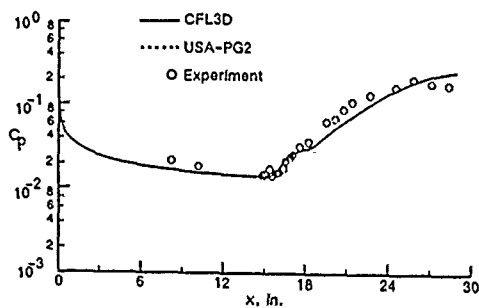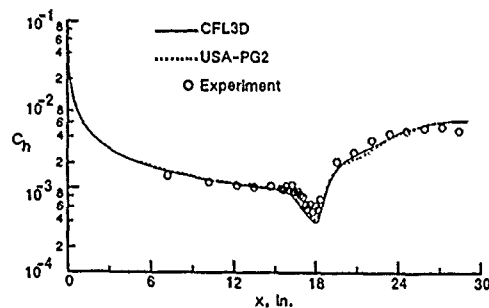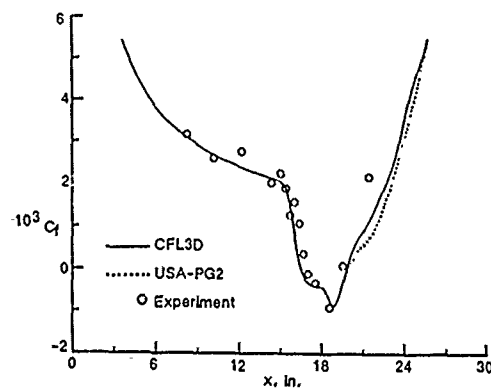
(d)　θ = 6.45°

Figure 16　Comparison between Navier–Stokes Solution and measurement
in shock induced laminar hypersonic separated flow.　(Ref. 14)

a) Mean flow configuration

b) Instantaneous pressure distribution

c) Time averaged pressure distribution
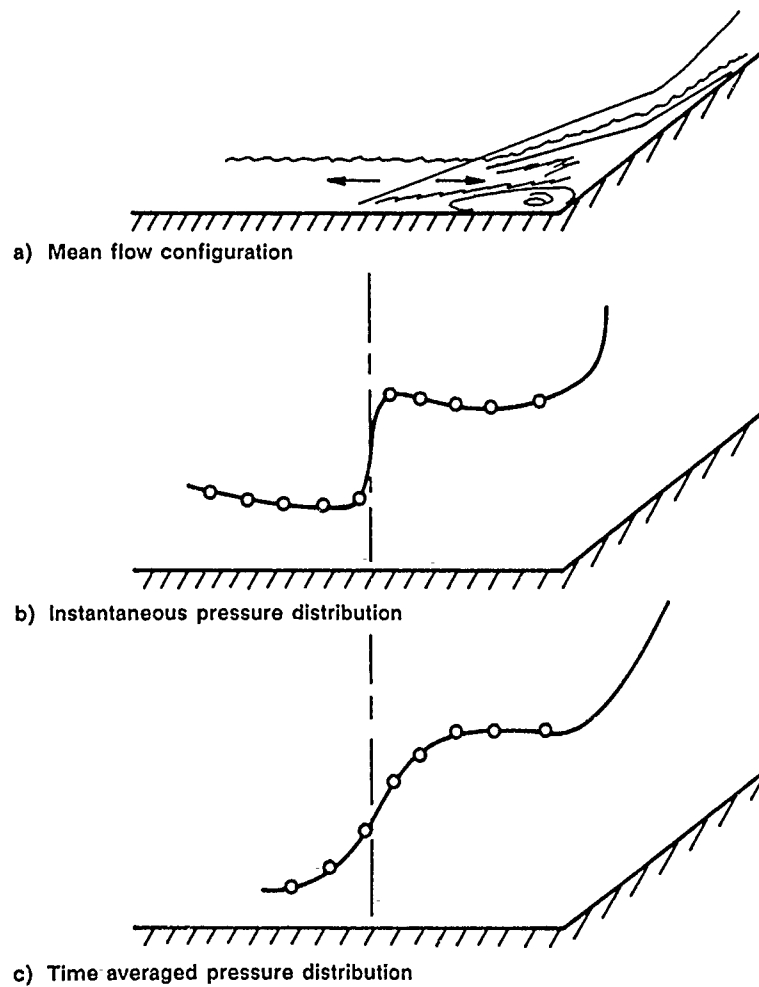
Figure 17 Measurements in unsteady separated turbulent flow
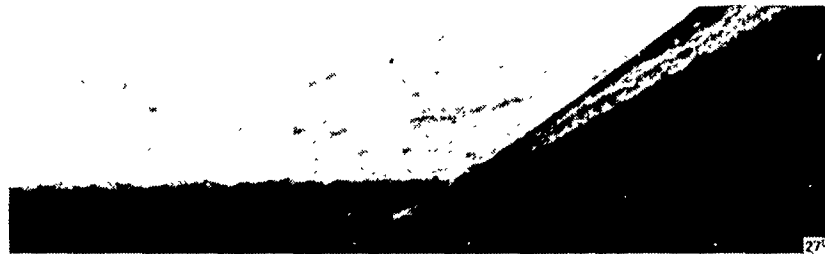
(a) WEDGE ANGLE = 27°
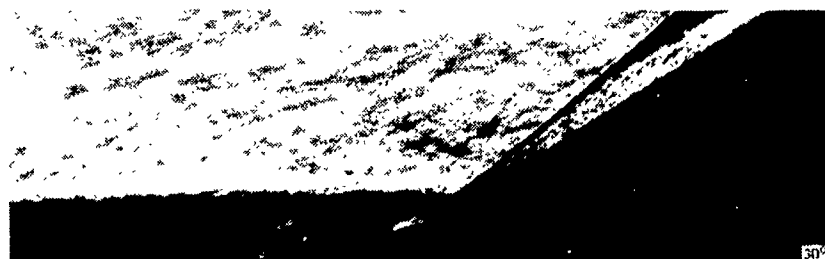
(b) WEDGE ANGLE = 30°
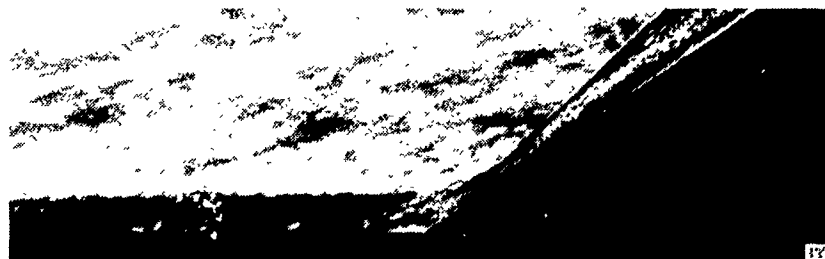
(c) WEDGE ANGLE = 33°

(d) WEDGE ANGLE = 36°

Figure 18 The development of a wedge-induced separated flow
$(M_\infty = 8.6 \ Re_L = 22.5 \times 10^6)$

(a) SHOCK GENERATOR ANGLE = 12.5°

(b) SHOCK GENERATOR ANGLE = 15°

(c) SHOCK GENERATOR ANGLE = 17.5°

(d) SHOCK GENERATOR ANGLE = 19.8°

Figure 19 The development of a shock–induced separated flow
(M_∞= 8.6 Re_L= 22.5 x 10^6)
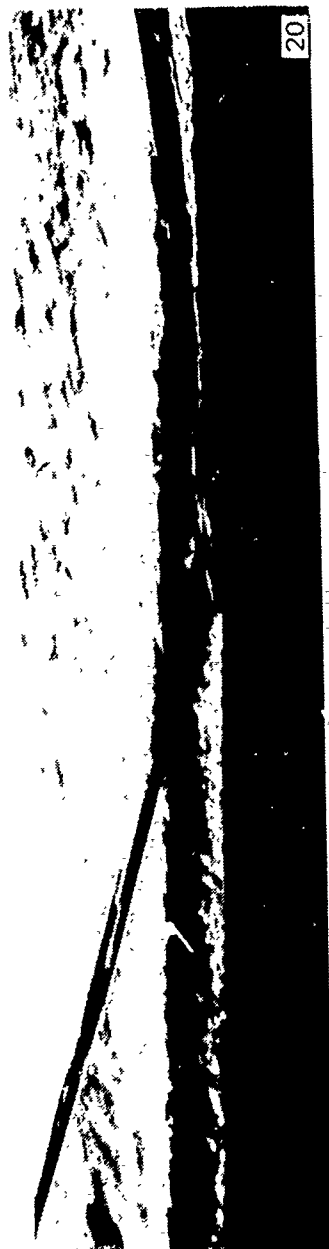
Figure 20 Incipient separation at mach 6.5 and $Re_L = 27 \times 10^6$
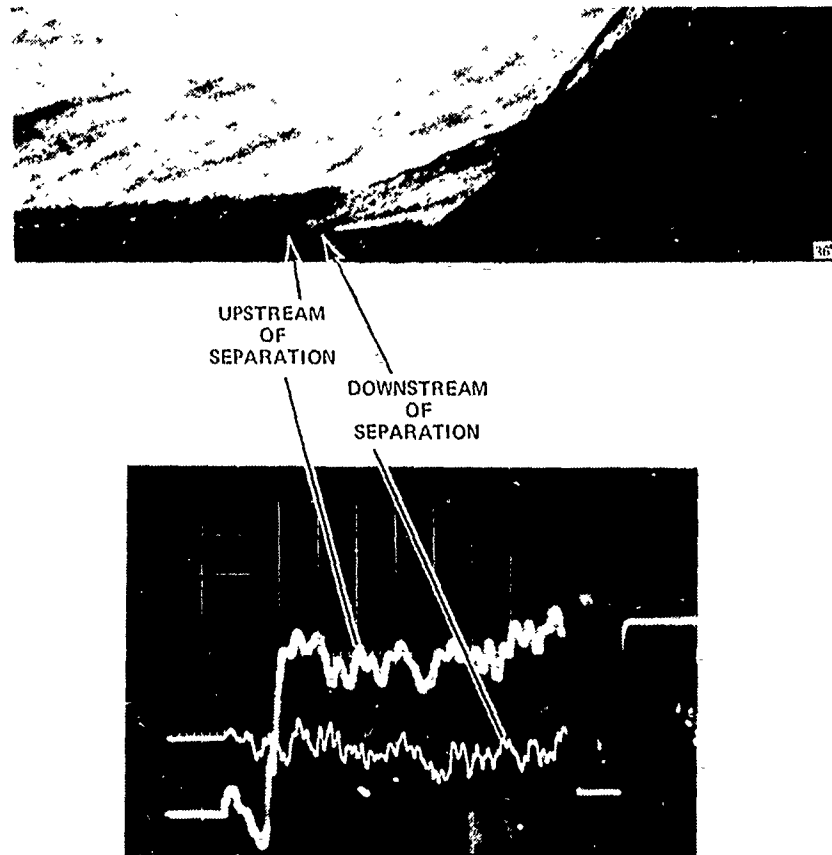
Figure 21 Output from skin friction gages in the separation region

SYM	
○	HOLDEN 1975
▢	
◇	
◹	
⬯	
⬠	ELFSTROM
⬠	STERRETT & EMERY
⊃	KUEHN
△	ROSHKO & THOMKE (1969)

$$\frac{P_I - P_o}{P_o}$$

$$M^3 C_{f_o}$$

SOLID SYM = SHOCK INDUCED INTERACTION
OPEN SYM = WEDGE INDUCED INTERACTION
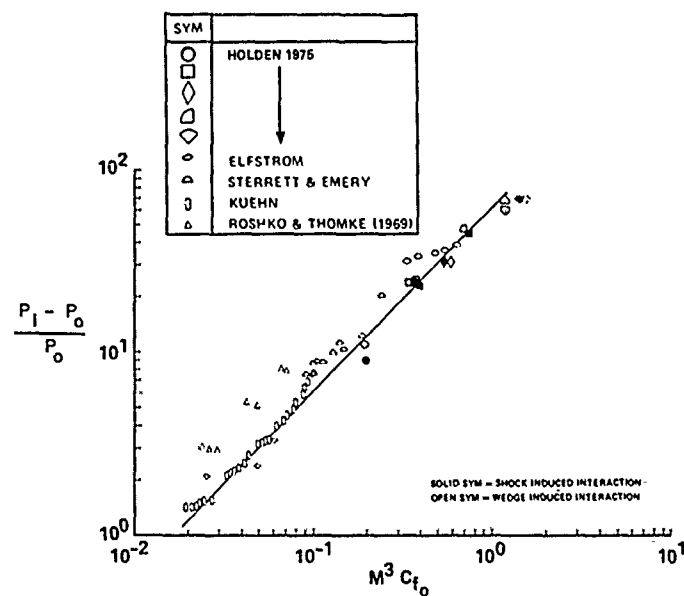
Figure 22 Correlation of incipient separation conditions for wedge–and shock–induced turbulent interaction regions

SYM	M	SOURCE	
▽	11.3	HOLDEN 1975	0°
▷			15°
△			30°
◁			45°
○	6.5	HOLDEN	
▢	7.9		
◇	8.6		
◹	11.4		
▽	13.0		
◁	1.435	LOVE	
◁	1.7-2.8	HEYSER & MAURER	
◇	2-3.5	CHAPMAN, KUEHN & LARSON	
○	2.5-4.0	BOGDONOFF	
▢	3.5 6.0	STERRETT & EMERY	
▽	6.5	TODISCO & REEVES	
△	3-5	ROSHKO & THOMKE	
△	7.3	WATSON ET AL.	
○	9-92	ELFSTROM	

SOLID SYM = SHOCK INDUCED INTERACTION
OPEN SYM = WEDGE INDUCED INTERACTION
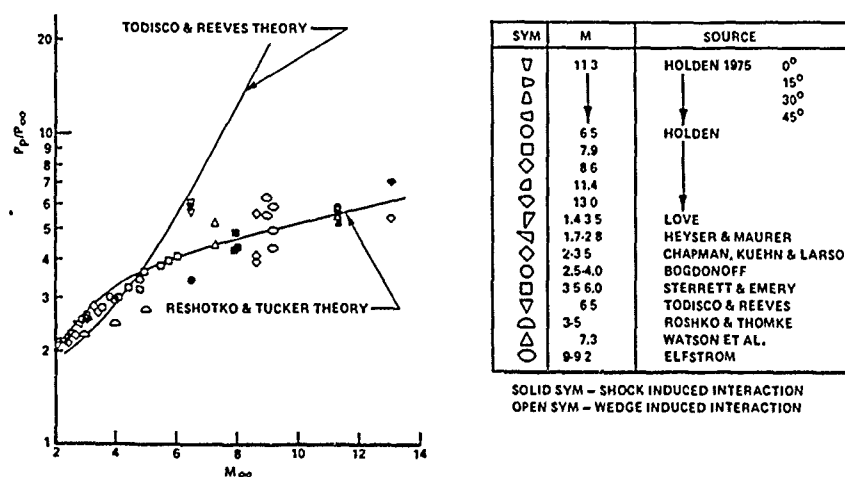
Figure 23 Correlation of plateau pressure measurements obtained in 2D and 3D flows showing little effect of crossflow on plateau pressure (REF. 41)
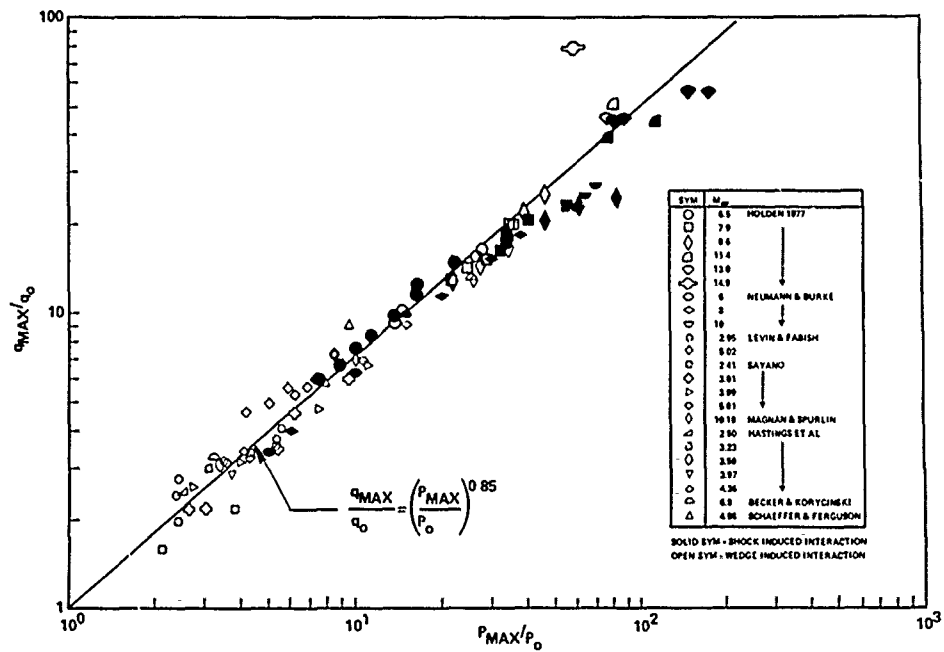
Figure 24 Correlation of maximum heating in wedge-and externally generated shock-induced turbulent separated flows
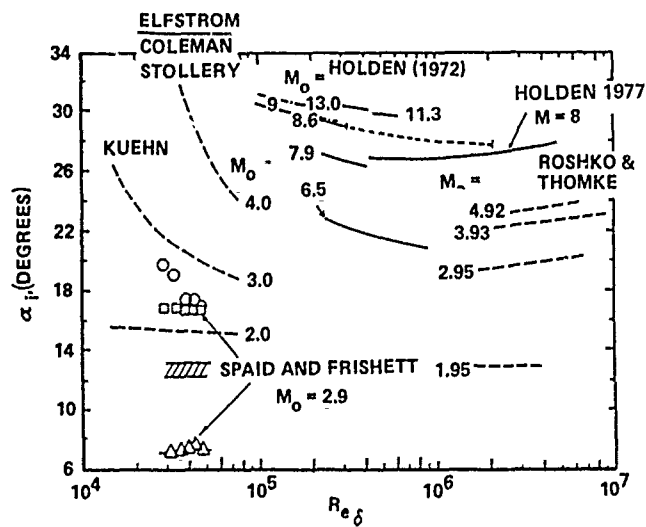
Figure 25 Wedge angle to induce incipient separation (REF. 41)
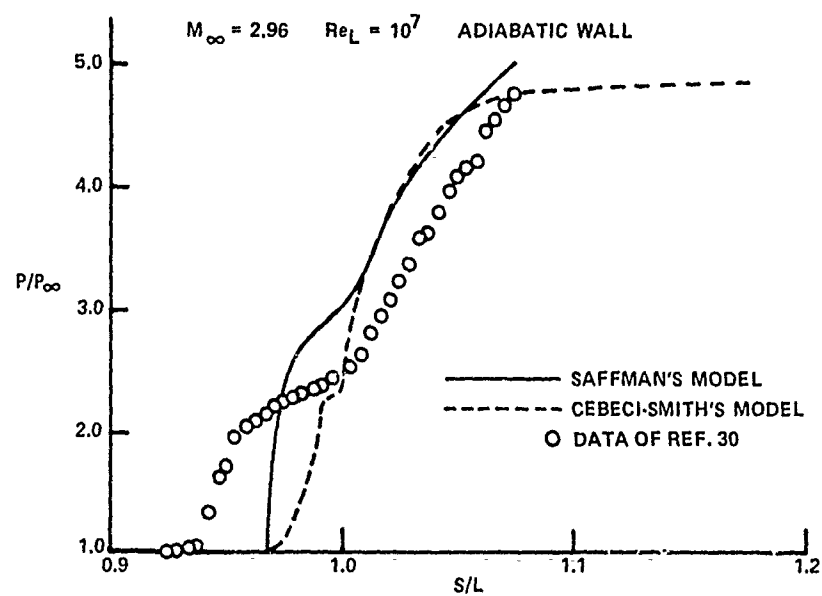
(a)
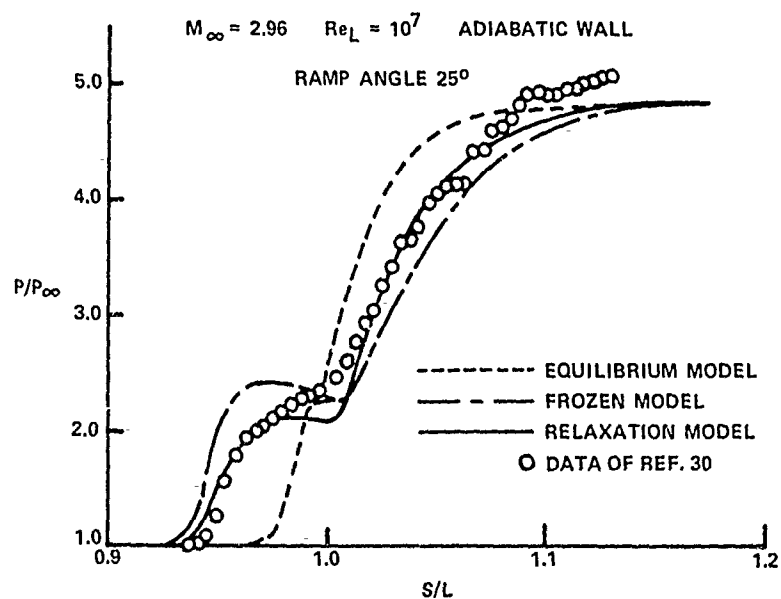
(b)

Figure 26 Comparison of different turbulent models with experiment
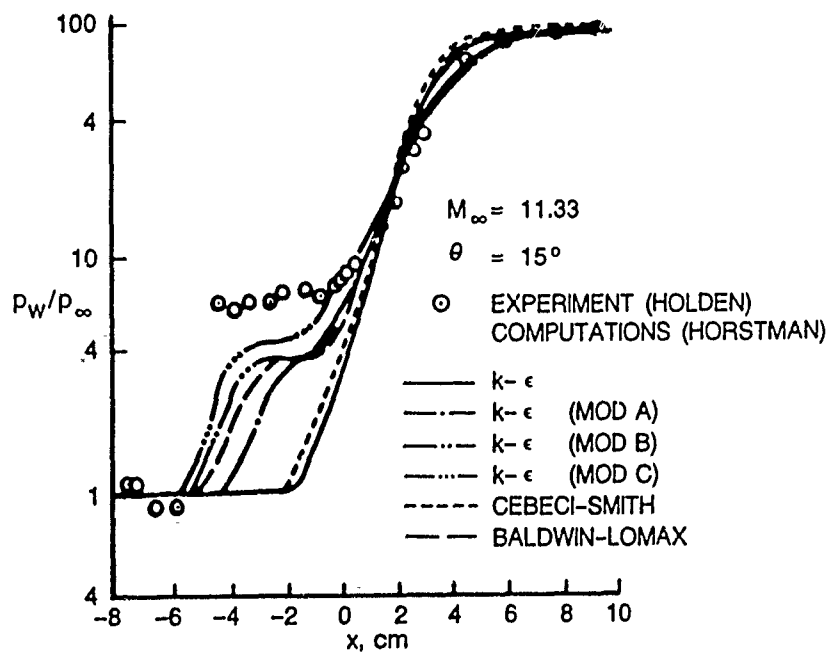
a) Surface pressure comparisons
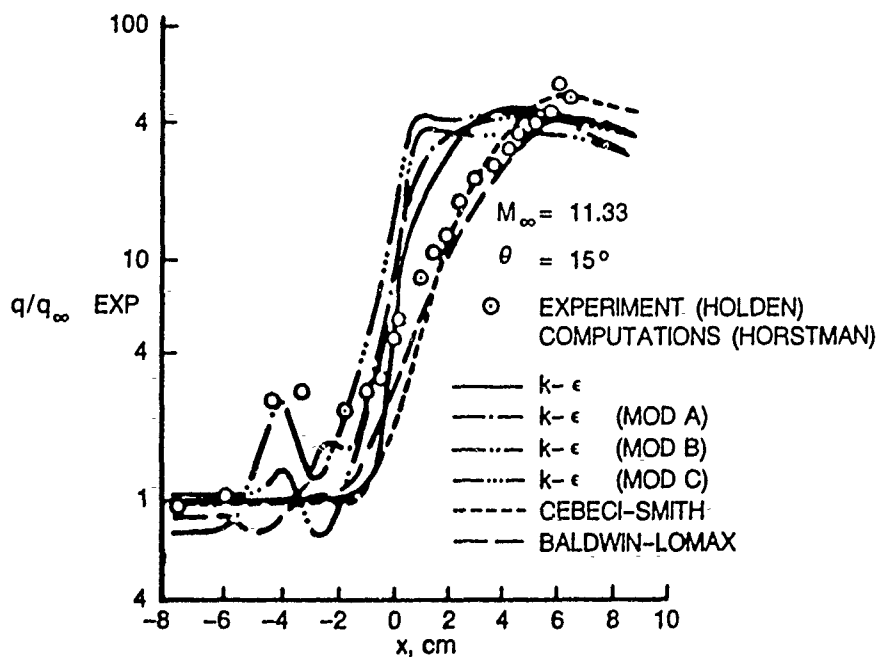
b) Surface heat transfer comparisons

Figure 27 Comparison between Navier–Stokes Solutions and measurements in
shock–induced turbulent separated flow at MACH 11

RUN 11
S.G. = 15°
SWEEP ANGLE = 30°

○ C_P/C_{P_o}
□ C_H/C_{H_o}

DISTANCE FROM PT. OF SHOCK IMPINGEMENT – inches
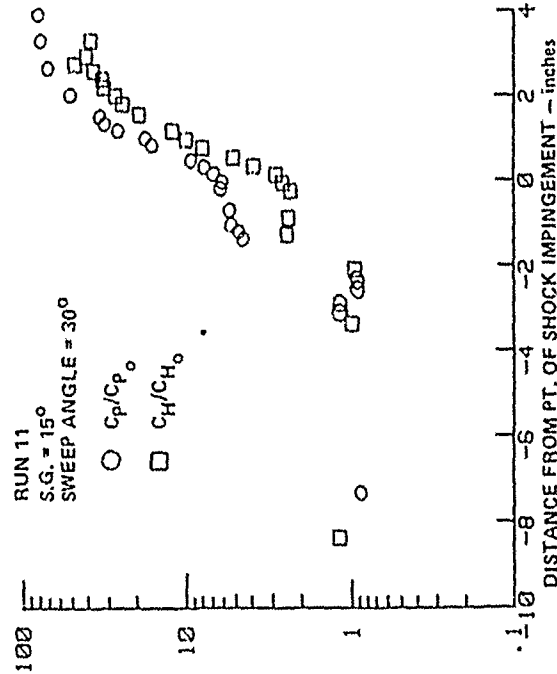
Figure 29 Streamwise distribution of heat transfer and pressure through skewed-oblique-shock interaction ($\theta = 15°$, $\psi = 30°$) (REF. 41)

RUN 6
S.G. = 15°

○ C_P/C_{P_o}
□ C_H/C_{H_o}

DISTANCE FROM PT. OF SHOCK IMPINGEMENT – inches
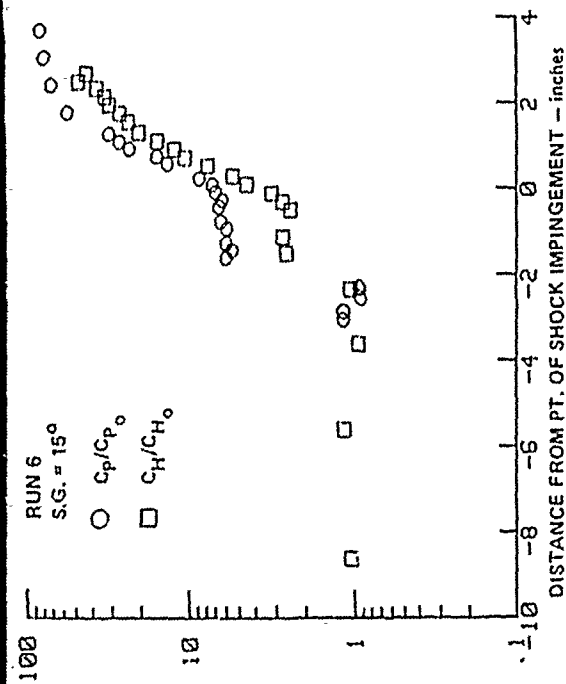
Figure 28 Streamwise distributions of heat transfer and pressure through skewed-oblique-shock boundary layer interaction ($\theta = 15°$, $\psi = 0°$) (REF. 41)

SYM	GEN/WED	SOURCE	Re_x
○	16°	SETTLES, PERKINS AND BOGDONOFF	18.7×10^6
□	16°	↓ (M = 3)	10.7×10^6
◇	12.5°	HOLDEN STUDY	50×10^6
△	15°	↓ (M = 11)	50×10^6
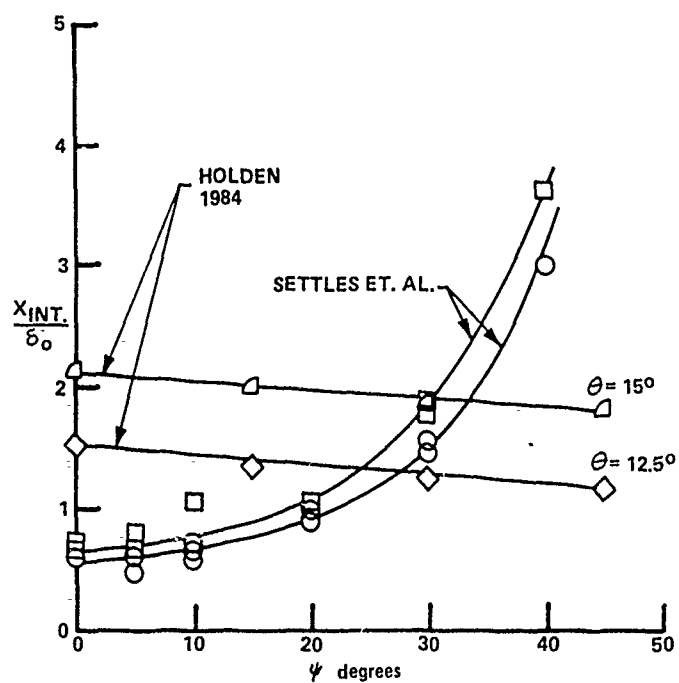
Figure 30 Variation of streamwise extent of interaction ahead of shock impingement (or corner) with sweep angle (Ref. 41)

AXIAL FLOW IN CORNERS AT SUPERSONIC AND HYPERSONIC SPEEDS [*]

by

Prof. Dr.-Ing. Dietrich Hummel
Institut für Strömungsmechanik
Technische Universität Braunschweig
Bienroder Weg 3
D-3300 Braunschweig
Federal Republic of Germany

SUMMARY

The intake-type of corner configurations basically formed by two intersecting wedges is treated in a survey. Symmetrical and unsymmetrical wedge/wedge combinations are considered including the limits of plate/plate and wedge/plate configurations. Variations of leading-edge sweep and corner angle are also taken into account.

The present knowledge on the supersonic and hypersonic axial flow in such configurations is summarized. On the basis of experimental investigations the structure of the flowfield and the pressure and heat transfer distributions at the surface are analyzed in detail. The effects of various geometric parameters as well as those of Machnumber and Reynoldsnumber are described.

The status of numerical solutions of the Euler and Navier-Stokes equations for the problem under consideration is also reviewed. Remarkable theoretical results have been achieved so far. Some details of the flow structure are still in question and further experimental and theoretical investigations are suggested.

List of Symbols

A	Source vector	s	Specific entropy
B	State vector	u,v,w	Components of V in x,y,z-directions
C	Chapman-Rubesin constant	$v_r, v_\vartheta, v_\varphi$	Components of V in r,ϑ,φ-directions
F,G,H,S	Flux vectors	x,y,z	Rectangular coordinate system
M	Machnumber	Θ	Corner angle
Pr	Molecular Prandtlnumber	ϕ	Leading edge sweep
Pr_t	Turbulent Prandtlnumber	$\bar{\Phi}$	Work done by the total stresses
Re	Reynoldsnumber	$\bar{\Phi}'$	Work done by the viscous stresses
R_1, R_2	Reattachment lines	σ	Shock angle
S_1, S_2	Separation lines	$\bar{\chi}$	Viscous interaction parameter
T	Temperature	Ψ	Angle between shear stress direction at the wall and the conical direction, positive towards the corner center
Tr	Triple point		
V	Velocity vector	γ	Ratio of specific heats ($\gamma = C_p/C_v$)
Y,Z	Conical coordinates ($Y=y/x$, $Z=z/x$), origin at x-axis	δ	Wedge angle normal to leading-edge
$\bar{Y}, \bar{Z}$	Conical coordinates, origin at the corner center	ρ	Density
a	Speed of sound	μ	Dynamic viscosity
e'	Specific total energy	τ	Total stress tensor
p	Pressure	τ'	Viscous stress tensor
$\dot{q}$	Local heat transfer rate at the wall	ξ	Static pressure ratio across a shock
		ζ	Total pressure ratio across a shock
r,ϑ,φ	Spherical coordinate system	Further notations are explained in the text	

Subscripts

C	Normal to conical ray	1	State upstream of a normal shock
E	Embedded shock	2	State downstream of a normal shock
W	State at a swept wedge	∞	Free stream conditions
Wa	State at the wall	*	Critical conditions
W,u	State at an unswept wedge		
t	Total condition (gas brought to rest isentropically)	n=0,1,2,3	Sections of the flowfield according to Fig. 10

1. INTRODUCTION

For the design of supersonic and hypersonic lifting vehicles corner flow problems are locally very important. On such configurations a lot of corners are present as sketched schematically in Fig. 1, e.g. in the junctions between wing/body, fin/wing, fin/body, pylon/wing, flap/wing as well as in the intake duct of airbreathing engines. In these corners a considerable increase of static pressure and heat transfer rate occurs. For instance severe interaction heating has been observed during the final flights of the X-15 research aircraft. Photos of the corresponding damage may be taken from R.D. Neumann [1].
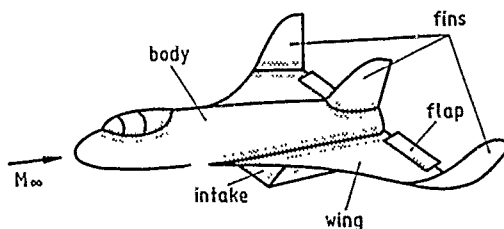
corner flowfield

Fig. 1: Corner flowfields on a supersonic/hypersonic vehicle.

In the survey lecture presented here the different corner flow problems which occur on supersonic and hypersonic flight vehicles are characterized briefly. They are related to different corner configurations which have been treated so far in the literature by means of experimental and theoretical investigations. It turns out that the symmetrical corner of two intersecting swept wedges may be regarded as the basic configuration for axial corner flows from which all other corner configurations and the corresponding flow structures may be deduced by systematic variation of geometric parameters. In the main part of the lecture the axial flow in symmetrical corner configurations formed by two swept wedges is treated in detail on the basis of experimental results. Finally theoretical investigations on axial flows in corners are summarized and compared with experimental data.
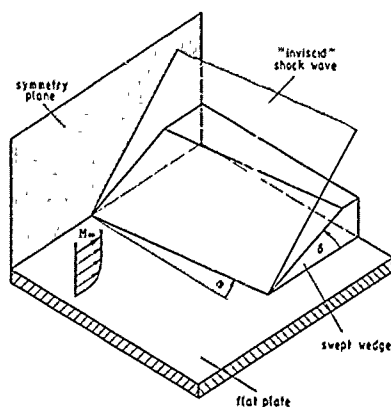
Fig. 2: Swept compression corner configuration on a flat plate.

2. SURVEY ON CORNER FLOW PROBLEMS

The corner flow problems which occur in the flowfield of a supersonic or hypersonic vehicle are related to some basic configurations:

2.1 Compression corner (ramp)

The wing/flap junction according to Fig. 1 is formed by a horizontal wedge on a flat plate as shown in Fig. 2. The wedge axis is parallel to the plane of the plate and the leading-edge is located on the plate. The corresponding compression corner is basically unswept which leads to a 2D formation of the flow, but small angles of sweep may also be present, which cause 3D effects. For the case of 2D flow the flowfield is well known: In invisci' flow from the corner an oblique shock wave emanates which is attached for small values of the wedge half-angle δ and detached for larger values of δ. In viscous flow this outer flowfield interacts with the fla. plat boundary layer which may be laminar or turbulent. Due to the pressure rise flow separations occur close to the corner region. In this case the shock wave is split up in two parts which are related to the separation and the reattachment point in the corner. Details may be taken from M.S. Holden [2], W.L. Hankey, M.S. Holden [3] and T.C. Adamson Jr., A.F. Messiter [4]. Recently the 3D effects resulting from a certain sweep of the corner as indicated in Fig. 2 have been investigated by G.S. Settles, J.J. Perkins and S.M. Bogdonoff [5], G.S. Settles, S.M. Bogdonoff [6] and G.S. Settles, H.Y. Teng [7]. For small angles of sweep a cylindrical symmetry in the 3D shock/turbulent boundary-layer interactions was found, whereas for larger angles of sweep the flowfield in the interaction region turned out to be conical. The boundary between these two flow regimes is basically a phenomenon of inviscid flow directly related to shock wave detachment. Solutions for this problem on the basis of the time-dependent Reynolds-averaged Navier-Stokes equations for 3D compressible flow, using the k-ε-eddy viscosity turbulence model, have been obtained by C.C. Horstman [8]. They are in good agreement with the experimental data according to G.S. Settles, H.Y. Teng [7]. The swept compression corner flow problem will not be covered in this lecture. It has been mentioned here in some detail for the sake of completeness and the reader is referred to the cited literature.

2.2 Glancing shock wave

Junctions between wing/body and fin/body according to Fig. 1 are related to the basic problem of a vertical wedge on a flat plate as shown in Fig. 3. In this case a glancing shock wave emanating from the leading-edge of the wedge interferes with the laminar or turbulent boundary layer on the flat plate. The most simple configuration of this kind is the unswept wedge (or fin or shock generator) with its leading-edge perpendicular to the flat plate. In this case the "inviscid" shock wave well away from the flat plate is plane and everywhere normal to the flat plate. The shock wave causes a pressure increase in flow direction in the boundary layer flow on the flat plate which may lead to flow separations there depending on the shock strength. Additional flow separations have been observed on the shock generator surface close to the corner center. Experimental investigations on such configurations are (among others) due to A. McCabe [9], C.H. Law [10], D.J. Peake [11], R.H. Korkegi [12], B. Oskam, S.M. Bogdonoff, I.E. Vas [13], H. Kubota, J.L. Stollery [14], D.S. Dolling, S.M. Bogdonoff [15] and W. McClure, D.S. Dolling [16]. Recently the effects of fin bluntness and sweep are of particular interest and they have been investigated in different places by D.S. Dolling [17], G.S. Settles, F.K. Lu [18] and N.R. Fomison, J.L. Stollery [19]. The problem of a glancing shock wave interacting with a flat plate boundary layer will be treated in detail in this lecture series. It is also mentioned here for two reasons:

i) The glancing shock wave problem contains a special case which is important also for axial corner flows in air intake ducts as indicated in Fig. 4. In the intake situation wedge and flat plate start from leading edges or lips which are mostly located in the same plane perpendicular to the free stream. The wedge generates a glancing shock wave which interacts with the flat plate flow, and the "inviscid" flowfield is the same as in the fin situation according to Fig. 3. The viscous flowfield however is different. In the fin situation a laminar or turbulent boundary layer without shock wave is present. In the intake situation due to boundary layer displacement effects a flat plate bow shock wave is formed at the lip and the glancing shock wave interacts with this weak shock wave as well as with the boundary layer underneath this shock wave. If the lip of the flat plate in Fig. 4 is moved upstream, the flat plate shock distance in the wedge region increases more and more and finally the situation according to Fig. 3 is achieved.
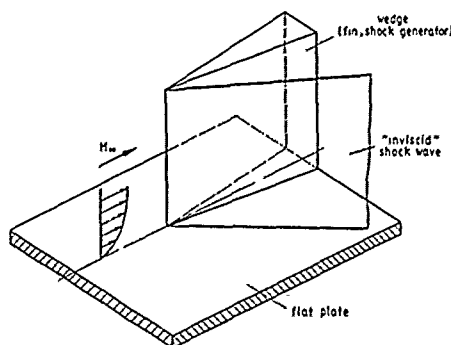
Fig. 3: Wedge configuration on a flate plate generating a glancing shock wave.
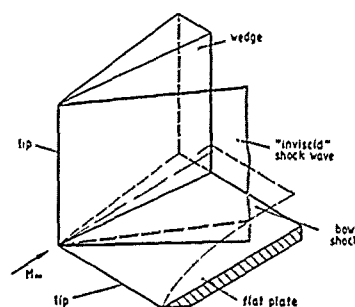
Fig. 4: Wedge/plate intake configuration with a glancing shock wave.

ii) For the glancing shock wave problem some very interesting theoretical approaches do exist, which might also be applied to the intake situation. The complete Navier-Stokes equations for laminar flow have been solved numerically by C.M. Hung, R.W. MacCormack [20] and later the same authors [21] extended their method to turbulent flow. In the equations the Reynolds stress tensor and the Reynolds heat flux have been added and turbulent closure has been accomplished by application of an eddy viscosity and turbulent Prandtl number turbulence model. In [21] an explicit numerical scheme was used, whereas D.D. Knight [23] applied a hybrid explicit-implicit numerical algorithm. Many details of the glancing shock wave problem have been calculated in [21] in good agreement with the experimental data due to C.H. Law [10], by C.C. Horstman and C.M. Hung [22] in comparison with measurements due to B. Oskam, S.M. Bogdonoff, I.E. Vas [13] and D.J. Peake [11] and by D.D. Knight [23] in agreement with data by W. McClure, D.S. Dolling [16].

Thus the glancing shock wave problem is closely related to axial corner flows in air intakes and the-oretical and experimental results for this problem have to be taken into account.

2.3 Intake corner flows

The flow in the intake duct of airbreathing engines leads to the problem of axial flow in the corner formed by two wedges as sketched in Fig. 5. In this case two shock waves are generated at the leading-edges of the wedges which interact in the corner region. Already in the inviscid outer flow far away from the corner line a very complicated flow structure turns out: Between the two wedge shocks a corner shock is formed, and from the line of intersection an embedded shock and a slip surface originate and pass towards the wedge surface and the corner center. Underneath this shock system a rather complicated viscous flow with primary and secondary vortex separations is found.
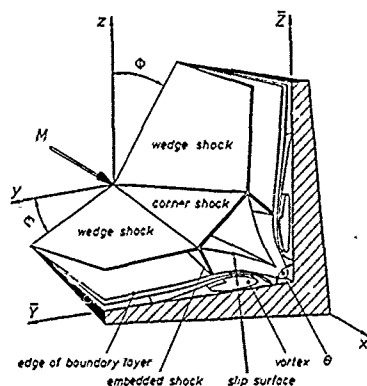
Fig. 5: Schematic view of the supersonic/hypersonic flow in a swept corner configuration.

If the two intersecting wedges have the same geometry a symmetrical flowfield with respect to the (ø/2)-line turns out, and the most important parameters for these corner flows are leading-edge sweep ø, corner angle θ, wedge angle δ and free stream Machnumber M. If in symmetrical flow the wedge angle of both wedges tends to zero, the problem of the axial flow in the corner between two flat plates turns out, which has often been investigated so far. With decreasing wedge angle the wedge shock strength decreases as well, but in the limit of two intersecting flat plates remains the interference of two weak flat plate bow shocks due to the viscous effects, which cause an effective wedge angle by the displacement effects of the boundary layers. For large distances from the leading-edges of the intersecting flat plates the shock system is located far away from the corner line, and in this case the problem of a compressible boundary layer for a uniform outer flow parallel to the corner turns out.

On the other hand, if the wedge angle δ or the sweep angle ø of the intersecting wedges is different on both sides, an unsymmetrical flowfield results. In the limit of one wedge angle tending to zero, the interference problem a wedge with a flat plate turns out. The wedge generates a glancing shock wave which interacts with the flat plate bow shock and the viscous layer underneath. This problem has already been sketched in Fig. 4. If the leading-edge of the flat plate moves upstream relative to the lip of the wedge the flat plate shock disappears and the interference of a glancing shock wave with a flat plate boundary layer without shock wave according to Fig. 3 turns out.

This discussion shows the central position of the axial corner flow problem of two intersecting wedges. Following here it will be reviewed on the basis of the available experimental and theoretical investigations.

3. EXPERIMENTAL INVESTIGATIONS ON AXIAL CORNER FLOWS

3.1 Literature survey

Early investigations of axial corner flow have been carried out for two intersecting flat plates by P.C. Stainback [24], [25] at Mach numbers 5 and 8. Pressure distribution and heat transfer measurements have been performed at the wall in the corner region and considerable increases of both parameters in the corner region have been found as compared with flat plate data. Similar investigations have been carried

out later by P.C. Stainback, L.M. Weinstein [26] for wedge/plate and wedge/wedge configurations at Mach numbers 8 and 20. The first flow field measurements in an axial corner are due to A.F. Charwat, L.G. Redekopp [27]. In these investigations the shock formation as sketched in Fig. 5 has been found. The tests have been carried out for two intersecting wedges at supersonic Machnumbers in the range $2.5 \leq M_\infty \leq 4.0$. The boundary layers were laminar, and due to the low Machnumbers the boundary layer thickness was relatively small as compared with the shock distance. The investigations were mainly concentrated on the inviscid part of the flow field, for which the effects of Machnumber on the formation of the shock system have been analyzed. The paper [27] contains also some exploratory tests on the effects of corner angle θ for symmetrical corners and on the shock formation in asymmetrical configurations with different wedge angles on both sides. Concerning the viscous part of the flow field some indications for flow separations in the corner flow field have been found. Similar investigations have been carried out in hypersonic flow by R.J. Cresci, S.G. Rubin, C.T. Nardo, T.C. Lin [28] at $M_\infty = 11,2$ on a flat plate configuration and by R.D. Watson, L.M. Weinstein [29] at $M_\infty = 20$ on plate/plate and symmetrical wedge/wedge configurations. It turned out that the basic features of the flowfield observed in supersonic flow are also present in hypersonic flow, but they are modified by thick boundary layers and large flow separations.

The 1971 state of knowledge on axial corner flows has been reviewed by R.H. Korkegi [30]. Up to that time almost all experimental work on corner flows involved laminar boundary layers, but the work of P.C. Stainback, L.M. Weinstein [26] indicated already that there exist some differences in the distributions of static pressures and heat transfer rates at the wall for laminar and turbulent flow. Experiments in supersonic flow at high Reynoldsnumbers are due to J.E. West, R.H. Korkegi [31]. It turned out that in laminar and turbulent flow the same features occur, but the interference region is much smaller in the case of turbulent boundary layers.

The problem of asymmetric axial corner flow had already been discussed by A.F. Charwat, L.G. Redekopp [27] for supersonic flow. Some exploratory experiments have been carried out for laminar flow in wedge/plate configurations and hypersonic Machnumber by J.R. Cooper, W.L. Hankey [32]. The flow field turned out to be very different from that sketched in Fig. 5 and only one triple point was found in the outer inviscid flow regime. On the flat plate side two flow separations were found in the corner region, but the interpretation of the flowfield by the authors gave rise to some doubts. Later R.H. Korkegi [33] used another review on flow separations to correct the view of the structure of this flow in the sense, that secondary separations underneath the primary vortex could clearly be indentified, see also D.J. Peake, M. Tobak, R.H. Korkegi [34]. A large variety of unsymmetrical configurations has been tested in supersonic flow by R.K. Nangia; some results are included in [60].

A comprehensive experimental program on axial flow in corners at hypersonic speeds has been carried out at Institut für Strömungsmechanik of TU Braunschweig. Symmetrical corners formed by unswept wedges have been investigated by K. Kipke [35] and K. Kipke, D. Hummel [36] at Mach numbers 12 and 16. Wedge angle δ and corner angle θ have been varied systematically. The flow field has been analyzed by pitot pressure surveys and flow visualizations at the wall and in addition the distributions of pressure and heat transfer rate at the wall have been measured. Similar experiments have been carried out by W. Möllenstädt [37], [38] for corner configurations with swept leading-edges. These measurements showed the structure of the flowfield for various sweep angles ϕ and corner angles θ. In almost all cases primary and secondary vortices have been found and the distributions of wall pressures and heat transfer rates could be correlated with the corresponding flow structure. The maximum values of wall pressure and heat transfer rate decrease considerably with increasing values of sweep angle ϕ and corner angle θ. The measurements have been carried out for laminar boundary layers. Summaries of the data have been given by D. Hummel [39], [40]. Similar investigations for turbulent boundary layers are missing up to now.

Type	Gun Tunnel
Maximum driver pressure	500 bar
Working section (size; type)	$\emptyset = 0.16$ m; open
Machnumber range	8 to 16
Stagnation pressure range	100 to 500 bar
Stagnation temperature range	900 to 1500 K
Typical model length	100 mm
Reynoldsnumber per mm (at maximum conditions)	$1.5 \cdot 10^3$ to $3 \cdot 10^4$
Running time	40 to 300 milliseconds
Usable measuring time	20 milliseconds
Test frequency	30 runs (shots) per day
Balance system	Strain-gauge balances (all six components)
Main use of tunnel	Basic research, force-, pressure- and heat-transfer measurements, flow visualization by oil-dot technique

Tab. 1 : Test parameters of the hypersonic gun tunnel of the Institut für Strömungsmechanik of Technische Universität Braunschweig

3.2 Testing techniques

Subsequently some of the results of the experimental program at Institut für Strömungsmechanik of TU Braunschweig will be discussed. Therefore the available facility and the testing technique are mentioned briefly.

The experimental investigations have been carried out in the gun tunnel of the institute, which has been described originally by K. Gersten, G. Kausche [41]. The actual data of this tunnel are compiled in Tab. 1. The tunnel is mainly operated at a driver pressure of 150 bar. Test gas is the air within the barrel (length 6 m, inner diameter 50 mm), which usually starts at atmospheric pressure and temperature and which is compressed by the piston to a stagnation pressure of about 150 bar and a stagnation temperature of about 1300 K. The flow expands through a conical nozzle the throat part of which can be changed in order to alter the Machnumber. At the beginning of each run the vacuum chamber at the downstream end of the facility starts at a minimum pressure of 0.4 mbar. The total running time at these conditions is about 100 msec.

Within this time margin the measurements of the aerodynamic quantities are taken. For surface pressure and heat transfer measurements 4 channels for the electric signals from the pressure transducers and from the thermo-couples are available. Within the running time of the tunnel on all 4 channels 400 values of the signals are taken and stored in the computer. From the time history of these 400 values the time interval can be determined in which constant aerodynamic parameters and thus steady flow conditions are present at the model. The corresponding measuring time is about 20 msec and the final measuring value for each channel is taken as the arithmetic mean value over the measuring time.

For atmospheric conditions within the barrel the obtainable Reynoldsnumbers depend on the stagnation pressure and the free-stream Machnumber. For a stagnation pressure of 150 bar and a characteristic model length of 100 mm the Reynolds number is $Re_\infty = 1.4 \cdot 10^6$ at a Machnumber of $M_\infty = 8$ and $Re_\infty = 1.7 \cdot 10^5$ at $M_\infty = 16$. The corresponding Knudsen numbers are $Kn = 8.5 \cdot 10^{-5}$ and $Kn = 12 \cdot 10^{-5}$ which indicates that continuum flows are present. In the flow tests all runs of the tunnel have been performed for stagnation pressures of 150 bar. The free stream Machnumber has been varied between $M_\infty = 12.3$ and $M_\infty = 16.0$ and the corresponding Reynoldnumbers, based on the model length l, were $Re_{l_\infty} = 5 \cdot 10^5$ and $Re_{l_\infty} = 1.7 \cdot 10^5$.

All corner configurations investigated so far were symmetrical with respect to the plane through the apex and the $(\theta/2)$-line, see Fig. 5. The corner angles were $\theta = 60°$, $90°$ and $120°$, the wedge angles normal to the leading-edges $\delta = 6.3°$, $8.0°$ and $10.0°$, and the sweep angles of the leading-edges $\phi = -30°$, $0°$, $15°$, $30°$, $45°$ and $60°$. In part I of the program corners between unswept wedges have been considered and the varied parameters were the Machnumber as well as the wedge angle and the corner angle. In part II corners between swept wedges were investigated and the varied parameter was the sweep angle at constant wedge angle and constant Machnumber. The dimensions of all models were l = 100 mm in free-stream direction and b = 50 mm perpendicular to it.

The test program for both parts of the investigations may be taken from Tab.2. Pitot pressure measurements have been carried out in a plane normal to the free-stream close to the model end at x = 0.9·l. In order to check the conicity of the flow field some measurements have also been performed at x = 0.4·l and x = 0.6·l. Four pitot probes with an outer diameter of 1 mm have been traversed simultaneously in an area of size 30 mm x 30 mm. About 800 runs of the tunnel were necessary to analyse all details of one flow field. The wall pressure and heat transfer measurements have been carried out in a section at x = 0.9·l. The heat transfer rates were determined by means of the transient thin skin technique as described by D. L. Schultz, T. V. Jones [42]. The measuring device which contained 11 thermo-couples could be adjusted in different positions in the surface of the corner models in order to achieve a dense distribution of measuring points within the section under consideration.

Part I. Corners between unswept wedges (K.Kipke, D.Hummel [36])						Part II: Corners between swept wedges (W.Möllenstädt [38])						

M_∞		12.3		16.0			M_∞			12.3			
δ		6.3°	8.0°	6.3°	8.0°	10.0°	δ			80°			
	60°		o	●	●	●	Φ	-30°	0°	15°	30°	45°	60°
θ	90°	●	●	●	●	●		60°		o	o	●	●	o
	120°	●	●	●	●	●	θ	90°	●	●	●	●	●	●
								120°		●		●	●	

o heat flux, oil flow pictures

● pitot pressure (flow field), wall pressure, heat flux, oil flow pictures

Tab. 2: Test program for the measurements in corner configurations

For the visualization of the flow at the wall an oil-dot technique has been applied. For this purpose a fluid had to be found with relatively low values of viscosity, which does not vaporize under vacuum condition of 0.5 mm Hg pressure and which leads to a distinct displacement of the droplets within the very short running time of 100 msec. Initially vacuum oil was used for this purpose, see K. Kipke, D. Hummel [36]. Later W. Möllenstädt [38] detected a well suited combination of an especially prepared model surface by means of an adhesive film and droplets of dibutylester ($C_6H_{22}O_4$) supplied with a red-coloured powder of formaldehyd-resin. During the tests the shear stress acts at the droplets and leads to considerable deformations. Local flow directions and qualitative values for the shear stress can easily be evaluated from deformed droplets after the run of the tunnel.
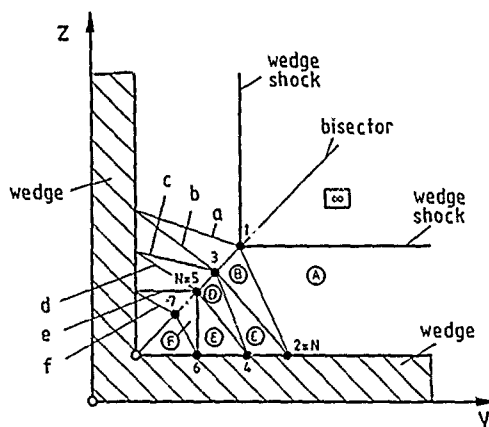
Fig. 6: Corner interference shock structure model according to [44].
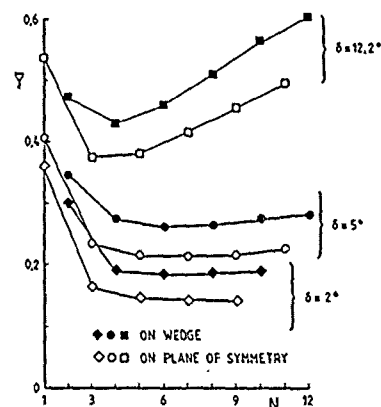
Fig. 7: Spanwise distance of shock intercepts in an unswept rectangular corner at M_∞ = 3.17 for different wedge angles δ according to [44].

3.3 Inviscid outer flow

3.3.1 Basic ideas for inviscid flow without boundary layer

Consider the cross section through a corner flow field formed by two intersecting wedges as sketched in Fig. 6. Each of the two wedges produces a bow shock. In the absence of viscous effects its distance from the wedge surface only depends on the free stream Machnumber M_∞ and the wedge (half) angle δ. The flow behind the wedge shock on one side is not parallel to the wedge surface on the other side and vice versa. In other words, the simple wedge flow does not fulfil the condition that in the case of two equal wedges the bisector must be a stream surface. These circumstances give rise to the question whether the boundary conditions on the wedge surfaces and in the bisector plane can be fulfilled simultaneously for bow shock waves which are planar up to their line of intersection in the bisector plane. For this purpose flow models have been developed by F.D. Hains [43] and R.H. Korkegi [44]. According to [44] the flow in the region A (Fig. 6) violates the tangential flow condition in the bisector plane and a plane shock wave a is necessary to fulfil this condition. The flow in region B behind this shock wave is parallel to the bisector plane but no longer tangential to the wedge surface. In order to correct this F.D. Hains [43] considered a steady flow deflecting for small wedge angles δ, whereas R.H. Korkegi [44] applied another plane shock wave b and due to the subsequent violations of the boundary conditions either in the bisector plane or on the wedge surface a shock system c , d , e ... according to Fig. 6 is necessary. The positions of the shock waves can easily be calculated from the shock relations [45]. The result is shown in Fig. 7 for a corner angle of θ = 90° and different wedge angles δ at M_∞ = 3.17. The lateral location of the shock intercepts N = 1,2,3... with the plane of symmetry and with the wedge initially move inboard, but finally they tend to move outboard and the shock waves intersect. It is concluded, that the region of interference of the corner of intersecting wedges in an inviscid supersonic stream extends outward into the flow beyond the planar intersection of the bow waves of the wedges. It turns out that planar bow shock waves up to their line of intersection are physically not possible at least for large wedge angles δ, since the boundary conditions in the bisector plane and on the wedge cannot be fulfilled simultaneously. Futher details may be taken from section 4.1.

In real flow the planar wedge shocks interfere by means of a corner shock as sketched in Fig. 5. From the line of intersection between wedge shock and corner shock an embedded shock and a slip surface emanate. If the flow field in a symmetrical corner configuration with leading edge sweep is considered, the inviscid flow structure is shown in Fig. 8 according to W. Möllenstädt [38]. Y = y/x, Z = z/x are conical coordinates with the origin at the apex of the corner configuration. For swept leading edges the corner angle θ would be slightly larger than 90°. In order to achieve a corner angle of θ = 90° the axes of the two wedges have to be turned about the X-axis at a small angle ϵ. The inviscid flow is conical with respect to the corner apex at X = Y = Z = 0. The corresponding flow structure is shown in conical coordinates. The velocity vector is splitted up in its components parallel and normal to the conical ray and the projection of the normal component into the Y, Z-plane is shown. In this kind of display the free stream flow V_∞ parallel to the X axis is represented by conical rays towards the center at Y = Z = 0 where the normal component disappears. The conical shock waves are indicated by double-lines. At a conical shock the component tangential to the conical ray is unchanged whereas the normal component undergoes a jump which is marked as a kink in the streamlines. Behind a plane corner shock the flow is parallel at a certain inclination in the bisector plane. Therefore the normal components of the velocity with respect to a conical ray with this inclination disappear and the flow in this region is focussed to a point on the bisector plane apart from the corner. The distance of this focus from the corner center depends on the strength of the corner shock. The slip surface through the triple point Tr of the shock system is the limiting streamline of this flow field behind the corner shock. The slip surface separates the streamlines through the corner shock from the ones which passed through the wedge shock. Behind the wedge shock the

a) Structure of the flowfield

b) Wall pressure
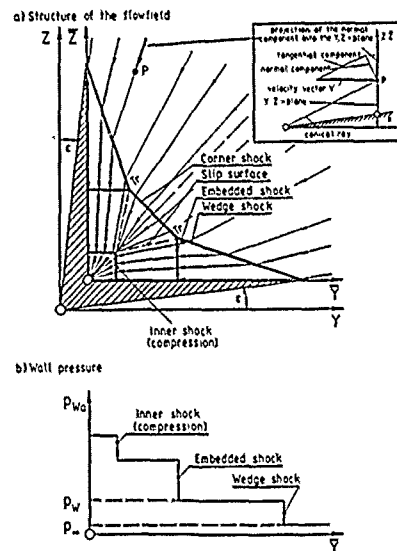
Fig. 8: Inviscid conical flow in a corner configuration with swept leading-edges (schematic view for plane shock waves) according to [38].

flow is parallel to the wedge surface and directed inboard. In order to meet the slip surface an embedded shock is necessary. At the slip surface the pressure is constant and across it a jump in entropy takes place which is equal to the difference in entropy rise between streamlines which pass through the corner shock on one side of the triple point Tr and streamlines which pass through wedge shock and embedded shock on the other side of the triple point. At the point of intersection of the slip surfaces from both sides the flow behind the corner shock is parallel to the bisector plane, but the flow in the adjacent area is not. Therefore this flow has to be deflected in order to become parallel to the symmetry plane. This can be achieved either by a steady compression or by a shock wave. In Fig. 8 a corresponding shock wave has been drawn for simplicity. Finally the flow at the corner center is parallel to the conical corner inter-section line and the streamlines are focussed with respect to this center. Related to this flow structure the wall pressure is also drawn schematically in Fig. 8. The pressure level between leading-edge and embedded shock is governed by the wedge flow, the level between embedded shock and inner (compression or) shock corresponds to the pressure behind the corner shock and the last pressure rise towards the corner center is due to the final flow deflection parallel to the corner line which is accompanied by a steep increase of pressure.

3.3.2 Inviscid outer flow in the presence of boundary layers

In the real flow with boundary layers at the intersecting wedges the structure of the inviscid outer flow is in principle the same as in purely inviscid flow. The displacement effect of the boundary layers is relatively small in supersonic flow, but it becomes very important in hypersonic flow. Due to the dis-placement effects the wedge shocks as well as the corner shock are located more outboard and their strengths are larger than in purely inviscid flow. Unfortunately the boundary layer development on the wedges and in the corner depends nonlinearly on the distance from the corner apex. This means that the flow is in principle non-conical. The viscous interaction parameter

$$\bar{\chi} = \frac{M_\infty^3}{\sqrt{Re_{x_\omega}}} \sqrt{C} \tag{1}$$

is a function of the distance from the corner apex. In the vicinity of the apex $\bar{\chi}$ reaches large values even for supersonic flow. Strong viscous interactions take place in this region and the flow is distinctly non-conical. Moving downstream the viscous interaction parameter reduces more and more. In the experiments of R.D. Watson, L.M. Weinstein [29] and K. Kipke, D. Hummel [36] the data were taken at a station corres-ponding to values $\bar{\chi} = 4$ and $\bar{\chi} = 3$ respectively and it has been shown that at this distance from the apex the flow is fairly conical with respect to a center which is located slightly upstream of the corner apex. A conical flowfield of this kind is drawn schematically in Fig. 9. Y,Z and $\bar{Y},\bar{Z}$ are conical coordinates with the origin at this center and in the corner. The displacement effect of the boundary layers at the wedges is taken into account. The two wedge shocks and the corner shock are located more outboard as compared with the purely inviscid flow according to Fig. 8, and the strengths of these bow shocks are in-creased. Correspondingly the point of intersection of the two slip surfaces on the bisector plane is also found more outboard. The adaptation of the flow behind the wedge shock to the no-crossflow condition at the slip surface can be achieved by an oblique embedded shock wave. Finally the flow has to be deflected in order to become parallel to the corner intersection line. This can be achieved by an inner shock as indicated in Fig. 9 or by a strong steady compression. This process is slightly different from the purely inviscid case, since the displacement thickness of the boundary layer is considerably reduced towards the corner center due to flow separations. This shape of the displacement surface leads to an expansion fan in the inviscid outer flow which interferes with the inner shock or compression in this region. The expected

a) Structure of the flowfield
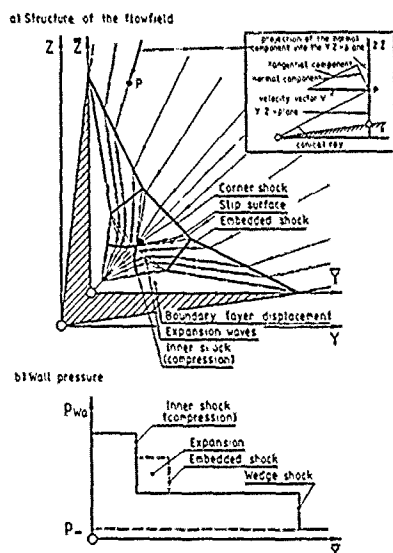
b) Wall pressure

Fig. 9: Inviscid conical outer flow in a corner configuration with swept leading-edges and boundary layer displacement (schematic view for plane shock waves) according to [38]

distribution of the wall pressure related to this flow structure is also indicated in Fig. 9. Due to the displacement effects the pressure level should be larger than in the purely inviscid case. In the region between the embedded shock and the inner compression the pressure increase caused by the embedded shock might be considerably reduced or even compensated by the expansion due to the shape of the displacement surface, but finally a steep pressure increase towards the corner center can be expected.

The inviscid outer flowfield is now analyzed on the basis of the experimental results for a $\phi = 30^\circ$ swept $\theta = 90^\circ$ rectangular corner at $M_\infty = 12.8$, as shown in Fig. 10. The flow is symmetrical with respect to the bisector plane. In the left upper half of the diagram the measured pitot pressure distribution is drawn and the right lower half of the flowfield is used for interpretation purposes. The pitot pressure data are given dimensionless as the ratio $\zeta = p_{t2}/p_{t2\infty}$, where $p_{t2\infty} = p_{t2_\infty}$ is the free stream pitot pressure in the region 0. Wedge shock and corner shock are marked by a steep increase of pitot pressure p_{t2} and the same applies for the embedded shock and the slip surface. Apart from the free stream region 0 the inviscid outer flow is divided in the regions 1, 2 and 3. The state of the flow in these parts of the flowfield can be analyzed quantitatively using the measured shock positions (which include the boundary layer displacement effects) and considering special measurements of the static pressure p_1 on swept wedges which are available as additional information. For the region 1 behind the wedge shock the
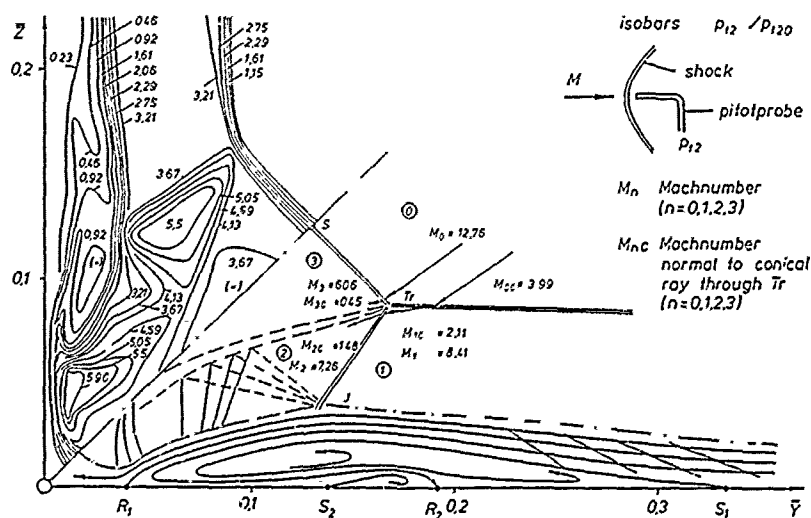
Fig. 10: Pitot pressure isobars and triple point analysis for the flowfield in a symmetrical $\phi = 30^\circ$ swept rectangular corner ($\delta = 8^\circ$) at $M_\infty = 12.8$ according to [38].

pitot pressure ratio may be written as

$$\zeta_1 = \frac{p_{t21}}{p_{t20}} = \frac{p_{t21}}{p_{t11}} \frac{p_{t10}}{p_{t20}} \frac{p_{t11}}{p_{t10}} \qquad . \qquad (2)$$

The first two factors indicate the ratio of pitot pressure p_{t2} to total pressure p_{t1} at the probe in the regions 1 and 0, which can be expressed by the corresponding Mach numbers for $\gamma = 7/5$ [45] as

$$\frac{p_{t21}}{p_{t11}} = \left[\frac{6M_1^2}{M_1^2 + 5} \right]^{7/2} \cdot \left[\frac{6}{7M_1^2 - 1} \right]^{5/2} \qquad (3a)$$

$$\frac{p_{t20}}{p_{t10}} = \left[\frac{6M_0^2}{M_0^2 + 5} \right]^{7/2} \cdot \left[\frac{6}{7M_0^2 - 1} \right]^{5/2} \qquad . \qquad (3b)$$

The free stream Mach number $M_\infty = M_0$ is known a priori. The Mach number M_1 can be expressed by the free stream Mach number M_0 and the pressure ratio $\xi_1 = p_1/p_0$ as

$$M_1 = \sqrt{\frac{M_0^2(6\xi_1 + 1) - 5(\xi_1^2 - 1)}{\xi_1(\xi_1 + 6)}} \qquad . \qquad (4)$$

The pressure p_1 has been measured separately and p_0 can be determined from the measured free stream pitot pressure p_{t20} according to [45] as

$$p_0 = p_{t20} \left[\frac{5}{6M_0^2} \right]^{7/2} \cdot \left[\frac{7M_0^2 - 1}{6} \right]^{5/2} \qquad . \qquad (5)$$

The last factor in equ. (2) is the ratio of total pressures at the wedge shock, which can be expressed by the ratio of the static pressures ξ_1 as

$$\frac{p_{t11}}{p_{t10}} = \left[\frac{6\xi_1 + 1}{\xi_1 + 6} \right]^{7/2} \cdot \left[\frac{1}{\xi_1} \right]^{5/2} \qquad . \qquad (6)$$

The evaluation of equ. (2) to (6) for the flow according to Fig. 10 leads to $\zeta_1 = 3,31$. The plateau of the data behind the wedge shock ($2.75 \leq \zeta_1 \leq 3.67$) is in good agreement with the calculated value.

Corresponding values for the regions 2 and 3 can be determined if the pressures

$$p_2 = p_3 \qquad (7)$$

are known. p_3 can be calculated from the corner shock angle σ_C in the bisector plane

$$\sigma_C = \tan^{-1} \frac{\sqrt{y_S^2 + z_S^2}}{x_M} \qquad , \qquad (8)$$

where y_S, z_S are the coordinates of point S in Fig. 10 in the corner apex fixed coordinate system and x_M is the distance of the measuring plane from the fictitious conical center upstream of the corner apex. The free stream Machnumber component normal to the corner shock is then

$$M_{0CS} = M_0 \cdot \sin\sigma_C \qquad , \qquad (9)$$

and this leads to the pressure ratio

$$\xi_3 = \frac{p_3}{p_0} = \frac{7M_{0CS}^2 - 1}{6} \qquad . \qquad (10)$$

For given p_0 according to equ. (5) the pressures p_2 and p_3 are known. The yet unknown distance x_M of the fictitious conical center located upstream of the corner apex can be determined using the measured position y_{Tr}, z_{Tr} of the triple point Tr and the wedge shock angle σ_W between the free stream flow $M_\infty = M_0$ and

the plane wedge shock

$$\sigma_W = \sin^{-1}\sqrt{\frac{6\xi_1 + 1}{7M_0^2}} \qquad . \qquad (11)$$

Finally x_M can be written as

$$x_M = y_{Tr} \cdot \tan\phi + z_{Tr}\sqrt{\frac{1}{\sin^2\sigma_W} - \frac{1}{\cos^2\phi}} \qquad , \qquad (12)$$

and for an unswept wedge $\phi = 0$ yields

$$x_M = z_{Tr} \cdot \cot\sigma_W \qquad \text{(unswept)} \qquad . \qquad (12a)$$

The values for the pitot pressure ratios ζ_2 and ζ_3 can be determined from equ. (2) to (6) by replacing ξ_1 by the ratios $\xi_2 = p_2/p_1$ and $\xi_3 = p_3/p_0$. For the flow in Fig. 10 the values $\zeta_2 = 5.98$ and $\zeta_3 = 4.17$ turn out. Both are in good agreement with the measured data. The pressure ratios at the various shocks are

Wedge shock	ξ_1	$= p_1/p_0 =$	7.60
Embedded shock	ξ_2	$= p_2/p_1 =$	2.42
Corner shock	ξ_3	$= p_3/p_0 =$	18.38 .

Due to equ. (7) the relation between the pressure ratios is

$$\xi_1 \cdot \xi_2 = \xi_3 \qquad . \qquad (12)$$

The corner shock wave is extremely strong, followed by the wedge shock, and the embedded shock is the weakest one in the field of the inviscid outer flow. From the pressure ratios ξ the Machnumbers behind the shocks can be evaluated for given Machnumbers upstream of the shocks according to equ. (4). This yields

Free stream	$M_\infty = M_0$	$= 12.76$
Region 1	M_1	$= 8.41$
Region 2	M_2	$= 7.26$
Region 3	M_3	$= 6.06$

The values indicate that in the whole region of the inviscid outer flow high supersonic or hypersonic Machnumbers are reached.

Finally the region in the immediate neighbourhood of the triple point Tr will be analyzed. The conical ray from the fictitious conical center towards the triple point Tr is known. In order to find the streamlines in conical coordinates according to Fig. 9 the Machnumber components normal to the conical ray M_{nc} (n = 0,1,2,3) have to be determined. Since the tangential component is unchanged through the shocks, for the normal components the ordinary shock relations [45] hold, and these normal components can be evaluated basically from equ. (4) according to W. Möllenstädt [38] as

Free stream	M_{0C}	$= 3.99$
Region 1	M_{1C}	$= 2.11$
Region 2	M_{2C}	$= 1.48$
Region 3	M_{3C}	$= 0.45$.

In the plane normal to the conical ray through the triple point Tr the deflection angle δ_1 at the wedge shock can be calculated from M_{0C} and ξ_1 as

$$\tan^2\delta_1 = \left[\frac{5(\xi_1 - 1)}{7M_{0C}^2 - 5(\xi_1 - 1)}\right]^2 \frac{7M_{0C}^2 - (6\xi_1 + 1)}{6\xi_1 + 1} \qquad , \qquad (13)$$

and corresponding formulas are valid for the deflection angles δ_2 and δ_3 at the embedded shock and at the corner shock. The angle σ_E between the Machnumber component M_{1C} and the embedded shock is

$$\sigma_E = \sin^{-1}\sqrt{\frac{6\xi_2 + 1}{7M_{1C}^2}} \qquad . \qquad (14)$$

Finally the shock system, which has been calculated in a plane normal to the conical ray through the triple point Tr, can be transformed in the Y,Z-plane. The result is shown in the right lower half of

Fig. 10. The shock directions in the vicinity of the triple point Tr are calculated from the measured data. The agreement with the pitot pressure data is evident. The flow on both sides of the triple point is also shown with the correct flow deflections at the various shocks. An intuitive view of the flow structure turns out.

Finally the shock polar diagram can be drawn for the plane normal to the conical ray through the triple point Tr. For the wedge shock the velocity ratio is [45]

$$\frac{V_{1C}}{V_{0C}} = \sqrt{1 - \frac{5(\xi_1^2 - 1)}{M_{0C}(6\xi_. + 1)}} \quad , \tag{15}$$

and similar equations hold for the two other shocks. For the vectors V_{0C} and V_{1C} at the angle δ_1 shown in Fig. 11 the shock polar for the wedge shock as well as the constant a_c^* for the diagram can be determined. The wedge shock angle σ_{wc} in the plane normal to the conical ray can be determined in the usual way. The shock polar for the embedded shock is also drawn in Fig. 11. The deflection angle δ_2 leads to the velocity V_{0C} behind the embedded shock and the corresponding shock angle according to equ. (14) can be evaluated also from Fig. 11. Concerning the corner shock the Machnumber component in the plane normal to the conical ray through the triple point Tr is subsonic. Hence the deflection angle δ_2 in combination with the V_{0C}-shock polar leads to the velocity V_{3C} behind the corner shock and the corresponding corner shock angle σ_{CC} is close to $\pi/2$. For the deflection angle yields

$$\delta_1 - \delta_2 = \delta_3 \quad . \tag{16}$$
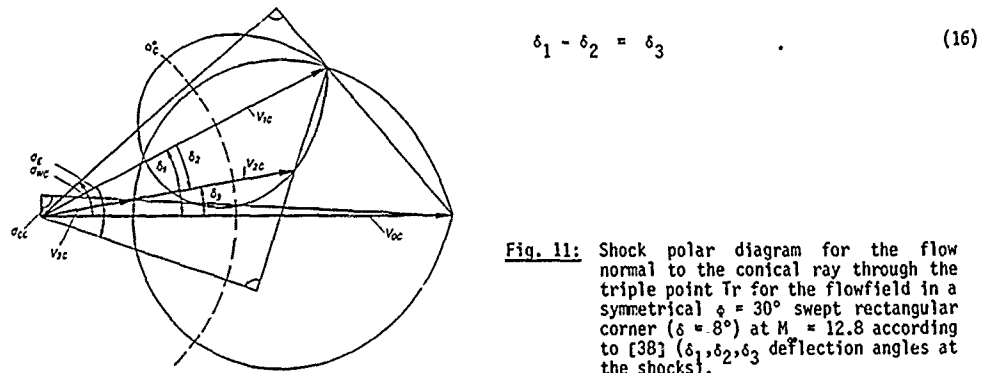
Fig. 11: Shock polar diagram for the flow normal to the conical ray through the triple point Tr for the flowfield in a symmetrical $\phi = 30°$ swept rectangular corner ($\delta = 8°$) at M $= 12.8$ according to [38] ($\delta_1,\delta_2,\delta_3$ deflection angles at the shocks).

On both sides of the slip surface the velocity vector components normal to the conical ray through the triple point Tr have the same direction, but the magnitude of this component is considerably different. Taking into account also the velocity component parallel to the conical ray through the triple point Tr, the velocities at the slip surface are in the same plane but their magnitude and direction are different. The slip surface represents a vorticity sheet. Originally at the triple point Tr this sheet is very thin, but far more inboard it develops like a free shear layer due to viscous effects. Unfortunately the relatively thick pitot probe is not able to give more details on the flow at the slip surface, but the steep pitot pressure increase between the two regions 2 and 3 is clearly indicated. The entropy jump across the slip surface can be calculated from the total pressures in both regions [45] as

$$\frac{\Delta s_{23}}{R} = - \ln \frac{p_{t13}}{p_{t12}} = - \ln \left[\frac{p_{t13}}{p_{t10}} \frac{p_{t10}}{p_{t11}} \frac{p_{t11}}{p_{t12}} \right] \tag{17}$$

and the total pressure ratios across the various shocks can be evaluated in principle from equ. (6) using the known static pressure ratios ξ_1, ξ_2 and ξ_3. For the present example in Fig. 10 the result is $\Delta s_{23}/R = 1.136$.

At the lower end of the flow in region 2 the pitot pressures decrease considerably, and this can be interpreted to be due to an expansion fan originating from the point of intersection J between the embedded shock and the boundary layer. The expansion waves are reflected from the slip surface and the bisector plane as compression waves and this leads again to a steep increase of the pitot pressure towards the corner center. Finally the flow is deflected parallel to the bisector plane and parallel to the wedge surface in the immediate neighbourhood of the corner by an inner shock or by a strong steady compression as indicated on the right-hand side of Fig. 10.

At the end of this analysis of the inviscid outer part of a corner flowfield it has to be born in mind that the input data were M_∞, p_{t20}, p_1, y_S, z_S and y_{Tr}, z_{Tr} and that all other quantities have been deduced from the shock relations [45]. The structure of the flowfield in the right hand lower half of Fig. 10 has been calculated on this basis and the agreement with the pitot pressure measurements is quite remarkable.

3.4 Boundary layer flow

The outer edge of the boundary layer is indicated in Fig. 10 by a sudden drop of the pitot pressure towards the wedge which is due to the total pressure loss within the boundary layer. The corresponding boundary layer thickness is largest in the region of the embedded shock.

The flow structure near the wall may be taken from the evaluation of the shear stress pattern, obtained from flow visualizations by means of the oil dot technique, according to Fig. 12. The flow on the $\phi = 30°$ swept wedge is parallel to the free stream up to a conical ray A. Upstream of this border the wedge flow is not influenced by the presence of the second wedge. Downstream of the line A the streamlines close to the wall move outboard. The angle Ψ between the streamlines and the conical rays from the corner apex reduces more and more. At S_1 a conical line with convergence of the streamlines is found which marks a separation line. At the wall the flow becomes parallel to this conical ray S_1. The crossflow component of the shear stress disappears at the separation line, but the longitudinal component does not. Therefore a deformation of the oil dots at the separation line in the direction of the conical ray is still present. The corresponding reattachment of the flow takes place at the conical line R_1, which is found very close

a)   b)   c)
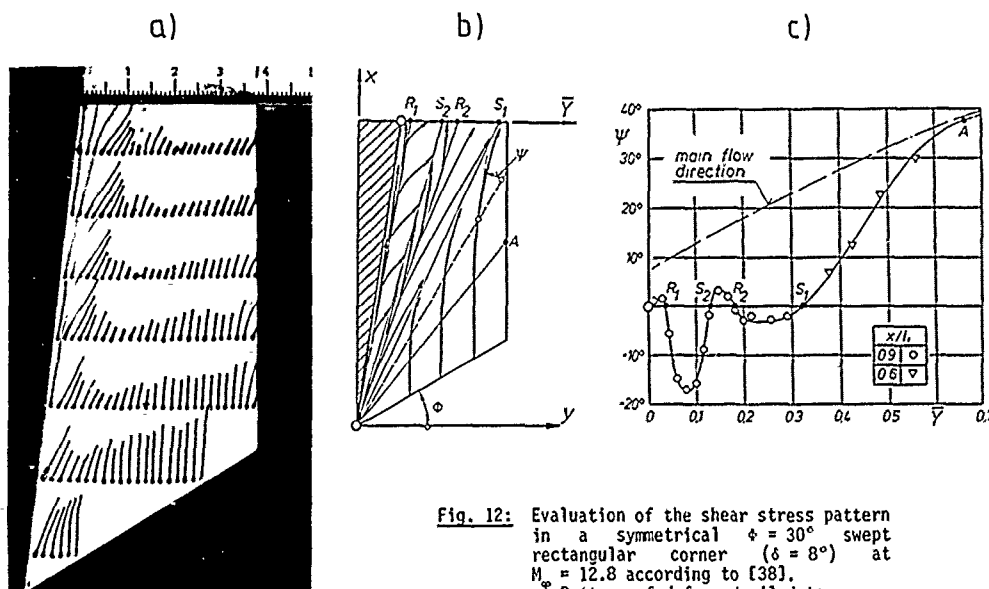
Fig. 12: Evaluation of the shear stress pattern in a symmetrical $\phi = 30°$ swept rectangular corner $(\delta = 8°)$ at $M_\infty = 12.8$ according to [38].
a) Pattern of deformed oil dots
b) Qualitative interpretation
c) Quantiative evaluation

to the corner. At this line streamline divergence is distinctly marked. In the region between the reattachment line R_1 and the corner the flow is directed towards the corner whereas in the region beyond the reattachment line R_1 the flow at the wall is directed outboard. S_1 and R_1 are related to a vortex which may be called the primary vortex. In the outboard flow between R_1 and S_1 another conical separation line S_2 with streamline convergence and another corresponding reattachment line R_2 with streamline convergence can be detected. They belong to a secondary vortex underneath the primary vortex.

The shear stress pattern can be evaluated with respect to the angle Ψ between the streamlines at the wall and the conical direction. The result is also shown in Fig. 12. If the flow is parallel to the conical direction $\Psi = 0$ turns out. $\Psi > 0$ means that the flow is directed inboard with respect to the conical rays and $\Psi < 0$ indicates the outboard direction of the flow. Using the results for the angle Ψ the flow pattern can be transferred into conical coordinates as shown in Fig. 10. The influence border A is located far outboard and it is not shown in the figure. Within the inboard flow between S_1 and R_1 the primary vortex is formed and underneath the secondary vortex is located between S_2 and R_2. It should be mentioned that in three-dimensional flow the separating stream surface and the attaching stream surface are different. Therefore the flow separations in three-dimensional flow take the form of vortices which are fed from outside with vorticity rather than closed separation bubbles which occur in two-dimensional flow. Primary vortex and secondary vortex show the opposite sense of rotation. Flow separations of this kind are well known, e.g. from the upper surface of slender delta wings as described by D. Hummel [46]; see also D.J. Peake, M. Tobak, R.H. Korkegi [34].

The occurrence of boundary layer separation is due to the pressure gradient caused by the embedded shock wave. Nevertheless it is an interesting result that the influence border A (in the example according to Figs. 10 and 12 situated at $\overline{Y} = 0.66$) is located far more outboard than the line of impingement J of the embedded shock and the boundary layer (situated at $\overline{Y} = 0.14$). This phenomenon is well known from two-dimensional flows with shock-induced pressure gradients as described by L. Lees, B.L. Reeves [47], M.S. Holden [2] and A.H. Shapiro [48]. If an external shock causes flow separation in a compressible

laminar boundary layer flow as sketched in Fig. 13, the boundary layer flow upstream of the shock is curved due to the displacement of the boundary layer and the separated region. In the supersonic part of the boundary layer and the adjacent inviscid outer flow a compression takes place which causes an increase of the static pressure at the wall upstream of the shock and this additional pressure rise finally leads to a separation point which is located far upstream of the shock impingement point. The displacement of the inviscid outer flow is largest in the region of the separation bubble at the shock impingement point. Behind the shock wave the separation bubble closes and the viscous displacement is considerably reduced. Therefore the inviscid outer flow passes an expansion and in the first instance the pressure rise due to the shock wave cannot be detected at the wall. Finally in the region of the reattachment point the flow is
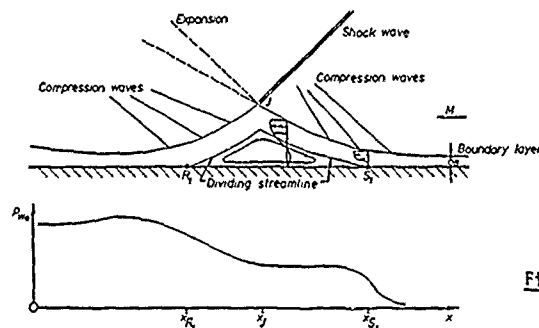
Fig. 13: Schock-induced boundary-layer separation in supersonic flow according to [47].

again turned parallel to the wall. This causes a compression in the inviscid outer flow which leads to the increase of static pressure at the wall in this region. This behaviour of the flow is in principle the same for two-dimensional and three-dimensional flow; the differences concerning the separating and re-attaching stream surfaces have already been mentioned. The boundary layer is very sensitive with respect to pressure gradients caused by external shock waves and it is the mechanism described here which smeares the effects of the pressure jump at the shock to large areas upstream and downstream of the shock.

3.5 Surface pressure distribution

Within the series of results presented later the experimental data for the configuration discussed so far are collected in Fig. 16. From these data the static pressure as well as the heat transfer distribution may be taken.

The pressure distribution at the wall is very similar to that observed in two-dimensional flow shown in Fig. 13. Far away from the corner the pressure starts at the value of a $\phi = 30°$ swept wedge and increases inboards due to the displacement caused by the flow separation far more inwards. The wall pressure reaches a relative maximum in the vicinity of the separation point S_1. In the region of the primary vortex at the impingement point of the embedded shock a flat minimum of the wall pressure is found, which might be related to the convex curvature of the displacement surface in this region which causes an expansion. The final pressure rise towards the corner center takes place in the region of the reattachment point R_1 where the inviscid outer flow is concave which leads to a steep pressure rise. By these effects the pressure jump of the embedded shock is smeared out: Separation occurs far outboard from the corner and the shock induced pressure rise is delayed by an expansion to the region of the reattachment point R_1. It might be that the reduction of the wall pressure in the separated flow region is also related to the flow separations as discussed by K. Kipke, D. Hummel [36] and R.H. Korkegi [33]. The flat minimum of static pressure is located underneath the primary vortex which could have caused the pressure reductions or at least an addition to it. Unfortunately the consequences of the expansion effect in the outer flow and the vortex effect in the separated viscous flow on the pressure distribution cannot be separated in the experimental results.

3.6 Surface heat transfer distribution

The measured distribution of the local heat transfer rate at the wall is also shown in Fig. 16. The maximum values are reached in the vicinity of the reattachment point R_1. From the structure of the flowfield, discussed so far, it is obvious that in this region stream surfaces reach the wall which originate from the outer part of the boundary layer. On these stream surfaces the original kinetic energy is large and therfore high temperatures are reached in the neighbourhood of the reattachment point R_1. The maximum value q_{max} related to the value $q_{W,u}$ at an unswept wedge with the same wedge angle δ is $q_{max}/q_{W,u} = 6$.

According to W. Möllenstädt [38] the heat transfer rate can be estimated by means of Crocco's analysis [49] for laminar boundary layers. If the flow proporties at the outer edge of the boundary layer are velocity V_1 and temperature T_1, the temperature distribution in a flat plate boundary layer in compressible flow is according to E.R. van Driest [50]

$$\frac{T}{T_1} = f_1\left(n\sqrt{\frac{V_1}{v_{Wa}x}}\right) = f_2\left(\frac{n}{\sqrt{x}}\right) = f_3\left(\frac{n}{\delta_B}\right) \qquad (18)$$

In this equation n is the coordinate normal to the flate plate. If the flow properties at the outer edge of the boundary layer as well as the temperature ratio T_{Wa}/T_1 are constant, the second relation in equ. (18) holds. If the local boundary layer thickness $\delta_B(x)$ is introduced, the variable $n/\sqrt{x}$ can be expressed as

$$\frac{n}{\sqrt{x}} = \frac{n}{\delta_B} \cdot \frac{\delta_B(x)}{\sqrt{x}} \sim \frac{n}{\delta_B} \qquad (19)$$

and since $\delta_B(x) \sim \sqrt{x}$ the second expression in equ. (19) is valid and the temperature distribution can be written in the form of the third relation in equ. (18). The temperature gradient at the wall may be calculated from equ. (18) as

$$\left[\frac{1}{T_1} \cdot \frac{\partial T}{\partial n}\right]_{Wa} = \left[f_3'\right]_{Wa} \cdot \frac{1}{\delta_B} \cdot \qquad (20)$$

It is now assumed that these relations for flat plate laminar boundary layers are also applicable for the laminar flow in the corner flow field. If equ. (20) is applied for an unswept wedge (subscript W, u) the constant $[f_3']_{Wa}$ can be expressed by the corresponding temperature gradient and from equ. (20) yields

$$\frac{\dot{q}}{\dot{q}_{W,u}} = \frac{[\partial T/\partial n]_{Wa}}{[\partial T/\partial n]_{W,u,Wa}} = \frac{\delta_{B,W,u}}{\delta_B} \cdot \qquad (21)$$

This simple result means that the heat transfer rate is proportional to the reciprocal value of the local boundary layer thickness. Thin boundary layers cause high heat transfer rates and vice-versa. The boundary layer thickness can be evaluated from the pitot pressure measurements. Typical results are plotted in Fig. 14 for the $\phi = 30°$ swept rectangular corner configuration. Since not every pitot pressure profile ends at a constant plateau outside the boundary layer, the boundary layer thickness has been taken as the distance of the inflection point of the pitot pressure profile from the wall for the swept and the unsept case as indicated in Fig. 14a. In the presence of an embedded vortex a corresponding vortex displacement thickness δ_v has been separated from the pitot pressure profile as shown in Fig. 14b, and it has been assumed that the heat transfer in such a flow is governed by the wedge flow part of the pitot pressure profile only. An evaluation of equ. (21) for the $\phi = 30°$ swept rectangular corner configuration is shown in Fig. 14c and compared with the measured data. The agreement between the estimation and the measurements is remarkable and the same applies to all other configurations investigated by W. Möllenstädt [38]. Some deviations are found in the region inboard of the reattachment line R_1 and underneath the primary vortex, which are due to the simplicity of the approximation. The variation of the flow properties at the outer edge of the boundary layer has not been taken into account and the effect of a vortex on the heat transfer rate has been omitted. Nevertheless the approximation according to equ. (21) leads to the correct value and position of the maximum heat transfer rate.
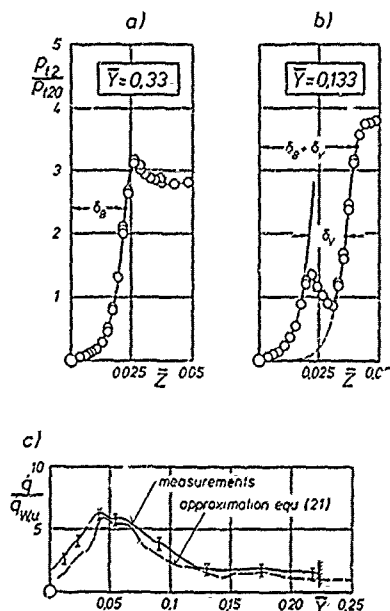
Fig. 14: Estimation of the surface heat transfer dristributuion through equ. (21) for the symmetrical $\phi = 30°$ swept rectangular corner ($\delta = 8°$) at $M_\infty = 12.8$ according to [38].
a) Pitot pressure distribution without vortex
b) Pitot pressure distribution with vortex
c) Distribution of surface heat transfer rate
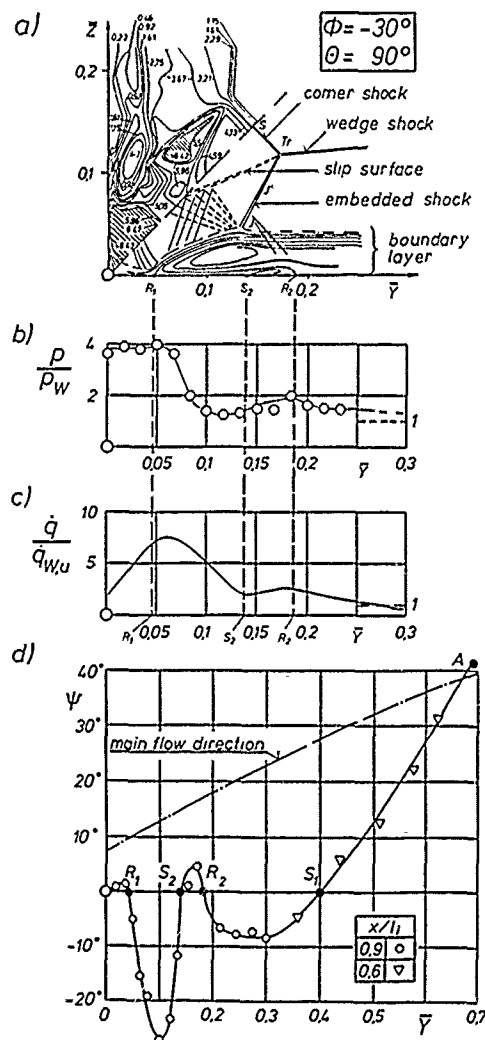
Fig. 15: Experimental results for the symmetrical -30° swept rectangular corner ($\delta = 8°$) at $M_\infty = 12.8$ [37].
a) Pitot pressure isobars p_{t2}/p_{t2_∞} in the flowfield
b) Wall pressure distribution
c) Wall heat transfer distribution
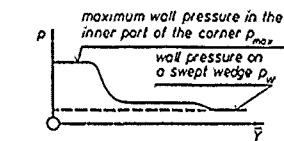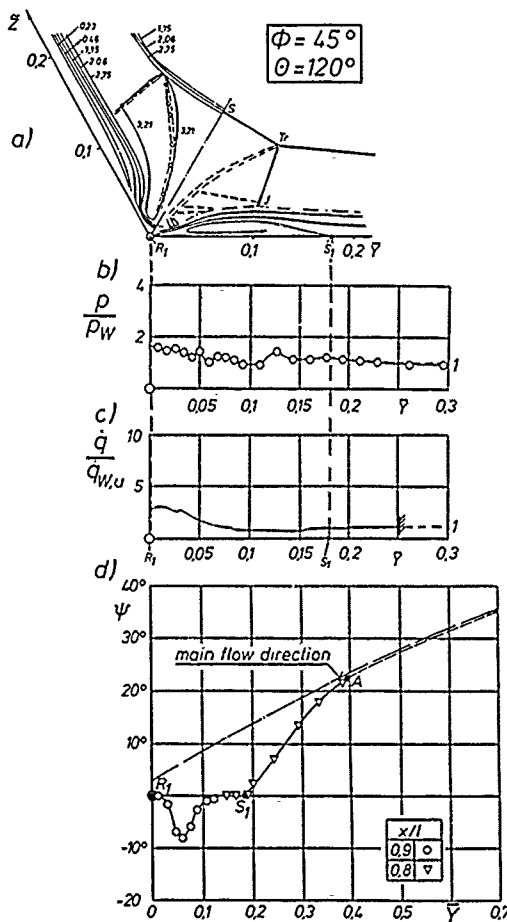d) Flow direction at the wall (reduced $\bar{Y}$-scale)
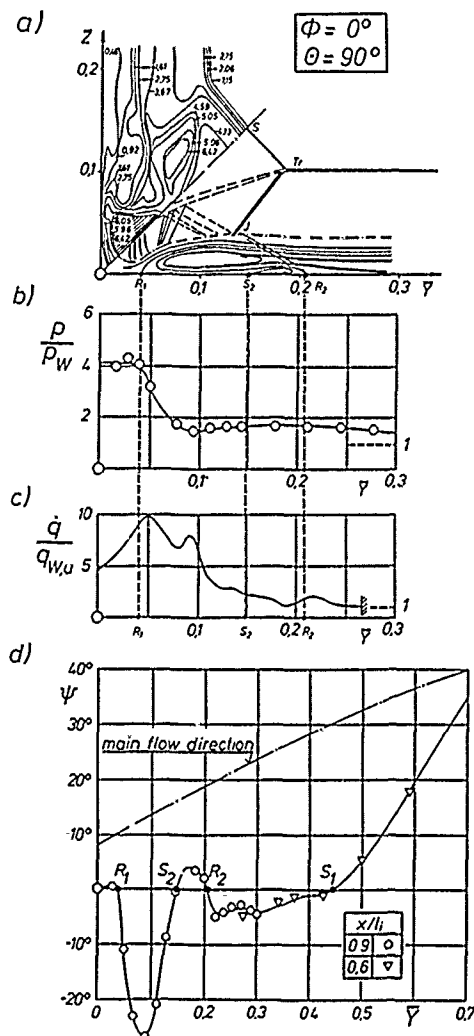
Fig. 16: Experimental results for the symmetrical unswept rectangular corner ($\delta = 8°$) at $M_\infty = 12.8$ [37].
a) Pitot pressure isobars p_{t2}/p_{t2_∞} in the flowfield
b) Wall pressure distribution
c) Wall heat transfer distribution
d) Flow direction at the wall (reduced $\bar{Y}$-scale)

3.7 Variation of geometric parameters

3.7.1 Effect of leading-edge sweep

The Figs. 15 to 18 show a series of experimental results in which the leading-edge sweep angle ϕ has been varied between $\phi = -30°$ and $\phi = +60°$. With increasing sweep angle ϕ the pitot pressure level in the corner region reduces, all shocks are weakened and the whole shock system moves slightly inboard as indicated by the partial diagrams a) in Figs. 15 to 18. For unswept wedges, Fig. 16a, the wedge shock is parallel to the $\bar{Y}$-axis. However, for swept wedges, Figs. 15a, 17a, 18a, the wedge shock is inclined against the $\bar{Y}$-axis since the distance of the wedge shock from the wedge changes in $\bar{Y}$-direction due to the increased or reduced distance between the leading-edge and the measuring plane depending on the sweep angle. With increasing sweep angle the slip surfaces meet closer to the corner center and the embedded shock impinges more and more normally on the viscous layer.

According to the partial diagrams in Figs. 15 to 18 for small sweep angles $|\phi| \leq 30°$ the maximum wall pressure in the corner reaches about 4 times the swept wedge value. The maximum wall pressure decreases considerably with increasing sweep angle ϕ and the width of the corresponding plateau is also reduced.
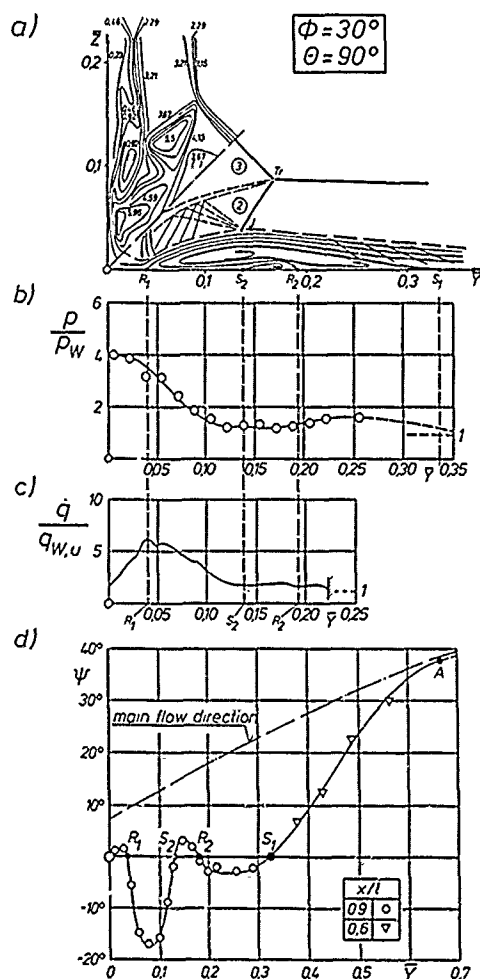
Fig. 17: Experimental results for the symmetrical 30° swept rectangular corner ($\delta = 8°$) at $M_\infty = 12.8$ [37].
a) Pitot pressure isobars $p_{t2}/p_{t2\infty}$ in the flowfield
b) Wall pressure distribution
c) Wall heat transfer distribution
d) Flow direction at the wall (reduced $\bar{Y}$-scale)
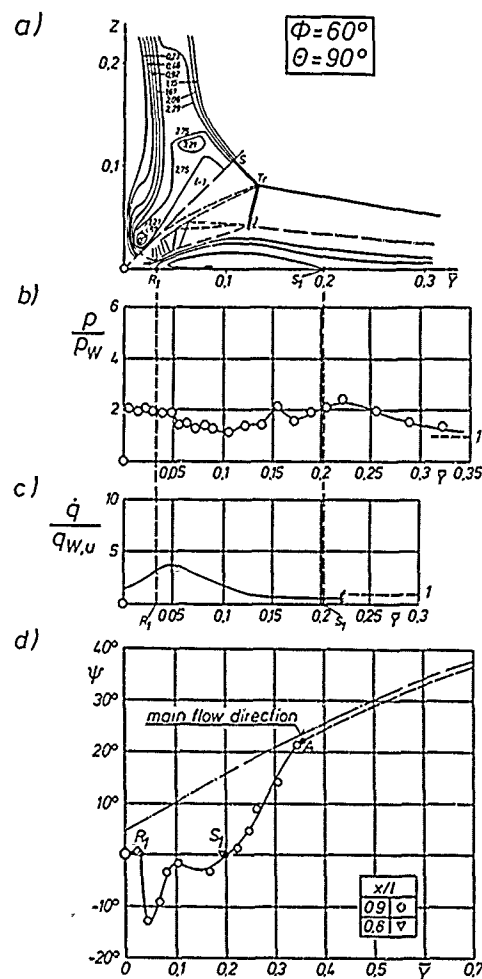
Fig. 18: Experimental results for the symmetrical 60° swept rectangular corner ($\delta = 8°$) at $M_\infty = 12.8$ [37].
a) Pitot pressure isobars $p_{t2}/p_{t2\infty}$ in the flowfield
b) Wall pressure distribution
c) Wall heat transfer distribution
d) Flow direction at the wall (reduced $\bar{Y}$-scale)

The partial diagrams c) in Figs. 15 to 18 show that the maximum heat flux in the vicinity of the reattachement line R_1 is highest for unswept corners, for which the maximum heat transfer rate is 10 times as large as for the unswept wedge. With increasing sweep angle ϕ the maximum local heat transfer rate is considerably reduced. Concerning Fig. 16c it has be noted that for $\phi = 0°$ a second heat transfer maximum has been measured underneath the primary vortex, which has not been found for other sweep angles ϕ, but which is in agreement with other investigations on unswept corner [29], [30], [33]. This matter is not fully understood, but the flow separation might be strongest for $\phi = 0°$ causing the additional heat transfer in this region.

According to the partial diagrams d) in Figs. 15 to 18 the influence border A is located at its outermost position at $\bar{Y} > 0.7$ for unswept wedges. The corner shock system is located at $\bar{Y} < 0.2$. This means that the interference effects between the two wedges extend through the boundary layer further outwards than the direct effect of the supersonic shock system. With increasing sweep angle ϕ the corner effect reduces considerably and the influence border moves inwards. Correspondingly the strengths of the primary vortices and of the secondary vortices within the viscous layer are reduced and for large sweep angles, Fig. 18d, the secondary separation disappears. The whole vortex system moves inwards with increasing sweep angle ϕ.

a) $\Phi = 45°$ $\Theta = 60°$

a) $\Phi = 45°$ $\Theta = 90°$
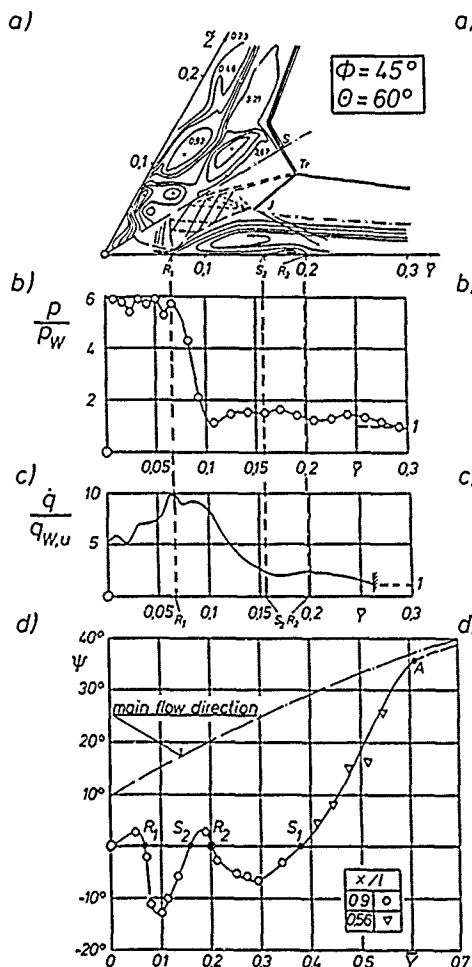
Fig. 19: Experimental results for the symmetrical 45° swept 60°-corner ($\delta = 8°$) at $M_\infty = 12.8$ [37].
a) Pitot pressure isobars p_{t2}/p_{t2} in the flowfield
b) Wall pressure distribution
c) Wall heat transfer distribution
d) Flow direction at the wall (reduced γ-scale)
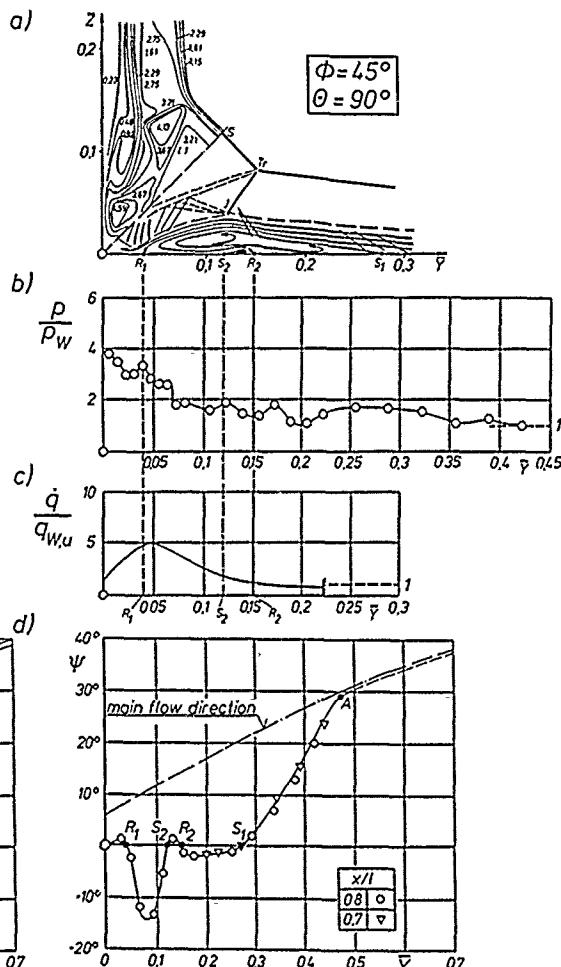
Fig. 20: Experimental results for the symmetrical 45° swept 90°-corner ($\delta = 8°$) at $M_\infty = 12.8$ [37].
a) Pitot pressure isobars p_{t2}/p_{t2} in the flowfield
b) Wall pressure distribution
c) Wall heat transfer distribution
d) Flow direction at the wall (reduced γ-scale)

3.7.2 Effect of corner angle

In Part I of the testprogram according to Tab. 2 the corner angle Θ has been varied systematically between $\Theta = 60°$ and $\Theta = 120°$ for corners between unswept wedges. The results have been published by K. Kipke, D. Hummel [36]. In the course of the investigations of W. Möllenstädt [38] the corner angle Θ has also been varied for corners between swept wedges. Examples of this kind are shown in Figs. 19 to 21 and discussed subsequently.

The partial diagrams a) indicate that the pitot pressure level in the corner region is considerably reduced for increasing corner angle Θ. The shock system moves inboard and all shocks weaken. The impingement angle between the embedded shock and the outer edge of the boundary layer is very flat for $\Theta = 60°$, but its value increases rapidly with increasing corner angle.

According to the partial diagrams b) in Figs. 19 to 21, at small corner angles a plateau of high wall pressures in the inner part of the corner exists. With incrasing corner angle Θ this pressure plateau disappears and the maximum wall pressure values are considerably reduced. This means that the pressure gradients are smaller and therefore the flow separations are weakened. The partial diagrams d) in Figs. 19 to 21 indicate weaker flow separations with increasing corner angle, and for $\Theta = 120°$ the secondary separation disappears at all. Corresponding to the inboard movement of the shock system with increasing corner angle the corner effects in the viscous layer decrease considerably in width. The influence border A as well as the separation lines S_1, S_2 and the reattachment lines R_1, R_2 move inwards with increasing corner angle.
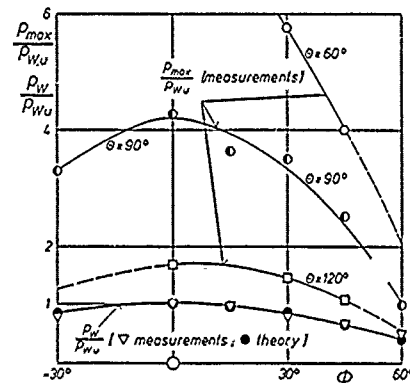
Fig. 22: Maximum wall pressure p_{max} as function of corner angle Θ and sweep angle ϕ in symmetrical corner configurations ($\delta = 8°$) at $M_\infty = 12.8$ [37].

Fig. 21: Experimental results for the symmetrical 45° swept 120°-corner ($\delta = 8°$) at $M_\infty = 12.8$ [37].
a) Pitot pressure isobars p_{t2}/p_{t2} in the flowfield
b) Wall pressure distribution
c) Wall heat transfer distribution
d) Flow direction at the wall (reduced γ-scale)

The partial diagrams c) in Figs. 19 to 21 show the effect of the corner angle on the heat transfer rates. Since the position of maximum heat flux is correlated with the reattachment line R_1, the region of maximum heat transfer moves inboard and the maximum values are reduced considerably with increasing corner angle.

3.7.3 Reduction of maximum values for wall pressures and heat transfer

In the course of the experimental investigations of K. Kipke, D. Hummel [36] and W. Möllenstädt [37, 38] reductions of the maximum values for static wall pressure and heat transfer rate due to variations of corner angle Θ and of leading-edge sweep ϕ have been found. The possible reductions of these maximum values by variations of the two governing parameters are summarized subsequently.

Fig. 22 shows a schematic diagram of the pressure distribution along the wall in a corner configuration. The maximum value in the corner center is p_{max} and far away from the corner the undisturbed value for the swept wedge p_W is reached. In the lower part of Fig. 22 the wall pressures are based on the wall pressure of an unswept wedge $p_{W,u}$. In order to be able to show the results in this manner, some additional pressure measurements on swept and unswept wedges far away from the corner have been carried out. The measured pressure ratio $p_W/p_{W,u}$ is plotted as a function of the sweep angle ϕ. The well known reduction of p_W with increasing ϕ turns out. The ratio $p_W/p_{W,u}$ has also been calculated from the shock relations using the measured shock positions and given in Fig. 22 as black dots. The agreement with the directly measured data is good. The diagram in Fig. 22 shows the maximum wall pressure $p_{max}/p_{W,u}$ as functions of the sweep angle ϕ for different corner angles Θ. Both parameters have a big influence. The highest values are found for unswept wedges, $\phi = 0°$, and with increasing sweep angle a considerable reduction is achieved. On the other hand the maximum wall pressure increases very much with decreasing corner angle Θ. In an unswept 90°-corner p_{max} is 4 times as high as in a 60°-swept 90°-corner. If the corner angle is reduced from 90° to 60° the wedges have to be 45°-swept to obtain the same maximum wall pressure as in the unswept 90°-corner. Small values of the maximum wall pressure are achieved for combinations of high sweep angles and large corner angles.

Finally Fig. 23 shows the maximum heat transfer rate as functions of the sweep angle ϕ for different corner angles θ. In the diagram the maximum heat transfer rate is based on the value for an unswept wedge. Measurements for swept wedges in the absence of a corner are not available. The maximum heat transfer rate decreases with increasing sweep angle and it increases with decreasing corner angle. In an unswept 60°-corner the maximum heat transfer rate is 14 times as high as for an unswept wedge. For 90°-corners the maximum heat transfer rate can be reduced to about 40% by applying a sweep angle of ϕ = 60°. If the corner angle is reduced from 90° to 60° the wedges have to be 45°-swept to obtain the same maximum heat transfer rate as in the unswept 90°-corner. Small values of the maximum heat transfer rate are achieved for combinations of high sweep angles and large corner angles.

3.7.4 Effects of wedge angle

Up to now symmetric corner configurations consisting of two intersecting wedges with the same wedge angle δ were considered at constant Machnumber. Systematic variations of the wedge angle have been carried out to some extend by K. Kipke, D. Hummel [36] for unswept 90° corners. Single symmetrical wedge/wedge configurations have been investigated by A.F. Charwat, L.G. Redekopp [27], J.E. West, R.H. Korkegi [31] and R.D. Watson, L.M. Weinstein [29]. Variations of the wedge angle for swept wedges and $\theta \neq$ 90° are missing. Configurations with two intersecting flat plates have also to be considered here because they form the limiting case for $\delta \to 0$. Investigations of this kind are due to P.C. Stainback [24], [25], P.C. Stainback, L.M. Weinstein [26] and H.J. Schepers [51]. For decreasing wedge angle the wedge shock angle σ_w as well as the corner shock angle σ_c decrease as well, and the corresponding shocks are weakend. In the limiting case $\delta \to 0$ rather weak bow shocks remain at the intersecting flat plates. They still cause an increase of static pressure and of local heat transfer rate at the wall towards the corner center and from their distributions some indications support the view that also flow separations are present in this limiting case. Flowfield investigations in symmetrical corners with small wedge angles or for flat plate configurations are missing.

3.7.5 Unsymmetric corner flows

Only a few investigations on unsymmetric corner configurations do exist. A.F. Charwat, L.G. Redekopp [27] published the first results for corner configurations with a base wedge δ_b = 12.2° and three inferferece wedges δ_i = 3.5°/7.5°/12.2° in supersonic flow. The resulting shock formation is shown in Fig. 24. The shock wave at the base wedge δ_b remains always in the same position σ_{bw}. With decreasing wedge angle of the interference wedge δ_i the wedge shock angle σ_{iw} decreases as well, but due to the different origins of the corner apex the interference wedge shock moves up. The shock pattern becomes unsymmetric as well and for all measured cases a corner shock wave and two triple points Tr have been found. On the side of the interference wedge the embedded shock moves inboard and shifts into line with the two-dimensional oblique shock of the base wedge as δ_i is decreased. On the base-wedge side the location of the shock-surface intersection point remains fixed. In this region the flow structure is very complicated and not yet fully understood. The pressure distribution on the base wedge according to [27] is shown in Fig. 25. A considerable reduction of the peak pressures with decreasing wedge angles of the interference wedge turns out. No data are available for the interference-wedge side. Theses experiments have been carried out in supersonic flow with relatively thin boundary layers. Although flow visualizations indicated flow separations within the viscous layer a detailed analysis of the corresponding flow pattern was not possible. Other investigations on unsymmetric corner configurations in supersonic flow may be taken from [60].

Another unsymmetric corner configuration has been investigated by J.R. Cooper, W.L. Hankey [32]. A δ_b = 15.0° base wedge formed a rectangular corner with a flat plate. Compared with the configuration of A.F. Charwat, L.G. Redekopp [27] this configuration forms the limiting case $\delta_i \to 0$. Concerning the inviscid outer flow the interference of a very strong wedge bow shock and a weak flat plate bow shock takes place and in this case only one triple point Tr has been found. The loss of a triple point for $\delta_i \to 0$ is not fully understood. The investigations have been carried out for a free stream Machnumber M_∞ = 12.5. The viscous layer was relatively thick and some details of their structure could be detected.
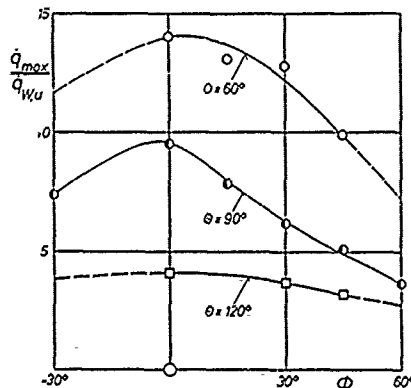
Fig. 23: Maximum heat transfer rate $\dot{q}_{max}$ as function of corner angle θ and sweep angle ϕ in symmetrical corner configurations (δ = 8°) at M_∞ = 12.8 [37].
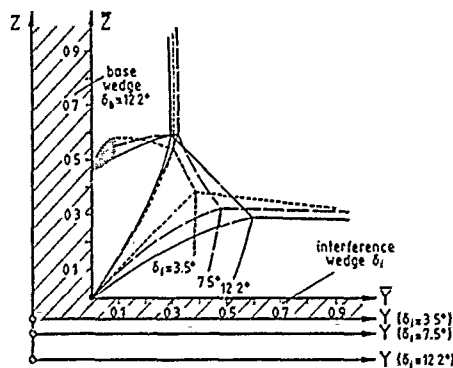
Fig. 24: Shock formation in unsymmetric corner configurations with different wedge angles (δ_b=12.2°, δ_i=3.5°/7.5°/12.2°) at M_∞=3.17 according to [27].
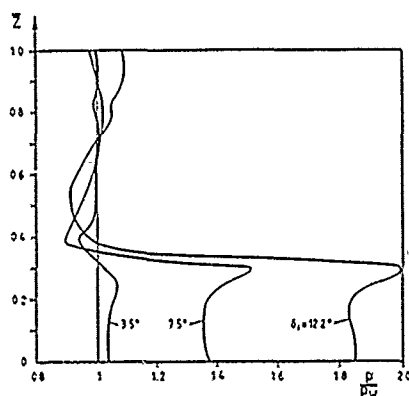
Fig. 25: Pressure distributions on the base wedge (δ_b=12.2°) of unsymmetric corner configurations with different interference wedge angles (δ_i=3.5°/7.5°/ 12.2°) at M_∞=3.17 according to [27].

Two separation lines and two reattachment lines have been found and they are interpreted to belong to two flow separations which follow each other in the flow towards the corner center. This view of the viscous flow gave rise to some doubts. K. Kipke [35] and K. Kipke, D. Hummel [36] were the first to explain these flow separations as primary and secondary separations which are well known from delta wings [46], and later R.H. Korkegi [33] and W. Möllenstädt [37], [38] used this interpretation as well. The paper of J.R. Cooper, W.L. Hankey [32] is mainly concentrated on the flow on the flat plate side and the wedge is considered only as a shock generator. No information about the flow behaviour on the wedge side of the configuration is available.

This section shows that the hypersonic axial flow in unsymmetric corner configuration is not yet understood in details. Therefore an extension of the research program (see Tab. 2) of the Institut für Strömungsmechanik at TU Braunschweig is presently carried out. In this new research program systematic experiments are performed for unsymmetric corner configurations, which contain the well known symmetric configurations [36], [38] as well as the limiting case of the wedge/plate combination. Unsymmetric flows are generated by different wedge angles δ and by different sweep angles ϕ on both sides as well as by combinations of both geometric parameters.

3.8 Effects of Machnumber and Reynoldsnumber

3.8.1 Viscous interaction parameter

For the axial corner flows under consideration the most important parameters governing the flow are the constant free stream Machnumber M_∞ and the Reynoldsnumber $Re_{x\infty} = \rho_\infty U_\infty x/\mu_\infty$, which is a linear function of the distance x from the corner apex, but which depends also on the free stream conditions. Hence the viscous interaction parameter for laminar flow (for derivation see e.g. W.D. Hayes, R.F. Probstein [52], J.L. Stollery [53]

$$\bar{\chi} = \frac{M^3_\infty}{\sqrt{Re_{x\infty}}} \sqrt{C}$$ (22)

with the Chapman-Rubesin constant

$$C = \frac{\mu_{Wa} \cdot \rho_{Wa}}{\mu_\infty \cdot \rho_\infty}$$ (23)

varies downstream. In the neighbourhood of the corner apex or the wedge leading-edge the viscous interaction parameter is very large and strong interactions between the viscous flow near the wall and the inviscid outer flow are present. Far more downstream the viscous interaction parameter $\bar{\chi}$ reduces more and more and only weak interactions of the two parts of the flowfield are observed. Measured pressure distributions p/p$_\infty$ in laminar flow indicate that the strong and weak interaction regions meet at $\bar{\chi}$ = 3.0.

At hypersonic Machnumbers the transition Reynoldsnumbers are very high so that strong turbulent viscous interactions are unlikely to occur. Nevertheless weak interactions have to be considered in the turbulent flow region and the corresponding turbulent viscous interaction parameter is according to J.L. Stollery [53]

$$\bar{\chi} = M^{9/5}_\infty \left(\frac{C}{Re_{x\infty}}\right)^{1/5}.$$ (24)

For all corner configurations, considered here, the inviscid flow would be conical, since the boundary conditions are conical. The flow including the viscous layer is principally non-conical. In the strong interaction region the pressure relation reads as

$$\frac{p}{p_\infty} = K_1(\gamma) \cdot \bar{\chi}$$ (strong interaction) (25)

(with K_1 as a constant) and this indicates that the flow cannot be conical there. Far more downstream, however, in the weak interaction region the pressure relation is

$$\frac{p}{p_\infty} = 1 + K_2(\gamma) \cdot \bar{x} \quad \text{(weak interaction)} \tag{26}$$

(with another constant K_2). For small values of $\bar{x}$ the pressure distribution will be constant, $p/p_\infty \approx 1$, and this means that the flow is conical. For all measurements in supersonic flow the viscous interaction parameter is indeed very small. Therfore all theses experiments have been carried out for weak interaction and conical flow has been found. In such tests, see e.g. A.F. Charwat, L.G. Redekopp [27], the flow is governed by the inviscid conical outer flow, and the boundary layers turned out to be very thin, indicating only weak interactions. In the hypersonic experiments of R.D. Watson, L.M. Weinstein [29] the measurements were taken at $\bar{x} = 4.0$ which is close to the border between strong and weak interaction, and the flow was conical there. The same is valid for the experiments of K.Kipke, D. Hummel [36] and W. Möllenstädt [37], for which K. Kipke [35] determined $\bar{x} = 3.0$, which is the border value. Some tests at different stations x/l, see Figs. 15-21 and [36], [38], led to the conclusion that the flow at the measuring station is fairly conical with respect to a fictitious corner apex which is located slightly upstream of the geometric one. This fact has been taken into account during the flowfield analysis in section 3.3.2.

In most experiments the flow at a corner configuration is analysed at a certain station x and the free stream Machnumber M_∞ as well as the Reynoldsnumber $Re_{x,\infty}$ are varied. In the case of weak interaction a variation of Machnumber at constant Reynoldsnumber influences primarily the properties of the outer inviscid flowfield. The boundary layer develops for the conditions prescribed by this outer flowfield and again a Machnumber effect may occur in the compressible boundary layer. On the other hand a variation of Reynoldsnumber at constant Machnumber for weak interaction has no significant effect on the inviscid outer flow, but the properties of the boundary layer may be strongly influenced by Reynoldsnumber . Subsequently effects of Machnumber and Reynoldsnumber are discussed for weak interaction.

3.8.2 Effects of Machnumber

The shock wave structure in the inviscid outer flowfield of the interference region is strongly influenced by Machnumber. A typical result for supersonic flow taken from A.F. Charwat, L.G. Redekopp [27] is shown in Fig. 26. At the left hand side the embedded shocks have been extrapolated to the wedge surface at the point of maximum slope of the wall-pressure distribution. The general features of the flowfield are unchanged. The entire interference region moves closer to the corner as the Machnumber increases. Similar results have been obtained by K. Kipke, D. Hummel [36] for hypersonic flow and weak interaction. Fig. 27 summarizes experimental data on the dependence of the maximum pressure in the neighbourhood of the corner center from the Machnumber. The maximum pressure increases considerably with increasing Machnumber. The same applies for the single two-shock flow model which assumes the intersection of two plane wedge shocks and which disregards the violation of the boundary conditions. The Machnumber M_1 behind the wedge shock can be calculated [45] from the free stream Machnumber M_∞ and the shock angle q_w. The pressure ratio p_{max}/p_W is then evaluated for $\gamma = 7/5$ [45] from

$$\frac{p_{max}}{p_W} = \frac{7 M^2_1 \sin^2 q_W - 1}{6} \tag{27}$$
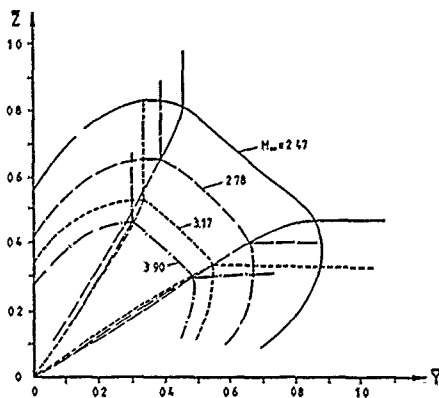
Fig. 26: Effect of Machnumber on the shock wave structure in a symmetrical, unswept, rectangular corner (δ_b=12.2°) at supersonic speed according to [27].
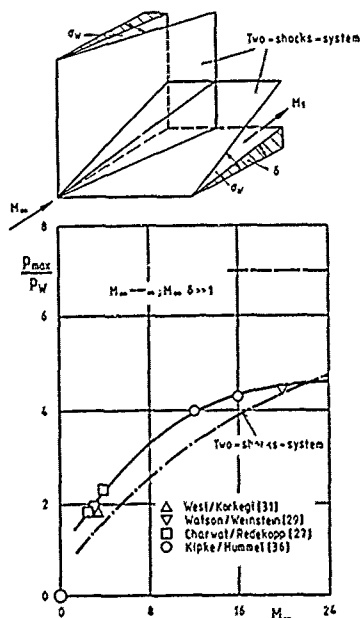
Fig. 27: Effect of Machnumber on the maximum pressure in an unswept, rectangular corner (δ=10°) at according to [36].
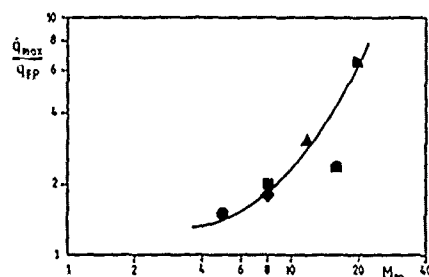
Fig. 28: Effect of Machnumber on the maximum heat transfer rate in an unswept rectangular corner of two intersecting flat plates ($\delta=0°$) at according to [29].
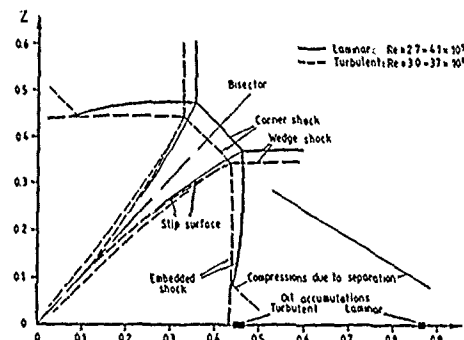
Fig. 29: Shock wave structure for laminar and turbulent boundary layers in a symmetrical unswept rectangular corner ($\delta=9.5°$) at $M_\infty=3.0$ according to [31].

and in the limit $M_\infty \to \infty$ with $M_\infty \cdot \delta \gg 1$ yields

$$\lim_{M_\infty \to \infty} \frac{p_{max}}{p_W} = \frac{2\gamma}{\gamma-1} = 7.$$ (28)

The strong increase of the maximum pressure is thus a characteristic feature of the inviscid outer flowfield.

The heat transfer distribution is principally the same for supersonic and hypersonic flow as compared by R.H. Korkegi [30]. R.D. Watson, L.M. Weinstein [29] have looked through the available experimental data for unswept 90° corner configurations. Their result for the peak heat transfer rate, based on the flat plate value (FP), as function of Machnumber is shown in Fig. 28. All these data are from the weak interaction region ($\bar{\chi} < 4.0$). The peak heat transfer rate increases considerably as the Machnumber increases.

3.8.3 Effects of Reynoldsnumber

Almost all experimental investigations on axial flow in corners were concerned with laminar flow. In this case strong flow separations occurred far outboard from the corner center and even secondary separations underneath the primary vortex were found. Only a few experimental data are available for turbulent boundary layers from J.E. West, R.H. Korkegi [31] and R. H. Korkegi [33]. These investigations have been carried out for a symmetric, unswept rectangular corner configuration of two intersecting 9.5° wedges at a Machnumber $M_\infty = 3$. For comparisons one flowfield has been measured at Re = 3.9 · 10^5, for which the boundary layer was laminar. The result is shown in Fig. 29. For turbulent boundary layers extensive tests for Reynoldsnumbers 3.0 to 37 · 10^6 showed no effect of Reynoldsnumber on the shock formation. The flow structure is basically the same as in laminar flow. The whole interference shock system is located slightly more inboard in the turbulent case. Although very low values of $\bar{\chi}$ are present and all results represent "weak" interaction, the displacement of the outer shock system due to the different boundary layer formation is distinctly marked. The surprising result is the different behaviour of the flow with respect to separations. For laminar flow a very early flow separation takes place marked by the oil accumulation line at $\bar{Y} = 0.87$. Hence a large primary vortex is formed which causes a large displacement in the flow and which moves the whole interference shock system outboard. The turbulent boundary layer flow is not very sensitive to pressure gradients. Flow separation takes place far more inboard and very close to the embedded shock. Therefore the flow separations are smaller in the case of turbulent boundary layer flow and the corresponding outboard displacement of the interference shock system is weaker. The paper of J.E. West, R.H. Korkegi [31] contains some very nice flow visualizations which show the transition from laminar to turbulent boundary layer and the corresponding inboard displacement of the primary separation line S_1.

Surface pressure distributions taken from [31] are shown in Fig. 30. For laminar boundary layer the pressure rise starts far outboard at the separation point and the compression in the flow is distinctly marked. The steep pressure increase caused by the embedded shock is delayed through the expansion around the primary vortex and finally the high plateau is reached in the reattachment zone. For turbulent boundary layers the pressure rise from the wedge value starts far more inboard and it is much steeper than for the laminar case. This indicates a strong compression or a lambda-formation of the embedded shock near the separation line. The second pressure rise is as in the laminar case associated with the flow impingement in the region of the reattachment line. The curve for a transitional section follows in the outer part the results for turbulent boundary layer and switches inboard towards the data for laminar boundary layer, since the inner portion of the flowfield has already experienced laminar boundary layer separation.

The heat transfer distribution has not been measured by J.E. West, R.H. Korkegi [31]. A few data are available from P.C. Stainback, L.M. Weinstein [26]. They indicate that in corner configurations the heat transfer rate in the vicinity of the reattachment point is considerably reduced for turbulent boundary layers as compared with the laminar case. Further investigations on this subject are needed.
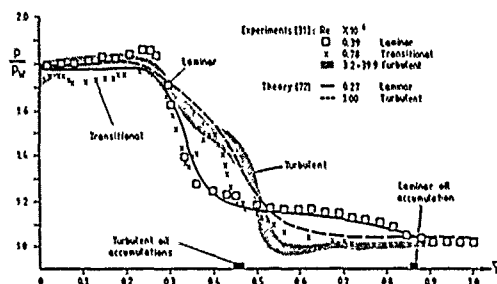
Fig. 30: Surface pressure distribution for different Reynoldsnumbers in a symmetrical, unswept, rectangular corner (δ=9.5°) at M_∞=3.0 according to [31]. Theory (numerical solution of the full Navier-Stokes equations) due to [72].

4. THEORETICAL INVESTIGATIONS ON AXIAL CORNER FLOWS AND COMPARISON WITH EXPERIMENTAL DATA

Up to 1970 theoretical work descriptive of supersonic flow in an axial corner was virtually nonexistent. Some early studies of the inviscid outer flowfield as well as of the boundary layer flow introduced assumptions and boundary conditions which were not representative of the supersonic interaction as found experimentally. In the last 20 years, however, theoretical modeling of the real axial corner flow has been achieved successfully. The approach was quite conventional, starting with inviscid flow theories followed by taking into account viscous effects up to the solution of simplified or the full Navier-Stokes equations. Concerning the region of hypersonic flows the theory is well established only for perfect gas properties. It will be outlined and reviewed subsequently up to this limit. Real gas effects such as dissociation and ionization will not be taken into account and the upstrem end of the strong interaction region with slip flow and free molecular flow will also not be covered. The review, following here, comprises theoretical work on the strong and weak interaction regions in axial corner flows for a perfect gas.

4.1. Inviscid flow

The linearized solution for supersonic flow near the intersection of two quarter-infinite wedges was obtained by R.M. Snow [54]. Later F.D. Hains [43] showed that at least for small wedge angles δ and not too small corner angles θ an exact solution exists, which allows the two wedge shocks to intersect as plane shock waves. For this purpose a single-embedded shock wave is necessary on each side. These shocks are followed by conical expansions which satisfy the boundary conditions at the wedge surfaces and which provide the conditions at the border of the inner elliptic region. J. Wallace, J.H. Clarke [55] found the same result on the basis of a second-order solution of the potential equation. Discontinuities in the potential and square-root singularities in the velocities are removed by a proper introduction of the bow shocks into the flowfield, which leads to the same flow structure as proposed by F.D. Hains [43]. Due to the conditions at the shocks the solution with direct intersection of two plane shock waves may be called a regular reflection configuration, whereas the other possible solution according to A.F. Charwat, L.G. Redekopp [27] may be considered as a Mach disk configuration. For some time both solutions were thought to exclude each other, but F. Marconi [56] has shown that in symmetrical corners for low wedge angles the regular reflection configuration and for large wedge-angles the Mach disk configuration of the shocks do exist. T.P. Goebel [57] analyzed the Mach disk shock configuration found in the experiments of A.F. Charwat, L.G. Redekopp [27], by means of an iteration technique to fulfil the shock relations and the compatibility conditions for the slip surface. As results the positions of the triple point Tr and the slope of the slip surfaces turned out and it was found that the slip surfaces meet at a certain distance from the corner center unlike the data of A.F. Charwat, L.G. Redekopp [27] but in agreement with the experiments of R.D. Watson, L.M Weinstein [29]. A unique solution for the embedded shock could not be given and so far no adequate method of predicting the inviscid flow structure for large wedge angles δ was available.

The first numerical solution of the Euler equations for axial corner flows has been carried out by P. Kutler [58]. According to this method examples have been calculated by V.Shankar, D. Anderson, P. Kutler [59] and D.A. Anderson, R.K. Nangia [60] and compared with experimental data. The Euler equations may be written in conservation form as

$$\frac{\partial \overline{F}}{\partial x} + \frac{\partial \overline{G}}{\partial y} + \frac{\partial \overline{H}}{\partial z} = 0 \tag{29}$$

where

$$\overline{F} = \begin{vmatrix} \rho u \\ \rho u^2 + kp \\ \rho uv \\ \rho uw \end{vmatrix} ; \quad \overline{G} = \begin{vmatrix} \rho v \\ \rho uv \\ \rho v^2 + kp \\ \rho vw \end{vmatrix} ; \quad \overline{H} = \begin{vmatrix} \rho w \\ \rho uw \\ \rho vw \\ \rho w^2 + kp \end{vmatrix}$$

and where $k = (\gamma - 1)/2\gamma$, γ beeing the ratio of specific heats. All quantities are dimensionless. Pressure and density are based on free-stream-stagnation conditions and the velocities on the maximum adiabatic velocity. The system of equations is made complete by the energy equation

$$p = \rho(1 - u^2 - v^2 - w^2). \tag{30}$$

These equations are transformed into nonorthogonal conical coordinates. In the y-direction the lower boundary is the interference wedge surface, where the tangency condition is satisfied. The upper boundary is chosen to fall in the region of known flow properties given by the base wedge δ_b. The base wedge shock location is known and beyond this free stream conditions are applied. An analogous procedure is used in the z-direction.

The second-order accurate predicator-corrector scheme according to R.W. MacCormack [61] is used to integrate equ. (29) iteratively until the term $\partial F/\partial x$ is zero, implying the establishment of a conical flowfield. Shock waves and slip surfaces that should exist form automatically and are correctly positioned within the computational network of points in the converged solution. Shocks are not treated explicitly as a discontinuity and the oblique shock relations are not used. The corresponding capturing technique is described by P. Kutler, H. Lomax [62].

Sample calculations have been carried out for experimental data available from the literature. Fig. 31 shows the computed flowfield with the shock and slip-surface structure according to V. Shankar, D. Anderson, P. Kutler [59] compared with the experimental results of A.F. Charwat, L.G. Redekopp [27]. The entire experimental wave structure is displaced outward relative to the inviscid numerical results because of the effective thickening of the body due to the presence of a laminar boundary layer. The difference between the experimental data and the inviscid numerical results suggests that the viscous effects are more dominant in the three-dimensional corner region than in the two-dimensional wedge flow region. Outboard of the embedded shock the inviscid flow is completely two-dimensional. The compression in this region, observed in the experiments, is caused by the separation of the laminar boundary layer. Thus the inviscid numerical solution turns out slightly different from the schematic view in Fig. 8. in which plane shock waves have been assumed. The details show that the corner shock and the embedded shock are also curved and that the flow behind them is not exactly parallel. Correspondingly the slip surfaces are curved and their intersection point in the bisector plane is therefore located far more inboard. The deflection of the flow in the vicinity of the corner center is achieved by a continuous compression.

A corresponding comparison between the inviscid numerical results according to P. Kutler [58] and the high Reynoldsnumber experimental data of J.E. West, R.H. Korkegi [31] is shown in Fig. 32. Again the embedded shock and the slip surface are slightly curved. The numerical corner shock is found more inboard than the experimental one, but the wedge shocks agree exactly. Again the experimental shock structure has moved outboard as compared with the inviscid numerical result, but this displacement is much weaker for the present case of turbulent boundary layers. A comparison of the numerical and experimental surface pressures for turbulent boundary layer is shown in Fig. 33. The first pressure rise in the experimental data with decreasing $\bar{Y}$ indicates the onset of separation. This is followed by a reduced gradient region which indicates separation and by a rapid pressure rise which is related to reattachment. The measured pressure between the reattachment point and the corner center is greater than that of the inviscid result. This indicates again an apparent thickening of the body in this region due to boundary layer displacement effects. Similar comparisons have been carried out by D.A. Anderson, R.K. Nangia [60] for swept and unswept corner configurations, which included also unsymmetrical cases and expansion flows.

Another approach for the numerical solution of the Euler equations has been carried out by F. Marconi [56]. The computational procedure utilizes again a second-order finite-difference marching technique and all discontinuities, shocks and slip surfaces, are fitted with the appropriate jump conditions. The triple points are computed exactly. Results according to this numerical approach are in excellent agreement with the shock-capturing results of P. Kutler [58] as shown in Fig. 32 for the shock structure and in Fig. 33 for the surface pressure distribution in a symmetrical configuration. For unsymmetrical configurations some differences between the shock-capturing and the shock-fitting solution were found. The paper of F. Marconi [56] contains some sample calculations which show the effects of parameter variations such as leading-edge sweep ϕ, corner angle θ and free stream Machnumber M_∞ on the shock structure. It is shown for inlet configurations that large portions of these flows are dominated by the conical flows originating at the corners.
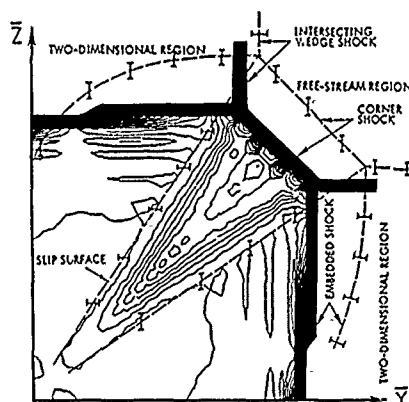
Fig. 31: Density contours plot in a symmetrical, unswept, rectangular corner ($\delta=12.2°$) at $M_\infty=3.17$. Comparison of the numerical solution of the Euler equations according to [59] with experimental data from [27] for laminar boundary layers.
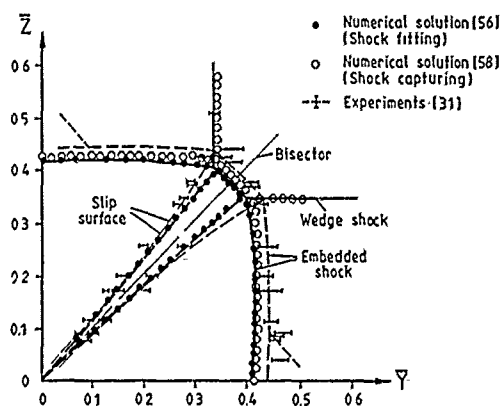
Fig. 32: Shock wave pattern in a symmetrical, unswept, rectangular corner ($\delta=9.5°$) at $M_\infty=3.0$. Comparison of the numerical solution of the Euler equations according to [56] and [58] with experimental data from [31] for turbulent boundary layers.
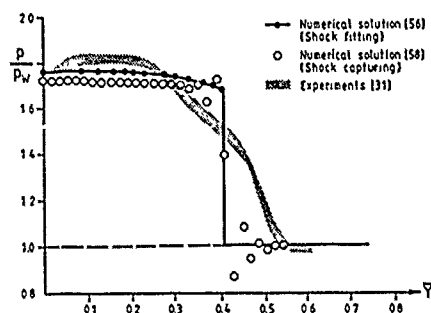
Fig. 33: Surface pressure distribution in a symmetrical, unswept, rectangular corner ($\delta=9.5°$) at $M_\infty=3.0$. Comparison of the numerical solution of the Euler equations according to [56] and [58] with experimental data from [31] for turbulent boundary layers.

Recently J.A. Martin [63] applied a shock-fitting numerical algorithm for the solution of the Euler equations to rounded corner configurations. It turns out that with increasing radius the shock system moves outward.

4.2. Viscous flow

For compressible viscous flow in corners several attempts exist to calculate the boundary layer flow for a given outer potential flow, see e. g. M.H. Bloom, S. Rubin [64], P.A. Libby [65], B.C. Weinberg, S.G. Rubin [66], K.N. Ghia, R.T. Davis [67] and A.G. Mikhail, K.N. Ghia [68]. In this kind of investigation the classical boundary layer concepts are applied. The inviscid outer flow is assumed to be smooth with only small transverse pressure gradients in comparison with the streamwise pressure gradient. In supersonic flow shocks are not taken into account. For the real axial corner flow problem these results are asymptotic solutions under particular flow conditions.

The behaviour of the viscous flow region in axial corner flows depends strongly on the shock wave structure in the inviscid outer flow. Realistic results can only be expected if this inviscid outer flowfield is taken into account properly. Therefore the problem is amenable to solution only through the use of the Navier-Stokes equations. Some attempts in this direction will be discussed subsequently.

4.2.1 Solutions of the full Navier-Stokes equations for laminar flow

Basis of the numerical calculations are the Navier-Stokes equations which may be written in conservation form as

$$\frac{\partial \bar{U}}{\partial t} + \frac{\partial \bar{F}}{\partial x} + \frac{\partial \bar{G}}{\partial y} + \frac{\partial \bar{H}}{\partial z} = 0 \tag{31}$$

where

$$\bar{U} = \begin{vmatrix} \rho \\ \rho u \\ \rho v \\ \rho w \\ \rho e' \end{vmatrix} \tag{32}$$

denotes the vector of the dependent variables ρ, $\rho \bar{V}$, $\rho e'$. The vector fluxes $\bar{F}$, $\bar{G}$ and $\bar{H}$ can be split up in their inviscid parts i and their viscous parts v as

$$\bar{F}_i = \begin{vmatrix} \rho u \\ \rho u u + p \\ \rho u v \\ \rho u w \\ \rho e'u + pu \end{vmatrix} ; \qquad \bar{F}_v = \begin{vmatrix} 0 \\ \tau'_{xx} \\ \tau'_{xy} \\ \tau'_{xz} \\ -\dot{q}_x + \phi'_x \end{vmatrix} \tag{33a}$$

$$\bar{G}_i = \begin{vmatrix} \rho v \\ \rho v u \\ \rho v v + p \\ \rho v w \\ \rho e'v + pv \end{vmatrix} ; \qquad \bar{G}_v = \begin{vmatrix} 0 \\ \tau'_{yx} \\ \tau'_{yy} \\ \tau'_{yz} \\ -\dot{q}_y + \phi'_y \end{vmatrix} \tag{33b}$$

$$\bar{H}_i = \begin{vmatrix} \rho w \\ \rho w u \\ \rho w v \\ \rho w w + p \\ \rho e' w + p w \end{vmatrix} \quad ; \quad \bar{H}_v = \begin{vmatrix} 0 \\ \tau'_{zx} \\ \tau'_{zy} \\ \tau'_{zz} \\ -\dot{q}_z + \phi'_z \end{vmatrix} \tag{33c}$$

In these equations e' is the specific total energy

$$e' = C_v T + \frac{u^2 + v^2 + w^2}{2} \tag{34}$$

and $\bar{\tau}'$ is the viscous stress tensor

$$\bar{\tau}' = \mu \mathrm{Def}\bar{V} + \lambda(\nabla \cdot \bar{V})\bar{I} \tag{35}$$

which contains the bulk viscosity term with $\lambda = -2\mu/3$ and $\bar{I}$ as the unit identity matrix and the shear viscosity terms with the deformation tensor

$$\mathrm{Def}\bar{V} = \begin{vmatrix} \frac{\partial u}{\partial x} & \frac{\partial u}{\partial y} & \frac{\partial u}{\partial z} \\ \frac{\partial v}{\partial x} & \frac{\partial v}{\partial y} & \frac{\partial v}{\partial z} \\ \frac{\partial w}{\partial x} & \frac{\partial w}{\partial y} & \frac{\partial w}{\partial z} \end{vmatrix} + \begin{vmatrix} \frac{\partial u}{\partial x} & \frac{\partial v}{\partial x} & \frac{\partial w}{\partial x} \\ \frac{\partial u}{\partial y} & \frac{\partial v}{\partial y} & \frac{\partial w}{\partial y} \\ \frac{\partial u}{\partial z} & \frac{\partial v}{\partial z} & \frac{\partial w}{\partial z} \end{vmatrix} . \tag{36}$$

The complete stress components can be obtained from the stress tensor

$$\bar{\tau} = \bar{\tau}' - p\bar{I}. \tag{37}$$

The work done by the viscous stresses is

$$\bar{\phi}' = \bar{V} \cdot \bar{\tau}' \tag{38}$$

and the heat flux is

$$\bar{\dot{q}} = -k\nabla T. \tag{39}$$

In inviscid flow the viscous terms in the above equations vanish

$$\bar{F}_v = \bar{G}_v = \bar{H}_v = \bar{\tau}' = 0$$

and the remaining set of equations can be easily transformed into the system of equ. (29), if the heat flux due to conductivity is omitted, $q = 0$.

For laminar flow closure of the problem is formally achieved by applying the equation of state for a perfect gas

$$p = \rho \cdot R \cdot T \tag{40}$$

with constant specific heats C_p and C_v (ratio $\gamma = C_p/C_v$), by Sutherland's viscosity law and by the application of a constant molecular Prandtl number ($Pr = 0.73$). This set of equations for laminar flow has been solved numerically by J.S. Shang, W.L. Hankey [69] and J.S. Shang [70] for the flow in axial corners at hypersonic speeds. It has to be mentioned, however, that another computer code has been written at about the same time by C.M. Hung, R.W. MacCormack [20]. Sample calculations by means of this code have been carried out for the glancing shock wave problem discussed briefly in section 2.2. A direct comparison of the results of both numerical approaches for the same configuration does not exist for axial corner flows. The details of the numerical procedures are not repeated here. The equations are transformed in a nonorthogonal conical coordinate system and they are solved using a two-step predictor-corrector scheme. For a proper capturing of the shock artificial viscosity-like terms were added to the difference equations. In the first paper [69] the numerical scheme was fully explicit, and correspondingly excessive computing time was needed. In the second paper [70] a partly implicit numerical scheme was used and thus the computing time was reduced by one order of magnitude. The same efficiency was achieved by C.M. Hung, R.W. MacCormack [20].

The sample calculations in [69], [70] were carried out for the unsymmetrical corner configuration measured by J.R. Cooper, W.L. Hankey [32]. Fig. 34 shows a comparison of experimental and theoretical pitot pressure contours. The bow shocks on the wedge side and the flat plate side are clearly indicated. On both sides the outer edge of the boundary layer is marked by a sudden drop of pitot pressure. In the experiments a series of triple points has been found within the intersecting shock system. Although the
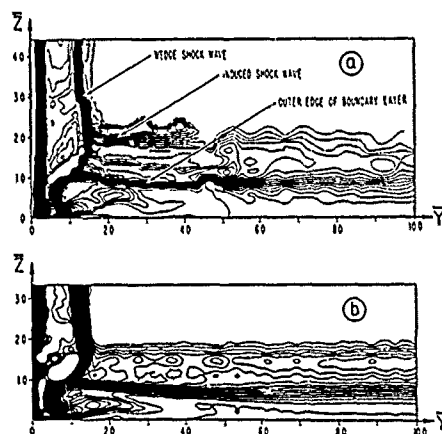
Fig. 34: Shock wave pattern in an unswept, un-symmetrical wedge ($\delta=15°$)/plate ($\delta=0°$) corner configuration at $M_\infty=12.5$ ($Re_{\infty_x}=1.2 \cdot 10^6$, $T_{Wa}=660°R$). Pitot pressure isobars from
a) experiments due to [32]
b) numerical solution of the full Navier-Stokes equations due to [69]
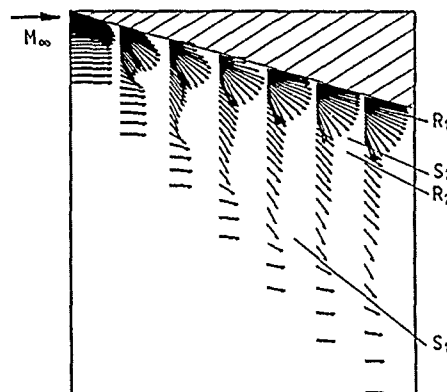
Fig. 35: Shear stress vector plot on the plate surface of an unswept, unsymmetrical wedge ($\delta=15°$)/plate ($\delta=0°$) corner configuration at $M_\infty=12.5°$ from the numerical solution of the full Navier-Stokes equations according to [69]. S_1, S_2 separation lines, R_1, R_2 reattachment lines.

theoretical result is in general agreement with the experimental data, the mesh-size was too coarse in order to find details. The numerical result exhibits a certain amount of shock wave smearing. The numerical solution indicates one triple point only, but more details as for example the location of the slip surface are missing. Within the boundary layer on the flat plate side two separation lines and two reattachment lines have been found in the experiments, indicating the formation of a primary and a secondary vortex. The theoretical result is shown in Fig. 35. Apart from the authors [32] interpretation both separations are clearly identified from the vector plot of the local shear stress and they are in good agreement with the experimental data. Unfortunately in the flowfield the secondary vortex was not captured properly due to the limited number of grid points. The overall result of the numerical solution was a nearly conical flowfield, but a detailed analysis of the situation in the strong and weak interaction regions of the flow depending on the viscous interaction parameter are still missing. The surface pressure and heat transfer distributions are shown in Fig. 36. The pressure distribution is in excellent agreement with the experimental data, showing the peak value at reattachment and some pressure reduction in the region of the primary vortex. The heat transfer maximum is also located in the reattachment region; experimental data are not available.

4.2.2 Solutions of the full Navier-Stokes equations for turbulent flows

For the case of turbulent flows the set of equ. (31) to (40) can be used in principle, but the tensor of the viscous stresses contains now the Reynolds stresses and the heat fluxes include a convective term due to the turbulent motion. To accomplish a simple means of effecting closure to the equations of motion the eddy-viscosity concept is adopted. The Reynolds stress tensor is represented by the product of the eddy viscosity and the mean flow velocity gradient. This leads to the viscous stress tensor as

$$\bar{\bar{\tau}}' = (\mu + \epsilon) \, \text{Def}\bar{V} - \frac{2}{3}(\mu + \epsilon)(\nabla \cdot \bar{V}) \, \bar{\bar{I}}. \tag{41}$$

Concerning the heat flux the effective conductivity can be taken into account by a turbulent Prandtl number ($Pr_t = 0.9$) and this leads to

$$\bar{q} = - c_p \left(\frac{\mu}{Pr} + \frac{\epsilon}{Pr_t} \right) \nabla T. \tag{42}$$

Thus the system of conservative equations reduces to the same form as that for laminar flow.

In the numerical solutions of the Navier-Stokes equations for turbulent flows which exist so far different eddy viscosity methods have been used. In the papers of C.M. Hung, R.W. MacCormack [21] and C.C. Horstman, C.M. Hung [22] an algebraic one-layer model has been used as

$$\epsilon(y) = \rho(Dl)^2\omega. \tag{43}$$

The eddy viscosity is proportional to absolute magnitude of vorticity

$$\omega = |\nabla \times \bar{V}| = \left[\left| \frac{\partial w}{\partial y} - \frac{\partial v}{\partial z} \right|^2 + \left| \frac{\partial u}{\partial z} - \frac{\partial w}{\partial x} \right|^2 + \left| \frac{\partial v}{\partial x} - \frac{\partial u}{\partial y} \right|^2 \right]^{1/2} \tag{44}$$
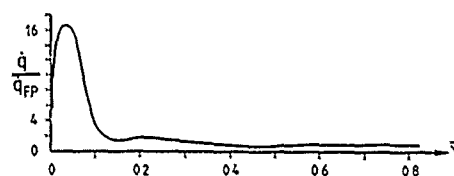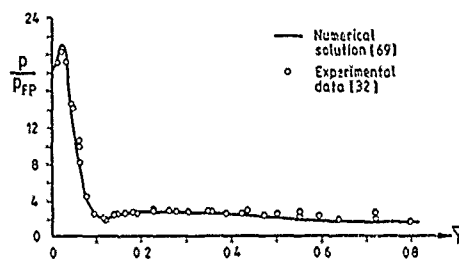
Fig. 36: Surface pressure and heat transfer distribution on the flat plate side of an unswept, unsymmetrical wedge $(\delta=15°)$/plate $(\delta=0°)$ corner configuration at $M_\infty=12.5°$ comparison of the numerical solution of the full Navier-Stokes equations [69] with experimental data [32].

and it vanishes automatically when the outer edge of the boundary layer is reached. D is the van Driest damping factor

$$D = 1 - \exp\left(-\frac{d}{26} \cdot \frac{\sqrt{\tau_{Wa} \cdot \rho_{Wa}}}{\mu_{Wa}}\right) \tag{45}$$

in which instead of the distance from the wall a modified distance d as

$$d = \frac{2yz}{y + z + \sqrt{y^2 + z^2}} \tag{46}$$

has been used. The mixing length scale l is chosen in a single function

$$l = \lambda\delta \tanh\left(\frac{0.41\, d}{\lambda\delta}\right) \tag{47}$$

were λ is a constant ($\lambda = 0.08$) and δ represents the value of d at the outer edge of the boundary layer. This kind of formulation fulfils the boundary conditions far away from the two walls in corner configurations.

Later in the paper by D.D. Knight [23] this turbulence model has been replaced by the well known two-layer algebraic eddy viscosity model of B.S. Baldwin, H. Lomax [71]. In the inner·region the Prandtl-Van Driest formulation according to the equ. (43) to (46) is used with the mixing length scale

$$l = 0.4 \cdot d \tag{48}$$

and in the outer region a modification of the original Clauser-formulation has been applied, see [71], which depends also on the magnitude of the vorticity ω. This removes again the necessity for finding the outer edge of the boundary layer. Nevertheless inner and outer region have to be adapted in such a way that the location of the switch from inner to outer region is improved in the subsequent steps of the iteration. In the papers of C.M. Hung. R.W. MacCormack [21], C.C. Horstmann, C.M Hung [22] and D.D. Knight [23] the sample calculations for corner flows have been carried out for the glancing shock wave problem as mentioned briefly in section 2.2. These computer codes have not yet been applied to analyze the structure of inlet type corner configurations although they would be very well suited for this task.

In the paper of J.S. Shang, W.L. Hankey, J.S. Petty [72] another two-layer eddy viscosity model is used. In the inner region the eddy viscosity is assumed as

$$\varepsilon_i = \rho(D'l)^2 \cdot \left|\frac{\partial q}{\partial n}\right|, \tag{49}$$

where l is the mixing length scale according to equ. (48) and (46) and D' is the modified van Driest damping factor

$$D' = 1 - \exp\left(-\frac{d}{26} \cdot \frac{\sqrt{\rho|\partial q|\partial n|}}{\mu}\right). \tag{50}$$

The eddy viscosity is related to $|\partial q|\partial n|$, where q is the magnitude of the velocity

$$q = \sqrt{u^2 + v^2 + w^2}\ . \tag{51}$$

In this formulation symmetrical corner configuration can easily be treated. In the outer region Clauser's velocity defect formulation is used in the form

$$\varepsilon_o = 0.0168 \cdot \rho \cdot q_{max} \int_0^{n_{max}} \left(1 - \frac{q}{q_{max}}\right) dn,$$

(a) $\bar{Z}$

$Re_{\infty x} = 0.27 \times 10^6$, laminar
• Shock waves
○ Slip surfaces } [31]
── Theory [72]

(b) $\bar{Z}$

$Re_{\infty x} = 1.1 \times 10^6$, turbulent
• Shock waves
○ Slip surfaces } [31]
── Theory [72]

Z(CMS)

── Theory [72]

--- Experimental
separation
line [31]

X(CMS)
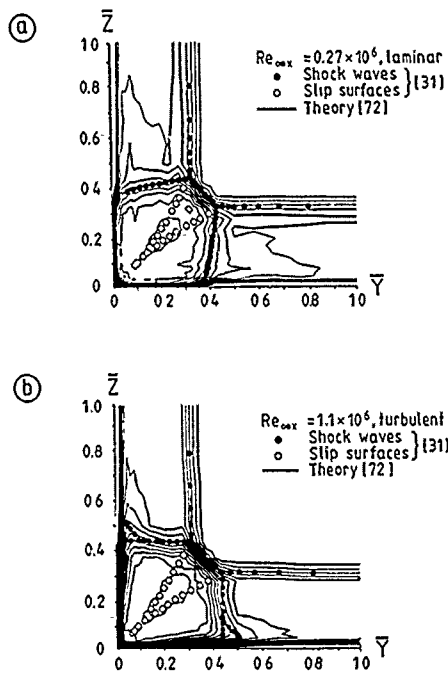
Fig. 37: Shock formation in a symmetrical, un-
swept, rectangular corner configu-
ration ($\delta = 9.5°$) at $M_\infty = 3.0°$ for
a) laminar, b) turbulent
boundary layer flow. Experimental data
according to [31], density contours
from numerical solutions of the full
Navier-Stokes equations [72].
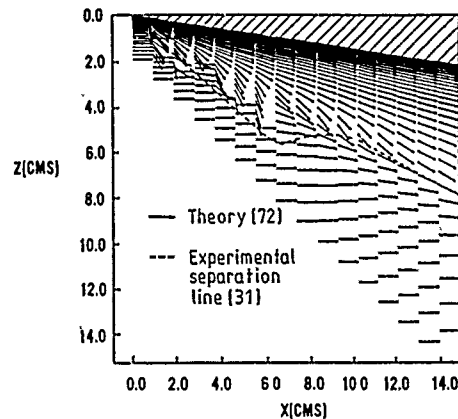
Fig. 38: Shear stress vector plot for the wedge
surface of a symmetrical, unswept,
rectangular corner configuration
($\delta = 9.5°$) at $M_\infty = 3.0°$ from the numerical
solution of the full Navier-Stokes
equations according to [72]; experi-
mental data from [31].

where n_{max} is the maximum dimension of the computational domain. Since the outer edge of the boundary layer is not clearly defined an intermittency correction in the law of the wake is not applied. In order to describe also transitional phenomena for the axial corner flow problem the entirely empirical tran-sition mode of S. Dhawan, R. Narasimha [73] has been applied in a version extended to three dimensions.

Sample calculations have been carried out by J.S. Shang, W.L. Hankey, J.S. Petty [72] for the symmetrical $\delta = 9.5°$ wedge corner configuration which has been investigated experimentally by J.E. West, R.H. Korkegi [31] at Machnumber $M_\infty = 3.0$ and high-Reynoldsnumbers. The numerical results indicate how - as the flow progresses downstream, undergoing transition from laminar to turbulent - the shock system readjusts itself to accomodate the distinctive change in length scale. Fig. 37 shows the shock wave structures and the associated slip surfaces for laminar and turbulent flow. Good agreement is observed between the computed and experimental values in the location of shock waves, triple points and slip surfaces. The corresponding pressure distributions have already been discussed in Fig. 30. Again the agreement between the experimental data and the numerical solution is excellent. Some differences might be due to the fact that the Reynoldsnumbers are not exactly the same. Fig. 38 shows the shear stress plot in which, however, only the orientation of the resultant stress is given, since the magnitude of the shear stress changes rapidly. The laminar/turbulent transition is clearly indicated and the corresponding shift of the separation line is in good agreement between theory and experiment. The boundary layers are very thin in this case. Therefore the limited number of grid points did not allow the study the flow separations in detail. The heat transfer rates had not been measured in the experimental investigation and therefore also theoretical results are not available.

4.2.3 Solutions based on thin-layer approximations of the Navier-Stokes equations

For the solution of the full Navier-Stokes equations large computer storage capacity as well as much computer time is needed even for implicit-explicit difference schemes. Therefore Prandtl's concept to omit comparatively small and insignificant expressions and to retain only the most important terms in the Navier-Stokes equations has been applied anew, and this led to the thin-layer approximation of the Navier-Stokes equations as described e.g. by B.S. Baldwin, H. Lomax [71]. The thin-layer approximation neglects the diffusion process parallel to the body surface as Prandtl's boundary layer theory does, but it retains all three of the momentum equations and makes no assumption about the pressure. This permits a straightforward computation of separated flow regions since no singularties occur at the separation points.

For a symmetrical flat plate corner configuration the Navier-Stokes equations according to equ. (31) to (40) are modified as follows: 1) All inviscid fluxes F_j, G_j and H_j are retained; 2) all velocity gradients in x-direction are neglected; 3) in y- and z-directions all derivatives are neglected which are perpendicular to the direction under consideration. For turbulent flow this leads to

$$\tau'_{xx} = \lambda \frac{\partial v}{\partial y} \;\; ; \;\;\; \tau'_{yy} = (\lambda + 2\mu + 2\epsilon) \frac{\partial v}{\partial y} \;\; ; \;\;\; \tau'_{zz} = (\lambda + 2\mu + 2\epsilon) \frac{\partial w}{\partial z} \;\; ; \tag{52}$$

$$\tau'_{xy} = 0 \;\;\; ; \;\;\; \tau'_{yx} = \mu \frac{\partial u}{\partial y} \;\; ; \tag{53a}$$

$$\tau'_{yz} = \mu \frac{\partial w}{\partial y} \;\; ; \;\;\; \tau'_{zy} = \mu \frac{\partial v}{\partial z} \;\; ; \tag{53b}$$

$$\tau'_{xz} = 0 \;\;\; ; \;\;\; \tau'_{zx} = \mu \frac{\partial u}{\partial z} \;\; ; \tag{53c}$$

where $\lambda = -2\mu/3$. The work done by the viscous stresses is then calculated from equ. (38), and for the heat flux components according to equ. (42) yields

$$\dot{q}_x = 0 \;\; ; \;\;\; \dot{q}_y = -C_p \left(\frac{\mu}{Pr} + \frac{\epsilon}{Pr_t} \right) \frac{\partial T}{\partial y} \tag{54a,b}$$

$$\dot{q}_z = -C_p \left(\frac{\mu}{Pr} + \frac{\epsilon}{Pr_t} \right) \frac{\partial T}{\partial z} \;\; . \tag{54c}$$

It has to be noted that the approximations according to equ. (53) are rather crude. It turns out that $\tau'_{xy} \neq \tau'_{yx}$, $\tau'_{yz} \neq \tau'_{zy}$, $\tau'_{zx} \neq \tau'_{xz}$, and the neglected derivatives can be in the same order of magnitude as the retained ones. The only argument for this is the fact that in a corner for small values of y and z the velocity components v and w as well as their derivatives are small.

The thin-layer approximated equations have been written in nonorthogonal coordinates for a wedge/plate corner configuration by C.M Hung, S.S. Kurasaki [74] and sample calculations have been carried out for the glancing shock wave problem and turbulent flow, which had already been treated on the basis of the full Navier-Stokes equations by C.M Hung, R.W. MacCormack [21]. The paper [74] contains no new results concerning corner flows, but good agreement between the full Navier-Stokes solution and the thin-layer approximation has been achieved at a 20% reduction of the required computation time. Calculations of this kind for the intake type of corner configurations, considered here, have not yet been carried out.

For the sake of completeness it may be mentioned that there exist also approximations of the Navier-Stokes equations for axial flow in corner configurations at high Machnumbers and low Reynoldsnumbers, which are valid in the strong interaction region at high values of $\bar{\chi}$ as well as in the slip flow regime. In this case the governing equations become parabolic and solutions of this kind have been published by R.J. Cresci, S.G. Rubin, C.T. Nardo, T.C. Lin [28].

4.2.4 Solutions based on local-conical approximations of the Navier-Stokes equations

The basis of this kind of approach are the Navier-Stokes equations in sherical r,ϑ,φ-coordinates. For the corner configurations under consideration the inviscid flow is conical and the viscous flow is nearly conical, at least for weak interaction. This means that all derivatives with respect to the radial distance r may be regarded as small. Applying this approximation, i. e. $\partial/\partial r = 0$, to all fluid quantities leads to the following "locally conical" Navier-Stokes equations

$$\frac{\partial \bar{U}}{\partial t} + \frac{\partial \bar{F}}{\partial \vartheta} + \frac{\partial \bar{G}}{\partial \varphi} + \bar{A} = 0 \tag{55}$$

where

$$\bar{U} = \bar{B} \sin\vartheta; \;\;\; \bar{F} = (v_\vartheta \bar{B} - \bar{S}_\vartheta)\sin\vartheta; \;\;\; \bar{G} = (v_\varphi \bar{B} - \bar{S}_\varphi) \tag{56}$$

$$\bar{B} = \begin{vmatrix} \rho \\ \rho v_r \\ \rho v_\vartheta \\ \rho v_\varphi \\ \rho e \end{vmatrix} \;\; ; \;\;\; \bar{S}_\vartheta = \begin{vmatrix} 0 \\ \tau_{\vartheta r} \\ \tau_{\vartheta\vartheta} \\ \tau_{\vartheta\varphi} \\ -\dot{q}_\vartheta + \phi_\vartheta \end{vmatrix} \;\; ; \;\;\; \bar{S}_\varphi = \begin{vmatrix} 0 \\ \tau_{\varphi x} \\ \tau_{\varphi\vartheta} \\ \tau_{\varphi\varphi} \\ -\dot{q}_\varphi + \phi_\varphi \end{vmatrix} \tag{57}$$

$$\overline{A} = \begin{vmatrix} 2\rho v_r \\ 2\rho v_r^2 - \rho v_\vartheta^2 - \rho v_\varphi^2 - (\tau_{rr} + p) + (\tau_{\vartheta\vartheta} + p) + (\tau_{\varphi\varphi} + p) \\ 3\rho v_r v_\vartheta - (\rho v_\varphi^2 + p)ctg\vartheta + (\tau_{\varphi\varphi} + p)ctg\vartheta - 2\tau_{r\vartheta} \\ 3\rho v_r v_\varphi - \rho v_\vartheta v_\varphi ctg\vartheta - \tau_{\vartheta\varphi}ctg\vartheta - 2\tau_{r\varphi} \\ 2v_r(\rho e + p) - v_r(\tau_{rr} + p) - v_\vartheta \tau_{r\vartheta} - v_\varphi \tau_{r\varphi} \end{vmatrix} \tag{58}$$

$$\tau_{rr} = -p - \frac{2}{3}\frac{\mu}{Re_{\infty r}}\left(2v_r + \frac{\partial v_\vartheta}{\partial\vartheta} + v_\vartheta ctg\vartheta + \frac{1}{sin\vartheta}\frac{\partial v_\varphi}{\partial\varphi}\right) \tag{59a}$$

$$\tau_{\vartheta\vartheta} = 2\frac{\mu}{Re_{\infty r}}\left(\frac{\partial v_\vartheta}{\partial\vartheta} + v_r\right) + \tau_{rr} \tag{59b}$$

$$\tau_{\varphi\varphi} = 2\frac{\mu}{Re_{\infty r}}\left(\frac{1}{sin\vartheta}\frac{\partial v_\varphi}{\partial\varphi} + v_r + v_\vartheta ctg\vartheta\right) + \tau_{rr} \tag{59c}$$

$$\tau_{r\vartheta} = \tau_{\vartheta r} = \frac{\mu}{Re_{\infty r}}\left(-v_\vartheta + \frac{\partial v_r}{\partial\vartheta}\right) \tag{59d}$$

$$\tau_{\vartheta\varphi} = \tau_{\varphi\vartheta} = \frac{\mu}{Re_{\infty r}}\left(\frac{\partial v_\varphi}{\partial\varphi} - v_\varphi ctg\vartheta + \frac{1}{sin\vartheta}\frac{\partial v_\vartheta}{\partial\varphi}\right) \tag{59e}$$

$$\tau_{\varphi r} = \tau_{r\varphi} = \frac{\mu}{Re_{\infty r}}\left(\frac{1}{sin\vartheta}\frac{\partial v_r}{\partial\varphi} - v_\varphi\right) \tag{59f}$$

$$\dot{q}_\vartheta = -\frac{1}{2}\frac{\mu}{Re_{\infty r}Pr}\cdot\frac{\partial T}{\partial\vartheta} \tag{60a}$$

$$\dot{q}_\varphi = -\frac{1}{2sin\vartheta}\cdot\frac{\mu}{Re_{\infty r}Pr}\cdot\frac{\partial T}{\partial\varphi} \tag{60b}$$

$$\Phi_\vartheta = v_r\tau_{\vartheta r} + v_\vartheta\tau_{\vartheta\vartheta} + v_\varphi\tau_{\vartheta\varphi} \tag{61a}$$

$$\Phi_\varphi = v_r\tau_{\varphi r} + v_\vartheta\tau_{\varphi\vartheta} + v_\varphi\tau_{\varphi\varphi}. \tag{61b}$$

In these equations the fluid properties, density ρ, velocity components v_r, v_ϑ, v_φ, internal energy e, pressure p, temperature T and the viscosity μ, have been nondimensionalized with respect to the free stream values ρ_∞, V_∞, V_∞^2, $\rho_\infty V_\infty^2$, $T_t \sim T_\infty$ and μ_∞, and the time t has been nondimensionalized by r/V_∞ correspondingly. For viscous flows a lenght scale is contained in the Reynoldsnumber $Re_{\infty r} = \rho_\infty V_\infty r/\mu_\infty$, which is related to the crossflow plane, in which the flow is calculated. The pressure is given as

$$p = (\gamma - 1)\rho\left(e - (v_r^2 + v_\vartheta^2 + v_\varphi^2)/2\right) \tag{62}$$

and the viscosity is accounted for by the Sutherland formula.

If the viscosity effects are neglected, $\mu = 0$, and for heat conductivity $k = 0$, the locally conical Euler equations result from equ. (55), (56) and

$$\overline{S}_\vartheta = \begin{vmatrix} 0 \\ 0 \\ -p \\ 0 \\ -v_\vartheta p \end{vmatrix} ; \quad \overline{S}_\varphi = \begin{vmatrix} 0 \\ 0 \\ 0 \\ -p \\ -v_\varphi p \end{vmatrix} ; \quad \overline{H} = \begin{vmatrix} 2\rho v_r \\ 2\rho v_r^2 - \rho(v_\vartheta^2 + v_\varphi^2) \\ 3\rho v_r v_\vartheta - (\rho v_\varphi^2 + p) ctg\vartheta \\ 3\rho v_r v_\varphi + \rho v_\vartheta v_\varphi ctg\vartheta \\ 2v_r(\rho e + p) \end{vmatrix}. \tag{63}$$

No length scale occurs in the Euler equations, which indicates that conical Euler equations describe strictly conical inviscid flows. The nonconicity is all introduced by the viscous effects.

The derivation of these equations as well as some exploratory sample calculations may be taken from N. Qin, B.E. Richards [75]. The predictor/corrector difference scheme is also described there. For acceleration of the convergence to steady state a multigrid procedure is applied and for stability reasons local variable time steps are used. To dampen numerical oscillations caused by strong shock waves an adaptive artificial viscosity term is used which is of significant magnitude only near shock waves. It has no effect within the viscous region itself.

Calculations according to this method for corner configurations have been carried out by K.W. Scriba [76] for the $\Phi = 30°$ swept $\Theta = 90°$ corner configuration measured by W. Möllenstädt [37], [38] at $M_\infty = 12,76$ according to Fig. 17. This flowfield has already been discussed in many details in sections 3.3.2 and 3.4. to 3.6. The calculations have been performed for the following additional data, taken from the experiments:

$$p_\infty = 68.48 \text{ Pa}; \qquad p_0 = 150 \cdot 10^5 \text{ Pa}; \qquad T_0 = 1300 \text{ K}; \qquad T_\infty = 38.73 \text{ K}; \qquad T_{Wa} = 300 \text{ K}.$$

The spherical computational surface was located at a distance $r = const.$, corresponding to a Reynoldsnumber $Re_{\infty r} = 4.5 \cdot 10^6$, where the experimental data have been taken.

A comparison of the measured and the computed flowfield is shown in Fig. 39. In the experimental data, the pitot pressure jumps at the shock waves and the slip surface are smeared due to the probe thickness. In the theoretical results the jumps are even more smeared due to the artificial viscosity which had to be introduced in order to damp the numerical oscillations near the discontinuity. Nevertheless the general properties of the flowfield are in excellent agreement between theory and experiment. This may especially be seen for the pitot pressure plateaus which are located behind the wedge shock, behind the corner shock, between embedded shock and slip surface, in the inner corner region as well as in the center of the primary vortex. The flow pattern in the corner cross-section according to the theory is drawn in Fig. 40 together with the author's [76] interpretation. The shock waves and slip surface formation is completely the same as measured by W. Möllenstädt [37]. The same applies for the structure of the viscous flow. The disturbance in the wedge flow occurs due to the flow separations generated by the embedded shock. The primary vortex is clearly detected in the flowfield. Underneath the primary vortex also a secondary vortex has been found by the theory in the correct position, but one has to bear in mind, that the resolution of this vortex is very poor due to the limited number of grid points in this region.

In the inviscid flow behind the embedded shock and below the slip surface, the theoretical result shows the formation of a vortex close to the bisector plane. This kind of vortex is new and it has not yet been found neither in experiments nor in other numerical solutions. This vortex may be called the corner vortex. It is located in the flow underneath the slip surface. The origin of this vortex is not yet understood. It might be associated with the inward flow of the two slip surfaces (which are actually vorticity layers) along the bisector, but this matter needs further investigations.

The wall pressure distribution is shown in Fig. 41. The separation at S_1 causes a static pressure rise which transmits through the boundary layer. The pressure increase in the flow due to the embedded shock is not found at the wall since the immediately following expansion compensates the effect on the wall pressure. The steep increase of the wall pressure takes place towards the reattachment point R_1. In this region some discrepancies between theory and experiment are present, which are due to the difficulties in the determination of the reattachment point R_1 in the experiments, and due to the fact that the very narrow pressure peak might not have been resolved by the few measuring stations in this region. The vortices in the flow obviously cause some local reductions in the wall pressure distribution, which are indicated by theory and experiment.
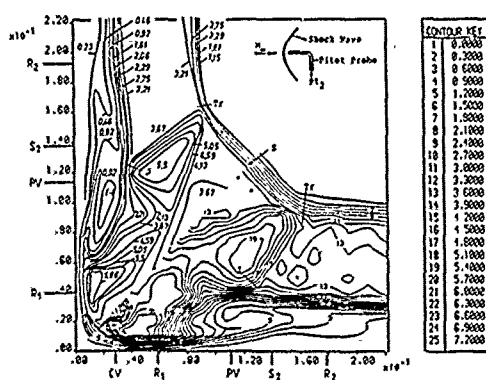
Fig. 39: Pitot pressure isobars in the flowfield of a a symmetrical, 30°swept, rectangular corner configuration ($\delta=8°$) at $M_\infty=12.8°$. Comparison of experimental results [37] with the numerical solution of the locally conical Navier-Stokes equations [76]. (S_1,S_2 separation lines, R_1,R_2 reattachment lines, PV, CV primary vortex, corner vortex).
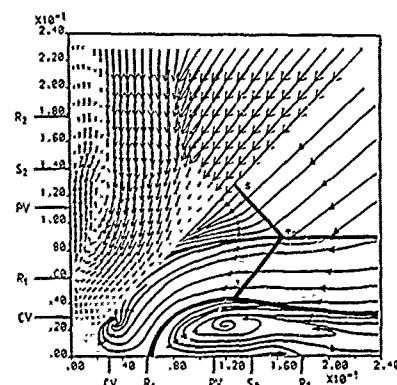
Fig. 40: Flowfield in a symmetrical, 30°swept, rectangular corner configuration ($\delta=8°$) at $M_\infty=12.8°$ according to the numerical solution of the locally conical Navier-Stokes equations according to [76]. (S_1,S_2 separation lines, R_1,R_2 reattachment lines, PV, CV primary vortex, corner vortex).
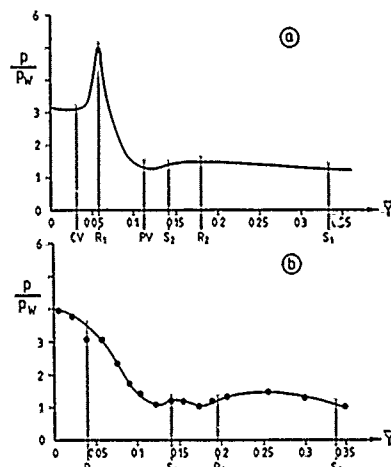
Fig. 41: Surface pressure distribution in a symmetrical, 30°swept, rectangular corner configuration (δ=8°) at M_∞=12.8°.
a) Numerical solution of the locally conical Navier-Stokes equations due to [76].
b) Experimental data due to [37] (S_1,S_2 separation lines, R_1,R_2 reattachment lines, PV, CV primary vortex, corner vortex).
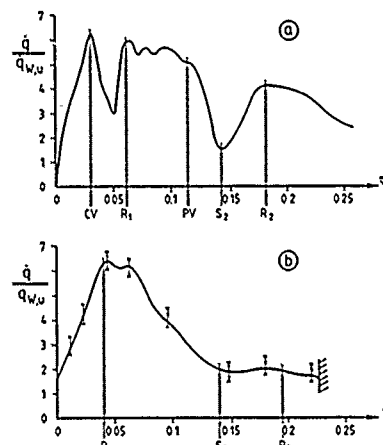
Fig. 42: Surface heat transfer distribution in a symmetrical, 30° swept, rectangular corner configuration (δ=8°) at M_∞=12.8°.
a) Numerical solution of the locally conical Navier-Stokes equations due to [76].
b) Experimental data due to [37] (S_1,S_2 separation lines, R_1,R_2 reattachment lines, PV, CV primary vortex, corner vortex).

The heat transfer distributions at the wall are shown in **Fig. 42**. The maximum value at the reattachment point R_1 as well as the minima at the separation points S_1 and S_2 are in good agreement between theory and experiment. In other regions large deviations between both have to be considered. It might be that the number of measuring stations was not enough to resove all details of the heat transfer distribution found by the theory. On the other hand one has to bear in mind that the theoretical heat transfer rates are calculated from the temperature gradients at the wall. It might be as well that the resolution of the numerical grid was not enough to calculate the heat transfer rates properly. This applies especially for the region underneath the primary vortex PV and the secondary vortex, where the largest deviations have been found. Other numerical solutions of the Navier-Stokes equations do not show such strong variations of the heat transfer rates along the wall. Further investigations on this subject are needed.

4.2.5 Final remarks

The comparisons between experimental data and numerical solutions of the Navier-Stokes equations for axial corner flows have shown very interesting results. Corner flows have relatively simple geometries and they are very well suited for the validation of computational fluid dynamics. This applies especially for laminar hypersonic flows, in which the boundary layers are thick so that flow separation phenomena can be studied in detail. It applies also for high Reynoldsnumber flows for which different methods of turbulence mcdeling can be tested.

Based on the present status of knowledge about axial corner flows, documented in this paper, further investigations should be carried out in order to improve numerical solutions and experimental data to achieve an even better understanding of the details of the flow behaviour. Further investigations should cover the following topics:

Theory:

i) Improvement of the resolution of the flowfield near the surface in the numerical solutions of the Navier-Stokes equations in order to
a) cover the secondary vortex properly
b) improve the heat transfer rates at the wall which are based on the temperature gradients.

ii) Improvement of the resolution of the flowfield in the vicinity of the slip surfaces in order to see more details of their structure especially at their intersection point and downstream of it.

iii) Detailed analysis of the flowfield in the inner corner region in order to clarify whether or not a corner vortex exists and why this vortex occurs. Comparison of solutions of the full and the locally conical Navier-Stokes equations.

iv) Extension of the numerical solutions to unsymmetric corner configuration in order to understand the changes in the outer inviscid flowfield from shock wave structures with two triple points to such with only one triple point, and to identify the corresponding flow separations, surface pressure and surface heat transfer distributions.

Experiments:

    i) Improvement of the resolution of the flowfield by the application of
       a) smaller pitot probes
       b) more measuring stations for static pressure and heat transfer rate at the corner surface.

    ii) Detailed analysis of the flowfield in the neighbourhood of the slip surfaces and downstream of
       their intersection point.

    iii) Investigations of the flowfield structure in the inner corner region in order to check the
       existence of a corner vortex.

    iv) Measurements on unsymmetrical corner configurations as a data base. Systematic variation of the
       governing geometric parameters. Analysis of the shock structure in the outer inviscid flowfield and
       the corresponding boundary layer flow including separations.

    An experimental program along these lines is presently carried out at Institut für Strömungsmechanik
of Technical University Braunschweig. A close connection with theoretically working groups is anticipated.
Further progress in this field is expected from such a cooperation between theory and experiment.

5. LITERATURE

[1] Neumann, R.D.: Special topics in hypersonic flow. In: Aerodynamic Problems of Hypersonic Vehicles. AGARD-LS-42 (1972), Vol. 1, 7-1 to 7-64.

[2] Holden, M.S.: Theoretical and experimental studies of separated flows induced by shock-wave-boundary-layer interaction. AGARD-CP-4 (1966), 147-180.

[3] Hankey, W.L. and M.S. Holden: Two-dimensional shock wave-boundary layer interactions in high speed flows. AGARDograph 203 (1975).

[4] Adamson, T.C. Jr. and A.F. Messiter : Analysis of two-dimensional interactions between shock waves and boundary layers. Ann. Rev. Fluid Mech. 12 (1980), 103-138.

[5] Settles, G.S., J.J. Perkins and S.M. Bogdonoff: Investigation of three-dimensional shock/boundary-layer interactions at swept compression corners. AIAA J. 18 (1980), 779-785.

[6] Settles, G.S. and S.M. Bogdonoff: Scaling of 2D and 3D shock/turbulent boundary layer interactions at compression corners. AIAA J. 20 (1982), 782-789.

[7] Settles, G.S. and H.Y. Teng: Cylindrical and conical flow regimes of three-dimensional shock/boundary-layer interactions. AIAA J. 22 (1984), 194-200.

[8] Horstman, C.C.: A computational study of complex three-dimensional compressible turbulent flowfields. AIAA J. 23 (1985), 1461-1462.

[9] McCabe, A.: The three-dimensional interactions of a shock wave with a turbulent boundary layer. Aeron. Quart. XVII (1966), 231-252.

[10] Law, C.H.: Three-dimensional shock wave-turbulent boundary layer interations at Mach 6. Aerospace Research Labs., Wright-Patterson-Air Force Base, Ohio, ARL TR 75-0179 (1975).

[11] Peake, D.J.: Three-dimensional swept shock/tubulent-boundary-layer separations with control by air injection. Nat. Res. Counc., Canada, Aeronautical Report LR-592 (1976).

[12] Korkegi, R.H.: On the structure of three-dimensional shock-induced separated flow regions. AIAA J. 14 (1976), 597-600.

[13] Oskam, B., S.M. Bogdonoff and I.E. Vas: Oblique shock wave/turbulent boundary layer interactions in three dimensions at Mach 3. Air Force Flight Dynamics Laboratory, AFFDL-TR-76-48 (1976).

[14] Kubota, H. and J.L. Stollery: An experimental study of the interaction between a glancing shock wave and a turbulent boundary layer. J. Fluid Mech. 116 (1982), 431-458.

[15] Dolling, D.S. and S.M. Bogdonoff: Upstream influence in sharp fin-induced shock wave turbulent boundary-layer interaction. AIAA J. 21 (1983), 143-145.

[16] McClure, W. and D.S. Dolling: Flowfield scaling in sharp fin-induced shock wave turbulent boundary layer interaction. AIAA Paper 83-1754 (1983).

[17] Dolling, D.S.: Comparison of sharp and blunt fin-induced shock wave/turbulent boundary-layer interaction. AIAA J. 20 (1982), 1385-1391.

[18] Settles, G.S. and F.K. Lu: Conical similarity of shock/boundary-layer interactions generated by swept and unswept fins. AIAA J. 23 (1985), 1021-1027.

[19] Fomison, N.R. and J.L. Stollery: The effect of sweep and bluntness on a glancing shock wave turbulent boundary layer interaction. AGARD-CP-428 (1987), 8-1 to 8-19.

[20] Hung, C.M. and R.W. MacCormack: Numerical solution of supersonic laminar flow over a three-dimensional compression corner. AIAA Paper 77-694 (1977).

[21] Hung, C.M. and R.W. MacCormack: Numerical solution of three-dimensional shock wave and turbulent boundary-layer interaction. AIAA J. 16 (1978), 1090-1096.

[22] Horstman, C.C. and C.M. Hung: Computation of three-dimensional turbulent separated flows at supersonic speeds. AIAA J. 17 (1979), 1155-1156.

[23] Knight, D.D.: Calculation of three-dimensional shock/turbulent boundary-layer interaction generated by sharp fin. AIAA J. 23 (1985), 1885-1891.

[24] Stainback, P.C.: An experimental investigation at a Mach number 4.95 of flow in the vicinity of a 90° interior corner aligned with the free-stream velocity. NASA TN D-184 (1960).

[25] Stainback, P.C.: Heat transfer measurements at a Mach number of 8 in the vicinity of a 90° interior corner aligned with the free stream velocity. NASA TN D-2417 (1964).

[26] Stainback, P.C. and L.M. Weinstein: Aerodynamic heating in the vicinity of corners at hypersonic speeds. NASA TN D-4130 (1967).

[27] Charwat, A.F. and L.G. Redekopp: Supersonic interference flow along the corner of intersecting wedges. AIAA J. 5 (1967), 480-488.

[28] Cresci, R.J., S.G. Rubin, C.T. Nardo and T.C. Lin: Hypersonic interaction along a rectangular corner. AIAA J. 7 (1969), 2241-2246.

[29] Watson, R.D. and L.M. Weinstein: A study of hypersonic corner flow interactions. AIAA J. 9 (1971), 1280-1286.

[30] Korkegi, R.H.: Survey of viscous interactions associated with high Mach number flight. AIAA J. 9 (1971), 771-784.

[31] West, J.E. and R.H. Korkegi: Supersonic interaction in the corner of intersecting wedges at high Reynolds numbers. AIAA J. 10 (1972), 652-656.

[32] Cooper, J.R. and W.L. Hankey Jr.: Flowfield measurements in an asymmetric axial corner at M = 12.5. AIAA J. 12 (1974), 1353-1357.

[33] Korkegi, R.H.: On the structure of three-dimensional shock-induced separated flow regions. AIAA J. 14 (1976), 597-600.

[34] Peake, D.J., M. Tobak and R.H. Korkegi: Three dimensional interactions and vortical flows with emphasis on high speeds. AGARDograph 252 (1980).

[35] Kipke, K.: Untersuchungen an längsangeströmten Ecken im Hyperschallbereich. ÜGFT/DGLR Jahrestagung 1973, Innsbruck. DGLR-Vorabdruck 73-114 (1973).

[36] Kipke, K. and D. Hummel: Untersuchungen an längsangeströmten Eckenkonfigurationen im Hyperschallbereich. Teil I: Ecken zwischen ungepfeilten Keilen. Z. Flugwiss. 23 (1975), 417-429.

[37] Möllenstädt, W.: Untersuchungen an längsangeströmten Eckenkonfigurationen im Hyperschallbereich. Teil II: Ecken zwischen gepfeilten Keilen. Z. Flugwiss. Weltraumforsch. 8 (1984), 405-414.

[38] Möllenstädt, W.: Untersuchungen an längsangeströmten, gepfeilten Eckenkonfigurationen im Hyperschallbereich. Dissertation TU Braunschweig 1984.

[39] Hummel, D.: Experimental investigations on blunt bodies and corner configurations in hypersonic flow. AGARD-CP-428 (1987), 6-1 to 6-16.

[40] Hummel, D.: Documentation of separated flows for computational fluid dynamics validation. AGARD-CP-437 (1988), Vol. 2, 15-1 to 15-24.

[41] Gersten, K. and G. Kausche: Die Hyperschallversuchsanlage (Gun Tunnel) der Deutschen Forschungsanstalt für Luft- und Raumfahrt. Z. Flugwiss. 14 (1966), 217-229.

[42] Schultz, D.L. and T.V. Jones: Heat-transfer measurements in short-duration hypersonic facilities. AGARDograph 165 (1973).

[43] Hains, F.D.: Supersonic flow near the junction of two wedges. J. Aerosp. Sci. 25 (1958), 530-531.

[44] Korkegi, R.H.: Limit case for supersonic inviscid flow in the corner of intersecting wedges. AIAA J. 7 (1969), 569-570.

[45] Ames Research Staff: Equations, tables and charts for compressible flow. NACA-Rep. 1135 (1953).

[46] Hummel, D.: On the vortex formation over a slender delta wing at large angles of incidence. AGARD-CP-247 (1978), 15-1 to 15-17.

[47] Lees, L. and B.L. Reeves: Supersonic separated and reattaching laminar flows: I. General theory and application to adiabatic boundary layer-shock wave interaction. AIAA J. 2 (1964), 1907-1920.

[48] Shapiro, A.H.: Compressible fluid flow. Vol. I/II. The Ronald Press Comp., New York 1954.

[49] Schlichting, H.: Boundary layer theory. 7th Ed. (1979), McGraw-Hill Book Co., New York. Grenzschicht-Theorie. 8. Auflage (1982), Verlag G. Braun, Karlsruhe.

[50] Driest, E.R. van: Investigation of laminar boundary layers in compressible fluids using the Crocco method. NACA TN 2597 (1952).

[51] Schepers, H.J.: Untersuchungen der wandnahen Strömung und des Wärmeübergangs im Bereich längsangeströmter Ecken bei Hyperschallströmung. DLR-FB 76-02 (1976).

[52] Hayes, W.D. and R.F. Probstein: Hypersonic flow theory. Academic Press, New York, London 1959.

[53] Stollery, J.L.: Viscous interaction effects on re-entry aerothermodynamics: theory and experimental results. AGARD-LS-42-Vol.1 (1972), 10-1 to 10-28.

[54] Snow, R.M.: Aerodynamics of thin quadrilateral wings at supersonic speeds. Quarterly Appl. Mathematics 5 (1948), 417-428.

[55] Wallace, J. and J.H. Clarke: Uniformly valid second order solution for supersonic flow over cruciform surfaces. AIAA J. 1 (1963), 179-185.

[56] Marconi, F.: Supersonic, inviscid, conical corner flowfields. AIAA J. 18 (1980), 78-84.

[57] Goebel, T.P.: A theoretical study of inviscid supersonic flow along a corner formed by the intersection of two wedges. Ph.D.thesis 1969, Univ. of Calif., Los Angeles.

[58] Kutler, P.: Supersonic flow in the corner formed by two intersecting wedges. AIAA J. 12 (1974), 577-578.

[59] Shankar, V., D. Anderson and P. Kutler: Numerical solutions for supersonic corner flow. J. of Computational Physics 17 (1975), 160-180.

[60] Anderson, D.A and R.K. Nangia: Comparison of numerical and experimental conical flow fields in supersonic corners with compression and/or expansion. Aeron. Quart. 28 (1977), 293-306.

[61] MacCormack, R.W.: The effect of viscosity in hypervelocity impact cratering. AIAA Paper 69-35A (1969).

[62] Kutler, P. and H. Lomax: Shock-capturing, finite-difference approach to supersonic flows. J. Spacecr. Rockets 8 (1971), 1175-1182.

[63] Martin, J.A.: Shock-fitting solution of the supersonic flowfield in a rounded internal corner. AIAA J. 23 (1985), 193-200.

[64] Bloom, M.H. and S. Rubin: High speed viscous corner flows. J. Aero. Sci. 28 (1961), 145-157.

[65] Libby, P.A.: Secondary flows associated with a supersonic corner region. AIAA J. 4 (1966), 1130-1132.

[66] Weinberg, B.C. and S.G. Rubin: Compression corner flow. J. Fluid Mech. 56, Part 4 (1972), 753-774.

[67] Ghia, K.N. and R.T. Davis: A study of compressible potential and asymptotic viscous flows for corner regions. AIAA J. 12 (1974), 355-359.

[68] Mikhail, A.G. and K.N. Ghia: Study of viscous compressible flow along an axial corner. AIAA Paper 77-685 (1977).

[69] Shang, J.S. and W.L. Hankey: Numerical solution of the Navier-Stokes equations for a three-dimensional corner. AIAA J. 15 (1977), 1575-1582.

[70] Shang, J.S.: Implicit-explicit method for solving the Navier-Stokes equations. AIAA J. 16 (1978), 496-502.

[71] Baldwin, B.S. and H. Lomax: Thin layer approximation and algebraic model for separated turbulent flows. AIAA Paper 78-257 (1978).

[72] Shang, J.S., W.L. Hankey and J.S. Petty: Three-dimensional supersonic interacting turbulent flow along a corner. AIAA J. 17 (1979), 706-713.

[73] Dhawan, S. and R. Narsimha: Some properties of boundary layer flow during the transition from laminar to turbulent motion. J. Fluid Mech. 3 (1958), 418-436.

[74] Hung, C.M. and S.S. Kurasaki: Thin-layer approximation for three-dimensional supersonic corner flow. AIAA J. 18 (1980), 1544-1546.

[75] Qin, N. and B.E. Richards: Numerical experiments with hypersonic flows beneath a cone-delta-wing combination. AGARD-CP-428 (1987), 20-1 to 20-14.

[76] Scriba, K.W.: Exploration of the importance of viscous effects on waverider configurations in simulated re-entry flow. University of Glasgow, Dept. of Aeronautics and Fluid Mechanics, March 1988.

GLANCING SHOCK-BOUNDARY LAYER INTERACTIONS

by

John L.Stollery
College of Aeronautics
Cranfield Institute of Technology
Cranfield, Bedford MK43 0AL
United Kingdom

1. INTRODUCTION

There is no universally agreed definition of glancing interaction but it is usually taken to include those situations where the shock wave generated by one body cuts across the boundary layer growing over another and the intersection line is swept.

Such flows are essentially three dimensional and are a sub-set of the many swept interactions shown in Fig.1. In the simplest glancing interactions the only shock wave of interest is that formed by the shock wave generator. Similarly the only boundary layer of interest is the one affected by shock impingement. The boundary layer development on the shock generator and any shock from the surface supporting the boundary layer are secondary in importance. Thus the more complex corner flows and shock-shock interactions are placed in categories of their own and enjoy individual treatment in this lecture series.

Here we will concentrate on just four of the many geometries shown in Fig.1. These four cover the effects of sweep and bluntness on a fin mounted at right angles to a flat plate. Hence we shall treat in turn

(i) sharp unswept fins,

(ii) sharp swept fins,

(iii) blunt unswept fins,

(iv) blunt swept fins.

These models can easily be tested experimentally with the fin mounted on a sharp leading edge flat plate or mounted directly from the wall of a wind tunnel test section.

However, even with these relatively simple geometries it would be foolish to ignore the mutual interference between the two surfaces. In particular the bow shock generated by a blunt fin will often cause boundary layer separation ahead of the fin root. This in turn generates an oblique shock which interacts with the bow shock so producing an example of the shock-shock interactions treated in detail elsewhere in this course. Similarly, a turbulent boundary layer at the base of a swept blunt fin may trigger leading-edge contamination along the attachment line with consequent increases in heat transfer rate. Hence wherever possible the flow pattern over both the plate and fin surfaces will be investigated.

The boundary layer over the plate can be laminar, transitional or turbulent. Wherever possible all three conditions will be described though most of the experimental data available are for turbulent boundary layers.

2. PREVIOUS SURVEYS

There have been many surveys of shock boundary layer interaction over the last 30 years. The general survey of Green (1970) contains a discussion of flows with swept shocks and draws attention to the continuing difficulty of defining incipient separation in a three-dimensional flow. The review of Korkegi (1971) covers a range of viscous interactions concentrating on hypersonic Mach numbers. He draws attention to the high heating rates that can occur with fin interactions and to the differences between laminar and turbulent flows. Peake and Tobak (1980) again concentrated on high speeds and covered a wide range of three-dimensional interactions as did Delery (1988) in his VKI lectures. As data has accumulated it has been possible to narrow the field surveyed. More recently Saida (1988) has reviewed blunt fin turbulent boundary layer interactions whilst most recently Settles and Dolling (1986) have written an excellent article on swept shock wave boundary layer interactions.

Each of these references in turn refers to a considerable body of published material now available.

3. SHARP UNSWEPT FINS (Fig.2)

Most of the experiments have been made at high Reynolds numbers so that the flat plate boundary layer was turbulent. For this reason we begin by describing turbulent interaction before presenting the smaller number of laminar results in §3.4.

3.1. Turbulent Flow

There have been many studies ranging from the work of Stanbrook (1961) and McCabe (1966), through the pioneering studies of Bogdonoff and his colleagues at Princeton who included Vas, Oskam (1975,1976), Dolling (1983) and Settles, to the studies of Kubota (1980) and Saida (1984). Comprehensive lists of references are given in the various surveys already referrred to.

Many investigators have used surface oil flow, following the early pictures of Stanbrook (1961). He used a very fluid oil mixture and was able to use one coating for a number of different wedge angles. He clearly showed how, as the wedge angle is increased, the oil flow lines from upstream coalesce into what he suggests is a separation line. Downstream of this line the oil also flows towards the line of coalescence though often very slowly. The formation of a line towards which the surface stream-lines converge is accepted here as the separation condition.

Some of the best oil flow pictures have been produced by Oskam et al (1975) and Kubota (1980). Copies from these are shown in Figs. 3a to 3c.

(i) at low wedge angles (e.g. up to α ~5° say) the 'surface flow' turns towards the plane of the shock-wave, the angle turned through can equal or exceed the wedge angle and the influence of the shock is felt well ahead of its 'inviscid position' i.e. its location in the freestream well away from the wall. Even at low α there is evidence of a small corner vortex as the higher pressure on th$\cdot$ wedge attempts to escape up the wall surface.

(ii) at moderate α (say between 5 and 10°) the streaklines ahead of the shock converge and at some wedge angle coalesce into what Kubota calls a line of complete convergence. This is taken to be the separation position. Similarly a line of divergence is also detectable on the wall surface close to the corner. In the corner the small corner vortex persists as shown by a convergence (i.e. separation) line on the wedge surface and a divergence (i.e. attachment) line on the wall.

The flow patterns proposed are shown in Fig.4. More recently the experimental work of Settles and Lu (1985) and the computations of Hortsmann (1986) have both confirmed the very flattened vortex which is formed along the wall. The calculations by Knight et al (1986) not only suggest the mean flow field structure shown in Fig.5 they also observe "a second small vortical structure within the fin boundary layer and close to the corner, in agreement with the experimental observations of Kubota and Stollery (1980)".

The broad features of the ineraction seem well established but more detailed questions remain. The shock affects the boundary layer and eventually causes separation, how does the affected boundary layer alter the shock pattern? Secondly what happens near the nose of the wedge where it intersects the wall? The vapour screen pictures by Kubota (1980) suggest the shock bifurcates near the wall and in their review Settles and Dolling sketched the pattern shown in Fig.6a drawing on the work of Oskam et al (1975) and Zheltovodov (1979).

Very recently Lu and Settles (1989) presented some laser light-screen pictures in a plane roughly normal to the inviscid shock. At $M_\infty = 3.44$ and a fin angle of 15° the main flow-field structure features are visible. They are interpreted in Fig. 6b. The lambda foot of the shock wave is clearly visible but more interestingly a curved line from the triple point curves round and impinges on the wall near the wall/fin junction. Using their interpretation the authors then considered the streamtube processed by the lambda shocks S2 and S3 and bounded by the slip surface (a) on one side and the vortical separation (b) on the other. They suggest that this streamtube curves and accelerates towards the test surface before finally decellerating through a normal shock S4. It is this streamtube (or supersonic jet) impinging on the surface that causes the high pressures and high heat transfer rates observed near flow attachment by many investigators. The figure (6b) is highly suggestive of the shock/shock interference fields studied by Edney (1968).

The figure is also similar in some ways to 'one half' of the flow in a corner. This is not surpirising and reference to the work on 90° corner flows of Charwat and Redekeopp (1967) and the magnificently detailed experimental (laminar) results of Kipke and Hummel (1975) and Mollenstädt (1984) shows many of the features now described by Lu and Settles (1989) for the case of turbulent glancing interaction.

An electron beam photograph (Bertram and Henderson 1970) taken in a helium tunnel at $M_\infty = 19$ for laminar flow through a 90° corner formed by two 10° wedges, clearly shows the slip line starting from the shock triple point and bending round to reach the surface. The photograph also shows how close this point is to the vortex attachment point and certainly in the German work referred to above, the peak values of pressure and heat transfer are allied to the main vortex attachment points.

Near the root of the fin, the fin penetrates the boundary layer whose local Mach number decreases as the wall is approached. At some point the wedge angle will reach the shock detachment angle and between this point and the sonic line within the boundary layer the shock will be detached. A possible flow pattern is shown in Fig.7. Such a pattern is supported by the oil flow pictures of Kubota but not obvious in those of Stanbrook and unfortunately not in the field of view in the pictures taken by Oskam. Obviously the feature is a minor one and depends on the wall boundary layer thickness and on how sharp the fin leading edge is.

From the design point of view, three features of great importance are the pressure distribution, heat transfer rate pattern and flow steadiness. Typical pressure distributions along lines parallel to the fin surface are shown in Fig.8. The way in which the viscous interaction smears out the abrupts rise occurring across the shock in the free stream is clearly visible. A complete map of the way in which the pressure distribution parallel to the free stream direction varies with wedge angle is shown in Fig.9 taken from the work of Oskam. Both Figs. 8 and 9 show how a 'plateau' of pressure develops as the boundary layer separates and this is reminiscent of '2D' separation.

To get a clearer picture of the overall pressure pattern it is necessary to plot out the isobars. This is done in Figs.10 and 11 and the approximately conical nature of the flow, apart from an 'inception region' near the nose, is immediately obvious. There have been many attempts to scale the flow using conical coordinates and among the latest is the paper by Lu et al (1987). We shall see later that the conical nature of the flow (in the sense of constant pressure, heat transfer and main flow visualisation lines lying along rays from an apex) also holds for laminar flow.

The pressure distributions in a plane normal to the wedge surface are replotted from Stanbrook in Fig.12. The pressure rises to the inviscid wedge pressure right in the corner. The correlation of Neumann and Hayes (1977) shows that in fact the peak pressure (and heat transfer rate) occurs on the wall close to the root of the fin. It is likely that the density of pressure tappings in Stanbrook's experiment may not have been sufficient to pick up this peak.

Korkegi (1976) has reviewed the structure of 3D glancing interactions and shown the connection between the flow features and the spanwise distributions of pressure and heat transer rate. These are reproduced in Figs. 13,14 and 15. There is no doubt that the correlations of Neumann and Token (1974) for pressure

and heat transfer peaks are very useful for design purposes as is the work of Scuderi (1978). The similarity between the pressure and heat transfer rate distributions when non-dimensionalised with respect to their freestream values is striking. This is often the case for turbulent separated flows.

From the considerable body of work available it is possible to construct the main features of both separated and unseparated flow. It remains to try to define the boundary between them.

3.2. Incipient Separation

Because incipient separation is difficult to define McCabe suggested the criterion that $\alpha = \alpha_i$ when the deflected surface flow becomes aligned with the inviscid shock. This enabled him to calculate the α_i vs M_∞ boundary shown in Fig.16. Korkegi (1975) found a better fit to the experimental data was given by $M_\infty.\alpha_i = 17°$. However, as many investigators have pointed out the flow can turn through larger angles than the wave angle before separation occurs, (as defined by the formation of a complete convergence line). A collection of actual separation measurements is shown in Fig.17. The dearth of data at hypersonic Mach numbers is immediately apparent. Tests by Goldberg (1973) locate α_i between 4° and 14°. In his paper the value of 9° is plotted at $M_\infty = 5.9$ but the value may have been influenced by the other walls of the tunnel test section. Holden (1984) measures a value of 6.5° at $M_\infty = 11$ based on the appearance of a plateau in the streamwise heat transfer distribution together with a marked increase in the fluctuation levels in the output from the local thin film gauges. Below $M_\infty = 5$ there seems reasonable agreement between the various sorts of data.

One thing is obvious, namely the values of α_i for glancing interaction are far below those for '2D' interactions (see Fig.18). This may have important implications where both types of interaction are likely to be present, as for example in rectangular wedge-type intake ducts. Goldberg's work shows how the two types of interaction can mutually affect one another.

3.3. Flow steadiness

Turbulent flows are by definition unsteady. Numerous measurements have been made, notably by Bogdonoff and his co-workers. This topic is covered elsewhere in the lecture programme.

3.4. Laminar Flow

When Korkegi surveyed sharp-fin glancing interactions in 1976 his first conclusion was that "the structure of the three dimensional interaction is not fundamentally different for laminar or turbulent flow; it is primarily dependent on the extent of separation."

He did of course point out that laminar boundary layers separate much more easily than turbulent ones. The amount of laminar data available is small.

Charwat and others have studied laminar corner flows but there was little else until VKI began a detailed investigation(of a wedge type fin mounted in the laminar boundary layer growing over a sharp edged flat plate) in about 1980. The paper by Degrez and Ginoux (1983) showed that even at $\alpha = 4°, M_\infty = 2.25$, the flow is already separated whereas α_i for turbulent flow is around 10? Further experiments showed the characteristic plateau in the pressure distributions for $\alpha = 4,6$ and 8° (Fig.19). The measured pressures scale reasonably well in conical coordinates (Fig.20) and a corresponding calculation by Degrez (1985) verifies the approximately concial nature of the isobars. The numerical results were obtained by solving the full compressible Navier Stokes equations. A comparison between the measured and computed pressure distributions is shown in Fig.22. The computation with a fine mesh gives better agreement with the experimental data. It also gives some evidence of a secondary separation which the coarse mesh does not (Fig.23). So far the investigation shows all the qualitative features of turbulent interaction but quantitatively separation occurs earlier and the interaction covers a large area.

Before leaving laminar flow it is worth noting that Möllenstädt (1984) measured peak heat transfer rates ten times the wedge value in a corner composed of two 8" wedges at right angles. The Mach number was 12.3, the flow was separated and the peak heat transfer occurred close to the attachment line

4. SHARP SWEPT FINS (FIG. 24)

Many of the flow features are qualitatively similar to the straight fin flows already described. However, there are two important additional points to consider. (i) As the fin is swept so the shock strength at the root, which causes the glancing interaction, is reduced. The reduction in strength as manifest by the shock wave angle at the centre line of the corresponding delta wing (one swept fin and its mirror image) is shown in Fig.25; (ii) sweeping the fin reduces the Mach number normal to the leading edge so that shock detachment from the leading edge occurs at a lower incidence as shown in Fig.26.

4.1. Turbulent Flow

Very little data exists but Lu (1983) and Settles and Lu (1985) studied a range of fins at $M_\infty = 3$ whilst more recently Fomison and Stollery (1987) examined fins with sweep angles between 0 and 75° at $M_\infty = 2.4$.

Both sets of investigators found the inviscid shock wave strength to be an important factor. Settles and Lu managed to correlate all their data on upstream influence (Fig.28) in terms of the normal Mach component (M_N) and initial boundary layer thickness Reynolds number ($Re_{\delta\delta}$). Fomison's data were taken with a much thicker turbulent boundary layer and he found that the proposed correlation was less successful for his results. The pressure distributions and isobars as measured by Fomison are shown in Figs.29 and 30. The isobars suggest the flow pattern is roughly 'conical' only ahead of the inviscid shock position. The pressure levels for a given incidence decrease as the sweep increases (Fig.30). This is expected since the shock strength is being reduced. Fomison non-dimensionalised his pressure measurements using the calculated pressures on the centre line of the corresponding delta wing. This seems to work

well (Fig.31) and suggests it is the total pressure rise through the interaction that is the important parameter.

The flow pattern development is very similar to the unswept case and the development is seen in Fig.32. The only changes to the flow proposed by Kubota are that (i) even at low fin incidences there seems to be a small separated region near the nose, (ii) as sweep is increased so the attachment line originally at the leading edge of the fin, moves down towards the root and the corner vortex moves closer to the corner. The 'streamsurface' and 'vortex skeleton' representations of the flow are shown in Fig.32 for the fin with 75° of sweep. The pressure distributions and flow characteristics normal to the shock wave are pictured in Figs. 33 and 34.

4.2. Laminar Flows

Currently there seems to be little data available. Murakami (1989) has made some interesting measurements at $M_\infty = 7$ on fins with 0 to 60° of sweep but his results await general publication. Again it is worth looking at the data for laminar flow past swept corners (e.g. Möllendstadt, 1984) which shows significant reductions in the surface pressure and thermal loading as the leading edge is swept back.

4.3. Incipient separation

If the inviscid shock strength at the root was the dominant factor then sweep would increase the incidence angle for incipient separation. Thus using Fig. 25 and taking $\alpha_i = 10°$ for $\Lambda = 0°$ and $M_\infty = 2.45$ we would assume that at $\Lambda = 75°$ α_i would be 19°. Yet the oil flow pictures and pressure distributions clearly indicate separated flow at α_i as low as 13°. However, reference to Fig.26 shows that at $\Lambda = 75°$ the leading edge is subsonic and that at smaller angles of sweep the leading edge shock will become detached at modest angles of incidence. Obviously the situation is complex and more data are required.

In the study by Settles and Lu at $M_\infty = 2.95$ (1985) they suggest incipient separation occurs when the inviscid shock angle (β_0) is 3½° more than the freestream Mach angle (μ_∞). The values of α_i corresponding to $\beta_0 = 19.8 + 3.5 = 23.3°$ for various sweep angles are given below:

$\Lambda =$	0	20	40	65
$\alpha_i =$	5	6	7	9

If we were to use the same criterion for Fomison's results at $M_\infty = 2.45$ then $\beta_0 = 24.6 + 3.5 = 28.1$ and the incipient separation angles of incidence are:

$\Lambda =$	0	30	45	60	75
$\alpha_i =$	5	6	7	8	11

Since the value of α_i at $\Lambda = 0$ seems too low and the oil flow picture at $\Lambda = 75$ shows the flow to be 'well separated' at $\alpha = 14$ the above values must be at best tentative and echo the need for further study.

5. BLUNT STRAIGHT FINS (FIG.35)

Immediately the leading edge is blunted the whole character of the interaction region is changed. Bluntness causes the 'inviscid shock' to stand off so that the part of the shock envelope ahead of the stagnation point is normal to the flow and the shock there is the strongest possible for a given Mach number.

A normal shock interacting with the side wall boundary layer will usually force separation which in turn modifies the shock pattern. Separation leads to the formation of one or more horseshoe vortices which encircle the nose. Ahead of the nose an oblique shock marks the start of the separation zone and this oblique shock interacts with the bow shock at some spanwise distance from the fin root. The ensuing shock-shock interaction can lead to complex jet-like flows which impinge on the fin leading edge giving high pressures and intense heat transfer rates. Shock-shock interactions form a separate part of this course where they are treated in detail.

5.1. Turbulent Flow

5.1.1. Fin at zero incidence

The most common geometry is a fin of constant thickness with a semi-circular nose. Sometimes just a circular cylinder is tested mounted on a flat plate. These are the only two configurations considered here. The inviscid shock shape must again be found experimentally. Even in the root region two dimensional results for the stand-off distance will be optimistic unless the span diameter ratio is very big (see Fig.36).

There have been many experimental investigations notably by Price and Stallings (1967), Kaufman et al (1972), Sedney and Kitchens (1977), Dolling and Bogdonoff (1982), Ozcan (1982) Saida and Hattori (1984) and Fomison (1986). Recently the problem has been studied mathematically by solving the Reynolds-averaged Navier-Stokes equations by Hung and Buning (1985). Agreement with experiment is very encouraging.

The broad features of the flow are common to all investigations and are sketched simply in Fig.37. The differences emerge when more detail is required. Most experimental studies have to rely on surface measurements and some 'rather cloudy' vapour screen pictures. Sidney and Kitchens took some excellent flow visualisation pictures, three of which are reproduced in Figs. 38-40. They found evidence of 2,4 or 6 horseshoe vortices encircling the cylinder depending on the Reynolds number. As Re increased so the number of pairs of vortices decreased. The position of the primary separation and attachment points varied very little but the structure between them changed significantly as sketched in Fig.40.

Fomison's oil flow pictures suggest four vortices though the one just in front of the fin is tucked into the fin-plate junction and can only be seen on the surface flow picture around the sides of the fin. One of Fomison's pictures is shown in Fig.41 and the interpretation is shown in Fig.42. Isometric views of the surface streamlines together with vortex skeleton representations are given in Figs.43 for large and small D/δ.

The flow shows many interesting features with the horseshoe vortices being stretched around the sides of the fin and appearing to weaken and lift off from the surface. The very high pressure air near the base of the fin escapes around the shoulder of the fin root and upwards over the fin giving a jet-like streak pattern. This has been noticed by many investigators.

A typical pressure distribution along the centre line is shown in Fig.45. The pressure starts to rise just ahead of the separation line as marked by the surface oil flow and is close to the extrapolated position of the oblique separation shock as might be expected. The first peak is close to the attachment point A, (Fig. 40 and 43) and the trough seems close to the secondary separation point (S_1 in Fig.40 and S_2 in Fig.43). The pressures close to the nose are difficult to measure but there is a second peak (see Fig.47) just before the fin is reached. This is probably associated with the attachment line A in Fig.40 (A_2 in Fig.43). The pressure values at this second peak are far higher than at the first peak but they fall short of the value behind a normal shock wave at the freestream Mach number (see Fig.47). Values greater than the stagnation pressure are measured in the region affected by shock/shock interaction and we shall return to this phenomenon later.

Dolling and Bogdonoff (1982) showed that the scaling parameter for the centre line pressure distribution over a wide range of M_∞ and D/δ was the leading edge diameter D (provided that the boundary layer was turbulent). Figure 46 shows the correlation. The upstream influence is between 2 and 3D and the pressure ratio at the first peak is around 2. There is an effect of Mach number as is clear from the work of Price and Stallings (Fig.47) but it is only really significant for the value of the second peak near the root of the fin.

Dolling and Bogdonoff also showed that for a given Mach number the whole side wall pressure field scaled with nose diameter D. This was confirmed by the work of Fomison (Fig.48) in which four different fins were used at $M_\infty = 2.45$. Pressure distributions at $y/D = 0,1,2,4,5$ and 8 are shown in Fig.48. The characteristic double peak pattern in the streamwise direction rapidly subsides into a single hump in the neighbourhood of the inviscid shock position as the spanwise distance is increased. This is also shown in the sidewall isobar plots shown in Figs. 49 and 50.

Dolling and Bogdonoff further showed (Fig.51) how the pressure distribution along the fin leading edge correlated with Z/D provided that the root shock wave structure is clear of the boundary layer thickness i.e. $D/\delta \geq 4$. At $M_\infty = 2.95$ the pressure peaks at $Z/D \approx 1$ and because of the shock/shock interactions part of the flow decellerates through a series of oblique shock waves instead of a single normal shock and so recovers to a pressure greater than the stagnation pressure ($p_w/p_{T2} > 1$). At $M_\infty = 2.95$ the ratio p_w/p_{T2} reaches 1.5 but at hypersonic speeds it can reach much higher values. The shock/shock interaction is type IV as described by Edney (1968).

As the value of D/δ is reduced so more and more of the shock interaction becomes submerged in the boundary layer. This is shown in the photographs taken by Fomison (Figs 52&35) and the effect on the fin leading edge pressure is shown in Fig.53. Some very useful measurements of heat transfer were made by Hung and Clauss (1980) on a flat plate from which a cylinder was mounted. For $H/D > 2$ (long protuberances) the heat transfer rate distributions along the plate centreline seem to scale with diameter D and the first signs of disturbances occur about 3 diameters upstream. The heat transfer centre line plots look similar in form to the pressure distributions as measured by other investigators.

Before leaving the blunt fin at zero incidence the numerical work of Hung and Buning must again be mentioned. They have simulated the flow numerically and despite the limited mesh resolution available and the complicated flow field, they achieved good agreement with the experimental data of Dolling et al. Only one pair of horseshoe vortices was found (Fig 54) but the surface pressure distributions agreed well. A sketch that Fomison made from his surface oil flow pictures at $M_\infty = 2.45$ is compared with the calculated limiting streamlines on the 'unwrapped' fin surface at $M_\infty = 2.95$ in Fig.55.

The calculations confirm that the spatial extent of the interaction is dominated by the inviscid characteristics of the flow i.e. the physical size of the fin, as found experimentally.

5.1.2. Fin at incidence

Both Dolling (1982) and Fomison have studied blunt fins at incidence. As might be expected the region near the nose is bluntness dominated but far away from the nose the flow becomes incidence dominated and must tend towards the results for a sharp fin. Dolling was able to sketch a rough boundary separating these two regions at $M_\infty = 3$ (Fig.56). Blunting the leading edge displaces the inviscid shock laterally but well away from the nose the shock angle must asymptote to that appropriate to a wedge and Fig.57 shows this to be the case. Pressure distributions measured in this far field region, relative to the shock position, should be similar, see Fig. 58.

Fomison's plots of the oil flow primary separation lines (Fig.59) show the nose dominated region and how, in the far field, the separation line is parallel to that for a sharp fin at the same incidence. The corresponding pressure distributions show how the results in the nose region are unaffected by incidence. The pressure levels downstream exceed the wedge values because of reflections from the bottom liner of the test section.

Once again the scaling factor D correlates the pressure distributions at a given incidence (Fig.60).

At hypersonic speeds the various domains are characterised by the parameters $M_\infty^2\alpha^2$ for incidence, $M_\infty^2 C_D^{2/3}(x/d)^{-2/3}$ for bluntness and $(M_\infty^9 C/Re_x)^n$ for viscous interaction where n is 2/7 for 1/5 for strong and weak interaction respectively. The relative size of these parameters will determine which is the dominant influence.

5.2. Laminar flow

Data are more sparse for laminar flow but as expected all investigators find that the area disturbed, for a given size of fin (or cylinder), is far greater than when the boundary layer is turbulent. Ozcan and Holt's (1984) studies at M_∞ = 2.36 clearly showed three separation lines on the flat plate ahead of the cylinder mounted on it. They examined the flow field postulated by Sedney and Kitchens (Fig.40) but could not confirm it by laser-velocimeter measurements. Instead their measurements suggested an unsteady and perhaps periodic flow field.

Their pressure measurements showed the interaction to begin up to 12 diameters ahead of the cylinder and that, for H/D > 4, the pattern did not change. For H/D < 4 the disturbed area reduces as the H/D ratio is reduced. Hung amd Clauss (1980) in their extensive set of heat transfer measurements at M_∞ = 5.3 also find the laminar interaction region extending to 12 diameters upstream for H/D > 2. This drops to 2 or 3 diameters for their turbulent flow results. In the laminar-flow disturbed region ahead of a cylinder the heat transfer initially drops below the flat plate value before rising to the first peak (Fig. 61). This is similar to the reduction found in 2D laminar separated regions and contrasts with the turbulent patterns already discussed.

5.3. Transitional Flow

Ozcan and Holt's study is one of the few to look at the effect of a transitional boundary layer. The distance to the primary separation line(S) increased very slightly with Reynolds number Re in the laminar range 0.1 x 10^6 < Re < 0.3x10^6. Further increase in Re_L saw the number of separation lines drop to two and then to one with the distance S decreasing with Re_L. When the flow was fully turbulent the ratio S/D had dropped to about 2 compared with the fully laminar value of around 7.5.

6. BLUNT SWEPT FINS

6.1. Turbulent flow

6.1.1. Fins at zero incidence

Price and Stallings reported the effects of sweep on glancing interactions as long ago as 1967. Figures 62 and 63 show how the centre-line pressure distribution collapses and the disturbed area (as measured to the first sign of increasing surface pressure) contracts as sweep is introduced.

More recently Hussain (1985) studied blunted fins at sweep angles up to 75° and incidence angles of 0 - 24°. The inviscid shock positions were found by testing the relevant delta wings (Fig.64). As can be seen from Fig.65 the bow shock is three dimensional. It only gradually approaches the (constant) two dimensional value of stand-off distance, calculated by considering the normal component of Mach number.

Hussain confirms the benefits of sweep in greatly reducing the level and extent of the disturbed pressure field (Fig.66). The characteristic double peaked pressure signature reduces dramatically in scale as the leading edge sweep is increased. With reduced pressure levels Price and Stallings question whether separation occurs at M_∞ = 3.71 for sweep angles above 45°. However, Fig.66 shows that the pressure rise to separation only changes slowly with sweep angle and certainly Hussain's oil flow pictures show a clear separation line S_1 up to the highest sweep tested (75°) at M_∞ = 2.45.

Nevertheless, the question of whether there is an incipient separation condition for blunt swept fins has to be considered and this is done in § 6.3. Hussain took many oil flow pictures. At sweep angles up to 30° the pattern looks similar to that for an unswept fin with two pairs of vortices ahead of the fin. However, Hussain interprets the 'jet like region' seen by Winkelmann and Fomison for example, (Fig.55) as the path of the vortex nearest to the fin root as it bends around the fin(see Fig.67a). When the fin is swept back this vortex is carried further outboard over the fin causing extensive separation over the fin surface (Fig.67b). Certainly the oil flow pictures are most complex and it must be remembered that interpreting them currently requires considerable conjecture. Moreover the real flows are to some extent unsteady.

A mathematical simulation of the flow past a swept blunt fin has been constructed by McMaster and Shang (1988) using the Baldwin-Lomax turbulence model. Calculations were made at M_∞ = 2.98 for sweep angles of 0, 30, 45, 60 and 68°. The results (Fig. 68) confirm the experimental findings of reduced disturbance with sweep. What is particularly interesting is that at the highest sweep angle of 68° the flow appears attached (see §6.3).

6.1.2. Fin at incidence

As for unswept fins the nose region is bluntness dominated. Figure 69 shows the centre-line pressure to be unaffected by incidence but away from the centre line the incidence effect becomes increasingly important.

When the blunt swept fin is at incidence the pressure on the fin windward surface is raised. The flow over the fin stays attached and separated flow regions are restricted to the plate surface and the corner. An interpretation of the flow past a 45° swept fin is shown in Fig.70.

6.2. Laminar and transitional flow

Very little data exists and most of the work reported is concerned with shock/shock interactions affecting the fin leading edge rather than the disturbed flow field over the plate from which the fin is mounted. Bushnell (1965) tested the configuration in Fig.71 covering the Reynolds number range Re_L from 10^6 to 10^7 at M_∞ = 8. At the lowest Re_L the boundary layer was laminar and a separated zone ahead of the cylinder (swept 57° relative to the wedge surface) can clearly be seen. This reduces progressively in size as Re_L is increased and for Re_L > 4 x 10^6 no separation is visible from the

schlieren pictures.

Hiers & Loubsky(1967) tested a blunt fin mounted on a flat plate at sweep angles of 0 to 45°. Burn marks, luminosity pictures and oil streak photographs taken at M_∞ = 14 indicated laminar separation (Re_L = 0.56 x 10^5) in a typical horseshoe shaped region encircling the fin. The plate was not instrumented. Thermocouple measurements along the fin leading edge showed how the extremely high local heat transfer rates arising from the separation-shock/bow-shock interaction could be dramatically reduced by sweep (Fig. 72).

6.3. Incipient separation for a blunt swept fin

For a straight blunt fin the bow shock always stands off but for a swept fin there is a sweep angle at which the shock can attach at the root. The equivalent 'inviscid' flow is that past a delta wing with hemi-cylindrical leading edges. Most investigators measure the shock position experimentally and Hussain found even at a sweep of 75° the bow shock is detached at the nose. In contrast both Price and Stallings (1967) and Winkelmann (1972) find no disturbance ahead of the nose of a 75° swept fin.

For an attached shock at the nose two conditions seem to be needed (i) the sweep must be small enough for the leading edges to be 'supersonic' in the sense that M_N > 1, (Fig. 73). This will ensure that the two halves of the blunt delta wing can't communicate with each other; (ii) the sweep must be large enough for the flow approaching the nose to turn along the leading edge attachment line through an attached oblique shock wave.

These two boundaries are shown in Fig.73 and if these are correct then for M_∞ < 2.2. or Λ < 44° the shock is always detached at the nose. Only in region A is an attached nose shock predicted. Every-where else the nose shock stands-off, the shock wave is therefore locally normal to the flow and would be expected to separate the boundary layer on a plate placed along the wing centreline.

Fins which lie in region A may separate the boundary layer if $(90 - \Lambda)$ exceeds $(\alpha_i)2_D$, the two-dimensional wedge angle for incipient separation. Values of α_i have been taken from Fig. 18. Of course these values of α_i may be pessimistic since the flow in the fin nose-root region is three dimensional.

Experimental evidence is scanty and often difficult to interpret. Jones (1964) records a small separated region ahead of 60° swept fin at M = 6 whilst Beckwith (1964) states that there was no separation ahead of a cylinder swept back 68° from the surface of a wedge over which the effective free-stream Mach number was 3.5. This latter value lies close to the 2D incipient separation line in Fig.73.

All we can say is that attached flow is likely in region A1, possible in region A2 and unlikely elsewhere.

6.4. Leading-edge contamination

The flow at the leading edge of a straight wing is laminar and, in particular, the heat transfer rate is the laminar stagnation point value. However swept wings can suffer from leading edge contamination. If the boundary layer at the wing body junction is turbulent then the flow there may contaminate the complete leading edge attachment line so significantly increasing the heat transfer rate values. Contam-ination depends on the sweep angle and radius of the leading edge as well as Mach number and Reynolds number. Poll(1983) has studied the problem and established the conditions under which contamination occurs.

As an example of this phenomenon Bushnell (1965) showed that when transition occurred on the wedge (fig.71) ahead of the cylinder it 'infected' the leading edge and the "increased heat characteristic of turbulent boundary layers persisted all the way along the cylinder for both sweep angles of 45° and 60°". The effect was typically to increase the attachment line heat transfer rates by 50% above the laminar value.

6.5. The effects of filleting

Using the 3D Navier-Stokes code provided by Dr. C.M.Hung of NASA Ames, Lakshmanan et al (1988) have studied the effects of filleting (and sweep). They showed numerically that with proper filleting the flow patterns lose much of their vortical character.

In particular they studied a blunt fin-with-a semicircular leading edge mounted on a flat plate, at M_∞ = 2.4. The horseshoe vortex interaction surrounding the fin was faithfully modelled. They found that in order to significantly weaken the interaction a large fillet (of radius equal to 3½ times the fin leading edge diameter) was required.

Although the mathematical model has been validated for unswept fins with no fillets, there seem to be no experimental data as yet for fin-body junctions with fillets added.

7. SUMMARY

7.1 Sharp fins

. Separation occurs more readily in glancing interactions than in two-dimensional interactions.

. The main features of the flow structure are reasonably well understood but many details require clarification.

. Leading edge sweep decreases the shock strength and hence the intensity and extent of the disturbed flow region on the wall. The wall pressure distributions can be correlated using the centre-line pressure of the corresponding delta wing.

7.2 Blunt fins

- Blunt unswept fins generate a very complex flow field. The strong bow shock always causes separation and the mean flow consists of a number of horseshoe vortices encircling the fin.

- The dominant scaling parameter is the leading edge diameter.

- At incidence the flow near the nose is bluntness dominated whereas the flow far away from the nose is incidence dominated.

- Sweep very significantly ameliorates the effects of bluntness. The scale and intensity of the disturbed region is reduced and at large sweep angles separation may be preven'ed.

- Problems peculiar to blunted fins are (i) shock/shock interactions which can lead to very high local pressure and heat transfer loading (ii) leading edge contamination causing the boundary layer to be turbulent along the attachment line of swept blunt fins.

REFERENCES

BERTRAM, M.H. and HENDERSON, A. (1970). Some recent research with viscous interacting flow in hypersonic streams. Proceedings of the ARL Symposium "Viscous interaction phenomena in supersonic and hypersonic flow". University of Dayton Press, 1970.

BUSHNELL, D.M. (1965). Interference heating on a swept cylinder in region of intersection with a wedge at Mach number 8. NASA TN D-3094 December 1965.

CHARWAT, A.F. and REDEKEOPP, L.G. (1967). Supersonic interference flow along the corner of intersecting wedges. AIAA J. vol 5 no 3 pp 480-488 March 1967.

DEGREZ, G and GINOUX, J.J. (1983). Three-dimensional skewed shock-wave/laminar boundary-layer interaction at Mach 2.25. AIAA Paper no 83-1755 July 1983 .

DEGREZ, G. (1985). Computation of three-dimensional skewed shock-wave/laminar boundary-layer interaction. AIAA Paper no 85-1565 July 1985 .

DELERY, J. (1988). Shock/shock and shock-wave/boundary-layer interactions in hypersonic flows. AGARD-FDP-VKI Special Course on Aerothermodynamics of Hypersonic Vehicles, May 1988.

DOLLING, D.S. (1982). Comparison of sharp and blunt fin-induced shock-wave/turbulent boundary-layer interactions. AIAA Journal, Vol 20 no 10 pp 1385-1391 Oct. 1982 .

DOLLING, D.S. and BOGDONOFF, S.M. (1982). Blunt fin-induced shock wave turbulent boundary layer interaction. AIAA Journal, vol 20 pp 1674-1680. December 1982.

EDNEY, B. (1968). Anomalous heat-transfer and pressure distributions on blunt bodies at hypersonic speeds in the presence of an impinging shock. FFA Report no 115.

FOMISON, N.R. and STOLLERY, J.L. (1987). The effects of sweep and bluntness on a glancing shock wave turbulent boundary layer interaction. AGARD Conference Procedures 428. 1987.

FOMISON, N.R. (1986). The effects of bluntness and sweep on glancing shock wave turbulent boundary layer interaction. PhD Thesis, Cranfield Institute of Technology, September 1986.

GOLDBERG, T.J. (1973). Three dimensional separation for interaction of shock waves with turbulent boundary layers. AIAA J. Vol 11 no 11 pp1573-1575, November 1973.

GREEN, J.E. (1969). Interactions between shock waves and turbulent boundary layers. RAE TR-69098 (May 1969); see also: Progress in Aerospace Sciences, Pergamon Press, Vol 11, pp 235-340 (1970).

HIERS, R.S. and LOUBSKY, W.J. (1967). Effects of shock-wave impingement on the heat transfer on a cylindrical leading edge. NASA TN D-3859, February 1967.

HOLDEN, M.S. (1984). Experimental studies of quasi-two-dimensional and three-dimensional viscous interaction regions induced by skewed-shock and swept-shock boundary-layer interaction. AIAA Paper no 84-1677.

HORSTMAN, C.C. (1986). Computation of sharp-fin-induced shock wave/turbulent boundary layer interaction. AIAA J. Vol 24, no 9, pp 1433-1440. September 1986.

HUSSAIN, S. (1985). A study of the interaction between a glancing shock wave and a turbulent boundary layer - the effects of leading edge bluntness and sweep. PhD Thesis. Cranfield Institute of Technology, November 1985.

HUNG, C-M. and BUNING, P.G.(1985). Simulation of blunt-fin-induced shock-wave and turbulent boundary-layer interaction. J Fluid Mech, Vol 154, pp 163-185. See also AIAA Paper 84-0457.

HUNG, F.T. and CLAUSS, J.M. (1980). Three-dimensional protuberance interference heating in high speed flow. AIAA Paper 80-289, January 1980.

KAUFMAN, L.G., KORKEGI, R.H. and MORTON, L.C. (1972). Shock impingement caused by boundary layer separation ahead of fins, ARL Report 72-0118, August 1972.

KIPKE, K. and HUMMEL, D. (1975). Investigations of the longitudinal flow in corner configurations in the hypersonic regime, Part I: Corners between unswept edges. Z.f.F. Vol 23, no 12, pp417-429, 1975.

KNIGHT, D., HORSTMAN, C., SHAPEY, S. and BOGDONOFF, S. (1986). The flowfield structure of the 3-D shock wave-boundary layer interaction generated by a 20 deg. sharp fin at Mach 3. AIAA Paper 86-0343, January 1986.

KORKEGI, R.H. (1971) "Survey of Viscous Interactions Associated with High Mach Number Flight". AIAA Journal, Vol.9, No 5, pp. 771-784 (May 1971).

KORKEGI, R.H. (1975). Comparison of shock-induced two- and three-dimensional incipient turbulent separation. AIAA Journal, vol, 13, no 4, pp 534-535 (April 1975).

KORKEGI, R.H. (1976). On the structure of three-dimensional shock-induced separated flow regions. AIAA Journal, vol 14, No 5, pp 597-600 (May 1976).

KUBOTA, H. A study of the interaction between a glancing shock wave and a turbulent boundary layer. PhD Thesis, Cranfield Institute of Technology, August 1980.

KUBOTA, H. and STOLLERY, J.L. (1980). An experimental investigation of the interaction between a glancing shock-wave and a turbulent boundary-layer. ICAS 80-14-1, pp 563-574. See additional refs. overleaf.

LAKSHMANAN, B., TIWARI, S.N. and HUSSAINI, M.Y. (1988). Control of supersonic interaction flowfields through filleting and sweep. AIAA/ASME/SIAM/APS First national fluid dynamics congress, July 1988.

LU, F.K. and SETTLES, G.S. (1989). Structure of fin-generated shock-wave boundary-layer interactions by laser light-screen visualisation. (To be published)

LU, F.K., SETTLES, G.S. and HORSTMAN, C.C. (1987). Mach number effects on conical surface features of swept shock boundary-layer interactions. AIAA Paper 87-1365.

McCABE, A. (1966). The three-dimensional interaction of a shock-wave with a turbulent boundary-layer. The Aeronautical Quarterly, Vol 17, Part 2, pp 231-252.

McMASTER, D.L. and SHANG, J.S. (1988). A numerical study of three-dimensional separated flows around a sweptback blunt fin. AIAA Paper No 88-0125 January 1988 .

MÖLLENSTÄDT, W. (1984). Investigations of the longitudinal flow in corner configurations in the hypersonic regime, Part II: Corners between swept wedges. Z.f.W. vol 8, no 6, pp 405-414, 1984.

MURAKAMI, A. An experimental study on three dimensional shock wave/laminar boundary layer interaction at Mach 7. University of Tokyo report - private communication.

NEUMANN, R.D. and TOKEN, K.H. (1974). Prediction of surface phenomena induced by three-dimensional interactions on planar turbulent boundary-layers. Paper no 74-058, International Astronautical Federation XXV Congress, Amsterdam, The Netherlands October 1974 .

NEUMANN, R.D. and HAYES, J.R. (1977). Prediction techniques for three-dimensional shock-wave/turbulent boundary-layer interactions. AIAA Journal, Vol 15, no 10, pp 1469-1473 October 1977 .

OSKAM, B., BOGDONOFF, S.M., and VAS, I.E. (1975). Study of three dimensional flow fields generated by the interaction of a skewed shock wave with a turbulent boundary layer. AFFDL-TR-75-21, Feb. 1975.

OZCAN, O. and HOLT, M. (1984). Supersonic separated flow past a cylindrical obstacle on a flat plate. AIAA Journal Vol. 22, No 5, pp 611-617, May 1984.

PEAKE, D.J. and TOBAK, M. (1980). Three-dimensional interactions and vortical flows with emphasis on high speeds. AGARDograph No 252 July 1980 .

POLL, D.I.A. (1983). The development of intermittent turbulence on a swept attachment line including the effects of compressibility. The Aeronautical Quarterly, vol 34, part 1. February 1983.

PRICE, A.E. and STALLINGS, R.L. (1967) Investigation of turbulent separated flows in the vicinity of fin type protuberances at supersonic Mach numbers, NASA TN-D-3804, February 1967.

SAIDA, N.(1988). A review of research on shock wave/boundary layer interactions. Japan Society of Mechanical Engineers.Part of Research & Investigation Sub-committee report P-SC91 "Generation, Propagation, Reflection & Refraction of Weak Shock Waves" (In Japanese) March 1988.

SAIDA, N. (1984). Interaction between shock waves and boundary layers induced by a sharp fin. Japan Soc. for Aeronautical and Space Sciences, vol 32, no 366, pp 403-409, 1984.

SAIDA, N. and HATTORI, H. (1984). Shock wave-turbulent boundary layer interactions induced by a blunt fin. Trans. Japan Soc. for Aeronautical and Space Sciences, vol. 27, no 76, pp 67-77, 1984.

SEDNEY, R. and KITCHENS, C.W. Jr. (1977). Separation ahead of protuberances in supersonic turbulent boundary-layers. AIAA Journal, vol 15, no 4, pp 546-552 April 1977 .

SCUDERI, L.F. (1978). Expressions for predicting 3-D shock wave turbulent boundary layer interaction pressures and heating rates. AIAA Paper 78-162, January 1978.

SETTLES, G.S. and DOLLING, D.S. (1986). Swept shockwave boundary layer interactions. AIAA Progress in Astronautics and Aeronautics. Vol 104, "Tactical Missile Aerodyamics" Ch 8, pp 297-379. September 1986.

SETTLES, G.S. and LU, F.K. (1985). Conical similarity of shock/boundary layer interactions generated by swept and unswept fins. AIAA Journal, vol 23, no 7, pp 1021-1027, July 1985.

STANBROOK, A. (1961). An experimental study of the glancing interaction between a shock wave and a turbulent boundary layer ARC CP 555. (HMSO London UK)

WINKELMANN, A.E. (1972). Experimental investigation of a fin protuberance partially immersed in a turbulent boundary layer at Mach 5. Naval Ordnance Laboratory Report NOLTR-72-33, January 1972.

ZHELTOVODOV, A.A. (1979). Properties of two- and three-dimensional separation flows at supersonic velocities, Izvestiya Akademii Nauk SSSR, Mekhanika Zhidkosti i Gaza, No 3, May - June 1979, pp 42-50.

ADDITIONAL REFERENCES

KUBOTA, H and STOLLERY, J.L. (1982). An experimental study of the interaction between a glancing shock wave and a turbulent boundary layer. J. Fluid Mech vol.116, pp. 431-458, 1982.

OZCAN, O. (1982). An experimental investigation of three-dimensional boundary-layer separation in supersonic flow past a circular cylinder on a flat plate. PhD Thesis, University of California, Berkeley, March 1982.

MOECKEL, W.E. (1949). Approximate method for predicting form and location of detached shock waves ahead of plane or axially symmetric bodies. NAGA TN 1921.

NEEDHAM, D.A. and STOLLERY, J.L. (1966) Boundary layer separation in hypersonic flow. AIAA Paper 66-455, June 1966.

SETTLES, G.S.; FITZPATRICK, T.J. and BOGDONOFF, S.M. (1978) "A Detailed Study of Attached and Separated Compression Corner Flowfields in High Reynolds Number Supersonic Flow". AIAA Paper No 78-1167 (July 1978); see also: AIAA Journal, Vol.17, No 6, pp. 579-585 (June 1979).

SPAID, F.W. and FRISHETT, J.C. (1972) "incipient Separation of a Supersonic, Turbulent Boundary-Layer, Including Effects of Heat-Transfer". AIAA Journal, Vol. 10, No 7, pp. 915-922 (July 1972).

KUEHN, D.M. (1959) "Experimental Investigation of the Pressure Rise Required for the Incipient Separation of Turbulent Boundary-Layers in Two-Dimensional Supersonic Flow". NASA Memo 1-21-59 A (Feb. 1959).

ROSHKO, A. and THOMKE, G.J. (1969) Supersonic Turbulent Boundary-Layer Interaction with a Compression Corner at Very High Reynolds Number". McDonnell Douglas, Paper 10163 (May 1969).

HOLDEN, M.S. (1972) "Shock-Wave/Turbulent Boundary-Layer Interactions in Hypersonic Flow". AIAA Paper No 72-74 (Jan. 1972).

LAW, C.H. (1974) "Supersonic, Turbulent Boundary-Layer Separation". AIAA Journal, Vol. 12, No 6, pp. 794-797 (June 1974).

DROUGGE, G. (1953) "An Experimental Investigation of the Influence of Strong Adverse Pressure Gradients on Turbulent Boundary Layers at Supersonic Speeds", FFA Report 47, Sweden, 1953.

KESSLER, W.C., REILLY, J.F. and MOCKAPETRIS, L.J. (1970) "Supersonic Turbulent Boundary Layer Interaction with an Expansion Ramp and a Compression Corner", MDC E0264, McDonnell Douglas, 1970.
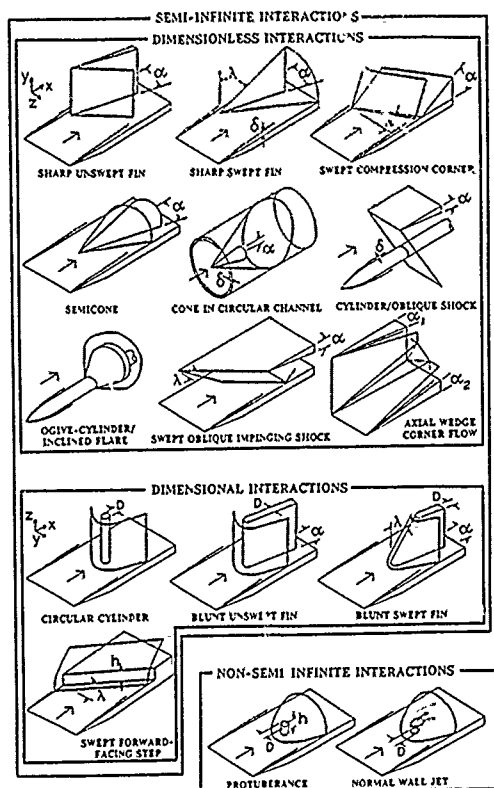
Fig 1 Types of swept shock wave/boundary-layer interaction.
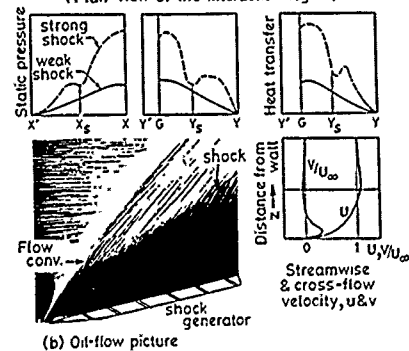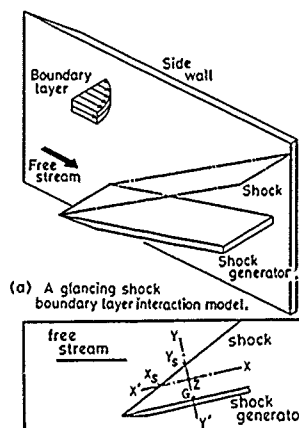
Fig 2 Characteristics of glancing interaction due to a sharp unswept fin.
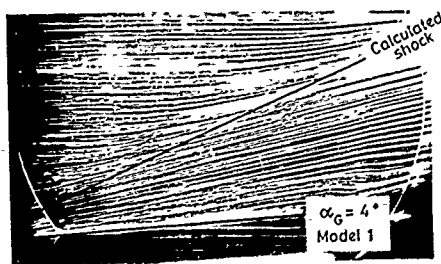
(a) α = 4°, Oskam et al (1975)
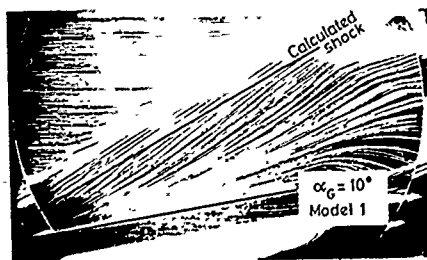
(b) α = 10°, Oskam et al (1975)
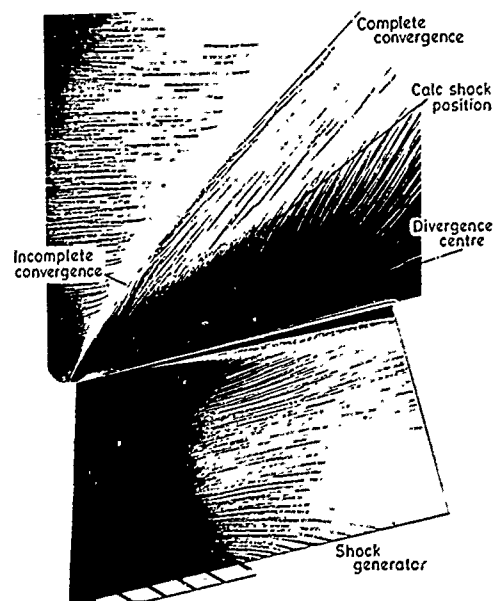
(c) α = 13°, Kubota (1980).

Fig 3 Surface oil Patterns
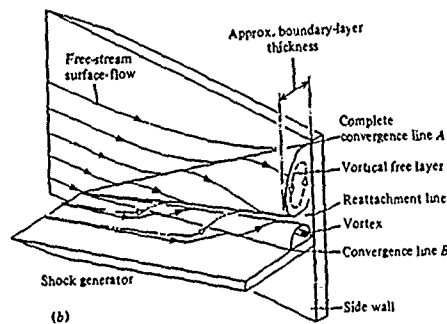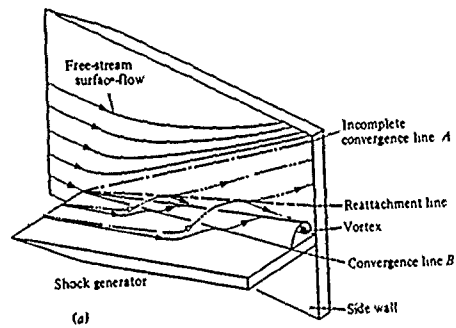
Streamlines in: (a) the attached flow field; (b) the separated flow field.
→ , surface streamline; ⇢ , free streamline.

Fig 4 The flow field model proposed by Kubota (1980).
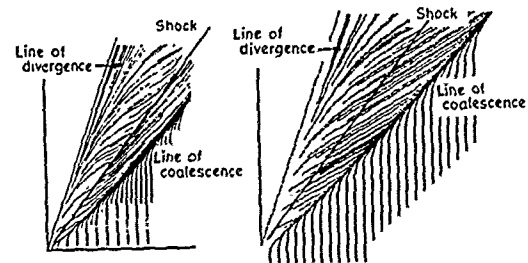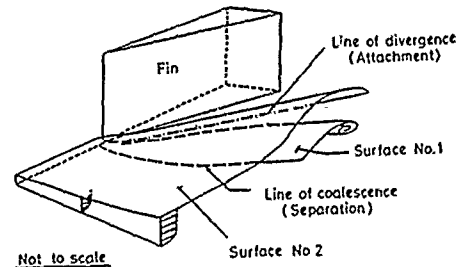
Fig 5 The flow field calculated by Knight et al (1986).
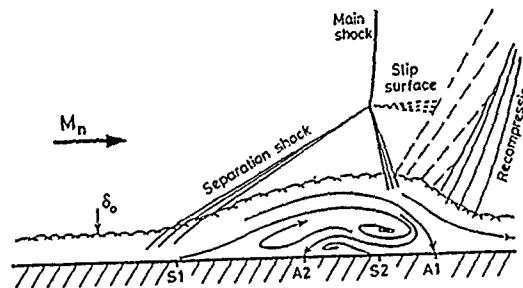
(a) Settles and Dolling (1986)
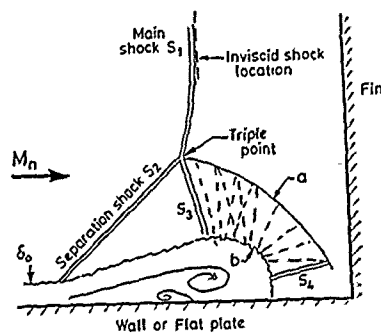
(b) Lu and Settles (1989)
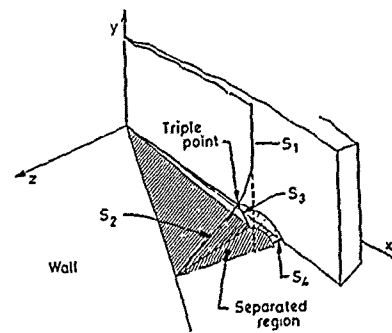
(c) Isometric sketch of the flow, Lu and Settles (1989).

Fig 6 Flow field models in a plane normal to the shock and an isometric sketch.
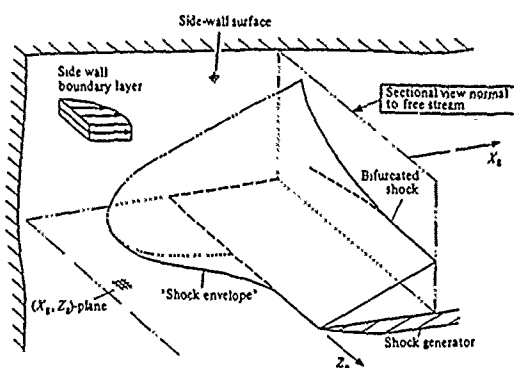
(a) Shock envelope near the fin root.　　　(b) Sectional view on the Xg, Zg plane.
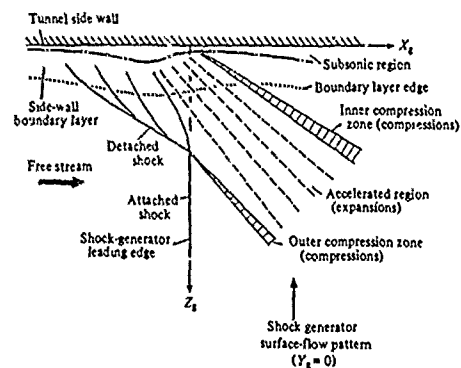
Fig 7
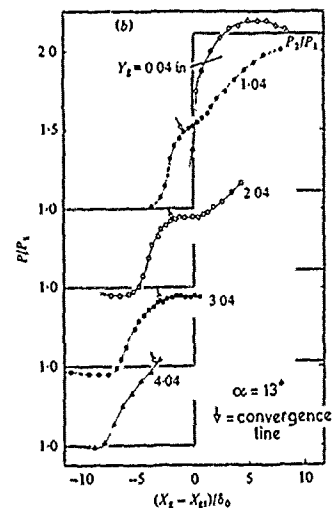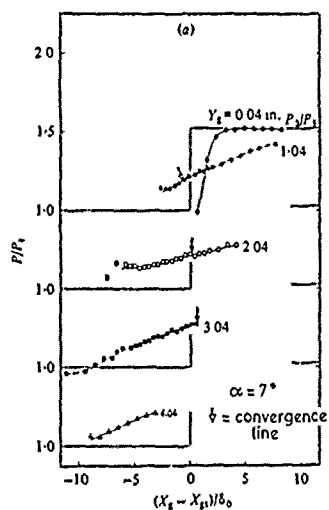
Fig 8　Wall surface pressure distributions (Kubota and Stollery, 1982).
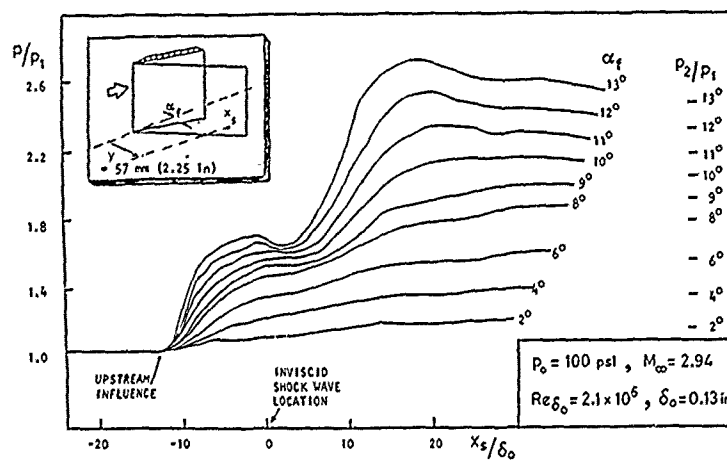
Fig 9　Wall surface pressure distributions, Oskam et al (1975).
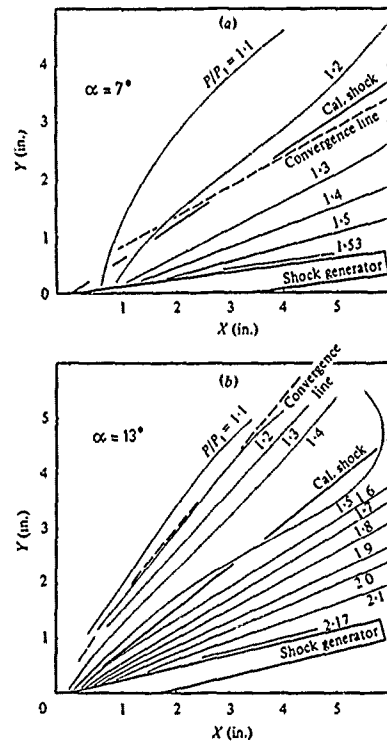
Fig 10 Wall isobars, Kubota and Stollery (1982).

Fig 11 Wall isobars, Oskam et al (1975).

Fig 12 Pressure distributions in a plane normal to
the fin surface, 0.85 inches (2.2cm) from
the fin leading edge.
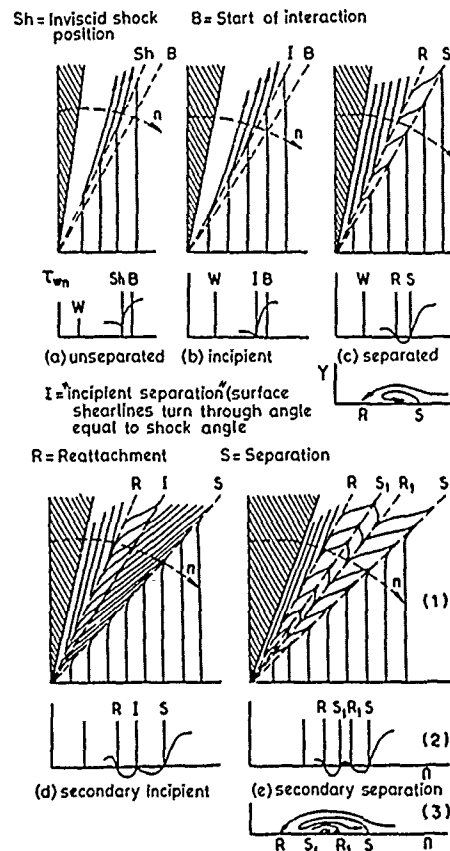
Fig 13 Glancing interaction. A schematic
representation of the flowfield
(Korkegi, 1976).
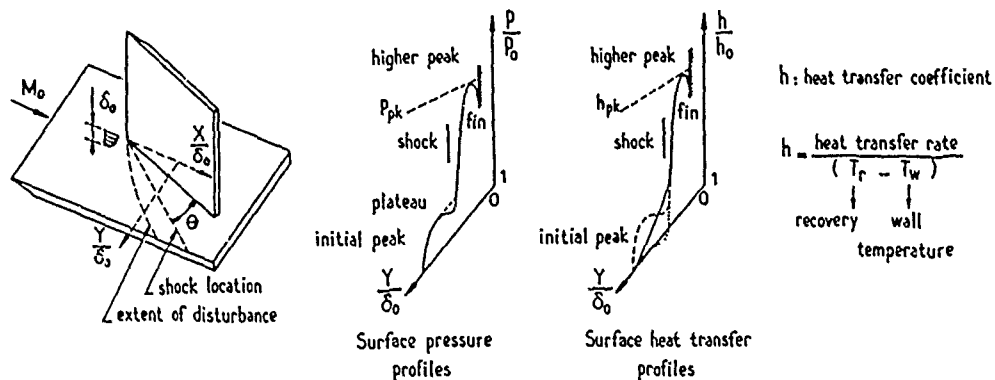
Fig 14 Glancing interaction. Typical wall pressure and wall heat transfer rate distributions.

a _ Peak pressure

b _ Stanton number
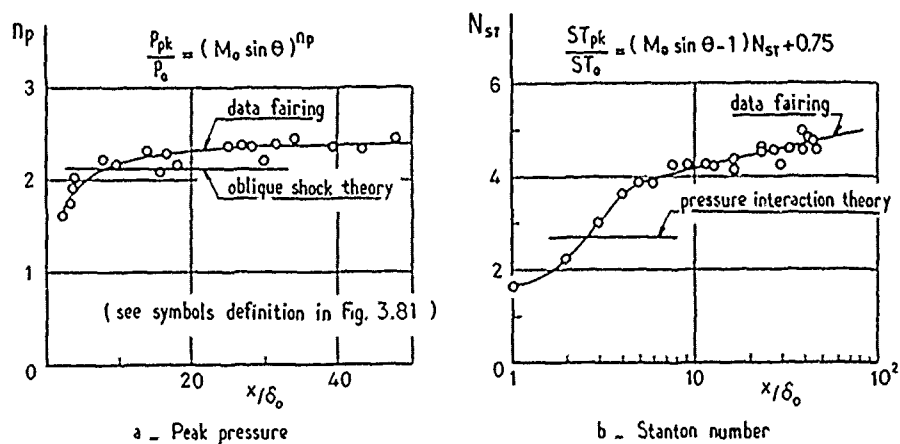
Fig 15 Glancing interaction. Correlations of peak pressure and peak heat transfer rates, (Neumann and Hayes, 1977).
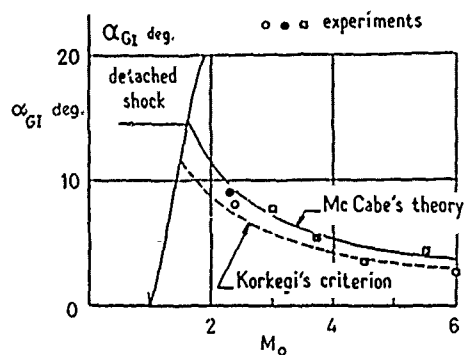
Fig 16 Incipient separation according to McCabe's separation criterion (Kubota and Stollery, 1982)
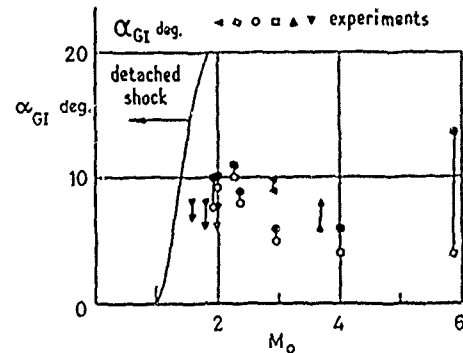
Fig 17 Incipient separation according to usual definition of separation (Kubota and Stollery, 1982)
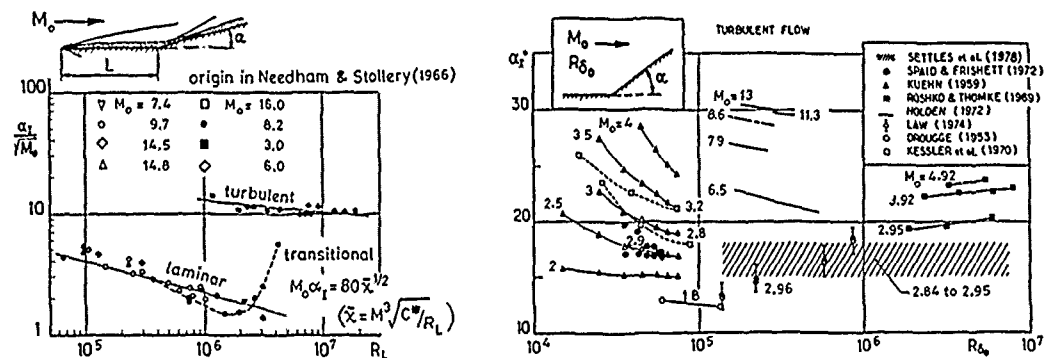
Fig 18 Shock induced incipient separation in supersonic and hypersonic flows over a compression corner.
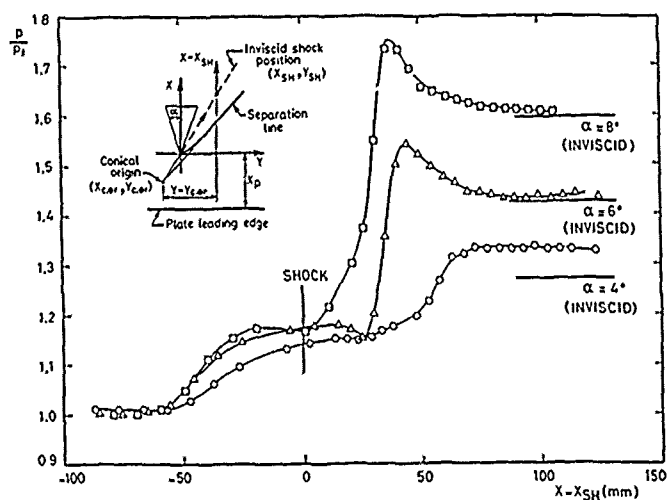
Fig 19 Pressure distribution on the wall Y = 5cm.
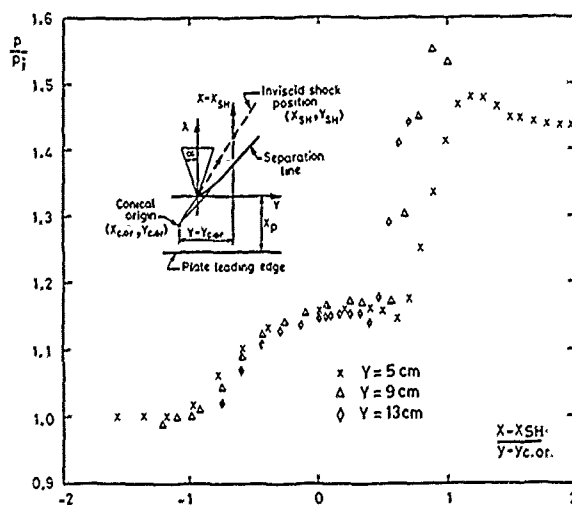
Fig 20 Wall pressure distribution in conical co-ordinates.
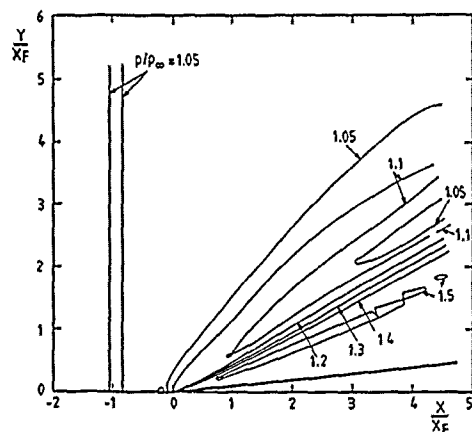
Fig 21 Navier - Stokes predictions of the wall isobars.
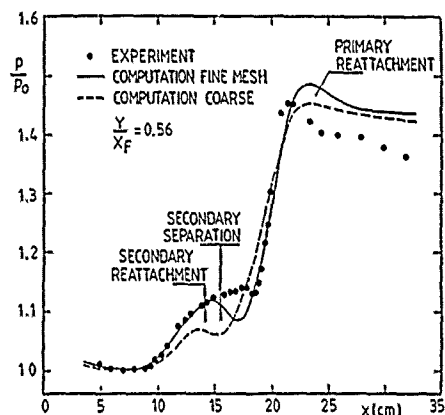
Fig 22 A comparison between the measured and calculated wall pressure distributions at Y = 5cm.
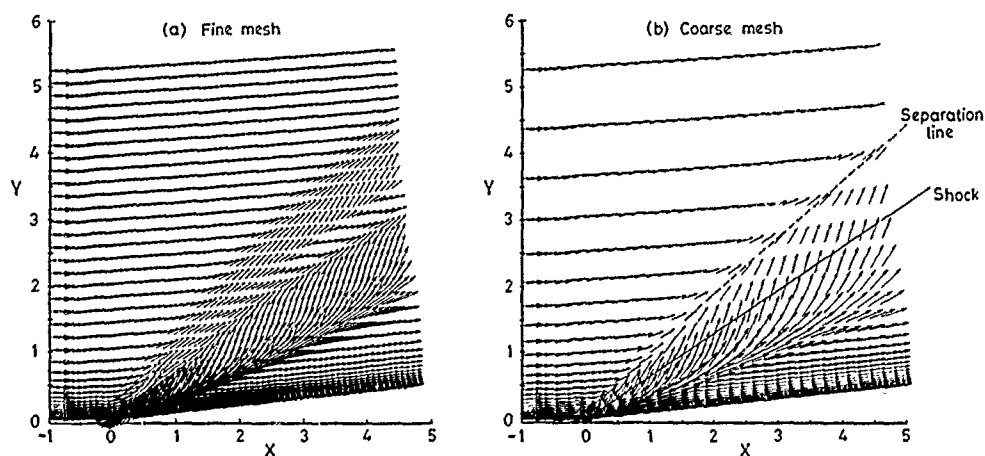
Fig 23 Calculated surface flow pattern using two meshes.
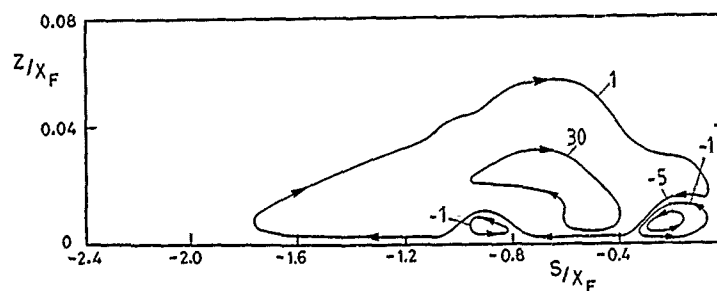
Fig 24 Calculated streamwise vorticity contour in the cut plane at $L_{SH}/X_F = 1.5$.

Figs 21 - 24 Taken from Degrez (1985).
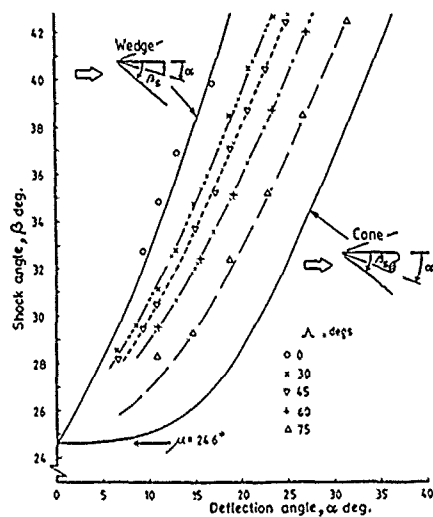
Fig 25 Delta wing centre-line shock wave angles.
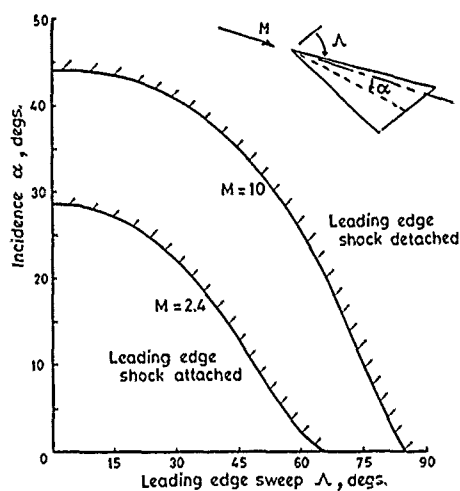
Fig 26 Shock detachment angle for a swept leading-edge.
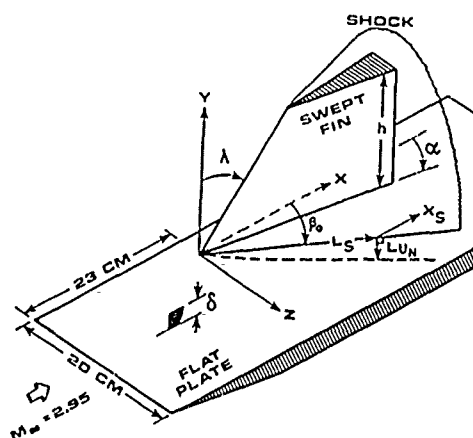
Fig 27 Swept fin geometry and notation.
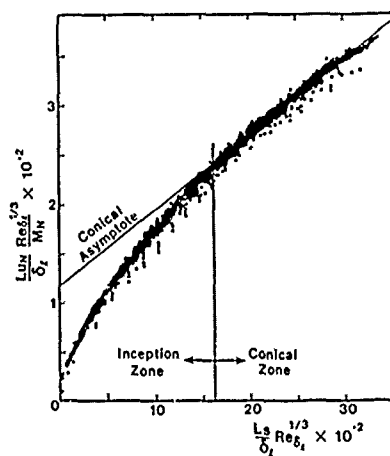
Fig 28 Scaling of the upstream disturbance length Lu_N, (Settles and Lu, 1985).
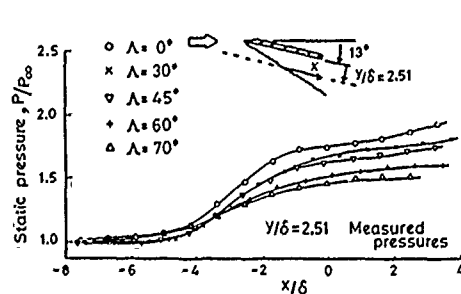
Fig 29 The effect of leading edge sweep on the wall pressure distribution (Fomison, 1986).
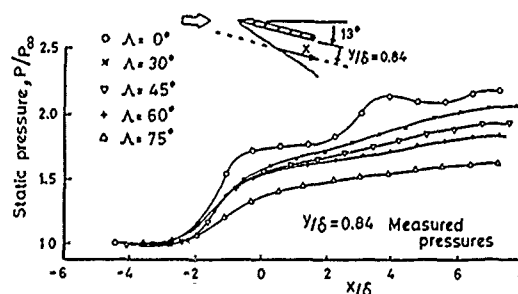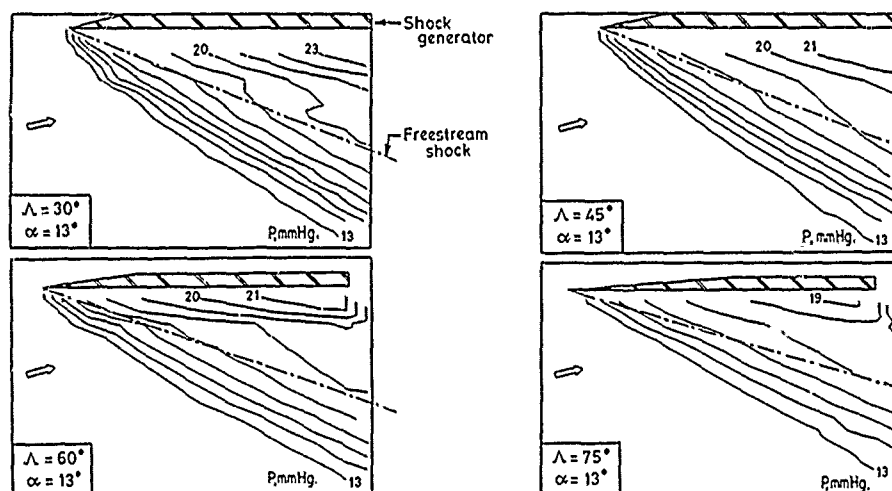
Fig 30 The effect of leading-edge sweep on the wall surface isobars (Fomison, 1986).
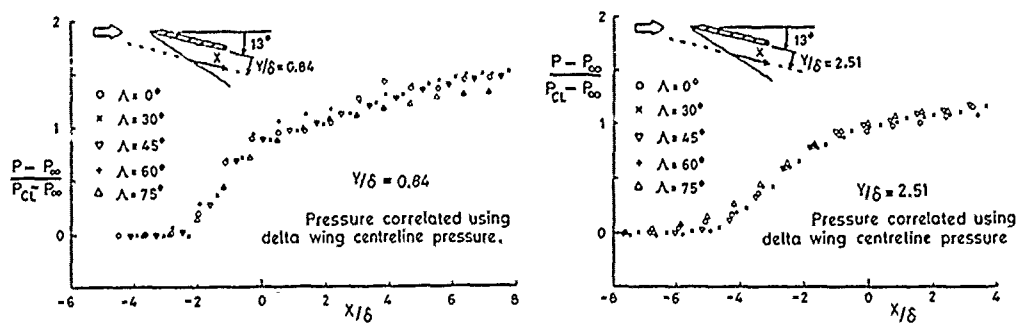
Fig 31 A correlation of the side wall pressures for various swept fin interactions (Fomison, 1986).
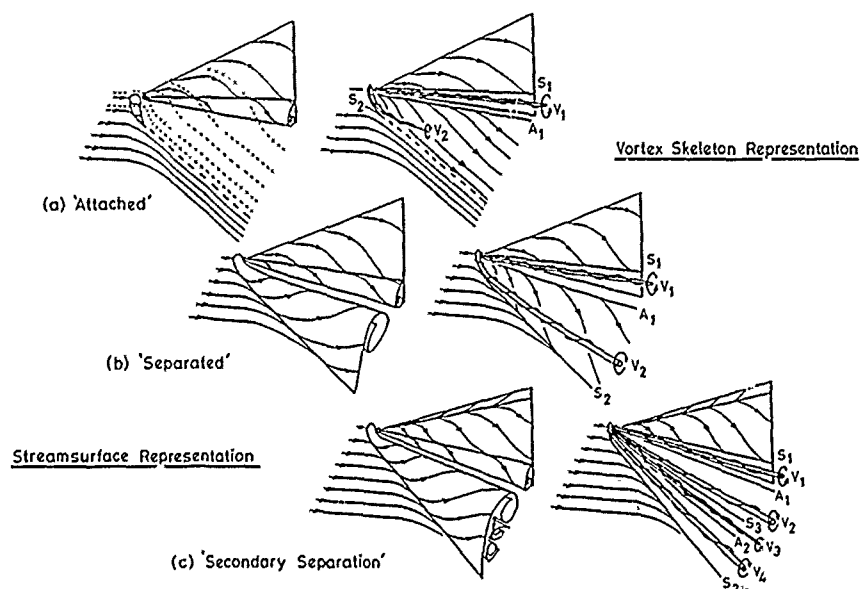
Fig 32 Suggested flow patterns for swept sharp fin/sidewall boundary layer interactions.
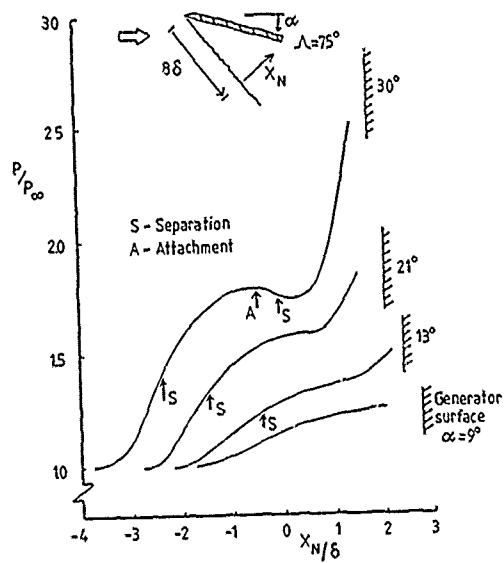
Fig 33 Pressure distribution in a transverse plane. Swept sharp fin, $\Lambda = 75°$.
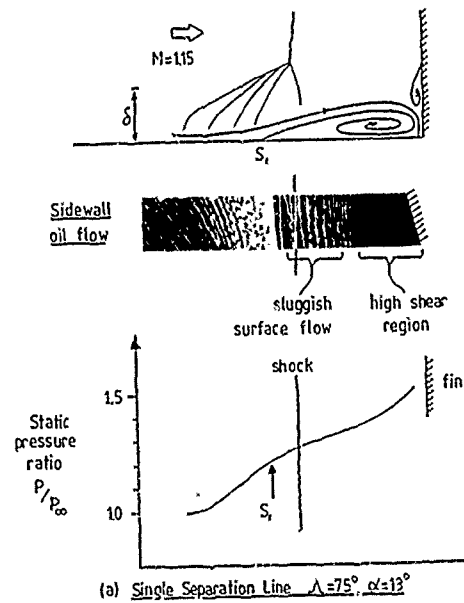
(a) Single Separation Line $\Lambda = 75°, \alpha = 13°$
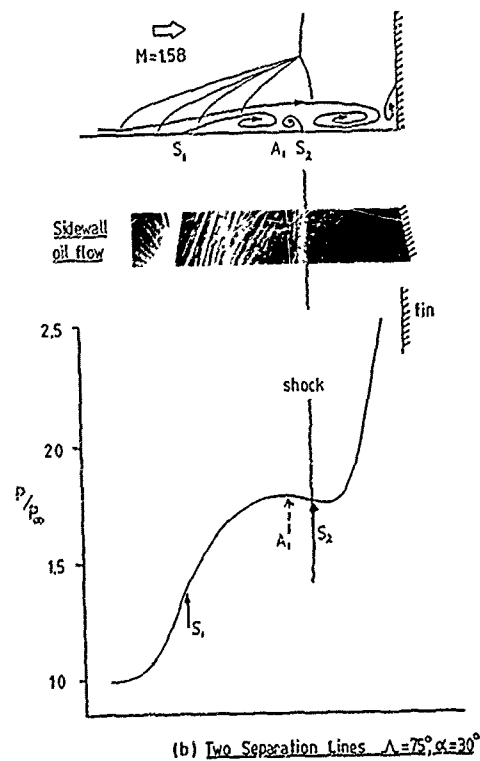
(b) Two Separation Lines $\Lambda = 75°, \alpha = 30°$

Fig 34 Suggested flow through the transverse plane. Swept sharp fin, $\Lambda = 75°$.
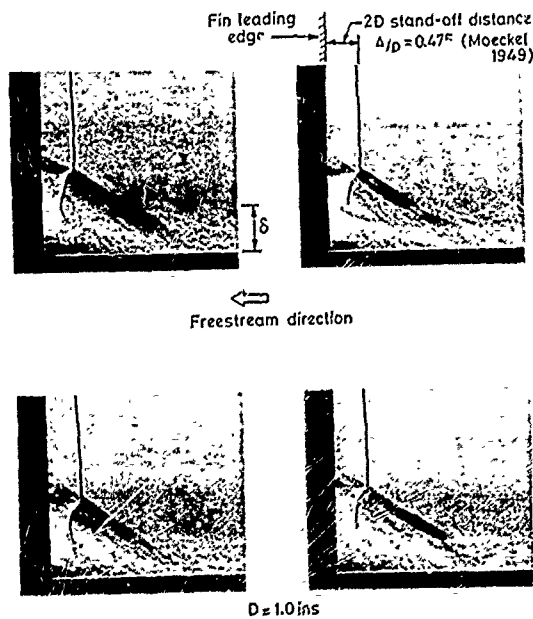
Fig 35 Four pictures of the same flow past a blunt fin, $D = 1.0" \approx 2.54$cm.
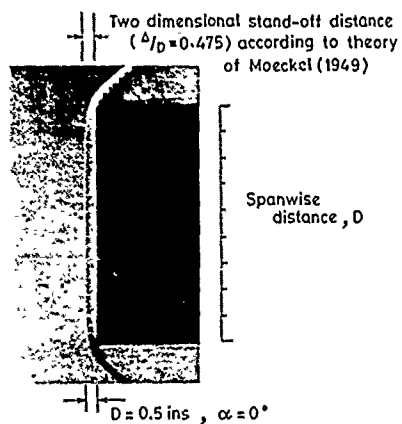
Fig 36 Bow shock ahead of a rectangular wing with a blunt (semi-cylindrical) leading edge.
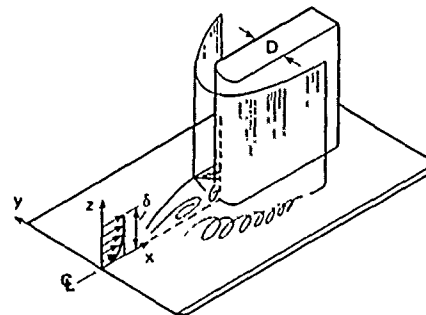
Fig 37 A very simple sketch of the interference at the root of a blunt fin.
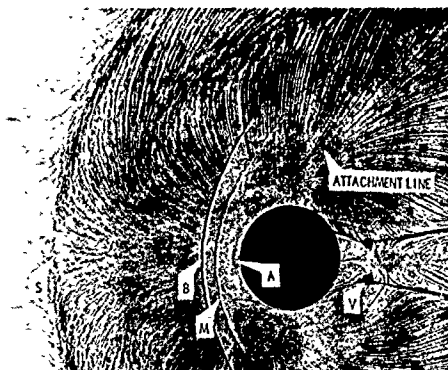
Fig 38 Combined surface flow and shadowgraph picture of the flow past a circular cylinder mounted on a flat plate. M = 2.5, Reg = 0.42 x 10^6, Where S = boundary layer thickness = 2.2cm. B = bow shock position (inviscid). S = separation line. A = attachment line. (Sedney and Kitchens 1977).
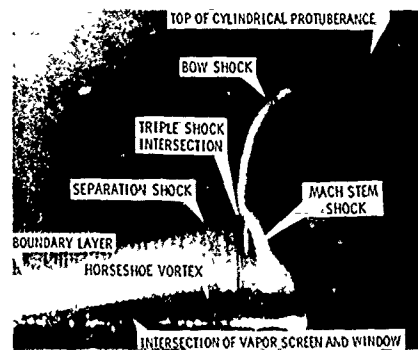
M = 2.5 , Re = 9.3 x 10^6 per metre

Fig 39 Vapour screen photograph. Light sheet in the symmetry plane and camera at 30° to sheet.
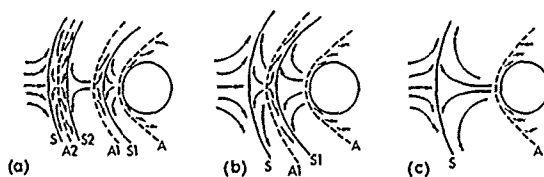
(a) Plan view of the surface flow patterns for 6, 4 and 2 vortices respectively.

(b) Oil flow picture for 6 vortices.
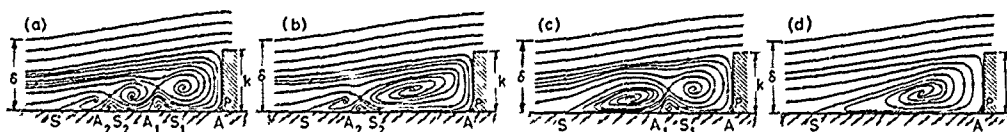
(c) Possible flow structure for 6, 4 and 2 vortices.

Fig 40 Flow ahead of a circular cylinder mounted on a flat wall. (Sedney and Kitchens, 1977)

D=025ins.   D=075ins.
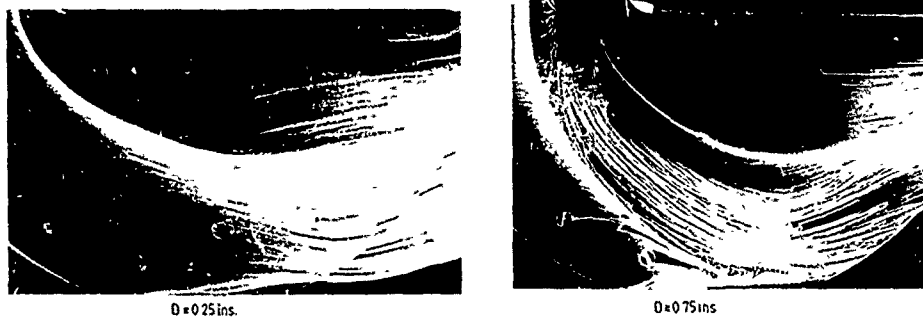
Fig 41 Oil flow pictures around the root of a blunt fin (Fomison, 1986).

Oil Flow Pattern Interpretation
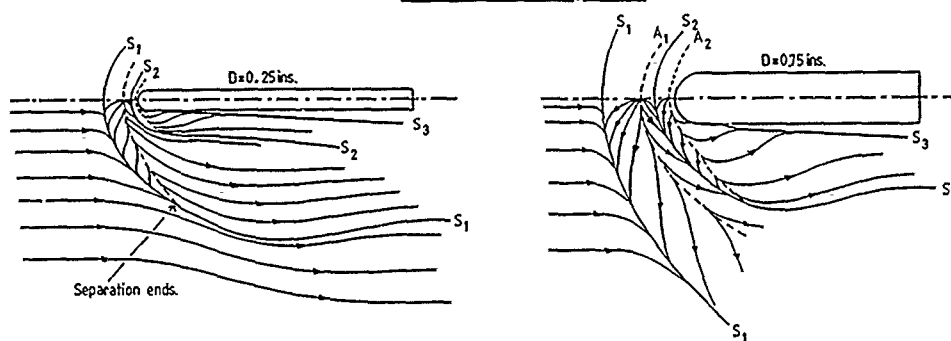
Fig 42 Interpretation of the pictures in Fig 41.

Surface
Streamlines

Vortex Skeleton
Representation

High pressure air
escaping from region
of nodal point of
attachment on A_2.

S - Separation line
A - Attachment line

Vortices V_1 and V_3
move off surface
and weaken.
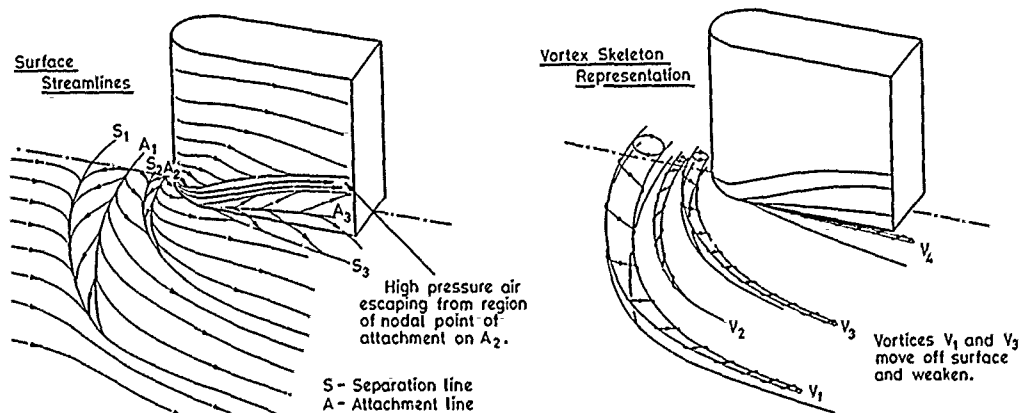
Fig 43 Sketches of the flow around a blunt fin, D/δ large, (Fomison, 1986).

Surface Streamlines.   Vortex Skeleton.

(a) $\alpha = 0°$

S - Separation line.   A - Attachment line.

(b) $\alpha > 0°$
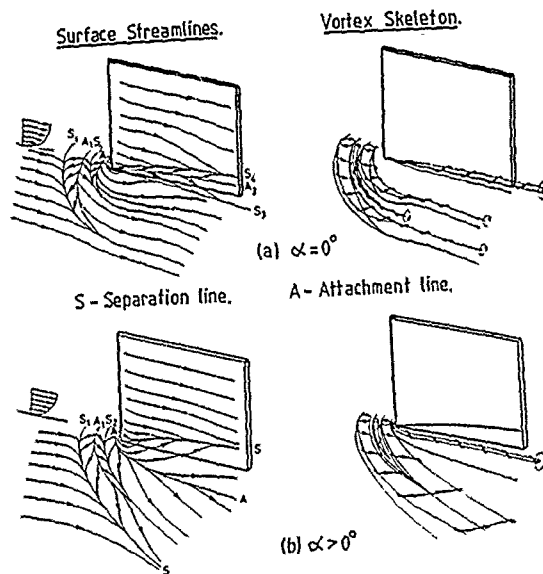
Fig 44 Sketches of the flow around a blunt fin, D/δ small, (Fomison, 1986).

$D = 10$ ins.
$\alpha = 0°$

Total pressure behind normal shock.
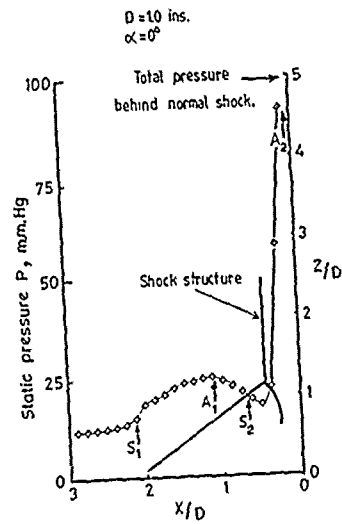
Shock structure

Fig 45 Pressure along the line of symmetry and shock structure, (Fomison, 1986).

D (CM)	δ(CM)		$M_\infty = 2.95$
□ 1.27	1.27		$R_f = 6.3 \times 10^7 H^{-1}$
△ 1.27	0.33		$Y/D = 2.0$
× 2.54	1.27		

δ(CM)	M_∞	D (CM)
□ 0.33	2.95	1.27
△ 1.27	2.95	1.27
+ 1.27	2.95	2.54
× 6.60	4.93	1.24
◇ 15.2	2.90	5.08
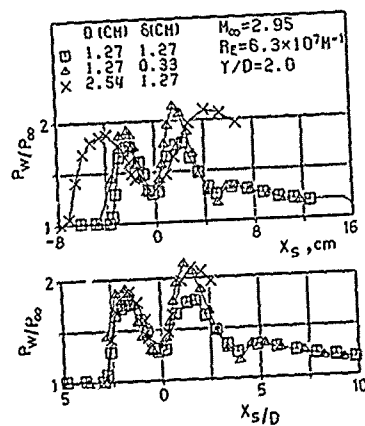
Fig 46 Pressure distributions as measured and correlated against X/D (Dolling and Bogdonoff, 1982).

$D = 5.08$ cm

M_∞	P_{stag}/P_∞
2.3 -------	7.3
2.98 ········	11.9
4.44 ——	25.8
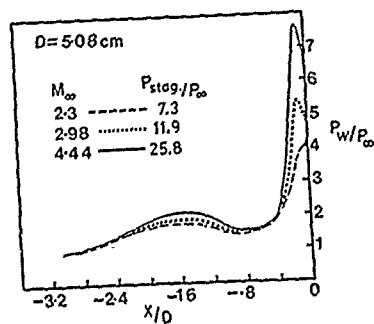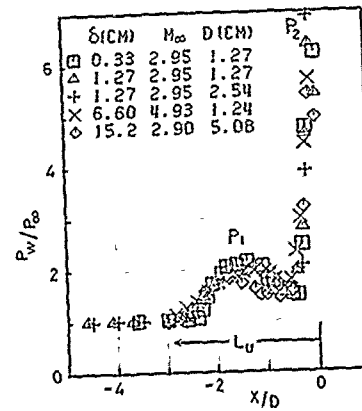
Fig 47 Variation of pressure distribution along the line of symmetry with Mach number.

$P_2 = 5.35$ ($P = 66$ mmHg)

D ins
◇ 10
□ 0.75
△ 0.5
▽ 0.25

$Y/D = 10$
$\alpha = 0°$
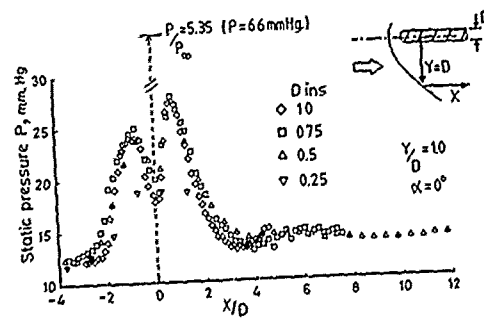
Fig 48 Pressure distributions correlated against X/D (Fomison, 1986).
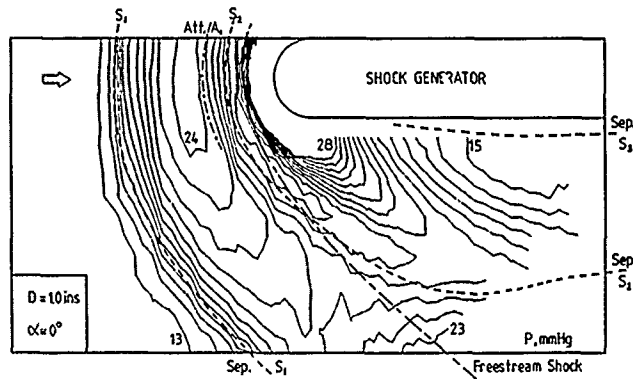
Fig 49 Isobars around a blunt fin (Fomison, 1986).
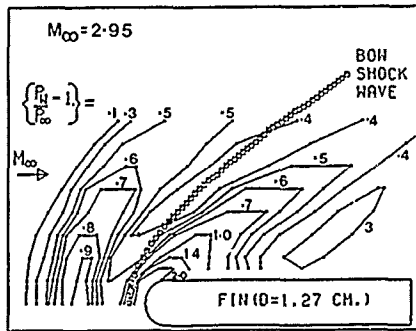
Fig 50 Isobars around a blunt fin (Settles and Dolling, 1986).
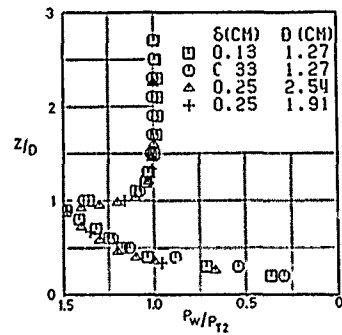
Fig 51 Pressure distribution along the leading edge of a blunt fin correlated against Z/D (Dolling and Bogdonoff, 1982).

Fin leading edge ──►
2D stand-off distance,
$\Delta/D = 0.475$, (Moeckel 1949)

⇐ Freestream direction

D = 0.375 ins
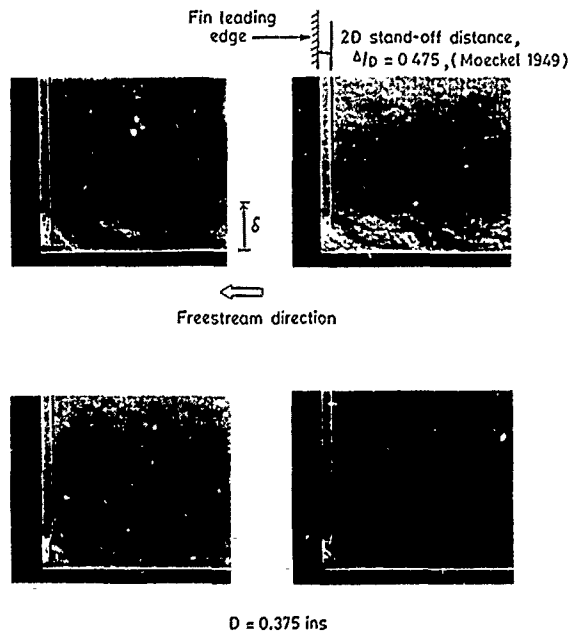
Fig 52 Bow shock interaction for D/δ small, compare with Fig 35 (Fomison 1986)
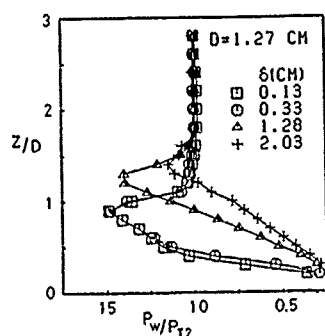
Fig 53 Effect of boundary layer thickness on fin leading edge pressure distribution (Dolling and Bogdonoff, 1982).
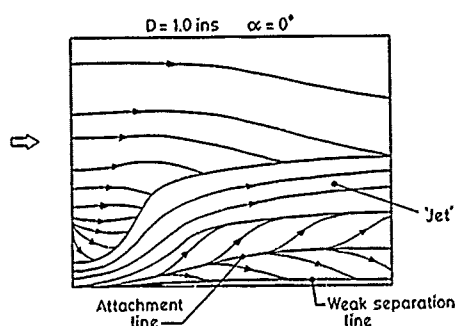
(a) from the oil flow picture by Fomison, 1956.
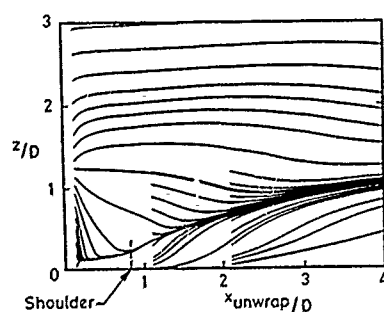
(b) from the calculations of Hung and Buning, 1985.

Fig 55 Limiting streamlines on the blunt fin,
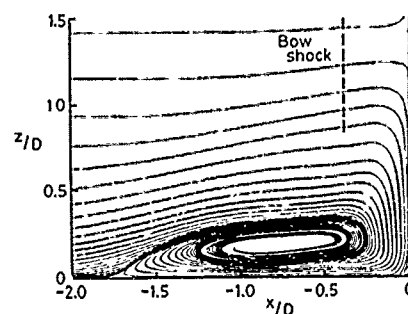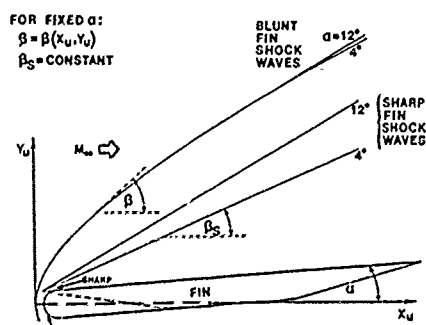
(a) Particle paths in the plane of symmetry
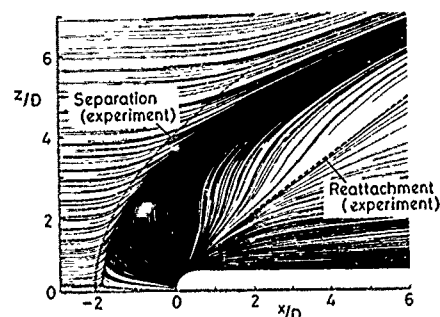
(b) Limiting streamlines on the flat plane.

Fig 54 Calculated flow around a blunt fin, (Hung and Buning, 1985).
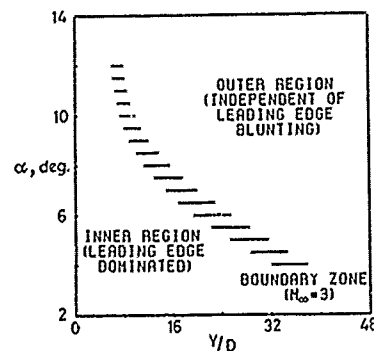
Fig 56 Flow regions around a blunt fin at incidence (Dolling, 1982).
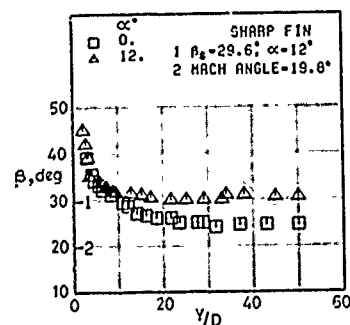
Fig 57 The shape of the shock wave generated by a fin.

D (CM)	Y (CM)	δ(CM)	Y/D
□ 0.41	3.50	0.25	8.60
⊙ 0.30	3.45	0.25	11.33
△ 0.20	3.41	0.25	16.79
+ 0.10	3.37	0.27	33.18
✕ SHARP	3.33	0.27	N/A

α = 10.0 DEG.
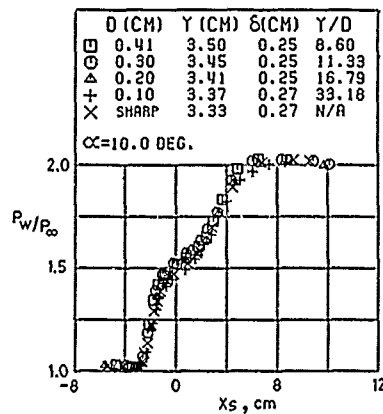
Fig 58 The wall pressure distribution measured at a fixed distance well away from the nose region, (Dolling, 1982).

Fig 59 Primary separation lines as measured by Fomison, 1986.

Fig 60 Scaling of the pressure distribution at Y/D = 10, α = 13°.
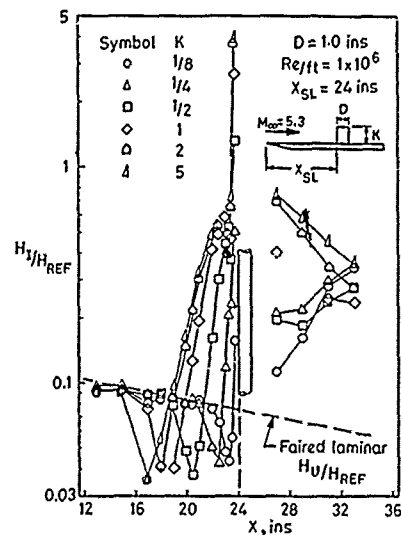
Fig 61 Heat transfer distribution along the line of symmetry for laminar flow. H Ref = stagnation point value. Hung and Clauss, (1980).

λ, deg	Model	h, cm
○ 0	8	25.40
□ 12.9	9	25.40
△ 30.0	7	25.40
◇ 45.0	10	25.40
▽ 60.0	11	25.40
◐ 75.0	12	15.24

$M_\infty = 4.44$

Fig 62 The effect of sweep on the pressure distribution along the line of symmetry of a blunt fin.

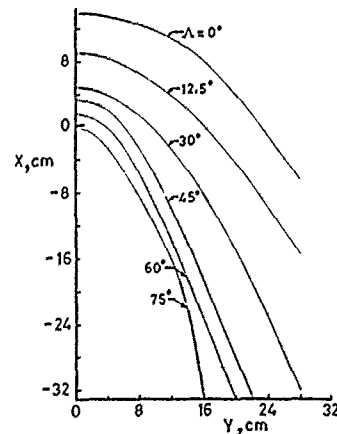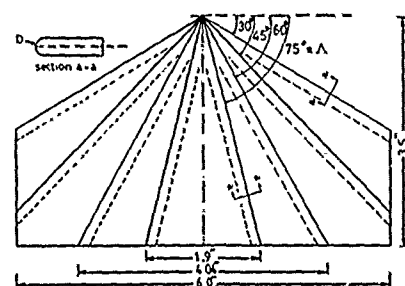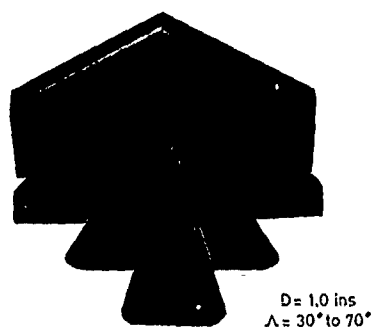**Fig 63** The effect of sweep on the primary separation lines around a blunt fin, D = 2" = 5.08cm. (Price and Stallings, 1967).

(a) Planform of delta models

D= 1.0 ins
Λ = 30° to 70°

(b) a typical set of delta models

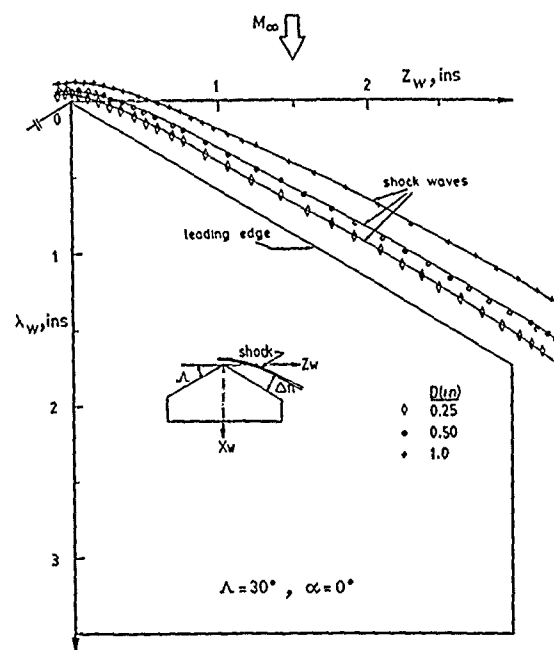Fig 64 The delta wing models tested by Hussain, 1985.

Fig 65 Bow shock stand-off distance ahead of a blunt delta wing, (Hussain, 1985).
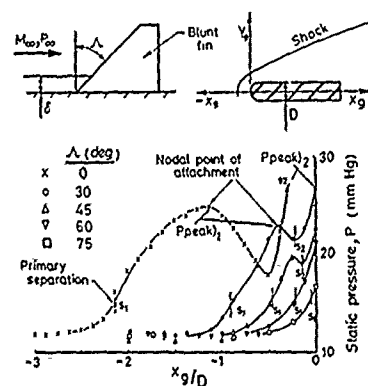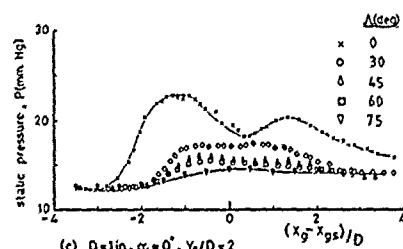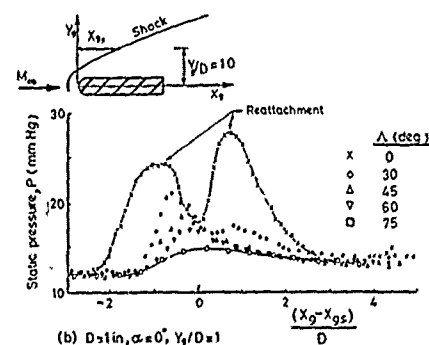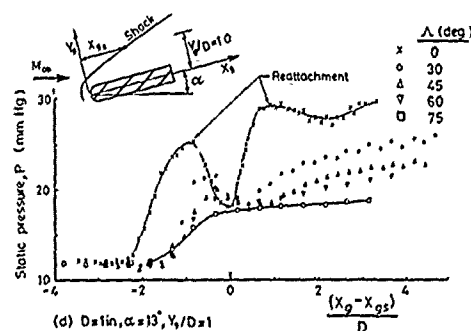

(a) Centre Line Pressure Distribution,
$D = 1$ in, $\alpha = 0°$, $Y_s/D = 0$

(b) $D = 1$ in, $\alpha = 0°$, $Y_s/D = 1$

(c) $D = 1$ in, $\alpha = 0°$, $Y_s/D = 2$

(d) $D = 1$ in, $\alpha = 13°$, $Y_s/D = 1$

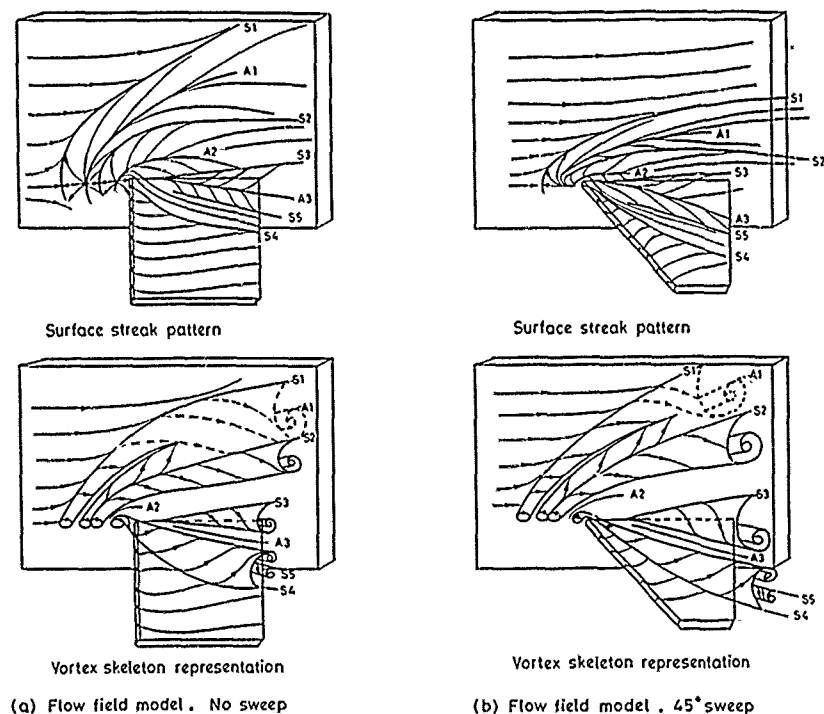Fig 66 The effects of sweep on the wall pressure distributions generated by a blunt fin (Hussain, 1985).

Surface streak pattern   Surface streak pattern

Vortex skeleton representation   Vortex skeleton representation

(a) Flow field model . No sweep   (b) Flow field model . 45° sweep

Fig 67 Suggested flow patterns around a blunt fin.

(a) Experiment, Λ=0°,   (d) Λ=45°, Calculation
    Dolling and Bogdonoff (1982)

(b) Λ=0°, Calculation   (e) Λ=60°, Calculation

(c) Λ=30, Calculation   (f) Λ=68°, Calculation
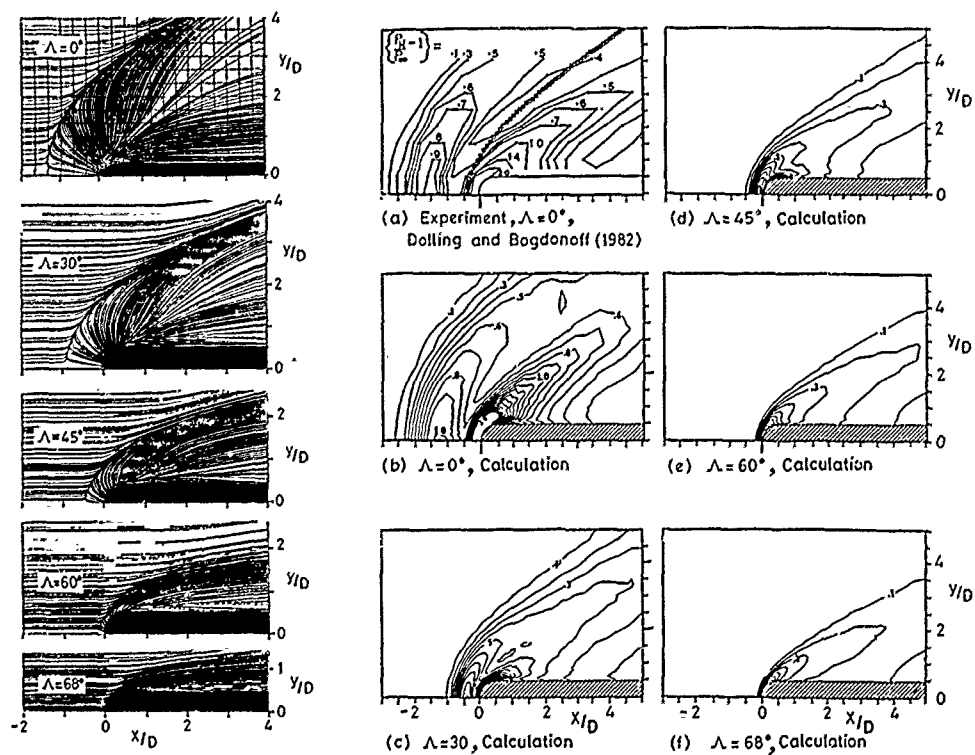
Fig 68 The mathematical simulation of flow around a blunt fin (McMaster and Shang,1988).

(a) Centre Line Pressure Distribution, $\Lambda = 30°$, $D = 1$in, $Y_s/D = 0$

(b) $\Lambda = 30°$, $D = 1.0$in, $Y_s/D = 0.5$

(c) $\Lambda = 30°$, $D = 1$in, $Y_s/D = 2$

(d) $\Lambda = 75°$, $D = 10$in, $Y_s/D = 0.5$

(e) $\Lambda = 75°$, $D = 10$in, $Y_s/D = 2.0$
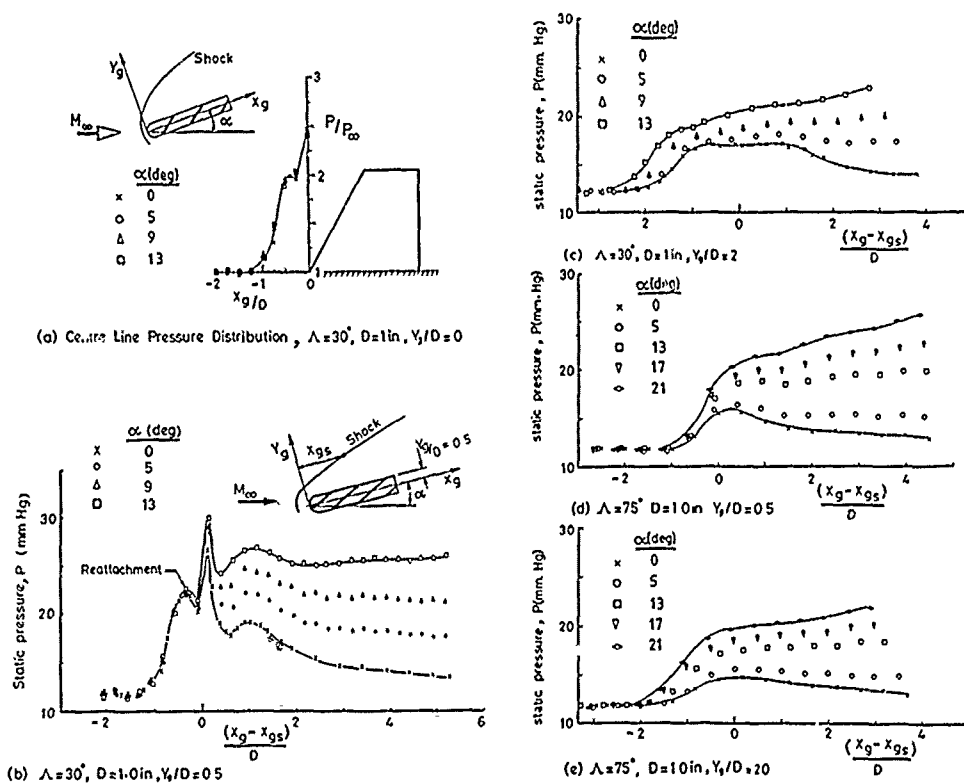
Fig 69 Pressure distributions generated by a blunt, swept fin at incidence (Hussain, 1985).

(a) An oil flow picture

Surface streak pattern

Vortex skeleton representation
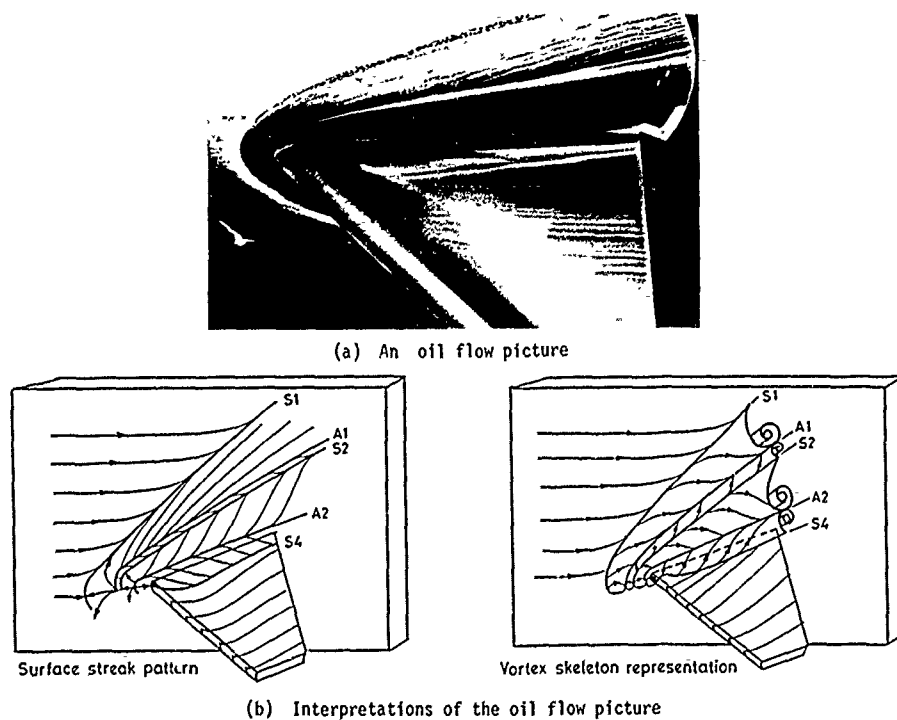
(b) Interpretations of the oil flow picture

Fig 70 Flow around a blunt swept fin at incidence $\Lambda = 45°$, (Hussain 1985).
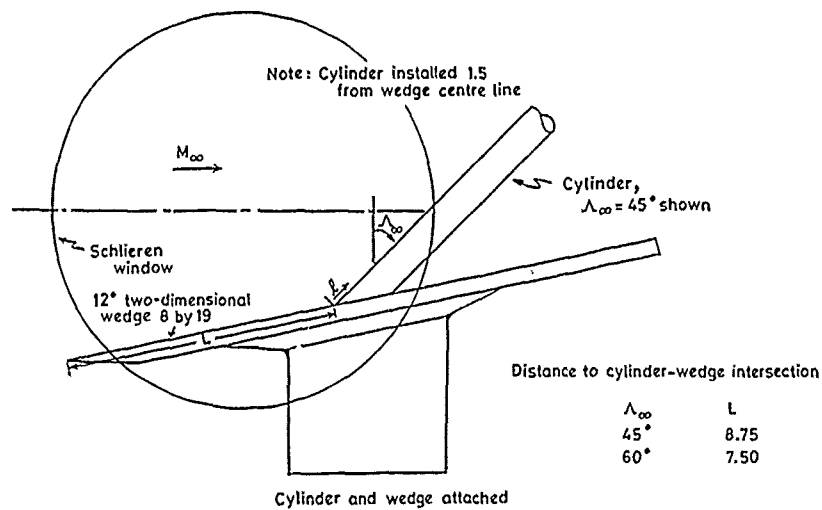
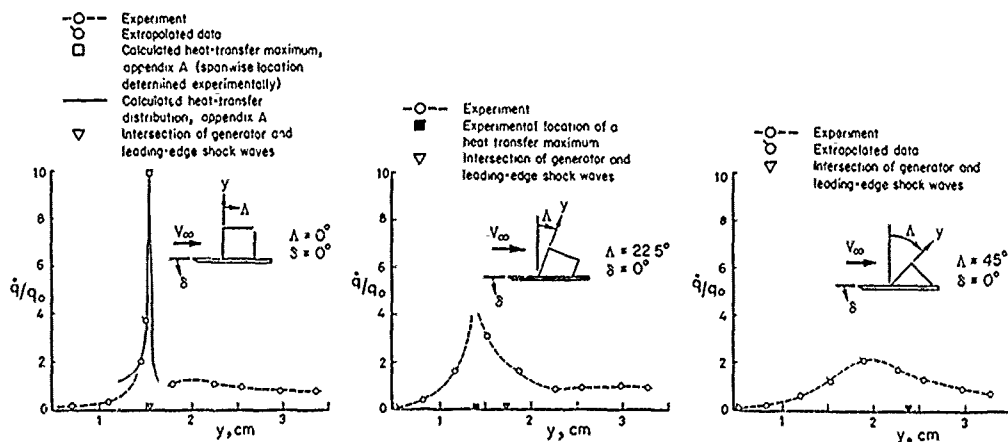Fig 71 The model tested by Bushnell (1965).

Fig 72 The effect of sweep on the heat transfer along the leading edge of a blunt fin (Hiers and Loubsky, 1967).
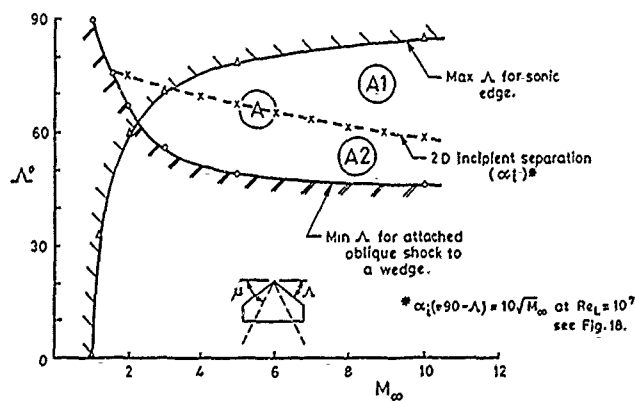

Fig 73 Suggested boundary for incipient separation at the nose/wall junction of a blunt swept fin.

UNSTEADINESS OF SUPERSONIC AND HYPERSONIC SHOCK INDUCED TURBULENT BOUNDARY LAYER SEPARATION

by
D.S. Dolling
Department of Aerospace Engineering and Engineering Mechanics
The University of Texas at Austin
Austin, Texas 78712, USA

SUMMARY

This review concerns the unsteadiness of supersonic and hypersonic shock-induced turbulent separated flows. Both two-dimensional (2-D) and three-dimensional (3-D) flows are discussed. For organizational reasons, more than physical ones, they are largely discussed in separate sections. The focus in both sections is mainly on the intermittent region, which is the streamwise zone in which the unsteady separation shock moves. The topics discussed include: (i) the qualitative description of the wall pressure signals and unsteady separation process (ii) quantitative aspects of the separation shock wave dynamics and the effects of model geometry and flow conditions and (iii) the mechanisms that have been proposed as being the cause of the unsteadiness. Also included, is a brief discussion of the dynamics of the separated flow and the outgoing boundary layer downstream of reattachment. Finally a few remarks are made regarding future work needed to answer some of the many remaining questions.

1. INTRODUCTION

This review deals with the unsteadiness of supersonic and hypersonic shock-induced turbulent separated flows. There has been sustained interest in such flows for more than 40 years now, largely because of their importance in such a wide variety of engineering applications. Buffeting in the transonic regime limits the maneuverablity of combat aircraft, and has much in common with other performance limiting phenomena such as dynamic inlet distortion and buzz: the latter may lead to compressor blade failure and large amplitude oscillatory structural loading, respectively. At higher speeds, interactions induced by deflected control surfaces, blunt and sharp fins at angle of attack, protuberances, forward and rearward facing steps, wall jets, and impinging shocks can be important. Such interactions can generate large scale, 3-D separated, vortical flows, and complex distributions of surface pressure and skin friction; at high Mach numbers, intense heat transfer rates may occur. To complicate the picture further, many of these flows are locally or globally unsteady.

There have been many experimental and computational studies of such phenomena. Only in a very small fraction of the experimental investigations have time-dependent measurements been made and, as far as is known, no time-dependent computations have been made. That many such flows are locally or globally unsteady is evident from high speed schlieren or shadow cinematography, or from examination of a series of individual microsecond exposure photographic frames taken at random intervals in time. In practice, since such photographs generally represent an integration of the light beam across the width of the tunnel, and the shock structure exhibits spanwise rippling, the data are usually qualitative. Figure 1 shows four frames taken at random intervals of flow upstream of a blunt fin at Mach 3. Changes in the separation shock position and structure are readily apparent.

Much of what is known quantitatively of flowfield unsteadiness comes from wall pressure fluctuation measurements. Some additional data comes from studies employing hot wire anemometry. In many studies the focus was on the unsteady separation shock and consequently these data and conclusions form the bulk of this review. Much less attention has been devoted to the dynamics of the separated flow, the reattachment process, or the dynamics of the outgoing boundary layer. A large fraction of the wall pressure fluctuation data has been taken in nominally 2-D flows generated by forward or rearward facing steps or unswept compression ramps. Far fewer experiments have been made in 3-D flows, and the data are more difficult to interpret since the boundary layer can be highly skewed.

In this review, only flows which are naturally unsteady are included. Forced unsteadiness, induced by oscillating boundaries or from time-varying upstream or downstream boundary conditions is excluded. The rich field of self sustaining coherent oscillations of impinging shear layers which was reviewed in the recent past by Rockwell (Ref. 1) is also excluded. Similarly excluded is the sub-class of unstable shock patterns associated with shock oscillations induced by spiked blunt bodies. Calarese and Hankey (Ref. 2) have recently reviewed this field. Further, since the emphasis is on supersonic and hypersonic flows, forced and self-excited oscillations in transonic diffuser flows are also largely excluded. From the late 1970's to the present wall pressure fluctuation data have contributed greatly to the progress made in the understanding of such phenomena and for details the reader is referred to References 3-7.

This paper is split into several parts. For organizational reasons, rather than physical ones, 2-D and 3-D flows are largely discussed in separate sections. However since they have a great deal in common they are

discussed together where appropriate. The focus is largely on the region bounded by X_o and 'S', where X_o is the interaction start (defined as where the mean pressure $\overline{P}_w$ first increases above the undisturbed level $\overline{P}_{wo}$) and 'S' is the separation location (as indicated by surface tracer techniques). Because of the nature of the wall pressure signal, this region is called intermittent. The topics covered in the discussion of the intermittent region include:

(a) the qualitative description of the unsteady shock-induced separation process.

(b) quantitative data and statistics of the separation shock wave

(c) the mechanisms that have been proposed as being the cause of the unsteadiness.

There is also some discussion of the dynamics of the separated flow and the outgoing boundary layer downstream of reattachment. The final part of the review consists of a few remarks regarding future work needed to answer some of the many remaining questions.

2. TWO-DIMENSIONAL FLOWS

2.1 Intermittent Region

2.1.1 Wall Pressure Signals and Intermittency

A typical pressure signal measured upstream of 'S' in a separated compression ramp flow at Mach 3 is shown in Figure 2. The moving separation shock generates an intermittent wall pressure signal, $P_w(t)$, whose level fluctuates between the range characteristic of the undisturbed turbulent boundary layer and that of the disturbed flow downstream of the shock. There is evidence to suggest that the instantaneous separation point and shock foot are essentially at the same location and that 'S' is the downstream boundary of a region of intermittent separation (Refs. 3, 8, 9). Some results from Ref. 9 are discussed in section 2.1.2. The fraction of the time that the flow at a point is downstream of the separation shock (given by the intermittency, γ) increases downstream of X_o until just upstream of 'S', $\gamma = 1.0$ (Fig. 2d). Kistler (Ref. 10) was probably the first to observe this behavior. The same phenomenon has since been seen in flows generated by unswept and swept compression ramps, hemicylindrically blunted fins, sharp fins at angle-of-attack, circular cylinders, and in shock-induced separation in transonic diffusers and on transonic airfoils.

2.1.2 Interpretation of Separation Lines from Surface Tracer Patterns

Surface tracer techniques are widely used in high speed flows to locate "separation lines" or "lines of coalescence". These methods are relatively easy to use and produce highly defined, repeatable "separation lines". In the case of the kerosene lampblack method, in which the pattern is lifted off the surface on large sheets of transparent tape, full scale undistorted records are obtained. An example, in a Mach 3 blunt fin interaction is shown in Fig. 3. Also shown are wall pressure signals measured upstream of 'S'. They show clearly that the separation shock wave moves well upstream of 'S' raising the question of the physical meaning of the latter.

This question has been addressed in Ref. 9 and the reader is referred to it for details. In brief, two pressure transducers with fixed separation were placed streamwise at different positions in the intermittent region upstream of a circular cylinder and wall pressure signals recorded. The Mach number was 5. Two typical data records, one for each of the channels, are shown in Fig. 4. Next, blocks of data corresponding to flow downstream of the instantaneous shock wave were extracted (one such block is indicated by the hatched band in Fig. 4) and cross-correlated. Cross-correlations at all of the stations in the intermittent region are shown in Fig. 5. They were essentially the same as those measured downstream of 'S' where the flow is always separated (Fig. 6). Maxima in the cross-correlation coefficient at both positive and negative time delay, corresponding to the separated shear layer eddies moving downstream and the backflow adjacent the wall respectively, occur at the same time no matter where the transducer pair is located in the intermittent region. These results confirm earlier hot film measurements (Ref 8) and show that separation occurs at, or just downstream of the instantaneous shock position. Hence the instantaneous separation point undergoes the same large-scale, low frequency motion as the separation shock wave. It appears that the separation line indicated by surface tracers is actually the downstream boundary of a region of intermittent separation. It should be emphasized that the results of Ref. 9 were obtained in one type of flowfield, namely that generated by a circular cylinder. The general applicability of the result remains to be demonstrated.

A plausible physical explanation for the latter result, based on the response of surface tracers to the time-varying wall shear stress is given in Ref. 8. It is summarized below. If the shock motion over a point is modelled as a step function as in Fig. 7a, then the instantaneous wall shear stress at that point will have two possible values. If the value corresponding to flow upstream of the shock wave (i.e., incoming boundary layer) is large

and positive, and the second value corresponding to back-flow is considerably smaller and negative then the wall shear stress time-history might look as sketched in Fig. 7b. If the ratio of their absolute values is large then even if there is backflow for a large fraction of the time (i.e., at high intermittency) the mean shear stress, as indicated by the hatched horizontal line, will still be positive. The surface tracer material, which has almost zero frequency response, will therefore move downstream. On this basis, the station at which the mean wall shear stress becomes zero will be at very high values of intermittency. It is there that the surface material will accumulate. It should be noted that this is a hypothesis; no wall shear stress measurements have been made. It does however explain the observed behavior of the surface tracer material and, on that basis, warrants further investigation.

2.1.3 RMS of Wall Pressure Fluctuations and Higher Order Moments

The unsteady shock causes a rapid increase in σ_P upstream of 'S'. A typical distribution of σ_P is shown in Figure 2c. For reference, the normalized distribution of mean pressure is also shown. Although the pressure fluctuations increase downstream of the shock wave (compare the signal at times t_1 and t_2 in Figure 2b), this contributes relatively little to the overall σ_P. The shape of the distribution upstream of 'S' appears to be common to all shock-induced turbulent separated flows. Similar distributions have been reported in studies in which the pressure signal was not shown or discussed explicitly and includes circular cylinders at transonic speeds, Refs. 11 and 12, impinging shock waves, Ref. 13, and axisymmetric flares and steps (Refs. 14, 15) over a wide range of flow conditions. Downstream of 'S' the shape appears to be a function of the type and scale of the separated flow. The maximum value of σ_P occurs upstream of 'S' and is a significant fraction of the local $\overline{P}_w$. Measured maximum values of σ_P in compression ramp flows, blunt fin flows and interactions induced by cylinders as reported by Dolling and Smith (Ref. 16) range from 0.15 to 0.3 $\cdot \overline{P}_w$.

A relatively simple analytical approximation expressing σ_P in terms of the contributions of the upstream and downstream pressure fields is given by Debieve and LaCharme (Ref. 17):

$$\frac{\sigma_P^2}{(\Delta P)_S^2} = (1 - \gamma)\frac{\sigma_{P_u}^2}{(\Delta P)_S^2} + \gamma\frac{\sigma_{P_d}^2}{(\Delta P)_S^2} + \gamma(1 - \gamma)$$

where $(\Delta P)_S$ is the mean pressure rise across the shock and subscripts u and d refer to the pressure fields upstream and downstream of the shock respectively. The only inherent assumption is that the upstream and downstream fields are statistically homogeneous. If σ_{P_u} and σ_{P_d} are small compared to $(\Delta P)_S$ which, based on experimental evidence, is a reasonable approximation, then the expression can be simplified to:

$$\frac{\sigma_P^2}{(\Delta P)_S^2} \simeq \gamma(1 - \gamma)$$

which has a maximum at $\gamma = 0.5$. As a check, $(\Delta P)_S$ was calculated from $(\sigma_P)_{max}$ for the 24°, Mach 3 compression ramp flow of Muck et al. (Ref. 18). The calculated shock pressure ratio was 1.6 compared to a value of about 1.7 "eyeballed" from the pressure signal. In practice, $(\sigma_P)_{max}$ appears to occur a little further downstream at $\gamma \approx 0.6 - 0.7$, but as a first approximation the above works well.

The third and fourth order moments about the mean (skewness and flatness respectively) which describe the shape of the probability density distribution of the fluctuation amplitude have the same streamwise behavior in different flows and can be correlated as a function of γ (Fig. 8). The skewness and flatness, both of which are sensitive to a few points in a data record being far from the mean, actually increase upstream of X_o, as do γ and σ_P. Dolling (Ref. 19) reports increases in skewness at $3.4D$ upstream of the leading edge of a blunt fin, in a flow in which X_o was at $2.8D$. High speed (35 kHz) schlieren photography by Degrez (Ref. 20) confirmed the presence of occasional shocks this far upstream.

2.1.4 Comments on Upstream Influence

Wall pressure signals show clearly the mechanism of upstream influence in shock-induced turbulent separated flows. The gradual increase in mean wall pressure near the upstream boundary of the interaction (i.e., downstream of X_o) is not the result of upstream propagation of disturbances in a nominally steady flow, but is a direct result of shock motion. Upstream influence varies continuously and the instantaneous value should be measured from the foot of the shock wave to whatever reference position (i.e., fin leading edge) is appropriate in that particular flow. The maximum and minimum values correspond to the furthest upstream and downstream locations of the shock wave (i.e., the variation in upstream influence is equal to L_S, the excursion of the shock wave).

Conventionally, upstream influence is measured from X_o to the downstream reference position and has a fixed value. The pressure signals show that X_o is simply the furthest upstream station at which an increment in $\overline{P}_w$ is detectable using conventional instrumentation. Actually, at X_o, γ is already about 0.03-0.05, $\sigma_P > \sigma_{P_o}$,

where subscript o refers to the undisturbed boundary layer and the skewness and flatness already have very large values. Hence if these parameters were used to define upstream influence, rather than $\overline{P}_w$, its magnitude would be considerably larger. In this sense, this length scale is somewhat arbitrary and using it for comparisons with predicted values is probably not a good test of a numerical method.

2.1.5 Shock Wave Structure

Muck et al. (Ref. 18) and Dussauge et al. (Ref. 21) made measurements using a rotatable wall plug in which 4 Kulite transducers were installed in a line with spacing, $\xi = 0.23\delta_o$. Simultaneously sampled signals upstream of 'S' in a Mach 3 separated compression ramp flow, with the transducers aligned streamwise are shown in figure 9. When the shock is upstream of a given transducer (i.e., the second one at time t_1), the pressure indicated by it and the downstream transducers is essentially the same, and about equal to the pressure level at 'S'. This observation suggests that the instantaneous shock structure in the intermittent zone can be described by a single leading shock wave. The traditional view, is that $\overline{P}_w$ increases through a continuous compression and may be incorrect. Drawing conclusions from visual inspection of wall pressure signals is somewhat speculative, and before any conclusions can be drawn about shock structure, quantitative data are needed. Ensemble-averaged values of shock strength as a function of position and the corresponding wall pressure values downstream would provide data on (i) shock strength as a function of position in the intermittent region and (ii) the strength of the compression system following the shock.

Pressure signals for the plug rotated 90°(Fig. 10) show that the shock front has spanwise ripples with wavelengths as small (if not smaller) than $0.23\ \delta_o$ and as large (if not larger) than $0.69\ \delta_o$. Dussauge et al (Ref. 21) also noted non-uniformities in the auto-correlations of the signals at different spanwise locations. The intermittency also displayed strong spanwise non-uniformities. All of these observations agree qualitatively with the surface flow visualization studies of Settles et al. (Ref. 22) which show the separation line has spanwise periodicity. Further evidence of non-uniformities are seen in space-time correlations obtained by Muck et al. (Ref. 23). Unlike the curves in the upstream boundary layer, which are symmetric with respect to the $\tau = 0$ axis (as expected in 2-D flow), assymmetries appear in the intermittent region. The authors speculate that this deviation of the flow from its mean longitudinal direction may be evidence of the cell structure of Taylor-Gortler vortices which are present in unstably curved flows. However, the observation that further downstream in the fully separated region, the spanwise space-time correlations were again symmetric about the $\tau = 0$ axis, suggested that the assymmetries seen in the intermittent region are more likely due to spanwise rippling of the shock wave. Since surface flow visualization shows evidence of streamwise vortices downstream of reattachment and since these probably originate in the upstream separated shear layer, or even in the incoming boundary layer, it is somewhat surprising that the correlations under the separated flow exhibit symmetry about the $\tau = 0$ axis. To resolve this question, additional work is required.

Spanwise wall pressure fluctuation measurements have also been made by Nordyke (Ref. 24) and Dolling and Nordyke (Ref. 25) in the intermittent region of a Mach 5, 28°, compression ramp interaction. One transducer (the reference one) was fixed in position at an intermittency of about 0.6 and the other moved spanwise relative to it. A span of about $4\delta_o$ was covered. Standard time series analysis techniques and a conditional sampling algorithm were used to analyze the data.

A new parameter, the co-intermittency, γ' was defined and is the fraction of the time that both channels are disturbed by the shock wave at the same time. The difference between γ' and γ'_{th}, the theoretical minimum co-intermittency as a function of spanwise separation, ϵ, is shown in Fig. 11. The theoretical co-intermittency is that value which would result from two statistically independent signals and is simply the product of the individual intermittencies. The hatched horizontal band represents results from statistically independent runs (SIR's). These latter cases were calculated to serve as a reference for comparison with the actual data. It can be seen that the $(\gamma' - \gamma'_{th})$ distribution decreases rapidly from its theoretical maximum of $(0.61 - 0.61^2)$ with increasing separation and then tails off at values just above the limit of the SIR's.

Fig. 12 shows the decay in the maximum cross-correlation coefficient, $(R_{pp})_{max}$, with spanwise spacing. The behavior is similar to that of $(\gamma' - \gamma'_{th})$. The coherence function for several spanwise spacings is shown in Fig. 13. The two upper curves show broad-band coherence, with the low frequencies of the shock motion highly coherent. As ϵ increases it can be seen that only the low frequency shock passages remain coherent. At $\epsilon = 1.97$ it can be seen that it is only the lowest frequency shock motions which cause $(R_{pp})_m$ and $(\gamma' - \gamma'_{th})$ to remain above the statistically independent limit. These data (and additional results in Refs 24 and 25 not cited here) are particularly difficult to interpret unambiguously but seem to support the view that "the shock moves as an almost planar unit on which is superposed a small scale rippling motion" (Ref. 24). Many questions remain concerning the scale of the rippling, the cause, etc. and is a fruitful area for future work.

2.1.6 Power Spectra in Intermittent Region

Power spectra at the location of $(\sigma_P)_{max}$ from Dolling and Brusniak (Ref. 26) and Dolling and Smith (Ref. 16) are shown in Figs. 14 and 15. The model geometries and flow conditions are given in the legend as is the frequency resolution, Δf, and the number of data records, NR, that the spectrum is based on. All of the results in Fig. 14 were obtained in the Princeton University Mach 3 blowdown tunnel either at Station 1 ($\delta_o \approx 1.6$cm) or at Station 2 ($\delta_o \approx 2.2$cm) in the tunnel floor boundary layer. The data in Fig. 15 were obtained in a Mach 5 blowdown tunnel at The University of Texas at Austin. The data in both figures are presented in the commonly employed form $f \cdot G(f)/\sigma_P^2$ vs. f, plotted in linear-log axes, where $G(f)$ is the one-sided, auto-spectral density function. The choice of plotting axes is an important consideration. Since $\sigma_P^2 = \int_o^\infty G(f)df$ then for visualizing the contribution of a given frequency range to σ_P^2, linear-linear axes, although awkward, are probably the least misleading. An alternative approach which has the advantage that the area under a given curve segment is linearly proportional to the contribution of that frequency range to σ_P^2 is to plot $f \cdot G(f)$ vs. f on linear-log axes. The frequency range of shock oscillation which is characterized by high amplitude fluctuations is then more evident than when plotted as $G(f)$ vs. f on log-log scales as is done for curve 1 in the inset at the top of the figure.

However, plotting $f \cdot G(f)$ vs. f does suffer from several drawbacks and care must be taken in the interpretation. Compared to the linear-linear form, the logarithmic representation may mask the low frequency component which is rejected to zero. Second, maxima in $f \cdot G(f)$ occur at each point where $G(f)$ vs. f in linear-linear form has a slope of -1. This point has no particular physical meaning and is not always in the dominant frequency range. Third, peaks evident in the original linear-linear plot can be aliased to lower frequencies leading to misleading interpretations. Normalizing by σ_P^2, to force the area under the curve to unity, can also be misleading, unless the true spectrum and the true σ_P^2 have been measured. If there exists a frequency cut-off, then as the area is forced to unity the low frequency range of the spectrum will be incorrect, even if the original dimensional spectrum was correct. In the incoming boundary layer and separated flow zones, frequency cut-off is a pervasive problem, and normalizing by σ_P^2 is not recommended. On the other hand at $(\sigma_P)_{max}$, where a large fraction of the energy is at low frequency, and is almost certainly captured by the transducer, little error will be incurred.

In all cases plotted it can be seen that the shock frequencies are broadband and at relatively low values. Typically the bandwidth is a few kHz supporting the statement made earlier that the shock motion is a low frequency phenomenon. For a given model type, certain trends with changes in geometry or incoming boundary layer can be seen. In the Mach 5 cylinder study, the center frequency decreases as the cylinder diameter increases in a fixed boundary layer, and for a fixed diameter cylinder the center frequency increases as the boundary layer becomes thinner. A similar trend is seen with the Mach 3 blunt fin flows. With compression ramps the center frequency decreases as the ramp angle and streamwise extent of separation increase. Conversely, in sharp fin flows there appears to be little change as the angle of attack is increased from 12° to 20°. There is currently no explanation of why these trends occur, nor why in a given boundary layer the spectrum and shock frequency are functions of model geometry.

Power spectra in the intermittent region of other 2-D flows, in transonic normal shock interaction in diffusers, and shock-induced separation on transonic airfoils, and in 3-D flows generated by sharp and blunt fins, all have similar characteristics. Even at very high freestream velocities and with thin boundary layers, which generates extremely small time-scales, δ/U_e, power spectra indicate low shock frequencies; spectral center frequencies are typically 2 kHz or less.

Although the range of shock frequencies can be deduced from power spectra, several authors have tried to isolate the shock motion component of the pressure signal, and determine the dynamics of the shock separately. A brief description of the techniques employed and some results follow in the next section.

2.1.7 Separation Shock Wave Zero-Crossing Frequency Estimates

To isolate the shock component of the pressure signal, several authors have employed conditional sampling algorithms [Dolling and Murphy (Ref. 27), Andreopoulos and Muck (Ref. 28), Narlo (Ref. 29), Dolling and Smith (Ref. 16)]. Their common feature is the conversion of the pressure signal (Fig. 16a) into a "box-car" of amplitude unity and varying frequency (Fig. 16b). The time T_i between consecutive passages of the shock over the transducer can be determined and statistics performed to obtain the probability distribution of T_i and the mean value $T_m (\equiv \frac{1}{N}\sum_{i=1}^{N} T_i)$, where N is the number of periods. It should be noted that $1/T_m$ is the shock zero crossing frequency, f_c, not the mean shock frequency. f_c is the number of crossings per second of the transducer by the shock wave, whereas the mean shock frequency is $\frac{1}{N}\sum_{i=1}^{N} f_i$, where $f_i = 1/T_i$. Since the pressure signal is of a turbulent flow, precautions must be taken to ensure that high-frequency turbulent fluctuations are not inadvertently counted as shock waves. This problem, and others, are discussed briefly below.

In earlier work (Ref. 27) a single threshold T was used, as indicated in Fig 16a. T was set equal to $\overline{P}_o + 3\sigma_{P_o}$ where subscript o refers to properties of the undisturbed boundary layer. Thus, when P_w increased above T, this indicated the start of the shock passage upstream over the transducer. When P_t fell below T this indicated the end of the shock passage. However, because drift and zero shifts cause small dc offsets from test to test the results can be inconsistent. Andreopoulos and Muck (Ref. 28) improved on this by "eyeballing" each signal and choosing T just above the largest fluctuations of the boundary layer fraction of this signal. This technique was used in the 24°compression ramp flow at Mach 3. T_m was found to be approximately $7.7\delta_c/U_\infty$. Further, T_m was independent of position in the intermittent region and ramp angle (i.e., independent of downstream flow conditions). f_c was equal to $0.13U_\infty/\delta_o$, which the authors claim is the same order as the estimated bursting frequency of the turbulent boundary layer. This result, and its implications, is discussed further in Section 2.1.10.

Although "eyeballing" the threshold avoids the problems noted above, it is subjective and difficult to apply consistently. However, a more serious problem is that many "false shocks" are counted. Fig. 16 illustrates the problem. Fig. 16b shows the "ideal" box-car, as judged by eye, for the pressure signal in Fig. 16a. Fig. 16c shows the box-car from the algorithm, in which turbulent fluctuations such as A and B (Fig. 16a) are inadvertently counted as shock waves. Because these "shocks" are actually turbulent fluctuations they occur at high frequency and their inclusion in the box-car drives f_c higher. No matter what level T is set at, fluctuations such as A and B or the series around C (Fig. 16a) will always create false shocks. That this problem is significant can be seen by locating the value of f_c ($0.13U_\infty/\delta_o \approx 3.1$kHz) on the corresponding power spectrum in Fig. 14. f_c is indicated by the arrow labelled "STM", and is around the upper boundary of the shock frequency range. This problem with the algorithm is also evident in the probability distributions for the shock wave period. With increased data sampling rate, f_s, T_m decreased significantly, from about 1.8 ms to 1.2 ms to 0.4 ms as f_S increased from 10 kHz to 20 kHz to 100 kHz. This is indicative of the capturing of progressively more and more high frequency turbulent fluctuations, which the algorithm cannot distinguish from shock waves.

To avoid this problem an algorithm using two thresholds was developed by Dolling and Narlo (Ref. 30). In this case, the upper threshold $T_2 = \overline{P}_o + 4.5\sigma_{P_o}$ and the lower one $T_1 = \overline{P}_o$. To calculate $\overline{P}_o$, a "window" of width ΔP is stepped through the pressure signal in small increments, starting at the minimum in the signal. At each step, the number of data points in the window is counted. Since the transducers used in these experiments showed that the pressure fluctuations in the undisturbed boundary layer are distributed normally the position at which the greatest number of data points occurs brackets $\overline{P}_o$. The standard deviation, σ_{P_o}, of the boundary layer portion of the signal is then calculated. $\overline{P}_o + 4.5\sigma_{P_o}$ was chosen for T_2, since the probability of finding points greater than $4.5\sigma_{P_o}$ above $\overline{P}_o$ is very low (i.e., 0.0000068). Hence, pressures above T_2 are characteristic of the flow downstream of the shock, and pressures below T_2 are characteristic of the undisturbed boundary layer. This approach sets T_2 consistently just above the largest fluctuations of the boundary layer, and automatically takes care of d.c. offsets or drift. The process requires no subjective input from the user.

Initially, if $P_w < T_2$, a flag is set "off". The algorithm then checks successive data points. If the first point is less than T_2 and the second point is greater than T_2 and the flag is "off", this marks the start of the passage of a shock. The counter that records the time between successive shock waves is then initialized and the flag is then set "on". Further crossings of T_2 are not counted until P_w is less than T_1. Termination of the shock occurs when this happens, and the flag is reset. As shown in Fig. 16d this process largely eliminates the counting of turbulent fluctuations as shock waves.

Distributions of f_c using this approach are shown in Fig. 17 for cylinder flows at Mach 5. f_c is a maximum at $\gamma \approx 0.5$ in all cases; about 1.6 kHz for $D = 1.27$cm and about 1.2 kHz for $D = 1.91$cm in the 0.54 cm thick boundary layer. These values are indicated by arrows labelled TTM on their corresponding power spectra in Fig. 15 and fall close to the center frequency of the spectrum. Narlo (Ref. 29) also calculated f_c using the single threshold method. These values are indicated by arrows labelled STM in Fig 15 and, consistent with the ramp results mentioned earlier, are significantly higher than the center frequency. The two-threshold algorithm was also used by Dolling and Narlo in Mach 3 blunt fin flows. With only a few measurement stations in the intermittent zone neither the distribution of f_c or $(f_c)_{max}$ could be defined very accurately. For $D = 1.27$cm and 2.54 cm $(f_c)_{max}$ was estimated to be about 1 kHz and 0.7 kHz, respectively. Again, these values fell close to the power spectra center frequencies (curves 6 and 7, Fig. 14).

However this algorithm introduces a new problem. If two shock passages are closely spaced P_w may not fall below $\overline{P}_o$ before increasing again, and the flag is not reset. Two shock passages are then counted as only one. To examine this, and also assess the sensitivity of f_c to the threshold settings, T_1 and T_2 were systematically varied. First, with $T_1 = \overline{P}_o$, T_2 was varied through a series of values give by $\overline{P}_o + n\sigma_{P_o}$, $3 \leq n \leq 9$. Next, T_1 was increased to $\overline{P}_o + 3\sigma_{P_o}$ and T_2 varied as before. With this higher value of T_1, P_w only has to fall back within the range of the turbulent boundary layer in order to reset the shock counter, whereas with $T_1 = \overline{P}_o$ the pressure must decrease to below the mean value. Some typical results at $\gamma \approx 0.2$ and 0.5 are shown in Fig. 18. At low γ, when relatively long periods of undisturbed boundary layer flow occur between successive shock passages, the choice of T_1 is less critical than at higher γ. Also, at higher values of γ, when $T_1 = \overline{P}_o + 3\sigma_{P_o}$, T_2 must be set significantly higher in order to avoid turbulent fluctuations being counted as shock waves (i.e., if T_1 and T_2 are too close the method becomes similar to a single threshold method and has similar problems). If T_2 is set $3\sigma_{P_o}$

above T_1 or higher, f_c is then relatively insensitive to further increases in T_2.

It is evident that although f_c cannot be pinpointed precisely, it can be bracketed within a narrow range. The lower boundary of the range corresponds to $T_1 = \overline{P}_o$, $T_2 = \overline{P}_o + 4.5\sigma_{P_o}$ since this requires that P_w fall below $\overline{P}_o$ between shock waves. The upper boundary is set by $T_1 = \overline{P}_o + 3\sigma_{P_o}$, $T_2 = \overline{P}_o + 6\sigma_{P_o}$. With these as bounds, f_c is in the range 0.55-0.65 kHz for $\gamma \approx .2$. At the higher γ, the variation is larger, 1.2-1.5 kHz.

In summary, results from single threshold methods give unrealistically high estimates of f_c. The two-threshold results are more representative and show that with physically sensible choice of T_1 and T_2, f_c can be bracketed within a fairly narrow range. Quantitatively, the values of $(f_c)_{max}$ from the two-threshold algorithm correlate reasonably well with the spectrum center frequency suggesting either technique could be used to estimate the maximum zero crossing frequency. However, statistical information concerning T_i and f_i can only be provided by conditional sampling algorithms.

2.1.8 Separation Shock Wave Period, Frequency and Persistence Distributions

From the box-car signals, probability density distributions or histograms of the shock wave period, T_i, frequency f_c, and persistence, P_i can be calculated. The persistence is defined as the time the signal stays 'hi' (i.e., the time-span that a given box-car has the value unity). Such distributions have been calculated by Nordyke (Ref. 24) in a 28°, Mach 5 compression ramp flow. Typical distributions of T_i, f_i and P_i based on about 1200 shock passages are shown in Figures 19, 20, and 21 respectively. All three were obtained from a transducer located at $\gamma \approx .63$.

All three distributions are highly skewed. The most probable shock period of about $300\mu s$ is approximately one quarter of the value of the mean period, $T_m(= 1050\mu s)$. The most probable persistence is about $50\mu s$ with a mean value, P_m of $650\mu s$ (Note that $P_m/T_m = .62$, nearly equal to the calculated γ at that station, which provides a check on the algorithm). The shock frequency distribution is truncated below 167 Hz because the algorithm did not store shock periods greater than $6000\mu s$. This frequency distribution shows that the most probable frequencies are below about 1 kHz, which agrees well with the power spectrum at the same location which is shown in Fig. 22.

2.1.9 Space-Time Correlations/Shock Speeds in Intermittent Region

Longitudinal space-time correlations $R_{pp}(\xi, \tau)$ calculated by Muck et al. (Ref. 18) in a Mach 3, 24°compression ramp flow are shown in Fig. 23. The spacing, ξ between transducers varied from 0.23-0.69δ_o although only curves for the smaller value are shown here. The case $X/\delta_o = -2.18$, has the upstream transducer at $(\sigma_P)_{max}$ and shows the features of such correlations and the difficulties of interpretation. One source of difficulty is that two different physical phenomena occur together. There is shock motion in the upstream and downstream directions superposed on convective transport of turbulent eddies largely in the downstream direction only. This leads to difficulties in interpreting the values of τ at which maxima in R_{pp} occur.

The correlation at $X/\delta_o = -2.18$ has two maxima; one at $\tau \approx -60\mu s$ and one at $\tau \approx +10\mu s$. The latter corresponds to turbulent eddy convection downstream. This is evident from correlations in the incoming boundary layer since the maximum in R_{pp} is at the same positive τ. It was suggested that the maximum at negative τ is "probably due to the shock motion". This has been confirmed by Baade and Dolling (Ref. 31). In this case, correlations were performed on the original signals, the box-cars obtained from the two-threshold algorithm, and a set of model signals. The model signals were either "nested" square waves (as would be generated by the box-car algorithm) with variable rise and fall times, T_r, and T_f (Fig. 24a) or "sequential" square waves with the delay time, T_d fixed for a given pair of waves but varying through the signal (Fig. 24b). These two signals have different cross-correlations with different physical interpretations. For the nested waves, maxima in R_{pp} occur at values of τ close to minima in T_r and T_f (Fig. 24c) and not at an average (or broadband) value of T_d as occurs for the sequential signals (Fig. 24d). Thus, although correlations of the box-car signals from the TTM reveal a maximum in R_{pp} at positive τ which corresponds to downstream motion of the shock wave, in addition to a maximum at negative τ corresponding to upstream motion, the shock speeds calculated from these values of τ and ξ are essentially maximum values, not broadband values.

In the Mach 5 cylinder interactions studied by Baade and Dolling the maximum upstream and downstream shock speeds deduced from cross-correlations of the box-cars were about 100 m/s. In the Mach 5 facility, 100 m/s is about 0.14 U_∞. At Mach 3, in Ref. 18, only cross-correlations of the original signals were made. Since the shock-induced fluctuations are also "nested" then the maximum in R_{pp} at negative τ is also heavily weighted towards the minimum T_r (maximum upstream velocity) rather than the broadband value. Further, it was noted by Dolling and Baade that correlations on the entire signal result in a somewhat higher τ (and smaller maximum velocity) than on the corresponding box-cars. Bearing this in mind, for a spacing of $0.23\delta_o(\approx 5.5mm)$ the maximum in R_{pp} at a τ of $-60\mu s$ corresponds to 92ms($\approx .16U_\infty$).

In a more direct attempt to calculate shock speeds, Fig. 24e, Andreopoulos and Muck (Ref. 28) identified individual pairs of nested box-cars from the 24°compression ramp flow and performed statistics on T_r and T_f.

The objective was to calculate the probability distribution for the shock speed but the small number of samples (only 64) precluded an accurate result (Fig. 25). The calculated speeds ranged from 0.05 - 0.8 U_∞ with a mean of about 0.15 U_∞. Upstream and downstream shock speeds were about the same order.

Shock speeds in both upstream and downstream directions calculated in the same way by Nordyke (Ref. 24) in a 28° Mach 5 compression ramp flow (at $\gamma \approx 0.63$) are shown in Fig. 25. The most probable speeds are a small fraction of U_∞ (=2400ft/s) and there is no evidence of any major differences between upstream and downstream values. The table below gives the mean speeds for the transducer pair at 3 different stations in the intermittent region.

Intermittency Channel 1/Channel 2	Upstream ft/s	Downstream ft/s
.44/.70	56	60
.21/.36	90	88
.14/.24	121	123

The upstream and downstream values are essentially the same with some evidence of a decrease with increasing intermittency. More detailed data at more streamwise stations and at different flow conditions are needed in order to draw conclusions about this result and the the validity of U_∞ as a normalizer.

2.1.10 Mechanism Driving Separation Shock Motion

In their Mach-3 compression ramp study Andreopoulos and Muck (Ref. 28) reported that the mean shock period, T_m, was independent of position in the intermittent region and independent of the ramp angle. The value of T_m corresponded to a value of $f_c(\equiv 1/T_m)$ of $0.13 U_\infty/\delta_o$. The authors claimed that this was the same order as the estimated bursting frequency in the incoming boundary layer. From this finding, they concluded that "the incoming boundary layer is largely responsible for the shock-wave motion". They also argued that the measured shock speeds were the same order as velocity fluctuations in the flowfield and that this "represents further evidence that the turbulence of the incoming boundary layer is largely responsible for the shock motion".

To this author, in the absence of measurements providing a direct correlation this seems to be a questionable conclusion at this stage. If the shock frequency is controlled by turbulent bursts and/or convected by velocity fluctuations then it might be anticipated that in a particular incoming boundary layer the shock zero crossing frequency, f_c, and streamwise length scale of its motion would be fixed. This is not the case. The spectral data, when plotted as $f \cdot G(f)/\sigma_p^2$ (curves 1, 2 and 3 of Fig. 14) show that the band of shock frequencies increases as the ramp angle decreases (in a fixed boundary layer). Also as noted earlier, for a circular cylinder of diameter D, the shock frequency f_c decreases as D increases, and the shock motion length scale increases as D increases, all in a fixed incoming boundary layer. Further, as shown in Ref. 12, the one-threshold algorithm used in Ref. 28 probably leads to overestimates in f_c due to its inability to discriminate between shock-induced pressure fluctuations and turbulent fluctuations. It is probable that a two-threshold approach would yield values of f_c of about half of those quoted in Ref. 28.

Andreopoulos and Muck's conclusions are also not supported by the results of Tran (Ref. 32) obtained using the VITA (Variable Interval Time Averaging) technique. Tran's work was done in the same Mach 3 blowdown facility in the same boundary layer but with a 20° compression ramp rather than a 24° model. One transducer was placed on the upstream influence line and the other further upstream in the incoming boundary layer. The upstream channel was used as a trigger and sampling was carried out on the downstream one. The threshold setting (which determines if an 'event' has occurred) was fixed and integration times varied from 16μs to 64μs. The latter had little effect on the magnitude of the downstream signals. Tran found little correlation between events detected on the upstream channel and the shock-induced pressure pulses on the downstream channel. Close observation showed that "in many instances, the details of the pressure fluctuations of the upstream signal were preserved at the downstream station at a time delay corresponding approximately to the time that it would take for the large-scale structure to travel between the two stations." Tran concluded that the pressure pulses in the intermittent region were independent of the large-scale structures in the upstream boundary layer which are convected into the interaction.

The results of the VITA analysis just discussed must also be treated with a certain amount of caution. The shock motion may be 'receptive' only to certain pressure-carrying eddies entering the interaction. The VITA technique most probably does detect these events but may average them with many other types of 'events' which could mask any correlation with the downstream shock motion. Further, in Tran's experiment only a single transducer was placed in the intermittent region, close to its upstream edge. It is quite possible that the shock was moving upstream and downstream in response to the incoming turbulent eddies but remained downstream of the transducer whose output was used to calculate the ensembles. It might be more appropriate to use the large pressure rise on the downstream channel as a trigger and ensemble average on the upstream channel in the undisturbed boundary layer. In this way, the trigger is a well defined and well-understood event, and ensemble averages on the upstream channel are more easily interpreted.

As a final comment, it is not necessary that the shock motion be connected with transport phenomena; the shock is an interface and its propagation speed depends on conditions in the regions upstream and downstream of it. Using this idea, a very simple 1-D analysis relating the shock speeds to the pressures upstream and downstream of the shock, was developed by Dolling and Smith (Ref. 16). It predicted shock speeds that agreed reasonably well with the measured ones. The calculated average downstream speed was also slightly higher than the upstream speed, a feature observed experimentally. At the present stage, the physical idea behind this, namely that either local or global pressure fluctuations in the separated flow drive the shock wave, must also be treated with considerable caution. No direct connection between the shock motion and separated flow pressure fluctuations has yet been established.

In transonic diffuser flow oscillations, characterized by a normal shock/turbulent boundary layer interaction combined with a subsonic, adverse pressure gradient region behind the shock, Boger et al. (Ref. 5) cite evidence suggesting that strong shock oscillations are sustained by a feedback loop of upstream propagating acoustic waves and downstream-convected perturbations in the boundary layer. In the ramp flow, the separation bubble contains a subsonic region in which a similar mechanism is feasible. To the best of the author's knowledge this has never been investigated.

In summary, other than in the diffuser problem just discussed, it must be stated that the driving mechanism of the separation shock motion is not known for any of the flows discussed and is a fruitful area for research.

2.1.11 Separated Flow Region

At 'S' or just downstream of it, the fluctuation amplitude distributions are again essentially Gaussian. If the separation length is large enough, both σ_P and $\overline{P}_w$ reach constant plateau levels [Chyu and Hanly (Ref. 14, Coe et al. (Ref. 15)]. Compared to the undisturbed attached flow, both σ_P and $\sigma_P/\overline{P}_w$ are significantly higher. Longitudinal space-time correlations for the Mach 3, 24°ramp are shown in Fig. 27. In this case, the extent of separation was relatively small, and the flow undergoes a continuous compression from separation through reattachment. $(R_{pp})_{max}$ is significantly less than in the upstream attached flow, and decreases much more rapidly with transducer separation distance suggesting a stronger contribution from high frequency (i.e., less correlated) fluctuations. An obvious feature is the double peak shape. However, the reasons for the second small peak at the larger positive τ are not clear. Estimates of the broadband convection velocity from the first maxima at positive τ gives a value of $0.6U_\infty$, or $0.8U_e$, where U_e is the local freestream velocity (deduced assuming a 10°deflection through the separation shock). This agrees well with attached flow results. Although reverse flow occurs, the fluctuations are much more highly correlated in the streamwise direction, and eddies moving downstream are the major contributors. For the closest spacing, a peak is just discernible at $\tau \approx -100\mu s$ but R_{pp} is low and of limited accuracy. Assuming that it reflects a physical feature present in the flow, it corresponds to an upstream convection velocity of about 55 m/s which is within a few percent of the maximum reversed flow velocities measured by Settles et al. (Ref. 33) in the same flowfield.

Correlations further downstream (Ref. 23) show that the maximum correlation at positive τ increases, and the maximum at negative τ disappears. It appears that convective phenomena dominate in the separated flow. Convection velocities at different separations were the same within the temporal resolution of the experiment. Spanwise correlations were symmetric about the $\tau = 0$ axis with a peak correlation coefficient of about 0.4. Thus, the eddies are not strongly correlated spanwise and the time-averaged flow can be regarded as uniform. These observations are in basic agreement with the work of Coe et al. Narrow-band convection velocities determined in the separated flow upstream of a 45°axisymmetric flare at Mach 2 varied from $0.2U_e$ (at $f\delta/U_e = 0.06$) to a maximum of about $0.8U_e$ (at $f\delta/U_e = 0.8$). Upstream convection was not detected. Clearly, broad-band velocities cannot be considered representative and the variation with frequency implies "that the predominant turbulence at different frequencies between $0.03 \leq f\delta/U_e \leq 0.8$ is generated at different levels of the boundary layer, ranging from slightly above the zero velocity line to the free shear layer."

Roos (Ref. 34) obtained similar correlations in studies of transonic airfoil buffeting. An 11% thick, single element Whitcomb supercritical airfoil and a conventional NACA 00012 airfoil were tested. For fully separated flow from the shock to the trailing edge, peak time delays were positive, indicative of disturbances moving downstream. By band-pass filtering before cross-correlation, the frequency dependence of the convection speeds was established. The results were similar to those of Coe et al. A more complex disturbance propagation pattern was found when shock-induced separation was followed by reattachment. The cross-correlations show upstream and downstream propagation of disturbances, indicative of acoustic and convective modes. In this case, the higher frequencies travelled downstream with the frequency-dependent speed characteristic of the convective mode, and the lower frequencies showed a mixed behavior.

Coe et al. tried to determine the extent of the interaction between the shock oscillation and pressure fluctuations in the separated flow by simultaneously sampling the signals in both regions and calculating correlations and coherence functions. The results showed that the fluctuations were related only at low frequencies, $f\delta/U_\infty < 0.04$ (in this case 200 Hz). The coherence at these low frequencies decreased rapidly downstream of the shock, but a coherence of about 0.2 persisted well into the separated region. Negative phase angles showed

that the convection of the mean related turbulence was upstream, indicating that at low frequencies turbulence in the separated flow has a strong influence on the shock oscillation.

Sajben and Kroutil (Ref. 4) reached a qualitatively similar conclusion in studies of the effect of initial boundary layer thickness on transonic diffuser flows. They observed that the turbulence in the rapidly thickening upper wall boundary layer (downstream of the shock) was associated with frequencies that decrease rapidly streamwise. At the end of the diffuser they could become low enough to be comparable to the shock oscillation frequency. Although the small bubble-type ramp flows do not appear to share similar spectral features, this idea has never been seriously examined.

Appropriate correlating parameters for the power spectra are not entirely clear. Chyu and Hanly (Ref. 14) normalized the power and frequency axes by $U_\infty/q_\infty^2\delta^*$ and δ^*/U_∞ respectively and obtained good correlation for $f\delta^*/U_\infty < 0.2$ (above that value it was M_∞ dependent). Coe et al. tested an assortment of 2-D and axisymmetric models and examined many normalizing parameters. Overall their best correlation was obtained using $U_\infty/q_\infty^2\delta$ and δ/U_∞. Dolling and Or (Ref. 35) have tried to correlate Mach 3 compression ramp data using the same parameters. The spectra had the same shape and roll-off rate over much of the frequency range but fell consistently below Coe's results.

2.1.12 Reattachment and Outgoing Boundary Layer

There exist few data near reattachment or in the outgoing boundary layer, largely because of tunnel constraints. Models such as compression ramps have to be long enough to avoid trailing-edge effects on reattachment, but short enough to avoid tunnel blockage. Generally outgoing boundary-layer lengths are short. In compression ramp flows $\sigma_P/\overline{P}_w$ increases towards reattachment (Fig. 28). Chyu and Hanly (Ref. 14) report the same behavior in axisymmetric flare studies, although these data must be interpreted with caution since the cut-off frequency was low. Downstream of R, σ_P progressively decreases, and continues to do so after $\overline{P}_w$ reaches a constant value. The slow readjustment is seen in the skewness and flatness coefficients (Fig. 29). The skewness passes through zero about $3\delta_o$ from the corner; close to where $\overline{P}_w$ becomes constant. It then decreases and levels off at around -0.2. It is difficult to judge whether it remains constant or increases slowly back to zero. The results for the flatness are equally confusing. At the downstream boundary of the measurement region, the value is about 3 and apparently increasing. The power spectra (Ref. 36) are suggestive of some unusual features in the outgoing boundary layer. Downstream of R, a "bulge" developed in the spectrum; at the furthest downstream station, it spanned the range of 5-12 kHz, corresponding to energetic structures of streamwise extent about $2\delta_o$.

Selig et al. (Ref. 37) made simultaneous wall pressure and mass flux measurements in the same compression ramp flow. Although correlations between the two signals were low and appeared to be dominated by tunnel noise, the mass flux measurements revealed some interesting results. From the wall to close to the middle of the boundary layer, probability density distributions centered around a single value equal to the incoming freestream mass flux. Further out than the middle of the boundary layer, the distribution centered around a single value equal to the mass flux downstream of the interaction. In the middle, the distributions were bimodal, indicative of an intermittent signal with peaks at both values. Similar findings have been reported by Hayakawa et al. (Ref. 38). Selig et al. suggest that this might be caused either by Taylor-Gortler vortices or low-speed eruptions from the separation bubble and suggest that the latter is the more likely cause. In support, they cite the microsecond schlieren photographs of Ardonceau (Ref. 39) which appear to show a "quasi-periodic" vortex sheet emerging from the separated flow and travelling downstream.

These observations agree qualitatively with the turbulence measurements of Lee (Ref. 40), Delery (Ref. 41) and Ardonceau (Ref. 39) although in some cases different conclusions are drawn from them. Lee made constant-temperature hot-wire measurements in 8°, 13°and 18°compression ramp flows at $M_\infty = 2.25$. These angles correspond to attached flow, incipient separation and separated flow respectively. The maxima in the power spectra were located near 25 kHz before and after the interaction, inferring large-scale structures of $0[2\delta_o]$ in extent in both cases. Some evidence of unsteadiness also was noted. The profiles close to the wall downstream of the interaction exhibited an intense peak around 1-10 kHz; asssuming that transport phenomena are responsible, this corresponds to flow structures up to $5\delta_o$ in extent. Lee concluded that this was not turbulence, but rather was due to "a global displacement of the boundary layer linked with the separation instability."

Delery used a laser velocimeter in three shock-induced separated flows in a 2-D transonic channel. The flows corresponded to incipient separation, well separated, and a case with a very large separated bubble. The downstream relaxation to a new equilibrium state was very gradual due to the long lifetime of the large structures in the outgoing flow which formed near the shock root, a region of intense turbulence production. Ardonceau made turbulence measurements in the same flows as Lee, using a laser velocimeter and a constant temperature hot wire. The longitudinal properties of the turbulent structure were investigated through spectal analysis of the hot-wire signal. It was concluded that a large amount of turbulent energy was contained in large-scale structures. A typical scale is $2\delta_o$ in the stream direction and $1\delta_o$ spanwise. As Lee's more qualitative work suggested, these structures do not lose their coherence during the interaction with the mean velocity field.

The corresponding probability density distributions for the shock frequency, f_i, are shown in Figure 34. Since $f_i = 1/T_i$ the distributions of f_i and T_i are not linearly related, so the inverse of the mean period is not the mean frequency, $\overline{f}$. The latter was defined earlier. The distributions are also plotted as $(N_i/N_T) \times (1/W)$ but unlike the shock period distributions $W(\equiv f_i - f_{i+1})$ is not constant. It decreases as T_i increases. The curves, particularly those for the tunnel floor tests exhibit considerable scatter. The mean frequencies, $\overline{f}$, are indicated by the vertical arrows. Although the range of possible shock frequencies is quite broad, low frequencies (typically < 1-2 kHz) are most probable in all cases. For a fixed D, the mean and most probable frequencies decrease in the thicker boundary layer.

Shock speeds and their distributions have been calculated by Dolling and Smith (Ref. 16) and Baade and Dolling (Ref. 31) in Mach 5 cylinder-induced flows. The shock speeds were calculated directly from individual pairs of nested 'box-car' signals as illustrated earlier in Fig. 24e. In Refs. 16 and 31 the two-threshold algorithm was used to generate the box car signal and at any given station, up to 750 pairs of nested box-cars were examined. Typical probability distributions of the shock speeds in both directions for two different diameter cylinders in the same boundary layer ($\delta_o = 1.62cm$) are shown in Figures 35 and 36. U_s is the shock speed, N is the number of occurrences of a given speed and N_T is the total number of events. The different curves correspond to different positions in the intermittent region and span the range $0.12 \leq \gamma \leq 0.87$. Mean upstream and downstream shock speeds for the different positions fell in the ranges $0.06 \leq \overline{U}_s/U_\infty \leq 0.07$ for the 1.27 cm case and $0.06 \leq \overline{U}_s/U_\infty \leq 0.13$ for the 1.91 cm case with no trends with intermittency. Downstream mean shock speeds were higher than upstream; 10-15% higher for the 1.27 cm cylinder and 15-30% higher for the 1.91 cm cylinder. The overall upstream and downstream mean shock speeds for the various cases, (i.e., the average value at all values of γ) including results from additional tests in a thinner boundary layer are given in the table below. Fewer data records were taken in the latter cases, so the average values are based on only 70-200 shock passages per station, rather than 400-750 for the thicker boundary layer cases. In summary, it appears that shock speeds are low and that position in the intermittent region, incoming boundary layer and model diameter have a relatively small affect on the values.

Overall Mean Shock Speeds

Overall Shock Speed	D = 1.91 cm	D = 1.27 cm	δ (cm)
Upstream	.068 U_∞	.062 U_∞	1.62
Downstream	.078 U_∞	.067 U_∞	1.62
Upstream	.056 U_∞	.049 U_∞	0.54
Downstream	.074 U_∞	.055 U_∞	0.54

It is possible that the discrepancy between the mean speeds in the ramp and cylinder studies is partly due to the smaller number of samples in the ramp study but it could also be due to the use of a single-threshold algorithm to generate the box-cars which biases the results to shorter times and hence higher speeds. At this stage, as noted earlier, there is no reason to assume that U_∞ is an appropriate normalizer. Even so, it is clear that in two different flows the shock speeds are a small fraction of U_∞. No satisfactory physical explanation for this result is available.

3.2.1 Separated Flow

In 3-D flow, a large variety of separated flow structures can exist depending on the model geometry, orientation, shock strength and incoming flow parameters such as Reynolds number and Mach number. In blunt fin and cylinder-induced flows, the qualitative structure can best be understood in terms of vortex systems; these include vortices that form in the upstream separated flow, the stretching of these around the leading edge (or cylinder) in a horseshoe shape, and in cylinder flows, the near-wake spiral vortices. This pattern is common to both laminar and turbulent flows, as well as to Mach numbers up to the hypersonic range. How many vortices occur appears to be primarily a function of Reynolds number, certain dimensionless parameters, and flow type [Sedney (Ref. 47)]. Since these vortices generate very large streamwise and spanwise pressure gradients it is obvious they they will play a dominant role in the wall pressure fluctuation behavior. This behavior is likely to be very complex.

There are very few results available. As seen in figure 31, for flow upstream of a blunt fin, σ_P continues to increase downstream of 'S'. It reaches a second peak whose magnitude is of the same order as that caused by the unsteady separation shock. The peak in the intermittent region maintains its position relative to the upstream influence line, the second peak is swept back and crosses underneath the inviscid shock at $X/D = 3$ (Figure 32). On center-line the second peak is about one diameter upstream of the fin leading edge, and corresponds approximately to the upstream limit of the embedded supersonic reversed flow region predicted in a numerical study by Hung and Buning (Ref. 48). As seen in Figure 32, the peak decays rapidly and further spanwise than $X/D = 4$ is no longer detectable. A third peak of greater magnitude than the other two occurs near the root of the shock generator leading edge, at $X/D \approx -0.1$ to -0.2. It is not clear if this is generated by the small secondary vortex at the generator root or by some other mechanism. All of these data were deduced from

measurements on a single channel; no space-time correlation data are available. Similarly no published data are available to provide information on the spectral content of the signal between 'S' and the leading edge.

3.3 Sharp Fin Flows

The only known data are those of Tan et al. (Ref 42), Tran et al. (Ref. 43) and Tran (Ref. 32). Tran made detailed measurements along a single survey line in the undisturbed freestream direction for fin angles of attack, α, of 10°, 12°, 16°and 20°. Distributions of the normalized mean wall pressure and normalized σ_P are shown in Figure 37. The spanwise location of the transducers is shown in the inset. On the figures 'UI' refers to the upstream influence line and 'C' refers to the line of coalescence of the surface streaks (generally considered as a line of separation). Both 'UI' and 'C' were obtained using the kerosene-lampblack method.

For the lowest inviscid shock strength ($\alpha = 10°$) the pressure signals were not intermittent and were Gaussian throughout the entire region surveyed. The distribution of σ_P shows no discernible peak. On the basis of earlier work by Debieve and LaCharme (Ref. 17), amongst others, Tran states that this case "may be viewed as reflecting the amplification of turbulence through a region of relatively mild adverse pressure gradient". With increased shock strength, the rise in σ_P becomes more abrupt and a peak develops. It is just discernible at 12°. The pressure signals show that this development is associated with development of an unsteady shock structure. Hence the pressure signal is intermittent, the same as in other 2-D and 3-D flows. Whether or not this flow is separated has been the subject of some controversy in recent years. To this author the evidence suggests that the development of an intermittent pressure signal is associated with the onset of separation. Whether this is the case in 2-D flows is not known since there exists no $P_w(t)$ data for boundary layers subjected to continuous compressions, as for example, on a concave surface.

As in 2-D flows, $(\sigma_P)_{max}$ occurs upstream of 'C'. Similar to large scale 2-D separated flows, between 'C' and the trace of the inviscid shock σ_P is essentially constant (as is $\overline{P}_w$) although, as expected, the value depends on the inviscid shock strength. Downstream of the shock, σ_P decreases. From extrapolations of the data in Figure 37, Tran estimated that a new equilibrium value would be reached $6 - 7\delta_o$ downstream of the inviscid shock.

Using a coordinate stretching technique, which makes use of the fact that the flowfield footprint is quasi-conical, Tran correlated the data from sharp fin, semi-cone and swept compression ramp flows (Figures 38 and 39). For a given inviscid shock strength, varying the geometry has little effect on the distribution of $\overline{P}_w/\overline{P}_{wo}$ and $\sigma_P/\overline{P}_w$, at least from X_o to the inviscid shock location. The inference is that the inviscid shock strength is the major governing parameter for such swept shock interactions, and that the shock location is the reference point from which comparisons should be made.

Tran also developed a procedure for correlating $(\sigma_P)_{max}$ in the intermittent region of 2-D and sharp fin flows. The data were correlated when plotted as (σ_P/σ_{P_o}) as a function of $d(\overline{P}_w/\overline{P}_{wo})/d(X_S/\Delta S)$ where ΔS is the distance along the shock wave from the fin leading edge (Fig. 39). Although tentative (the degree of overlap between 2-D and 3-D flow was small) the result has interesting implications. First, in the sharp fin flow, ΔS develops quasi-conically and, as indicated by the correlating parameter, the boundary layer thickness does not occur. This could be construed as evidence that the shock is not convected by the large scale structures in the incoming flow.

Power spectra at 8 stations along the survey line for $\alpha = 16°$ and 20° have been reported by Tran. Both cases have common features. Between UI and C the shock-induced fluctuations are the major contributor to σ_P and are centered around 2 kHz (Figure 40). At C, the low frequency content decreases and the higher frequency range increases. In the plateau region of the σ_P distribution, the shape is unchanged with the higher frequency range centered around 10 kHz. Downstream of the inviscid shock, the shape of the spectra relaxes towards that of the incoming boundary layer. In the intermittent region these results are qualitatively the same as in 2-D flows, and other 3-D flows. The shock frequency of about 2 kHz is in the same range as blunt fin flows, but a factor of about 4 higher than in the compression ramp (all for the same incoming freestream and boundary layer).

In the fin flows, the shock front appears to ripple less than in 2-D ramp flows. Space-time correlations were made by Tran along UI for both cases. Figure 41 shows the maxima of the space-time correlations as a function of transducer spacing. For close spacings, the signals are highly correlated for the swept flow; for the ramp it has already dropped significantly at $\xi/\delta_o = 1$. For larger spacings, the correlation is essentially zero for the ramp, but for the swept case is still relatively significant even at $\xi/\delta_o = 3$. The corresponding plots of the coherence function are shown in Figure 42. For the swept case, the high frequency components drop off rapidly while the low frequency components (due to shock oscillation) remain highly correlated. The ramp data demonstrate clearly the uncorrelated shock front rippling motion.

In addition to the 20°ramp study mentioned earlier, Tran also applied the VITA technique near the interaction start in the sharp fin flows. The transducer configuration was similar; one in the undisturbed and the other on the upstream influence line. The same findings as reported for the 2-D flow were observed here. Similar reservations also apply as discussed earlier.

4. SUGGESTIONS FOR FUTURE WORK

4.1 Driving Mechanism

The single most important question from a fundamental point of view is that of the mechanism driving the shock motion. Identifying the source of the unsteadiness is important on two counts. The first count concerns numerical modelling. Given a powerful enough computer, appropriate algorithms, and a physically accurate turbulence model, there is no reason to suppose that 3-D, time-accurate Navier-Stokes codes cannot be used to predict the phenomenon. This is probably not likely in the near future. If the mechanism was understood then it might prove possible to devise simpler models which do not require such a sophisticated, and expensive approach. The second count concerns controlling the shock motion, or eliminating it altogether. This calls for some understanding of the basic physics. In the author's view, considering the status of 3-D, turbulent, separated shock-boundary layer interaction computations, it is more likely that the physical mechanism will be identified through experiment than through calculation. This is a challenging task and is made more complex by the possibility that the mechanism may differ from one flowfield to another.

In the author's own laboratory some work is being done on this topic. Some current data have shown that ensemble-averaged pressures under the separated shear layer in a compression ramp flow rise and fall as the separation shock wave moves downstream and upstream respectively (Ref. 49). One question, not answered by these data, is whether the downstream pressure changes are a result of, or the cause of, the shock motion. In a new experiment underway, pressure transducers are placed in the intermittent region, close to its downstream boundary, and further downstream under the separated shear layer. The same experiment is being done in interactions induced by compression ramps and circular cylinders. In the analysis, those occasions when the shock changes its direction from downstream to upstream are detected. Pressures recorded by the downstream transducers are ensemble-averaged over a large number of these direction-change events. The objective is to determine if the decrease in pressure under the shear layer precedes or follows the shock direction change.

In a second experiment, transducers are located in the incoming boundary layer and in the intermittent region. As the shock crosses the downstream transducer, ensemble averages are calculated on the upstream channel. The objective is to determine whether the shock motion is preceded by "events" in the incoming boundary layer. It is possible that the shock is "receptive" to certain types of incoming turbulent eddies. The ensemble-averages should indicate whether shock motion is preceded by "pressure-carrying" eddies with large amplitude fluctuations. This analysis differs from the VITA technique, as used by Tran and discussed in Section 2.1.10. These events in the incoming boundary layer were detected from the VITA signal and averaging done on the downstream channel. The new technique avoids the difficulties discussed earlier. At the time of writing, the experiments are done, but the analysis is not completed.

4.2 Swept Flowfields

Other than the work of Tran (Ref. 32), nearly all of the measurements have been made in nominally 2-D flows, or on the plane of symmetry in such 3-D flows as those generated by blunt fins or circular cylinders. The qualitative and quantitative character of the shock dynamics in swept flows is largely unknown. Considering that so many of the interactive flows of engineering interest are swept, one example being the side wall interactions in inlets, this lack of attention is somewhat surprising. There are some very interesting questions to be addressed For example, using the terminology defined earlier it is known that the separation shock motion occurs in the region bounded by X_o and 'S'. In flows such as those generated by sharp fins at angle of attack, or by highly swept compression ramps the flowfields are essentially conically symmetric. The upstream influence line (i.e., X_o), the separation line 'S' and the trace of the inviscid shock on the test surface lie along rays emanating from either the fin leading edge (or ramp apex) or a virtual origin close to the latter. Wall pressure distributions can be collapsed in conical coordinates. Hence the distance from X_o to 'S' increases linearly with increasing spanwise distance. Whether the separation shock continues to move over this ever-increasing distance and if it does, at what frequencies and speeds, are intriguing questions whose answers are unknown. In fact, these questions may be premature, or inappropriate, since even qualitative features of the unsteady shock structure and its dynamics are unknown. Whether there exists an unsteady separation shock with intermittent separation at all spanwise stations, or whether the flowfield structure changes at large distances from the leading edge (or apex) are unknown. Whether the swept separation shock 'flaps' in some coherent fashion with a definable large scale wavelength, or simply undergoes small-scale local rippling along its length are unknown. Answers to such questions are inherently related to the mechanism responsible, be it the turbulence of the local incoming boundary layer or oscillations or instabilities in the large scale vortical separated flow structure in the interaction itself. Clearly, much interesting work remains to be done.

REFERENCES

1. Rockwell, D., 1983, "Oscillations of Impinging Shear Layers", *AIAA J.*, 21, 656-664.

2. Calarese, W. and Hankey, W.L., 1985, "Modes of Shock-Wave Oscillations on Spike-Tipped Bodies", *AIAA J.*, 23, 185-192.

3. Chen, C.P., M. Sajben and J.C. Kroutil, 1979, "Shock Wave Oscillations in a Transonic Diffuser Flow", *AIAA J.*, 17, 1076-1083.

4. Sajben, J. and J.C. Kroutil, 1981, "Effects of Initial Boundary Layer Thickness on Transonic Diffuser Flows," *AIAA J.*, 19, 1386-1393.

5. Bogar, T.J., M. Sajben and J.C. Kroutil, 1983, "Characteristic Frequencies of Transonic Diffuser Flow Oscillations", *AIAA J.*, 21, 1232-1240.

6. Sajben, M., T.J. Bogar and J.C. Kroutil, 1984, "Forced Oscillation Experiments in Supercritical Diffuser Flows", *AIAA J.*, 22, 465-474.

7. Bogar, T.J., 1986, "Structure of Self-Excited Oscillations in Transonic Diffuser Flows", *AIAA J.*, 24, 54-61.

8. Gramann, R. and D.S. Dolling, 1986, "Unsteady Separation in Shock Wave Turbulent Boundary Layer Interactions", AIAA Paper 86-1033.

9. Gramann, R., and D.S. Dolling, 1988, "Detection of Turbulent Boundary Layer Separation Using Fluctuating Wall Pressure Signals", AIAA Paper 88-4676.

10. Kistler, A.L., 1964, "Fluctuating Wall Pressure Under a Separated Supersonic Flow", *J. Acoust. Soc. of America*, 36, 543-550.

11. Robertson, J.E., 1969, "Characteristics of the Static and Fluctuating-Pressure Environments Induced by Three-Dimensional Protuberances at Transonic Mach Numbers", Wyle Lab Rept. WR-69-3.

12. Robertson, J.E., 1971, "Prediction of In-Flight Fluctuating Pressure Environments Including Protuberance Induced Flow", Wyle Lab Rept. WR-71-10.

13. Speaker, W.V. and C.M. Ailman, 1969, "Spectra and Space-Time Correlations of the Fluctuating Pressures at a Wall Beneath a Supersonic Turbulent Boundary Layer Perturbed by Steps and Shock Waves", NASA CR-486.

14. Chyu, W.J. and R.D. Hanly, 1969, "Power and Cross Spectra and Space-Time Correlations of Surface Fluctuating Pressures at Mach Numbers Between 1.6 and 2.5", NASA TN-D-5440.

15. Coe, C.F., W.J. Chyu and J.B. Dods, 1973, "Pressure Fluctuations Underlying Attached and Separated Supersonic Turbulent Boundary Layers and Shock Waves", AIAA Paper 73-996.

16. Dolling, D.S. and Smith, D.R.S., 1988, "Unsteady Shock-Induced Turbulent Separation in Mach 5 Cylinder Interactions", AIAA Paper 88-0305.

17. Debieve, J.F. and J.P. Lacharme, 1986, "A Shock Wave/Free Turbulence Interaction", Proceedings, IUTAM Symposium, Turbulent Shear-Layer/Shock-Wave Interactions, Springer-Verlag, 393-403.

18. Muck, K.C., J.P. Dussauge and S.M. Bogdonoff, 1985, "Structure of the Wall Pressure Fluctuations in a Shock-Induced Separated Turbulent Flow", AIAA Paper 85-0179.

19. Dolling, D.S., 1983, "On Upstream Influence in Shock Wave Turbulent Boundary Layer Interaction", *Royal Aero. Soc. J.*, 324-327.

20. Degrez, G., 1981, "Exploratory Experimental Investigation of the Unsteady Aspects of Blunt Fin-Induced Shock Wave Turbulent Boundary Layer Interactions", MAE Dept., MS Thesis 1516-T, Princeton University.

21. Dussauge, J.P., K.C. Muck and J. Andreopoulos, 1985, "Properties of Wall Pressure Fluctuations in Separated Flow Over a Compression Ramp", Proceedings, IUTAM Symposium, Turbulent Shear-Layer/Shock-Wave Interactions, Springer-Verlag.

22. Settles, G.S., T.J. Fitzpatrick and S.M. Bogdonoff, 1979, "Detailed Study of Attached and Separated Compression Corner Flowfields in High Reynolds Number Supersonic Flow", *AIAA J.*, 17, 579-585.

23. Muck, K.C., Andreopoulos, J. and Dussauge, J.P., 1987, "The Structure of a Separated Flow Over a Two-Dimensional Compression Ramp", submitted to *AIAA Journal*.

24. Nordyke, R., "Spanwise Properties of the Unsteady Separation Shock in a Mach 5 Unswept Compression Ramp Interaction", Aerospace Engineering Dept., University of Texas, MS Thesis, Dec. 1987.

25. Dolling, D.S. and R. Nordyke, "Exploratory Study of Spanwise Separation Shock Motion in Compression Ramp Interactions", AIAA Paper 88-3802, 1st National Fluid Dynamics Congress, Cincinnatti, July 1988.

26. Dolling, D.S. and L. Brusniak, 1987, "Separation Shock Motion in Fin, Cylinder and Compression Ramp-Induced Turbulent Interactions", AIAA Paper 87-1368.

27. Dolling, D.S. and M.T. Murphy, 1983, "Unsteadiness of the Separation Shock Wave Structure in a Supersonic Compression Ramp Flowfield", *AIAA J.*, 21, 1628-1634.

28. Andreopoulos, J. and K.C. Muck, 1986, "Some New Aspects of the Shock Wave Boundary Layer Interaction in Compression Ramp Flows", AIAA Paper 86-0342.

29. Narlo, J.C., II, 1986, "Experimental Investigati 1 of the Driving Mechanisms of Separation Shock Wave Motion in Interactive Flows", MS Thesis, ASE/EM Dept., The University of Texas at Austin.

30. Dolling, D.S. and J.C. Narlo, II, 1987, "Driving Mechanism of Unsteady Separation Shock Motion in Hypersonic Interactive Flow", AGARD Symposium on Aerodynamics of Hypersonic Lifting Vehicles, AGARD CP428, Paper #7.

31. Baade, H., and D.S. Dolling, "Separation Shock Wave Dynamics in Mach 5 Turbulent Flow", submitted to JFM.

32. Tran, T.T., "An Experimental Investigation of Unsteadiness in Swept Shock Wave/Turbulent Boundary Layer Interactions", Ph.D. dissertation (T-1763), Mechanical & Aerospace Engineering Dept., Princeton University, 1987.

33. Settles, G.S., "An Experimental Study of Compressible Turbulent Boundary Layer Separation at High Reynolds Number", Ph.D. dissertation, Mech. and Aero. Engineering Dept., Princeton University, Sept. 1975.

34. Roos, F. W., "Some Features of the Unsteady Pressure Field in Transonic Airfoil Buffeting," *Jnl. of Aircraft*, Vol. 17, No. 11, 781-788.

35. Dolling, D.S and C.T. Or, 1985, "Unsteadiness of the Shock Wave Structure in Attached and Separated Compression Ramp Flowfields", Exp. in Fluids, 3, 24-32.

36. Murphy, M., 1983, "An Experimental Investigation of the Separation Shock Wave Unsteadiness in a Compression Ramp Flowfield", M.S.E. Thesis 1605-T, MAE Dept., Princeton University.

37. Selig, M.S., J. Andreopoulos, K.C. Muck, J.P. Dussauge and A.J.Smits, "Simultaneous Wall Pressure and Mass Flux Measurements Downstream of a Shock Wave/Turbulent Boundary Layer Interaction", AIAA Paper 87-0550.

38. Hayakawa, K., A.J. Smits and S.M. Bogdonoff, 1984, "Turbulence Measurements in a Compressible Reattaching Shear Layer", *AIAA J.*, 22, 889-895.

39. Ardonceau, P.L., 1984, "The Structure of Turbulence in a Supersonic Shock Wave Boundary Layer Interaction", *AIAA J.*, 22, 1254-1262.

40. Lee, D.H., 1979, "Study of the Evolution of Turbulence in a Shock Wave Boundary Layer Interaction", Thesis (Docteur Ingenieur), University of Poitiers.

41. Delery, J.M., 1983, "Experimental Investigation of Turbulence Properties in Transonic Shock/Boundary Layer Interactions", *AIAA J.*, 21, 180-185.

42. Tan, D.K.M., T.T. Tran and S.M. Bogdonoff, 1985, "Surface Pressure Fluctuations in a Three Dimensional Shock Wave/Turbulent Boundary Layer Interaction", AIAA Paper 85-0125.

43. Tran, T.T., D.K.M. Tan and S.M. Bogdonoff, 1985, "Surface Pressure Fluctuations in a Three Dimensional Shock Wave/Turbulent Boundary Layer Interaction at Various Shock Strengths", AIAA Paper 85-1562.

44. Dolling, D.S. and S.M. Bogdonoff, 1981, "An Experimental Investigation of the Unsteady Behavior of Blunt Fin-Induced Shock Wave Turbulent Boundary Layer Interactions", AIAA Paper 81-1287.

45. Settles, G.S. and D.S. Dolling, 1987 'Swept Shock Wave Boundary Layer Interaction", AIAA Progress Series, Volume 104, Tactical Missile Aerodynamics.

46. Dolling, D. S. and S. M. Bogdonoff, 1982, "Blunt Fin-Induced Shock Wave/Turbulent Boundary Layer interaction," *AIAA Jnl.*, Vol. 20, No. 12, 1674-1680.

47. Sedney, R., June 1973, "A Survey of the Effects of Small Protuberances on Boundary Layer Flows", *AIAA Journal*, Vol. 11, 782-792.

48. Hung, C.M. and P.E. Buning, 1984, "Simulation of Blunt Fin-Induced Shock Wave and Turbulent Boundary Layer Interaction", AIAA Paper 84-0457.

49. Erengil, M, Private Communication, November, 1988.
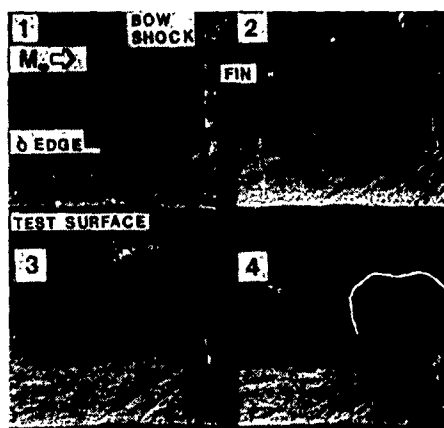
Figure 1   Micro-Second Exposure Shadow Photographs of Flow Upstream of a Blunt Fin at Mach 3. [from Ref. 44]

Figure 2   Compression Ramp flow at Mach 3 a) Model, b) Wall Pressure Signals Upstream of 'S' (c) distribution of mean pressure and rms of pressure fluctuations (d) intermittency

Figure 3   Kerosene-Lampblack Surface Tracer Pattern and Wall Pressure Signals in a Mach 3 Blunt Fin Flow. [from Ref. 9]
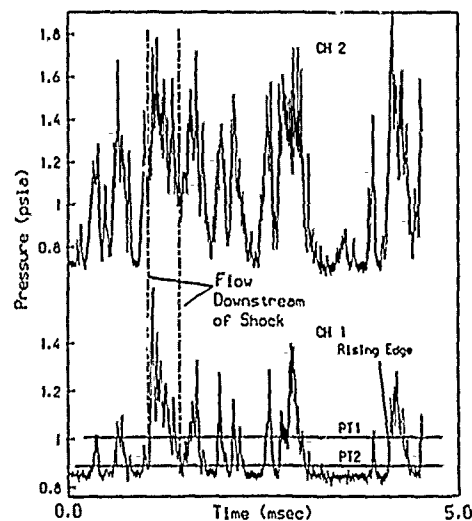
Figure 4   Simultaneously Sampled Wall Pressure Signals from Transducers Placed Streamwise in Intermittent Region. [from Ref. 9]
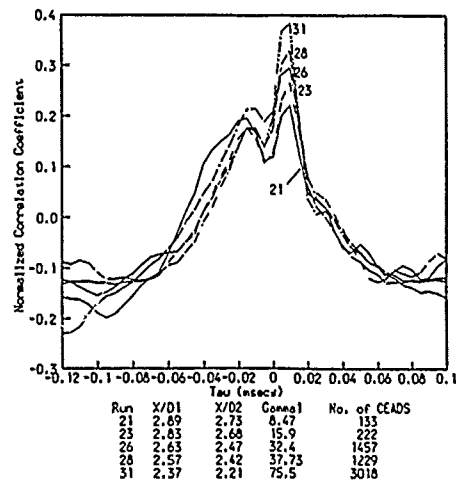
Figure 5   Cross-Correlations of Conditionally Sampled
            Data Blocks at Various Stations in the Inter-
            mittent Region. [from Ref. 9]

Run	X/D1	X/D2	Connel	No. of CEADS
21	2.89	2.73	8.47	133
23	2.83	2.68	15.9	222
26	2.63	2.47	32.4	1457
28	2.57	2.42	37.73	1229
31	2.37	2.21	75.5	3018
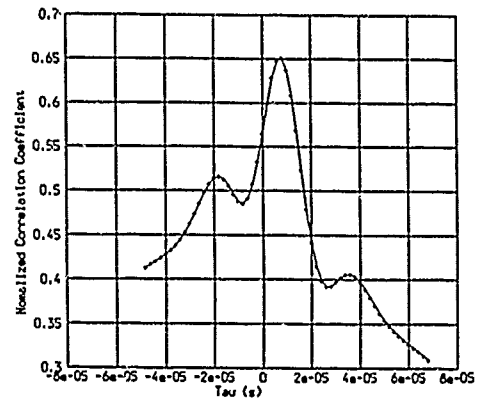
Figure 6   Cross-Correlation of Streamwise Transducers
            in Separated Flow Downstream of 'S'. [from
            Ref. 9]
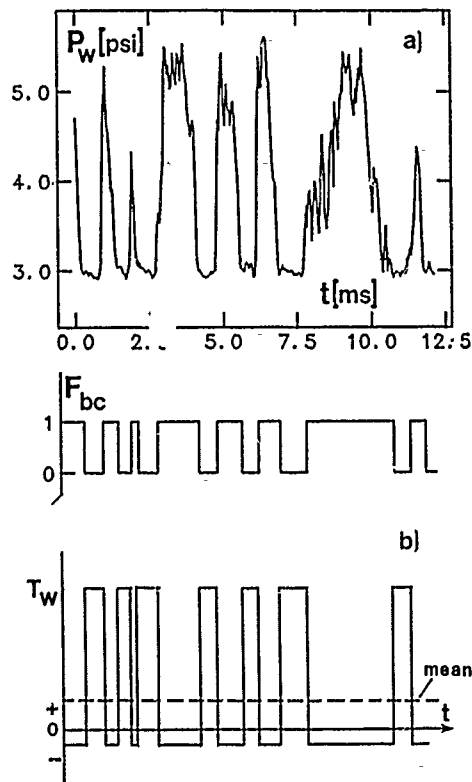
Figure 7   Model of Time Varying Wall Shear Stress in
            Intermittent Region
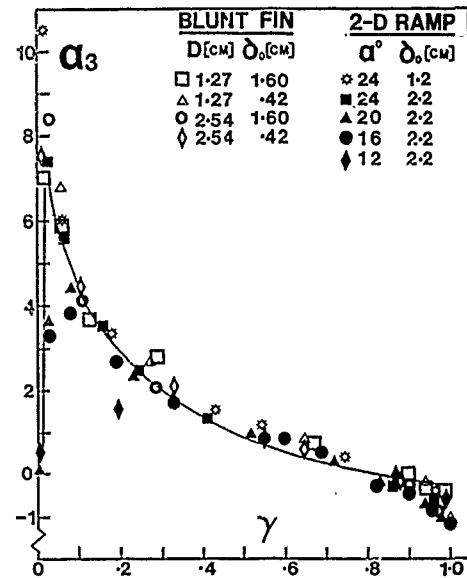
Figure 8   Skewness Coefficient of Wall Pressure Fluctu-
            ations as a Function of Intermittency. [from
            Ref. 35]
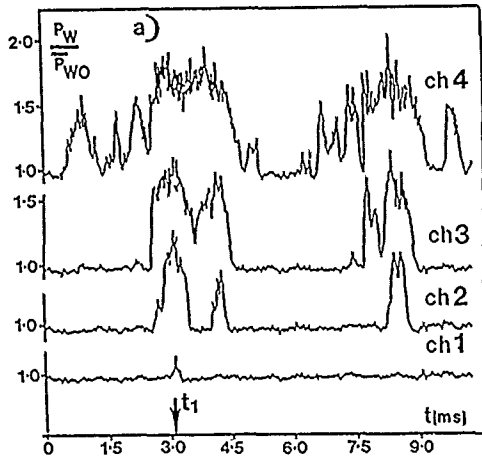
Figure 9 Wall Pressure Signals at Four Streamwise Stations in the Intermittent Region in a Mach 3 Compression Ramp Interaction. [from Ref. 18]

Figure 10 Wall Pressure Signals at Four Spanwise Stations in the Intermittent Region in a Mach 3 Compression Ramp Interaction. [from Ref. 18]
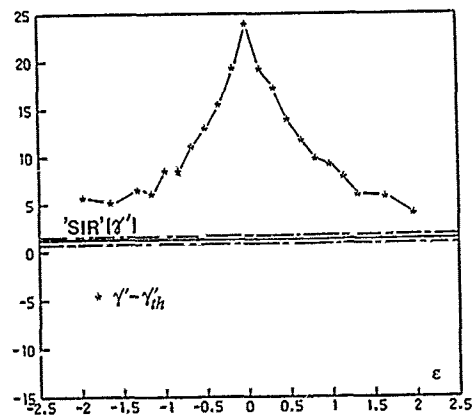
Figure 11 Spanwise Variation of $(\gamma' - \gamma'_{th})$ in a Mach 5 Compression Ramp Interaction (ϵ =spanwise distance normalized by δ_o)[from Ref. 25]
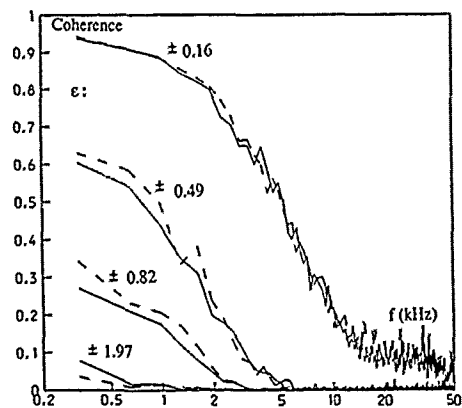
Figure 13 Coherence Function for Four Spanwise Separations in the Intermittent Region in a Mach 5 Compression Ramp Interaction. [from Ref. 25]
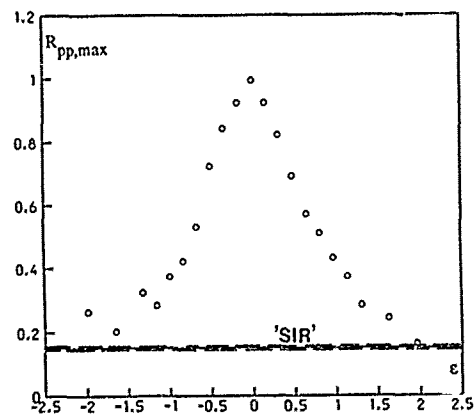
Figure 12 Spanwise Variation of the Maximum Cross-Correlation Coefficient in the Intermittent Region in a Mach 5 Compression Ramp Interaction [from Ref. 25]

Curve	Stat./Geom.	σ_{p_w}	Δf[Hz]	NR
1	2/24° ramp	0.85	39	-
2	2/24° ramp	0.80	488	750
3	1/24° ramp	0.72	488	600
4	2/20° ramp	0.64	195	200
5	2/16° ramp	0.47	195	200
6	1/D=1.27 cm	0.70	156	36
7	1/D=2.54 cm	0.84	156	36
8	1/16° sharp fin	0.21	97	≥72
9	1/20° sharp fin	0.33	97	≥72
10	1/12° sharp fin	-	97	≥72

- indicates unknown; σ_{p_w} in psi

Figure 15 Power Spectra at $(\sigma_{P_w})_{max}$ in Mach 5 Cylinder Flows. [from Ref. 16]

Figure 14 Power Spectra at $(\sigma_{P_w})_{max}$ for Various Mach 3 Interactions (curves 1-3 on axes shown, curves 4-10 are each shifted 0-3 units of $f \cdot G(f)/\sigma_{P_w}^2$ upwards). [from Ref. 26]
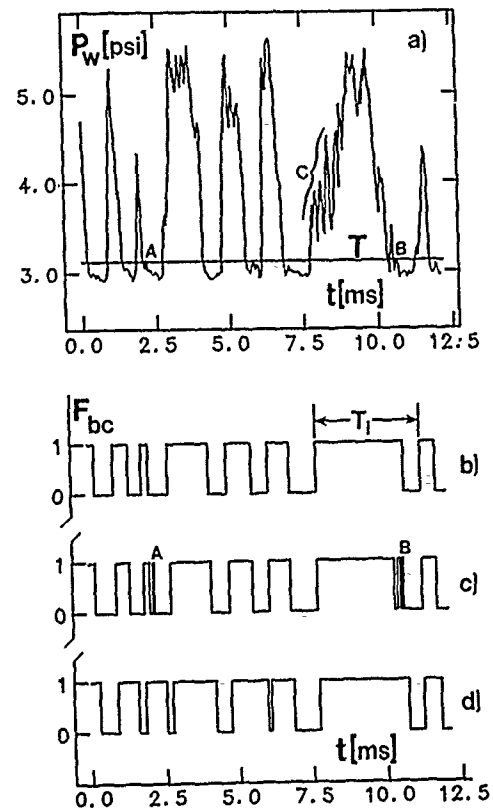
Figure 16 Conversion of Intermittent Wall Pressure Signal into Box-Car Function [from Ref. 26]
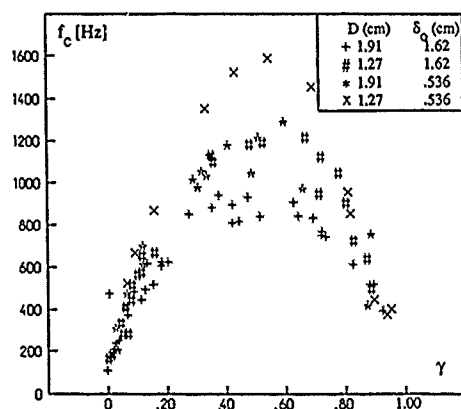
Figure 17   Shock Zero Crossing Frequency as a Function
of Intermittency in Mach 5 Cylinder Flows.
[from Ref. 16]
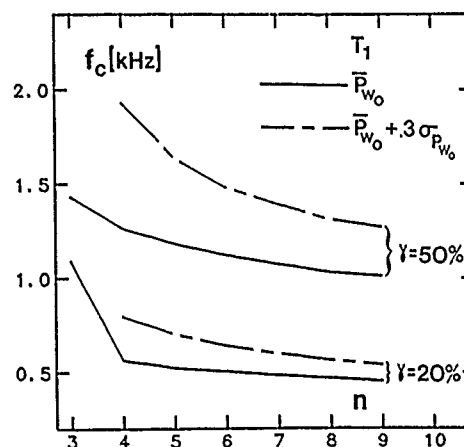
Figure 18   Effect of Threshold Settings on Shock Zero
Crossing Frequency. [from Ref. 26]
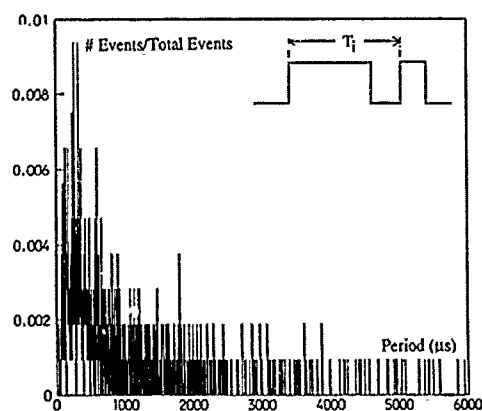
Figure 19   Histogram of Shock Periods, T_i, at $\gamma = 0.63$
in a Mach 5 Compression Ramp Interaction.
[from Ref. 24]
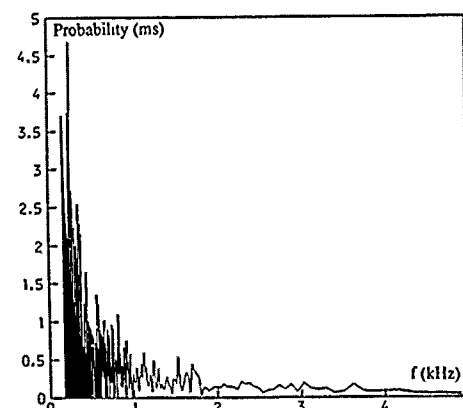
Figure 20   Histogram of Shock Frequencies, f_i, at $\gamma = 0.63$ in a Mach 5 Compression Ramp Interaction. [from Ref. 24]
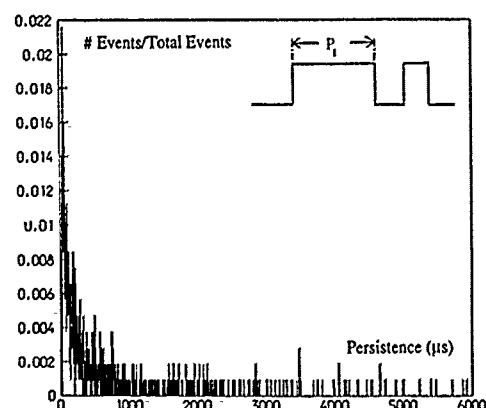
Figure 21   Histogram of Shock Persistence, P_i at $\gamma = 0.63$
in a Mach 5 Compression Ramp Interaction.
[from Ref. 24]
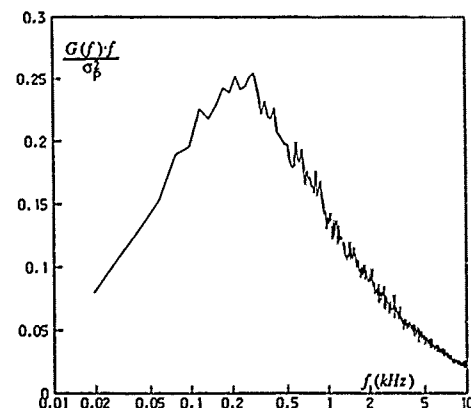
Figure 22   Power Spectrum at $\gamma = 0.63$ in a Mach 5 Compression Ramp Interaction. [from Ref. 24]
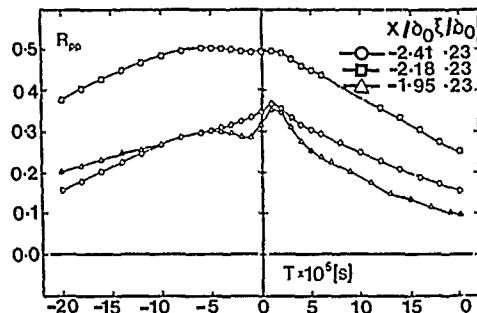
Figure 23   Longitudinal Space-Time Correlations in the Intermittent Region in a Mach 3 Compression Ramp Interaction [from Ref. 18]

Figure 24   Cross-Correlations of Nested Box Cars and Sequential Signals and Method of Calculating Shock Speeds from Box-Car Signals
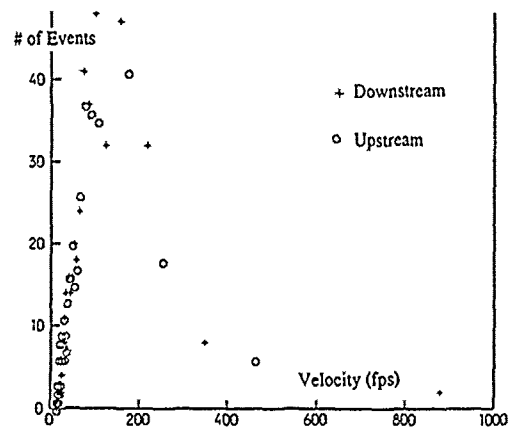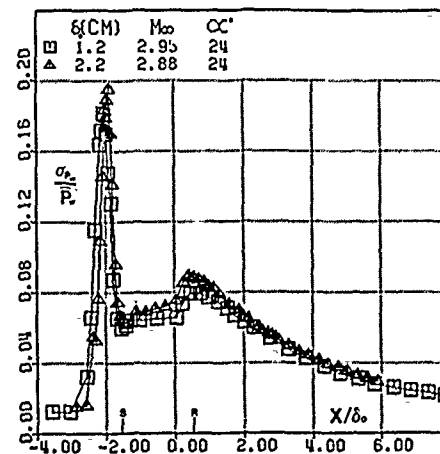

Figure 25   Shock Speeds in a Mach 3 Compression Ramp Interaction. [from Ref. 28]

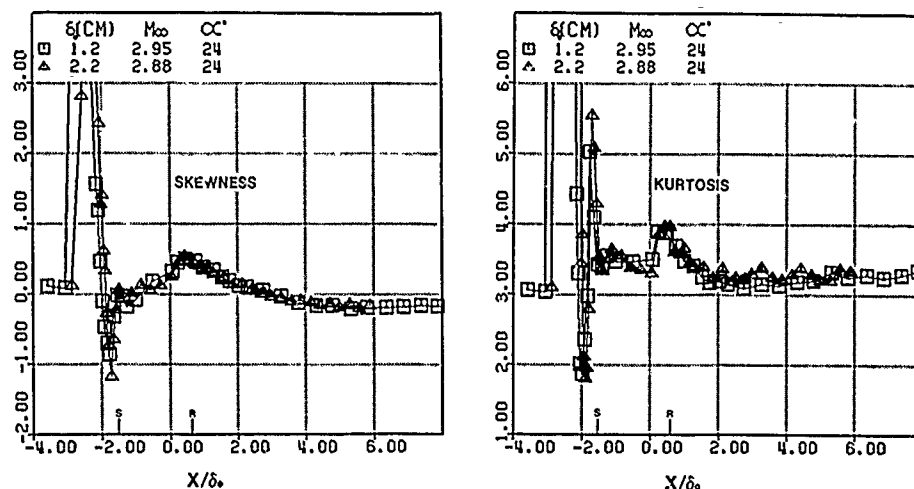Figure 26   Probability Distribution of Shock Speeds in a Mach 5 Compression Ramp Interaction. [from Ref. 28]

Figure 27   Longitudinal Space-Time Correlation Under the Separated Shear Layer in a Mach 3 Compression Ramp Interaction. [from Ref. 23]

Figure 28   Normalized Distribution of RMS of Pressure Fluctuations in a Mach 3 Compression Ramp Interaction. [from Ref. 36]

Figure 29   Skewness and Flatness Coefficients in a Mach
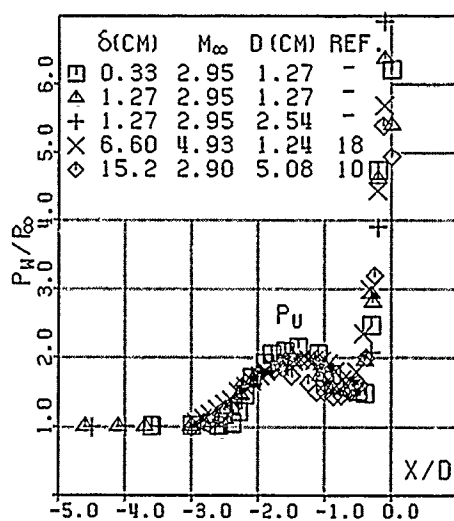3 Compression Ramp Interaction. [from Ref.
36]

Figure 30   Mean Wall Pressure Distributions Upstream
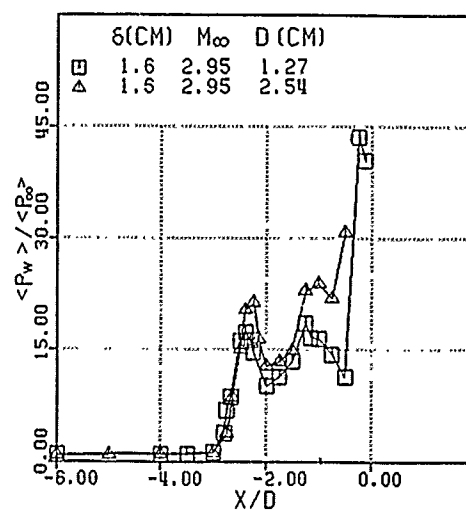of a Blunt Fin at Mach 3. [from Ref. 44]

Figure 31   Normalized RMS of Pressure Fluctuations on
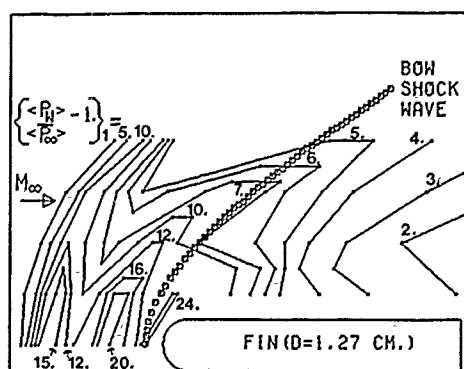Centerline Upstream of a Blunt Fin at Mach
3. [from Ref. 44]

Figure 32   Contours of the RMS of Pressure Fluctuations
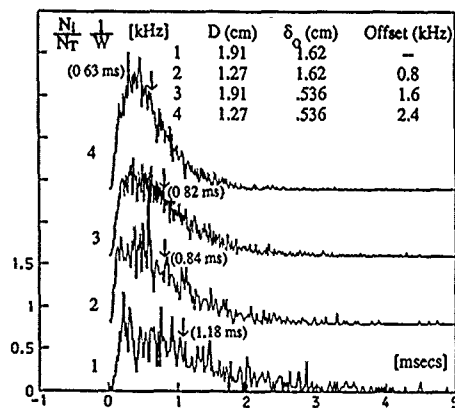in a Blunt Fin Interaction at Mach 3. [from
Ref. 44]

$\frac{N_i}{N_T}$ $\frac{1}{W}$	[kHz]	D (cm)	δ_q (cm)	Offset (kHz)
(0 63 ms)	1	1.91	1.62	—
	2	1.27	1.62	0.8
	3	1.91	.536	1.6
	4	1.27	.536	2.4

Figure 33 Probability Density Distributions of the Shock Period in Mach 5 Cylinder Interactions. [from Ref. 16]

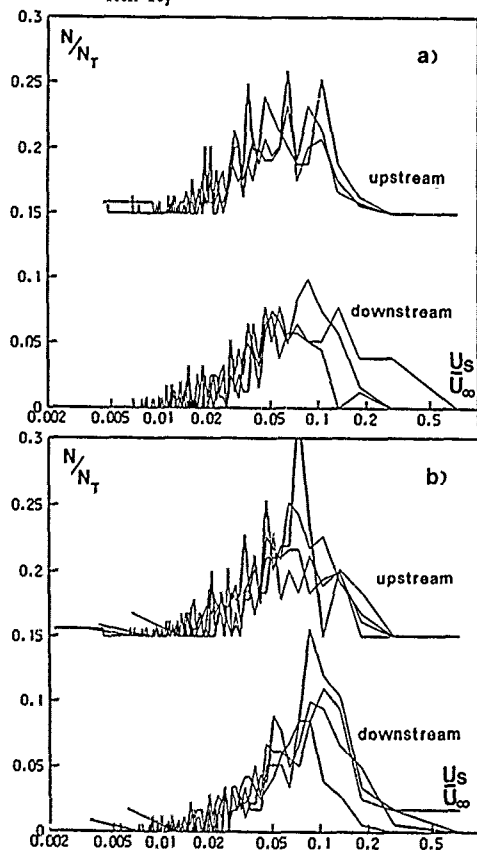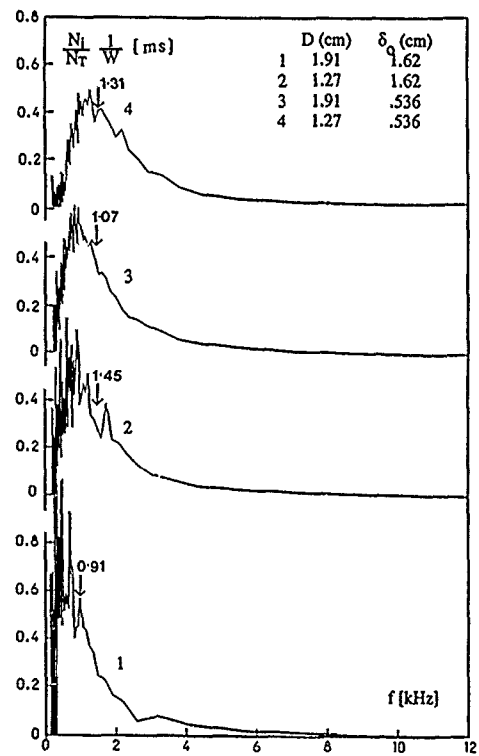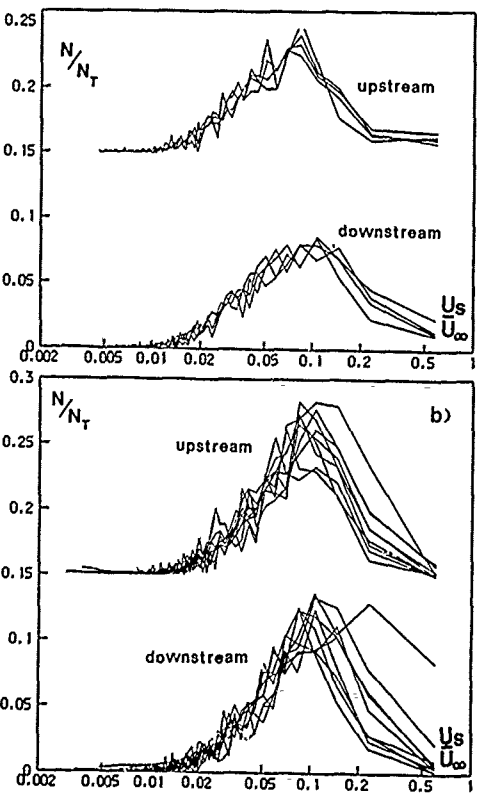| $\frac{N_i}{N_T}$ $\frac{1}{W}$ [ms]		D (cm)	δ_q (cm)
	1	1.91	1.62
	2	1.27	1.62
	3	1.91	.536
	4	1.27	.536

Figure 34 Probability Density Distributions of the Shock Frequencies in Mach 5 Cylinder Interactions. [from Ref. 16]

Figure 35 Probability Density Distributions of Shock Speeds in Mach 5 Cylinder Interactions ($D = 1.27$cm, 1.91 cm, $\delta_o = 0.54$cm). Curves of Upstream Speeds Shifted 0.15 Units Upwards [from Ref. 31]

Figure 36 Probability Density Distributions of Shock Speeds in Mach 5 Cylinder Interactions ($D = 1.27$cm, 1.91 cm, $\delta_o = 1.62$cm). Curves of Upstream Speeds Shifted 0.15 Units Upwards [from Ref. 31]

Figure 38 Correlation of Mean Wall Pressure Distributions in Sharp Fin, Semi-Cone, and Swept Compression Ramp Flows. [from Ref. 32]

Figure 39 Correlation of RMS of Fluctuations in Sharp Fin, Semi-Cone, and Swept Compression Ramp Flows. [from Ref. 32]
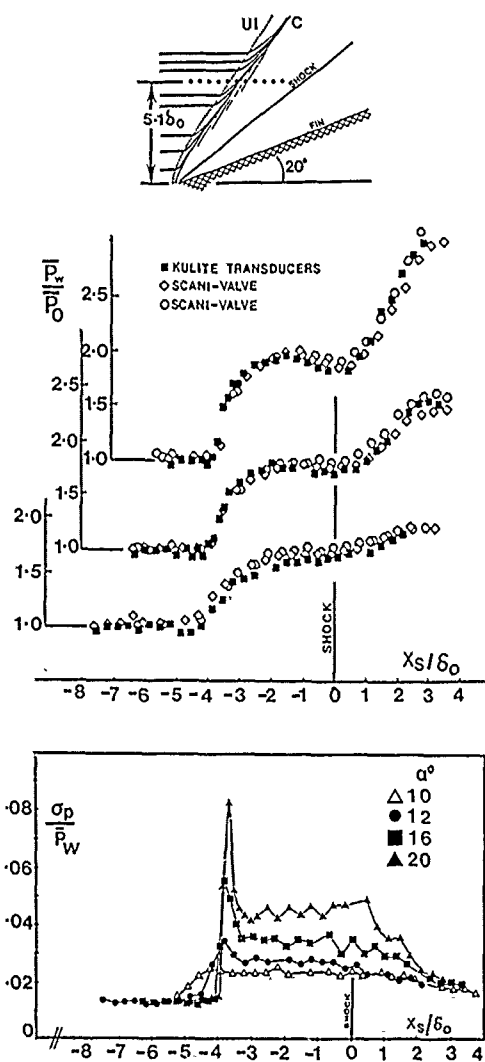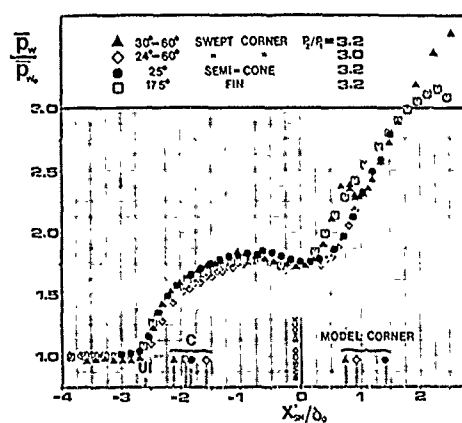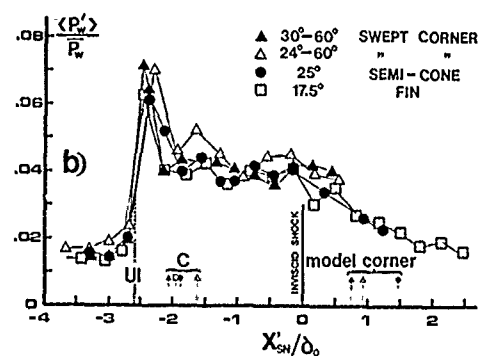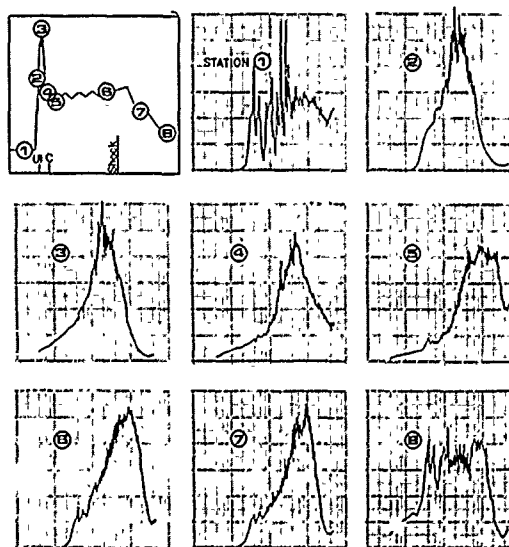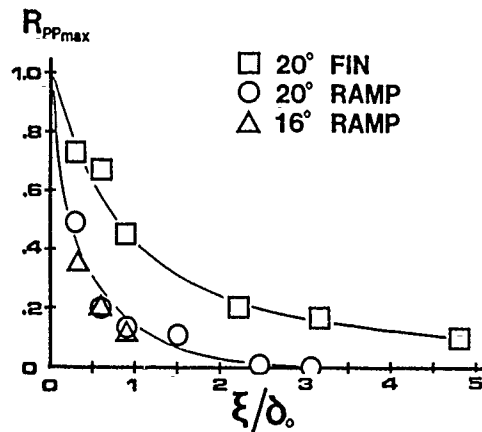

Figure 37 Distributions of Normalized Mean Wall Pressures and RMS of Fluctuations in Mach 3 Sharp Fin Flows. [from Ref. 32]

Figure 40 Power Spectra in Mach 3 Sharp Fin Flows. [from Ref. 32]

$R_{PP_{max}}$

□ 20° FIN
○ 20° RAMP
△ 16° RAMP

1.0

.8

.6

.4

.2

0

ξ/δ_o

1   2   3   4   5

Figure 41   Maxima of Space-Time Correlation Coefficients as a Function of Spacing for Transducers Aligned in the Shock Direction [from Ref. 32]

$\gamma^2(\xi_1,\xi_2,f)$

c) $\xi/\delta_o = .9$

b) $\xi/\delta_o = .6$

frequency, kHz

a) $\xi/\delta_o = .3$

c) $\xi/\delta = .9$

b) $\xi/\delta = .6$

frequency, kHz
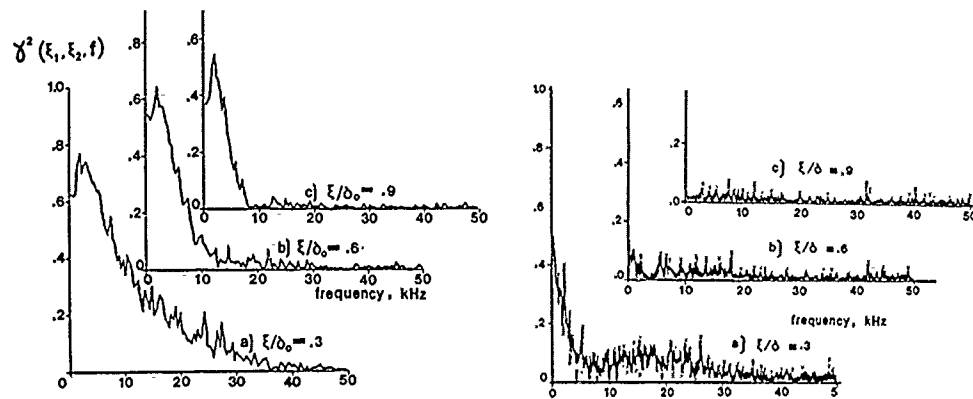
a) $\xi/\delta = .3$

Figure 42   Coherence Function for Transducers Aligned in the Shock Direction a) Sharp Fin, b) Compression Ramp. [from Ref. 32]

AGARD-FDP-VKI Special Course

"THREE-DIMENSIONAL SUPERSONIC AND HYPERSONIC FLOWS INCLUDING SEPARATION"
<u>REACTING FLOWS</u>

by

George S. Deiwert and Graham V. Candler
Aerothermodynamics Branch
NASA Ames Research Center, Moffett Field, California 94035
United States

SUMMARY

Features of chemically reacting separated hypersonic flows are identified and issues concerning their analysis and simulation are discussed. Emphasis is placed on flows of high temperature dissociating and ionizing air and current methods for studying and characterizing these flows, including separation, are reviewed. The aeroassist orbital transfer vehicle and its flight trajectory are used for illustration. Thermochemical nonequilibrium phenomena are emphasized and extension of continuum analysis to the high altitude slip-flow regime is considered.

SYMBOLS

a	Speed of sound.
A_{im}	Constants for use in equilibrium reaction constant.
A_{sr}	Constant used in Millikan and White vibrational relaxation model, see (3.37).
A_s, B_s, C_s	Constants used in Blottner viscosity model, see (3.29).
A', B'	Jacobians of F' and G', see (4.13).
A'_+, A'_-	Flux-split Jacobians of F'.
B'_+, B'_-	Flux-split Jacobians of G'.
c_s	Mass concentration of species s, $c_s = \rho_s/\rho$.
c_s	Thermal speed of species s, see (3.41).
c_p	Mass-averaged specific heat at constant pressure.
c_v	Mass-averaged specific heat at constant volume.
c_{vs}	Translational-rotational specific heat at constant volume of species s.
$c_{vtr\,s}$	Translational specific heat at constant volume of species s.
$c_{vrot\,s}$	Rotational specific heat at constant volume of species s.
$c_{vvib\,s}$	Vibrational specific heat at constant volume of species s.
C	Jacobian of W with respect to U.
$C_A, C_{A'}$	Jacobians used in diagonalization of A', see (4.15).
C_{f_m}	Constant for use in the Arrhenius form of reaction rates, see (3.51).
$\mathcal{D}$	Diffusion coefficient of uncharged species.
$\mathcal{D}_s$	Diffusion coefficient of species s.
d_s	Molecular diameter of species s.
e	Electron charge.
e_e	Electron translational energy per unit mass.
$e_{el\,s}$	Electronic energy of species s per unit mass, see (3.26).
e_{vs}	Vibrational energy per unit mass of species s.
$e^*_{vs}(T)$	Vibrational energy per unit mass of species s at the local T.
E	Total energy per unit volume.
E_e	Electron translational energy per unit volume.
E_{vs}	Vibrational energy per unit volume of species s.
E_s	Total energy per unit volume of species s.
E_i	Electric field in the i direction.
F, G	Flux vectors in the x and y directions.
F', G'	Rotated flux vectors in the ξ and η directions, see (4.7).
F'_I, F'_v	Inviscid and viscous components of F'.
G'_I, G'_v	Inviscid and viscous components of G'.
g_{is}	Degeneracy of electronic states for state i of species s, see (3.26).
h_s	Enthalpy per unit mass of species s, see (3.25).
h°_s	Heat of formation of species s.
i, j	Indices used for vector components and also to denote grid points.
k	Boltzmann constant.
k_{f_m}	Forward reaction rate of reaction m, see (3.51).
k_{b_m}	Backward reaction rate of reaction m, see (3.51).
K_{eq_m}	Equilibrium constant of reaction m, see (3.51).
Kn	Knudsen number.
$\mathcal{L}e$	Lewis number, see (3.33).
M	Mass-averaged atomic weight.
$\mathcal{M}$	Mach number.
M_s	Atomic weight of species s.
n	Number of species or time level of computation.
N_s	Number density of species s.
$\hat{N}$	Avogadro's number.

p	Pressure.
p_s	Species s partial pressure.
P_{si}	Momentum transfer rate of species s in direction i.
P_{sr}	Probability of vibration energy transfer, see (3.47).
q_j	Translational-rotational heat conduction in direction j.
q_{ej}	Electron translational heat conduction in direction j.
q_{tj}	Total heat conduction in direction j.
q_{vsj}	Vibrational heat conduction of species s in direction j.
Q_{vs}	Vibrational energy transfer rate of species s.
Q_{e-vs}	Electron-vibration energy transfer rate of species s.
Q_{T-e}	Translation-electron energy transfer rate.
Q_{T-vs}	Translation-vibration energy transfer rate of species s.
Q_{v-vs}	Vibration-vibration energy transfer rate of species s.
r_n	Nose radius.
R	Gas constant.
$\mathcal{R}$	Reaction, see (3.42).
R_A	Rotation matrix.
Re	Reynolds number based on nose radius or total length.
R_s	Gas constant of species s.
$\bar{R}$	Mass-averaged gas constant.
S	Jacobian of V with respect to U.
S_s	Exponent for use in the diffusion model of vibrational relaxation, see (3.39).
t	Time.
T	Translational-rotational temperature.
T_e	Electron translational temperature.
T_{vs}	Vibrational temperature of species s.
$\bar{T}$	Average temperature for use in reaction rates.
$u,\ v$	Mass-averaged velocity components in x and y direction.
u_j	Mass-averaged velocity vector.
u_{sj}	Species s velocity vector.
v_{sj}	Species s diffusion velocity vector.
$u_s,\ v_s$	Diffusion velocities of species s in x and y directions.
$u',\ v'$	Mass-averaged velocity components normal and tangential to a surface.
U	Vector of conserved quantities.
V	Vector of non-conserved variables.
w_s	Mass source term due to reaction of species s.
W	Source vector.
$x,\ y$	Cartesian coordinates.
x_j	Cartesian coordinate vector.
X_s	Molar concentration of species s.
Z_s	Charge number of species s.
Z_{sr}	Number of $s-r$ collisions per unit time.
$\bar{\gamma}$	Effective ratio of specific heats.
δ_{ij}	Kronecker symbol.
δU	Implicit change in the vector of conserved quantities.
Δt	Time step.
ΔU	Explicit change in the vector of conserved quantities.
ε_{vs}	Vibrational energy per particle of species s.
η_m	Constant for use in Arrhenius form of reaction rate for reaction m, see (3.51).
$\theta_{cl\ is}$	Electronic activation energy of state i for species s, see (3.26).
θ_m	Characteristic temperature of reaction for reaction m.
θ_s	Characteristic temperature for use in diffusive model of vibrational relaxation.
θ_{vs}	Characteristic temperature of vibration of species s.
κ	Conductivity of translational-rotational temperature.
κ_e	Conductivity of electron translational temperature.
κ_{vs}	Conductivity of vibrational temperature of species s.
λ	Second coefficient of viscosity.
$\Lambda_{A'}$	Diagonal matrix of convection speeds of characteristic variables for A'.
$\Lambda_{A'+},\ \Lambda_{A'-}$	Diagonal matrices of positive and negative convection speeds of characteristic variables for A'.
μ	Viscosity of mixture.
μ_s	Species viscosity.
$\xi,\ \eta$	General coordinate directions, ξ along the body and η normal to the body.
ρ	Density.
ρ_s	Density of species s.
σ_{sr}	Collision cross-section for species s and r. (Specific to the process.)
τ_{cs}	Collision limited vibrational relaxation time of species s.
τ_{es}	Electron energy relaxation time of species s.
τ_{ij}	Shear stress tensor.
τ_{sij}	Species shear stress tensor.
τ_{sL-T}	Landau-Teller vibrational relaxation time of species s, see (3.37).
τ_{vs}	Vibrational relaxation time of species s, see (3.40).
ϕ_s	Parameter for use in Wilke mixing model, see (3.31).
ψ	Reactivity of the gas.

$$\frac{D_+Z_{ij}}{\Delta\xi} \equiv Z_{i+1j} - Z_{ij} \qquad \frac{D_-Z_{ij}}{\Delta\xi} \equiv Z_{ij} - Z_{i-1j}$$

$$\frac{D_+Z_{ij}}{\Delta\eta} \equiv Z_{ij+1} - Z_{ij} \qquad \frac{D_-Z_{ij}}{\Delta\eta} \equiv Z_{ij} - Z_{ij-1}$$

1. INTRODUCTION

Computational fluid dynamics involves the numerical simulation of the equations of motion which are the conservation of mass, momentum and energy. The general form these equations for continuum flows are the compressible Navier-Stokes equations. Many flowfields have been well simulated for a variety of shapes and flow conditions where strong viscous/inviscid interactions and/or flow separation are important by solving these equations in a time-like manner until a steady state is asymptotically achieved. Real gas effects include thermo-chemical nonequilibrium, where finite rate processes for chemical and energy exchange phenomena occur, and radiative transport is a coupled process. To account for chemical reactions, conservation equations for each chemical species must be added to the flowfield equation set. There are 5 flowfield equations; one continuity, three momentum, and one energy equation. For dissociating and ionizing air there may be typically 11 reacting species (N_2, O_2, N, O, NO, O^+, N^+, O_2^+, N_2^+, NO^+, e^-). The inclusion of conservation equations for each of these species nearly triples the number of equations to be solved. When there are combustion processes or gas/surface interactions or ablation products, the number of species increases dramatically. To account for thermal nonequilibrium there are additional energy equations to describe the energy exchange between the various energy modes (translational, rotational, vibrational, electronic, etc.) To further complicate the analysis the range of time scales involved in thermo-chemical processes is many orders of magnitude wider than the mean flow time scale. This is the single most complicating factor in reacting flow simulation. Coupled radiative transport results in a system of integrodifferential equations which are exceedingly difficult to solve. Simplifying assumptions, such as optical transparency, or gray gas, or tangent slab models, are generally used to reduce this level of complexity. A wide variety of simplifications are used to alleviate problems associated with widely disparate time scales and are discussed briefly next.

Many flows can be adequately approximated by assuming an equilibrium real gas. Here all the reaction rates are assumed to be fast enough relative to the fluid motion rate so that the gas is everywhere in local equilibrium and both the thermal and chemical state of the gas can be defined solely by the local temperature and pressure. Reactions are allowed to occur but are completely uncoupled from the flowfield equations. This is a good approximation for lower altitudes and can be used for a major portion of the analysis of such vehicles as hypersonic aircraft which fly in the sensible part of the atmosphere. In the other extreme, reactions are sometimes so slow that the gas can be considered frozen in a particular chemical state. This phenomenon typically occurs in regions of rapid expansion such as in jets or base regions of body shapes, but can sometimes be used behind compressive shocks as well.

When the thermal and chemical time scales are not negligible compared to the fluid dynamic time scale, finite rate processes must be considered. If the chemical time scale is of the order of the fluid dynamic time scale and the thermal time scale is very small (as typically occurs at lower temperatures, say of the order of just a few thousand degrees K) then thermal equilibrium can be assumed. Here we need to consider finite chemical rates along with the fluid motion. In the more general case (as will occur at higher temperatures) both the thermal and chemical rate processes must be considered. In this case the chemical rate processes are typically strongly dependent on the nonequilibrium thermal state of the gas. The time scales can now vary over an extremely wide range, resulting in a stiff behavior of the complete equation set. To accurately resolve all the time scales the flowfield, species, and internal energy equations must be solved in a fully coupled manner. In cases when the chemical rates are either relatively fast or relatively slow, the species equations can be effectively uncoupled from the flowfield equations and solved separately in a loosely coupled manner, often by a different (typically implicit) numerical technique.

To validate these real gas codes both ground based and flight experiments are necessary to assess the effects of chemical kinetics, high enthalpy, low density and scale. Shown in Fig. 1 are flight domains in terms of Reynolds number and flight speed and enthalpy (Fig. 1a) and in terms of altitude and flight speed (Fig. 1b) for typical aerospace vehicles in hypersonic flight. Typically, at speeds above 8,000 fps there are significant levels of oxygen dissociation, above 15,000 fps nitrogen dissociates, and above 30,000 fps there are significant levels of ionization. When the Reynolds number is large, corresponding to high density, low altitude flight, the chemical reactions (dissociation and ionization) occur sufficiently fast that the assumption of chemical equilibrium is generally appropriate. As the density (and Reynolds number) decreases with increasing altitude, the molecular mean-free-paths increase and finite rate thermo-chemistry becomes important. At even higher altitudes assumptions related to continuum flow break down and slip boundary conditions and higher order constitutive relationships for momentum and energy transport must be considered. Lower density regimes are desribed by the Boltzmann equation and ultimately by free molecule flow.

One aerospace vehicle, the aeroassist orbital transfer vehicle (AOTV), is chosen in the present context to best illustrate the features of three-dimensional chemically reacting flows with separation and will be the basis for most of the subsequent discussion. Other aerospace vehicles, such as transatmospheric vehicles (TAVs) and boost-glide vehicles (BGVs), can be analyzed with the tools that are developed for AOTV simulation, and in some cases the analyses can even be simplified.

In the analyses developed herein we are concerned with fairly low flight Reynolds numbers, which indicate laminar flows, due to the low density associated with high altitude flight. Hence, the added complexity of turbulent transport will not be considered. For slender vehicles flying in the lower atmosphere turbulence will be an important consideration, but here the effects of finite rate chemistry are minimal, particularly in the localized regions where there may be flow separation. The problems of turbulence and flow separation are treated in another section of this lecture series by Mr. Cousteix and by Prof. Dolling.

2. QUALITATIVE DESCRIPTION OF AOTV FLOWFIELD

The qualitative aspects of a typical AOTV flowfield are discussed in this section, with attention paid to where particular physical effects must be included in an analysis. This will indicate what type of numerical modeling will be adequate in each region of the flow.

2.1 AOTV Forebody Flowfield

The AOTV forebody flowfield, illustrated schematically in Fig. 2a, is dominated by the presence of the strong bow shock wave and the consequent heating, and chemical reaction of the gas. At typical flight conditions (about $M_\infty = 30$ and 80 km altitude), the

thermal excitation and chemical reaction of the gas occur slowly enough that a significant portion of the flowfield is in a state of thermo-chemical nonequilibrium. A second important effect is the presence of the thick boundary layer along the surface of the AOTV. In this region there are large thermal and chemical species gradients due to the interaction of the gas with the wall. Also at high altitudes the shock wave and the boundary layer may become so thick that they merge; in this case the entire shock layer is dominated by viscous effects.

A gas is in thermal nonequilibrium if, for a given density and internal energy, it is in a thermodynamic state where the internal energy modes cannot be characterized by a unique temperature, and is in chemical nonequilibrium if its chemical state does not satisfy chemical equilibrium conditions. As was asserted above, a portion of an AOTV forebody flowfield is in thermo-chemical nonequilibrium. This can be seen by considering the trajectory of a control volume of air that enters the AOTV flowfield. The translational modes of this piece of gas are heated strongly as it passes through the bow shock wave. The translational modes transfer their energy to the other internal energy modes of the molecules through inter-molecular collisions. Also chemical reaction of the gas species occur such as dissociation and ionization. These processes require some number of collisions for equilibrium to be reached. Thus as the element of gas is convected through the shock layer, these energy exchanges and chemical reactions occur at finite rates until, at some point on the streamline, equilibrium is achieved. Therefore there will be significant thermo-chemical nonequilibrium near the bow shock wave and near equilibrium a large distance along the fluid element's streamline. The rate at which equilibration occurs is dependent on the free-stream density and speed, or altitude and Mach number. A parameter that quantifies the degree of chemical nonequilibrium for a particular condition may be derived as follows; a similar parameter may be derived for the relaxation of energy modes.

Consider the species s mass conservation equation for a steady-state condition

$$\frac{\partial}{\partial x_j}(\rho_s u_{sj}) = w_s,$$ (2.1)

where w_s is the mass source term due to chemical reactions. We may non-dimensionalize this equation with the free-stream (∞) conditions and the reference length, L, as

$$\frac{L}{\rho_\infty u_\infty}\frac{\partial}{\partial x_j}(\rho_s u_{sj}) = \frac{L w_s}{\rho_\infty u_\infty},$$

$$\frac{\partial}{\partial \bar{x}_j}(\bar{\rho}_s \bar{u}_{sj}) = \frac{L w_s}{\rho_\infty u_\infty} = \psi.$$ (2.2)

The non-dimensional quantity, ψ, which is a form of the Damköhler number, may be thought of as the ratio of the fluid time scale to the chemical time scale, or as the ratio of the chemical reaction rate to the fluid motion rate. For the case of chemical equilibrium, the chemical rates are infinitely fast, or $\psi \to \infty$, and for frozen-flow case where the fluid rates are much larger than the chemical rates, $\psi \to 0$. For conditions between these two limits the flow is, to some degree, in chemical nonequilibrium.

A more useful form of the parameter ψ may be derived by considering the primary reaction that occurs in high-temperature air flows, which is the dissociation of diatomic oxygen by collisions with diatomic oxygen and nitrogen. In this case we have

$$w_s = w_{O_2} = k_f \rho_{O_2}\left(\frac{\rho_{O_2}}{M_{O_2}} + \frac{\rho_{N_2}}{M_{N_2}}\right) = k_f \rho_{O_2}\frac{\rho}{M}.$$ (2.3)

If we substitute expression the Arrhenius form for the forward reaction rate, $k_f = CT^\eta \exp(-\theta_{O_2}/T)$, and use the hypersonic limit for the density change across the shock, we have

$$\psi_{O_2} = K_{O_2} T_{shk}^{-1} \exp(-59500/T_{shk})\frac{\rho_\infty L}{u_\infty},$$

$$K_{O_2} = c_{O_{2\infty}}\left(\frac{\gamma+1}{\gamma-1}\right)^2\frac{C}{M} \simeq 3.4 \times 10^{16} c_{O_{2\infty}} \ (\text{m}^3 \text{ K}/\text{kg s}),$$ (2.4)

where we have substituted the values of the constants that were used in the computations. The post-shock temperature, T_{shk}, can be approximated using the hypersonic shock relation

$$T_{shk} \simeq \frac{2\gamma(\gamma-1)}{(\gamma+1)^2}M_\infty^2 T_\infty.$$ (2.5)

We have assumed that the peak reaction rate occurs immediately behind the normal shock wave, and for simplicity that the reaction is governed by the translational temperature only. Alternatively, we can write ψ_{O_2} in terms of the Reynolds number (based on the reference length) as

$$\psi_{O_2} = K_{O_2} T_{shk}^{-1} \exp(-59500/T_{shk})\frac{Re\,\mu_\infty}{u_\infty^2}.$$ (2.6)

This parameter is most strongly influenced by the exponential term in the post-shock temperature, which is proportional to the square of the free-stream Mach number. For the aeroassist flight experiment (AFE) $\psi_{O_2} = 310$ at perigee conditions ($M_\infty = 32$ and 78 km altitude) and $\psi_{O_2} = 64$ at an entry condition where $M_\infty = 36$ at 87 km altitude. Thus for AOTV-like conditions $\psi_{O_2} = \mathcal{O}(10^2)$; we will see that there is a significant degree of thermo-chemical nonequilibrium in this regime and that consideration of these effects is required for accurate results.

A second important effect in the AOTV forebody region is the interaction of the wall with the thermally excited and reacted gas in the boundary layer. Because of the high altitudes the Reynolds number is relatively small for AOTV conditions (typically on the order of 10^4 based on free-stream conditions and nose radius). Thus the boundary layer will be thick and viscous effects will dominate much of the flowfield. Also, as the boundary layer is influenced by the cool wall, chemical reactions can be slowed or halted in the vicinity of the wall. The wall can also interact chemically with the flowfield due to catalytic effects that promote the recombination of reacted species at the wall. Thus the inclusion of viscous effects for AOTV forebody flowfield analyses is mandatory. At high altitudes, the usual assumption of perfect thermal accomodation and no-slip at the wall breaks down. Therefore, for some conditions, temperature and velocity slip effects must also be included.

Another effect related to the low density regime in which AOTV's would operate is the thickening of the bow shock wave to encompass a large volume of the flowfield. The bow shock wave is several mean-free-paths thick and at high altitudes, this implies that the bow shock thickness is an appreciable fraction of the shock standoff distance and can merge with the thick boundary layer.

For these thick shock waves, relaxation of internal modes occurs within the shock wave; this effect must be included in any analysis where rarefaction occurs. Also it has been shown that the Navier-Stokes equations under-predict the shock thickness and misrepresent the separation between the density and temperature profiles within a shock wave (Fiscko and Chapman[1]). Thus for some regimes the predicted shock thickness using Navier-Stokes solvers is suspect.

2.2 AOTV Afterbody Flowfield

The flow about the AOTV afterbody, illustrated in Fig. 2b, is dominated by two phenomena; the presence of the rapid expansion as the highly compressed gas flows around the shoulder of the vehicle and the related initiation of separation of the gas near the vehicle corner. These two effects require specific modeling approaches and capabilities.

The expansion, which is dominated by inviscid effects, has the effect of rapidly lowering the translational temperature, density and pressure of the gas. However, the chemical state of the gas and the temperatures that characterize the energy in the internal modes will tend to remain constant, or frozen. This results in a flow where the vibrational and electronic temperatures of the gas are higher than the translational temperature and where the gas is more dissociated and excited than predicted by equilibrium conditions. As the gas flows downstream, recombination occurs slowly the vibrational temperature rises still higher; a result of a portion of the chemical energy of recombination being put into the vibrational modes of the gas. This can cause the gas to radiate significantly in the afterbody region. Another important effect present in the inviscid, expanded region is the presence of species gradients across the wake. This is caused by some portion of the gas having passed through a relatively weak oblique shock wave where it hardly reacts, and another part of the gas having passed through the strong forebody shock where reactions are substantial. Thus the gas near the center of the wake tends to be more dissociated than that in its extremities and consequently γ, the ratio of specific heats, varies across the wake.

A second inviscid effect associated with the wake structure is the presence of a wake shock. As the flow expands around the shoulder of the vehicle, some of it is directed toward the centerline of the body. However, this supersonic flow must change direction and a reflecting shock and an oblique shock wave is formed. The gas becomes compressed in this region, and as there is are high vibrational and electronic temperatures due to freezing, the gas can radiate significantly.

The location of the separation on the back face of the AOTV is affected by: the state of the boundary layer on the shoulder, the Reynolds number, whether the flow is turbulent or laminar, the ratio of specific heats, and the body geometry. For many cases of interest, particularly at high altitude, the flow can remain attached over a significant portion of the vehicle's afterbody. The location of separation influences the dimension of the recirculation zone and the strength of the shear-layer that forms between the recirculating gas and the external, rapidly expanding, supersonic flow. The recirculation zone entrains gas that was in the forebody boundary layer which is relatively cool but highly dissociated. This recirculation zone will be unsteady, the magnitude of which depending on how the shear-layer behaves and the feedback between the body motion and the state of the gas in the separated region.

The modeling of the free shear-layer must account for large gradients of velocity, temperature, density and species concentration across it, and for the possibility that the flow may be turbulent and unsteady. The numerical treatment of the problem is particulary difficult because of these effects and also due to the uncertain location of this structure.

The AOTV afterbody flowfield is characterized by the presence of thermo-chemical nonequilibrium, large gradients in thermodynamic quantities and chemical state, and a large separated region. The combination of these factors stretches computation fluid dynamics beyond it current capabilities.

3. MATHEMATICAL FORMULATION

In this section the set of coupled partial differential equations that describes the dynamics of a high temperature flowfield is derived. This equation set is the Navier-Stokes equations expanded so that it is applicable to a gas that is vibrationally and electronically excited, chemically reacting and weakly ionized. The corresponding equation of state for this gas is also developed. The assumptions underlying the current description are discussed and the limitations are exposed. The models that represent the transfer of mass between different chemical species and the transfer of energy between different energy modes is described.

3.1 Basic Assumptions

The nonequilibrium flowfields that are of interest here are assumed to conform to particular criteria as outlined below, which make the derivation of the governing equations feasible and are the basis for the entire solution technique.

The flowfields are assumed to be accurately described by a continuum formulation. The Knudsen number, Kn, is defined to be the ratio of the mean-free-path associated with the flow conditions to the characteristic length scale of the body or of the flow itself. The continuum formulation is valid for Knudsen numbers much less than one[*] where there are a large number of molecules within a computational volume. This implies that there is little statistical variation at any point, and as a result, the continuum description of the viscous fluxes is consistent. A second requirement of this approach regards the treatment of the interaction between the gas and the surface of the body. It is assumed that there are a large enough number of collisions of the gas molecules with the wall so that there is no velocity or temperature slip at the wall. This condition is also satisfied with a small Knudsen number.

It is assumed that the thermal state of the gas can be described by separate and independent temperatures. The energy in the translational modes of all the heavy-particles, i.e. everything except the electrons, is assumed to be characterized by a single translational temperature. The rotational state of the diatomic molecules is assumed to be equilibrated with this translational temperature. Thus, we have a single temperature, T, that characterizes the translational-rotational state of the gas. This assumption is reasonable at conditions within the continuum regime where, for air species rotational equilibrium with translation takes of the order of five collisions because of the low characteristic temperature of rotation.

The energy contained in the vibrational modes of diatomic species s can be described by the vibrational temperature, T_{vs}, which is not related to the rotational state of the gas. The vibrational state is assumed to conform to the harmonic oscillator description at all vibrational temperatures. A second assumption implicit in the formulation of the vibrational state is that rotational-vibrational coupling

---

[†] This requirement is usually met with $Kn < 0.1$ and flowfields for this Kn have been computed.

is not significant. Each diatomic species is assumed to have a separate vibrational energy, and a corresponding vibrational temperature. The translational energy of the free electrons is quantified by the electron temperature, T_e. The excited electronic states of the molecules are assumed to be in a Boltzmann distribution corresponding to the electron translational temperature. The gas may be only weakly ionized, which implies that there the mass fraction of ions is less than one percent[tt]. Although this assumption is not implemented explicitly in the derivation of the governing equations, several terms that can have a significant influence in a highly ionized plasma have been ignored.

3.2 The Conservation Equations

The time-dependent equations that govern the motion of a gas mixture are derived in this section. First the individual species mass, momentum, and energy conservation equations are discussed and then these are combined to yield the complete equation set.

The equations that describe the conservation of mass, momentum, and energy for the chemical species s of the gas may be written as follows. The species mass conservation is given by[2-4]

$$\frac{\partial \rho_s}{\partial t} + \frac{\partial}{\partial x_j}\left(\rho_s u_{sj}\right) = w_s. \tag{3.1}$$

The species momentum conservation is written as

$$\frac{\partial}{\partial t}\left(\rho_s u_{si}\right) + \frac{\partial}{\partial x_j}\left(\rho_s u_{si} u_{sj} + p_s \delta_{ij} + \tau_{sij}\right) = N_s e Z_s \tilde{E}_i + P_{si}, \tag{3.2}$$

and the species energy conservation as

$$\frac{\partial E_s}{\partial t} + \frac{\partial}{\partial x_j}\left((E_s + p_s)u_{sj} + u_{si}\tau_{sij} + q_{tsj}\right) = N_s e Z_s \tilde{E}_i u_{si} + Q_s, \tag{3.3}$$

where u_{si} is the species velocity in the i direction. The terms appearing on the right-hand side of these equations, w_s, P_{si}, and Q_s, represent the mass, momentum, and energy transfer rates respectively. The mass source term, w_s, is the rate of production of species s due to chemical reactions. P_{si} is the rate of momentum transfer between species s and the other molecules due to collisions and force-field interactions in the i direction. And Q_s represents the rate of energy transfer to and from the various energy modes of s due to interactions with other species. The quantity $\tilde{E}_i$ is the electric field in the i direction due to charge separation; it acts on ions and electrons only. τ_{sij} is the shear stress tensor and q_{tsj} is the total heat flux vector of species s.

The vibrational energy conservation equation for each diatomic species may be derived by considering the conservation of the vibrational energy per particle, ε_{vs}, as it is convected at a velocity u_{si}. If there is no conduction of vibrational energy or energy transfer, then we have simply

$$\frac{\partial \varepsilon_{vs}}{\partial t} + u_{sj}\frac{\partial \varepsilon_{vs}}{\partial x_j} = 0. \tag{3.4}$$

The vibrational energy per particle is related to the vibrational energy per unit volume by the relation

$$E_{vs} = \rho_s e_{vs} = \rho_s \varepsilon_{vs}\frac{\hat{N}}{M_s}. \tag{3.5}$$

If we multiply equation (3.4) by $\rho_s \hat{N}/M_s$, and use expression (3.5), we have the equation

$$\frac{\partial \rho_s e_{vs}}{\partial t} - e_{vs}\frac{\partial \rho_s}{\partial t} + \frac{\partial}{\partial x_j}\left(\rho_s e_{vs} u_{sj}\right) - e_{vs}\frac{\partial}{\partial x_j}\left(\rho_s u_{sj}\right) = 0. \tag{3.6}$$

The vibrational energy conservation equation results by multiplying equation (3.1) by e_{vs} and adding it to equation (3.6), to get

$$\frac{\partial E_{vs}}{\partial t} + \frac{\partial}{\partial x_j}\left(E_{vs} u_{sj}\right) = -\frac{\partial q_{vsj}}{\partial x_j} + Q_{vs} + w_s e_{vs}, \tag{3.7}$$

where the vibrational heat conduction and energy transfer rate have also been included. The term $w_s e_{vs}$ in this equation results from the derivation and is due to the fact that vibrational energy is conserved on a per-particle basis, not on a volumetric basis. It represents the amount of vibrational energy that is added to or taken away from the vibrational energy due to the production or destruction of species s. We have not taken into account any preferential removal of vibrational energy due to dissociation with this approach. That is, the diatomic molecules that dissociate tend to be those in the highly excited vibrational levels; thus they carry more than the average vibrational energy with them and a dissociation reaction suppresses the vibrational temperature[5-7]. However, as indicated by Park[8,9], ignoring the effect of preferential removal is appropriate because the dissociation reaction rates that are available currently were computed without including this effect and this approach is consistent with the use of these rates.

In principle, the n component gas could be represented by solving equations (3.1-3) and (3.7) for each species. However, this would entail the solution of n momentum equations and the evaluation of the momentum exchange term P_{si}. This approach is not feasible for a two or three-dimensional flowfield with more than a few species. The problem may be simplified by assuming that the species velocities, u_{si}, are approximately the same size as the mass-averaged velocity, u_i, defined by

$$u_i = \sum_{s=1}^{n}\frac{\rho_s}{\rho}u_{si}, \qquad \rho = \sum_{s=1}^{n}\rho_s. \tag{3.8}$$

[tt] Weak ionization depends on having a small Coulomb cross-section relative to the electron-neutral cross-section (see Section 3.6.2).

Then we define the diffusion velocity, v_{si}, to be the difference between the species velocity and the mass-averaged velocity

$$v_{si} = u_{si} - u_i. \tag{3.9}$$

Expressed with these new variables, the species mass conservation equation, (3.1), becomes

$$\frac{\partial \rho_s}{\partial t} + \frac{\partial}{\partial x_j}\left(\rho_s u_j\right) = -\frac{\partial}{\partial x_j}\left(\rho_s v_{sj}\right) + w_s. \tag{3.10}$$

The species momentum equation, (3.2), may be summed over all species to yield the mass-averaged momentum equation

$$\frac{\partial}{\partial t}\left(\rho u_i\right) + \frac{\partial}{\partial x_j}\left(\rho u_i u_j + p\delta_{ij}\right) = -\frac{\partial}{\partial x_j}\sum_{s=1}^{n}\rho_s v_{si}v_{sj} - \frac{\partial \tau_{ij}}{\partial x_j} + \sum_{s=1}^{n}eN_s Z_s \tilde{E}_i, \tag{3.11}$$

where the total pressure, p, and shear stress τ_{ij}, are defined as the sum of the species quantities. By making this summation, the interspecies momentum transfer terms, P_{si}, sum identically to zero, which is a significant simplification. However, the sum of the induced electric field forces is not zero due to the differing charge numbers on ions and electrons.

A similar summation may be made to the species energy equation, (3.3), to yield the total energy equation for the mixture

$$\frac{\partial E}{\partial t} + \frac{\partial}{\partial x_j}\left((E+p)u_j\right) = -\frac{\partial}{\partial x_j}\left(q_j + q_{vj} + q_{ej}\right) - \frac{\partial}{\partial x_j}\left(u_i \tau_{ij}\right)$$
$$-\frac{\partial}{\partial x_j}\sum_{s=1}^{n}v_{si}\left(h_s\delta_{ij} + \tau_{sij}\right) + \sum_{s=1}^{n}eN_s Z_s \tilde{E}_i\left(u_i + v_{si}\right). \tag{3.12}$$

The heat conduction vector has been expressed in component form, where each term is due to gradients in the different temperatures in the flowfield.

In addition to the total energy equation, we require an equation for each form of energy that is treated separately. In this case, we are using the approach where a vibrational energy for each diatomic species and the electron energy are computed. Thus, for a gas with m diatomic species, we need to solve m vibrational energy equations, (3.7), which may be re-written as

$$\frac{\partial E_{vs}}{\partial t} + \frac{\partial}{\partial x_j}\left(E_{vs}u_j\right) = -\frac{\partial}{\partial x_j}\left(E_{vs}v_{sj}\right)$$
$$-\frac{\partial q_{vsj}}{\partial x_j} + Q_{T-vs} + Q_{v-vs} + Q_{e-vs} + w_s e_{vs}. \tag{3.13}$$

The various mechanisms to transfer energy to the vibrational energy modes have been represented here. Q_{T-vs}, Q_{v-vs}, and Q_{e-vs} are respectively the rates of translation-vibration, vibration-vibration, and electron-vibration energy exchange.

The dynamics of the electron translational energy, E_e, are computed with the solution of the electron energy equation which is a species energy equation, (3.3), applied to electrons. This may be written as

$$\frac{\partial E_e}{\partial t} + \frac{\partial}{\partial x_j}\left((E_e + p_e)u_j\right) = -\frac{\partial}{\partial x_j}\left((E_e + p_e)v_{ej}\right) - \frac{\partial q_{ej}}{\partial x_j}$$
$$-\frac{\partial}{\partial x_j}\left((u_i + v_{ei})\tau_{eij}\right) - N_e e \tilde{E}_i(u_i + v_{ei}) + Q_{T-e} - \sum_{s=1}^{m}Q_{e-vs} + w_e e_e. \tag{3.14}$$

Where Q_{T-e} is the translation-electron energy exchange rate. We should note that the transport of electron energy is fundamentally different than that of vibrational energy. The vibrational energy of a species is convected at the local velocity u_i, whereas the electron energy convection speed is also a function of the local electron pressure, p_e.

These differential equations describe the flow of an n species, the first m of which are diatomic, weakly ionized gas. The solution of these equations yields the dynamics of the conserved flow variables $\rho_1 \ldots \rho_n$, ρu_i, E_v: E_{vm}, E_e', and E.

3.2.1 Simplifications to the Conservation Equations

Some minor simplifications to the governing equations may be made which make it possible to determine an algebraic expression for the electric field. Consider the species momentum equation, (3.2), applied to electrons

$$\frac{\partial}{\partial t}\left(\rho_e u_{ei}\right) + \frac{\partial}{\partial x_j}\left(\rho_e u_{ei}u_{ej} + p_e\delta_{ij}\right) = -\frac{\partial \tau_{eij}}{\partial x_j} - eN_e \tilde{E}_i + P_{ei}. \tag{3.15}$$

If we take the ratio of the dynamic pressure of the electron gas to the electron pressure and assume that the electron speed and temperature are about the same as the bulk gas, we have

$$\frac{\rho_e u_e^2}{p_e} = \frac{M_e u_e^2}{RT_e} \simeq \frac{M_e u^2}{RT} \simeq \frac{M_e}{M}\mathcal{M}^2. \tag{3.16}$$

The ratio of electron mass to heavy particle mass, M_e/M, is of the order of 10^{-6} and for conditions of interest the square of the Mach number will be of the order of 10^3 at most. Therefore we can neglect the electron dynamic pressure relative to the electron pressure. The electron shear-stress is also small relative to the electron pressure, and because we are solving for a steady-state, we may neglect

the time derivative of the momentum. The momentum transfer rate due to inter-species collisions, P_{ei}, is assumed to be small for electrons due to their small collision cross-section. Therefore, by neglecting these terms, the electric field may be expressed as

$$\breve{E}_i \simeq -\frac{1}{N_e e}\frac{\partial p_e}{\partial x_i}. \tag{3.17}$$

This simplification eases the solution considerably because the electric field is fundamentally represented by a set of electro-dynamic equations[4]

A further modification to this expression is required to diagonalize the equation set for efficient numerical solution, as will be seen in the following section. Namely, the term $\frac{\partial}{\partial x_j}p_e u_j$ will be moved to the right-hand side and treated as a viscous term, taking the equation set out of conservation-law form. Then (3.14) becomes

$$\frac{\partial E_e}{\partial t} + \frac{\partial}{\partial x_j}\left(E_e u_j\right) = -\frac{\partial}{\partial x_j}\left(E_e v_{ej}\right) - p_e\frac{\partial}{\partial x_j}\left(u_j + v_{ej}\right) - \frac{\partial q_{ej}}{\partial x_j}$$
$$+ Q_{T-e} - \sum_{s=1}^{m} Q_{e-vs} + w_e e_e, \tag{3.18}$$

where we have assumed that the electron shear stresses are negligible. The final assumption is that the terms which involve the square of diffusion velocities or are products of species shear-stresses and diffusion velocities are negligible; this alters (3.11) and (3.12).

3.5 Equations of State

The relationship between the conserved quantities and the non-conserved quantities such as pressure and temperature are derived in this section. The total energy, E, is made up of the separate components of energy which may be written as

$$E = \sum_{s\neq e}^{n} \rho_s c_{vs}T + \frac{1}{2}\sum_{s\neq e}^{n}\rho_s u_i u_i + \sum_{s=1}^{m} E_{vs} + E_e + \sum_{s\neq e}^{n}\rho_s h_s^o + \sum_{s\neq e}^{n}\rho_s e_{cls}. \tag{3.19}$$

This expression may be inverted to yield the energy in the translational-rotational modes, and consequently T. The constants of specific heat at constant volume, c_{vs}, are the sum of the specific heat of translation, $c_{vtr\,s}$, and the specific heat of rotation, $c_{vrot\,s}$. These are given by

$$c_{vtr\,s} = \frac{3}{2}\frac{R}{M_s},$$
$$c_{vrot\,s} = \begin{cases} \frac{R}{M_s}, & \text{for } s = 1, m; \\ 0, & \text{otherwise.} \end{cases} \tag{3.20}$$

The vibrational temperature of species s is determined by inverting the expression for the vibrational energy contained in a harmonic oscillator at the temperature T_{vs}

$$E_{v_s} = \rho_s\frac{R}{M_s}\frac{\theta_{vs}}{e^{\theta_{vs}/T_{vs}} - 1}, \tag{3.21}$$

where θ_{vs} is the characteristic temperature of vibration. The electron temperature is determined by inverting the relation between the electron energy, E_e, and the energy contained in the electron thermal and kinetic energy

$$E_e = \rho_e c_{ve}T_e + \frac{1}{2}\rho_e u_i u_i. \tag{3.22}$$

The electronic excitation energy of the molecules which is characterized by T_e has been included in the total energy and not in the free electron translational energy. The total pressure is the sum of the partial pressures,

$$p = \sum_{s\neq e}^{n}\rho_s\frac{R}{M_s}T + p_e, \tag{3.23}$$

and the electron pressure is given by

$$p_e = \rho_e\frac{R}{M_e}T_e. \tag{3.24}$$

The enthalpy per unit mass, h_s, is defined to be

$$h_s = c_{vs}T + \frac{p_s}{\rho_s} + e_{vs} + h_s^o + e_{cls}. \tag{3.25}$$

The expression for the energy contained in the excited electron states comes from the assumption that they are in a Boltzmann distribution governed by the electron translational temperature, T_e (Lee[2]). This yields

$$e_{cls} = \frac{R}{M_s}\frac{\sum_{i=1}^{\infty} g_{is}\theta_{cl\,is}\exp(-\theta_{cl\,is}/T_e)}{\sum_{i=0}^{\infty} g_{is}\exp(-\theta_{cl\,is}/T_e)}, \tag{3.26}$$

where g_{is} is the degeneracy of state i and $\theta_{cl\,is}$ is the excitation energy of that state. In this study only the terms in the sum up to $i = 1$ are included.

3.5 Shear Stresses, Heat Fluxes, and Diffusion Velocities

The shear stresses are assumed to be proportional to the first derivative of the mass-averaged velocities and the Stokes assumption for the bulk viscosity is made. Therefore the expression for the shear stress tensor is

$$\tau_{ij} = -\mu\left(\frac{\partial u_i}{\partial x_j} + \frac{\partial u_j}{\partial x_i}\right) - \lambda\frac{\partial u_k}{\partial x_k}\delta_{ij}, \qquad \lambda = -\frac{2}{3}\mu \tag{3.27}$$

And the heat conduction vectors are are assumed to be given by the Fourier heat law

$$q_j = -\kappa\frac{\partial T}{\partial x_j},$$
$$q_{vsj} = -\kappa_{vs}\frac{\partial T_{vs}}{\partial x_j}, \tag{3.28}$$

The flux of electron energy, q_{ej}, has been taken to be zero. This assumption is reasonable because the proportion of electron energy in the total energy is very small. The assumptions of a linear relation between the shear stress and the velocity gradients and between the heat fluxes and the gradients of temperature are suspect as hypersonic Mach numbers. A more accurate description is a topic of current and future research (Fiscko and Chapman[1]).

A viscosity model for reacting air developed by Blottner et al.[10] may be used to determine the species viscosity, μ_s. The model uses three constants for a curve fit and yields

$$\mu_s = 0.1\exp\left[(A_s\ln T + B_s)\ln T + C_s\right], \quad \text{(in kg/m s)} \tag{3.29}$$

where A_s, B_s, and C_s are found in the Appendix. The curve fits for the viscosity are appropriate for temperatures up to 10,000 K and for weak ionization.

The conductivity of the translational-rotational and vibrational temperatures for each species may be derived from an Eucken relation[1]. With this method it is assumed that the transport of translational energy involves correlation with the velocity, but the transport of internal energy (rotational and vibrational) involves no correlation. The result is that

$$\kappa_s = \mu_s\left(\frac{5}{2}c_{vtr\,s} + c_{vrot\,s}\right) \qquad \kappa_{vs} = \mu_s c_{vvib\,s} \tag{3.30}$$

The total viscosity and conductivity of the gas are then calculated using Wilke's[11] semi-empirical mixing rule.

$$\mu = \sum_s\frac{X_s\mu_s}{\phi_s}, \qquad \kappa = \sum_s\frac{X_s\kappa_s}{\phi_s},$$

where

$$X_s = \frac{c_s M}{M_s}, \qquad M = \left(\sum_s\frac{c_s}{M_s}\right)^{-1}, \tag{3.31}$$

$$\phi_s = \sum_{r\neq e}X_r\left[1 + \sqrt{\frac{\mu_s}{\mu_r}}\left(\frac{M_r}{M_s}\right)^{1/4}\right]^2\left[\sqrt{8\left(1 + \frac{M_s}{M_r}\right)}\right]^{-1}.$$

If we assume that the diffusive fluxes due to pressure and temperature gradients are negligible, then the diffusion velocity of each component of the gas mixture is proportional to the gradient of the mass concentration. With the additional assumption of binary diffusion where species s diffuses into a mixture of similar particles, we have

$$\rho_s v_{sj} = -\rho\mathcal{D}_s\frac{\partial c_s}{\partial x_j}. \tag{3.32}$$

The diffusion coefficient, $\mathcal{D}_s$, is derived by assuming a constant Lewis number, $\mathcal{L}e$, which by definition is given by

$$\mathcal{L}e = \frac{\mathcal{D}\rho c_p}{\kappa}. \tag{3.33}$$

The uncharged particles all have the same $\mathcal{D}$, but the diffusion coefficient for ions is assumed to be doubled (i.e. the ambipolar diffusion assumption holds) because of the existence of an electric field. The diffusion velocity of electrons is computed using

$$\mathcal{D}_e = M_e\frac{\sum_{s=\text{ions}}\mathcal{D}_s\rho_s/M_s}{\sum_{s=\text{ions}}\rho_s}, \tag{3.34}$$

which is derived from Lee[2].

3.6 Energy Exchange Mechanisms

The energy exchange mechanisms that appear on the right hand side of equations (3.13) and (3.14) must be modeled. The models that have been proposed are simplifications of the complicated energy exchange processes that occur on a molecular level. This phenomenologic treatment has inadequacies because it does not fully embody the physics of molecular interactions.

3.6.1 Translation-Vibration Energy Exchanges

The rate of energy exchange between vibrational and translational modes has been discussed extensively[8,9,12-14]. The rate of change in the population of the vibrational states at low temperatures is described well by the Landau-Teller formulation where it is

---
[1] See Vincenti and Kruger[3], pp. 15–21.

assumed that the vibrational level of a molecule can change by only one quantum level at a time (Vincenti and Kruger[3]). The resulting energy exchange rate is

$$Q_{T-v s_{L-T}} = \rho_s \frac{e_{vs}^*(T) - e_{vs}}{<\tau_{s_{L-T}}>}.$$
(3.35)

Where $e_{vs}^*(T)$ is the vibrational energy per unit mass of species s evaluated at the local translational-rotational temperature and $<\tau_{s_{L-T}}>$ is the molar averaged Landau-Teller relaxation time given by Lee (1985).

$$<\tau_{s_{L-T}}> = \frac{\sum_r X_r}{\sum_r X_r / \tau_{sr_{L-T}}}, \quad \text{for } r \neq e.$$
(3.36)

An expression developed by Millikan and White[12] yields the Landau-Teller inter-species relaxation times, $\tau_{sr_{L-T}}$, in seconds using the function

$$\tau_{sr_{L-T}} = \frac{1}{p} \exp\left[A_{sr}(T^{-1/3} - 0.015 \mu_{sr}^{1/4}) - 18.42\right], \quad p \text{ in atm},$$
$$A_{sr} = 1.16 \times 10^{-3} \mu_{sr}^{1/2} \theta_{vs}^{4/3},$$
$$\mu_{sr} = M_s M_r / (M_s + M_r).$$
(3.37)

However, at high vibrational temperatures the vibrational ladder climbing process due to heavy particle collisions is diffusive in nature[8,9,13,15]. Park (1987) proposes an empirical bridging function between the Landau-Teller and diffusive rates of the form

$$Q_{T-vs} = \rho_s \frac{e_{vs}^*(T) - e_{vs}}{<\tau_{s_{L-T}}>} \left| \frac{T_{shk} - T_{vs}}{T_{shk} - T_{vs\,shk}} \right|^{S_s - 1},$$
(3.38)

where the exponent, S_s, has the form

$$S_s = 3.5 \exp(-\theta_s / T_{shk}).$$
(3.39)

The quantities T_{shk} and $T_{vs\,shk}$ are the translational-rotational and species vibrational temperatures evaluated just behind the bow shock wave. At low temperatures, the relaxation is governed by the Landau-Teller rate, and at high temperatures, by the slower diffusive rate. The characteristic temperatures, θ_s, for use in calculating the exponent, S_s, are assumed to be as given in the Appendix.

A second modification to the translational-vibrational relaxation rate is made to account for the limiting collision cross-section at high temperature. The Landau-Teller rate expression from Millikan and White yields a relaxation rate that is unrealistically large at high temperatures due to an overprediction of the collision cross-section. The addition of the limiting cross-section rate corrects this inaccuracy. As suggested by Park[13], a new relaxation time, τ_{vs}, that is the sum of the Landau-Teller relaxation time and the collision limited relaxation time, τ_{cs}, corrects this inadequacy. Thus if we use equation (3.38) with this new rate, we have the final form of the energy exchange mechanism

$$Q_{T-vs} = \rho_s \frac{e_{vs}^*(T) - e_{vs}}{\tau_{vs}} \left| \frac{T_{shk} - T_{vs}}{T_{shk} - T_{vs\,shk}} \right|^{S_s - 1},$$
$$\tau_{vs} = <\tau_{s_{L-T}}> + \tau_{cs},$$
(3.40)

where

$$\tau_{cs} = \frac{1}{c_s \sigma_v N_s}.$$
(3.41)

c_s is the average molecular speed of species s, $c_s = \sqrt{8RT/\pi M_s}$ and N_s is the number density of the colliding particles. The expression for the limiting collision cross-section, σ_v, is assumed to be as given by (Park[13])

$$\sigma_v = 10^{-21}(50,000/T)^2 \quad \text{m}^2.$$
(3.42)

3.6.2 Translation-Electron Energy Exchanges

The energy transfer rate between the heavy-particle and electron translational modes, Q_{T-e}, is given by an expression derived from Lee[2]

$$Q_{T-e} = 3R\rho_e(T - T_e)\sqrt{\frac{8RT_e}{\pi M_e}} \sum_{r \neq e} \frac{\rho_r \hat{N}}{M_r^2} \sigma_{er},$$
(3.43)

where σ_{er}, $r \neq$ ions, are the collision cross-sections for electron-neutral interactions. The functional form of these parameters is not well known and for this work a constant σ_{er} equal to 10^{-20} m^2 was assumed. For the case of electron-ion interactions the effective Coulomb cross-section is given by (Lee[2])

$$\sigma_{e,\text{ions}} = \frac{8\pi}{27} \frac{e^4}{k^2 T_e^2} \ln\left[1 + \frac{9k^3 T_e^3}{4\pi N_e e^6}\right].$$
(3.44)

3.6.3 Electron-Vibration Energy Exchanges

The coupling of the electron energy with the vibrational energy of diatomic nitrogen is strong, but between the other vibrational states it is negligibly weak (Lee[16]). The rate of energy transfer between electron translational modes and nitrogen vibrational modes, Q_{e-vs}, is assumed to be

$$Q_{e-vs} = \rho_e \frac{M_s}{M_e} \frac{e_{vs}^*(T_e) - e_{vs}}{\tau_{es}}, \quad \text{for } s = N_2$$
(3.45)

Lee[16] derived an expression for the rate of electron-vibration energy transfer, τ_{es}, by solving the system of master equations that accounts for transitions of multiple levels. τ_{es} was curve-fit to the results of Lee using two quadratics in the logarithm (base 10) of the electron temperature. This expression is

$$\log(p_e \tau_{es}) = \begin{cases} 7.50(\log T_e)^2 - 57.0 \log T_e + 98.70, & \text{for } T_e < 7000 \text{ K}; \\ 2.36(\log T_e)^2 - 17.9 \log T_e + 24.35, & \text{for } T_e > 7000 \text{ K}, \end{cases} \tag{3.46}$$

where p_e is in atmospheres and the resulting τ_{es} is in seconds.

3.6.4 Vibration-Vibration Energy Exchanges

In a mixture of diatomic gases that have been thermally excited, the vibrational temperature of each constituent relaxes toward the translational temperature at a finite rate. However, as one species becomes vibrationally excited, it tends to transfer its vibrational energy to the other species in vibration-vibration ($v-v$) energy exchanges which drives the separate vibrational temperatures together. A rate of vibrational energy transfer between species can be derived from kinetic theory and experimentally determined probabilities of vibrational energy exchange during a collision. This expression is (Candler and MacCormack[17].)

$$Q_{v-vs} = \sum_{r\neq s}^{m} \left[\hat{N} \sigma_{sr} \sqrt{\frac{8RT}{\pi \mu_{sr}}} \left(P_{sr} \frac{\rho_s}{M_s} E_{vr} - P_{rs} \frac{\rho_r}{M_r} E_{vs} \right) \right]. \tag{3.47}$$

The probabilities of an exchange, P_{sr}, have been measured for several different molecules (Taylor et al.[18]). For temperatures of interest (above 2000 K), they are typically of the order of 10^{-2}, and for this work have been assumed to be constant at that value. The collision cross-sections for this process are computed with the expression $\sigma_{sr} = d_s d_r$, where d_s are the collision diameters.

3.7 Chemical Source Terms

The chemical source terms are derived from the reactions that occur between the components of the gas. The expressions for these mass transfer rates are derived below and the treatment of the reaction rates is discussed.

For high temperature ionized air there are seven primary constituents, which may be ordered as follows, N_2, O_2, NO, NO^+, N, O, and e^-. The most important chemical reactions between these species are

$$\begin{aligned} N_2 + M &\rightleftharpoons 2N + M \\ O_2 + M &\rightleftharpoons 2O + M \\ NO + M &\rightleftharpoons N + O + M \\ N_2 + O &\rightleftharpoons NO + N \\ NO + O &\rightleftharpoons O_2 + N \\ N + O &\rightleftharpoons NO^+ + e^-, \end{aligned} \tag{3.48}$$

where M represents any particle that acts as a collision partner in the reaction and is not altered. The first three are dissociation reactions, the fourth and fifth are exchange reactions and the last is an associative ionization reaction. Each reaction is governed by forward and backward reaction rate coefficients, k_{f_m} and k_{b_m}, respectively. The six reactions may be written in order as

$$\begin{aligned} \mathcal{R}_1 &= \sum_m \left[-k_{f_{1m}} \frac{\rho_{N_2}}{M_{N_2}} \frac{\rho_m}{M_m} + k_{b_{1m}} \frac{\rho_N}{M_N} \frac{\rho_N}{M_N} \frac{\rho_m}{M_m} \right] \\ \mathcal{R}_2 &= \sum_m \left[-k_{f_{2m}} \frac{\rho_{O_2}}{M_{O_2}} \frac{\rho_m}{M_m} + k_{b_{2m}} \frac{\rho_O}{M_O} \frac{\rho_O}{M_O} \frac{\rho_m}{M_m} \right] \\ \mathcal{R}_3 &= \sum_m \left[-k_{f_{3m}} \frac{\rho_{NO}}{M_{NO}} \frac{\rho_m}{M_m} + k_{b_{3m}} \frac{\rho_N}{M_N} \frac{\rho_O}{M_O} \frac{\rho_m}{M_m} \right] \\ \mathcal{R}_4 &= -k_{f_4} \frac{\rho_{N_2}}{M_{N_2}} \frac{\rho_O}{M_O} + k_{b_4} \frac{\rho_{NO}}{M_{NO}} \frac{\rho_N}{M_N} \\ \mathcal{R}_5 &= -k_{f_5} \frac{\rho_{NO}}{M_{NO}} \frac{\rho_O}{M_O} + k_{b_5} \frac{\rho_{O_2}}{M_{O_2}} \frac{\rho_N}{M_N} \\ \mathcal{R}_6 &= -k_{f_6} \frac{\rho_N}{M_N} \frac{\rho_O}{M_O} + k_{b_6} \frac{\rho_{NO^+}}{M_{NO^+}} \frac{\rho_e}{M_e}. \end{aligned} \tag{3.49}$$

Thus the source terms that represent the inter-species mass transfer rates may be constructed as

$$\begin{aligned} w_{N_2} &= M_{N_2}(\mathcal{R}_1 + \mathcal{R}_4) \\ w_{O_2} &= M_{O_2}(\mathcal{R}_2 - \mathcal{R}_5) \\ w_{NO} &= M_{NO}(\mathcal{R}_3 - \mathcal{R}_4 + \mathcal{R}_5) \\ w_{NO^+} &= -M_{NO^+} \mathcal{R}_6 \\ w_N &= M_N(-2\mathcal{R}_1 - \mathcal{R}_3 - \mathcal{R}_4 - \mathcal{R}_5 + \mathcal{R}_6) \\ w_O &= M_O(-2\mathcal{R}_2 - \mathcal{R}_3 + \mathcal{R}_4 + \mathcal{R}_5 + \mathcal{R}_6) \\ w_e &= -M_e \mathcal{R}_6. \end{aligned} \tag{3.50}$$

We should note that the sum of the mass transfer rates is identically zero and that elemental conservation holds, as required.

The forward and backward reaction rates of reaction m have the functional form

$$\begin{aligned} k_{f_m}(\tilde{T}) &= C_{f_m} \tilde{T}^{\eta_m} \exp(-\theta_m/\tilde{T}), \\ k_{b_m}(\tilde{T}) &= \frac{k_{f_m}(\tilde{T})}{K_{eq_m}(\tilde{T})}, \end{aligned} \tag{3.51}$$

where the constants C_{f_m}, η_m, and θ_m and the expression for K_{eq_m} are experimentally determined. As discussed by Park[8,9,19], the reaction rates will be a function of different temperatures depending on the type of reaction. Take, for example, the first three reactions where the impacting particle, M, is a heavy species (i.e. not an electron). The forward reaction rate will be a function of the vibrational excitation of the diatomic molecule and the translational temperature of the impacting heavy particle. Thus we can postulate an average temperature that governs this reaction rate to be (Park[9])

$$k_{f_{lm}} = k_{f_{lm}}(\bar{T}), \quad \bar{T} = \sqrt{TT_{vl}}, \quad \text{for } l = 1,3 \quad \text{and } m = 1,6. \tag{3.52}$$

However, the backward reaction rates will depend only on the translational temperature of the impacting particles,

$$k_{b_{lm}} = k_{b_{lm}}(T), \quad \text{for } l = 1,3 \quad \text{and } m = 1,6. \tag{3.53}$$

For the case where the impacting particle is an electron, the forward rate will depend on the average of the vibrational temperature and the electron translational temperature,

$$k_{f_{l4}} = k_{f_{l4}}(\bar{T}), \quad \bar{T} = \sqrt{T_{vl}T_e}, \quad \text{for } l = 1,3. \tag{3.54}$$

Similarly, the backward reaction rate is governed by an average temperature

$$k_{b_{l4}} = k_{b_{l4}}(\bar{T}), \quad \bar{T} = \sqrt{TT_e}, \quad \text{for } l = 1,3. \tag{3.55}$$

The forward and backward rates of reactions 4 and 5 will depend only on the relative speed of the impacting molecules, which implies that $\bar{T} = T$. The forward rate of reaction 6 will also be governed by the translational temperature of the impacting atoms. However, its backward reaction rate will depend on the vibrational temperature of the NO$^+$ and translational temperature of the electrons,

$$k_{b_6} = k_{b_6}(\bar{T}), \quad \bar{T} = \sqrt{T_{NO^+}T_e}. \tag{3.56}$$

The magnitudes of the published reaction rate coefficients vary greatly, especially at high temperatures. However, the use of the two-temperature rate model tends to lower the effective temperature and decrease the variation. The forward reaction rates for the first five reactions were taken from Park[19]. The coefficients for the sixth reaction came from Wray (Bussing and Eberhardt[20]). The expressions for the equilibrium constants, K_{eq_m}, were taken from Park[19]. These data are listed in the Appendix.

3.8 Boundary Conditions

The boundary conditions for the problem are as follows. The free-stream is supersonic so that all flow variables are fixed on the boundary outside of the bow shock wave. The outflow is also supersonic or within the boundary layer and, therefore, we can impose a zero-gradient exit condition. The wall boundaries are specified by assuming either an adiabatic or fixed-wall temperature, a no-slip velocity condition, and a zero normal gradient of pressure at the wall. In the results presented below the wall was assumed to be fully non-catalytic, which implies that the normal gradient of each species mass concentration is zero at the wall. The wall was considered to be adiabatic for the electron temperature.

3.9 Summary of Governing Equations

The governing differential equations are summarized in this section. For the case of interest, there is one mass conservation equation for each of the n chemical species. These equations may be written as

$$\frac{\partial \rho_s}{\partial t} + \frac{\partial}{\partial x_j}(\rho_s u_j) = -\frac{\partial}{\partial x_j}(\rho_s v_{sj}) + w_s. \tag{3.57}$$

There are d momentum conservation equations, where d is the spatial dimension of the problem.

$$\frac{\partial}{\partial t}(\rho u_i) + \frac{\partial}{\partial x_j}(\rho u_i u_j + p\delta_{ij}) = -\frac{\partial \tau_{ij}}{\partial x_j} - \sum_{s=1}^{n} \frac{N_s}{N_e} Z_s \frac{\partial p_e}{\partial x_i}. \tag{3.58}$$

The conservation of vibrational energy for each of the m diatomic species is represented as

$$\frac{\partial E_{vs}}{\partial t} + \frac{\partial}{\partial x_j}(E_{vs} u_j) = -\frac{\partial}{\partial x_j}(E_{vs} v_{sj})$$
$$- \frac{\partial q_{vsj}}{\partial x_j} + Q_{T-vs} + Q_{v-vs} + Q_{e-vs} + w_s e_{vs}. \tag{3.59}$$

The electron energy is conserved according to the equation

$$\frac{\partial E_e}{\partial t} + \frac{\partial}{\partial x_j}(E_e u_j) = -\frac{\partial}{\partial x_j}(E_e v_{ej}) - p_e \frac{\partial u_j}{\partial x_j} - \frac{\partial q_{ej}}{\partial x_j} + Q_{T-e} - \sum_{s=1}^{m} \Omega_{e-vs} + w_e e_e. \tag{3.60}$$

And finally the conservation of total energy is represented by

$$\frac{\partial E}{\partial t} + \frac{\partial}{\partial x_j}((E+p)u_j) = -\frac{\partial}{\partial x_j}(q_j + q_{vj} + q_{ej}) - \frac{\partial}{\partial x_j}(u_i \tau_{ij})$$
$$- \sum_{s=1}^{n} \frac{\partial}{\partial x_j} v_{sj} h_s - \sum_{s=1}^{n} \frac{N_s}{N_e} Z_s \frac{\partial p_e}{\partial x_i} u_i. \tag{3.61}$$

Thus the flowfield is represented with $n+d+m+2$ coupled differential equations. These equations have been written with the inviscid fluxes on the left-hand side and the viscous fluxes and source terms on the right-hand side. The solution technique that was used to solve these equations is discussed in the next section.

4. NUMERICAL SOLUTION PROCEDURE

In this section we briefly discuss the technique for solving the set of governing equations. This is done in the context of a general implicit numerical scheme, and demonstrates that many numerical techniques that are used for perfect gases also apply to thermo-chemical nonequilibrium gases. The description of a specific numerical method may be found elsewhere (Candler[21] and MacCormack[22]).

4.1 The Conservation-Law Form of the Governing Equations

The governing equations for the nonequilibrium flow that were presented in the previous section may be written in a form that is more suitable for the derivation of a numerical method. This is the conservation-law form of the differential equations where the time rate of change of the vector of conserved quantities is balanced by the gradients in the flux vectors and the source vector. In two dimensions the governing equations written in this form are

$$\frac{\partial U}{\partial t} + \frac{\partial F}{\partial x} + \frac{\partial G}{\partial y} = W, \tag{4.1}$$

where the vector of conserved quantities, U, is given by

$$U = (\rho_1, \rho_2, \ldots, \rho_n, \rho u, \rho v, E_{v1}, \ldots, E_{vm}, E_e, E)^T. \tag{4.2}$$

The quantities u and v are the mass-averaged velocity components in the x and y directions respectively. The x direction flux is written as

$$F = \begin{pmatrix} \rho_1(u + u_1) \\ \rho_2(u + u_2) \\ \vdots \\ \rho_n(u + u_n) \\ \rho u^2 + p + \tau_{xx} \\ \rho uv + \tau_{xy} \\ E_{v1}(u + u_1) + q_{v1x} \\ \vdots \\ E_{vm}(u + u_m) + q_{vmx} \\ E_e(u + u_e) + q_{ex} \\ (E + p + \tau_{xx})u + \tau_{xy}v + q_x + q_{vx} + q_{ex} + \sum_{s=1}^{n} \rho_s h_s u_s \end{pmatrix}. \tag{4.3}$$

where the quantity u_s is the x component of the diffusion velocity of species s. The y direction flux has a similar form. The source vector that is made up of terms that represent the mass, momentum, and energy transfer rates may be written as

$$W = \begin{pmatrix} w_1 \\ w_2 \\ \vdots \\ w_n \\ -\sum_{s=1}^{n} Z_s \frac{N_s}{N_e} \frac{\partial p_e}{\partial x} \\ -\sum_{s=1}^{n} Z_s \frac{N_s}{N_e} \frac{\partial p_e}{\partial y} \\ Q_{T-v1} + Q_{v-v1} + Q_{e-v1} + w_1 e_{v1} \\ \vdots \\ Q_{T-vm} + Q_{v-vm} + Q_{e-vm} + w_m e_{vm} \\ -p_e\left(\frac{\partial u}{\partial x} + \frac{\partial v}{\partial y}\right) + Q_{T-e} - \sum_{s=1}^{m} Q_{e-vs} + w_e e_e \\ -\sum_{s=1}^{n} Z_s \frac{N_s}{N_e}\left(u\frac{\partial p_e}{\partial x} + v\frac{\partial p_e}{\partial y}\right) \end{pmatrix}. \tag{4.4}$$

Equation (4.1) is written in Cartesian coordinates, however we are interested in applying the numerical method to a general grid and thus we must make a transformation to a general coordinate system, ξ and η. Using the chain rule of differentials, we can write

$$\frac{\partial}{\partial x} = \frac{\partial \xi}{\partial x}\frac{\partial}{\partial \xi} + \frac{\partial \eta}{\partial x}\frac{\partial}{\partial \eta},$$
$$\frac{\partial}{\partial y} = \frac{\partial \xi}{\partial y}\frac{\partial}{\partial \xi} + \frac{\partial \eta}{\partial y}\frac{\partial}{\partial \eta}. \tag{4.5}$$

Thus the Cartesian derivatives in equation (4.1) may be replaced to yield

$$\frac{\partial U}{\partial t} + \frac{\partial}{\partial \xi}\left(\frac{\partial \xi}{\partial x}F + \frac{\partial \xi}{\partial y}G\right) + \frac{\partial}{\partial \eta}\left(\frac{\partial \eta}{\partial x}F + \frac{\partial \eta}{\partial y}G\right) = W. \tag{4.6}$$

If we define

$$F' = \frac{\partial \xi}{\partial x}F + \frac{\partial \xi}{\partial y}G,$$
$$G' = \frac{\partial \eta}{\partial x}F + \frac{\partial \eta}{\partial y}G, \tag{4.7}$$

our set of governing equations becomes

$$\frac{\partial U}{\partial t} + \frac{\partial F'}{\partial \xi} + \frac{\partial G'}{\partial \eta} = W. \tag{4.8}$$

This is the basic equation that will be used in the derivation of the numerical method.

4.2 Numerical Methodology

The basic equation set written in conservation-law form, equation (4.8), may be first-order finite differenced in space and time to yield the implicit difference equation

$$U^{n+1} - U^n + \Delta t \left[\frac{D}{\Delta \xi} F'^{n+1} + \frac{D}{\Delta \eta} G'^{n+1} \right] = \Delta t\, W^{n+1}, \tag{4.9}$$

where we have assumed that the solution is known at time level n. The equation is expressed entirely at the future time level, $n+1$ where the solution is unknown. The spatial difference operators are generic; the direction of the differencing will become apparent later. Both of the flux vectors may be broken into two parts, the flux due to the inviscid terms and that due to the viscous terms. For example

$$F' = F'_I + F'_v, \tag{4.10}$$

where the subscripts denote the inviscid and viscous terms of F' respectively. The inviscid part of the flux may then be linearized to yield the expression

$$F'^{n+1}_I = F'^n_I + A'^n(U^{n+1} - U^n) + \mathcal{O}(\Delta t^2), \tag{4.11}$$

where A' is the Jacobian of F'_I with respect to U. Due to the homogeneity of F'_I, we can also express the flux at time level n in terms of the Jacobian A' as

$$F'^n_I = A'^n U^n = \left(A'^n_+ + A'^n_- \right) U^n, \tag{4.12}$$

where A' has been broken into the elements of the fluxes moving in the positive ξ direction, A'_+, and those moving in the negative ξ direction, A'_-. This partitioning is performed by diagonalizing A'. We can do this by writing

$$A' = \frac{\partial F'_I}{\partial U} = \frac{\partial U}{\partial V} \cdot \frac{\partial V}{\partial U} \frac{\partial F'_I}{\partial V} \cdot \frac{\partial V}{\partial U}, \tag{4.13}$$

where V is a vector of non-conserved flow variables introduced for convenience. The choice of V is not unique, but in this case we have used

$$V = \left(\rho_1, \rho_2, \ldots, \rho_n, u, v, e_{v1}, \ldots, e_{vm}, e_e, p \right)^T. \tag{4.14}$$

With this choice of V the diagonalization of $\frac{\partial V}{\partial U} \frac{\partial F'_I}{\partial V}$ is straight-forward and the result may be written as

$$\frac{\partial V}{\partial U} \frac{\partial F'_I}{\partial V} = C_{A'}^{-1} \Lambda_{A'} C_{A'}, \tag{4.15}$$

where $\Lambda_{A'}$ is a diagonal matrix. If we define $S = \frac{\partial V}{\partial U}$ and a rotation matrix R_A, such that $C_{A'} = C_A R_A$, we have

$$A' = S^{-1} R_A^{-1} C_A^{-1} \Lambda_{A'} C_A R_A S, \tag{4.16}$$

Let the diagonal matrix $\Lambda_{A'+}$ be made up of the positive elements of $\Lambda_{A'}$ and $\Lambda_{A'-}$ be composed of its negative elements. Then we have

$$\begin{aligned} A'_+ = S^{-1} R_A^{-1} C_A^{-1} \Lambda_{A'+} C_A R_A S, \\ A'_- = S^{-1} R_A^{-1} C_A^{-1} \Lambda_{A'-} C_A R_A S, \end{aligned} \tag{4.17}$$

which represent the split-flux Jacobians of the inviscid flux vector F'_I. The inviscid flux entering or leaving a volume across a surface is given in equation (4.12), however the grid point where each term should be evaluated is ambiguous. We do not have data stored at the surface itself, and therefore an approximation must be made. The flux traveling in the positive ξ direction originates at the point i,j and that traveling in the negative ξ direction comes from point $i+1,j$. Therefore the inviscid flux across surface $i+\frac{1}{2},j$ is given by

$$F'^n_{I\,i+\frac{1}{2},j} = A'^n_{+\,i+\frac{1}{2},j} U^n_{i,j} + A'^n_{-\,i+\frac{1}{2},j} U^n_{i+1,j}. \tag{4.18}$$

We need a scheme to determine at what grid point we should evaluate the Jacobians. Two methods have been used in this study. The primary technique used was proposed by MacCormack[23] and MacCormack and Candler[24] and has been shown to have favorable characteristics for the treatment of a boundary layer. With this method, both of the Jacobians, A'_+ and A'_-, are always evaluated at the same place. The point used is alternated between i,j and $i+1,j$. The second method was proposed by Steger and Warming[25] and the flux-splitting is performed so that

$$F'^n_{I\,i+\frac{1}{2},j} = A'^n_{+\,i,j} U^n_{i,j} + A'^n_{-\,i+1,j} U^n_{i+1,j}. \tag{4.19}$$

The second technique is very dissipative and shows poor results in a boundary layer (MacCormack and Candler[24]), but was used in the work presented below in strong pressure gradient regions to maintain numerical stability and to capture shock waves[1]. For simplicity, the subscript $i+\frac{1}{2},j$ will be left on A' to imply that either flux-splitting method may be used.

Having made these approximations, we can express the inviscid fluxes at time level $n+1$, using (4.11), (4.18), and the definition $\delta U^n \equiv U^{n+1} - U^n$, as follows

$$\begin{aligned} F'^{n+1}_{I\,i+\frac{1}{2},j} &\simeq A'^n_{+\,i+\frac{1}{2},j} U^n_{i,j} + A'^n_{-\,i+\frac{1}{2},j} U^n_{i+1,j} + A'^n_{+\,i+\frac{1}{2},j} \delta U^n_{i,j} + A'^n_{-\,i+\frac{1}{2},j} \delta U^n_{i+1,j}, \\ G'^{n+1}_{I\,i,j+\frac{1}{2}} &\simeq B'^n_{+\,i,j+\frac{1}{2}} U^n_{i,j} + B'^n_{-\,i,j+\frac{1}{2}} U^n_{i,j+1} + B'^n_{+\,i,j+\frac{1}{2}} \delta U^n_{i,j} + B'^n_{-\,i,j+\frac{1}{2}} \delta U^n_{i,j+1}. \end{aligned} \tag{4.20}$$

---

[1] At any point where the pressure changes by 25% across a surface, the Steger-Warming flux-splitting, (4.19), is used.

The source vector may be linearized in a similar fashion so that we have

$$W_{ij}^{n+1} = W_{ij}^n + C_{ij}^n \delta U_{ij}^n + O(\Delta t^2), \tag{4.21}$$

where C is the Jacobian of W with respect to U.

Using these approximations for $F_{1i+\frac{1}{2},j}^{'n+1}$, $G_{1i,j+\frac{1}{2}}^{'n+1}$ and W_{ij}^{n+1}, we can devise an implicit numerical scheme for the solution of (4.8). This has been discussed in detail bay Candler[21] and by Candler and MacCormack[17] for the particular case of an implicit flux-split Gauss-Seidel line relaxation method. However, the concepts discussed here, namely the homogeneity of the flux vectors and the splitting of the flux Jacobians, can be exploited for many different numerical schemes. Grossman and Cinnella[26] use these ideas in the derivation of Van Leer flux-vector split and Roe averaged algorithms.

5. NUMERICAL RESULTS

In this section we discuss some numerical results obtained with the model for air described in Section 3. The equation set was solved using the implicit Gauss-Seidel line-relaxation technique of MacCormack[23]. We briefly discuss some cases where computed results are compared to experiments in an attempt to validate the physical model and the solution procedure. There is good agreement in all cases. The numerical method is then used to compute the flow about an axisymmetric AOTV-like vehicle at two flight conditions, which correspond to perigee for the Aeroassist Flight Experiment (AFE) vehicle and to the approximate limit of the continuum regime where the gas model is applicable.

Several test cases are presented which demonstrate that the model for high temperature air gives results that agree with experiment. These calculations are discussed more extensively by Candler and MacCormack[17] and Candler[27]. The model for air uses seven chemical species: N_2, O_2, NO, NO^+, N, O, and e^-. There are six temperatures that describe the gas at every point: one translational-rotational, vibrational for each diatomic species, and an electron-electronic temperature.

5.1 RAM-C Flight Experiment

The first case to be discussed is a comparison of the peak electron number density about a sphere-cone vehicle traveling in the atmosphere at near satellite speed (7.65 km/s). The experimental vehicle[28-30] was 0.1524 m nose radius sphere attached to a $9°$ half-angle cone, which was instrumented at several locations to measure peak electron number density. The flowfield about this vehicle was computed at three altitudes on a 35×50 mesh for about ten nose radii of the vehicle. Figure 3 shows the comparison with the experimental results and the computed results along the axis of the cone for these three flight conditions (61 km, 71 km, and 81 km altitude). We see that for these three fight conditions, there is very good agreement.

5.2 Hot Nitrogen Flow About a Cylinder

The flow about a 2-inch (5.08 cm) diameter cylinder in hot, partially dissociated nitrogen ($C_{N_2 \infty} = 0.927$, $C_{N \infty} = 0.073$) was computed using the thermo-chemical nonequlibrium algorithm. This case replicates an experiment of Hornung[31], in which interferograms were made of this flowfield. The free-stream conditions are $u_\infty = 5.59 \text{ km/s}$, $T_\infty = 1833 \text{ K}$, and $p_\infty = 2910 \text{ Pa}$. To compare the computed results with experiment, we relate the density change, $\Delta \rho$, to the fringe pattern using an expression from Hornung[31]

$$\Delta \rho = \frac{4160 F \lambda}{\ell(1 + 0.28 c_N)}, \quad (\rho \text{ in kg/m}^3), \tag{5.1}$$

where F is the fringe number, λ is the wavelength, and ℓ is the experiment's geometrical path. Contours of constant fringe number are plotted in Figure 4. The shapes of the computed contours are very similar to the experimental fringe patterns and the location of the experimental and computed shock waves coincide. Thus, the multi-temperature model predicts the correct distribution of density within this reacting flow. Several other teat cases have also been computed using the thermo-chemical nonequilibrium algorithm and also show very good comparison with experiment[27].

5.3 AOTV Flowfield

The flowfield around an axisymmetric AOTV was computed for two conditions in the proposed trajectory. The first is for the perigee conditions at 78 km and a free-stream velocity of 8.91 km/sec. The second is at 90 km and 9.89 km/sec which is the approximate limit of the continuum regime. Both cases were run with an assumed fixed wall temperature of 1000 K and a non-catalytic wall. Table I gives the free-stream conditions for each case. The composition of the air at 78 km was assumed to be 79% N_2 and 21% O_2 and at 90 km to be 76.6% N_2, 23.23% O_2 and 0.17% O (by mass). A plot of the grid used for the low altitude case is presented in Figure 5.

Table I. Free-stream Conditions for AOTV Test Cases.

	78 km	90 km
u_∞ (m/s)	8910	9890
T_∞ (K)	197	188
ρ_∞ (kg/m³)	2.78×10^{-5}	3.14×10^{-6}
Re	43400	5670
M_∞	31.6	36.4

5.3.1 AOTV Forebody

The perigee conditions of the AFE flight trajectory will expose the vehicle to the highest radiative and convective heating and the largest drag forces. The accurate prediction of these aerothermal loads is critical to the design of an AOTV. A discussion of the nature of the flowfield and the surface heating follows.

Figure 6, shows the density distribution along the stagnation streamline. The shock layer and the boundary layer are distinct in this case. If the standoff distance is defined to be the point where the density rise is six times the free-stream density, the shock standoff is 0.137 m, or 5.96% of the nose radius. Figure 7 is a plot of the molar concentrations along the stagnation streamline. The peak molar concentration of NO^+ ions is 1.83×10^{-5}.

The translational-rotational, nitrogen vibrational, and electron-electronic temperature distributions on the stagnation streamline are plotted in Figure 8. The other three vibrational temperatures are not plotted, because they have a similar behavior as that of nitrogen. There is a strong degree of thermal nonequilibrium near the shock, but for this case, the electron and vibrational temperatures equilibrate with the translational-rotational temperature within about 50% of the distance to the wall. The electron temperature rises near the shock due to translation-electron exchanges, and rises further downstream as the vibrational temperature becomes excited and the electron-vibration energy exchanges become more efficient.

Figures 9a and 9b show the calculated convective and radiative heating to the body surface as a function of distance from the nose. The stagnation point convective heating value is 16.5 W/cm^2. The heating rises on the ellipsoidal part of the body to a peak of 19.3 W/cm^2 and then drops to a nearly constant 14 W/cm^2 for the length of the cone. The rise in the heat transfer away from the nose is postulated to be a result of the ellsoidal surface curvature. The gas accelerates around the ellipsoidal nose, causing the boundary layer to thin, and increasing the temperature gradients and the heat transfer. The surface pressure distribution also has an interesting behaviour, as shown in Figure 9c. The gas experiences an adverse pressure gradient after the ellipsoid-cone juncture at $\xi = 0.9$ m. This is a result of centrifugal forces decreasing the pressure on the ellipsoidal surface as compared to the adjacent conical surface. These effects have been observed experimentally[32]. The stagnation point convective heating is similar to the 15.2 W/cm^2 predicted by Fay and Riddell with Goulard's correction for a non-catalytic wall[33,34], but it is considerably lower than the 24.8 W/cm^2 that Moss et al.[35] calculated. This discrepancy is probably due to the inclusion of a catalytic wall boundary condition in their study. The influence of a catalytic wall on the convective heat transfer can be profound for cases where the flowfield is highly reactive[3].

The peak radiative heating for this case occurs at the stagnation point and is computed to be 5.94 W/cm^2. This decreases rapidly and reaches a fairly constant value of about 2 W/cm^2 on the conical surface. The stagnation point radiative heat transfer agrees very well with the 6.63 W/cm^2 result of Park[9].

The next figures give a more qualitative description of the flowfield in the form of contour plots. Figure 10 is a plot of the percent N_2 mass concentration and shows that the gas is most highly dissociated near the stagnation point and the degree of dissociation decreases with axial distance. Figure 11 plots the contours of translational-rotational temperature. A comparison with Figure 12, which presents N_2 vibrational temperature contours, shows that these two temperatures are nearly in equilibrium for a large part of the flowfield. However, Figure 13 shows that the electron temperature remains lower than both other temperatures.

Figure 14 is a contour plot of the radiative emission power from the flowfield. The largest emission occurs on the stagnation streamline where the temperatures and the density are highest. The radiative power falls off rapidly from this point to a fairly constant level on the conical section of the body.

In summary, the results from this case indicate that the flowfield is highly reactive and radiative. The stagnation point heat transfer results are consistent with previously published experimental work. A major portion (26%) of the total heat transfer to the stagnation point is from radiation for this non-catalytic wall case. The maximum convective heat transfer occurs off of the nose, near the ellipsoid-cone juncture. The inclusion of thermal nonequilibrium for this case is mandatory for the accurate calculation of radiation because approximately a 5% error in the vibrational and electron temperatures results in a factor of two error in the radiative emission.

The second case is at an altitude of 90 km and a speed of nearly 10 km/s. Although the vehicle does not experience its peak heat transfer at this point, the aerothermal characteristics are still important because they help determine the total heat load and flight trajectory. The conditions at this point are similar to the previous case except that the density is considerably (9 times) lower and the speed is slightly greater.

The first series of plots for this case show the characteristics of the flow on the stagnation streamline. The standoff distance based on the six-fold density increase is 0.167 m or 7.24% of the nose radius. Figure 15 is a semi-log plot of the molar concentrations and Figure 16 is a plot of three temperatures on the stagnation streamline. The translational-rotational temperature reaches a peak of 40,000 K, the vibrational temperature of nitrogen rises to 13,000 K, and the electron temperature peaks at 7200 K. This case is characterized by a high degree of thermal nonequilibrium with a relatively minor excitation of the vibrational and electron modes.

The calculated convective and radiative heating are plotted in Figure 17. The distribution is similar, though about 10% lower, than the 78 km case. The increase in the heat transfer off of the stagnation point is also evident for this case. The stagnation point heat transfer of 15.8 W/cm^2 is similar to the 18.4 W/cm^2 reported by Moss et al.[35] The stagnation point radiative heat transfer is 0.112 W/cm^2, which is much smaller than the convective component (164 times less) and the radiative heat transfer for the previous case (53 times less). The much smaller thermal excitation and the lower density of this case has caused the radiative heat transfer to be less significant. Figure 17b also shows that the maximum radiative heat transfer occurs at the stagnation point. There is also a peak of nearly the same magnitude at $\xi \simeq 2.6$ m. The reason for this will become evident when the following contour plots are discussed.

Figure 18 is a contour plot of the N_2 mass concentration and shows that the minimum concentration of diatomic nitrogen occurs, not at the nose, but on the shoulder of the body ($x \simeq 0.75$ m and $y \simeq 2.25$ m). The next three figures are plots of the translational-rotational temperature (Fig. 19), N_2 vibrational temperature (Fig. 20), and the electron temperature (Fig. 21). The first, Fig. 19, shows that the maximum translational-rotational temperature occurs behind the shock on the stagnation point, as expected. However, the peak vibrational and electron temperatures (Figs. 20 and 21) are on the shoulder of the body. This phenomenon is most evident for the electron temperature, which reaches its maximum of nearly 8500 K at this point, as opposed to 7200 K on the stagnation streamline.

The reason why a peak in the degree of chemical reaction and thermal excitation occurs off the stagnation point is made clear by considering Figure 22, which is a streamline plot. Particles are introduced in the free-stream and traced through the flowfield. Consider the streamline that enters the flowfield at $y \simeq 0.9$ m. It passes through an oblique, though strong shock wave, and flows around the body, far enough away from the surface that it does not enter the cool boundary layer. This fluid element experiences rather severe heating inside the entire shock layer and because it travels a significant physical distance, it undergoes appreciable reaction and thermal excitation. Thus, because of the nonequilibrium nature of the flow, the peak degree of reaction can occur off the stagnation point. Figure 23 is a plot of the radiative emission from the flowfield. The peak radiation power occurs near the shoulder of the body ($x \simeq 0.75$ m and $y \simeq 2.25$ m) where the maximum thermal excitation of the gas has occurred. It should be noted that this effect would be more pronounced for a full scale aerobrake because the gas would have a larger distance to thermalize and would become more radiant.

This case demonstrates that thermo-chemical nonequilibrium can have a large influence on the state of the gas. The largest degree of reaction and thermal excitation do not occur at the stagnation point, and as a result, neither does the peak radiative emission.

5.3.2 AOTV Afterbody

Several notable features of the AOTV afterbody flowfield will be discussed at the two conditions of interest using contour plots. Consider Figs. 24a and 24b, which are contours of translational-rotational temperature at the two flight conditions. We see that the peak temperature occurs at the stagnation point of the body in both cases. The wake region is much cooler because the gas expands rapidly as it flows over the body shoulder. The result is that most of the afterbody flowfield has a translational-rotational temperature of less than $10,000K$. In the 78 km case, we see evidence of reheating of the gas where it is recompressed near the centerline; here the temperature returns to about 7000K. This region is where the wake closes and is forced to turn parallel to the centerline. Similarly for the 90 km case the temperature peaks at something less than $10,000K$.

The next figures, 25a and 25b, show contours of nitrogen vibrational temperature for both conditions. (The other three vibrational temperatures and the electron-electronic temperature are similar, and are not plotted.) These figures demonstrate the different behavior of the vibrational state of the gas compared to the translational-rotational state. We see that much of the afterbody flowfield has a higher vibrational temperature than translational-rotational temperature because vibrational energy is frozen at high levels as the gas expands around the body shoulder. In this shoulder region the flow speed is high and the rate of vibrational equilibration is low (it is proportional to the pressure), so that little energy is transfered from vibration to the cooler translational modes of the gas. Both altitude cases show this type of behaviour, with the 90 km condition having a higher vibrational temperature in the wake.

Figures 26a and 26b plot the difference between the translational-rotational temperature and the nitrogen vibrational temperature, $T - T_{vN_2}$. They cleary show the phenomenon of vibrational freezing where the vibrational temperature remains high while the translational temperature has dropped due to the expansion. It i. also interesting to note that near the centerline of the body, these two temperatures are nearly equal. Thus for the flow immediately behind the vehicle, there is a state of near vibrational equilibrium. The elevated vibrational temperature has ramifications in the design of the vehicle because this gas will radiate much more than a gas in equilibrium. As a further illustration of the state of nonequilibrium of the gas we can consider a non-dimensional number, ψ_v, that measures the rate of vibrational energy exchange relative to the local flow rate. Let us define

$$\psi_v = \frac{L}{u\tau_v}, \tag{5.2}$$

where τ_v is the characteristic time for vibrational equilibration (see equation (3.40)), u is the local speed, and L is the characteristic length of the body. Figures 27a and 27b plot the logarithm (base 10) of this quantity. We see that in much of the wake this parameter is between 10^{-3} and 10^{-2}, indicating that the rate of fluid motion is much greater than the rate of vibrational relaxation, thus the vibrational energy remains frozen in the gas. It is only in the region of recirculation, which will be shown later to be immediately behind the body, where there is sufficient residence time for the gas to equilibrate.

Figures 28a and 28b are plots of the percent mass fraction of N_2. There is significant dissociation of the gas in the nose region; this gas is swept around the body and remains reacted through much of the wake. Thus we see evidence of chemical freezing in the same region where vibrational freezing occurs. A parameter that describes the degree of nonequilibrium of the nitrogen mass fraction can be written as

$$\psi_{N_2} = \frac{w_{N_2}L}{u\rho}, \tag{5.3}$$

where w_{N_2} is the rate of production of N_2 due to chemical reaction (see equation (3.50)). This parameter is about the same magnitude as the ψ_v for most of the wake, indicating that the gas is not in chemical equilibrium in the wake. Because of this phenomenon, there is a large gradient of mass fraction between the centerline of the body and the free-stream. This affects the atomic weight of the gas, the isentropic exponent, the speed of sound, and consequently the dynamics of the gas in the wake region. This important effect must be included in any analysis of this type of wake flow.

The next plots, Figures 29a and 29b, are pathline tracings in the region immediately behind the vehicle. Both cases show the same general features: separation of the flow on the back face of the vehicle, a strong recirculation region driven by the high speed gas that expands over the shoulder, and a reattachment point on the centerline. However, the two conditions are significantly different also. The separation point on the base moves further down the back of the body at the higher altitude, due to the lower Reynolds number of this flow. Also the recirculation region is much smaller for this case. It is also interesting to note that the location of the vortical structure is different in each case. The location and size of these features is dependent on the correct modeling of the gas, not only its thermo-chemical state, but also resolving or modeling any effects of turbulence that may be present. The presence of turbulence will influence the location of the attachment point in the wake, the thickness and location of the shear layer and the structure of the recirculation region. Because of the coarse grid used in these simulations and the neglect of transition and turbulence the detailed structure of the recirculation region should be considered only in a qualitative sense at this time.

6. Summary

The multi-temperature chemical nonequilibrium technique has been shown to reproduce a number of experiments over a wide range of conditions, validating its use for the calculation of flows about AOTV's. The forebody and afterbody regions of an axisymmetric version of an AOTV have been computed for two conditions. In these results we have seen the influence that thermo-chemical nonequilibrium can have on the flowfield, including the location of the peak radiative emission, and the effect of vibrational temperature overshoot in the wake. Some other effects have been mentioned and their importance in modeling these flows has been discussed. These flows show that the correct modeling of a separated, chemically reacting, hypersonic flow has many effects that must be included.

Extensions of the two dimensional AOTV analysis to three dimensions is currently being treated by several investigators (e.g. Gnoffo[37], Li[38], and Palmer[39]). Additional extension of the analysis method to include rotational nonequilibrium and slip boundary conditions necessary for application at even higher altitudes have been considered by Gokcen and MacCormack[40].

REFERENCES

[1] Fiscko, K.A., and Chapman, D.R., Comparison of Shock Structure Solutions Using Independent Continuum and Kinetic Theory Approaches. *SPIE Proceedings on Sensing, Discrimination, and Signal Processing and Superconducting Materials and Instrumentation 879*, pp. 113–122, 1988.

[2] Lee, J.H., Basic Governing Equations for the Flight Regimes of Aeroassisted Orbital Transfer Vehicles. *Thermal Design of Aeroassisted Orbital Transfer Vehicles*, ed. H.F. Nelson, *Progress in Aeronautics and Astronautics, 96*, pp. 3–53, 1985.

[3] Vincenti, W.G. and Kruger, C.H., Jr., *Introduction to Physical Gas Dynamics*. Krieger Publishing Company, Florida, 1965.

4   Appleton, J.P. and Bray, K.N.C., The Conservation Equations for a Non-equilibrium Plasma. *J. Fluid Mech.* 20, pp. 659–672, 1964.
5   Marrone, P.V. and Treanor, C.E., Chemical Relaxation With Preferential Dissociation from Excited Vibrational Levels. *Physics of Fluids,* 6, pp. 1215–1221, 1963.
6   Treanor, C.E. and Marrone, P.V., Effect of Dissociation on the Rate of Vibrational Relaxation. *Physics of Fluids,* 5, pp. 1022–1026, 1962.
7   Park 1988.
8   Park, C., Assessment of Two-Temperature Kinetic Model for Dissociating and Weakly Ionizing Nitrogen. *AIAA Paper No. 86–1347,* 1986.
9   Park, C., Assessment of Two-Temperature Kinetic Model for Ionizing Air. *AIAA Paper No. 87–1574,* 1987.
10 Blottner, F.G., Johnson, M. and Ellis, M., Chemically Reacting Viscous Flow Program for Multi-Component Gas Mixtures. *Report No. SC-RR-70-754, Sandia Laboratories, Albuquerque, New Mexico,* 1971
11 Wilke, C.R., A Viscosity Equation for Gas Mixtures. *J. Chem. Phys.,* 18, pp. 517–519, 1950.
12 Millikan, R.C. and White, D.R., Systematics of Vibrational Relaxation. *J. of Chem. Phys.,* 39, pp. 3209–3213, 1963.
13 Park, C., Calculation of Nonequilibrium Radiation in the Flight Regimes of Aeroassisted Orbital Transfer Vehicles. *Thermal Design of Aeroassisted Orbital Transfer Vehicles,* ed. H.F. Nelson, *Progress in Aeronautics and Astronautics,* 96, pp. 395–418, 1985.
14 Parker, J.G., Rotational and Vibrational Relaxation in Diatomic Gases. *Physics of Fluids,* 2, pp. 449–462, 1959.
15 Keck, J. and Carrier, G., Diffusion Theory of Nonequilibrium Dissociation and Recombination. *J. Chemical Physics,* 43, pp. 2284–2298, 1965.
16 Lee, J.H., Electron-Impact Vibrational Excitation Rates in the Flowfield of of Aeroassisted Orbital Transfer Vehicles. *Thermophysical Aspects of Re-entry Flows,* eds. J.N. Moss and C.D. Scott, *Progress in Aeronautics and Astronautics,* 103, pp. 197–224, 1986.
17 Candler, G.V. and MacCormack, R.W., The Computation of Hypersonic Ionized Flows in Chemical and Thermal Nonequilibrium. *AIAA Paper No. 88-0511,* 1988.
18 Taylor, R.L., Camac, M. and Feinberg, R.M., Measurements of Vibration-Vibration Coupling in Gas Mixtures. *Proc. of Eleventh Symposium on Combustion,* pp. 49-65, 1966.
19 Park, C., On Convergence of Computation of Chemically Reacting Flows. *AIAA Paper No. 85-0247,* 1985.
20 Bussing, T.R.A. and Eberhardt, S., Chemistry Associated with Hypersonic Vehicles. *AIAA Paper No. 87-1292,* 1987.
21 Candler, G.V., "The Computation of Weakly Ionized Hypersonic Flows in Thermo-Chemical Nonequilibrium," Ph.D. Thesis, Aeronautics and Astronautics Dept., Stanford Univ., Stanford, California, 1988.
22 MacCormack 1987.
23 MacCormack, R.W., Current Status of the Numerical Solutions of the Navier-Stokes Equations. *AIAA Paper No. 85-0032,* 1985.
24 MacCormack, R.W. and Candler, G.V., The Solution of the Navier-Stokes Equations Gauss-Seidel Line Relaxation. *Presented at the Symposium in Honor of G. Moretti's* 70th *Birthday,* Polytechnic Univerisity, Long Island, 1987.
25 Steger, J. and Warming, R.W., Flux-Vector Splitting of the Inviscid Gasdynamics Equations with Application to Finite Difference Methods. *NASA TM-78605,* 1979.
26 Grossman, B. and P. Cinnella, "Flux-Split Algorithms for Flows With Non-Equilibrium Chemistry and Vibrational Relaxation," Interdisciplinary Center for Applied Mathematics Report 88-08-03, Virginia Polytechnic and State University, Blacksburg, Virginia, 1988.
27 Candler, G.V., "The Computation of Shock Shapes in Nonequilibrium Hypersonic Flows," *AIAA Paper No. 89-0312,* 1989.
28 Akey N.D. and Cross, A.E., Radio Blackout Alleviation and Plasma Diagnostic Results From a 25,000 Foot per Second Blunt-Body Reentry. *NASA TN D-5615,* 1970.
29 Granthan, W.L., Flight Results of 25,000 Foot per Second Reentry Experiment Using Microwave Reflectometers to Measure Plasma Electron Density and Standoff Distance. *NASA TN D-6062,* 1970.
30 Jones, W.L., Jr. and Cross, A.E., Electrostatic Probe Measurements of Plasma Parameters for Two Reentry Flight Experiments at 25,000 Feet per Second. *NASA TN D-6617,* 1972.
31 Hornung, H.G., "Non-equilibrium Dissociating Nitrogen Flow Over Spheres and Circular Cylinders," *J. Fluid Mechanics,* 53, pp. 149–176, 1972.
32 Kemp, N.H., P.H. Rose, and R.W. Detra, "Laminar Heat Transfer Around Blunt Bodies in Dissociated Air," *J. Aeronautical Sci.,* Vol. 26, pp. 421-430, 1959.
33 Fay, J.A. and Riddell, F.R., Theory of Stagnation Point Heat Transfer in Dissociated Air. *J. Aeronautical Sci.* 25, pp. 73–85, 1958.
34 Goulard, R., On Catalytic Recombination Rates in Hypersonic Stagnation Heat Transfer. *Jet Propulsion,* 28, pp. 737–745, 1958.
35 Moss, J.N., Bird, G.A. and Dogra, V.K., Nonequilibrium Thermal Radiation for an Aeroassist Flight Experiment Vehicle. *AIAA Paper No. 88-0081,* 1988.
36 Scott, C.D., Ried, R.C. and Maraia, R.J., An AOTV Aeroheating and Thermal Protection Study. *Thermal Design of Aeroassisted Orbital Transfer Vehicles,* ed. H.F. Nelson, *Progress in Aeronautics and Astronautics,* 96, pp. 309–337 1985.
37 Gnoffo,P. A., Application of Program LAURA to Three Dimensional AOTV Flowfields. *AIAA Paper No. 8-0565,* 1986.
38 Li, C. P., Computation of Three-Dimensional Flow about Aerobrake Configurations. *AIAA Paper No. 86-0566,* 1986.
39 Palmer, G., An Efficient, Explicit Finite-Rate Algorithm to Compute Flows in Chemical Nonequilibrium. *AIAA Paper No. 89-0522,* 1989.
40 Gokcen, T. and MacCormack, R., Nonequilibrium Effects for Hypersonic Transitional Flows Using Continuum Approach. *AIAA Paper No. 89-0461,* 1989.

a) Ground Based Simulation Capability - (Reynolds number vs flight speed)
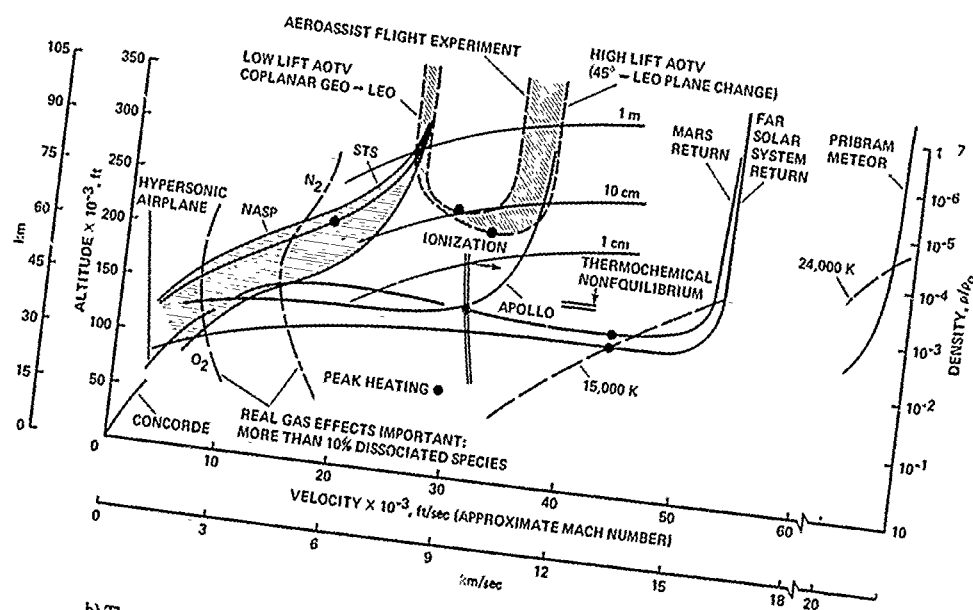
b) Thermochemical Nonequilibrium Regimes - (Altitude vs flight speed)

Fig. 1 Vehicle flight regimes in earth atmosphere

a) Forebody flowfield

b) Afterbody flowfield
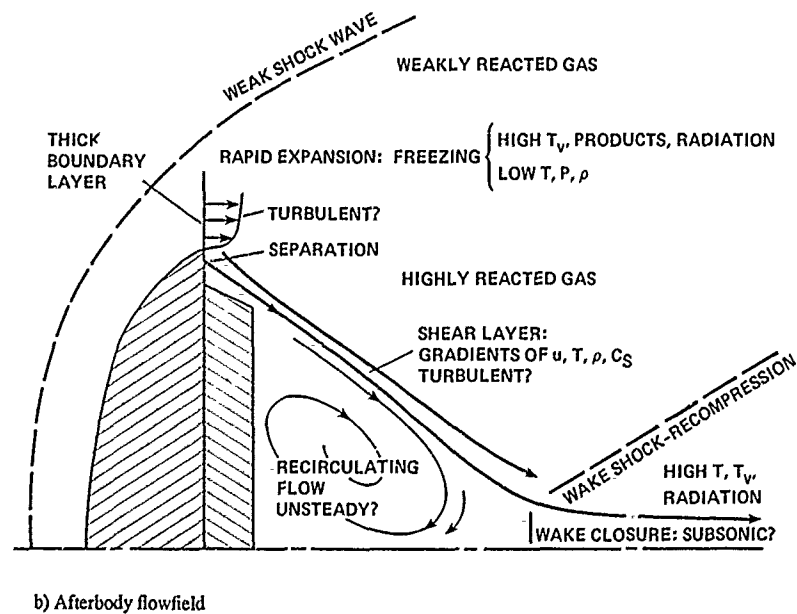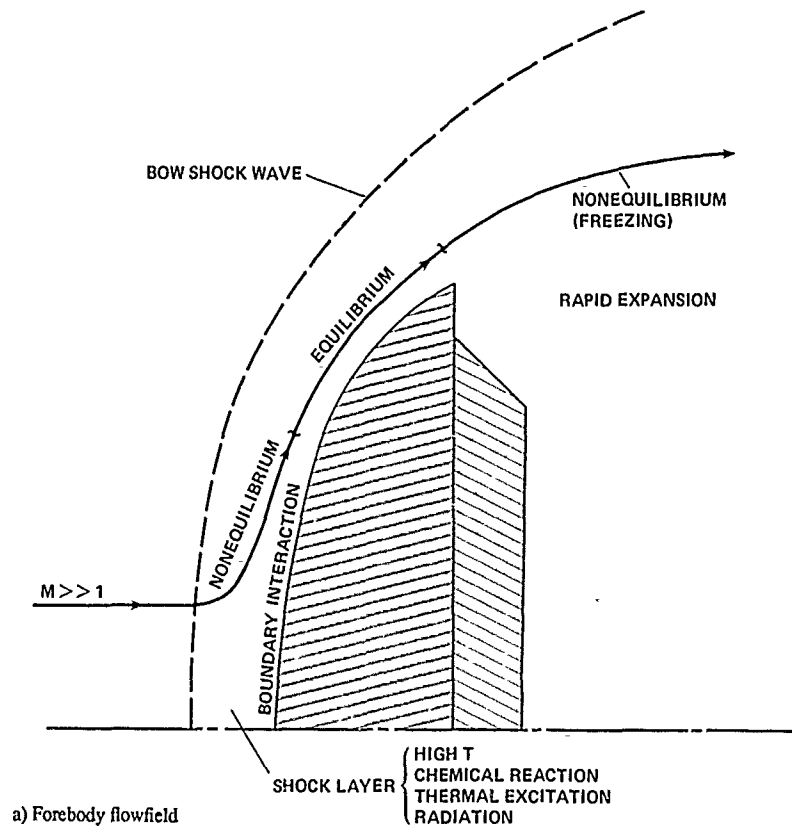
Fig. 2   AOTV flowfield schematic
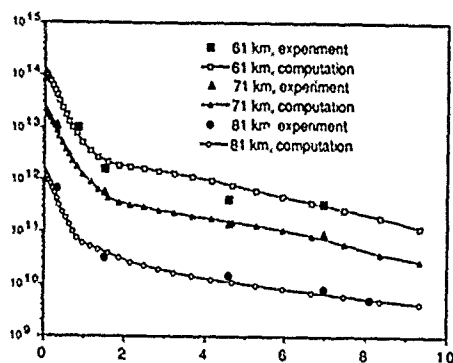
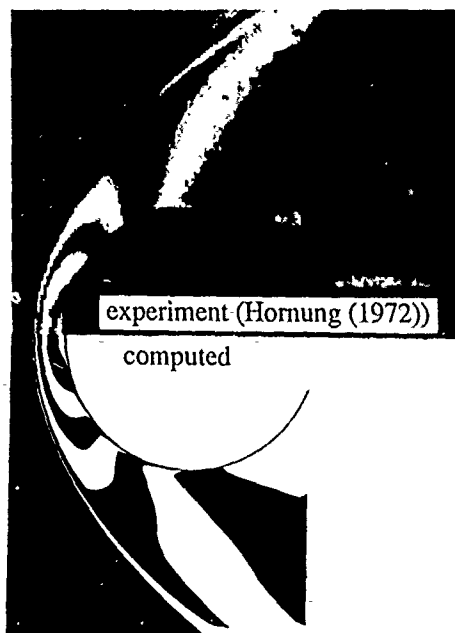Fig. 3 Peak electron density distributions over RAM-C flight vehicle.

Fig. 6 Stagnation streamline density distribution for AOTV at 78km.

experiment (Hornung (1972))

computed

Fig. 4 Computed and experimental interferogram fringe pattern over right circular cylinder.

$M_\infty = 6.1, Re = 6000, u_\infty = 5.6\,km/s.$

Fig. 7 Stagnation streamline molar concentrations for AOTV at 78km.
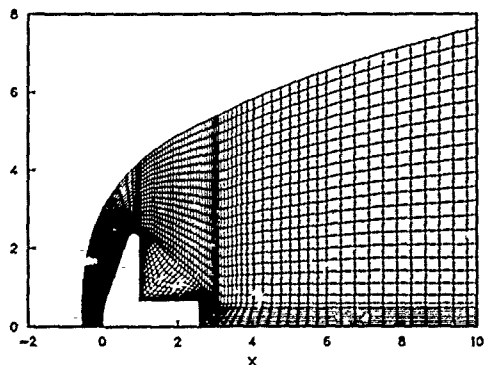
Fig. 5 Computational Grid for AOTV Flowfield
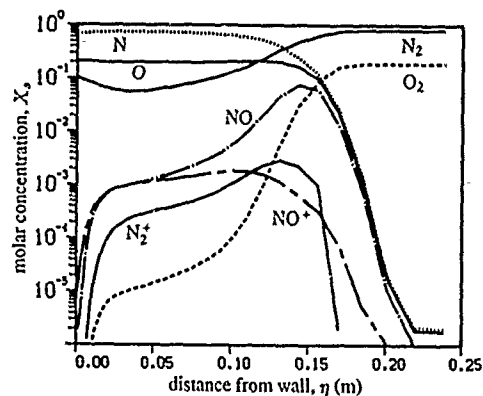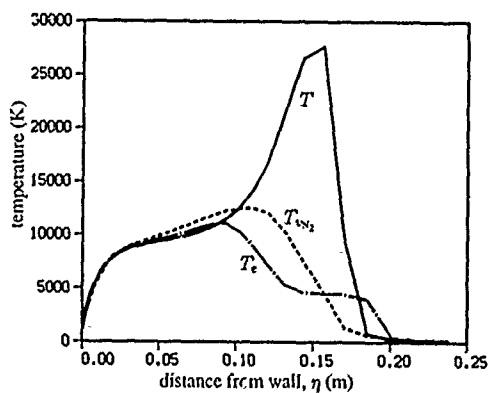
Fig. 8 Stagnation streamline temperature distributions for AOTV at 78km.
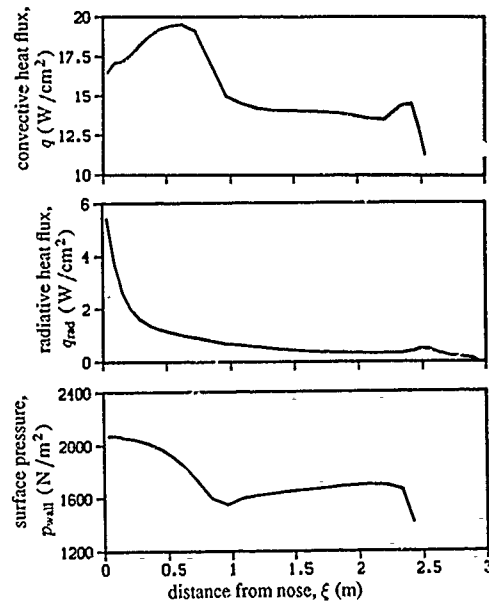
Fig. 9 Convective and radiative surface flux and surface pressure distributions for AOTV at 78km.
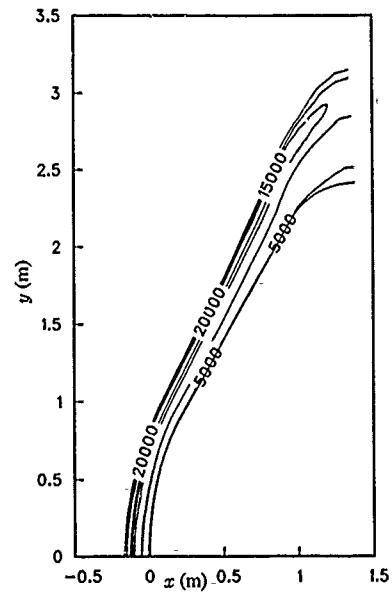
Fig. 11 Translational-rotational temperature contours for AOTV at 78km.
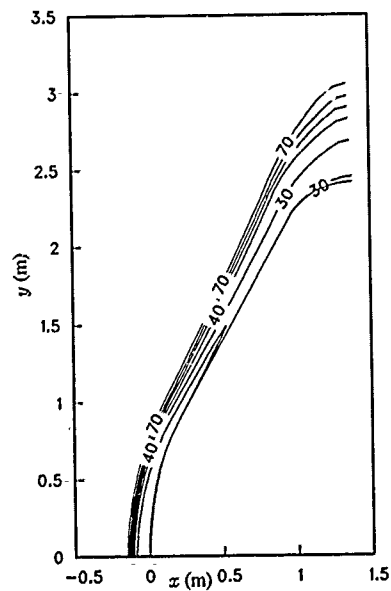
Fig. 10 Percent N_2 mass concentration contours for AOTV at 78km.
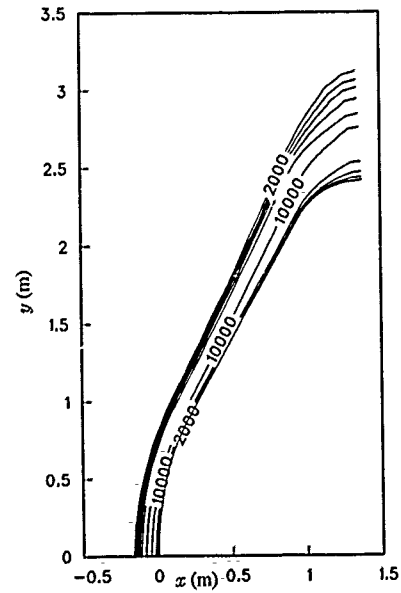
Fig. 12 N_2 vibrational temperature contours for AOTV at 78km.
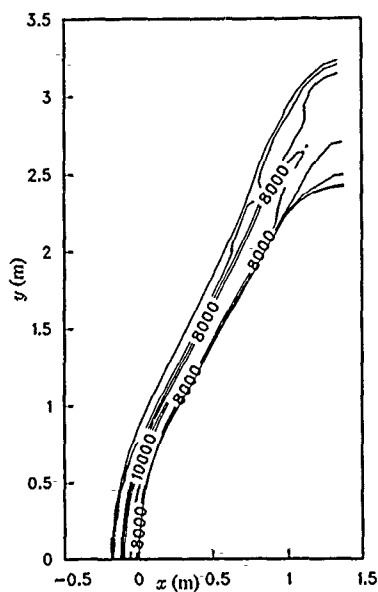
Fig. 13 Electron translational temperature contours for AOTV at 78km.
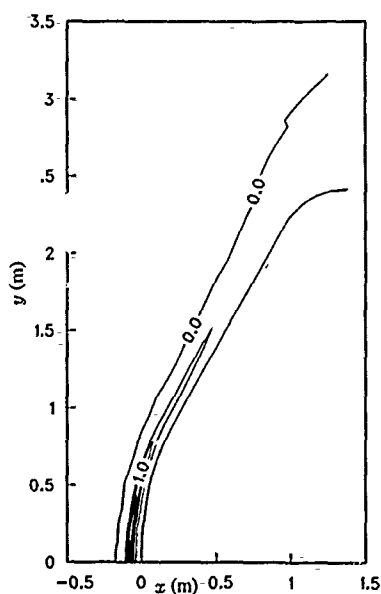
Fig. 14 Radiation intensity contours for AOTV at 78km.
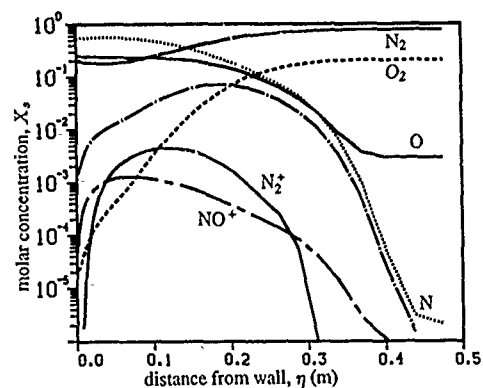
Fig. 15 Stagnation streamline molar concentrations for AOTV at 90km.
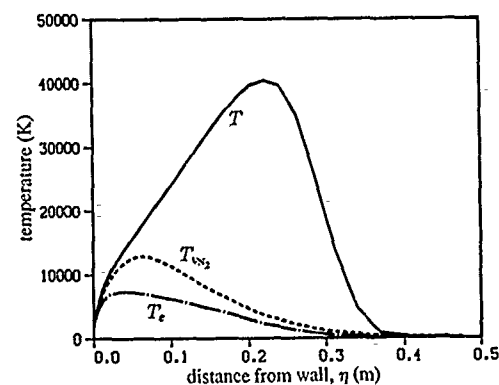
Fig. 16 Stagnation streamline temperature distributions for AOTV at 90km.
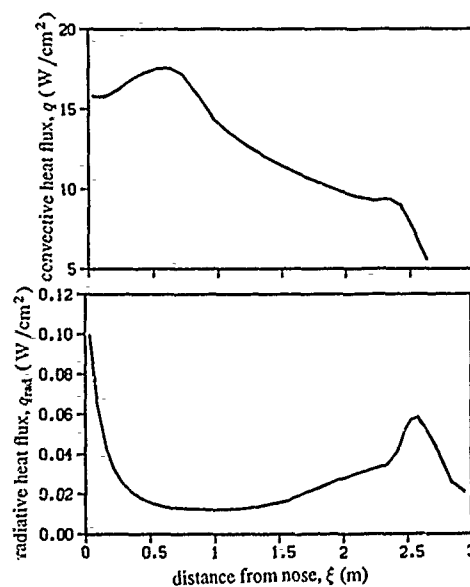
Fig. 17 Convective and radiative surface heat flux distributions for AOTV at 90km.
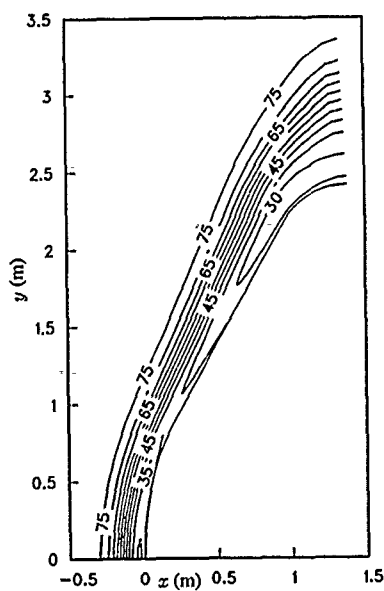
Fig. 18 Percent N_2 mass concentration contours for AOTV at 90km.
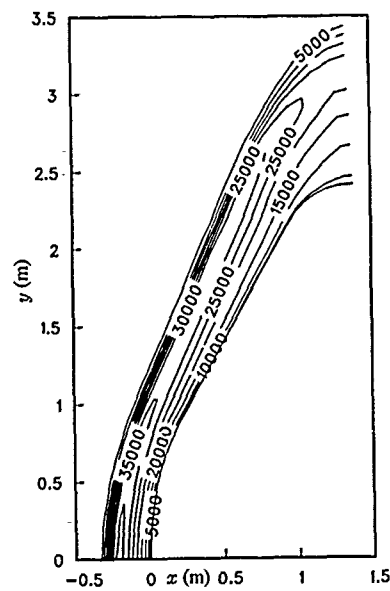
Fig. 19 Translational-rotational temperature contours for AOTV at 90km.
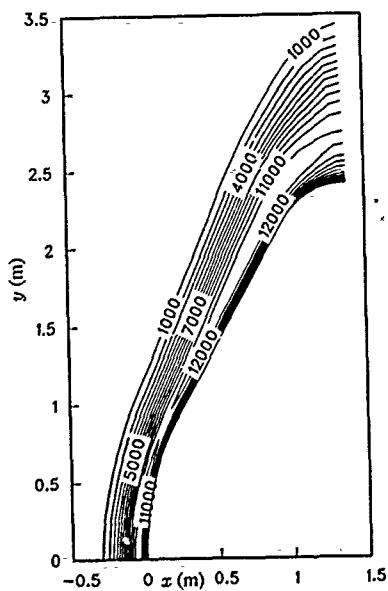
Fig. 20 N_2 vibrational temperature contours for AOTV at 90km.
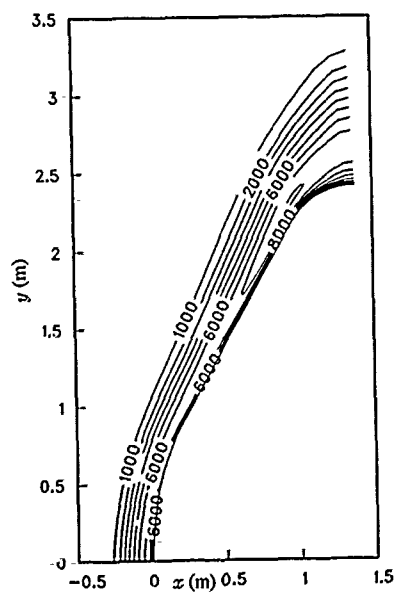
Fig. 21 Electron translational temperature contours for AOTV at 90km.
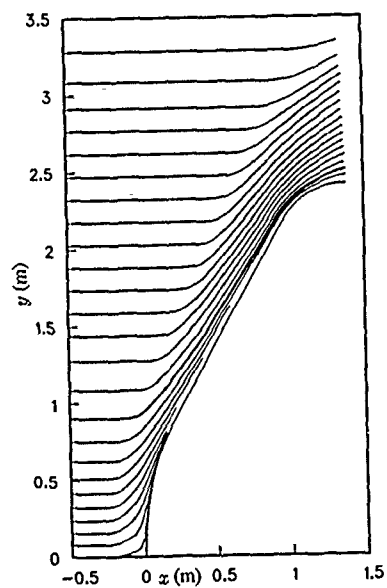
Fig. 22 Streamlines for AOTV at 90km..
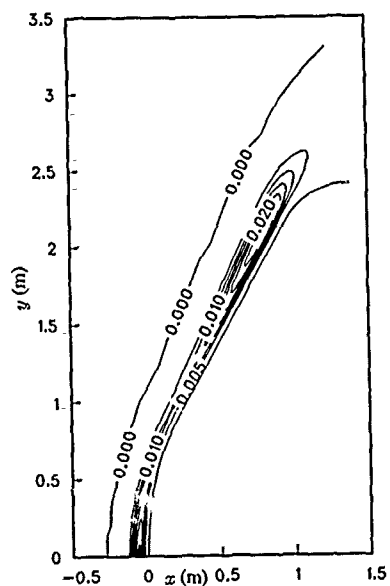
Fig. 23 Radiation intensity contours for AOTV at 78km.
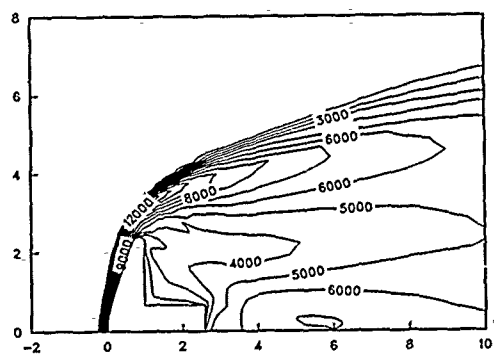
a) 78 km altitude, $M_\infty = 31.6$
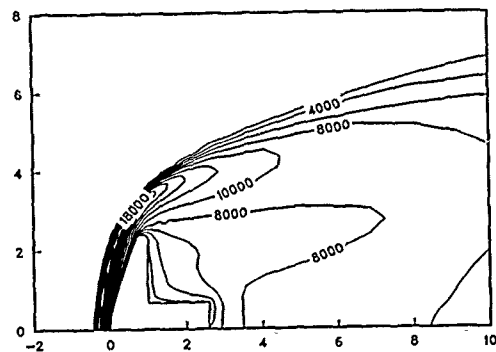
b) 90 km altitude, $M_\infty = 36.4$

Fig. 24 Computed translational temperature contours over AOTV
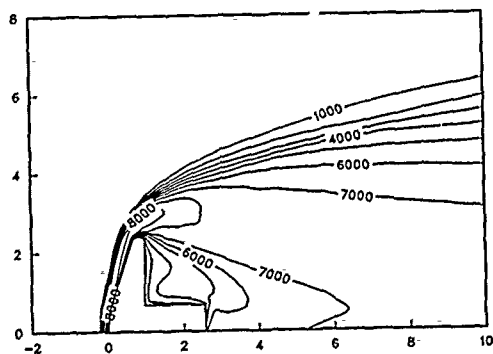
a) 78 km altitude, $M_\infty = 31.6$
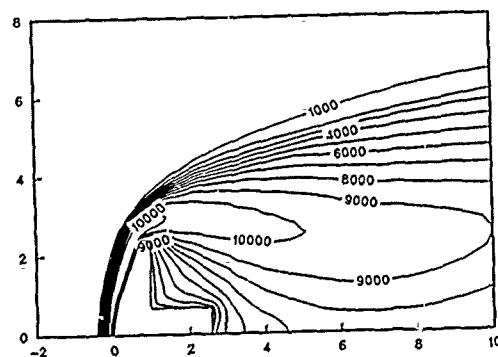
b) 90 km altitude, $M_\infty = 36.4$

Fig. 25 Computed nitrogen vibrational temperature contours over ATOV

a) 78 km altitude, $M_\infty = 31.6$

b) 90 km altitude, $M_\infty = 36.4$
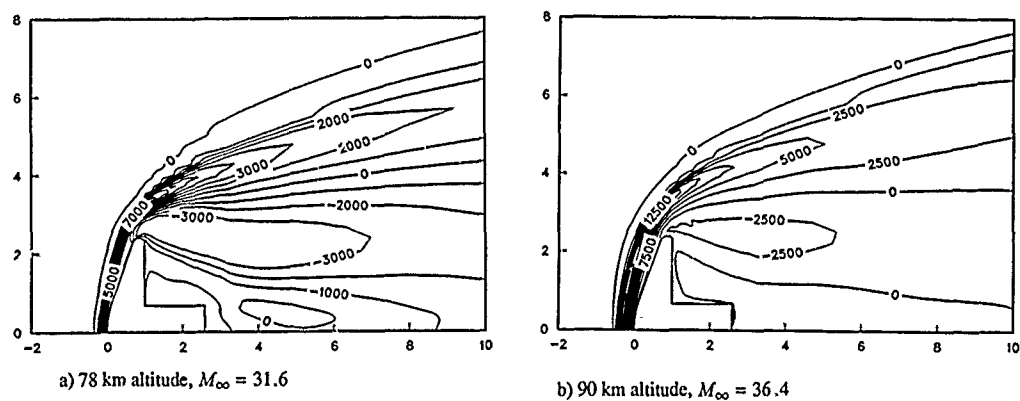
Fig. 26 Temperature difference contours $(T - T_{N_2,v})$ for AOTV

a) 78 km altitude, $M_\infty = 31.6$

b) 90 km altitude, $M_\infty = 36.4$
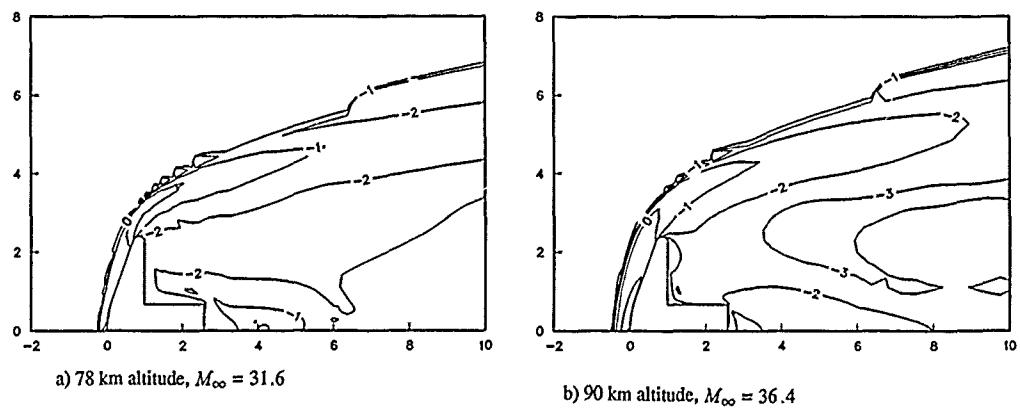
Fig. 27 Logarithm of Damkohler number for nitrogen vibrational relaxation.

a) 78 km altitude, $M_\infty = 31.6$

b) 90 km altitude, $M_\infty = 36.4$
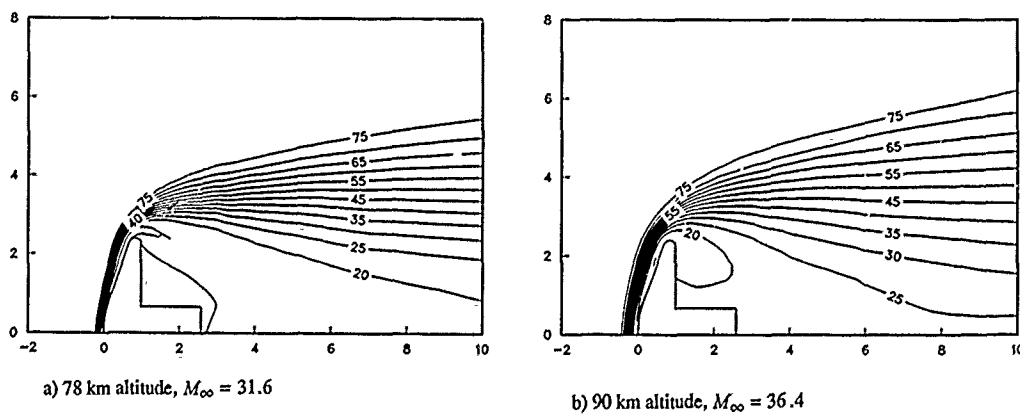
Fig. 28 Computed nitrogen (N_2) mass fraction contours for AOTV

a) 78 km altitude, $M_\infty \approx 31.6$

b) 90 km altitude, $M_\infty = 36.4$
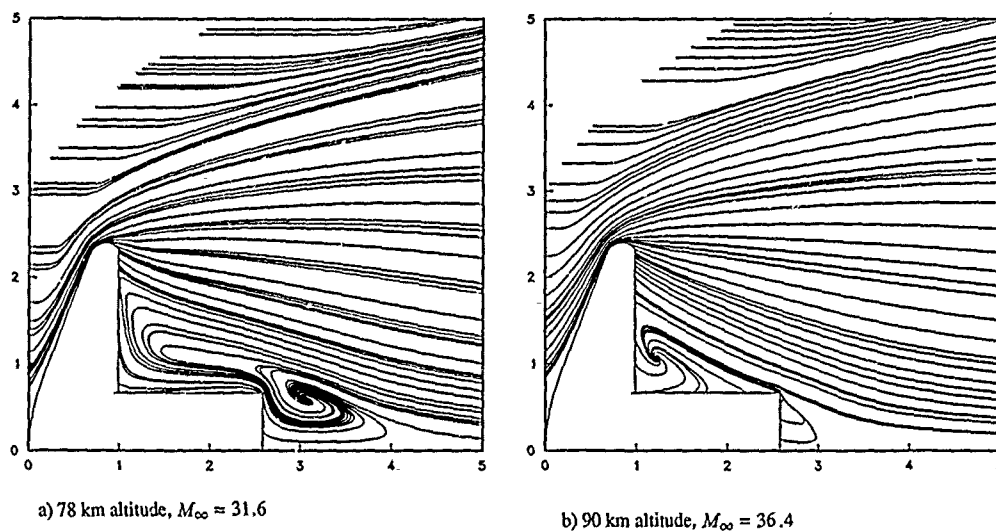
Fig. 29   Computed pathlines over AOTV

APPENDIX

CONSTANTS USED IN AIR MODEL

In this section the various constants that were introduced in the discussion of the physical model of air. The heats of formation of the seven chemical species used are listed below.

Table A.1 Heats of formation (J/kg).

Species	h_s°
N_2	0.0
O_2	0.0
NO	2.996123×10^6
NO^+	3.283480×10^7
N	3.362161×10^7
O	1.543119×10^7
e^-	0.0

The coefficients required for the viscosity model of Blottner[10] *et al.* are given in the following table.

Table A.2 Viscosity Coefficients for Blottner Model

Species	A_s	B_s	C_s
N_2	0.0268142	0.3177838	-11.3155513
O_2	0.0449290	-0.0826158	-9.2019475
NO	0.0436378	-0.0335511	-9.5767430
NO^+	0.3020141	-3.5039791	-3.7355157
N	0.0115572	0.6031679	-12.4327495
O	0.0203144	0.4294404	-11.6031403

The Arrhenius coefficients required for the calculation of the forward reaction rates for the six reactions and the possible collision partners are given in the following table. These were taken from Park[19] and Bussing and Eberhardt[20].

Table A.3 Arrhenius coefficients for forward reaction rates.

Reaction	Partner	C_m (m³/kg s)	η_m	θ_{dm} (K)
1	N₂	3.700×10^{18}	-1.600	113200
	O₂	3.700×10^{18}	-1.600	113200
	NO	3.700×10^{18}	-1.600	113200
	NO⁺	3.700×10^{18}	-1.600	113200
	N	1.110×10^{19}	-1.600	113200
	O	1.110×10^{19}	-1.600	113200
	e⁻	1.110×10^{21}	-1.600	113200
2	N₂	2.750×10^{16}	-1.000	59500
	O₂	2.750×10^{16}	-1.000	59500
	NO	2.750×10^{16}	-1.000	59500
	NO⁺	2.750×10^{16}	-1.000	59500
	N	8.250×10^{16}	-1.000	59500
	O	8.250×10^{16}	-1.000	59500
	e⁻	1.320×10^{19}	-1.000	59500
3	N₂	2.300×10^{14}	-0.500	75500
	O₂	2.300×10^{14}	-0.500	75500
	NO	2.300×10^{14}	-0.500	75500
	NO⁺	2.300×10^{14}	-0.500	75500
	N	4.600×10^{14}	-0.500	75500
	O	4.600×10^{14}	-0.500	75500
	e⁻	7.360×10^{16}	-0.500	75500
4	–	3.180×10^{10}	0.100	37700
5	–	2.160×10^{5}	1.290	19220
6	–	6.500×10^{8}	0.000	32000

The characteristic temperatures used in the harmonic oscillator model (equation (3.21)) and the diffusion model (equation (3.38)) are given in Table A.4. The table also includes the collision diameters for use in the vibration-vibration coupling model (equation (3.47)).

Table A.4 Molecular constants for use in the harmonic oscillator model for vibration, the diffusion model of vibrational excitation, and the vibration-vibration coupling model.

Species	θ_{vs} (K)	θ_s (K)	$d_s \times 10^{10}$ (m)
N₂	3395	5000	3.709
O₂	2239	3350	3.608
NO	2817	4040	3.534
NO⁺	2817	4040	3.534

The equilibrium constants for the chemical reactions are computed using the expression in Park[19], which is a curve fit to experimental data. This is done using

$$K_{eq\,m} = \exp\left(A_{1m} + A_{2m}Z + A_{3m}Z^2 + A_{4m}Z^3 + A_{5m}Z^4\right),\tag{A.1}$$

where $Z = 10,000/T$, (T in K) and the constants are given in Table A.5.

Table A.5 Constants for computing equilibrium reaction constants.

Reaction	A_{1m}	A_{2m}	A_{3m}	A_{4m}	A_{5m}
1	3.898	-12.611	0.683	-0.118	0.006
2	1.335	-4.127	-0.616	0.093	-0.005
3	1.549	-7.784	0.228	-0.043	0.002
4	2.349	-4.828	0.455	-0.075	0.004
5	0.215	-3.652	0.843	-0.136	0.007
6	-6.234	-5.536	0.494	-0.058	0.003

REPORT DOCUMENTATION PAGE

1. Recipient's Reference	2. Originator's Reference	3. Further Reference	4. Security Classification of Document
	AGARD-R-764	ISBN 92-835-0537-9	UNCLASSIFIED

5. Originator	Advisory Group for Aerospace Research and Development North Atlantic Treaty Organization 7 rue Ancelle, 92200 Neuilly sur Seine, France

6. Title	THREE-DIMENSIONAL SUPERSONIC/HYPERSONIC FLOWS INCLUDING SEPARATION

7. Presented at	the von Kármán Institute, Rhode-Saint-Genèse, Belgium, on 8—12 May 1989 and as a Short Course at NASA Ames Research Center, Moffett Field, USA, on 10—14 July 1989.

8. Author(s)/Editor(s)	9. Date
Various	January 1990

10. Author's/Editor's Address	11. Pages
Various	396

12. Distribution Statement	This document is distributed in accordance with AGARD policies and regulations, which are outlined on the Outside Back Covers of all AGARD publications.

13. Keywords/Descriptors

Supersonic flow
Hypersonic flow
Three-dimensional flow

Boundary layer separation
Computation
Turbulence

14. Abstract

The objective of this AGARD-FDP-VKI Special Course was to provide a status report on our understanding and ability to predict three-dimensional compressible flows including the complex effects of flow separation. Stimulation for this course arose from a variety of projects underway or receiving strong consideration in many countries: the next-generation supersonic transport, HERMES, the National Aerospace Plane, HOTOL, SANGER, the 'ORIENT EXPRESS' etc.

An overview presentation of the requirements for this technology — showing applications and problem areas — set the stage for the course. This was followed by two lectures which discussed topics that are basic to all that followed. First, the capabilities and limitations of computational fluid dynamics to describe these complex flows was addressed; and second a review of turbulence models appropriate to compressible flows was presented.

The next four lectures concentrated on a series of generic shock-shock boundary-layer interaction problems which may be viewed as either a means to understand flow physics or as building blocks for vehicle design. The course closed with a discussion on how the chemical reactions present in highly hypersonic flows will influence three-dimensional hypersonic flows fields.

The course and the material assembled in this book were prepared under the combined sponsorship of the Fluid Dynamics Panel, the von Kármán Institute, and the Consultant and Exchange Program of AGARD. Presentations were made at the von Kármán Institute, Rhode-Saint-Genèse, Belgium, on 8—12 May 1989 and at NASA's Ames Research Center, Moffett Field, California, USA, on 10—14 July 1989.

	AGARD-R-764
AGARD Report No.764 Advisory Group for Aerospace Research and Development, NATO THREE-DIMENSIONAL SUPERSONIC/HYPER- SONIC FLOWS INCLUDING SEPARATION Published January 1990 396 pages The objective of this AGARD-FDP-VKI Special Course was to provide a status report on our understanding and ability to predict three-dimensional compressible flows including the complex effects of flow separation. Stimulation for this course arose from a variety of projects underway or receiving strong consideration in many countries: the next-generation supersonic transport, HERMES, the National Aerospace Plane, HOTOL, SANGER, the "ORIENT EXPRESS" etc. P.T.O.	Supersonic flow Hypersonic flow Three-dimensional flow Boundary layer separation Computation Turbulence

	AGARD-R-764
AGARD Report No.764 Advisory Group for Aerospace Research and Development, NATO THREE-DIMENSIONAL SUPERSONIC/HYPER- SONIC FLOWS INCLUDING SEPARATION Published January 1990 396 pages The objective of this AGARD-FDP-VKI Special Course was to provide a status report on our understanding and ability to predict three-dimensional compressible flows including the complex effects of flow separation. Stimulation for this course arose from a variety of projects underway or receiving strong consideration in many countries: the next-generation supersonic transport, HERMES, the National Aerospace Plane, HOTOL, SANGER, the "ORIENT EXPRESS" etc. P.T.O.	Supersonic flow Hypersonic flow Three-dimensional flow Boundary layer separation Computation Turbulence

	AGARD-R-764
AGARD Report No.764 Advisory Group for Aerospace Research and Development, NATO THREE-DIMENSIONAL SUPERSONIC/HYPER- SONIC FLOWS INCLUDING SEPARATION Published January 1990 396 pages The objective of this AGARD-FDP-VKI Special Course was to provide a status report on our understanding and ability to predict three-dimensional compressible flows including the complex effects of flow separation. Stimulation for this course arose from a variety of projects underway or receiving strong consideration in many countries: the next-generation supersonic transport, HERMES, the National Aerospace Plane, HOTOL, SANGER, the "ORIENT EXPRESS" etc. P.T.O.	Supersonic flow Hypersonic flow Three-dimensional flow Boundary layer separation Computation Turbulence

	AGARD-R-764
AGARD Report No.764 Advisory Group for Aerospace Research and Development, NATO THREE-DIMENSIONAL SUPERSONIC/HYPER- SONIC FLOWS INCLUDING SEPARATION Published January 1990 396 pages The objective of this AGARD-FDP-VKI Special Course was to provide a status report on our understanding and ability to predict three-dimensional compressible flows including the complex effects of flow separation. Stimulation for this course arose from a variety of projects underway or receiving strong consideration in many countries: the next-generation supersonic transport, HERMES, the National Aerospace Plane, HOTOL, SANGER, the "ORIENT EXPRESS" etc. P.T.O.	Supersonic flow Hypersonic flow Three-dimensional flow Boundary layer separation Computation Turbulence

An overview presentation of the requirements for this technology — showing applications and problem areas — set the stage for the course. This was followed by two lectures which discussed topics that are basic to all that followed. First, the capabilities and limitations of computational fluid dynamics to describe these complex flows was addressed; and second a review of turbulence models appropriate to compressible flows was presented.

The next four lectures concentrated on a series of generic shock-shock boundary-layer interaction problems which may be viewed as either a means to understand flow physics or as building blocks for vehicle design. The course closed with a discussion on how the chemical reactions present in highly hypersonic flows will influence three-dimensional hypersonic flows fields.

The course and the material assembled in this book were prepared under the combined sponsorship of the Fluid Dynamics Panel, the von Kármán Institute, and the Consultant and Exchange Program of AGARD. Presentations were made at the von Kármán Institute, Rhode-Saint-Genèse, Belgium, on 8–12 May 1989 and at NASA's Ames Research Center, Moffett Field, California, USA, on 10–14 July 1989.